europhysics
conference
abstracts

16 th European Conference on

Controlled Fusion and Plasma Physics

Venice, March 13-17, 1989

Editors: S.Segre, H. Knoepfel, E. Sindoni

Contributed Papers
Part III

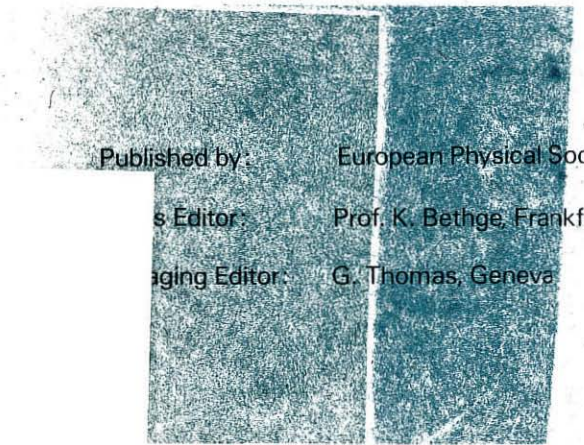

Published by: European Physical Society
s Editor: Prof. K. Bethge, Frankfurt/M.
aging Editor: G. Thomas, Geneva

VOLUME 13 B Part III

XVI FUSION VENEZIA 1989

S. Giorgio Maggiore Island

D
E
F1
F2
F3
F4
F5

16th European Conference on

Controlled Fusion and Plasma Physics

Venice, March 13-17, 1989

Editors: S. Segre, H. Knoepfel, E. Sindoni

Contributed Papers

Part III

EUROPHYSICS CONFERENCE ABSTRACTS is published by the
European Physical Society,

PREFACE

The 16th European Conference on Controlled Fusion and Plasma Physics was held in Venice, Italy, from 13th to 17th March 1989 by the Plasma Physics Division of the European Physical Society (EPS).

The Conference has been organized under the sponsorship of the Italian National Research Council (CNR), the Italian Commission for Nuclear and Alternative Energy Sources (ENEA) and the International School of Plasma Physics "Piero Caldirola" (ISPP).

The programme, format and schedule of the Conference were determined by the International Programme Committee which was appointed by the Plasma Physics Division of the EPS.

The programme included 17 invited lectures, 23 orally presented contributed papers and more than 450 contributed papers presented in poster sessions.

This 4-volume publication contains all accepted contributed papers received in due time by the Organizers. It is published in the Europhysics Conference Abstracts Series. The 4-page extended abstracts were reproduced photographically using the camera-ready manuscripts submitted by the authors. The invited papers will be published in a special issue of the journal "Plasma Physics and Controlled Fusion" and sent free of charge to each registered participant.

The organizers would like to acknowledge the skillful and dedicated support given by Maria Polidoro of the ENEA Fusion Department at Frascati to the editing of these four volumes.

The Editors

INTERNATIONAL PROGRAMME COMMITTEE

S. Segre (Chairman), University of Rome II, Rome, Italy
K. Appert, CRPP, Lausanne, Switzerland
H.A.B. Bodin, Culham Laboratory, Abingdon, United Kingdom
F. De Marco, ENEA, Frascati, Italy
E. Fabre, Ecole Polytechnique, Palaiseau Cedex, France
M. Fontanesi, CNR, Milan, Italy
V.E. Golant, Joffe Physics Institute, Leningrad, USSR
J. Jacquinot, JET, Abingdon, United Kingdom
G.M. Mc Cracken, JET, Abingdon, United Kingdom
J. Nührenberg, MPI, Garching, F.R.G.
J. Tachon, CEN, Cadarache, France
F. Wagner, MPI, Garching, F.R.G.
R.R. Weynants, ERM, Brussels, Belgium

ORGANIZING COMMITTEE

M. Fontanesi (Chairman), CNR, Milan
H. Knoepfel, Associazione Euratom-ENEA, Frascati
M. Lontano, CNR, Milan
G. Malesani, CNR, Padua
E. Sindoni, University of Milan, Milan
M. Polidoro, ENEA, Frascati

CONTENTS

PAPER IDENTIFICATION

Each paper is identified with a 6 character code. The code u v wx yz has the following structure:

u - type of contribution; u = O, P for oral and poster contributed paper

v - the day of event; v = 1,2,3, ...9 for Monday morning, Monday afternoon, Tuesday morning, ... to Friday morning

wx - the topic and subtopic of the contribution

yz - progressive number within session and topic

Example

P4 F6 11

P	4	F6	11
↓	↓	↓	↓
Paper type	Half-day number of event	Topic and Subtopic	Progressive number
↓	↓	↓	↓
Poster	Tuesday afternoon	Plasma heating and current drive Current drive and profile control	Poster number 11

TITLE LIST OF CONTRIBUTED PAPERS

A. TOKAMAKS

A1. Experiments

A3. Theory

B. STELLARATORS

C. ALTERNATIVE MAGNETIC CONFINEMENT SCHEMES

C1. Reverse field pinch

D. INERTIAL CONFINEMENT

F2. Electron cyclotron resonance heating (ECRH)

F3. Lower hybrid heating (LHH)

F4. Alfvén and other RF-methods

G. GENERAL PLASMA THEORY

H. DIAGNOSTICS

I. BASIC COLLISIONLESS PLASMA PHYSICS

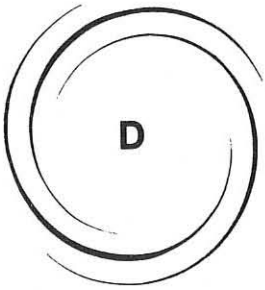

INERTIAL CONFINEMENT

EFFECT OF REDUCED COHERENCE ON THE INTERACTION OF A LASER BEAM WITH A LONG SCALELENGTH PRE-FORMED PLASMA

A. Giulietti
Istituto di Fisica Atomica e Molecolare, Pisa, Italy

T. Afshar-rad, S. Coe, O. Willi
Imperial College, London, U.K.

Z.Q. Lin, W.Yu
Institute of Optics and Fine Mechanics, Shanghai, China

Instabilities occurring in the interaction of an intense laser beam with a plasma can be detrimental for the laser plasma coupling and for the optimization of laser driven compression of fusion targets. In particular self-focusing and filamentation of the laser beam are the most serious of these instabilities because of their low irradiance threshold. As a consequence the laser irradiance is increased locally thus inducing several other instabilities. It has been suggested that these processes can be suppressed by the reduction of the degree of coherence of the laser beam [1]. Some experimental results are already available [2]. Because large millimeter sized plasmas are expected from reactor targets, we designed an experiment in which a laser beam interacts with a pre-formed plasma axially along a millimeter path, to study the effect of different degrees of coherence on filamentation, stimulated Brillouin and stimulated Raman scattering (SBS and SRS).

The experiment was performed at the Central Laser Facility of the Rutherford Appleton Laboratory (UK) using the Nd laser system "Vulcan" operating in second harmonic (λ= 527 nm). A cylindrical homogeneous plasma 1 mm in length and several hundred μm in diameter was produced by a line focus arrangement. Two pairs of two opposite laser beams (heating beams) were focused onto a thin foil target by the off-axis lens mirror configuration [3]. The size of the line focus was 1 mm by 0.2 mm. All four laser beam were superimposed to give an irradiance of 10^{14} W/cm^2 in a 800 ps pulse. The target consisted of a metal stripe .

A fifth laser beam (interaction beam) was focused axially into the pre-formed plasma. The density and temperature of the pre-formed plasma where changed by varying the delay of the interaction pulse with respect to the heating pulse.In a series of shots a Random Phase Plate (RPP) was inserted in front of the focusing optics.In another series we used an Induced Spatial Incoherence system (ISI)[4].In this case the bandwidth of the laser was increased from 0.5 to 15 A. The target position in respect to the best focus of the interaction beam was carefully adjusted in order to have the same irradiance at different degrees of coherence.The main diagnostics of this experiment were: multiframe equivalent plane imaging, in order to have time integrated, spatially resolved images of the focal spot; time -resolved imaging of the exit surface of the plasma using both a gated image intensifier (100 ps) and an optical streak-camera; SBS and SRS backscattered energy measurements and time-resolved SBS and SRS spectroscopy.

Self- focusing and filamentation

From the time-resolved images of the exit surface with ordinary coherent interaction beam, clear evidence of the evolution of whole beam self- focusing (WBSF) of the laser beam during the interaction with the preformed plasma is observed (see Fig.1 right side). The growth of the initial inhomogeneities (Fig.1 left side) into filaments was observed as well as the subsequent cahotic clustering of these filaments. This was not observed in the beam when no preformed plasma was present.The final cross section of the beam and the growth time of WBSF both drastically decreased with increasing Z (from Al to Bi) due to improved thermal self focusing. On the other hand the random phased beam splits in a number of beamlets because of the interference between the waves diffracted from each element of the phase plate [2]. Its pattern is shown in Fig.2 left side. What is very important, is that these beamlets do not change their position in time and do not cluster (see Fig.2 right side). No evidence of whole beam self-focusing was observed with the random phased beam.

Stimulated Brillouin scattering

The backscattered SBS energy was found to be reduced with the random phased beam for interaction intensities from 10^{14} to 10^{15} W/cm^2. Spectral features were different with and without the RPP. With the ordinary beam the spectrum was multi-component, with some late time components showing very high temperature regions in the plasma that can only be explained by filamentation [5].With the random phased beam, SBS spectra were found generally single-component, with reduced red shift [6] indicating a lower temperature.

Also the SRS energy scattered backwards was reduced with the random phased beam. The spectral features were completely different at different degrees of coherence of the beam. With the ordinary beam the SRS spectra were broadband, with distinct structures moving quckly in the time-wavelength domain; with the random phased beam the SRS spectra were found to be very faint, not structured, narrower in the spectral band and shorter in time [6].

In conclusion the use of a Random Phase Plate makes it possible to control filamentation of a laser beam into a long scalelength plasma and to suppress whole beam self- focusing. Also other important instabilities, such as stimulation of ion-acoustic and electrostatic waves are depressed with the random phased beam. Similar results have been obtained with an Induced Spatial Incoherence system but a detailed analysis of ISI data is still in progress. These results are encouraging for laser fusion since they clearly indicate inhibition of non-linear instabilities in a long scalelength plasma when the coherence of the laser beam is reduced.

The authors are grateful to L. Gizzi for his help in the paper edition.

References

[1] D. Bassett, N. Islava, O. Willi, A. Giulietti, RAL Annual Report, pp. 53-56 (1987)

[2] Y. Kato, K. Mima, N. Miyanaga, S. Arinaga, Y. Kitagawa, M. Nakatsuka and C. Yamanaka, Phys. Rev. Lett. **53**, 1057 (1984)

[3] I.N. Ross, E.M. Hodgson, J. Phys.E: Sci Instr., **18**, 169 (1985)

[4] R.H. Lehmberg, A.J. Schmitt end S.E. Bodner, J. Appl. Phys., **62**, 2680 (1987)

[5] O. Willi, D. Bassett, A. Giulietti and S.J. Karttunen, submitted to Optics Comm. (1988)

[6] A. Giulietti, T. Afshar-Rad, S.Coe, O. Willi, Z. Q. Lin, W.Yu Proc. of 19th ECLIM - Madrid 1988

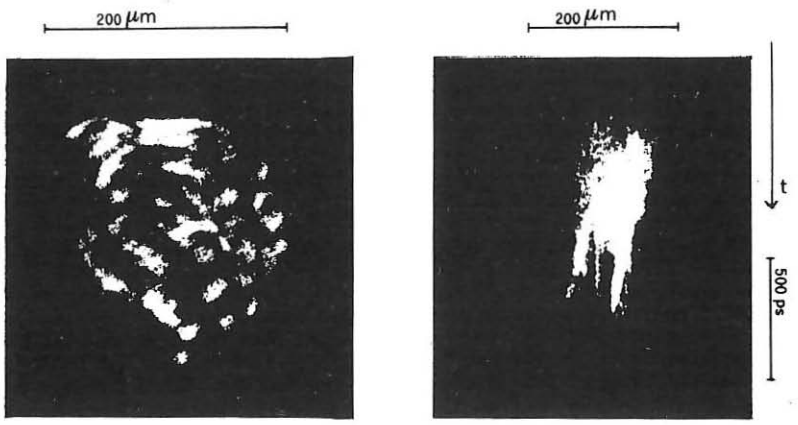

Fig.1. Pattern and evolution of the ordinary beam. Left:image of the beam pattern without target, obtained with a gated (100ps) intensifier.Irradiance 5.0 10^{14} W/cm^2. Right: beam evolution during the interaction with a pre-formed plasma from 700nm Al target. Shot# 172888.Heating-interaction delay 1.7 ns. Irrad. 7.7 10^{14} W/cm^2.

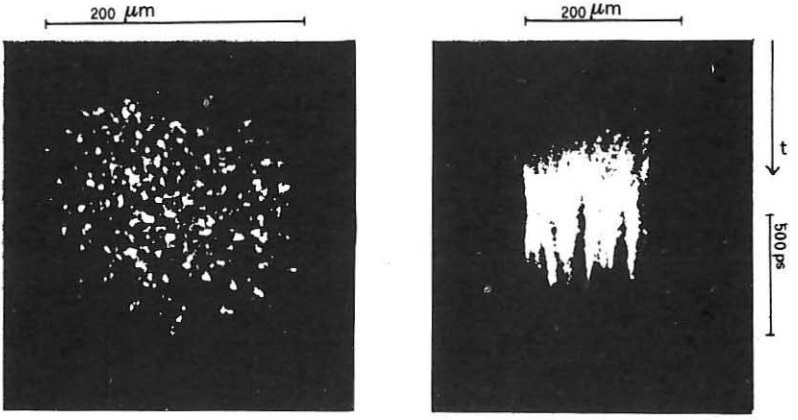

Fig. 2. Pattern and evolution of the random phased beam. Left:image from gated (100ps) intensifier. Irrad. 9.7 10^{14} W/cm^2. Right:evolution during interaction with 700nm Al target. Shot# 328788. Heating-interaction delay 1.7 ns. Irrad. 7.2 10^{14} W/cm^2.

2ω AND 3/2ω GENERATION IN LASER PRODUCED PLASMAS FROM VERY THIN PLASTIC FILMS

D. Batani, I. Deha, A. Giulietti, D. Giulietti,
L. Gizzi, L. Nocera, E. Schifano.

Istituto di Fisica Atomica e Molecolare - CNR
Via del Giardino 7, I-56100 Pisa

The irradiation of very thin films is useful to study the laser-plasma interaction in a variety of conditions of interest for the inertial confinement fusion; these conditions can be controlled essentially through laser intensity and pulse duration, film thickness and material. In this paper we report on data from an experiment of irradiation of plastic (formvar) films 0.3 to 1.9 μm in thickness at 1.064 μm laser wavelength and 3ns FWHM pulse duration. The intensity on the target was up to 5 10^{13} W/cm^2 in a spot of 60μm in diameter. The film thickness was chosen in order to allow the plasma to become underdense during the laser pulse. In this way during the pulse, the interaction volume was extended to the whole plasma depth and several instabilities could be stimulated and studied. Of course the interaction conditions evolve in time because of the expansion of the plasma and the time-profile of the laser pulse. A first extimation of the evolution of the plasma parameters (electron temperature, density and scalelength: T, n, L) has been done using a self-similar model [1] which is in good agreement with numerical simulations.

A critical aspect of this kind of experiment is the level of pre-lasing (level of laser power before the main pulse). We have been able to achieve a pre-lasing less than 10^{-4} timesthe peak power, and the lack of any plasma formation before the main pulse have been verified shot by shot. However some shots were affected by higher pre-lasing : in these cases we found completely different behaviour. In what concerns 2ω and (3/2)ω generation, it was completely missing in case of pre-lasing because the main pulse interacted weakly with a plasma already underdense. Finally we must stress that the laser power was affected by modulations due to mode beating in the laser cavity. These modulations allowed to reach higher intesity for few tens of picoseconds, several times during the pulse.

Data on the three-halves and second harmonic emissions have been obtained at 90° to the laser beam. Both time-resolved imaging and time-resolved spectroscopy have been performed.

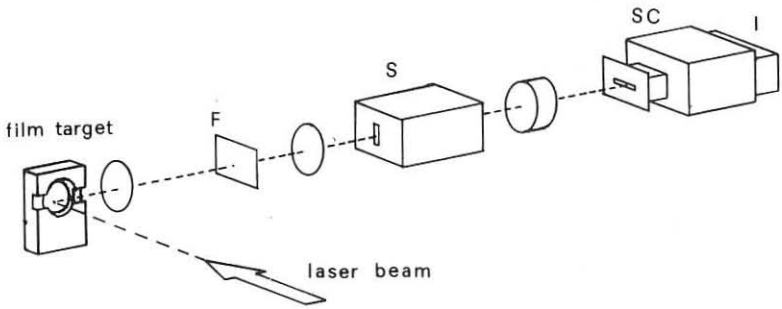

Fig. 1 Set-up for time-resolved spectroscopy at 90°.
F: filter rejecting 1.06 μm radiation; S: spectrometer; SC: streak camera; I: intensifier.

In Fig. 1 the set-up for the time-resolved spectroscopy is shown. The interaction region was imaged on the entrace slit of a spectrometer with a dispersion of 60 Å/mm. The exit plane of the spectrometer was demagnified to have both $(3/2)\omega$ and 2ω (λ=0.709 and 0.530 μm respectively) into the same streak-image. To obtain time resolved images we directely imaged the interaction region on the streak-camera slit with a magnification 10:1. A typical time-resolved spectrum is shown in Fig. 2.

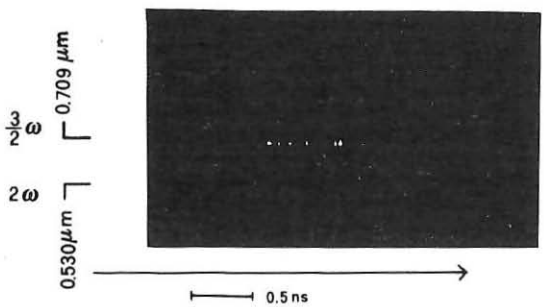

Fig. 2 Time-resolved spectrum showing both $(3/2)\omega$ and 2ω emission. Shot 061209-Laser intensity: 1.28 10^{13} W/cm^2; Formvar film thickness: 1.34 μm.

The $(3/2)\omega$ and 2ω lines are present for a time shorter than the pulse duration, and the emission shows very sharp peaks in time, following the power maxima due to the laser modulation. The $(3/2)\omega$ line originates from two-plasmon-decay instability (TPDI) in the plasma region where $n \simeq n_c/4$ [2]. The intensity threshold for TPDI, in precence of a density gradient of scalelength L at $n_c/4$, is [3] :

$$I \simeq \frac{4\ 10^{15}\ T}{\lambda_o\ L}\ (W/cm^2) \qquad (1)$$

where T is measured in KeV, λ_o and L in μm. The threshold is exceeded for the first time when intensity and scalelength both fullfil the condition (1). If the film is thick enough, the plasma will keep a $n_c/4$ layer during the whole pulse, and $(3/2)\omega$ emission will stop when the laser intensity will drop under threshold. With thinner films, the $(3/2)\omega$ will vanish because of the plasma rarefaction below $n_c/4$. In fact we observed that the duration of the $(3/2)\omega$ emission decreased with the film thickness below 0.8 μm and no $(3/2)\omega$ emission was found with films thinner than 0.6 μm. Putting the plasma parameters given by the model in expression (1) a threshold for TPDI of the order of 10^{13} W/cm^2 is found. From this value we could expect a continuous $(3/2)\omega$ emission with targets thicker than 1 μm. On the contrary, Fig. 2 clearly shows that the threshold is exceeded only a few times for very short (tens of picoseconds) peaks. This point has to be clarified with a careful experimental study of the intensity evolution in the plasma.

Let's now consider the 2ω component of the spectrum. At early times the 2ω emission can in principle be ascribed to resonance absorption near the critical density (but 90° emission is difficult to explain). If we consider a 2ω time-resolved image, as Fig. 3, the early stage corresponds toa well localised emission close to the film position. Notice that it originates from both front and rear side, probably due to filament driven fast burn-through of the film. At later times there will be no critical layer in the plasma, and 2ω emission must be attributed to a different process. The extension of the 2ω sources in a region of the order 1 mm perpendiculary to the film (see Fig. 3) confirms that 2ω originates from a plasma definitely underdense. A possible mechanism for 2ω generation is the sum of frequency between the laser light and the light backscattered by the plasma (stimulated Brillouin scattering) [4]. This process allows 2ω radiation at 90° due to the current

$$\underline{j}_{2\omega} = (e^3/2im^2\omega^3)\ [\ \underline{E}\ \underline{E}^b + \underline{E}^b\underline{E}\ ]\cdot \underline{\nabla} n$$

where $\underline{E}^b$ is the field of the backscattered wave. In a previous experiment [5] in gas we observed 2ω emission forward but we

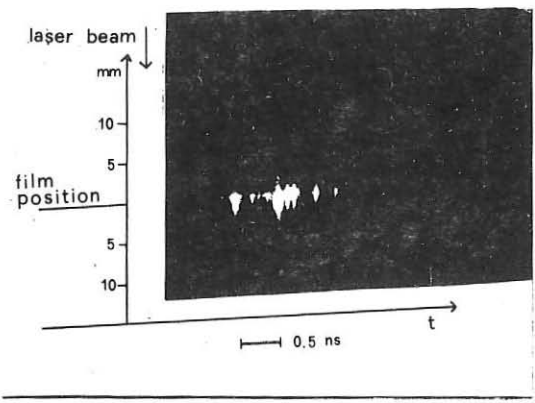

Fig. 3 Time -resolved image in 2ω light. Shot 141109- Laser intensity: 2 10^{13} W/cm^2; Formvar film thicknesss: 1.25 μm.

failed to observe 2ω at 90°.Emission was shown to mix to zero (due to destructive interference) as the detector elongated from the beam axis. The mixing effect disappears if a backscattered or reflected radiation contributes to the 2ω emission [4], this being a clear difference between experiments in gases and on solid targets. However, the formation of density gradients orthogonal to the beam axis remains a necessary requirement for 90° 2ω emission. According to [4] we can ascribe this to self-focusing which therefore remains a typical hallmark for 2ω emission.

Time-resolved spectroscopy of the two lines with higher resolution is in progress. It can give information on plasma temperature and its evolution as well as on some hydrodynamic parameters. The role played by filamentation in the interaction process havé also to be clarified.

The authors are very grateful to S. Bartalini for his creative technical support. Contribution to the self-similar model handling is due to F. Bianconi. This work was supported by Consiglio Nazionale delle Ricerche.

References

[1] R.A. London and M.D. Rosen, Phys. Fluids, 29, 3813 (1986)
[2] S.J. Karttunen, Las. Part. Beams, 3, 157 (1985)
[3] W.L. Kruer in "Laser-Plasma Interaction" vol. 3 Ed. by M.B. Hooper (SUSSP Publications, Edimburg) pag 79 (1986)
[4] J.A. stamper, R.H. Lehmberg, A. Schmitt, M.J. Young, J.H. Gardner and S.P. Obenschain, Phys. Fluids, 28, 2563 (1985)
[5] D.Giulietti, G.P.Banfi, I.Deha, A.Giulietti, M.Lucchesi, L.Nocera,Z.Z.Chen, Las. Part. Beams, 6, 141 (1988)

CORE-CORONA COUPLING IN A LASER-IRRADIATED SPHERICAL Z LAYERED PLASMA TARGET

V.Palleschi, D.P.Singh and M.Vaselli

Istituto di Fisica Atomica e Molecolare del C.N.R.
Via del Giardino, 7 - 56127 Pisa, Italy

ABSTRACT

In many experimental situations of laser-fusion interest, the superthermal electrons are produced at the plasma resonance surface. The electrons make tangential orbits around the dense plasma core creating a 'hot cloud' and heat the plasma core up to the depth of their mean free path. The equipartition of energy exists between the cold electrons of the plasma pellet core and the hot electrons in the overlapping region. The efficiency of heat transfer from the hot corona to the cold core depends on the laser wavelength and the mean temperature of the overlapping region. Earlier studies on core-coronal heating were limited up to the simple spherical pellet geometry in the absence of any Z layer. The presence of Z layer is likely to reduce the mean free path of the hot electrons thereby reducing the width of the overlapping region. The aim of the present paper is to study the laser wavelength scaling of the core-coronal heating in Z layered spherical plasma pellet. The effect of the width of the Z layer on core-corona coupling would also be investigated in some detail.

1. INTRODUCTION

When an intense laser beam impinges on the surface of a solid DT pellet, the superthermal electrons are likely to be produced at the plasma resonance surface where the electron-plasma frequency equals to the laser frequency. This nonthermal heat flux component with large mean free path has been predicted in computer simulation (Friedberg et al. 1972) and has also been observed in laser-plasma interaction experiments (Kephart et al. 1974; Kolodner et al. 1976). In the case of symmetric multibeam laser pellet implosion, the plasma pellet is surrounded by a hot electron 'halo'. The formation of hot electron cloud may result from the deflection of hot electrons from inward radial direction either due to some local plasma inhomogeneity or due to the self-generated magnetic field in the corona itself. The width of the hot electron cloud might be of the order of mean free path of the hot electrons and consequently the self-regulation model for the core-corona coupling may be applied. Earlier studies (Kidder & Zink 1972; Singh et al. 1988) on core-coronal coupling were limited up to the simple case of spherical unlayered pellet.

The aim of the present paper is to study the core-corona coupling in a spherical Z layered DT pellet. The presence of Z layer would reduce the electron mean free path and subsequently would affect the core heating by the surrounding corona.

2. ANALYSIS OF CORE-CORONA COUPLING

It is assumed that the hot electrons generated at the plasma critical surface have a uniform temperature (T_h) and density (n_c) in the whole plasma ablation region equal to that at the critical layer. The core-corona coupling essentially depends on two competing processes simultaneously occurring in the plasma ablation zone, namely, the rate of laser energy transfer to the hot electrons and the cooling rate of the hot corona by the cold dense core. The hot electrons are heated by the incident laser beam almost instantaneously while the heating of the dense plasma core depends on the energy-equipartition time of the electrons present in the overlapping region between the core and the corona. The rate at which the hot corona is cooled may be given as

$$S = \frac{3}{2} k_B \frac{(T_h - T_d)}{\tau_{eq}} \int_{r_c}^{r_e} n\, r^2\, dr \quad , \tag{1}$$

where r, n, k_B, T_c and τ_{eq} are the radial coordinate, electron density in the overlapping region, Boltzmann constant, core electron temperature and the energy equipartition time between the core and coronal electrons in the overlapping region respectively. r_e and r_c are the plasma ablation radius and critical radius.

The energy equipartition time may be written as

$$\tau_{eq} = \frac{3}{4} \sqrt{\frac{m}{\pi}} \frac{(k_B T)^{3/2}}{e^4 n_c \ln \Lambda} \quad , \tag{2}$$

where e, m, $\ln \Lambda$ and T (= $(T_h + T_c)/2$) are the electronic charge, electronic mass, Coulomb logarithm and the mean electron temperature in the overlapping region respectively. The expression (2) is derived on the assumption that the equipartition of energy is established between the superthermal and thermal electrons having Maxwellian velocity distributions with kinetic temperature T_h and T_c respectively. It may be further mentioned from the energy exchange interaction in the overlapping region that the electron temperature from the equipartition state decreases exponentially with characteristic time τ_{eq} if the mean electron temperature does not change appreciably. The radial variation of core electron temperature being small is neglected. As the computer simulation calculation indicate, the plasma density in the expanding region decreases as $1/r^3$ i.e.

$$n\, r^3 = n_c\, r_c^3 \quad , \tag{3}$$

Substituting the expression for the electron density (n) from eq.(3) into eq.(1) and applying the self-regulation condition, we obtain,

$$S = \frac{3}{4} n_c r_c^3 k_B \frac{(T_h - T_d)}{\tau_{eq}} \ln\left(1 + 2\frac{\lambda_e}{r_c}\right) \quad , \tag{4}$$

where λ_e (=$(k_B T)^2 / (\pi e^4 (Z+1) n_c r_c \ln \Lambda)$) is the electron mean free path.

The total mass of the pellet core may also be written as

$$M = \frac{m_i n_c r_c^3}{3} \left[\left(1 - \frac{D}{r_e}\right)^3 + \frac{A}{Z} \frac{n_z}{n_c} \frac{n_c}{n_o} \left\{ 1 - \left(1 - \frac{D}{r_e}\right)^3 \right\} + \frac{A}{Z} \ln \frac{n_o}{n_c} \right] \quad , \tag{5}$$

where m_i, D, r_e and n_z are the ion mass, width of the Z layer, pellet core radius and electron density in Z layer respectively. In deriving eq.(5), we have assumed that the plasma density is constant (n_o) up to the core radius r_e and the Z layer has constant electronic density (n_z), beyond that the density varies as ($1/r^3$) in the coronal region.

Considering the energy balance between the core and the surrounding corona, the expression for core-corona coupling (τ_c^{-1}) may be obtained as

$$\tau_c^{-1} = \frac{3}{2}\tau_{eq}^{-1} \frac{\ln\left(1 + 2\frac{\lambda_e}{r_c}\right)}{\left[\left(1 - \frac{D}{r_e}\right)^3 + \frac{n_z}{n_c}\frac{n_c}{n_o}\left\{1 - \left(1 - \frac{D}{r_e}\right)^3\right\} + \ln\frac{n_o}{n_c}\right]}, \qquad (6)$$

Eq.(6) along with eq.(2) describes the analytic expressions for core-corona coupling. The maximum value of core corona-coupling can be obtained by differentiating expression (6) with respect to mean electron temperature. The relevant numerical results are plotted in the figures.

3. DISCUSSION

The core-corona coupling, in general, depends on the laser wavelength, the width of the Z layer and the mean temperature of the electrons in the overlapping region between the cold core and the hot corona.

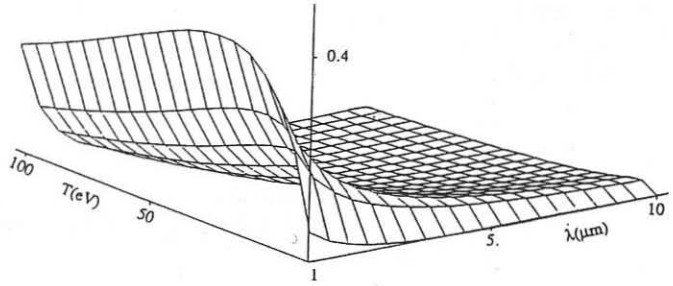

Fig. 1- Dependence of core-corona coupling on laser wavelength and mean electron temperature for aluminium layered target $4\pi M = 2000\ \mu g$, $r_e/D=100$, $n_o/n_c=10^4$.

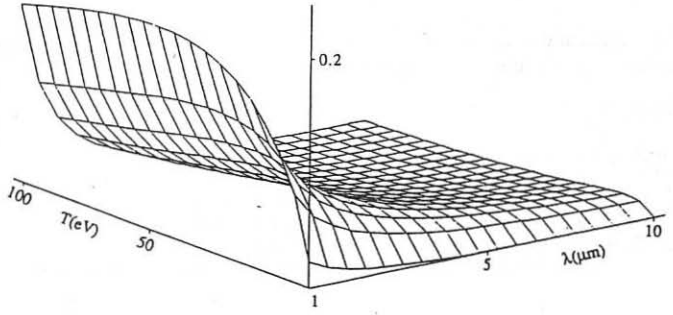

Fig. 2- Dependence of core-corona coupling on laser wavelength and mean electron temperature for molybdenum layered target $4\pi M = 2000\ \mu g$, $r_e/D=100$, $n_o/n_c=10^4$.

Figs.(1) and (2) show the dependence of core-corona coupling on laser wavelength and the mean electron temperature in the ablation region for aluminium and molybdenum layered spherical targets respectively. It is obvious that there exists an optimum temperature at which the coupling is maximum leading to the conclusion that the increase of hot electron temperature enhances the heating rate of the core up to a certain extent and beyond that further laser flux transfer to the hot corona makes the corona more tenuous only and decoupling of the core from the surrounding corona occurs. It is also seen that the heat transfer from the hot corona to the core is favoured for short laser wavelengths which is due to the fact that the short wavelength lasers are able to penetrate deeper into the interior of the plasma pellet. Fig.(3) exhibits the variation of maximum core-corona coupling ($\tau_c^{-1}{}_{min}$) with aspect ratio (r_e/D) for aluminium target.

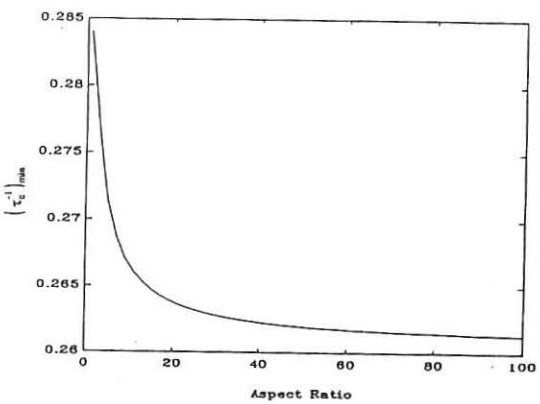

Fig. 3- Variation of maximum core-corona coupling with the aspect ratio (r_e/D) for aluminium layered target $4\pi M = 2000$ μg, λ=1.06 μm, $n_o/n_c = 10^4$.

It can be concluded that $\tau_c^{-1}{}_{min}$ decreases marginally for high aspect ratio plasma targets for the parameters mentioned in figure captions.

REFERENCES

FRIEDBERG, J.P. et al. 1972 *Phys.Rev.Lett.* 28, 795.
KEPHART,J.F. et al. 1974 *Appl.Phys.Lett.* 25,108.
KIDDER,R.E. & ZINK,J.W. 1972 *Nuclear Fusion* 12, 325.
KOLODNER,P. & YABLONVITCH,E. 1976 *Phys.Rev.Lett.* 37, 1754.
SINGH,D.P. et al. 1988 *Laser & Particle Beams* (in press).
SPITZER,L.Jr. 1962 *"Physics of Fully Ionized Gases"* 2nd Eds. Interscience, New York.

EFFECT OF RANDOM PHASE PLATE IRRADIATION ON BACK SCATTERING

Isao MATSUSHIMA, Toshihisa TOMIE, Kazuyoshi KOYAMA, and Masaaki YANO

Electrotechnical Laboratory, 1-1-4, Umezono, Tsukuba, 305, Japan

ABSTRACT

Back scattering from a high density plasma under the irradiation with a randomly distributed phase plate is studied using the second harmonic of a glass laser. Brillouin scattering is observed to be suppressed compared to the case of the irradiation without the phase plate. For the emission at three halves laser frequency, any effect of the random phase plate irradiation is not observed.

INTRODUCTION

One of the most important issues in laser-fusion is the uniform compression. Among some ideas for improving the uniformity, the irradiation scheme using a randomly distributed phase plate (RDPP) is technically the simplest.[1] In the RDPP irradiation, however, there are many spikes in the focused pattern, although large scale uniformity is significantly improved. These spikes may have some bad effects on the compression. One of them is the possibility of the enhancement of back scattering.

We studied back scatterings at laser frequency and three halves frequency. In this paper, the experimental results about those back scatterings are reported and the effect of RDPP irradiation is discussed.

EXPERIMENT

The experiment was performed by irradiating the second harmonic of a glass laser onto solid polyethylene (CH_2) target at oblique incidence angle (40°). The laser energy was 10J at λ_L = 532nm, and the pulse duration was t_L = 0.5ns (FWHM). The laser beam of D=75mm diameter was focused by a lens of focal length f=500mm. A RDPP with the pixel size d=2mm was inserted in front of the lens. The focal spot size was 270 μm which is given by $2\lambda_L$ f/d. Experiment was also performed without using the RDPP. In this case, the focal spot size was varied from 80 μm to 300 μm. The scattered light back through the focusing lens was observed by a spectrometer equipped with an optical multichannel analyzer.

Figure 1 shows a typical spectrum observed around the laser frequency (ω_0) in the irradiation without RDPP. The left side peak has exactly the same wavelength with that of the incident laser. The right side signal is generated through Brillouin scattering (BS) and the peak was red-shifted by 2~3 Å from the laser wavelength. The intensities of two peaks normalized to the input laser energy are plotted on Fig. 2 as a function of the laser power density for various irradiation conditions. The red-shift component was observed only for the irradiation without RDPP.

The threshold of BS was $I = 5 \times 10^{12}$ W/cm^2 . The reflectivity R

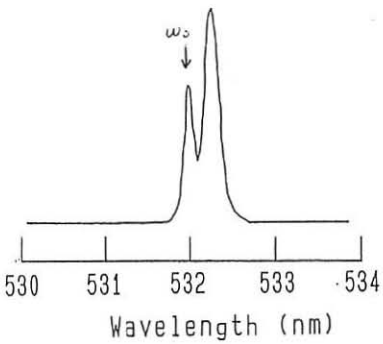

Fig. 1 A typical observed spectrum around ω_0 without RDPP. Two peaks are observed. One is a scattered laser light with the same wavelength of the laser. The other is a red-shifted peak suggesting Brillouin scattering.

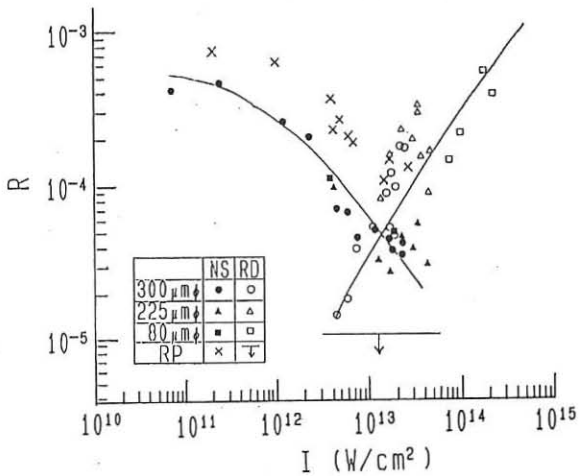

Fig. 2 Intensities of red-shifted peaks (RD) and non-shifted peaks (NS) observed around ω_0 for ordinary irradiations with indicated focused spot diameters and for RDPP irradiations (RP). The values are normalized as the reflectivity R to the input laser energy. For the cases without RDPP, the red-shifted peak has a threshold at $I = 5 \times 10^{12}$ W/cm², and the reflectivity R increased with the laser power density, I, as $R \propto I^{1.4}$. As red-shifted components were not found in the RDPP irradiation, the noise level at the wavelength corresponding to the red-shifted peaks in the ordinary irradiation is indicated as a horizontal line and an arrow. Non-shifted scattering component decreases with the laser power and scattering efficiency was higher for the RDPP irradiation.

increased with the laser power density, I, as $R \propto I^{1.4}$. When the RDPP was placed, no red-shift component was observed within the detection level up to $I=3\times 10^{13}$ W/cm^2 . Non-shifted scattering component decreases with the laser power and scattering efficiency was higher for the RDPP irradiation.

The emission spectrum at around $3\omega_0/2$ is shown in Fig. 3. The band width was about 30Å and the peak was red-shifted by 20 Å . The band width and the amount of the red-shift had power density dependence. Figure 4 shows the peak intensities as a function of the laser power density for various irradiation conditions. The efficiency G of the $3\omega_0/2$ emission increased as $G \propto I^{2.5}$. The threshold was higher for the smaller focused spot diameter. The threshold in the RDPP irradiation was nearly the same with that for the irradiation of 300μm spot diameter without RDPP.

DISCUSSION

In RDPP irradiation, the focused laser pattern consists of many small spikes. The size of the spikes is given by $2\lambda_L$ f/D and it was 7μm in our case. The peak intensity of the spikes exceeded ten times average intensity. Therefore, we could expect the enhancement of non-linear phenomena. On the other hand, the small spikes modulate the plasma and the scale length will be reduced. The growth rate of parametric instabilities in an inhomogeneous plasma is proportional to the scale length of the phase-mismatch, L_{ph}. Therefore, the existence of the small spikes in the focused pattern may be suppress parametric instabilities.

As shown in Fig. 2, the threshold of BS was higher for RDPP irradiation. The result can be understood if BS occurred near the critical surface where the small spikes would produce temperature and density modulations. The modulation will reduce the scale length and elevate the threshold. Near the critical surface the scale length will be independent on focal spot size. Therefore, BS near the critical surface is one explanation of the observed independence of BS on focal spot size. The assumption that BS occurred near the critical surface is consistent with the observed red-shift of 2~3 Å . If the Doppler shift can be neglected, which will be a good assumption at low power density of 10^{13}W/cm^2 , BS is estimated to have occurred at the electron density, $n_e=(1/2\sim 3/4)\, n_c$. Non-shifted component is considered to be diffuse scattering caused by the roughness of the reflection surface. Larger diffuse scattering in RDPP irradiation could be due to to the density modulation by the small spikes.

$3\omega_0/2$ emission is considered to be generated by the non-linear mixing of an incident photon of frequency ω_0 and a plasma wave of frequency $\omega_0/2$. The plasma wave of $\omega_0/2$ can be generated at 1/4 n_c by the two-plasmon decay (TPD) instability. For the TPD instability, L_{ph} is nearly equal to the density scale length L_d . When the focal spot size is large enough, the plasma expands one dimensionally. The density scale length L_d at low electron density region will be given by $L_{d1}=\tau c_s$, where τ is the laser pulse duration and c_s is the ion sound velocity. In our case at around 10^{12}w/cm^2 , $L_{d1}\sim 80\mu$m. The distance of 1/4 n_c region from the critical surface will be about 80 μm. Therefore, the density modulation of 7μm generated by the small spikes in RDPP irradiation will be well smoothed out in the region where TPD occurs. This can explain nearly the same $3\omega_0/2$ emission in RDPP irradiation with that for 300 μm focal spot size without RDPP. When the focal spot size becomes comparable to L_{d1}, the plasma expands two-dimensionally and the scale length, L_{d2}, is proportional to the focal spot size. The increasing TPD threshold for smaller focal spot size observed in Fig. 4 can

be explained by the reduced density scale length L_{d2}.

CONCLUSION

In the irradiation with a randomly distributed plate, there are lots of small spikes in the focused pattern. These spikes could enhance back scatterings due to the very high peak intensity. The experimental result, however, was that no enhancement of BS and TPD instabilities was observed in RDPP irradiation. Rather, BS signal was suppressed. The reason of the suppression will be reduced scale length caused by the small spikes. If the non-enhancement of TPD and suppression of BS as observed in the present work can be observed also for larger scale plasma, RDPP irradiation will be a very attractive scheme for the uniform compression.

REFERENCES

[1] Y. Kato, K. Mima, N. Miyanaga, et. al. Phys. Rev. Lett. 53(1984)1057.

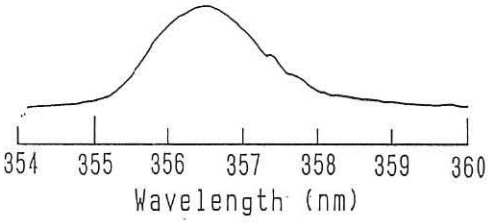

Fig. 3 A typical observed back-scattered spectrum around $3\omega_0/2$

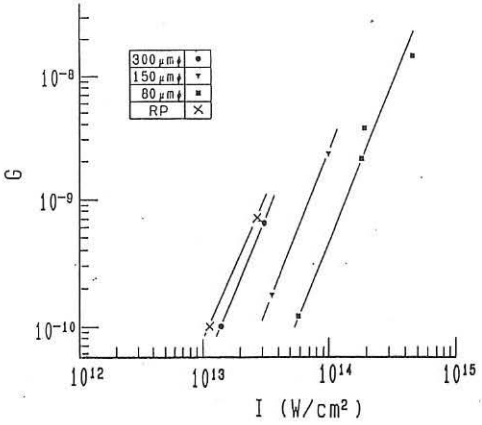

Fig. 4 Intensities of the peaks which were observed in the spectrum around $3\omega_0/2$ for each focused spot diameter without RDPP and for an irradiation with RDPP (RP). The each peak value is normalized to the laser energy and indicated as a generation coefficient, G. The threshold of the harmonic generation was higher for the smaller focused spot diameter. The threshold in the RDPP irradiation was nearly the same with that for the irradiation of 300 μm spot diameter without RDPP. For each of the focal conditions, the efficiency G depends the laser power density as $G \propto I^{2.5}$.

EXPERIMENTAL STUDY OF LASER-PLASMA INTERACTION PHYSICS WITH SHORT LASER WAVELENGTH

C. LABAUNE, F. AMIRANOFF, E. FABRE, G. MATTHIEUSSENT, C. ROUSSEAUX, S. BATON

Laboratoire pour l'Utilisation des Lasers Intenses,
Ecole Polytechnique, CNRS, 91128 Palaiseau Cédex, FRANCE

Many non-linear processes can affect laser-plasma coupling in fusion experiments[1,2]. The interaction processes of interest involve three or more waves, including the incident electromagnetic wave and various selections of electromagnetic, electrostatic and acoustic waves. Whenever plasma waves are involved (stimulated Raman scattering, two-plasmon decay instability, parametric decay instability and others), energetic electrons are created through the various damping processes of these waves : these energetic electrons in turn deleteriously affect the compression phase in laser fusion experiments through pre-heating of the fuel core. Some parametric processes lead primarily to loss of incident laser energy (stimulated Brillouin scattering) while others, such as filamentation[3], lead to strongly enhanced local laser intensies through the focusing of part (or all) of the laser beam into filaments of very small dimensions with a concomitant expulsion of the plasma out of these regions. So filamentation destroys the uniformity of energy deposition in the plasma and prevents high compression efficiency of the target.

These interaction effects are typically of parametric nature, with their thresholds and growth rates depending critically on plasma scale lengths. Since these scale lengths increase with available laser energy and since millimeter sized plasmas are expected from reactor targets which will be used in direct drive implosion experiments, a good understanding of these processes and their saturation mechanisms becomes imperative. We report here the results on absolute energy measurements and time-resolved spectra of SRS and SBS obtained in various types of plasmas where the major changes were the inhomogeneity scale lengths.

EXPERIMENTAL SET-UP

In the experiments reported here one or two beams of the neodymium:glass laser of the LULI Laboratory at Ecole Polytechnique were used. Two irradiation techniques were achieved in order to produced three different types of plasmas:

1. Thick foil, directly irradiated by the main beam, produces a short scale length, in the range of 5 to 10 μm, with linear like density profile and plasma temperature of 1 keV.

2. Thin plastic foil (0.3 - 1.5 μm) irradiated by the main beam expands and becomes underdense during the pulse, with a parabolic like density profile and a plasma temperature of 600 eV. Top of this profile provides a ~100 μm plasma length in which SRS may develop.

3. Long and quasi-homogeneous plasmas were generated by irradiation of a thin (0.3 - 0.8 μm) and narrow (0.5 - 1 mm) plastic foil with a first laser beam focused onto a rectangular

focal spot (2mm -150μm). This beam was frequency converted from 1.053 μm to its second harmonic at 526 nm; the pulse width was around 0.5 ns and the incident intensities ranged around (1 to 2×10^{13} W/cm^2). Under these conditions we have found from previous interaction studies[4] that relatively homogeneous, 500 μm plasma length (focal depth of the lens is 250μm), of $n_e/n_c \lesssim 0.2$ and $T_e \sim 400$ eV could be obtained 0.6 ns after the peak of the pulse. The interaction beam was tightly focused along the long direction and at the center of this preformed plasma which is roughly uniform over the cross section.

Last two types of plasmas are schematized in fig. 1. The experimental lay-out is shown on fig. 2 for the two beam-experiment. In the one beam-experiment the lay-out is exactly the same except that the plasma producing beam is missing . The interaction beam was frequency converted to its second (526 nm) and to its fourth (263 nm) harmonics; it was focused by an f/2.5 lens to a spot of approximately 50 μm diameter so that the maximum intensity was 2×10^{15} W/cm^2 .The main diagnostics are:

a. absolute time-integrated measurements of backward and forward Raman scattering, backreflected light into the lens at the fundamental frequency (Brillouin backscattering) and transmitted light of the interaction beam through the plasma.

b. time-resolved spectra of backward and forward Raman scattering and Brillouin backscattering.

c. hot electron energy spectra between 30 and 250 keV in various directions

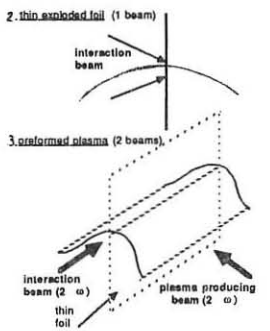

Figure 1
Generation of plasmas type 2 and 3

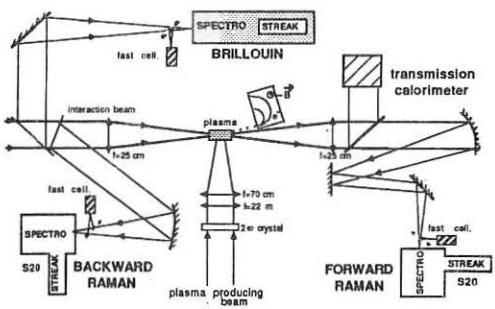

Figure 2
Experimental set-up

EXPERIMENTAL RESULTS

Stimulated Raman scattering

1 One beam-experiment at 0.53 and 0.26 μm :

-Figure 3 shows typical time-resolved spectra of the backward and the forward Raman scattered light recorded in one beam, 2ω, thin exploded foil experiment. The Raman light starts in a narrow density region and shifts towards lower density during the pulse.The emitting densities were in the range $(0.03 - 0.17)n_c$.A previous model[5] has shown that these spectra can be well predicted by assuming the Raman to be occuring in a L~100μm region at the top of a parabolic density profile, using well accepted threshold estimates. The low density limit of

backward Raman can be attributed to Landau damping of the generated plasma waves at an electron temperature of around 500 eV. The forward Raman signal is observed with an intensity only sligthly greater than the continuum plasma ligth emission.

- Absolute conversion efficiency of backward Raman is very sensitive to the initial foil thickness; with same conditions we have measured 10^{-6}, 2×10^{-5}, $10^{-3}$and 4×10^{-3} respectively for thick targets, 1.5μm, 6000Å and 3000Å, in the 2ω experiment.

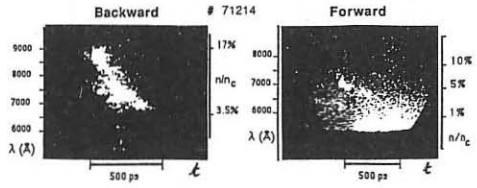

Figure 3
Typical exploded foil spectra
CH 0.3μm, I= 10^{15}W/cm^2

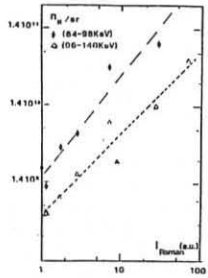

Figure 4
Correlation between hot electons and Raman light. 1.5μm foils.

- Hot electron emission with energies in the range (64-98)keV and (96-140)keV, which correspond to channels 4 and 5 of the electron spectrometer is correlated with Raman intensity as shown on fig.4 . These hot electrons are only observed on the laser axis or within an angle lower than the aperture lens, as expected for Raman instability.

- Experiments with the 4ω light show a decrease, by a factor of ten , of Raman energy and hot electron emission compared to the 2ω experiments.

2 Two beam experiment at 0.53μm

-In preformed plasmas typical Raman spectra are very narrow, with wavelength decreasing slowly with time (fig.5);the plasma density as measured from Raman spectra depends on the initial foil thickness and in all cases forward and backward Raman are emitted at the same density ,as can be seen in fig.6, indicating the presence of a rather homogeneous plasma . Plasma density evolution during the interaction laser pulse calculated in two-dimensional hydrodynamic simulations using the code SAGE shows that the plasma heated from the central region is expelled and decrease of density versus time[4] is the same as the one observed from time resolved spectra. The short wavelength limit of the backward spectrum gives an upper limit of the electron temperature of the plasma of ~400eV.

- Raman intensity increases with initial foil thickness (fig.7),and so with plasma density ; maximum conversion efficiency is 6×10^{-3} for backward Raman and $\leq10^{-8}$ for forward Raman.

-Hot electron are not observed in preformed experiments: the temperature of the plasma is too much low and no background electrons can be trapped and accelerated in the plasma waves.

Stimulated Brillouin scattering

Backreflected light in the focusing optics at the fundamental frequency produces a measurement of Brillouin intensity as there is no critical density in preformed plasma or in thin exploded foil, and so there is no specular reflection.At 0.53μm, with thin exploded foil (3000-6000)Å the backscattered level is very low ~3 10^{-4} of incident energy but with preformed plasmas the level is

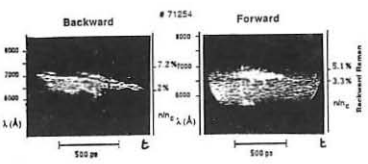

Figure 5
Typical preformed plasma Raman spectra CH 0.6μm, $I=10^{15} W/cm^2$

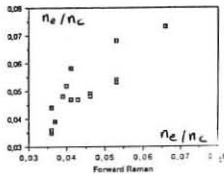

Figure 6
Backward versus forward plasma density of Raman.

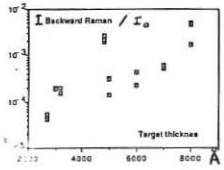

Figure 7
Raman intensity versus initial foil thickness

much higher ~0.02 .The main difference between these two plasmas is probably the velocity scale length that can reduce a lot Brillouin instability in the fast expanding plasma.

Time-resolved spectra are also very different: in thin exploded foils they are quite broad ~10Å and in preformed plasmas they are very narrow and constant in time. In the first case the emission may come from regions with different densities, temperatures and velocities whereas in the second case the plasma is quite homogeneous in density and temperature. These features have already been observed in previous experiments[7] which were using a different geometry of irradiation to preform plasmas; in these past experiments it was also shown that Brillouin backscattering was lower than 10^{-4} at 0.26μm in preformed plasmas.

CONCLUSION

Conversion efficiency of Raman scattering is strongly dependent on plasma inhomogeneity and is increased by a factor of ~10000 for density scale length variing from 10μm (linear profile) to 100-300 μm (homogeneous profile). In hot plasmas, energetic electrons are correlated with Raman instability, so this process could have dramatic effect in large plasmas. By using 0.26μm laser light, Raman efficiency is decreased by a factor of 10; this is due to collision damping of em and plasma waves.

Brillouin backscattering has been observed but is still at a very low level (≲2%) at 0.53μm ,even in homogeneous plasma of ~300um length. Short wavelength (0.26μm) reduces the backscattered level by a factor of ~200.

REFERENCES

1. D.FORSLUND,J.KINDEL and L.LINDMAN Phys. Fuids 18, 1002 and 1017 (1975)
2. P.DRAKE,E.WILLIAMS,P.YOUNG,K.ESTABROOK and W.KRUER Phys. Rev. Lett. 60,1018 (1988)
3. B.COHEN and C.MAX Phys. Fluids 22, 1115 (1979)
4.C.LABAUNE,F.AMIRANOFF,G.MATTHIEUSSENT,C.ROUSSEAUX,S.BATON,J.L.LACAZE,W.SEKA,S.CRAXTON Proceeding of the 19th ECLIM Conference, Madrid 1988
5.C.LABAUNE,H.BALDIS,E.FABRE,F.BRIAND,D.VILLENEUVE,K.ESTABROOK to be published in Phys. Fluids
6. C.ROUSSEAUX,F.AMIRANOFF,C.LABAUNE,B.MABILLE,G.MATTHIEUSSENT Rev. Phys. Appl. 23, (1988)
7. C.LABAUNE,E.FABRE,A.MICHARD,F.BRIAND Phys.Rev. A 32, 577 (1985)

GENERATION OF SUPERHOT ELECTRONS FROM LASER PLASMAS AT THE DELPHIN INSTALLATION

Gamaly E.G., Lokteva O.V., Nikolaev F.A., Stukov O.I.

Moscow Aviatiom Institute,
Volokolamskoeshosse 4, Moscow 125871, USSR

Superthermal electrons generated in laser-produced plasmas are known to have a significant influence on the hydrodinamic behavior of the target. The influence is two-fold: the energy of the superthermals is decoupled from the implosion process, resulting in decreased hydrodynamic efficiency; and high-energy superthermals penetrate to and preheat the target core. So the investigation of energy spectrum of superthermal electrons and mechanism of their generation is the important task.

The energy yields of superhot electrons with energies above 200 keV were measured at the Delphin installation when irradiating spherical shell highaspect targets ($R/\Delta R \approx 10^2$) 0,4 mm in diameter by laser pulse $2 \cdot 10^{-9}$ s in duration with energy $\sim 10^3$ J. The electrons were recorded by Cherencov detectors, that registered only those electrons whose energy was larger than some threshold energy determined by radiator material. Different transparent materials were used as the radiators of Cherencov detectors: water, glicerin, polymethylmetacrylate. Such materials possess of low sensitivity to x-ray emission. Furthermore Cherencov detectors are not sensitive to any corpuscular emanation from laser plasma.

Aluminium foils were placed in front of detectors. They cut off soft component of electromagnetic radiation and reduced hard one. So the contribution of radiator fluorescence when x-ray emission was passing through the detector was neglected. Electrons lose some part of its energy when passing through the foil, so the minimum energy E_{cut} of electrons registed is larger than threshold energy E_{th} . Moreover one can change the cut off energy by means of changing the thicness of foil.

At first one Cherencov detector was used for the purpose of discovering the generation of superhot electrons. So only one value of energy yield

$$Y = \int_{E_{cut}}^{\infty} N(E) \cdot f(E,x)\, dE$$

was measured for every laser pulse. Here $N(E)$ is the energy spectrum of electrons, $f(E,x)$ is the detector response func-

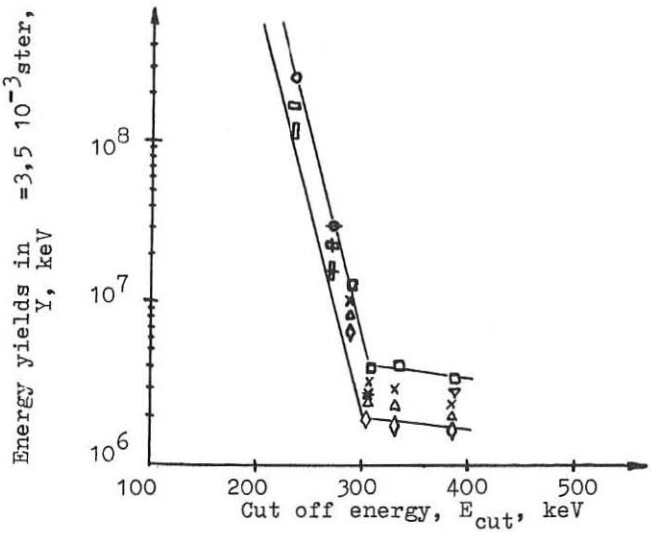

Fig.1. The energy yields of superhot electrons versus the cut off energy. The energy of laser pulse was (J): ○ - 1082, □ - 890, ▯ - 640, ⊖ - 1100, ⊕ - 863, ⊞ - 843, ▫ - 1085, × - 780, △ - 602, ◊ - 345, ✳ - 663.

tion, and x is the thickness if aluminium foil. In the following experiments the godoscope of four Cherencov detectors was used. Aluminium foils with different thickness were placed in front of detectors. It allowed to measure several values of energy yields for every laser flash and to obtain the distribution of energy yields as the function of E_{cut}.

The amplitudes of signals from detectors were measured by one oscilloscope. These signals were delayd with respect to each other by cable delay line and after mixing entered the fast oscilloscope. Synchronous launching of the oscilloscope was carried out by signal from scitillator detector which recorded x-ray emission from laser plasma.

The experimental results are shown in Fig.1, where the energy yields Y of superthermal electrons are plotted versus the cut off energy. One can see, that there is considerable yield of electrons for cut off energy $E_{cut} \geq 300$ keV. Moreover the absolute yield of fast electrons increas with the growth of laser energy. The dependence of electron energy

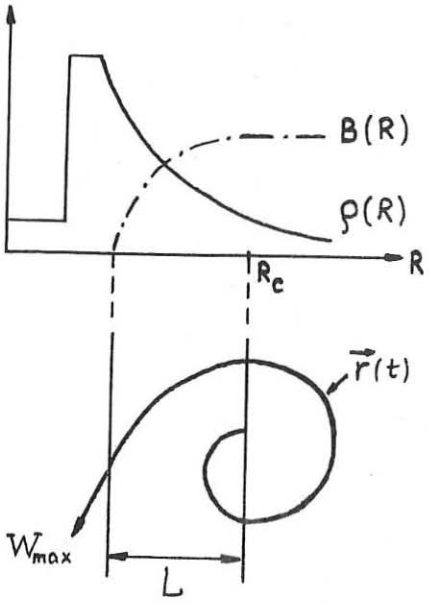

Fig.2. Ecceleration of electrons by multiple interaction with resonance plasma oscillations in the presence of magnetic fields.

yield in logarithmic scale upon E_{cut} is linear and there is the break near $E_{cut} \approx 300$ keV.

Such shape of distribution function is typical when electrons accelerating after multiple interactions with resonance plasma oscillations in the presence of magnetic fields, as is shown in Fig.2. Magnetic fields influence at most on the fastest electrons, that is on electrons in the tail of distribution function. Dispersion length of electron exceeds its Larmor's radius at energies $W > (3 \cdot 10^4 Z^2/B)^{2/3}$ keV. The amount of interactions with resonance fields, ensured by madnetic field, is large even for not very strong fields: $N \approx 10^7 \cdot B \cdot \tau$. For $\tau = 10^{-9}$ s and $B = 10^5$ G the amount of interactions is equal to $N \approx 10^3$. So the practical restriction on maximum energy of fast electrons is determined by magnitude of magnetic field, that is the acceleration is stopped when Larmor's radius becomes equal to the distance between ecceleration region and the field boundary L. The maximum energy in this case is

$$W_{max} = mc^2 \sqrt{1 + (eBL/mc^2)^2}$$

and it allows to obtain information about the size of magnetic fields in laser plasma. For the case of cut off energy 300 keV one can obtain $BL \approx 2 \cdot 10^7$ G·μm. The typical dimention of field is equal to the distance from critical surface to the plasma boundary, that is $L \approx 100$ μm in our experiments. Then the magnitude of magnetic field is equal to $2 \cdot 10^5$ G.

SOLITONIC PROPAGATION OF LASER PULSES IN A COLLISIONLESS PLASMA

F.F. Koermendi

Institute H.T.M., Belgrade, Yugoslavia

The solitonic propagation of laser pulses in a collisionless plasma may be treated quantumelectrodynamically as a process of elastic scattering of n photons, representing the wave packet, from free electrons, in such a way that the effective cross section does not depend on the frequency of the photons in the laser pulse.

If n photons of four-momenta $k_o/\vec{k}_o, iw_o/$ elastically scatter from a free electron of initial and final four-momenta $p_o/\vec{p}_o, iE/$ and $p/\vec{p}, iE/$, respectively, into a mode $k/\vec{k}, iw_o/$, the four-momentum conservation law

$$p_o + nk_o = p + nk$$

results in a kinematical relation

$$n = \frac{p_o/\, k_o - k\, /}{k_o k}$$

or, explicitly,

$$n = \frac{|\vec{p}_o| \,/\, \sin\theta \, \cos\varphi - \cos\varphi_o \,/}{w_o \,/\, 1 - \cos\alpha \,/} \equiv \frac{|\vec{p}_o|}{w_o} L$$

where φ_o is the angle between $\vec{p}_o$ and $\vec{k}_o$, $/\theta, \varphi /$ define the angle between $\vec{p}_o$ and $\vec{k}$, while α is the angle between $\vec{k}_o, \vec{k}$.

The transition probability per unit time may be evaluated with the help of Feynman diagrams, shown below ,

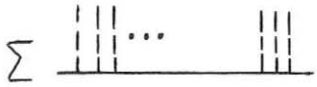

where the full line represents the electron propagation function and the dashed lines are the incoming or scattered photon functions. Σ denotes the sum of all possible graphs in which the number of incoming and scattered photons are equal.

The transition probability per unit time P' is given by

$$P' = 2\pi |M|^2 \varrho_F \quad ,$$

where M is the transition matrix element and

$$\varrho_F = \varrho_e \left| \frac{\partial E_F}{\partial E} \right| = \frac{E |\vec{p}_o| V \, d\Omega}{(2\pi)^3} \left| \frac{2}{n} \right| .$$

Evaluating the P' , the differential cross section becomes

$$\frac{d\sigma}{d\Omega} = f K^n \quad ,$$

where f is a factor independent of the photon frequency w_o, while K reaches its maximal value

$$K \to 1$$

at incident light intensities

$$I/w_o/ \to \frac{w_o^2 \, m_o \qquad L^4}{2\pi r_o \quad \cos^2\beta \, \cos^2\gamma} \quad ,$$

m_o and r_o being the rest-mass and the classical radius of the electron, β the angle between $\vec{p}_o$ and $\vec{\mathcal{E}}_o$ -the polarization vector of the incoming photons, γ -the angle between $\vec{p}_o$ and $\vec{\mathcal{E}}$ -the polarization vector of the scattered photons. Thus the laser pulses may propagate as solitons if the spectral distribution of the intensity has the form

$$I/w/ = k \frac{w^2 m_o}{2\pi r_o} \frac{L^4}{\cos^2\beta \cos^2\gamma},$$

where $k \gg 1$.

As is shown in /1/ , an appropriate threshold intensity appears at photon absorption by free electrons which has the value

$$I_a = \frac{w^3}{2\pi r_o (\vec{\mathcal{E}}_o \vec{\mathcal{E}})}$$

During the initial period of the laser irradiation in IC fusion experiments most of the outer electrons have propagation directions toward the outer space, opposite to the laser beam propagation direction. In this case $L \to 1$, $\cos\beta \to 0$ and thus I /w/ becomes much higher than I_a which shows that in the outer, collisionless region of the created plasma photon absorption prevails at incident laser beam intensities

$$I_a \leq I \leq I/w/.$$

REFERENCES

/1/ Körmendi F., Optica Acta, 31, 301, 1984.

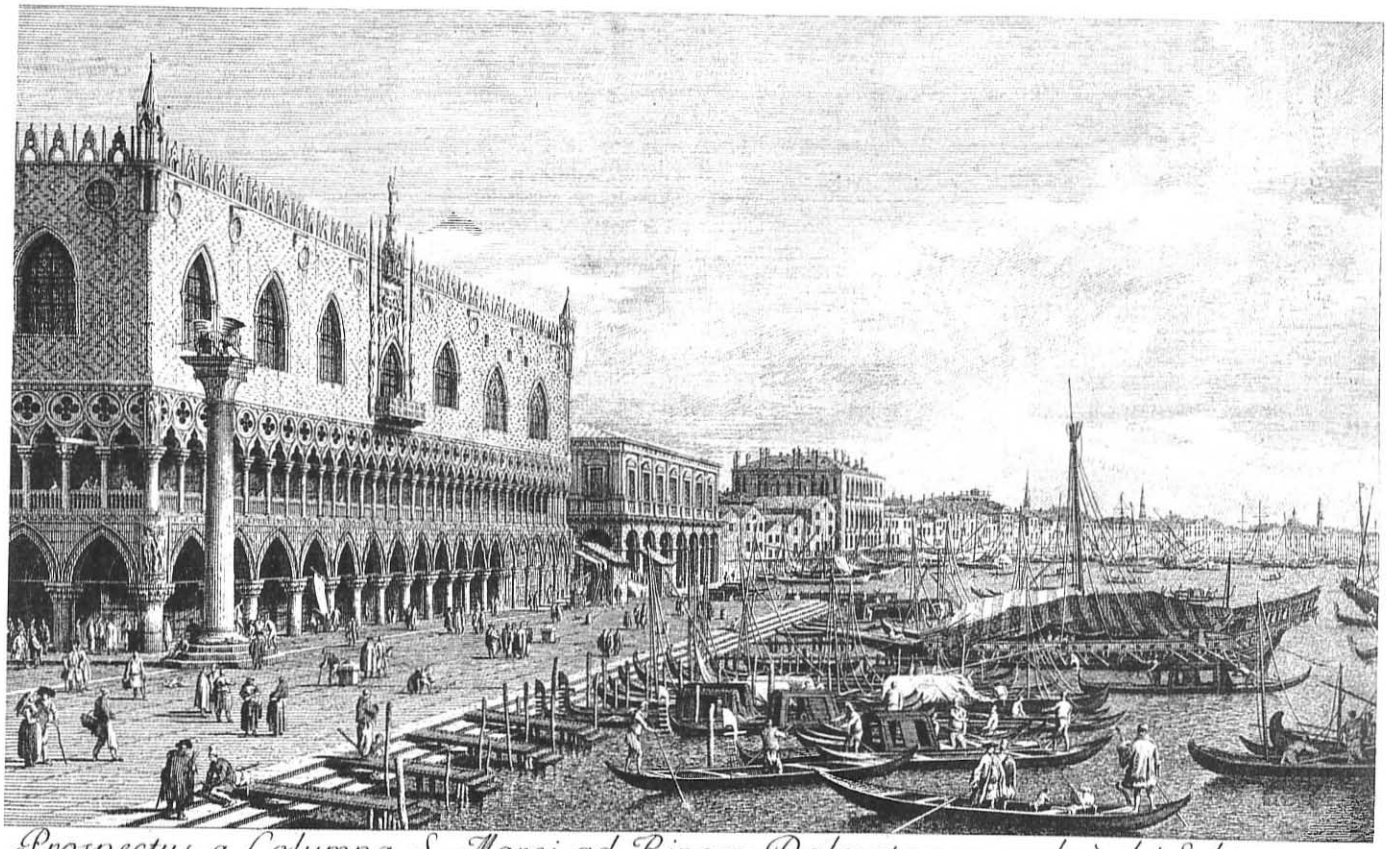

Prospectus a Columna S. Marci ad Ripam Dalmatarum vulgò de' Schiavoni. JJ.

OBSERVATIONS AND TWO DIMENSIONAL FOKKER–PLANCK CALCULATIONS OF A SHORT PULSE, HIGH POWER KrF LASER–SOLID INTERACTION

O Willi, G Kiehn, J Edwards, V Barrow, R A Smith, J Wark*, G J Rickard, A R Bell,[1] E Turcu[2], E M Epperlein[3]

[1]Imperial College of Science, Technology and Medicine, The Blackett Laboratory, Prince Consort Road, London SW7 2BZ, *Now at University of Oxford, Clarendon Laboratory, [2]Rutherford Appleton Laboratory, Chilton, Didcot and [3]LLE University of Rochester, NY, USA.

Abstract

The generation of hot, high density plasmas with 3.5 picosecond, 1 J KrF laser pulses focussed onto solid targets with irradiances up to $10^{17}Wcm^{-2}$ has been studied using time resolved X–ray spectroscopy. Fully ionised aluminium plasmas were observed, and densities above $10^{23}cm^{-3}$ were inferred from observations of Stark widths and continuum lowering. Both 1–D hydrodynamic and 2–D Fokker–Planck codes were employed to model the experiment. The latter uses a diffusive approximation and is solved by the alternating direction implicit (ADI) method, with ions modelled hydrodynamically. Substantial departures from Spitzer heat flow are found, especially along the surface of the target where the heat flow is inhibited. As a result even for 10 micron diameter laser spots, the heat flow into the target is not strongly reduced by lateral transport.

The recent development of high power picosecond lasers have opened up exciting possibilities of producing very hot high density plasmas. This is because the laser energy is absorbed very close to the initial target surface since no significant hydrodynamic motion can occur on a subpicosecond time scale.

This paper describes experimental observations and computational modelling on the interaction of a 3.5ps high power KrF laser pulse with solid targets at irradiances up to $10^{17}Wcm^{-2}$. Fully ionized Al plasmas close to solid density with temperatures of 400eV were observed when the prepulse level was low. The results were modelled by a 1–D hydrodynamic and a 2–D Fokker–Planck computer code.

The experiments were carried out at the SERC Central Laser Facility (Rutherford Appleton Laboratory) using the recently developed short pulse, high power KrF laser system SPRITE [1]. A 3.5ps pulse was amplified to energies up to 2.5J in discharge and electron beam pumped KrF amplifiers. The laser beam was focused onto target with an f/2.5 aspheric lens to a 20μm focal spot. Irradiances up to $10^{17}Wcm^{-2}$ were achieved. The primary diagnostic used to study the plasma was a time resolved crystal spectrograph. A flat TLAP crystal was coupled to an x–ray streak camera operating in the 5–7 A spectral window. The spectral and temporal resolutions were 15mA and 15ps respectively.

The experimental observations were modelled with the 1–D Lagrangian hydrocode MEDUSA [2] and a 2–D Fokker–Planck code [3]. With the latter code electron thermal transport occurring both into and along the surface of the laser irradiated targets were simulated. The code has been written to solve the Fokker–Planck equation for electrons

in one or two spatial dimensions in the diffusive approximation. The equation is solved using the alternating direction implicit (ADI) method.

Time resolved x−ray spectra were recorded on aluminium targets irradiated by the short KrF pulse. When the ASE prepulse was less than 10^{-5} a very wide and intense Al Heβ ($1s^2$ − 1s3p) transition was observed which dominates the spectrum. The Heγ ($1s^2$−1s4p) transition turns on approximately 15ps after the Heβ transition. In addition, the higher members of the H−like and He−like series are extremely faint.

In contrast a distinctly different X−ray spectrum is observed when large prepulses are superimposed upon the short pulse. The experimental spectrum shows the full He−like and H−like series. In addition, the X−ray radiation is emitted without significant change in brightness for several hundred picoseconds, indicating a large plasma corona. The electron density was obtained by comparing the experimental Stark profiles predicted by the atomic physics codes RATION and SPECTRA [4]. Figure 1 compares synthetic line profiles with a microdensitometer trace of Heβ and Heγ line profiles recorded when the ASE prepulse level was very low and not detectable by an optical diode. The trace was taken 15ps after the start of the emission. The best fit was found for an electron density of $1.6\times10^{23}cm^{-3}$. The calculations of the synthetic spectra assume small opacity corrections and an electron temperature of 400 eV.

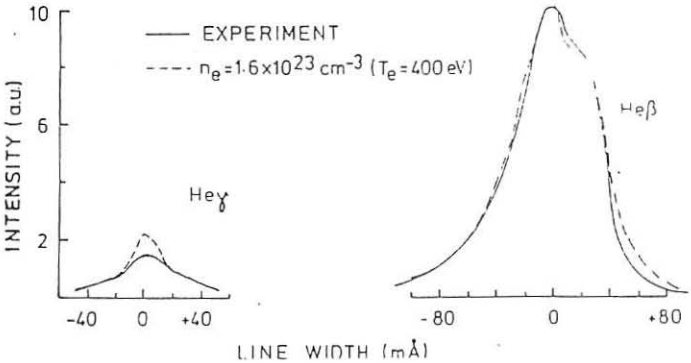

Figure 1. Comparison of experimental line profiles of Al Heγ and Al Heβ with predicted profiles calculated with T_e = 400eV and $n_e = 1.6 \times 10^{23}cm^{-3}$.

The electron density was also obtained for spectra recorded on targets with large ASE prepulses. The Stark width was again compared with synthetic spectra produced by RATION and SPECTRA and good agreement was found for $n_e = 3\times10^{22}Wcm^{-2}$. This is consistent with x−ray emission from densities close to critical ($1.6\times10^{22}cm^{-3}$) for 248nm laser light.

Detailed hydrodynamic simulations were carried out using the 1−D hydrocode MEDUSA to predict and analyze the experimental data. All the simulations were performed with a laser wavelength of 248nm and target materials of aluminium. The interaction was modelled for a 3.5ps FWHM laser pulse with 0.55 J total energy, $3\times10^{16}Wcm^{-2}$, to simulate the experimental data shot shown in figure 1.

The deposition of laser energy is calculated assuming inverse bremsstrahlung to be effective upto the critical density surface. A fraction f_R of 0.2 of the remaining energy is dumped at the critical density surface to simulate resonance absorption. The fraction of resonantly absorbed energy producing hot electrons was taken to be 0.9. A flux limiter of 0.1 times the classical free streaming limit was used.

Figure 2 shows the results of the simulations during and after the laser pulse. Electron density and temperature as well as the average ionization profiles are plotted. As can be seen in figure 2, the simulations predict higher electron densities during the laser pulse than are observed experimentally. This is due to the temporal smearing of the experimental measurements caused by the finite 15 ps temporal resolution of the X−ray spectrograph. After the laser pulse the predicted electron density agrees closely with the observations.

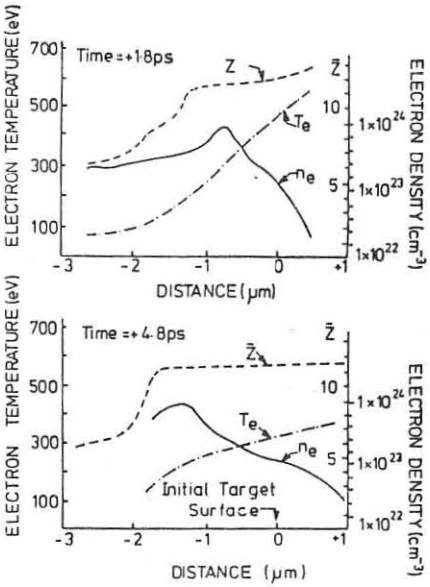

Figure 2. Hydrodynamic simulations of a 3.5 ps laser pulse without prepulse showing the evolution of the electron density, temperature, and average ionization during and after the laser pulse.

The effects of a prepulse in the target and plasma conditions were also stimulated. A gaussian laser pulse, 20 ns in duration, containing 30% of the total energy, 0.8J, was superimposed with the short pulse. A flux limiter of 0.03 times the classical free streaming limit was used. The predictions of the plasma conditions are now distinctly different. During the prepulse, several microns of plastic are ablated. The electron temperature drops off sharply above critical density. This implies that the x−ray

radiation is emitted from electron densities close to critical, in agreement with the experimental observations.

The validity of the 1−D hydrocode simulations under the prepulse and prepulse free conditions is corraborated by 2−D Fokker−Planck simulations. When the short pulse alone is incident upon the target, the Fokker−Planck simulations show that almost all of the total absorbed energy is transported into the target, ie towards higher electron densities, calculating a flux of 0.1 times the free streaming limit even for 10μm diameter focal spots. Figure 3 shows temperature contours and vector plots of the heat flow for a 20 μm diameter spot. In the case of the large ASE prepulse, the Fokker−Planck code shows that the short pulse is completely absorbed in the large low density plasma corona and most of the absorbed energy is transported laterally across the target surface predicting a flux of 0.03X the free streaming limit into the target.

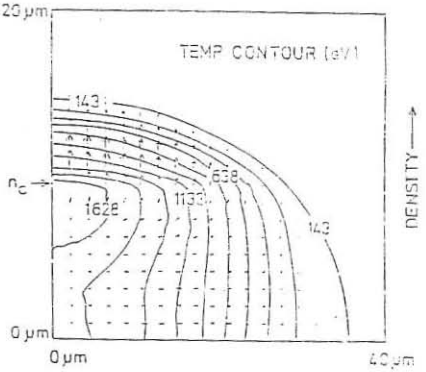

Fig 3. Temperature contours and heat flow vector plots for a 20μm heat spot size from the 2−dimensional Eulerian code shortly after the peak of the 3.5ps laser pulse.

In summary, this letter reports on spectroscopic X−ray observations demonstrating that fully ionized aluminium plasmas are produced with a single 3.5 ps high power KrF laser pulse. Comparison of atomic physics predictions with measured Stark profiles and observed continuum lowering indicated that X−ray radiation is emitted from plasmas with electron densities above $10^{23}cm^{-3}$ when there is no prepulse. Plasmas with similar conditions were predicted by hydrodynamic simulations when 20% of the incident laser energy was dumped at the critical density to model resonance absorption. These simulations were in agreement with 2−D Fokker−Planck calculations. For very short pulses a substantial departure from Spitzer heat flow was found, especially along the target surface.

References

1. J M Barr et al, Opt. Comm. 60, 127 (1988).
2. J P Christiansen et al, Comp. Phys. Comm, 7 271 (1974).
3. G J Rickard et al Comp. Phys. Comm., to be published.
4. A R W Lee, B L Whitten and R E Stout II, J. Quant. Radiat. Transfer 32,91 (1984).

SIMULATION STUDIES ON THE DYNAMICS OF IMPLODING SHOCK WAVES IN SPHERICAL PINCH EXPERIMENTS

D.P.Singh, M.A.Harith*, V.Palleschi, G.Tropiano and M.Vaselli

Istituto di Fisica Atomica e Molecolare del C.N.R.
Via del Giardino, 7- 56127 Pisa, Italy

and

E.Panarella**

Advanced Laser and Fusion Technology, Inc.
P.O. Box 8763, Alta Vista Terminal
Ottawa, Canada KIA OR6

Abstract

The earlier theoretical studies on the scaling laws for Spherical Pinch (SP) experiments obtained under the conditions of substantial expansion of the central plasma and the well defined time delay between the creation of central plasma and the launching of the peripheral shock capable of confining central plasma sufficiently long to achieve breakeven conditions for plasma fusion led to the conclusion that, in realistic situations of SP experiments, negative time delays should be adopted i.e. the launching of the imploding shock wave should precede the formation of the central plasma. However, the interaction of converging shock wave with the central plasma causing an additional heating and compression of the central plasma leading to favorable scaling laws was not taken into account. Starting from the hydrodynamic equations of the system, the proposed simulation code deals with the propagation of converging shock waves and its interaction with the expanding central plasma. Relevant simulation results on the dynamics of shock wave propagation are also compared with the predictions of point strong explosion theory.

1. INTRODUCTION

The dynamics of blast wave propagation in laser produced plasmas in gases has been investigated experimentally and theoretically in great details in past years [1,2]. More recently, the convergent spherical shock waves have been employed to contain the central plasma in Spherical Pinch experiments[3] . SP is a novel variation of inertial confinement fusion scheme in which the preformed central plasma is confined by the converging shock waves which are capable enough to contain the plasma for a sufficiently long time to reach plasma breakeven conditions. In a recent pilot experiment of Panarella[3], the plasma confinement time is found to

* Physics Department, Faculty of Sciences, University of Cairo (EGYPT)
** Also with National Research Council, (CANADA) and Department of Physics, University of Florence (ITALY)

be as large as ≈ 5.4 μsec. and the neutrons emitted were ≈ 10^7 per shot. The plasma temperature was ≈ 730 eV and the product $n\tau \approx 1.74 \times 10^{14}$ cm^{-3} sec. On the other hand, the theoretical analysis[3,4] attempted so far to lay an insight into optimising plasma and shock wave parameters for plasma breakeven conditions have not gone beyond the stage of first approximations. The recent analytical studies on SP were limited to the scaling laws involving the substantial expansion of the central plasma and the finite time delay between the creation of central plasma and the initiation of the peripheral imploding shock waves. It was concluded that in the case of simultaneous creation of central plasma and the launching of imploding shock, the central plasma is confined to as large as half of the radius of the spherical vessel and it has further been suggested that, in realistic SP experiments, negative time delays should be adopted i.e. the launching of the peripheral shock should precede the formation of central plasma. Obviously, the experimental and theoretical results obtained so far inspire not only the need of using improved diagnostics such as laser holography or spectroscopy to determine plasma density directly and spatially resolved X-ray emission spectra giving clear picture of the heated core region of the pinch but also a realistic and sophisticated numerical modelling for the theoretical support. The aim of the present paper is to provide some preliminary results on hydrodynamics of shock wave propagation with one dimensional simulation code. The present study improves further over the previous ones, in the sense that it also includes the interaction of imploding shock waves with the expanding central plasma. The additional heating of the central plasma by converging shock waves is likely to reduce the amount of energy to be deposited in the central region of the pinch to achieve plasma ignition temperature.

Sec. 2 deals with the details of the simulation results and the point strong explosion theory. A brief discussion of the simulation results on the shock wave dynamics are compared with the predictions of point strong explosion theory in Sec. 3.

2. HYDRODYNAMICS OF SHOCK WAVE PROPAGATION

A. Simulation analysis

The present simulation program is a one dimensional fluid code which employs a single fluid, one temperature and the hydrodynamical equation for perfect gas. The relevant fluid equations are written in Lagrangian coordinates using standard reference configuration. Each fluid element is labeled with a certain value called Lagrangian coordinate and retains it as it moves about. Obviously, one dimensional character of the simulation analysis rules out the possibilities to include the effects of self-generated magnetic fields. The original differential equations describing the hydrodynamical properties of the fluid on discrete space and time meshes are replaced by a set of finite difference equations which considerably facilitates to provide more information about the motion of of each fluid element. Since the viscosity may play important role on very short scale lengths, similar to other laser fusion codes, the rigorous viscous terms have been neglected. However, an artificial viscosity has been incorporated in few layers around the shock front and the corresponding original expression for viscosity developed by von Neuman and Richtmeyer[5] has been included which has the advantage that the pseudo viscous terms do not alter the stability of the usual difference equations for smooth flow of the fluid element.

B. Point Strong Explosion Theory

It is considered that the energy deposition at the periphery of the spherical cell occurs instantaneously. The ambient gas counterpressure is also assumed quite small in comparison with the pressure of the shock wave. In this situation, the hydrodynamics of the shock wave

may be easily described by point strong explosion theory and the dimensional analysis of the relevant fluid equations reveals that the two parameters namely, the initial gas density and the energy absorbed in the explosion are sufficient to describe the motion of the shock wave[6].

3. RESULTS AND DISCUSSION

Fig. 1 illustrates the comparison of simulation results on temporal evolution of expanding shock wave with the predictions of point strong explosion theory. Different continuous curves obtained from the simulation analysis correspond to the radial boundaries of different concentric cells. The shock wave front corresponds to the region of maximum compression of the gas in the corresponding cell. It is obvious that the time evolution of the shock wave front obtained through the above mentioned analysis is in excellent agreement with the predictions of the point strong explosion theory (triangles in the figure).

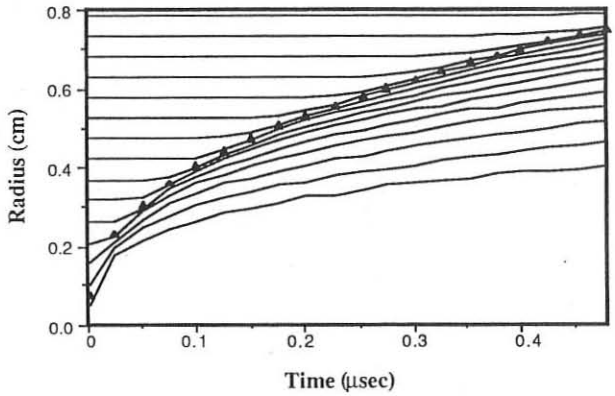

Fig.1 - Time evolution of the shock wave front in a D-T mixture with an unperturbed density $\rho = 10^{-3}$ g/cm^3. At the time t=0 a 100J laser energy is absorbed in the most internal cell. The triangles correspond to the prediction of point strong explosion theory.

The dynamics of the imploding shock wave and the expanding central plasma in the case of simultaneous launching of the peripheral shock wave and the creation of central plasma is displayed in fig.2a which provides an estimate about the confinement of the central D-T plasma. This numerical estimate is quite realistic from the experimental point of view as the interaction of the imploding shock wave with the expanding central plasma is included self-consistently in the numerical code.The unperturbed density of the gas corresponds to 10^{-3} g/cm^3, the absorbed laser energy is 100J, while the energy of the converging shock wave is 10^8 J/g.

Taking into consideration a negative time delay, as suggested in earlier analytical studies[3,4], a numerical simulation of such case is displayed in fig. 2b, adopting the same input physical parameters considered in fig.2a.

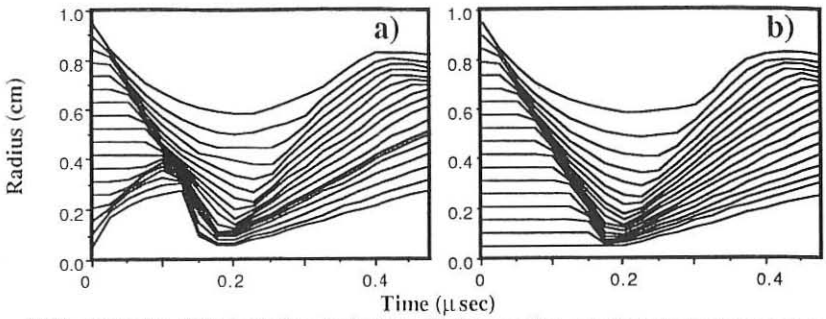

Fig.2 - Interaction of the imploding shock wave with the expanding central plasma in the case of a) simultaneous launching of the peripheral shock wave and the initiation of the central plasma; b) negative time delay between the launching of the shock wave and the initiation of the plasma.

Fig. 4 exhibits the variation of central plasma temperature during the expansion phase and the subsequent compression by the converging shock wave. The same negative time delay is considered. It is clear from the figure that the interaction of the shock wave with the central plasma results in an abrupt increase in its temperature followed by a relatively slow cooling down.

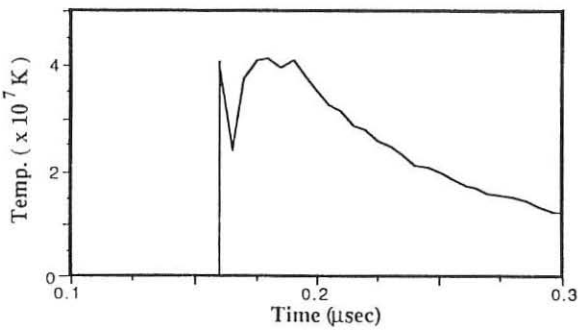

Fig.4 - The time dependence of the plasma temperature.

REFERENCES

1 -Hohla, K. et al. 1969 Z. *Naturforschung* 24a, 1244.
2 -Gatti, M. et al. 1988*Optics Comm.* 69 141 ; Harith, M. A. et al. 1988 *Opt. Comm.* (submitted).
3 -Panarella, E. 1987 *J. Fusion Energy* 6 , 285.
4 -Singh, D.P. et al. 1988 *Laser and Particle Beams* (submitted).
5 - Richtmeyer, R.D. et al. "Difference Methods for Initial-value Problems" Interscience NEW YORK (1967)
6 -Sedov, L. "Similarity and Dimensional Methods in Mechanics", MIR MOSCOW (1982).

IMPLOSION EXPERIMENTS AT 0.26 μm LASER WAVELENGTH

E. FABRE, M. KOENIG, A. MICHARD, Lab. L.U.L.I, Centre National de la Recherche Scientifique, Ecole Polytechnique, Palaiseau, France

P. FEWS, Bristol University, Great Britain

Short wavelength lasers have been demonstrated as the most efficient drivers for laser inertial confinement fusion : efficient absorption, low fast electron preheat, high ablation rate and ablation pressure. We present here some results dealing with the studies of implosions of large aspect ratio target driven with laser light in the UV at 0.26 μm.

The experimental conditions are as follow : the output of the six beam Nd glass laser facility from LULI Laboratory is frequency quadrupled with KdP cristals with an average efficiency of 35 %. This provides us, for experiment, a total amount of 200 J in a 500 picosec. pulse for the six beams configuration. Target illumination is made by using large aperture quartz lenses f : 1. The focus of each lenses is located, for best condition of uniformity of illumination, beyond the target at a distance L from center with L/R ranging from 1.8 to 2.5. The value L/R = 2 corresponds to tangential illumination. Targets are 10 ath D-T filled glass microshells from KMS Inc. with diameter ranging from 250 μm to 450 μm and wall thickness from 0.8 μm to 2 μm.

The diagnostics in these experiments are X-ray photography in the KeV range by pinhole or streak camera which gives us information on the implosion dynamic and symetry. The others main diagnostics are particle yield determination, for neutron with scintillators, and for α particles and protons using the tracks on C.R. 39 foils giving measurements of shell ρΔR and fuel temperature at the time of particles emission.

The main parameter in these experiments was the target wall thickness and to some extent the target aspect ratio R/e which was ranging from 100 to 280. The experimental data have been analysed using this paramater by comparison with the numerical prediction of the I-D Lagrangian code F.I.L.M.

The first set of results is related to the implosions dynamic obtained from X-ray streak photograph. On figure 1 is shown the R (t) diagram obtained from experiment and compared with numerical results.

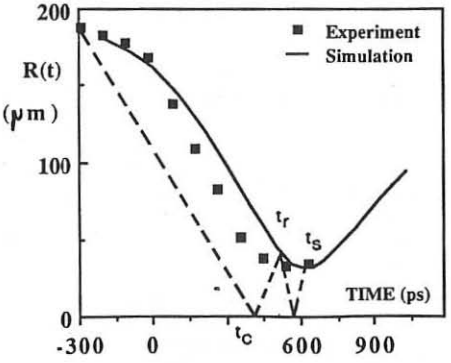

Fig. 1 : Comparison of experimentals (■) and numerical (–) R(t) diagrams
The dotted curve simulates. The shock wave propagation.

On figure 2 are plotted for various experimental conditions, target diameter, wall thickness, the experimental values of the squared implosion velocity versus numerical values with again a fairly good agreement.

This shows that with a moderate flux inhibition described by an harmonic average of thermal flux close to the non local flux theory and corresponding to a flux limit of 0.1, the numerical simulation gives a good description of the implosion dynamic.

The second set of experimental data is related to the fusion reactions. Here the agreement is rather poor as shown on figure 3. On this figure are plotted the experimental yields normalized to the yields given by numerical simulation at the time called t_r when the shock wave, driven by ablation pressure, suffers its first reflexion on the imploding wall, after its convergence at target center at time called t_c and before stagnation at time t_s as shown on figure 1.

These results show that experimental yield are smaller by two or three orders of magnitude than predicted values and that the discreapancy decreases when the target aspect ratio increases.

A better agreement could be found if experimental yield were normalised with yield at time t_c indicating that fusion reaction should occur at this time but other diagnostics deseagre with this assumption. Firstly the measurements of shell $\rho\Delta R$ from α particle slowing down show that $\rho\Delta R$ values agrees with numerical prediction at t_r. Secondly implosion photographs show that implosion behave relatively uniform untill late stage when the shell is strongly decelerated, process which occur significantly between t_r and stagnation.

Other, interesting data have been obtained from these experiments as shown on figure 4 where the neutron yields are plotted versus fuel temperature obtained from α particle spectrum broadening. On this figure is also plotted the $\langle\sigma_{DT}.V\rangle$ average cross section versus temperature. This shows that the major influence for particle production is

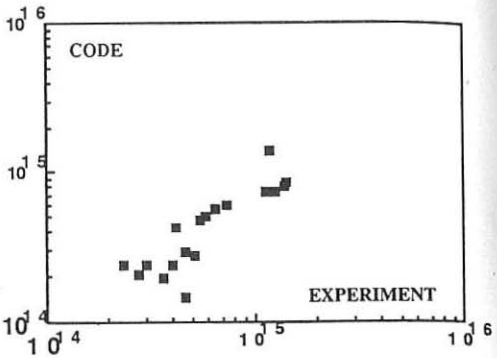

Fig. 2 : Plot of the numerical values of the squared implosion velocity ($cm^2.s^{-2}$) versus the experimental determination.

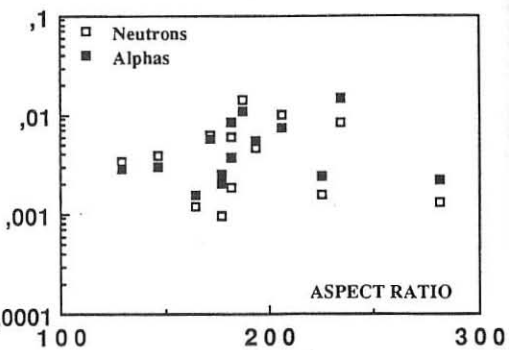

Fig. 3 : Experimental neutron and α yield normalized to numerical yield at reflexion versus aspect ratio.

the fuel temperature as expected. The remaining descreapancy could be attributed to the difference in each experiments for $n\tau$ values and the total number of fuel particles involved in the fusion reactions.

Another interesting result is the determination of hydroefficiency. This has been estimated in two way. First by estimating the value of thermal energy in the fuel $E_{th} = 3 N_o k T_f$ where N_o is the total number of deuterons or tritons, T_f the measured fuel temperature. This determination is surely an over estimate because the fraction of fuel involved in fusion reactions can be small excepted at the stagnation phase.

The second determination for hydroefficiency is the measurement of shell kinetic energy by the quantity $E_k = 2 \Pi R_f^2 (\rho\Delta R) V^2_{imp}$ where R_f is the shell radius at the end of implosion measured from pinhole photograph, $(\rho\Delta R)$ is the shell areal mass measured from α particle and V_{imp} is the implosion velocity.

This assume that R_f and $(\rho\Delta R)$ are determined at the same phase of implosion and consequently the hydroefficiencies obtained could be under estimated. The figure 5 gives these values plotted versus wall thickness.

What is seen on this figure is that the agreement between the two kinds of measurement is better for the thin shells. Some optimum value could be found near 1.2 to 1.3 μ wall thickness. However for the present conditions, small number of experiments and lack of precision, such conclusion is premature. The decrease for the thick shells in the kinetic energy is not only due to implosion velocity decrease but also and strongly to the small amount of shell which is given this velocity in contradiction with what could be expected from simple interpretation of ablation rate.

Nevertheless it is possible to estimate that the hydro efficiency can reach values in the range of 6 % to 12 % for optimum conditions.

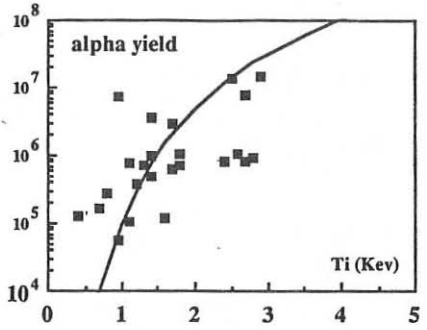

Fig. 4 : α yield versus ion temperature T_i. The solid line corresponds to the variation of $\langle\sigma v\rangle_{D-T}$ in this domain.

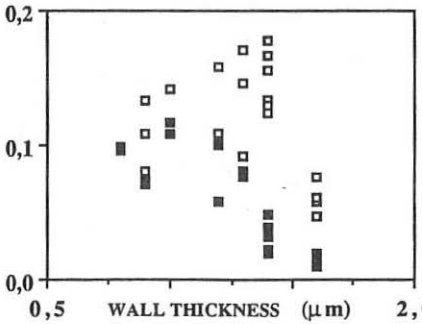

Fig. 5 : Hydroefficiency determination from kinetic ■ or thermal □ measurements.

In these experiments the most intriguing problem is the level of particle yield which is much lower than predicted. Certainly the implosion stops nearly around the time t_f at which the shell suffers a strong decelleration, owing to the relatively non uniform illumination conditions. Because of the strong shell preheat by shock or radiation, this non uniformity effect is more or less smoothed by shell expansion and favors thinner shells for breaking in later phase of implosion closer to stagnation. This would agree with the shell ($\rho\Delta R$) measured which are comparatively larger for thin shells than for thick shells by comparison with expected values from numerical simulation. The fuel temperature is also smaller than expected and it could be explained by some wall-fuel mixing occuring since the early stage of implosion before shell breaking.

These experiments have shown that for short wavelength lasers the implosion dynamic seems correctly described by numerical simulation with moderate transport inhibition. Hydro efficiency in the range of 6 to 12 % are obtained. The implosions behave relatively uniform untill late stage of implosions when the shell is strongly decelerated and shell preheat can explained this. However the strong descreapancy between experimental and predicted yields is not well understood yet. Fuel wall mixing during the early stage of implosion could explain this.

This is however not entirely sufficient and shell breaking time needs to be known implying more refine diagnostics on fusion reactions chronology.

PHOTON TRANSPORT AND RADIATION LOSSES IN LASER-CREATED PLASMAS

I. Toubhans and R. Fabbro

Laboratoire pour l' Utilisation des Lasers Intenses, Ecole Polytechnique, 91128 Palaiseau (France).

J.C. Gauthier

Laboratoire de Physique des milieux Ionisés , Ecole Polytechnique, 91128 Palaiseau (France).

M. Chaker and H. Pepin

Institut National de la Recherche Scientifique-Energie, Université du Québec, P.O. Box 1020, Varennes,Québec (Canada).

I) Introduction

Radiation energetics is a key issue in inertial confinement studies. At the high particle densities prevailing in laser-created plasmas, the electron energy balance is strongly influenced by photon transport through absorption and emission processes. In the dense part of the target, the medium is optically thick to line radiation and heating of the material by sub-keV photons is likely to occur. In the coronal part of the laser blowoff, the plasma is optically thin and radiation can escape freely. For these reasons, laser-created plasmas are copious sources of pulsed X-rays. For medium-Z (Z ~ 30) materials, peak emissions are found in the 100-2000 eV range with typical durations of a few ps to several ns. In this paper, we will focus on the measurement of X-ray conversion efficiencies in well-defined experimental conditions where plane copper targets are irradiated by laser light at 0.26, 0.53 and 1.06 μm with pulse durations of 600 ps, 3 ns and 30 ns and various laser intensities. Results will be compared with the predictions of a 1D hydrocode incorporating photon transport physics.

II) Experimental setup

Experiments were carried out at the LULI Laser facility (Palaiseau) with laser irradiances from 10^{10} to 10^{15} W/cm2. Copper has been chosen as a target material for its handling readiness and its high L-band emissivity in the keV range (1). Two low-spectral resolution spectrographs have been used: a multichannel X-ray diode spectrometer (1,2) and a transmission grating spectrograph. The first instrument gives absolute intensity measurements in wide energy channels (a few hundred eV) while the second allows for more detailed spectral analysis with a few Å resolution. Exploitation of the experimental results involve the analysis of experimental spectra at constant irradiance for the three wavelengths and pulse durations available. Conversion efficiencies (2π steradians) in the 100-750 eV range (sub-keV) and in the

750-2000 eV range (keV) have been deduced from measured, spectrally-integrated, absolute X-ray intensities and laser energy.

III) Hydrocode simulation

A one dimensional (plane geometry) lagrangian code using a fully implicit integration scheme for the solution of the conservation equations of mass density, matter velocity and internal energy has been developed. Laser deposition by inverse bremsstrahlung and resonance absorption together with flux-limited electron thermal conduction are treated classically (3). An accurate equation of state (4) is used to close the sytem of conservation equations. Photon transport is evaluated by using a multigroup, multiangle solution of the radiative transfer problem. The average charge state and the emission and absorption coefficients of the ionized matter are calculated within the framework of the average atom model (5) under non-LTE conditions. Front and rear side emission spectra, conversion efficiencies and plasma parameters are calculated as a function of time and can be compared directly to experiments.

IV Results

Figure 1 shows the experimental spectra obtained from the diode spectrometer and from the grating spectrograph in a laser shot at 1.06 μm, 3 ns pulse duration and 2. 10^{13} W/cm^2 laser irradiance. Good agreement is found between the results from the two instruments in the sub-keV range. Grating spectrograph results are much smaller in the keV range. This can been accounted for by errors in the film calibration or grating imperfections. Code predictions, assuming a measured focal spot diameter of 200 μm are also shown in figure 1. It is worth to mention that there are no adjustable parameters in the hydrodynamic calculations apart from the heat flux limitation factor that we have set to its standard value of 0.03 at 1.06 μm.

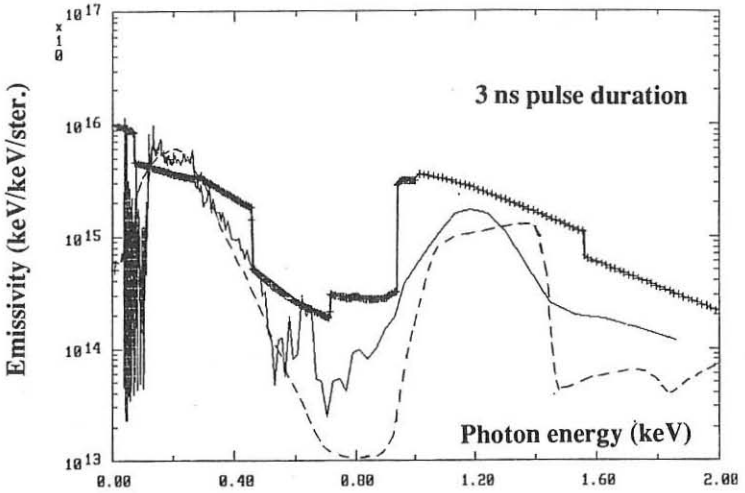

Figure 1 : Diode spectra (heavy line), grating spectra (light line) and code results (dashed line) between 0 and 2 keV for a shot at 2. 10^{13} W/cm^2 and 1.06 μm.

Figure 2 gives the conversion efficiency at 1.06 μm , 0.53 μm and 0.26 μm as a function of laser intensity. Sub-keV conversions are found to increase from 8% to 30 % when the wavelength varies from 1.06 μm to 0.26 μm at 10^{12} W/cm^2 laser irradiance. At larger laser irradiances, conversion efficiencies slightly decrease. Hydrocode results show a stronger influence of plasma reabsorption at higher electron densities. In the keV range, a threshold occurs around 5.10^{12} W/cm^2. Then, the conversion efficiency increases to reach an optimum at about 10^{13} W/cm^2 . This behavior can easily be explained by the minimum temperature of about 300 eV which is needed to produce L-band emitting ions. Code simulations are also presented in figure 2. Experimental conversion efficiencies are well reproduced by the calculations except at 1.06 μm in the keV range where a discrepancy of a factor of 2 occurs. This is due to the poor description of resonance absorption used in the calculations.

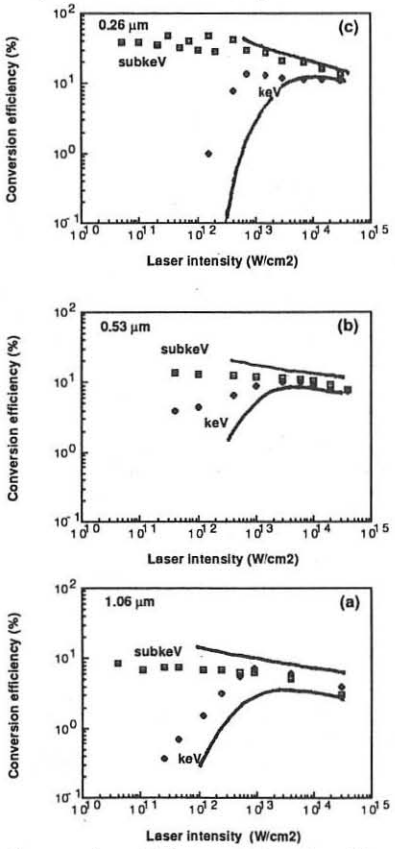

Figure 2 : Experimental conversion efficiency as a function of laser intensity for 1.06, 0.53 and 0.26 μm laser wavelength at 600 ps laser duration. Codes results are given by full lines.

Figures 3a and 3b give the measured conversion efficiency in the sub-keV and the keV range as a function of pulse duration ,respectively. In the sub-keV range, the conversion efficiency increases with pulse duration. The hydrocode predicts an increase of the electron density scale-length at temperatures (~150 eV) where sub-keV emissions take place. keV conversion is more sensitive to electron temperature. Cooling effects by lateral expansion decrease the conversion for very long pulse lengths. We have also shown that a prepulse enhances the conversion efficiency at a given deposited laser energy.

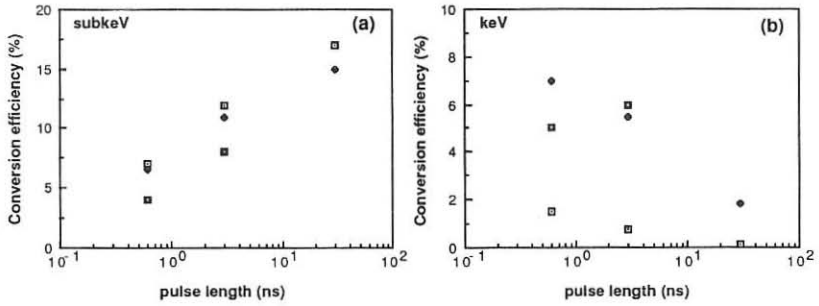

Figure 3 : Conversion efficiency as a function of pulse length at 1.06 μm. light squares : 1.10^{12} W/cm^2, full squares : 1.10^{13} W/cm^2, heavy squares : 1.10^{14} W/cm^2.

V) Conclusion

We have studied experimentally the dependence of X-ray conversion efficiency as a function of laser intensity, wavelength and pulse duration for copper targets. Results are in very good agreement with hydrocode simulations incorporating radiation tranport effects. Conversion efficiencies of more than 30% in the sub-keV range can be obtained at 0.26 μm. Taking into account frequency quadrupling efficiency, X-ray conversion efficiency at 1.06 μm and 0.26 μm are similar. The present study , together with the Z-scaling presented in Ref. 6, can help in designing pulsed, intense X-ray sources for many practical applications such as X-ray lithography and microscopy.

References

1) P. Alaterre, H. Pepin, R. Fabbro and B. Faral Phys. Rev. A34,4184(1986).
2) I. Toubhans, Thèse de Doctorat (Palaiseau,1989).
3) "Laser-plasma Interaction",eds. R. Baliant and J.C. Adam (North Holland, Amsterdam,1982).
4) R. M. More,K. H. Warren, D.A. Young and G. B. Zimmerman Report UCRL 96675 (1987) and Phys. Fluids (to be published).
5) J.P.Geindre and J.C. Gauthier, Report PMI 1971 (1988).
6) M. Chaker, H. Pepin, V. Bareau, B. Lafontaine, I. Toubhans, R. Fabbro and B. Faral

2-D SIMULATIONS OF THE IMPLOSION, COLLAPSE AND STAGNATION OF LASER FUSION SHELLS

S. Atzeni, A. Guerrieri*

Associazione EURATOM-ENEA sulla Fusione, C. R. E. Frascati,
C.P. 65 - 00044 - Frascati, Rome, Italy

INTRODUCTION

We discuss the method, model and first results of 2-D numerical simulations of the entire *history* of gas-filled shells irradiated by laser pulses with long wavelength non-uniformities.

Although this issue has already been addressed in connection with the design of reactor targets [1], or with the interpretation of experimental results [2,3], a complete, clear, and quantitative picture of the relevant phenomenology is still missing [see, e.g., 1 and 4].

In general, the history of a target can be divided into three phases, namely, the acceleration and inertial phase of the implosion (I; $t \leq t_0$; see **Fig. 1**), the shock collapse and reflection (II, $t_0 \leq t \leq t'_0$), and the stagnation ($t'_0 \leq t \leq t_1$). In a previous study [5], we were able to study quantitatively phase I and to get some qualitative information on phase II. At $t \simeq t_0$, however, negative area zones occurred in the mesh of our purely Lagrangian code [6], and the simulations became unreliable.

We have now upgraded our code, by introducing an automatic mesh-rezoning package, which allows us to follow with reasonable accuracy phases II and III of the target implosion.

MODEL

We use the 2-D, quadrilateral-zone, Lagrangian code DUED [6], including single fluid, two-temperature hydrodynamics, flux-limited conductivities, real matter equations of state, nuclear reactions, and ray tracing of the laser light.

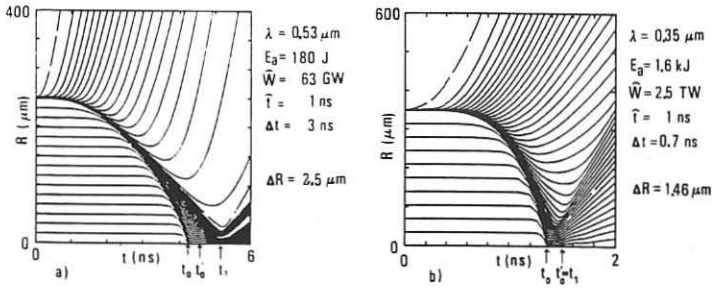

Fig. 1 - Radius vs time history of targets a) and b), respectively

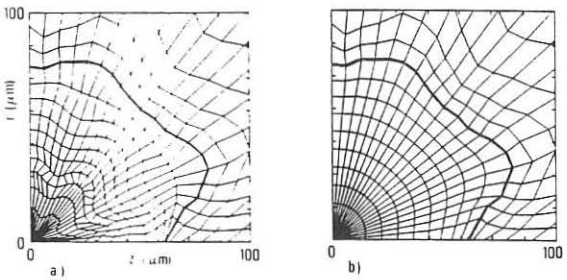

Fig. 2 - Example of mesh rezoning. A new mesh is defined inside the marked line (interface between gas and shell). a) and b) mesh before and after the rezoning, respectively

The rezoning package [7], once a strong mesh deformation has been detected, defines a new mesh and then maps physical quantities from the old mesh to the new one. Grid re-generation is performed separately on the different materials (or regions of a same material) in the target, thus allowing for the interface tracking properties of the Lagrangian approach to be maintained. In the simplest cases of interest, as e.g., in Fig. 2, we only rezone the mesh in the filling gas, no rezoning being needed for the somewhat distorted, but not pathological mesh of the glass shell. The new mesh is generated by a suitably modified form of a variational algorithm [8] allowing us to obtain a compromise between mesh smoothness, orthogonality and volume control [7]. Mapping of the *densities* of the conserved quantities is performed by assuming that each *density* is constant inside a mesh zone, both in the new and in the old mesh, using the scheme of Ref. 9.

PROBLEM SET UP

We simulate D-T gas filled, thin glass shells, and we assume centrally focussed irradiation, with laser intensity perturbation described by a single Legendre mode, with amplitude coefficient C_ℓ, i.e. $C_\ell P_\ell (\cos\theta)$, with ℓ=2-12. We restrict our attention to two sets ((a) and (b), respectively) of laser and target parameters (detailed in Ref. 5; see also Fig. 1), which are chosen to allow for sufficiently general results as well as for their relevance to several laboratory experiments. The respective 1-D R-t evolutions are shown in Fig. 1. Case a) is representative of the *purely ablative regime of implosion* with a long stagnation phase (see Fig. 1a). Case b) has the parameters of an experiment performed at LLE [2] and may be taken as representative of the *stagnation-free* regime of implosion.

RESULTS

During phase I the shell is subjected to a secular deformation, induced by the non uniform irradiation, as clearly shown for a typical case in Fig. 3 (see Ref. [5] for details and parametric studies). In Fig. 4a we plot the relative deformation ε of the gas-shell interface vs the quantity $x^{(\ell)}=(C(t)-1)\Delta I/I$, (for target b) at time t_0, and for several values of ℓ and C_ℓ), where C is the convergence ratio of the interface (ratio of initial to actual radius), and $\Delta I/I$ is the peak-to-valley intensity perturbation. The solid line is the result of a model neglecting any non-uniformity smoothing mechanism [5]. Figure 4b shows that the measured amounts of smoothing agree with a simple model implying steady

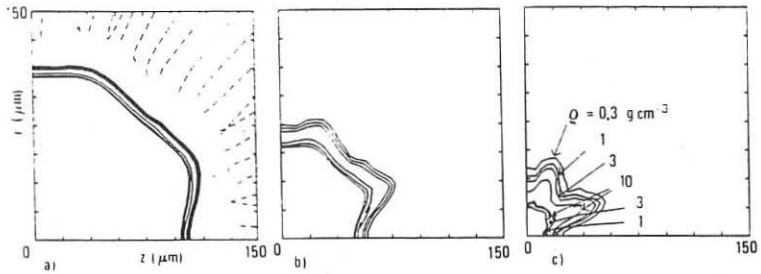

Fig. 3 - Implosion of target a), with $\ell = 8$, and $C_8 = 0.10$. The shell position is indicated by the isodensity contours. a) t = 3.75 ns; b) t = 4.5 ns; c) t = 5.10 ns

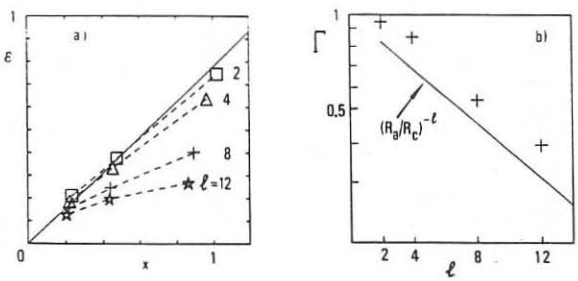

Fig. 4 - (For target b): a) Relative shell deformation vs x; b) smoothing factor vs mode number ℓ; crosses: simulations; solid line: model (R_c/R_a measured at t = 0.9 ns)

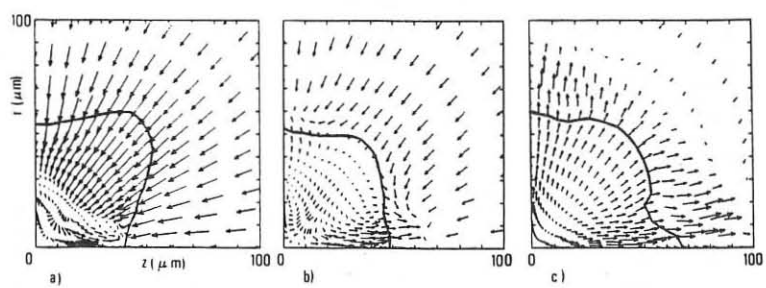

Fig. 5 - Target b) with $\ell = 4$ and $C_4 = 0.10$: Shock reflection and shock-shell collision illustrated by the velocity vectors at selected times. The solid curve is the gas-glass interface a) t = 1.40 ns; b) t = 1.45 ns; c) t = 1.50 ns

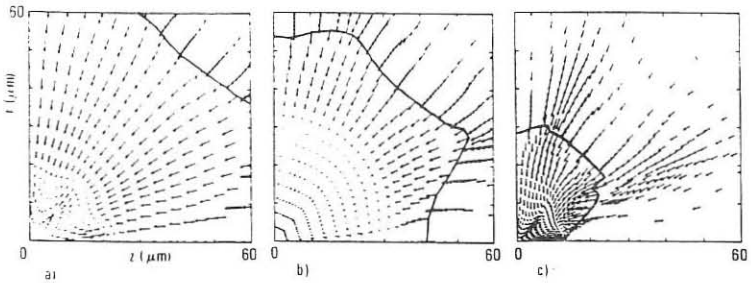

Fig. 6 - Target a) with $\ell = 8$ and $C_8 = 0.10$: shock reflection and stagnation phase. a) t = 4.5 ns; b) t = 4.67 ns; c) t = 5.1 ns

state thermal conduction between critical and ablation radius [5]. Higher ℓ modes are increasingly smoothed.

Higher ℓ modes, on the other hand, are more effective in inducing perturbations of the mass distribution inside the shell, which, in turn may seed unstable modes of the Rayleigh-Taylor instability at the ablation front [5].

When the imploding shock-wave propagating through the filling gas collapses and is reflected at the center (phase II), outwardly directed jets of matter form in correspondence to the maxima of the laser intensity (see Figs. 5 and 6).

For the stagnation phase (III), we have obtained the first qualitative results, illustrated by Figs. 5 and 6. For case b) targets (Fig. 5) there is no real stagnation, but rather, as the reflected shock collides with the shell, the latter is reflected (and considerably distorted by the collision with the highly non symmetric shock). In case a), instead, we observe several reflections of the shock waves in the gas (see Fig. 6) without further substantial distortion of the gas-shell interface.

We are now performing a parametric study of these targets and will also simulate thermonuclear targets to gain a better (and reactor relevant) insight into the processes occurring in phases II and III. The results will be reported in due time.

FOOTNOTE AND REFERENCES

* ENEA Student

[1] R.L. Mc Crory and C.P. Verdon: Proc. of the School and Workshop on Inertial Confinement Fusion (Varenna 6-16 September 1988) Editrice Compositori, Bologna, in press

[2] M.C. Richardson et al.: Phys. Rev. Lett. **54**, 1656 (1986)

[3] H. Takabe: in Proc. of the 19th ECLIM (Madrid, 3-7 October 1988) World Scientific, Singapore, in press

[4] S. Atzeni: Plasma Phys. Controlled Fusion **29**, 1535 (1987)

[5] S. Atzeni: 2-D Studies of Non-uniformly Irradiated spherical Shells, to appear in Laser Particle Beams (1989), see also paper O8-C7 in Proc. of the 19th ECLIM (Madrid 3-7 October 1988) World Scientific, Singapore, in press

[6] S. Atzeni: Computer Phys. Commun. **43**, 107 (1986)

[7] S. Atzeni and A. Guerrieri: to be published

[8] J.U. Brackbill and J.S. Salzmann: J. Comput. Phys. **46**, 342 (1982)

[9] J.D. Ramshaw: J. Comput. Phys. **59**, 193 (1985)

FUSION GAIN CALCULATIONS FOR IDEAL ADIABATIC VOLUME COMPRESSION AND IGNITION WITH 100 MJ HF-LASER DRIVING.

Heinrich Hora, L. Cicchitelli, G. Kasotakis, C. Phipps*, G.H. Miley ** and R.J. Stening.

Department of Theoretical Physics, University of New South Wales,
Kensington, 2033, Australia.

High fusion gains due to ideal adiabatic compression of DT gas filled pellets have now been demonstrated in GEKKO 12 using a pusherless direct drive with high aspect ratio. Thus similarly high gains might be expected with only moderate compression (100 times the solid state) if MJ laser input were available, because volume ignition will then take place. This will provide additional driving from the reaction products and will yield temperature up to 100 keV. Earlier calculations without ignition showed undesirably high optimum temperatures, but a new treatment, using the latest available cross sections, and including ignition, results in an optimum temperature of only 4.5 keV if bremsstrahlung re-absorption is negligible. This result is in agreement with the fact that reaction energy just compensates bremsstrahlung at 4.5 keV. For cases with considerable reabsorption, the optimum temperature drops to 1 keV only, with gains up to 1200 and 80% fuel burn. In view of the low cost 100 MJ HF compact laser system, gains for this laser energy range are reported for DT and for clean fuel reactions.

1. Introduction

The argument against laser fusion in 1980 was the statement by Brueckner [1] that the then best numbers of DT fusion neutrons from Shiva were ten thousand times less than expected from theory. Apart from the change of the scenario by the confirmation from underground test experiments that inertial confinement fusion with energy input of 10 to 100 MJ radiation energy does result in sufficiently high exothermal energy for power production [2], the mentioned factor of ten thousand may now be considered to be overcome by two facts:
(a) The direct driving of the pusher modes for the Shiva experiment could be improved by a factor of about 100 as demonstrated by the Omega laser experiment [3] when using Kato's random phase plate [4].
(b) Pusherless [5] shock free volume compression known as Yamanaka compression of the pellets led to a drastic increase of the neutron gains [6], approximately providing the remaining factor of 100 called for by Brueckner.

The random phase plate (RPP) technique introduced in 1983 [8] and induced spatial incoherence (ISI) [9] as well as broad band laser beams [10] seemed to be a method to overcome the difficulties observed in laser-plasma interaction. Another tool for overcoming these difficulties is the indirect hohlraum drive [11] of Nuckolls, which achieves a quite smooth drive. However the conversion of the laser radiation into x-rays and their 50% use for driving a pellet compression causes a loss by a factor three or more in the gains expected relative to direct drive. The difficulties of the interaction have been shown to be not due to SRS or SBS [12]. We show, on the basis of numerical results at ILE Rochester in 1974 [13], that the pulsating interaction which does describe these difficulties is due to the cyclic appearance

---

* On Sabbatical from Los Alamos Nat. Lab., USA.
** Fusion Studies Lab. Univ. Illinois, Urbana Ill., USA.

and disappearance of a density ripple in the plasma corona caused by the standing wave component of the laser field. The ripple produces a peripheral reflection, followed by hydrodynamic relaxation of the ripples within about 10 psec, subsequent low reflectivity and strong pushing etc. [14]. It can then be directly explained why RPP, ISI and broad band lasers are so successful in achieving smooth interaction.

This paper discusses the mentioned second improvement of laser fusion which arises from pusherless volume compression, as realized experimentally by Yamanaka, Nakai et al [6,7].

2. Volume Compression.

In order to understand the significance of the Yamanaka compression as the realization of the ideal shockfree adiabatic compression of the pellet, reference is given to the results of the sixties for calculating the fusion gain G_o for DT. If an energy E_o is introduced into a sphere of uniform density n_o and radius R_o where n_s is the solid state density and E_{BE} the break even energy,

$$G_o = \left(\frac{E_o}{E_{BE}}\right)^{1/3}\left(\frac{n_o}{n_s}\right)^{2/3} = Cn_oR_o \qquad (1)$$

The result was first published in 1970 [15] and an identical second result in 1974 [16]. The empirical constants involved in these two formulations gave gains which agreed numerically to with a factor of 3. This corresponded to a variation of the break even energy between 1.6 and 50 MJ and of the optimum temperature for which Eq. (1) was formulated, between 10 and 17 keV.

If one assumed that only 25% of the fuel would have been burned the maximum gain would have been near 70 only. This was definitely too low considering the low efficiency of lasers and other losses. Alternatively, the spark ignition concept was introduced in which the laser driven ablation of the pellet results in a sequence of shocks (Guderley scheme) [11] such that a little part of the pellet material in the centre is compressed to 10000 times the solid state at optimum temperature between 10 and 17 keV. Then the fusion reaction triggers a self sustained fusion combustion wave through the surrounding fuel. Very high gains should be expected [17]. The scheme included the rather impossible conditions of 10000 time solid state compression, and left the well known difficulties in understanding the fusion combustion wave open [18]. However, it was considered as the only way to achieve gains higher than the value of 70 predicted by Eq. (1) for the simple adiabatic volume burn, while remaining within sensible experimental conditions.

The attractiveness of the simple volume burn was restored [19] when the alpha self heat apart from the losses by fuel depletion and by bremsstrahlung were included. It was discovered that a volume ignition (like in a Diesel engine) is possible with drastically lower initial temperature and high gains.

3. High Gain, Self-driven Volume Ignition with Selfdriving

Our improvements of the computations of the volume ignition included the following points:

(a) The depletion of fuel, initially included in the number of the reacting atoms only [19], has now been taken into account for the adiabatic compression and expansion hydrodynamics. The corrections are not severe but the model can now be considered as complete with respect to fuel depletion.

(b) The inclusion of bremsstrahlung losses has confirmed that this does not affect the results of Eq. (1) for high values of the optimum burn temperature, but it does become important at the

lower temperatures applying to volume ignition. The re-absorption of bremsstrahlung was included in the following calculations. In contrast to the approximation formula used by other authors, we used a detailed spectral distribution of the bremsstrahlung and its density and temperature dependence to calculate the mean free path of the photons for each time step of the plasma dynamics.

In order to test the results with regard to earlier known facts, Fig. 1 shows the time dependence of the plasma temperature T for the case of an initial density 100 times the solid state with an initial volume of one cubic millimeter. Three cases are given in Fig. 1. The fusion gains G are 2.01; 22.38 and 103.3.

The ignition process can be seen in a very pronounced way not only from the strong increase of the gain G with little increase of input energy, but also from the observed temporal increase of the temperature. In the first case, the temperature is, for a long time, nearly constant because the temperature loss by bremsstrahlung and by adiabatic expansion (sometimes called adiabatic loss) is compensated by the alpha self-heat until a strong drop of the temperature occurs with the fast expansion.

A ten percent higher energy input results in the appearance of ignition instead of the simple burn: the input of heat into the plasma from the alphas produced outweighs the losses and the temperature of the pellet after the input of the driver energy of 12 MJ increases. A maximum temperature of nearly 10 keV is reached before the fast expansion and adiabatic cooling drop the temperature. Increasing the input energy again by about 10 percent results in strong ignition with a maximum temperature of 31 keV and a high gain above 100.

The initial temperatures in the three cases of Fig. 1 are 3.95; 4.31; 4.67 keV respectively. This is just a little bit less than the simple case [20] where the generated fusion energy is equal to the generated bremsstrahlung. Only a small part of the bremsstrahlung is re-absorbed in the pellet. This corresponds to the well known temperature [20] of 4.5 keV where the loss of bremsstrahlung is compensated by fusion energy generation. Lower initial temperatures as low as 1.5 keV were achieved when re-absorption of bremsstrahlung was strong, e.g., for 40 MJ input energy at compression to 1000 times the solid state with fuel depletion of 62%.

While the calculations described in Fig. 1 were only the expansion phase of the reaction, we calculated the full cycle of implosion and expansion together with the volume burn and the volume ignition determining the gain. The results based on fusion cross-sections by Feldbacher et al [21] are shown in Fig. 2.

4. Further Results and Discussions

We extended the computations for the case of the ideal neutron free reaction of hydrogen and boron-11. The inclusion of the bremsstrahlung loss indicated a high initial temperature of 115 keV for the optimum cases of volume burn only. We found cases with input energies in the 100 MJ range in which the temperature increased after burning due to volume ignition. The gains were then in the range between 5 and 10. The calculations were done with the nonrelativistic bremsstrahlung formula. The inclusion of the exact relativistic formula is being evaluated and may result in lower initial temperatures and consequent higher gains.

Use is made from the scheme of the compact HF laser producing 100 MJ broad band pulses for a projected price of $800 Mill. [22]. The basing of fusion reactors on these scales for DT in turn reconfirm the otherwise explored conditions [2] under which inertial confinement fusion power stations may be economically realized in the not too distant future.

References

[1] W. Sullivan, New York Times, 129, Jan. 13, p.42 (1980); [2] W.J. Broad, New York Times, March 21, 1988; [3] R.L. McCrory, Laser Focus, April 1985; [4] Y. Kato, K. Mima et al, Phys. Rev. Lett. 53, 1057 (1984); [5] K. Mima, H. Takabe, and S. Nakai, Oct. 1987

Conf. Rpt., K. Niu ed. (IPP Nagoya, Febr. 1988) p.124, Laser and Particle Beams 7, No. 2 (1989); [6] C. Yamanaka and S. Nakai, Nature 319, 747 (1986); [7] C. Yamanaka, S. Nakai, T. Yamanaka, Y. Izawa, K. Mim, K. Nishihara, Y. Kato, T. Mochizuki, M. Yamanaka, M. Nakatsutam and T. Yabe, Laser Interaction and Related Plasma Phenomena, H. Hora and G.H. Miley eds. (Plenum, New York, 1986) Vol. 7, p.395; [8] K. Mima and Y. Kato, Anomalous Absorption Conf. June 1983; [9] S.P. Obenschain et al., Phys. Rev. Lett. 56, 2807 (1986); [10] Lin Zunqi et al, Laser and Particle Beams 4, 223 (1986); [11] J.H. Nuckolls, Physics Today 35 (no. 9) 24 (1982); [12] R.P. Drake, Laser and Particle Beams 6, 235 (1988); E. Fabre, US-Japan Semin., August 1988, Laser and Particle Beams 7, No. 3 (1989); [13] H. Hora, Laser Plasma and Nuclear Energy (Plenum, New York, 1975), Fig. 7.7a and b; [14] Gu Min and H. Hora (submitted); [15] H. Hora and D. Pfirsch, Conf. Digest 6th Int. Conf. Quantum Electronics (Kyoto 1970), p.10; [16] R.E. Kidder, Nuclear Fusion 14, 797 (1974); [17] J. Meyer-ter-Vehn, Nuclear Fusion 22, 561 (1982); [18] L. Cicchitelli et al., Laser and Particle Beams 6, 163 (1988); [19] H. Hora and P.S. Ray, Z. Naturforsch 33A, 890 (1978); [20] S. Glasstone and R.H. Loveberg, Controlled Thermonuclear Reactions (New York, 1960); [21] W. Feldbacher and M. Heindler, Nucl. Instr. Meth. A271, 65 (1988); [22] C. Phipps, Jr., 3rd Int. Conference on Lasers, Xiamen 1987.

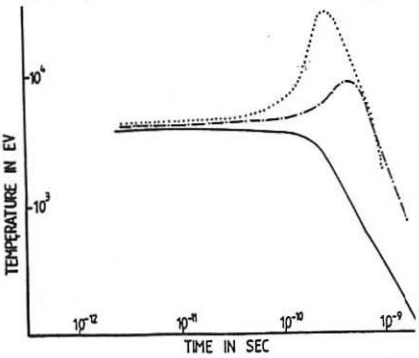

Fig. 1: Dependence of the temperature T of a pellet on the time t at initial compression to 100 times the solid state and initial volume of 1 mm^3. For the cases of the (fully drawn; dashed; dotted) lines respectively, the input energies were 11; 12; 13 MJ.

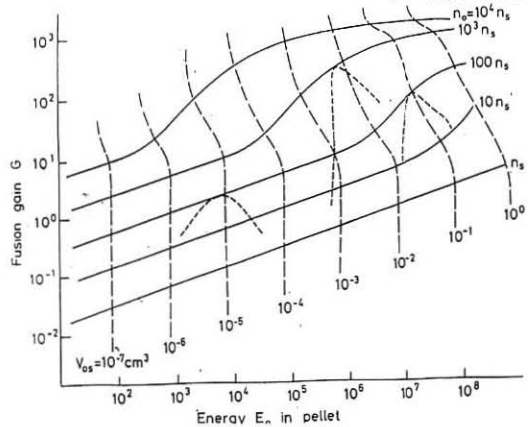

Fig. 2: Optimum fusion gains G for DT related to the energy E_o put into the pellet for various densities n_o. V_{os} is the solid state volume of the pellets.

HYDRODYNAMICS OF LAYER STRUCTURED TARGETS IMPINGED BY INTENSE ION BEAMS

J. Dávila y A. Barrero

Departamento de Ingeniería Energética y Mecánica de Fluidos
E.T.S.I. Industriales. Universidad de Sevilla. Spain

To minimize the energy loss in the corona outflow, a layer structured spherical hollow shell has been proposed to be used as target in inertial confinement fusion. For ion beam drivers, the major part of the beam energy is absorbed in the middle layer, which is called either absorber or pusher. The outer layer, called tamper, slows down the outward expansion of the absorbed low density region. The materials of the tamper and pusher are usually lead and aluminium, respectively, and the fuel (deuterium-tritium) is located in the inner layer. The knowledge of the hydrodynamics of the interaction of an intense beam with a structured target is then an essential point in order to achieve break-even conditions in ion-beam fusion.

In a recent paper, Fernández and Barrero (1986) found that the hydrodynamics of the ion beam-plasma interaction depends on a dimensionless number,

$$\delta = 2\pi^3 e^{11} Z_b^5 (\ln \Lambda)^3 I_o n_o^2 \tau^3 m_b^3 m_e^{-3} m_i^{-1} E_o^{-5} \quad , \qquad (1)$$

which is the ratio of pressure to inertial forces and contains the basic beam and plasma parameters; Z_b, m_b, E_o, I_o and τ are atomic number, particle mass, maximum energy per nucleon, current intensity per unit area, and pulse duration respectively, m_i n_o, $\ln \Lambda$, e and m_e are the undisturbed, mass density, Coulomb logarithm and electron charge and mass.

Two asymptotic hydrodynamic regimes appear for small and large values of the parameter δ. For δ small, the beam energy heats the target without developing significant convection there, while for δ large thermal and kinetic energies of the material are comparable. The asymptotic analysis showed that for $\delta >> 1$ there are two different flow regions: a compression zone separated by a shock from the undisturbed material, and a region where beam absorption occurs. A well defined ablation surface lies in between.

These ideas may be applied to describe the hydrodynamic behaviour of both tamper and absorbed. As it may be seen from (1) for a given beam pulse (E_o, I_o and τ given) the value of the parameter δ is different in the tamper than in the absorber. The relation between these two values of δ is

$$\delta_{Al} = \gamma^{-5} \left[\frac{(n_o)_{Al}}{(n_o)_{Pb}}\right]^2 \frac{(m_i)_{Pb}}{(m_i)_{Al}} \delta_{Pb} = .26\, \delta_{Pb}/\gamma^5 >> \delta_{Pb}$$

where γ is the fraction of the total beam energy absorbed by the target. -- For example, for a protom beam (1 MeV, 10^6A cm^{-2} and 20 ns) one has $\delta_{Pb} \cong .18$ and $\delta_{Al} \cong 4.74$ if γ=1 is assumed. For heavy ion beams, (uranium, 500 MeV, 10^4 A cm^{-2}, 20 ns) one has $\delta_{Pb} \cong .24$ and $\delta_{Al} \cong 6.15$ (if a value of 50 is taken for the effective beam charge). A value equal to 6 has been arbitrarily taken - for the Coulamb logarithm in the above calculations.

Accordingly, with the asymptotic regime $\delta << 1$, there will not be convection in the tamper except in a very thin layer (compared with the tamper thickness) where the plasma expands to the vacuum. The momentum equation - for the beam is

$$m_b n_b v_b dv_b/dx = - R_1 - R_2 \quad , \tag{2}$$

where the momentum per unit volume and time transferred from the beam to - both free and bound electrons is respectively given by[2]

$$R_1 = a \ln \Lambda \, Z_i \frac{n \, n_b}{v_b^2} \Phi \left[v_b/(2 k T_e/m_e)^{1/2} \right] \quad , \tag{3}$$

$$\Phi(y) = 2\pi^{-1/2} \left[\int_o^y \exp(-t^2) dt - y \exp(-y^2) \right] \quad , \tag{4}$$

and

$$R_2 = a (Z-Z_i) \frac{n \, n_b}{v_b^2} \ln (2 m_e v_b^2/\bar{I}) \quad , \tag{5}$$

$a = 4\pi e^4 Z_b^2/m_e$ and $\bar{I}$ is the mean ionization potential of the tamper. Using a mean ionization degree, which is assumed to be constant, neglecting the - logarithmic dependence in both R_1 and R_2, and assuming that functional Φ is equal to 1, equation (2) may be integrated. If L is the tamper thickness - the beam velocity at the tamper-absorber interface is given by

$$v_b(o,t) = \left[\frac{2 E_b(t)}{m_b} \right]^{1/2} \left[1 - \left(\frac{m_b}{2 E_b(t)} \right)^2 A L \right]^{1/4} \quad \text{for } t \geq t_o \quad , \tag{6}$$

where $A = a\left[Z_i \ln \Lambda + (Z-Z_i) \ln (2m_e v_b^2/\bar{I})\right]/m_b$ and t_o is obtained from the condition $2E_b(t_o)/m_b = (A L)^{1/2}$; notice that the origin has been taken at the interface. For typical values of interest in ion beam fusion the maximum beam energy E_o satisfies the inequality $E_o >> m_b (A L)^{1/2}$ so that the - lag-time t_o is much smaller than the pulse duration τ and consequently -- $v_b(o,t) \cong (2 E_b(t)/m_b)^{1/2}$.

Now, if one considers planar geometries and elastic collisions to simplify the analysis it is easy to show that flow in the absorber becomes self-similar if the beam parameters depend on time as $E_b = E_o (t/\tau)^{2/3}$ and $I_b = I_o (t/\tau)^{1/3}$. The hydrodynamics self-similar equations are

$$\bar{n}_b \, u_b = 1 \quad , \tag{7}$$

$$\frac{du_b}{d\xi} = - \frac{\bar{n}}{u_b^3} \, \Phi \, (\beta \, u_b / \theta^{1/2}) \quad , \tag{8}$$

$$\frac{d\bar{n}}{d\xi} = \frac{\bar{n}}{\xi - u} \frac{du}{d\xi} \quad , \tag{9}$$

$$\bar{n} \left[u - 4(\xi - u) \frac{du}{d\xi} \right] = - \delta \frac{d}{d\xi} \left[(Z_i + 1) \, \bar{n} \, \theta \right] \quad , \tag{10}$$

$$\bar{n} \left\{ (Z_i + 1)\theta + \frac{4u^2}{3\delta} - 2(\xi - u) \frac{d}{d\xi} \left[(Z_i + 1)\theta + \frac{4u^2}{3\delta} \right] \right\} =$$

$$- \frac{4}{3} \frac{d}{d\xi} \left[(Z_i + 1) \, \bar{n} \, u \, \theta \right] - Z_i \frac{du_b^2}{d\xi} \quad ; \tag{11}$$

the self-similar dimensionless variables (beam density and velocity $\bar{n}_b$ and u_b and plasma density, velocity and temperature $\bar{n}$, u and θ) were defined in Ref. 1.

System (7)-(11) must be solved subject to the following boundary conditions:

* for $\xi \geq \xi_f$ (ξ_f being the boundary with the undisturbed aluminium)

$$\bar{n} = 1 \quad , \quad u = \theta = 0 \tag{12}$$

* at $\xi = 0$ (the tamper-absorber interface)

$$u = 0 \quad , \quad \bar{n}_b = u_b = 1 \tag{13}$$

The asymptotic solution, for $\delta \gg 1$, of system (7)-(11) with conditions (12) and (13) yields the profiles of all variables in the absorber - (see figures 1 and 2). In particular, one finds that a shock propagates into the undisturbed medium with a velocity $v_f \cong (W_o / n_o m_i)^{1/3} \, (t/\tau)^{1/3}$; where $W_o = E_o I_o / e Z_b$ is the maximum beam power per unit area. There is a well defined ablation surface moving behind the shock with a velocity $v_a \cong 0.82 \, v_f \cong 0.82 \, (W_o / n_o m_i)^{1/3} \, (t/\tau)^{1/3}$. The pressure at this surface (the ablation pressure) takes the value $P_a \cong 4.08 \, (m_i n_o)^{1/3} \, W_o^{2/3} \, (t/\tau)^{2/3}$ (for a maximum power of 10^{12} W cm^{-2} one obtains a shock velocity of 1.5×10^4 m s^{-1} and an ablation pressure of 2.6×10^{12} Pa). Between the ablation surface and the target-absorber interface there exists a very low density region of high temperature where the beam energy absorption occurs. Therefore, the absorber may be divided in two zones of comparable extent: the compression region behind the shock which acts as a pusher followed of the low density region that behaves as the absorber itself. Clearly, the solution presented

here will remain valid until the shock reaches the deuterium-tritium layer.

REFERENCES

(1) FERNANDEZ A. and BARRERO A. (1986) Plasma Phys. Contr. Fusion 28, 989.

(2) MELHORN T.A. (1981) Sandia National Lab. Report SAND 80-0038.

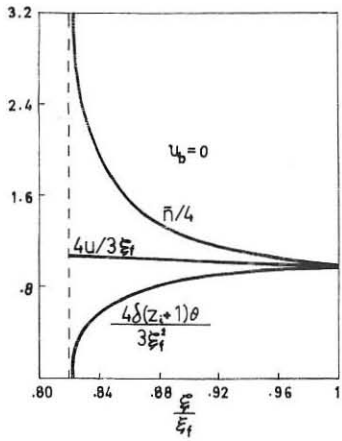

Figure 1. Self-similar density $\bar{n}$, velocity u, and temperature θ vs. distance ξ in the compression region.

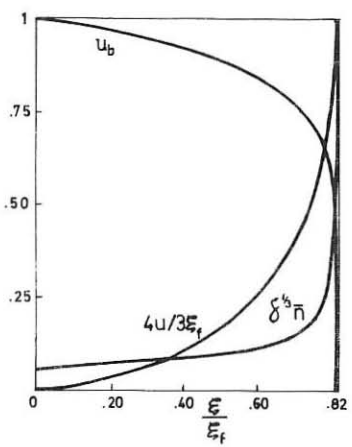

Figure 2. Self-similar plasma density $\bar{n}$, velocity u, and beam velocity u_b vs. distance ξ in the absorption region.

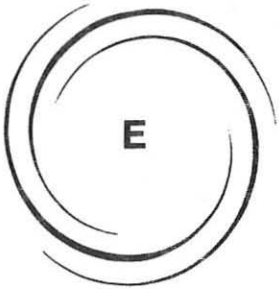

PLASMA EDGE PHYSICS

IMPURITY PRODUCTION AND TRANSPORT AT THE JET BELT LIMITER

C S Pitcher*, G M McCracken***, P C Stangeby** and D D R Summers

Joint European Torus, Abingdon, Oxon OX14 3EA, UK

* Canadian Fusion Fuels Technology Project, Toronto, Canada
** JET and University of Toronto Institute for Aerospace Studies, Canada
*** Culham Laboratory UKAEA, Abingdon, UK

1 Introduction

Under certain operating conditions in JET the impurity content of the discharge can be high, thus reducing the fusion reaction rate through the dilution of the hydrogenic fuel. The dilution in most discharges is predominantly due to carbon impurities [1]. In order to understand how carbon impurities are produced and transported into the plasma, detailed measurements have been made with a CCD camera looking at the graphite limiter with interference filters centered on intense spectral lines of the low ionization states of carbon (C I, C II, C III) as well as the fuel species ($D\alpha$) and helium (He I).

2 Experiment

The viewing geometry is sketched in the upper portion of Fig. 1. The CCD camera is mounted at the top of the torus and looks at the bottom belt limiter. The boundary plasma conditions are determined with Langmuir probes built into the belt limiter and with a fast reciprocating probe (RP) at the top of the torus [2]. The built-in probes give the time dependence of the electron density and temperature in the edge plasma while the RP provides radial profiles from the wall to several centimetres inside the last closed flux surface (LCFS). The boundary plasma conditions obtained with the probes are essential in the interpretation of the spectral emission observed around the limiter.

3 Spatial Distributions

Figure 1 shows the spatial distributions of C I, C II, C III, $D\alpha$ and He I observed in a discharge with Ohmic heating only, a plasma current $I_p = 3.1\,MA$, toroidal magnetic field $B_T = 2.3T$ and volume-average density $\overline{n_e} = 1.5 \times 10^{19} m^{-3}$. In this discharge the plasma is limited by the lower belt only and helium is present as a trace impurity. In general, all of the emissions are centered about the magnetic field tangency point. The $D\alpha$ and He I distributions appear strikingly similar with both having their maxima at the tangency point. This is in contrast to the C I distribution which has its maximum shifted away from the tangency point to the ion drift side. The C II and C III distributions show a progressive broadening and shift in the ion drift direction.

The transport of the carbon atoms and ions originating from the limiter has been modelled using the two-dimensional impurity transport code LIM [3]. Carbon atoms are assumed to be produced by physical sputtering and are launched from the limiter surface into a plasma grid. The plasma density ($n_e(r)$) and temperature ($T_e(r)$) profiles in the boundary plasma are specified in the code from probe measurements and are approximated by exponential functions.

Once ionized, the C^+ ion is heated by the background plasma and starts to disperse. The code tracks the dispersal of the ions along and across the magnetic field lines, taking into account the effects of ionization to higher stages, heating, classical parallel diffusion and anomalous cross-field diffusion. When the impurity ion densities in the vicinity of the limiter are determined, the line of sight integrations of the emitted radiation are calculated using the radiating efficiencies of the atoms and ions [4].

Results from the code appear in Fig. 2. The following SOL parameters are assumed by the code; $\lambda_T = 17mm$, $\lambda_n = 6mm$, $T_e(a) = 60eV$ and $n_e(i) = 2n_e(e) = 1.5x10^{18}m^{-3}$. These values are consistent with the RP measurements allowing for the compression of the magnetic surfaces from the probe position to the limiter. The higher density on the ion drift side of the limiter is required to reproduce the asymmetric C I distribution obtained experimentally. Further, to obtain the observed drift of the C II and C III, the background plasma is assumed to have a flow velocity of $10^4 m/s$ (Mach number ~ 0.1) in the ion drift direction. The carbon ions thus appear to be swept in the ion direction by friction associated with a background plasma flow.

4 Particle Fluxes

The experimental photon fluxes for the above conditions have been converted with the aid of theoretical photon efficiencies at $T_e = 50eV$ into total particle influxes. The error in this conversion is estimated to be a factor of ~ 2. Within this uncertainty, the C I, C II and C III influxes are similar and are approximately $\sim 4x10^{20} carbons^{-1}$, compared with the total deuteron influx of $\sim 4x10^{21} Ds^{-1}$. The LIM simulation gives C I, C II and C III influxes that are in reasonable agreement with these values. The observed effective yield appears to be high $\Gamma_C/\Gamma_D \sim 0.1$ but, within experimental error, can be explained by deuteron and carbon physical sputtering.

The fact that the fluxes of the low ionization states of carbon are similar means that negligible scrape-off layer screening is occurring for these ionization states resulting in little prompt redeposition of impurities. This is predicted by the code and to be expected, since the SOL in low density (Ohmic) boundary plasma conditions is nearly transparent to sputtered carbon atoms.

5 ICRH Power Scaling

As the input power is increased through the application of ICRH the central density of the plasma increases without external gas puffing. This behaviour is shown in Fig. 3 for well-conditioned 3.3 MA, 3.4 T discharges. The resulting edge density rise is somewhat greater, being roughly proportional to the total input power. The increase in density is such that the electron temperature in the boundary remains constant at $T_e(a) \sim 55eV$. Similarly, λ_n (22 mm) remains approximately constant as measured by the RP, as does Z_{eff} (2.3), and the radiated power fraction ($P_{rad}/P_{tot} \sim 0.4$). The carbon sputtered from the limiter, as measured by the C I, increases roughly in proportion to the edge density (Fig. 3). This is expected since a constant electron temperature implies a constant sputtering yield and a constant photon efficiency for the radiating atoms. Similar results are obtained in reference [5].

6 High Power Operation

As shown by Fig. 3, the power scaling of impurity production at the limiter is relatively simple, the sputtered carbon flux is proportional to the edge density which is proportional to the total input power. During high power operation, however, this scaling breaks down as enhanced carbon erosion occurs at "hot spots" that appear at the limiter tile edges, typically with an area of $\sim 10 cm^2$. In Fig. 4 the C III emission associated with a single hot spot on the lower belt limiter and the edge plasma conditions as measured by the built-in Langmuir probes are shown as a function of time. On the application of ~ 28 MW of combined ICRH and NBI heating the edge density rises and the electron temperature remains constant, as observed at lower powers. The C III emission rises in proportion to the edge density up to a point, ~ 0.5 s after the start of the heating, where the signal abruptly rises and saturates. The temperature of the hot spot at this time had risen to approximately 1600 C as estimated from the black-body emission measured with the CCD camera. As a result of the massive influx of carbon from this and other locations, the discharge detaches, the total radiation abruptly jumps from ~ 40% to ~ 100%, and the edge density and temperature drop significantly. Once the heating power is reduced the discharge re-attaches and the edge signals and radiated power revert to more typical values. These observations taken in limiter discharges are consistent with measurements in high-power X-point and inner wall discharges.

From the C III observation it appears that enhanced erosion is occurring at ~ 1600 C probably due to radiation-enhanced sublimation [6]. Unfortunately, the majority of the limiter surface is not observed and it may be that some spots are hot enough for thermal sublimation to be important.

7 Conclusions

Dilution in JET plasmas can be serious and thus the production and transport from a major source of these impurities, the limiter, has been studied. The spatial distributions of the C I, C II and C III have been modelled with a two-dimensional Monte Carlo code and are in reasonable agreement with experiment. Little prompt redeposition at the limiter appears to be occurring in Ohmic discharges with most of the atoms being ionized on closed field lines and thus free to disperse and contaminate the plasma. The application of auxiliary heating has little effect on the boundary except to increase the density and thus the limiter sputtering in proportion; this results in a constant Z_{eff} in the centre of the discharge. During high power operation, isolated "hot spots" on the limiter reach temperatures of > 1600 C and appear to emit carbon at an enhanced rate, consistent with radiation enhanced sublimation.

References

1. K Behringer et al, J N Mat 163-165 (1989) to be published.
2. S K Erents et al, J N Mat 163-165 (1989) to be published.
3. P C Stangeby et al, JET-P(87)61 and Nucl Fusion (to be published).
4. K Behringer, J N Mat 145-147 (1987) 145.
5. M F Stamp et al, these proceedings.
6. J Roth, J N Mat 145-147 (1987) 87 and private communication.

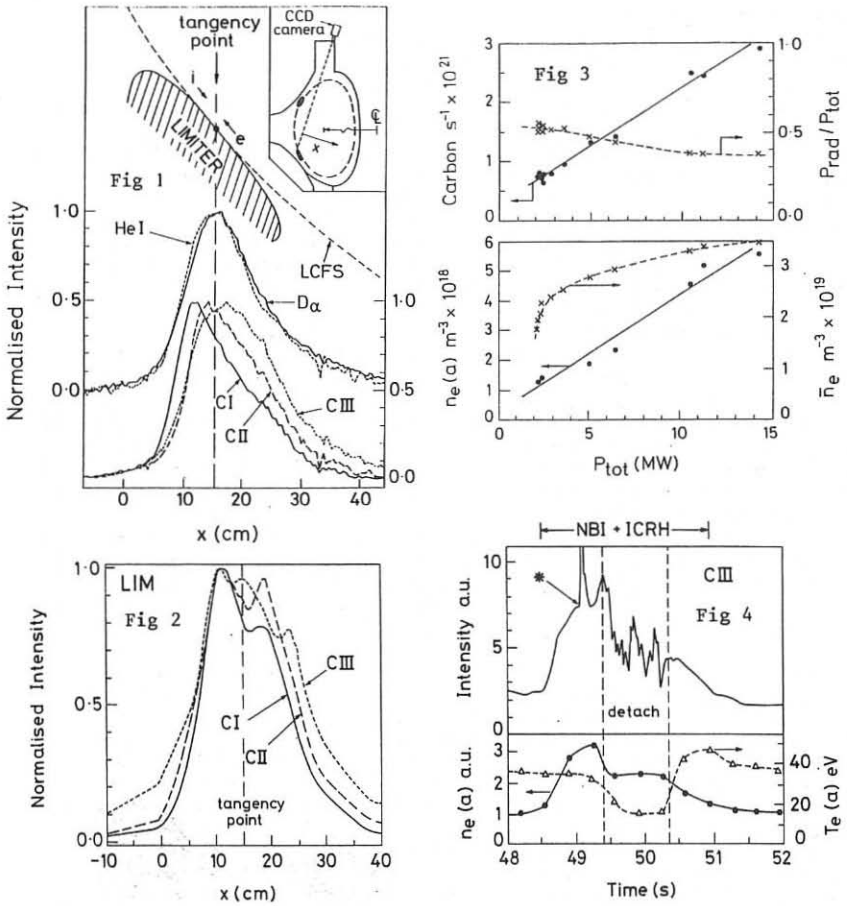

Fig. 1 Spatial distributions of the low ionization states.

Fig. 2 Spatial distributions of C I, C II and C III as predicted by the LIM code.

Fig. 3 The ICRH power scaling of the carbon influx, the radiated power fraction P_{rad}/P_{tot}, the edge density $n_e(a)$ and the volume-averaged density $\bar{n}_e$.

Fig. 4 The C III intensity associated with a hot spot on the lower belt limiter and the edge plasma conditions during ~ 28 MW combined heating. $I_p = 5MA$, $B_T = 3.2T$, discharge balanced between upper and lower limiters. "*" denotes hot spot temperature ~ 1600 C.

SOL-PLASMA TEMPERATURES OF T-10 OBSERVED WITH LANGMUIR PROBES

A.Herrmann, M.Laux, P.Pech, H.-D.Reiner

Central Institute of Electron Physics, 1086 Berlin, GDR

Langmuir probes of different type are used to investigate the scrape-off layer (SOL) of T-10 for several years now. Radial profiles as well as temporal evolutions of SOL-plasma density n and electron temperature T_e were obtained at different locations in the vessel and for a variety of discharge conditions [1-3]. The exponential character of the density profiles was established [1,2] and influences of different disturbances like auxiliary heating or pellet injection were studied additionally [3,4]. As a further step the SOL parameters were compared to results of other diagnostics as the line-averaged central density [5] or impurity fluxes to a deposition probe [6].

Despite the fact that T_e is affected in some cases [2] the majority of the interpretations concentrate on density effects in the SOL up to now, because the evaluation of T_e from measured UI-characteristics is less reliable and very often the observed T_e varies not more than 50% (even after strong disturbances). Consequently, it is the aim of this paper to concentrate on T_e effects and to discuss attempts using the shape of the characteristics for an estimation of T_i/T_e.

It is well known [7] that in tokamaks the evaluation of T_e by an exponential fit of a measured single probe characteristics can be misleading because the strong magnetic field brings about remarkable deviations of the electron current from a simple exponential law at probe potentials U_p above the floating point U_f (Fig.1). A simple restriction to potentials $U_p \leq U_f$ meets the difficulty that U_f itself is a parameter resulting from the fit. Accordingly, the new U_f obtained during every fit gives rise to a change of the set of useful UI-points thus suggesting a self-consistent procedure. Applying such a procedure to experimental characteristics from the SOL of T-10 the parameters were found to react very sensitive to the sucessive changes of the point set. Table I summarizes typical examples of the parameter behaviour reaching from fast convergence to limiting cycles.

From this more methodical result it can be concluded that a consistent and converging procedure should be choosen to derive physically reasonable temperature values from single probe characteristics measured in the SOLs of tokamaks.

On the other hand an attempt was made to extract additional physical information out of the distorted part of the characteristics. Assuming an electron current reduction due to the magnetic field [8] and following the ideas of [9] the potential dependence of the ratio of the electron current to the ion saturation current can be calculated with a

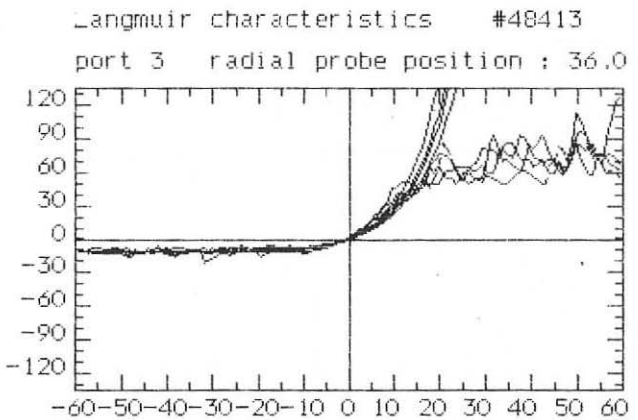

Fig.1 UI-characteristics (-60V <= U_p <= +60V,I in arbitrary units) of a single Langmuir probe in the time intervall 480 to 540 ms during the stationary phase of a T-10 -discharge. The figure shows the saturation of electron (I_e, right branch) as well as ion current (I_s, left branch) with a ratio of about 7:1 (much lower than the expected 60:1). From a simple log-I-fit in the range -20 V <= U_p <= +20 V electron temperatures of 7.6, 8.3, 8.6 and 9.2 eV are obtained for the four characteristics (see exponential curves). The iteration procedure restricted to values below U_f gives quite different temperatures ranging from 3.5 to 14.7 eV.

reduction factor r and T_i/T_e as parameters. If the saturation of this current ratio at high (positive) potentials U_p is observed experimentally, one of the parameters, say r, can be eliminated and the shape of the curve is determined by T_i/T_e only. Therefore T_i/T_e can be choosen to fit the experimental values of $(I-I_s)/I_s$. Unfortunately, this reverse conclusion is in practice not unambiguous taking the experimental uncertainties into account and the sensitivity of the shape to changes of T_i/T_e differs remarkably for different values of T_i/T_e. Nevertheless, in several cases a good fit of the experimental points by reasonable model parameters was achieved (Fig. 2). In all those cases T_i/T_e was found to be larger than 3, probably even larger than 10. Using the typical electron temperatures just below 10 eV this points to ion temperatures of roughly 100 eV in the SOL of T-10 in agreement with earlier estimates from investigations of the lattice damage of Si single crystals and D_2^- desorption experiments with C samples exposed to T-10 shots.

Applying the consistent and converging procedure mentioned above typical effects of ECRH on T_e in the SOL of T-10 were investigated as an example using five single probes at essentially different locations. Probes 1-4 are two pairs of directional tips covered with an isolating

Table I: Convergence behaviour of U_f and T_e in the iteration procedure

Iteration step	fast converg.		converging		lim. cycle	
	U_f/V	T_e/eV	U_f/V	T_e/eV	U_f/V	T_e/eV
1	4.7	17.6	0.5	11.5	3.1	12.0
2	7.5	21.1	9.2	22.0	1.0	8.8
3	7.7	21.8	2.7	16.5	5.2	13.5
4	7.7	21.8	6.3	19.1	0.3	8.3
5	7.7	21.8	3.8	17.1	9.0	16.6
6	7.7	21.8	5.5	18.5	0.8	8.7
7	7.7	21.8	4.3	17.5	5.2	13.5
8	7.7	21.8	4.9	18.0	0.3	8.3
9	7.7	21.8	4.9	18.0	9.0	16.6
10	7.7	21.8	4.9	18.0	0.8	8.7

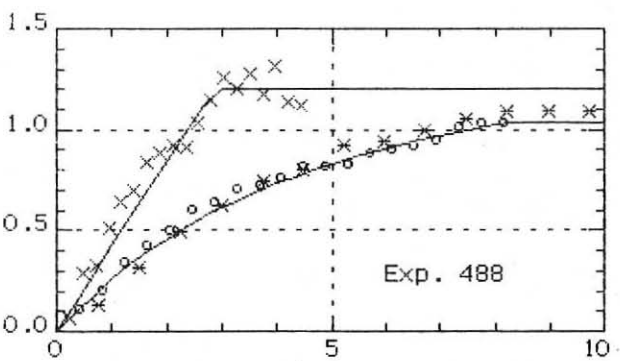

Fig.2 Logarithmic current ratio $(I-I_s)/I_s$ as a function of normalised probe potential $(U_p-U_f)/kT_e$ and calculated curves with T_i/T_e =14, r= 112 , I_e/I_s =16.04 (upper curve) and T_i/T_e =12, r=1.613, I_e/I_s =10.79 (lower curve).

layer on either its electron- or ion-side. The pairs were situated toroi-dally 90 degrees to the electron side of the main limiter section and poloidally mounted at the top and the bottom of the machine, respectively. Probe no. 5 was an omnidirectional tip introduced into the main limiter port from below and poloidally neighbouring the rail limiter plate. In the typical heated T-10 discharge about 2 MW ECRH-power was applied from the 420th millisecond on using 11 gyrotrons at all four main ports of the vessel.

Compared to the preceeding pure ohmic phase (before 420 ms) a

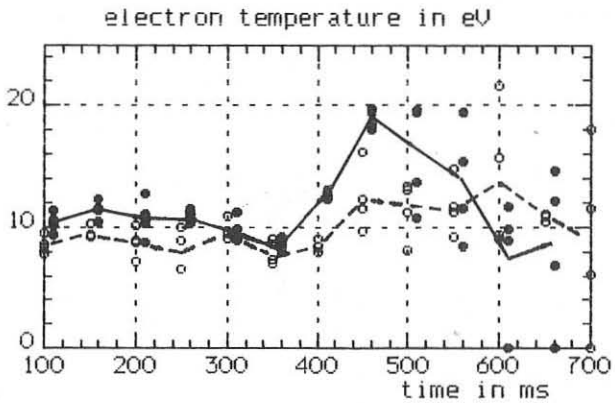

Fig.3 Rise of T_e at the onset of ECRH (420 ms) averaged over four comparable tokamak pulses. At probe 1 (full circles) pointing to the ion side an approximate doubling of T_e was observed whereas at probe 2 (open circles) pointing to the electron side the rise reaches only 30% .

significant rise of T_e with the onset of the heating pulse was detectable at all five probes, but the effect is differently pronounced (Fig. 3). There were clear differences between tips situated at the same position and pointing into different toroidal directions, but these relations are contradictory at the top and the bottom of the vessel. Therefore it can be concluded that concerning the T_e-rise initiated by ECRH the SOL of T-10 is directional as well as poloidally structured at a fixed toroidal position.

The authors are indebted to the T-10 staff for making the experiments possible. The helpfull discussions and the technical support by V.Vershkov, A.Chankin and S.Grashin are gratefully acknowledged.

References:

[1] K.F.Alexander et al.,Int.Conf.on Plasma Phys.,Lausanne 1984,II P25-1
[2] M.Laux et al.,Proc. 12th Europ.Conf.on Contr.Fus. & Plasma Phys., Budapest 1985,II p.551
[3] D.Hildebrandt et al.,Proc. 12th Europ.Conf.on Contr.Fus. & Plasma Phys., Budapest 1985,II p.615
[4] D.Hildebrandt et al., Contr. Plasma Phys., Vol. 28 (1988) 85
[5] K.F.Alexander et al., Nucl. Fusion, Vol. 26 (1986) 1575
[6] M.Laux et al., 8th PSI Conf., Julich 1988, poster A 25
[7] J.A.Tagle et al., Plasma Phys. and Contr.Fusion, Vol. 29 (1987) 297
[8] D. Bohm et al., Characteristics of Electrical Discharges in Magnetic Fields, 1949
[9] P.C. Stangeby, J. Phys. D, Vol.15 (1982) 1007

DIVERTOR PLASMA CHARACTERISTICS DURING H-MODE IN JFT-2M TOKAMAK

I.Nakazawa*, T.Shoji, H.Aikawa, K.Hoshino, S.Kasai, T.Kawakami, H.Kawashima, T.Kondoh**, H.Maeda, T.Matsuda, H.Matsumoto, Y.Miura, M.Mori, C.R.Neufeld***, K.Odajima, H.Ogawa, T.Ogawa, H.Ohtsuka, S.Sengoku, N.suzuki, H.Tamai, Y.Uesugi, T.Yamamoto, T.Yamauchi, O.Hanawa, K.Hasegawa, A.Honda, I.Ishibori, Y.Kashiwa, M.Kazawa, K.Kikuchi, H.Okano, E.Sato, N.Seki, T.Shibata, T.Sihiina, K.Suzuki, T.Tani, T.Tokutake and S.Uno

Japan Atomic Energy Research Institute
Tokai-mura, Naka-gun, Ibaraki, 319-11, Japan
* on leave from Mitsubishi Electric Co., Tokyo, Japan
** on leave from University of Tsukuba, Ibaraki, Japan
*** on leave from Hydro-Quebec, Varennes, Quebec, Canada

1. Introduction and experimental set up

The JFT-2M [1] tokamak has capability of elongated limiter and open divertor discharges, and in both configurations the high confinement mode(H-mode) has been observed [2]. In this paper, a detail measurement of the plasma at divertor was performed and the single null divertor properties are discussed. A single null divertor plasma (see fig.1) is with a major radius 1.31m and a minor radius of axb=0.28x0.39m, a distance between the null point and a divertor plate (divertor length) is 9cm. Toroidal magnetic field is 1.27 T and plasma current is 230 kA. The divertor plates are made of graphite, and also the inside wall of vacuum vessel are covered with graphite tiles. Hydrogen neutral beams with each maximum power of 0.8MW are injected tangentially (balanced co- and counter-injection).

The divertor plasma is measured by using single Langumir probes. Fourteen probes are set on the divertor plates in the poloidal direction (see fig. 1), supplied saw-tooth voltage from -80v to 80v in the interval of 5ms simultaneously. Electron temperature (T_{ed}), electron density (n_{ed}), space and floating potential are calculated by fitting exponential curve to obtained probe voltage-current curve for each channels. Temporal behavior can be measured during 200ms (40 temporal points).

2. The property of divertor plasma

2.1 Ohmic heating phase

The peak values of T_{ed} and n_{ed} at ohmic phase are plotted verses main plasma density (n_e) in figure 2. By changing the direction of toroidal magnetic field (B_T), ion and electron sides can be exchanged. When the direction of B_T is counter-clock-wise (CCW) in the top view of JFT-2M, inner divertor is to be "ion side". At lower n_e, both inner and outer divertor plasma densities increase with n_e, and their temperatures decrease with n_e. However, at higher n_e, the densities begin to decrease and the temperatures begin to rise up with n_e. In this region, particle flux into

divertor does not increase with proportional to n_e, since some instabilities occurred or neutral particles built up. Dense and cold divertor plasma is realized more easily at the ion side than the electron side.

2.2 NBI heating phase

The behavior of main plasma and the time evolution of ion saturation current (I_s) (CCW's) are shown in figure 3-1. NBI power (total 1.3MW) is added into main plasma at 700ms during 200ms. L-H transition occurs at 710ms. The thershold heating power needed for L-H transition is 290kw (CCW) and 480kw (CW), also it is 560kw in double null plasma. Since the confinement of main plasma is improved, I_s decreases quickly. Also H-H transition [3] occurs at 820ms, and then I_s decreases again.

The spatial and temporal behaviors of the obtained T_{ed} and n_{ed} are shown in figure 3-2 (a), (b) respectively. T_{ed} at outer divertor (el. side) is higher than at inner's . On the other hand, inner's n_{ed} is larger than outer's. This results correspond to the facts that I_s at inner is larger than outer's and I_s*T_{ed} (heat flux) at inner is much smaller than outer's (see fig. 3-3). From figure 3-2, 3-3, the width which divertor plate receives heat flux does not much change temporally.

The property of divertor plasma at NBI heating phase is shown in figure 4. The ion saturation current and divertor plasma density increase with NBI heating power, while divertor plasma temperature is not effected. The maximum density is about $3\times10^{19}/m^3$ for ion side and $1.6\times10^{19}/m^3$ for electron side. The temperature T_{ed} is about 25eV for electron side and 15eV for ion side.

3. Continuous measurement of floating potential

Continuous measurement of floating potential (V_{fp}) is performed by using high resistance in place of bias voltage supplier. Figure 6 is shown line averaged density, radiation, D_α, floating potential at outer divertor in CCW's case. The signal of the inner divertor is out of the range (plus side) of measurement. V_{fp} in the outer divertor is about +7V. After L-H transition V_{fp} rises up to +15 V and its fluctuation becomes small. The negative spikes on V_{fp} are also observed to synchronize with D_α spikes.

ACKNOWLEDGEMENTS

The authors are grateful to Drs. S.Shimamoto, M.Tanaka, M.Yoshikawa and S.Mori for continuous encouragement. The author (I.Nakazawa) is gratefúl to Dr. T.Morikawa(MELCO).

REFERENCES

[1] T.Shoji et al., in Proc. of 11th Europ. Conf., (Achen 1983) Vol.1,p55
[2] K.Odajima et al., in Proc. of 11th Int. conf. on Plasma Phys. and Cont. Nucl. Fusion Research, (Kyoto 1986), IAEA-CN-47/A-III-2
[3] T.Shoji et al., in Proc. of 15th Europ. Conf., (Dubrovnik, 1988) Vol.1, P219

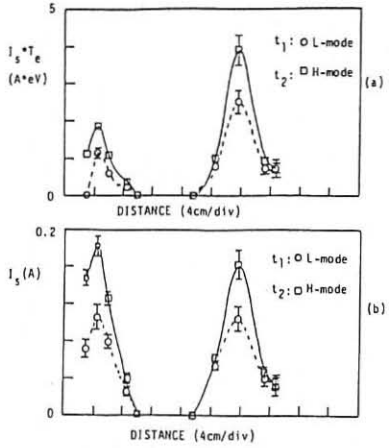

Fig. 3-3 The profiles of I_s*T_{ed} and I_s in L and H modes, (a) I_s*T_{ed}, (b) I_s.

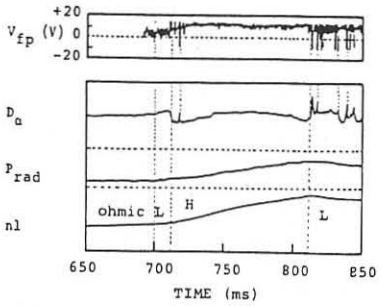

Fig. 5 Temporal evolutions of floating potential (V_{fp}), D_α, radiation (P_{rad}), line averaged density of main plasma (nl).

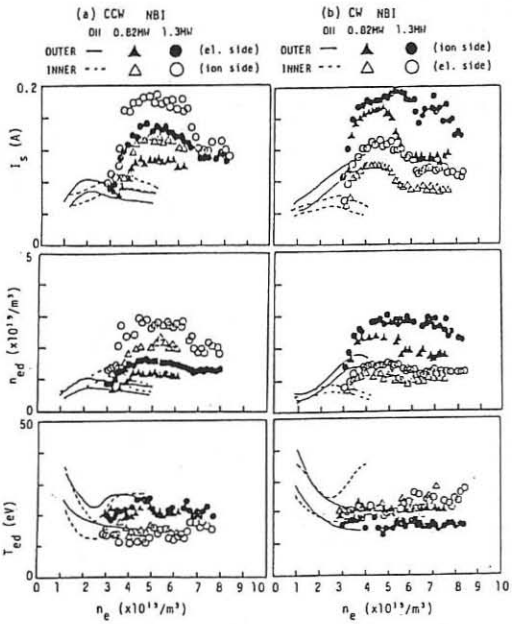

Fig. 4 T_{ed} and n_{ed} dependences on main plasma density at NBI heating phase (input power 1.3MW and 0.82MW) (a) CCW, (b) CW.

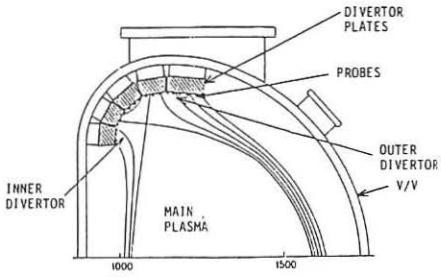

Fig. 1 Experimental set up and single null divertor configuration in JFT-2M

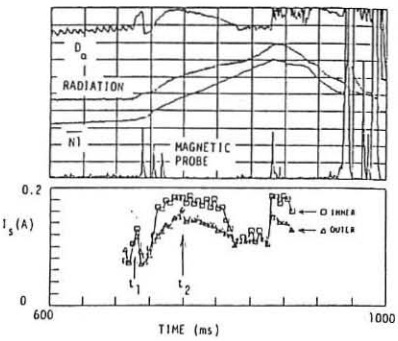

Fig. 3-1 Temporal evolutions of D_α, radiation, line averaged density, magnetic fluctuation, and ion saturation current (CCW's) L/H transition occurs at 710ms.

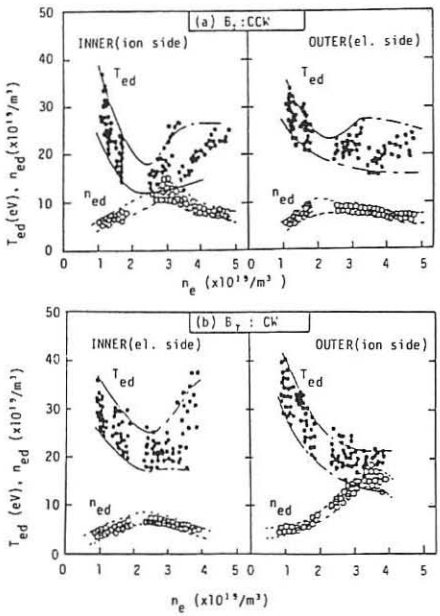

Fig. 2 T_{ed} and n_{ed} dependences on main plasma density at ohmic heating phase, (a) CCW, (b) CW.

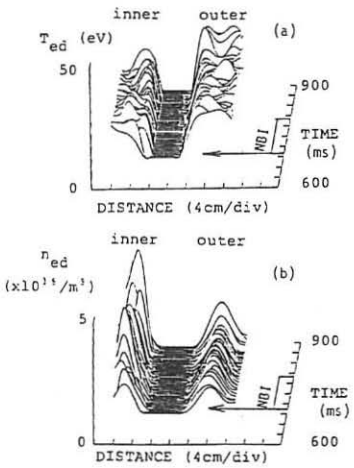

Fig. 3-2 Spatial and temporal behavior of divertor plasma parameter (CCW's), at NBI heating phase, (a) T_{ed}, (b) n_{ed}

EDGE PHYSICS AND ITS IMPACT ON THE IMPROVED OHMIC CONFINEMENT IN ASDEX

M. Bessenrodt-Weberpals, A. Carlson, G. Haas, K. McCormick, J. Neuhauser, N. Tsois, H. Verbeek and the ASDEX Team*

Max-Planck-Institut für Plasmaphysik
EURATOM Association, D – 8046 Garching
*N.R.C.N.S. Democritos, Athens, Greece

1. Introduction

The edge conditions play a crucial role in achieving and maintaining the improved ohmic confinement (IOC) regime in ASDEX as has been stated by Haas et al. (1988) and Söldner et al. (1988). This new regime is obtained after divertor reconstruction in deuterium discharges when the gas puffing is substantially reduced. IOC is then characterized by peaked density profiles and the linear scaling of the energy confinement time τ_E with the line-averaged density $\overline{n}_e$ is recovered up to the density limit.

In this paper, we discuss the evolution of the *edge* parameters in the transition from the linear (LOC) and then saturated (SOC) to the improved (IOC) ohmic regime. In addition, we describe the edge plasma mainly in terms of edge parameters like the *separatrix* density instead of bulk parameters such as the *line-averaged* density. This gives us the opportunity to identify and separate edge effects from the central behaviour.

The data in the vicinity of the separatrix stem mainly from the single-pulse multipoint Thomson scattering system, the lithium beam spectroscopy, the Langmuir probe, and the time-of-flight spectrometer in ASDEX. For comparison, we will sometimes use measurements in the divertor chamber by electric triple probes and ionization gauges.

2. Temporal evolution of the edge parameters

To get detailed information about the temporal evolution of the SOC to IOC transition in ASDEX we change the external gas puff a few times during the same discharge (cf. Figure 1). Thus we build up the density with successive plateaus at $\overline{n}_e = 2.5 \times 10^{19}$ m^{-3} (LOC), $\overline{n}_e = 4.0 \times 10^{19}$ m^{-3} (IOC1), and $\overline{n}_e = 4.9 \times 10^{19}$ m^{-3} (IOC2) each separated by a linear density ramp (SOC1, SOC2) (cf. Figure 1). The temporal evolutions of the electron density and temperature at the separatrix are taken from the Thomson scattering diagnostics. The results show that the separatrix density in the SOC regime is remarkably higher than in the corresponding IOC case as is confirmed by the lithium beam data (cf. Figure 1). At the same time, the temperature evolution is similar in both regimes. The triple probe determines the density in the divertor to behave similar and the divertor temperature to be slightly higher in the IOC regime. This also holds for the mean energy of the particles detected by the

time-of-flight spectrometer. According to these data, the pressure $p_e = n_e k_B T_e$ stays approximately constant.

Evaluating the error bars, we see that the comparison of different edge diagnostics suffers from the fact that the separatrix position is determined with an accuracy of only $\pm$ 1 cm in ASDEX. This value is about the same order of magnitude as the radial e-folding lengths of the electron data and thus implies a significant uncertainty for all edge studies. We suppose that the separatrix position will be approx. 1 cm more outside compared with the magnetic measurements. Moreover, we have indications from edge diagnostics at different toroidal positions that the edge structure itself is helical and even ergodized near the separatrix. The problem of the separatrix position is thus further investigated by Tsois et al. (1989). In the following, we will rely on the magnetically determined separatrix position.

3. Edge scans

To identify edge correlations, we plot the temperature at the *separatrix* T_{es} versus the corresponding *separatrix* density n_{es} (cf. Figure 2). For the SOC case, we observe the usual decrease of T_{es} with increasing n_{es}. For the IOC case, we follow approximately the same curve. An empirical scaling law given by Kaufmann et al. (1989) for a large number of different ASDEX discharges (ohmic, L mode, pellets) yields $T_e \sim n_e^{-0.5}$ at 35 cm minor radius. This is consistent with our experimental data from the separatrix at 40 cm (cf. Figure 2). In addition, we consider the simulation code by Schneider et al. (1988) which is based on the combination of a one-dimensional hydrodynamic plasma code and a two-dimensional neutral particle Monte-Carlo simulation. This study evaluates also a reasonable fit with a good agreement for the relative dependence but a factor of 2.2 lower temperatures (cf. Figure 2). This may be explained by the 1 cm shift of the separatrix position as determined experimentally (cf. Section 2).

A similar analysis is performed for other edge data e.g. the particle flux and the mean energy measured by the time-of-flight spectrometer. This reveals the same scaling with separatrix density in both the SOC and the IOC regime. Thus, the physics at the separatrix does not change significantly between the SOC and the IOC cases. What really is different seems to be the scaling of the neutral recycling fluxes versus the separatrix density. Since these fluxes contribute a significant portion to the total particle flux, this may be a hint for the different behaviour of the SOC and the IOC regimes.

In order to relate the energy confinement time τ_E quantitatively to specific edge conditions, we correlate τ_E with n_{es}. Starting at low densities and low confinement times, τ_E rises proportional to n_{es} in the LOC regime. With larger n_{es}, τ_E saturates (SOC1) until the gas flux is reduced. Now, n_{es} drops immediately thus establishing the IOC phase with peaked density profile and with τ_E slowly going up (IOC1). Opening the gas valve results in a sudden drop of the particle as well as the energy confinement. This gives higher densities at the separatrix (SOC2). Then, the gas flux is reduced again. For a second time τ_E goes upwards with decreasing n_{es} reaching up to about

twice the value of the SOC phase (IOC2).

4. Particle transport

To gain deeper insight into the recycling processes in the scrape-off and diverted region, we calculate the total particle flux across the separatrix in the main chamber. This comprehends the particle fluxes from the bypass, the slits and the recycling zone in ASDEX as well as the change in the total particle content and the external flux through the valve. Because of the various atomic physics processes in the scrape-off layer only a part of this flux which is determined by the fuelling efficiency (Mayer et al., 1982) enters the plasma. This particle flux Φ leeds also to a convective energy flux P. Assuming equal ion and electron temperature it is $P = 5k_BT\Phi$. From the total particle flux, we also get an estimate for the global particle confinement time. The calculations show that the contribution of the convective energy flux to the total power across the separatrix drops when the confinement is improved. Simultaneously, the global particle confinement time rises to approximately the same extent as the energy confinement which is clearly seen in Figure 3.

5. Summary

To investigate the transition from the saturated to the improved ohmic confinement in ASDEX, the edge conditions are analyzed in detail. The results show that the reduction of the gas feed leeds to an immediate drop of the separatrix density. This drop seems to be the trigger of a change in the bulk transport and hence leeds to the peaking of the density profiles in the bulk. Simultaneously, the temperature at the separatrix increases slightly during the transition. According to these data, the pressure stays approximately constant at the separatrix during the SOC to IOC transition. In addition, we evaluate that the contribution of the convective energy flux to the total power across the separatrix drops during the SOC to IOC transition. Then, the global particle as well as the global energy confinement time are improved by about the same factor.

References

G. Haas, W. Poschenrieder, J. Neuhauser, S. Kaesdorf, ASDEX- and NI-Team, *8th Int. Conf. Plasma Surface Interactions in Controlled Fusion Devices*, Jülich (1988).

M. Kaufmann, M. Bessenrodt-Weberpals, K. Büchl, O. Gruber, O. Kardaun, et al., *these proceedings* .

H.-M. Mayer, F. Wagner, G. Becker, K. Behringer, D. Campbell et al., *J. Nucl. Mater.* **111-112** (1982) 204–210.

W. Schneider, J. Neuhauser, G. Haas, K. McCormick, N. Tsois, and R. Wunderlich, *Contrib. Plasma Phys.* **28** (1988) 387–392.

F. X. Söldner, E. R. Müller, F. Wagner, H. S. Bosch, A. Eberhagen et al., *Phys. Rev. Lett.* **61** (1988) 1105–1108.

N. Tsois, M. Bessenrodt-Weberpals, A. Carlson, G. Haas, K. McCormick, et al., *these proceedings* .

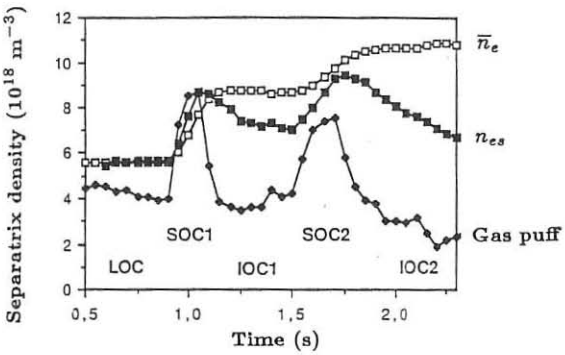

Figure 1 :
Temporal evolution of the gas puff (a.u.), the line density $\overline{n}_e$ (a.u.), and the separatrix density $\overline{n}_{es}$.

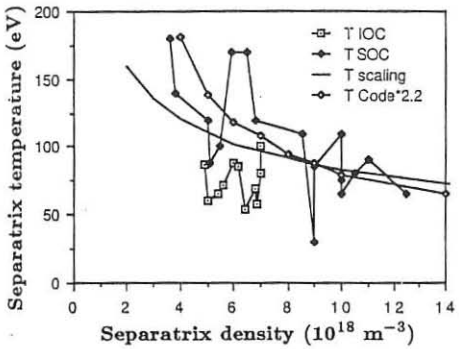

Figure 2 :
Separatrix temperature versus separatrix density for SOC and IOC regime.

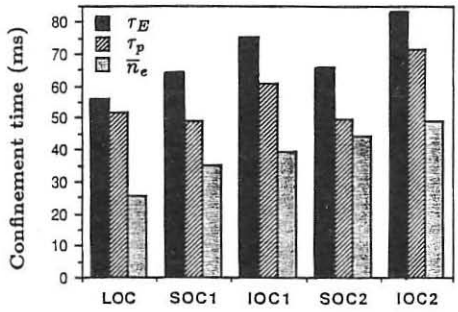

Figure 3 :
Global energy and particle confinement time.

SCALING OF EDGE PARAMETERS FOR OHMICALLY-HEATED DISCHARGES ON ASDEX

K. McCormick, Z.A. Pietrzyk*, E. Sevillano**,
G. Haas, H.D. Murmann, H. Verbeek and the ASDEX Team

Max-Planck-Institut für Plasmaphysik, EURATOM Association,
Garching bei München, Fed. Rep. of Germany

ABSTRACT: The scrape-off-layer (SOL) density profile on ASDEX has been investigated over a wide range of parameters ($\bar{n}_e$ = 0.8 - 5.3 x 10^{13}/cm^3; I_p = 150 - 425 kA; B_t = 1.9 - 2.5 T; H_2, D_2) for a carbonized vessel with the new divertor configuration (DV-II), and can be described by regression formulae of the form: n_s, $\lambda_n \propto \bar{n}_e^{\alpha} I_p^{\beta} B_t^{\gamma} q_a^{A}$, where n_s is the separatrix density and λ_n the exponential fall-off length. Values for the exponents are given in Table 1. Essentially $\lambda_n(H^+) \sim \lambda_n(D^+)$. $n_s(H^+)$ is greater than $n_s(D^+)$ by up to 70 %. Operation of ASDEX in the IOC mode (non-carbonized walls) yields n_s values as much as 40 % lower than for SOC conditions; λ_n experiences only moderate (< 10 %) changes during IOC.

INTRODUCTION: The SOL relative density profiles have been measured by the Li-beam technique /5/ and calibrated using the YAG Thomson scattering system. A description of the discharge series, and a regression analysis of global plasma properties, as well as the edge YAG n_e, T_e values are in /1/.

RESULTS AND DISCUSSION OF PARAMETER SCANS (carbonized wall): Figure 1 reveals many of the systematic trends of n_s and λ_n: For both H_2 and D_2 the lowest value of n_s (for $\bar{n}_e$ = 0.8 x 10^{13}/cm^3) increases only very moderately with I_p, whereas the maximum attainable n_s is a much stronger function of I_p. Further, $n_s(H^+) > n_s(D^+)$. λ_n decreases with I_p over I_p= 150 - 250 kA.

In more detail, plots of n_s vs. $\bar{n}_e$ for a given I_p (Fig. 2) show $n_s \propto \bar{n}_e$, with the constant of proportionality becoming larger with I_p. Regression fits (see Table 1 and Fig. 3) quantify these observations. The isotopic dependence of n_s is confirmed by Thomson scattering, which also shows the effect is most apparent near the edge.

For I_p > 200 kA and $\bar{n}_e$ > 1.5 x 10^{13}/cm^3, λ_n increases slowly with q_a (and with B_t for D^+), and has no $\bar{n}_e$ dependence (Fig. 5, top). For $\bar{n}_e$ = 1.5 → 0.8 x 10^{13}/cm^3, λ_n increases by about 25 % (not shown). In the case of $I_p \leq$ 200 kA, λ_n depends strongly on I_p and, to lesser extent, on $\bar{n}_e$ (Fig. 5, bottom). Note that for I_p = 250 - 425 kA (q_a ~ 2.2 - 5), λ_n varies by ~ 0.4 cm, whereas for $I_p \leq$ 200 kA (q_a = 4.6 - 8.5), λ_n ~ 2 → 7 cm.

Examination of the SOL density profiles (Fig. 4), with I_p as a parameter, illustrates the extreme flatness for I_p = 150 kA. Stepping I_p to 200 kA reduces n_e outside the separatrix (R_s = radial separatrix position). Then, at 250 kA, n_s increases to produce a shoulder in the profile for R-R_s > 2 cm, and finally I_p = 425 kA leads almost to the disappearance of the shoulder. Presumably, at $I_p \leq$ 200 kA the edge electron temperature (Fig. 1) is too low to support a "normal" value of n_s; hence the discharge reacts to higher $\bar{n}_e$ values by producing peaked profiles with an ever-broader SOL (larger λ_n). Also, $I_p \leq$ 200 kA discharges are prone to unstable conditions

* CRPP, Lausanne
** GA Technologies, San Diego

at the edge. This is responsible for some of the large scatter in points for Fig. 5 (I_p < 250 kA). Note that the λ_n values quoted here characterize only the region $0 \leq R\text{-}R_s \leq 2$ cm.

The general scatter in the D_2 graphs comes from a tendency towards non-stationarity at the edge, as well as changes in other parameters not included in the regression (wall condition, gas puff rate...?).

TEMPORAL PARAMETER EVOLUTION (non-carbonized wall): Alteration of the divertor has permitted ASDEX to access an IOC regime (only for D^+) which is initiated by a reduction in the gas puff (GP) rate. It is characterized by peaked density profiles, accompanied by lower n_s (see /2-4/ for more details). Figure 6 illustrates during the $\bar{n}_e$ ramp-up phases of the discharge, that n_s tracks with $\bar{n}_e$, T_e(39.4 cm) decreases, and the global density profile broadens (Q_{n14} decreases). During the 2nd and 3rd plateaus, n_s decreases, and T_e(39.4) remains constant.

The response of λ_n to the 1st $\bar{n}_e$ ramp is to initially decrease, then increase, only to again decrease as the GP rate is reduced. For both ramps, λ_n experiences about a 15 % variation, but the changes during all three plateaus is less than 10 %. This example makes clear that λ_n is not determined strictly by I_p and B_t alone.

The D^0 flux to the wall (ϕ) /4/ is roughly proportional to n_s (Fig. 6). The divertor pressure P_D is related to the time history of the discharge and n_s. P_D tracks with n_s in the 1st $\bar{n}_e$ ramp, but then decays less rapidly than n_s in the 2nd $\bar{n}_e$ plateau (Fig. 6). A repetition of this phenomena in the subsequent phases of the discharge leads to a 70 % increase in the ratio P_D/n_s over the course of the discharge.

CONCLUDING COMMENTS: Comparing regression fits on ASDEX with the old /5,6/ and new divertors reveals about the same global dependence (and absolute values) for λ_n on q_a (q_a < 5). Thus, as before, the behavior of λ_n is not inconsistent with the formulation $\lambda_n \propto \sqrt{D_\perp \tau_\parallel}$ /5/. Determinations of $D_{\perp e}$ near the edge of the plasma column indicate a factor of ten reduction in $D_{\perp e}$ for $\bar{n}_e = 0.8 \rightarrow 3 \times 10^{13}/cm^3$ /6/. λ_n varies less than 25 % over this range. Thus, $D_\perp$(SOL) does not appear to reflect $D_{\perp e}$ in a strong manner.

For the parameter scan, the ratio $n_s/\bar{n}_e$ varies over ~ 0.21 - 0.33 for H_2 and ~ 0.13 - 0.25 for D_2 (for q_a < 5). This is a much larger span than found for the old divertor. For typical conditions ($\bar{n}_e = 3 \times 10^{13}/cm^3$, I_p = 380 kA, B_t = 2.2 T) $n_s(H^+)/n_s(D^+)$ ~ 1.5.

REFERENCES

/1/ F. Wagner et al., this conference
/2/ F.X. Söldner et al., Phys.Rev.Lett. 61, 1105 (1988); this conference
/3-4/ M. Bessenrodt-Weberpals et al., H. Verbeek et al., this conference
/5/ K. McCormick, Z.A.Pietrzyk et al., J.Nucl.Mater. 145-147, 215 (1987)
/6/ O. Gehre, this conference.

Table I. Regression fits of the form $A\bar{n}_e^{\alpha}I_p^{B}... + B$. Standard error is in the adjacent column. R is the regression coefficient.

CONDITIONS		A		B		ne		Ip		Bt		qa		R
H+	ns	0.051	-0.039	1.01	0.054	0.3	0.077	0	0	0	0	0	0	0.978
D+	ns	0.0024	-0.03	0.753	0.033	0.853	0.048	-0.049	0.121	0	0	0.947		
H+ / <200kA	λ_n	0.27	-0.661	0.462	0.113	0	0	0	0	1.324	0.238	0.858		
D+ / <200kA	λ_n	0.155	-0.096	0.481	0.069	0	0	0	0	1.524	0.148	0.865		
H+ / >200kA; >1.2e13	λ_n	1.321	-0.011	0	0	0	0	0	0	0.295	0.054	0.828		
D+ / >200kA; >1.2e13	λ_n	1.375	-0.069	0	0	0	0	0.255	0.084	0.156	0.049	0.411		

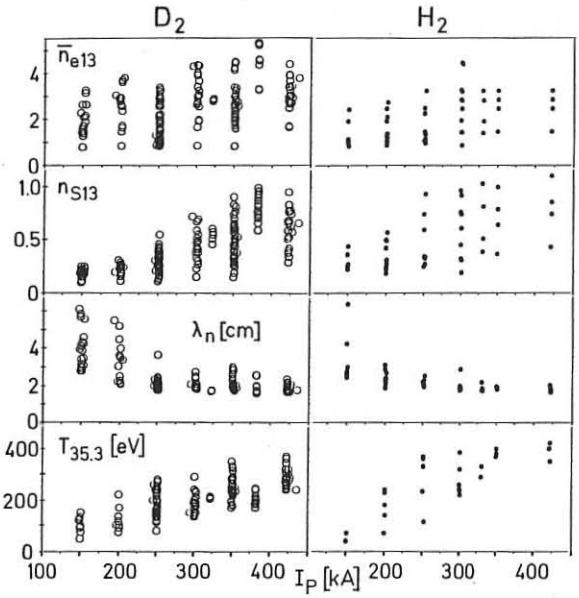

Fig.1: Global overview of the $\bar{n}_e$, n_s, λ_n and $T_e(r=35.3\ cm)$ ranges vs. I_p, for the D_2, H_2 parameter scans

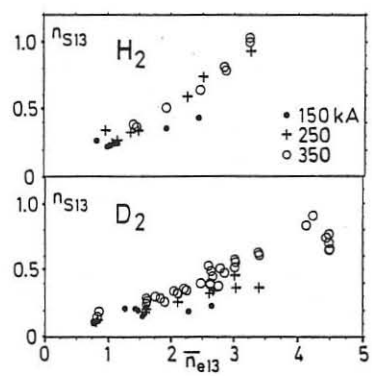

Fig.2: Separatrix density n_s [$10^{13}/cm^3$] vs. $\bar{n}_e$ with I_p as a parameter

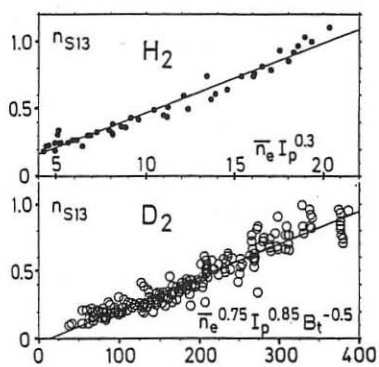

Fig. 3: n_s regression fits for the D_2, H_2 parameter scans.

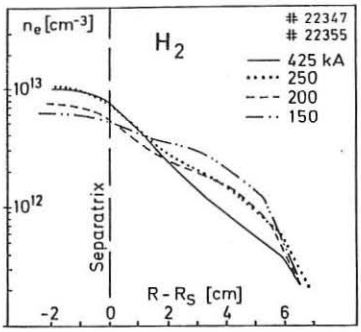

Fig. 4: Density profiles at the plasma edge for an I_p scan. B_t = 2.2 T, $\bar{n}_e$ = 2.5 x 10^{13}/cm^3

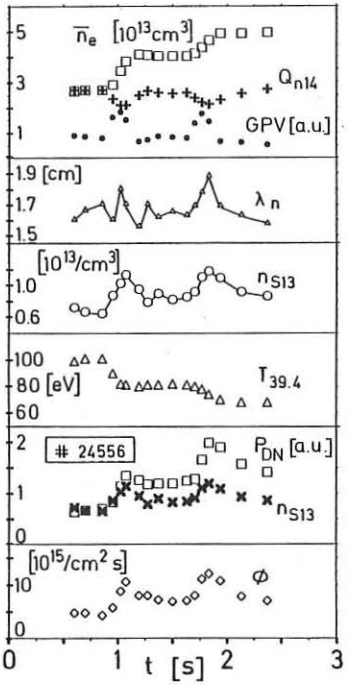

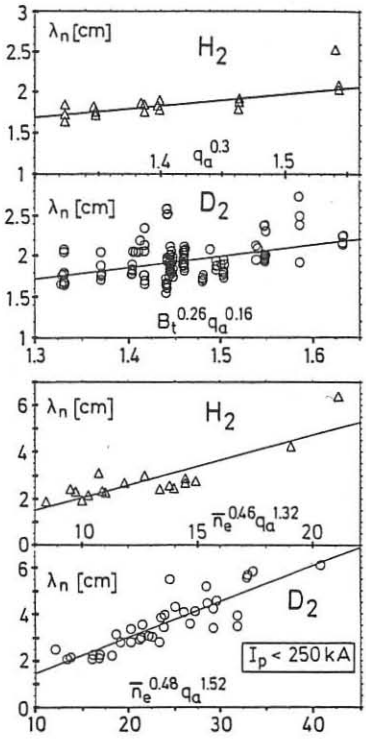

Fig. 5 (above) λ_n regression fits for I_p > 200 kA (top) and I_p < 250 kA (bottom) for the D_2, H_2 parameter scans.

Fig. 6 (left): Temporal evolution of global and edge parameters for a discharge exhibiting IOC characteristics. B_t = 2.2 T, I_p = 380 kA,
Q_{n14} = $\bar{n}_e$ (0)/$\bar{n}_e$ (0.75a);
GPV = volt. on GP valve;
$T_{39.4}$ = T_e (39.4 cm) from YAG Thomson scattering.
P_{DN} = upper, outer divertor pressure, normalized to n_s at t = 0.7 s;
Ø = D° flux to wall.

IMPURITY PRODUCTION AT THE DIVERTOR PLATES AND DEPOSITION IN ASDEX

J.Roth, G.Janeschitz, R.Behrisch, G.Fußmann, E.Taglauer,
N.Tsois, M.Wielunski, H.R.Yang

Max-Planck-Institut für Plasmaphysik, EURATOM Association
D-8046 Garching/München, FRG

Abstract:

In the divertor tokamak ASDEX the metal atoms released from the divertor plates have been investigated after the change of the plate material from Ti to Cu. Erosion rates measured spectroscopically and with collector probes have been found consistent with sputtering rates due to the divertor plasma. The comparison of erosion rates with the Cu content in the plasma yields values for the divertor retention efficiency, which is strongly dependent on plasma density. The final sink for the Cu atoms could be determined by detailed mapping of the vessel walls using long term collector probes and analysing wall structures. Deposition mainly occurs at the walls of the divertor chamber, only to a small fraction at the main plasma vessel wall. Erosion rates at the divertor plates are not balanced by redeposition back to the plates.

Introduction:

In today's fusion experiments the main plasma wall interaction occurs at limiters /1/ or divertor plates /2/. When the boundary plasma interacts with the divertor plates a secondary divertor plasma is formed, which is dominated by the boundary plasma parameters and by recycling processes at the divertor plate. This leads to a considerable reduction of the divertor plasma temperature and an increase of particle fluxes to the plate. Details of the erosion at the plate, ionization and transport in the divertor plasma are still poorly understood /3,4/. However, the knowledge of these processes is important to estimate lifetimes of future divertor plates as well as radiation losses and dilution due to plasma impurities /5/. In ASDEX the erosion processes /6-8/ as well as the divertor retention for impurities /9/ and final redeposition /10/ have been investigated for the first time in a divertor tokamak.

Experimental:

After 7 years of operation the ASDEX divertor plates were changed from Ti to a watercooled Cu structure /11/. This offered the possibility to study the transport of Cu to the surface structures of the vessel walls. The erosion of Cu is determined from absolute measurements of the Cu I (3247 Å) line radiation in front of the plates /9/ as well as by collecting the eroded Cu after ionization on the time resolving rotating collector probe /12/. The erosion rates are compared to sputtering rates calculated using divertor plasma parameters /13/ and sputtering yield data /2,14/. In order to determine the divertor retention capability /9/ the erosion rates are compared to central plasma Cu concentrations measured spectroscopically

/15/. The deposition of Cu atoms is finally determined by analyzing a large number of poloidally and toroidally distributed C and Si long term probes on the vessel walls /10/.

Results and discussions:

Figure 1 shows the Cu erosion profile in front of the divertor plate for an ohmic deuterium discharge at a central plasma density n_e of $4 \cdot 10^{13}$ cm^{-3}. Integrating the profile and multiplying with the divertor circumference a total erosion of $2.5 \cdot 10^{19}$ Cu/s can be evaluated. The deuterium ion flux distribution impinging onto the divertor plate was obtained from the measured divertor plasma temperature and density profiles /13/ and used to calculate the neutral Cu flux profile, as shown in fig. 1 (solid line). This profile was recalculated for the observation geometry into an emission profile of the Cu I line, exited in the divertor plasma (dashed line) and agrees well with the experimental data /16/.

Figure 2 shows the total sputtered Cu atom flux as calculated from sputtering due to divertor plasma ions compared with data from spectroscopy and collector probe as function of average plasma density. Sputtering due to the divertor plasma can explain the observed fluxes within the experimental uncertainties both for ohmic and neutral beam heated (NBI) plasmas. The increase of sputtered Cu atoms for ICRH heating is by far smaller than for NBI, while ICRH leads to a much stronger increase of atoms sputtered from the main plasma vessel wall /2/. For comparison with long term deposition measurements the average source strength of Cu atoms over a discharge period including ICRH, NBI and ohmic discharges at various densities can be estimated to about $3 \cdot 10^{19}$ Cu/s.

The central plasma concentration of impurities originating from the divertor plates varies with average plasma density much stronger than the eroded flux (fig. 2 and 3). The strong decrease of the Cu concentration with increasing plasma density indicates that the retention capability of the divertor increases with density /9/. Taking a central confinement time of about 50 ms a Cu content of 10^{15} at high densities and a production rate of $1 \cdot 10^{19}$/s results in a retention probability of 98%. At low densities, however, the retention probability decreases to 90%. Similar values are obtained for neutral beam heating and ICRH /2,9/.

The estimates of the divertor retention indicate, that the largest part of the impurity flux remains in the divertor chamber. However, only a detailed balance can tell, which fraction returns to the divertor plate and can possibly reduce the net local erosion by redeposition. For 3 operation periods the distribution of Cu atoms deposited on the walls of the main vessel and on the shield opposite to the outer divertor plates have been investigated. Further, a metal oxide layer deposited on the divertor plates was stripped using adhesive tape and analysed. All three distributions show the same pattern and roughly the same deposition rate. As an example the pattern for the last period from October 1987 through June 1988 is shown in fig. 4.

While on most vessel areas the deposited layer is of the order of $2 \cdot 10^{16}/cm^2$, the shields opposite to the outer divertor plates are covered with layers up to $6 \cdot 10^{18}/cm^2$. Integrating over the whole circumference these areas alone yield a coverage with $1.6 \cdot 10^{23}$ atoms while the vessel

walls are covered with $6 \cdot 10^{21}$ atoms only. This deposition equals more than 50% of the total eroded Cu, amounting for about 4000 discharges at an average length of 2.5 s to $3 \cdot 10^{23}$ atoms. The metal layer covering a 3 cm wide band outside the separatrix intersection with up to $1 \cdot 10^{19}$ Cu/cm^2 contained a total amount of $5 \cdot 10^{22}$ atoms, i.e. about 17% of the eroded material.

With the knowledge of the divertor plasma parameters the probability for sputtered neutral Cu atoms to escape ionization before redeposition at surfaces can be evaluated. Figure 5 shows the neutral Cu density in the divertor region for a medium density discharge ($4 \cdot 10^{13}$ cm^{-3}). It can be seen, that the direction of highest escape probability before ionization is in an upward direction away from the separatrix. The areas where the largest deposition was found on the divertor shields and on the plate are indicated in fig. 5. This may lead to the conclusion, that the Cu atoms reach the shield predominantly as neutral atoms, while the coverage on the plate originate from backstreaming Cu ions. The streaming pattern of hydrogen and impurity ions in the divertor and back to the main plasma, however, awaits its modelling by 2D-comupter simulation /3,4/.

Conclusion:

The detailed investigations on the production and transport of divertor impurities lead to the following conclusions:

- The measured erosion fluxes are in good quantitative agreement with sputtering by ions from the divertor plasma.
- The divertor retention is strongly dependent on average plasma density and reaches in the best (high density) cases values of 98%.
- Redeposition fluxes at the target plate are only a minor fraction of the eroded fluxes and do not significantly reduce the net local erosion.
- The large deposition on the shields opposite to the intersection of the separatrix with the divertor plates may possibly originate from neutral Cu atoms escaping ionization in the divertor plasma.

References

/1/ G.M.McCracken, Plasmaphysics and Controlled Fusion 29, 1273 (1987)
/2/ J.Roth, G.Janeschitz, submitted to Nuclear Fusion
/3/ J.Neuhauser, R.Wunderlich, J. Nucl. Mat. 145-147, 877 (1987)
/4/ J.Brooks, J. Nucl. Mat. 145-147, 837 (1987)
/5/ D.Post et al., 12th Int. Conf. Plasma Phys. Contr. Nucl. Fusion Res., Nice, France (1988)
/6/ G.Staudenmaier, J. Vac. Sci. Technol. A3, 1099 (1985)
/7/ H.Verbeek et al., J. Nucl. Mat. 145-147, 523 (1987)
/8/ E.Taglauer, G.Staudenmaier, J. Vac. Sci. Technol. A5, 1352 (1987)
/9/ G.Janeschitz et al., J. Nucl. Mat., in press (PSI 1988)
/10/ W.M.Wang, J.Roth, R.Behrisch, G.Staudenmaier, as ref. /9/
/11/ H.Niedermeyer et al., 15th Europ. Conf. Contr. Fusion Plasmaphys. Dubrovnik (1988)
/12/ E.Taglauer, A.P.Martinelli, G.Janeschitz, as ref. /9/
/13/ N.Tsois, private communication
/14/ W.Eckstein, private communication
/15/ G.Janeschitz, L.B.Ran et al., these proceedings
/16/ H.R.Yang, G.Fußmann, to be published

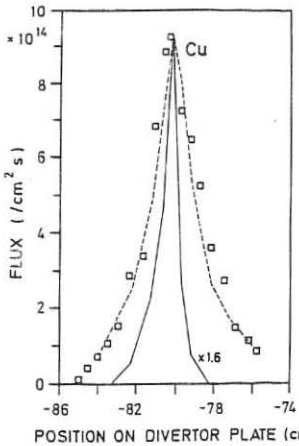

Fig.1: Distribution of sputtered Cu flux in front of divertor plate (curves see text).

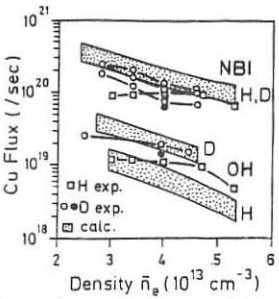

Fig.2: Comparison of measured Cu flux with calculations from sputtering.

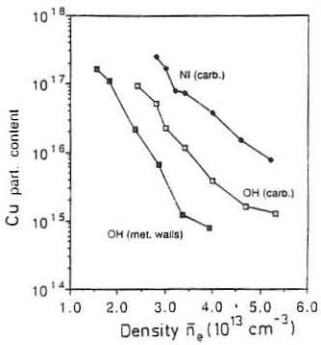

Fig.3: Dependence of the Cu content on the main plasma on plasma density.

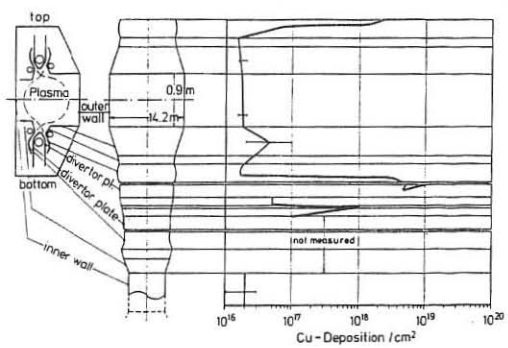

Fig.4: Deposition of Cu on the wall structures of ASDEX.

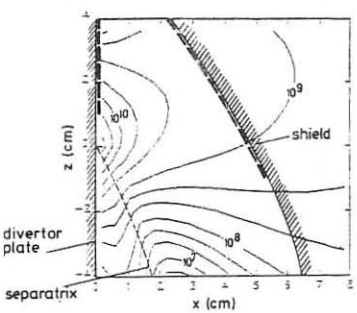

Fig.5: Contour lines of neutral Cu density in the divertor plasma.

THE PARTICLE FLUXES IN THE EDGE PLASMA DURING DISCHARGES WITH IMPROVED OHMIC CONFINEMENT IN ASDEX

H.Verbeek, W.Poschenrieder, Fu J.-K., F.X.Söldner and the ASDEX Team

Max-Planck-Institut für Plasmaphysik, EURATOM Association,
8046 Garching/München, FRG

In the recent experimental period of ASDEX a new regime of Improved Ohmic Confinement (IOC) was discovered /1,2/. So far the energy confinement time τ_E increased linearly with increasing line averaged density $\bar{n}_e$ up to $n_e = 3 \cdot 10^{13}$ cm^{-3} saturated, however, at higher densities. In the new IOC regime τ_E increases further with increasing $\bar{n}_e$ up to $\sim 5 \cdot 10^{13}$ cm^{-3}. The IOC regime is achieved for D_2 discharges only since the last modification of the ASDEX divertor which substantially increased the recycling from the divertor through the divertor slits. It also led to a reduction in gas consumption for a discharge by a factor of about 2. As it appears, the high fuelling rate required during a fast ramp-up of the plasma density leads to a transition into the Saturated Ohmic Confinement (SOC) regime. Vice versa, the strong reduction in the external gas feed when the preprogrammed density plateau is reached seems to be essential for establishing the IOC. It is characterized by a pronounced peaking of the density profile.

During the transition from the SOC to the IOC regime large variations in the signals of all edge and divertor related diagnostics are observed. In this paper we concentrate on the results of the Low Energy Neutral Particle Analyser (LENA), the sniffer probe, on the mass spectrometers measuring the divertor exhaust pressure.

The LENA based on a time-of-flight technique measures the charge exchanged neutral particle flux in the energy range of 30 eV to 2.8 keV. This flux is dominated by low energy particles which orginate from the areas close to the plasma edge /3,4/. The neutral particle flux observed in these measurements is to a large extent produced by the plasma recycling at the tip of the large graphite limiter positioned at the outward edge of the SOL in close proximity to the LENA. The neutral particle flux Φ scales very well with the particle content in the SOL namely with $n_S \cdot \lambda_n$ i.e. with the density at the separatrix n_S times the decay length of the density outside the separatrix λ_n as measured with the Li-beam diagnostic /5/.

In the plasma chamber 2 cm behind the protective limiter the sniffer probe is located. It measures charged particle fluxes parallel to the magnetic field in the boundary plasma. The ion fluxes can be obtained from the pressure rise in the exhaust of the probe with the response time of 120 ms. It has also an integrated Mach probe which can be biased to draw ions or electrons and yields a very fast response to flux changes. A good agreement between ion saturation current and measured H- flux has been found. It is therefore related to the recycling in the main chamber /6/.

The exhaust pressure of the upper and lower divertors of ASDEX is measured with mass spectrometers. They can be repeatedly scanned over a group of masses (normally 1 to 4) in $\sim$125 ms, thus delivering the time dependent partial pressures, or can be set to a specific mass (4 in this paper) which yields better time resolution. This divertor pressure results

from the plasma flux in the scrape-off layer streaming into the divertor. The divertor pressure in turn is the direct measure for the neutral gas recycling into the main chamber via the bypasses /7/.

In each of figs. 1 and 2 a shot with substantially improved confinement and another one with little improvement are compared.

In fig. 1 shot # 23351 with clean steel walls shows the IOC regime, while in shot # 23862 with carbonized walls only a modest improvement of the confinement occurs in this otherwise equal discharge. For both shots $\bar{n}_e$ was ramped up to a flat top at $\bar{n}_e = 4.5 \cdot 10^{13}$ cm^{-3} by the controlled gas valve. GASV shows the voltage at this piezo valve, while Q_{GAS} is the total amount of gas used to maintain this discharge. The changes in the confinement time τ_E are shown in the last row. While $\bar{n}_e$ is ramped up at 0.7 sec τ_E rolls over and even decreases somewhat in the SOC regime. At 1.2 sec τ_E increases again with the beginning of the IOC regime. This increase is much less in the case of carbonized walls (# 23862). In the third row the neutral particle flux ϕ is shown. It increases as $\bar{n}_e$ increases. With the onset of the IOC regime ϕ decreases rapidly. The signal of the sniffer probe I_{SN} behaves quite similar. In this case the Mach probe was biased positively; it measures therefore the plasma electron flux. The close relation of the neutral particle flux ϕ and the plasma flux in the region outside the SOL shows that ϕ is dominated by the recycling at the protection limiter located in close proximity. With some delay, owing to the vacuum time constants involved, also the divertor pressure decreases after the onset of the IOC. In the case of carbonized walls, where only a poor improvement of τ_E occurs only a modest reduction of ϕ and the divertor pressure is seen. I_{SN} behaves accordingly.

The strong reduction in recycling fluxes shown by the neutral flux ϕ, the divertor pressure, and the sniffer probe signals mark an improvement in the particle confinement. Obviously the reduction in τ_E is the consequence of this improved particle confinement.

Figure 1 shows that an alteration of the walls - carbonisation hereby - has a large impact on the plasma edge. In the case of carbonization, after the ramp-up of $\bar{n}_e$, the divertor pressure, the neutral flux, and the plasma flux in the boundary (sniffer probe) reach much higher values. The gas consumption Q_{GAS} shows an opposing behavior: The Q_{GAS} is high during the ramp-up and low in the good IOC regime achieved with steel walls and, conversely, is first low and then high in the $\bar{n}_e$-plateau with carbonized walls.

It should be mentioned that the ratio of the pressure in the upper and lower divertors (not shown in fig. 1) has a minimum where the maximum of the edge diagnostics discussed here (at 1.2 sec) occurs. This indicates a change of the anomalous transport which is partly responsible for this divertor asymmetry.

In fig. 2 two discharges with a slightly different toroidal field B_T and thus q_a but otherwise equal parameters are compared. The density was ramped up to 3 plateaus with $\bar{n}_e = 2.6$, 4.0, and $4.6 \cdot 10^{13}$ cm^{-3}. The neutral flux, the divertor pressure, and the gas consumption indicate that the IOC regime is reached in the second and third density plateaus for $q_a = 2.77$. This is much less pronounced in the discharge with $q_a = 3.01$. Again, all the edge particle flux measurements consistently show the same tendency. This demonstrates once more the critical dependence of the IOC regime on the plasma edge conditions, since the decay length λ_n in the SOL scales proportional with q_a.

Though it was hoped for, that a more detailed study of the plasma-edge fluxes and recycling might reveal some more clues to the chain of causality responsible for loss and reestablishment of the regime with linear increase of confinement, the question of the actual trigger remain still unresolved. The fuelling rate from the feed-back controlled gas valve appears here to be an important parameter. An analysis of many shots shows that IOC conditions are only reached if this rate is above 20 mbar l/s during ramp-up. If it stays below, as is typical for carbonized walls, only SOC has been observed.

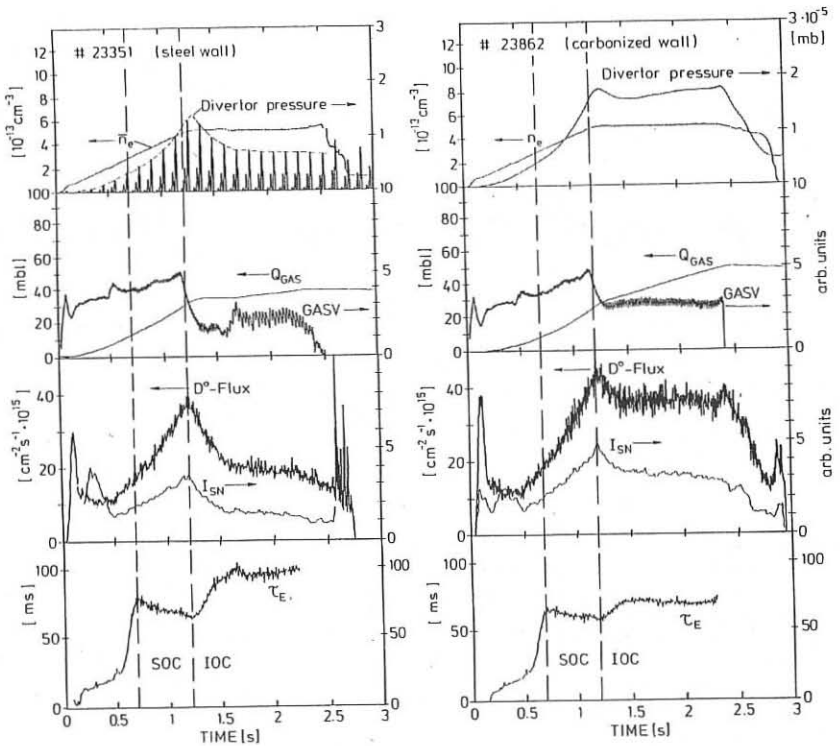

Fig. 1: Time evolution of the line averaged density $\bar{n}_e$, the pressure in the lower divertor, the voltage at the controlled gas valve GASV, the consumed gas Q_{GAS}, the neutral flux, the electron current from the sniffer probe I_{SN}, and the energy confinement time τ_E for D_2-discharges with steel walls (left) and carbonized walls (right) but otherwise equal parameters.

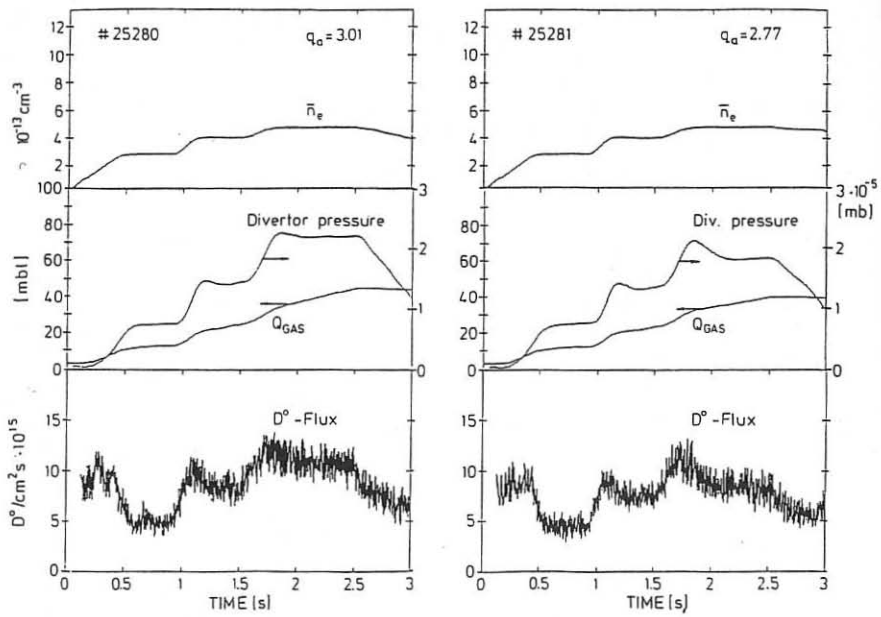

Fig. 2: Time evolution of the time averaged density $\bar{n}_e$, the divertor pressure, the consumed amount of gas Q_{GAS}, and the neutral particle flux D_2-discharges with q_a = 3.01 (B_T = 2.36 T) (left) and q_a = 2.77 (B_T = 2.17 T) (right) but otherwise equal parameters.

References:
/1/ E.R.Müller et al., Europhysics Conf. Abstr. 12B (1988) 19
/2/ F.X.Söldner et al., Phys. Rev. Lett. 61 (1988) 1105
/3/ H.Verbeek, J. Nucl. Mat. 145-147 (1987) 523
/4/ H.Verbeek et al., Proc. 8th PSI-Conf., Jülich 1988
/5/ K.McCormick et al., this conference
/6/ W.Poschenrieder et al., Europhys. Conf. Abstr. 9F (1985) 587
/7/ G.Haas, W.Poschenrieder et al., Proc. 8th PSI Conf. Jülich 1988

SCRAPE-OFF LAYER INVESTIGATIONS BY LANGMUIR PROBES IN ASDEX

N.Tsois*, M.Bessenrodt-Weberpals, A.Carlson, G.Haas, K.McCormick, J.Neuhauser, G.Siller, H.Würz**, and the ASDEX-Team

Max-Planck-Institut für Plasmaphysik, EURATOM-Association
Garching near Munich, Fed.Rep.Germany

Introduction: The scrape-off layer (SOL) of ASDEX in the hardened divertor configuration (DV-II) was investigated by two fast moving Langmuir probes. Multiple tip heads have been used in several arrangements: standard triple probe for n_e, T_e, Φ_{fl} profiles and/or time evolution, a configuration to measure fluctuations and Mach number probe. The main chamber probe scans 10 cm in radial direction in the equatorial plane. For the divertor probe, a tilt mechanism permits scanning in both radial and poloidal directions. Thus the recycling region close to the divertor plate can be investigated in two dimensions. The two probes are nearly at the same toroidal position on top of each other and can be correlated along field lines by adjusting q(a), typically around q≈3. The experimental set-up is shown in fig.1.

Experimental results: The SOL plasma parameters have been proved to be strong functions not only of main plasma parameters, ($\overline{n}_e$, plasma current, toroidal field) but also of wall conditions, instantaneous and time integrated gas puff, pumping and confinement regime /1,2/. In an attempt to make detailed comparison between midplane and divertor probe data as well as between probe and other SOL diagnostics (Thomson scattering, lithium beam, microwave interferometry, infrared thermography), simultaneous measurements have been done. A set of typical radial profiles from Langmuir probes in midplane and divertor are shown in fig.2. The profiles display the same qualitative characteristics as in the old , uncooled divertor configuration (DV-I) /1,3,4/: clear profile maxima in the divertor just outside the separatrix, roughly exponential decay close to the separatrix, followed by a plateau type shoulder a few cm outside with high, radially increasing, low frequency fluctuations. The shoulders are narrower now everywhere, as are the divertor slits.

The radial range of midplane profiles was extended further inward than previously /5,6/, in a few cases beyond the nominal separatrix /6/.The electron temperature and density profiles obtained in midplane agree with those inferred from laser scattering and lithium beam measurements till a "turning point" located approx. 1-1.5 cm outside from the nominal separatrix. Its exact nature is not yet clear, but the electron temperature reaches about 40 eV there and the triple probe approaches its limit. Strong heating and even melting of the tips was sometimes also observed in this high power region, despite the short residence time there (10-20 ms).Extrapolating the exponential part to the nominal separatrix radius, we regain the values of T_{es} and n_{es} of the

laser and lithium beam within ±25 percent. As discussed below, the true separatrix position is very likely about 1 cm outside the nominal one, requiring a downward adjustment of the separatrix plasma parameters.

Apart from the global similarity /1,3,4/ there are also clear differences from the old divertor: The relation of peak electron temperature and density in the divertor to the average line density $\bar{n}_e$ in the main chamber deviates from the previous relation for $\bar{n}_e > 3*10^{19}$ m^{-3}, with $T_{e,new} > T_{e,old}$ and $n_{e,new} < n_{e,old}$. Also the positively charged region around the separatrix is maintained to a higher n_e than previously /4/. These differences are marked during density plateau phases (low gas puff rate) and strongly diminished during density ramp up (high gas puff). They are correlated with changes in the mid plane separatrix density and are attributed to different confinement regimes (SOC, IOC /2/).

The new 3 mm microwave interferometer installed in the upper outer divertor permits an independent check on the probe density data.Good agreement was obtained over the entire range of divertor densities, when the geometric probe area was extended by the local ion Larmor radius (similar to /7/).

Due to the thermal charcteristics of the copper target plates /8/, comparison of probe data with thermography is possible in the new divertor only with auxilliary heating. In the few ICRH and NI heated discharges good agreement both in absolute value and width of the power deposition is found. The glancing incidence of the magnetic field lines on the target plates (now about 3 degrees), however, introduces an uncertainty.

Profiles taken for similar shots but different toroidal magnetic field direction and plasma current (thus indicative for the up/down asymmetry) reveal some pecularities (fig.3): With reversed polarity the "negative dip" /4/ is very strong and shifted inside away from the plasma profile maxima. Also the peaks of ion saturation current and temperature profiles are less closely in this case. As was pointed out in /4/, we believe the negative dip (produced by hot electrons leaving the plasma immediately at the boundary between open and closed field lines) represents the accurate, local separatrix position, which may differ by several millimeters or more from the magnetically determined one. The difference between the two profiles in fig.3 therefore seems to be relevant. Such a deviation is theoretically expected e.g. from the E X B drift (E being the poloidal presheath field), yielding typically a poloidal ion gyroradius, which is in fact several millimeters for ASDEX edge parameters.

Identification of the potential dip with the separatrix implies that the power deposition profile on the target plates is always situated in the expected part of the SOL, i.e. where field lines are connected to the main chamber.

Comparison with numerical simulations: The Langmuir probe results of fig.2 were compared with numerical simulations using a simplified version of the 2D multifluid edge code of B.Braams /9/, together with a quite realistic numerical neutral gas model. Starting with experimental values for ion and electron power and particle input into the scrape-off layer, the radial transport

coefficients, the divertor recycling and the impurity radiation were varied. A reasonable fit is obtained with $D \approx 1 m^2/s$ and $\chi \approx 1.5 m^2/s$ in the steep part near the separatrix, corresponding roughly to Bohm diffusion (see fig.4 and points in fig.2). The plateau region 2 cm outside, however, could be fitted only by multiplying the coefficients by at least a factor of three, yielding numbers definitely above the local Bohm value. This tendency correlates with the fact that the fluctuation spectrum changes qualitatively in this region /10/. The reason for the high absolute transport coefficients is not clear, but might be connected with the plasma parameters at the target plate and the electric sheath there.

The connection of the two sets of profiles of fig.2 along field lines assuming approx. electron pressure constancy according to the numerical simulation (see pressure profiles of fig.2) leads to the location of the separatrix in the midplane at 1-1.5 cm outside of the nominal position. The same deviation was inferred from the study of soft x-rays produced by suprathermal electrons hitting the Langmuir probe shield /11/.

As in earlier simulations with a 1D code coupled to the DEGAS neutral Monte Carlo code /12/, classical heat conduction along field lines with only a moderate flux limitation must be assumed, if the corrected separatrix position is taken.

Conclusions: Detailed Langmuir probe measurements in main chamber and divertor give a quite consistent picture of the SOL structure in ASDEX. The results agree reasonably with other edge measurements. Numerical simulations yield Bohm diffusion near the separatrix and even higher values farther out. In addition, The parallel heat flux is best described by classical heat conduction with only a moderate flux limit. Simultaneous fit of midplane and divertor profiles require that the actual separatrix position in midplane is 1-1.5 cm outside the nominal one.

* NRCNS "Demokritos", Athens, Greece

** Nuclear Research Centre Karlsruhe, Germany

/1/ Y.Shimomura et al., Nucl. Fusion 23, 869 (1983)
/2/ F.Söldner et al., Phys.Rev.Lett. 61, 1105 (1988)
/3/ G.Fussmann et al., J.Nucl.Mater. 128/129, 350 (1984)
/4/ N.Tsois et al., Europhys.Conf.Abstr. 11D, 658 (1987)
/5/ M.ElShaer, IPP Report III/96 (1984)
/6/ M.Lenoci, G.Haas, IPP Peport III/113 (1986)
/7/ I.G.Brown et al., Phys.Fluids 14, 1377 (1971)
/8/ H.Würz et al., Proc. 15th SOFT, Utrecht (1988), to be publ.
/9/ B.Braams, NET Report No.68 (1987), EUR-FU/XII-80/87/86
/10/ A.Rudyj et al., this conference
/11/ J.Neuhauser et al., Bull.Am.Phys.Soc. 32, 1839 (1987)
/12/ W.Schneider et al., Contr.to Plasmaphys. 28,387 (1988)

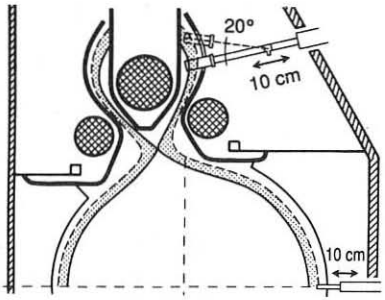

Fig.1. Langmuir probe location in the SOL of ASDEX

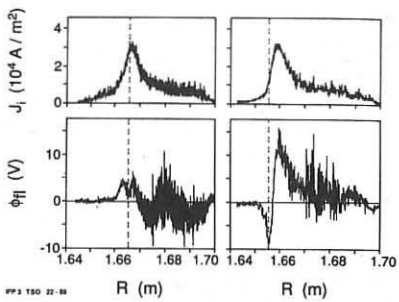

Fig.3. Divertor ion saturation current and floating potential for normal (left) and reversed (right) magnetic field polarity.

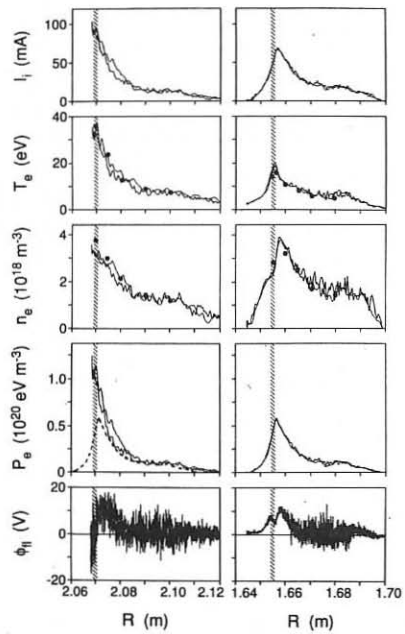

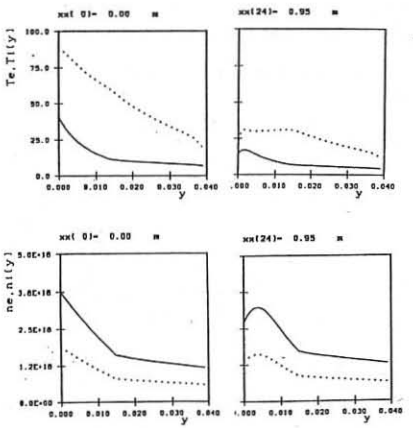

Fig.4. Numerical temperature and density profiles for parameters similar to those of fig.2.

Fig.2. Profiles of plasma parameters in the midplane (left) and divertor (right). $\bar{n}_e = 2.7*10^{19}$ m^{-3}, $P_{OH} \approx 350$ kW.

THERMAL FLUX ASYMMETRIES IN THE FT EDGE PLASMA

M. Ciotti, C. Ferro, G. Maddaluno

Associazione EURATOM-ENEA sulla Fusione, C. R. E. Frascati,
C.P. 65 - 00044 - Frascati, Rome, Italy

INTRODUCTION

A magnetized plasma loses energy through two main channels: by radiation diffusing uniformly to the vacuum chamber enclosing the plasma and by means of particles flowing along flux tubes to localized zones of the chamber. A knowledge of the relative amount of the two channels as a function of the plasma parameters is important for formulating models of the scrape-off layer (SOL) and for developing credible designs of the structures necessary to control the plasma (limiters/divertor plates) and improve the plasma performances (launcher structures for auxiliary heating).

The best method for investigating the thermal loads is surface thermography by infrared techniques, which can provide spatially- and temporally-resolved information during a discharge. When, as in FT, the machine compactness rules out this possibility, a set of thermocouples distributed in different zones in the vacuum chamber can be conveniently used to measure the total energy deposited per discharge in the different zones.

In FT we have used this philosophy inserting thermocouples in the vacuum chamber, the limiter and in other structures. Some experimental results have already been presented [1,2], and in this paper we report data obtained from two thermocouples embedded in the protective plates of the RF launcher structure.

EXPERIMENT

In FT the heating of the plasma with lower hybrid radiofrequency has been performed with different launcher structures. The current one, at 8 GHz, is an antenna of 16 waveguides with overall dimensions near the plasma of about 15 cm in the poloidal direction and 2.6 cm in the toroidal direction. The launcher structure is located on the outer equatorial plane at 90° toroidally from the main limiter. On both the electron and ion sides, a stainless steel protective plate has been mounted bearing a thermocouple embedded at 1.6 mm under the surface facing the plasma flow (normal to the toroidal field) and at about 3 mm from the waveguide tip. The radial position of the launcher structure has always been in the shadow of the limiter, which has a radius of 20 cm, and between 20.5 and 21.5 cm from its poloidal center of curvature.

RESULTS

Among the discharges which the guide temperature was monitored for, we only selected the ones not showing abnormal event such as disruptions, runaways, strong MHD activities, MARFEs. Because of the lack of time resolution during a discharge, the average values of the plasma position, density, energy and current were used in looking for any dependence of the thermocouple data on plasma parameters. In this way a total

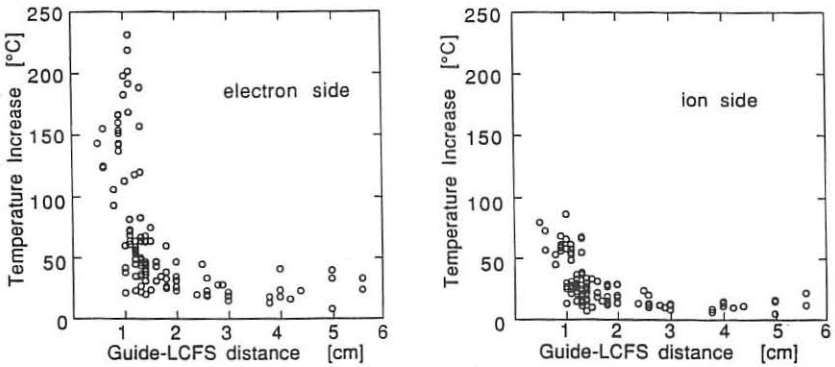

Fig. 1 - Electron (a) and ion (b) side temperature increase of the r.f. guide as a function of the distance from the last closed flux surface

of 120 discharges covering a wide range of plasma parameters was analyzed. The plasma current varied from 280 to 410 kA, the energy from 500 to 800 kJ, and the average electron density from 0.3×10^{14} cm^{-3} to 2.1×10^{14} cm^{-3}.

In order to estimate the effective distance of the structure from the plasma edge, the shift of the plasma center from the chamber toroidal axis was taken into account and the last closed flux surface (LCFS) was considered as in Ref. [3]. Figures 1a and 1b report the temperature increases measured in the electron and ion sides as a function of the distance between the launcher structure and the LCFS.

With reference to the power absorbed by the structure, the maximum temperature in Fig. 1a corresponds to a value of about 20 kW, i.e., 3% of the total ohmic input power.

The experimental data plotted in Fig. 1 refer to discharges with the toroidal magnetic field antiparallel to the plasma current. Electron and ion sides show a similar trend with the ion side values systematically lower by a factor ranging between 1.5 and 3.5. Some shots were also run with the toroidal field parallel to the plasma current. They showed a reversed, although not symmetric, electron to ion side ratio. In Fig. 2, a comparison is made between discharges with similar plasma parameters, but different toroidal field direction.

In order to rule out the not easily estimable dependence of the power load on the plasma displacement, only the shots with a well-centered plasma position are reported in Fig. 3. An exponential-like decrease of the structure heating with the distance from the LCFS can be noticed.

DISCUSSION AND CONCLUSIONS

In a compact high field machine like FT, the particle and energy fluxes to the material structures inside the vacuum chamber are critically dependent on the radial position. In fact, both the density [4] and the energy [2] decay lengths are very short. The sharp increase of the temperature when the grill mouth approaches the plasma edge (Figs. 1a, 1b) just reflects the exponential dependence of the energy flux on the radial distance.

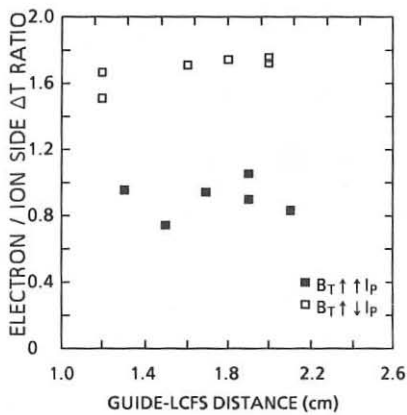

Fig. 2 - Electron to ion side temperature increase ratio for B_T parallel and antiparallel to I_p

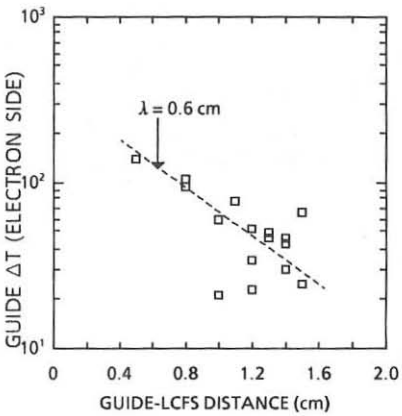

Fig. 3 - Electron side temperature increase for well-centered plasma discharges

On the other hand, the bulk parameters are also known to influence the boundary plasma. On FT a strong dependence of the scrape off density on both the bulk density and current was inferred from Langmuir measurements [4].

The scatter of the experimental data can be attributed to both this dependence on bulk parameters and the influence of the plasma horizontal displacement. The latter affects the energy fluxes to the structures in a fairly complicated way owing to the change of the connection lengths (i.e., of the energy decay lengths) and the extension of areas *wetted* by the plasma. In this respect, the flatness of the temperature vs plasma-guide distance curve beyond 2 cm (mostly related to inward shifted plasma position) seems to indicate the onset of a drastic change in the spatial distribution of the conductive-convective energy losses. As a result, the thermal load on the grill mouth becomes almost independent of the distance from the plasma edge.

With regard to the directional asymmetries of the thermal loads, it must be considered that the connection length on the electron side is larger than on the ion side by a factor of about 3. Assuming an exponential decay of the power flux in the scrape off layer and taking into account the dependence of the e-folding length λ_E on the connection length $L_\parallel$ ($\lambda_E \propto \sqrt{L_\parallel}$), an electron to ion ratio of 1.7 should be expected, irrespective of the toroidal field direction.

Both the scatter in the values of this ratio for B_T antiparallel to I_p and, especially, its inversion when B_T is reversed, seem to rule out a simple geometric explanation of the directional asymmetry observed. It can be attributed to nonpoloidally uniform plasma parameters in the scrape off layer of a limiter-controlled discharge [5].

The dependence on the bulk plasma parameters of the total value as well as of the electron/ion side asymmetry of the thermal load are under critical review.

REFERENCES

[1] C. Ferro et al.: Proc. 12th European Conf. on Controlled Fusion and Plasma Physics (Budapest, 1985) 9F, 2, 555
[2] G. Maddaluno, M. Ciotti, C. Ferro: ENEA Report RT/FUS/86/1
[3] S.K. Erents et al.: Nucl. Fusion 28, 1209 (1988)
[4] V. Pericoli-Ridolfini: Plasma Phys. and Controlled Fusion 27, 493 (1985)
[5] A.S. Wan et al.: J. Nucl. Mater. 145-147, 191 (1987)

EROSION-REDEPOSITION PROCESSES ON THE FT LIMITER STUDIED BY PROBES OF DIFFERENT MATERIAL

G. Maddaluno

Associazione EURATOM-ENEA sulla Fusione, C. R. E. Frascati,
C.P. 65 - 00044 - Frascati, Rome, Italy

A.P. Martinelli

Max-Planck-Institut für Plasmaphysik, Euratom Association,
D-8046 Garching (F.R.G.)

INTRODUCTION

The erosion-redeposition processes occurring on the limiter of a high field, high density tokamak like FT [1] play a great part in the global behaviour of the discharge. In fact in these machines the limiter is by far the major source of impurities.

A knowledge of the extent of the erosion-redeposition phenomena as well as of their poloidal and directional (electron versus ion side) asymmetries can give useful information about the limiter geometry and material to be used on the future devices. Following previous measurements [2,3], efforts have been made in this work for a better understanding of the erosion-deposition processes occurring on the FT limiter.

EXPERIMENT

A set of long-term deposition probes was mounted on the lateral sides of the full poloidal stainless steel limiter support (Fig. 1), between 10 and 25 mm from the plasma edge (the part of the limiter closest to the plasma consisted of mushroom-shaped Inconel pieces). The set included: four couples of graphite (Ringsdorff EK 98) and titanium targets close together, distributed on both the electron and the ion side of the limiter support at about 70° above and below the outer equatorial plane; four graphite targets mounted at about 30° above and below the inner equatorial plane, on both the ion and electron sides; a further couple of graphite and titanium targets (henceforth named CØ and Ti 45) mounted on the electron side at about 30° above the outer equatorial plane. Unlike the other targets, which had their collecting surfaces perpendicular to the toroidal direction, the titanium target of this couple was inclined at 45 degrees and collected only particles travelling between 20 and 25 mm from the plasma edge. In turn, the graphite target was able to collect only the particles reflected or emitted by the titanium surface.

In the summer 1987 experimental period, the targets were exposed to ohmically and rf heated deuterium discharges, with the toroidal magnetic field B_T antiparallel to the plasma current I_p. About 30% of the discharges ended with a disruption. The total time of exposure was 415 s. After removal from the limiter, the targets were surface analyzed by PIXE. Before and after the plasma exposure, the weight of the targets was carefully measured.

RESULTS

Large metal concentrations (Ni, Fe, Cr) were found on all the targets directly exposed to the plasma, the Ti 45 included. Radially averaged values range between $1 \cdot 10^{18}$ and $5.5 \cdot 10^{18}$ atoms cm^{-2}, depending on the poloidal as well as on the directional

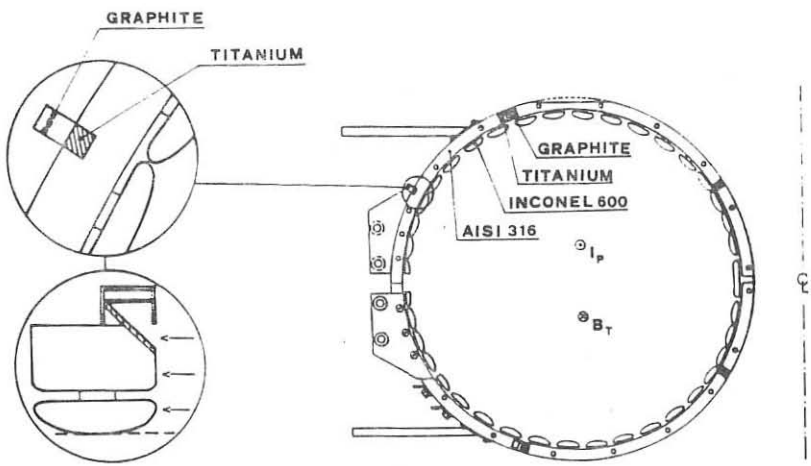

Fig. 1 - Schematic view of the full poloidal FT limiter with the long-term target positions

position (Fig. 2). Much lower amounts ($\sim 3.8 \cdot 10^{16}$ atoms cm^{-2}) were found on the graphite target CØ.

The elemental composition of the metal deposit resembles Inconel 600, as nickel is by far the major component. Above the equatorial plane, the largest amounts of metallic impurities are on the graphite targets facing the ion side, while in the bottom half of the limiter, the pattern is reversed. The radial profile of the metal deposition shows a composite asymmetric pattern too. Short lengths (0.4÷1.4 cm) are observed on the electron upper side and the ion lower side, whereas the deposits on the lower electron and upper ion side are rather flat. A similar trend is observed on the titanium targets, but the differences in the amount of metal between the electron and the ion side are much smaller.

The weight changes of the closely mounted graphite and titanium targets are reported in Table I. The net erosion of three of the graphite targets as well as the weight increase of all the titanium targets is evident. A weight loss was also measured on the other graphite targets.

Very low titanium concentrations (maximum one monolayer) were found on the graphite targets mounted on the support sides, and nothing at all on the target CØ.

DISCUSSION

The erosion and deposition processes occurring at the limiter during an experimental period can be conveniently investigated with long-term targets by simultaneously performing weight change and impurity concentration measurements. Further information about erosion and its mechanisms can also be obtained from the combination of an erosion target and a collector, as well as from the use of two different materials as erosion target. In this respect the most striking result is the net erosion of the graphite targets (except one) in comparison with the weight increase of the titanium ones (the amount of the metal deposit being the same). This result could be justified by assuming that physical sputtering is the main cause of the graphite erosion, at least in the observed radial range. As a matter of the fact, at the energy the ions

Table I

MATERIAL	POLOIDAL POSITION*	SIDE	WEIGHT CHANGE (mg)
C	110°	e⁻	+ 0.34
Ti	110°	e⁻	+ 0.30
C	110°	i+	-10
Ti	110°	i+	+ 5.5
C	250°	e⁻	-10
Ti	250°	e⁻	+ 0.78
C	250°	i+	-0.26
Ti	250°	i+	+ 0.55

** 0° on the inner equator, counterclockwise rotation*

are expected to impinge with ($E \sim 5k\,T_e \sim 75$ eV; $T_e \sim 15$ eV [4]) the sputtering yield by deuterium is ten times higher for carbon than for titanium. Chemical sputtering of carbon probably plays a minor role because the temperature of the targets, as inferred from subsequent thermocouple measurements in the same radial position, seldom reached the value which the hydrocarbon production is enhanced at [5].

The negligible erosion of medium-z materials beyond 1 cm from the plasma edge is confirmed both by the low (Ni, Fe, Cr) or no (Ti) metal deposit on the graphite target CØ and by the elemental composition of the metal coverage of the targets, which resembles Inconel rather than stainless steel.

With regard to the asymmetries in the impurity deposition, from a comparison with a previous set of graphite targets exposed to discharges with B_T parallel to I_p [3], a dependence on the B_T direction of these poloidal and directional asymmetries can be inferred (Fig. 3). With $B_T \uparrow \uparrow I_p$ the largest metal concentrations are found on the electron side above, and on the ion side under, the equatorial plane. The opposite is true for $B_T \downarrow \uparrow I_p$. The macroscopic damages on previous FT limiters showed the same dependence on the toroidal field direction.

The composite top-bottom electron-ion side asymmetry of the impurity radial profiles is reversed too, by changing the B_T direction.

The pattern of the radial profiles of the metal deposit in the present experiment is reminescent of the poloidal asymmetries in electron density e-folding lengths, as found on Alcator-C using Langmuir probes [6]. In effect, by adding up the electron and ion side contributions, the poloidal asymmetries of the impurity radial profiles are in qualitative agreement with the trend of the density decay lengths (longer at the outside than at the inside). Nevertheless, in this case, the most evident feature is the existence of a directional asymmetry, which Langmuir probes were not able to discern.

CONCLUSION

Long-term targets of different material (graphite and titanium) have been used on the FT limiter to get information about the erosion and deposition processes.

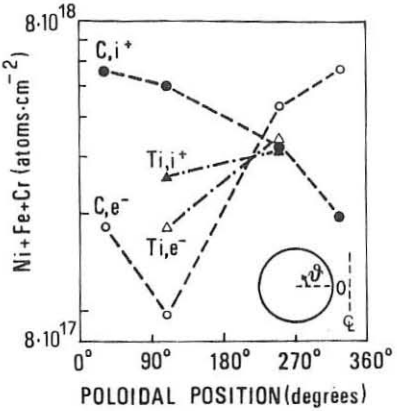

Fig. 2 - Radially averaged poloidal distribution of the metal impurities on the graphite and titanium targets

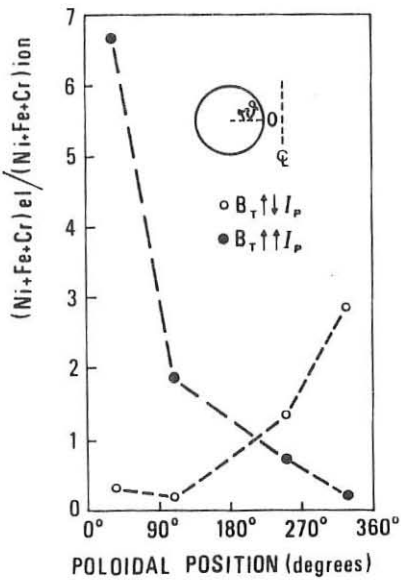

Fig. 3 - Electron to ion side ratio of the metal coverage for both the B_T directions

From impurity concentration and weight change measurements, graphite targets were found to be more eroded than titanium ones beyond 1 cm from the plasma edge, probably as a result of the different sputtering yield. A poloidally and directionally asymmetric pattern of the metal deposit was found too; the pattern depends on the B_T direction. The low erosion of medium-z material on the limiter support could mean a tolerable metal contamination of the graphite mushrooms in the metal-graphite limiter envisaged for FT [7].

REFERENCES

[1] F. De Marco et al., Nucl. Fusion 26, 1193 (1986)
[2] G. Maddaluno, A.P. Martinelli, 14th European Conf. on Controlled Fusion and Plasma Physics, Madrid (1987), part II, p. 786
[3] G. Maddaluno, A.P. Martinelli, 8th Int. Conf. on Plasma-Surface Interactions (Jülich, FRG, May 1988), to be published on J. Nucl. Materials
[4] V. Pericoli-Ridolfini, Plasma Phys. and Controlled Fusion 27, 493 (1985)
[5] R.A. Langley et al., Nucl. Fusion, special Issue (1984)
[6] F. La Bombard, M.I.T. Plasma Fusion Center Report PFC/RR-86-6 (1986)
[7] C. Ferro, private communication

FTU PUMP LIMITER

C. Alessandrini, M. Ciotti, A. De Matteis, G. Maddaluno, G. Mazzitelli

Associazione EURATOM-ENEA sulla Fusione, C. R. E. Frascati,
C.P. 65 - 00044 - Frascati, Rome, Italy

DESIGN

The control of the refuelling and recycling of the plasma is crucial in providing enhanced performances in tokamaks and steady-state operation in future reactos.

In this paper, we report details of the design and analysis for the pump limiter to be incorporated into the FTU tokamak. The FTU, presently under commissioning, is a compact, high field (B=8 T), medium high density, circular cross section machine with small accesses. The dimensions of the equatorial port (width 8 cm) would reduce the length of the entrance throat to a few centimeters, which is unacceptable for efficient particle trapping. We have, therefore, designed a rotating blade of the pump limiter head that, in the working position, extends in the toroidal direction inside the vacuum chamber (Fig. 1).

A simple model [1] of the scrape-off layer (SOL) has been adopted for the analysis and design of the pump limiter. The principal assumptions are that the SOL plasma density and temperature are given by

$$n(x)=n_0(r=a)\exp(-\frac{x}{\lambda_n})$$

and

$$T(x)=T_0(r=a)\exp(-\frac{x}{\lambda_T})$$

a = plasma radius

where λ_n and λ_T are the e-folding lengths for the density and temperature respectively. These two parameters could be calculated theoretically, but due to the poor knowledge of transport coefficients, we have chosen to extrapolate the values from the results obtained on FT [2]. With λ_n=1 cm and λ_T=3 cm the e-folding lengths for the particle flux are therefore λ_Γ=0.86 cm and λ_q=0.66 cm.

The pump limiter design is always a compromise between high particle exhaust and the capability of handling high power fluxes.

In FTU an exhaust efficiency of 5÷10% with an average throat length and width, respectively, of 12 cm and 2 cm seems to be feasible. The thickness of the blade of the head goes from 0.2 cm at the leading edge to 1.5 cm in the middle. The length of the entrance throat should be sufficient to ionize a neutral product at the deflector plate before it can return to the plasma.

By utilizing a 3 D Monte Carlo code NIMBUS [3] having as input parameters the ionic flux to the entrance throat the density and temperature in the SOL, together with a simplified geometrical model of the pump limiter, we have obtained the following results: 30% of the neutrals produced go directly to the pump system, 60% are ionized

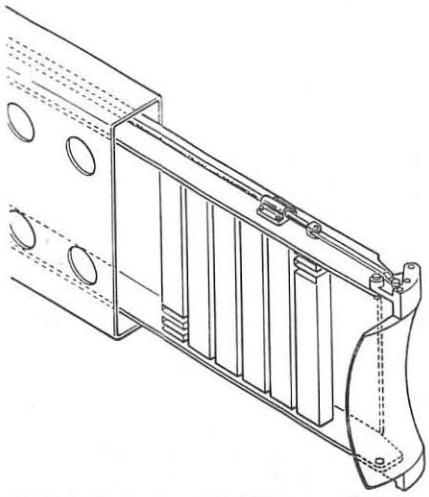

Fig. 1 - Artistic view of the FTU pump limiter

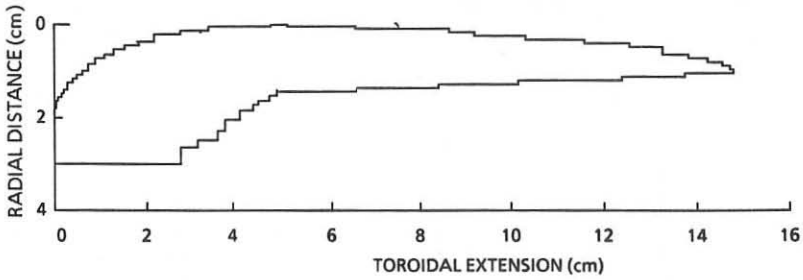

Fig. 2 - Pump limiter head geometry used for thermal load analysis

in the throat and 10% stream back to the plasma. the exhaust efficiency is ε=4%, which should be sufficient for plasma density control. It is worthwhile noting that the phenomenon of plasma plugging is not taken into account in the code [1].

THERMAL LOAD

A thermal load analysis on the FTU pumped limiter has been carried out to evaluate both the regime-temperature reached by the AISI 304 limiter and the amount and location of melted material during a single discharge. A finite difference heat conduction code [4] has been used with the following hypothesis: a) a 2D geometry (Fig. 2) has been used because of the poloidal symmetry; b) the limiter receives a power density given by

$$\begin{cases} P(x)=P_L e^{-x/\lambda_E/2\theta a\lambda_E} & 0<t\leq 1s \\ P(x)=0 & t>1s \end{cases}$$

where r is the radial distance from the plasma edge, θ the poloidal extension, λ_E the energy decay length and P_L the total power flowing to the limiter; c) cooling by radiation is admitted.

Figure 3 shows the depth of melted material in the leading edge belt for a single discharge as a function of the total power P_L. This is the zone where the penetration of fused material is maximum. To evaluate the regime-temperature of the limiter, especially in the zone where the rotation axis of the limiter head is placed, a set of discharges with power P_L = 650 kW and a duty cycle of then minutes was simulated. In these conditions, a regime temperature of 350°C has been estimated. The P_L value corresponds to the ohmic power fraction expected to be transported by conduction and convection to the limiter according to the measurements on the FT machine [5].

PUMPING SYSTEM

Bulk getter pumps will be employed to exhaust the particles trapped in the limiter throat. They were chosen becuse the pumps must be installed as close as possible to the geometry and the magnetic fields rule out cryogenic and turbomolecular pumps. The performance of nonevaporable getter pumps under transient load conditions was successfully tested at pressure higher than 1.33 Pa [6], and the problem related to the embrittlement of the getter material during the discharge cleaning operation [7] can be overcome by a suitable temperature increase of the pump.

An array of six or seven *wafer* modules (metallic strips pleated and coated with Zr-V-Fe getter material) will be installed directly behind the limiter head between 10 and 50 cm from the neutralizer plate. The nominal pumping speed of each module for

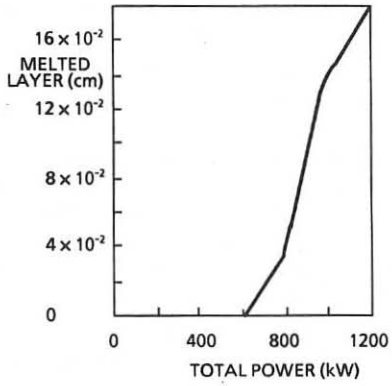

Fig. 3 - Calculated melt depth at the leading edge vs total power flowing to the limiter

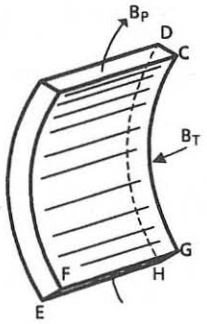

Fig. 4 - Model of the pump limiter head for electromagnetic load analysis

deuterium at room temperature is ~800 $l \cdot s^{-1}$. Due to the conductance limitations, the total pumping speed for thermal particles of six modules is expected to be ~3700 $l \cdot s^{-1}$. A value of ~4200 $l \cdot s^{-1}$ can be reached by covering the wall of the supporting structure with metallic foils coated with the getter material. This pumping speed corresponds to 85% of that required to get 10% exhaust efficiency at the maximum particle flux expected in FTU (~$1.2 \cdot 10^4$ $Pa \cdot l \cdot s^{-1}$).

ELECTROMECHANICAL LOADING

The main mechanical loading experienced by the pumped limiter head results from the interaction between the toroidal magnetic field and the eddy currents induced in the limiter itself during plasma disruptions.

In order to quantify the mechanical forces and torques applied to the limiter, a simple analytical model was used. An exponential decay of the plasma current, $I(t)=I_0 \exp(-t/\tau_d)$ was assumed, with $I_0=1.6$ MA and $\tau_d=3.0 \cdot 10^{-3}$ s. The limiter head was modelled by a part of a stainless steel 30×15×1.5 cm^3 cylindrical shell, with a curvature radius equal to the plasma minor radius (Fig. 4).

Within the approximation of concentric circular magnetic surfaces and of fixed plasma position during the disruption, the angle between the poloidal field and the limiter surface is different from zero only on the small top and bottom areas (ABCD and EFGH in Fig. 4).

The eddy current induced on these surfaces was calculated according the equation

$$\frac{di}{dt} + \frac{R}{L} i = \frac{A}{L} \frac{B_p(0)}{\tau_d} \exp(-\frac{t}{\tau_d})$$

$$i(t) = \frac{A B_p(0)}{R(\tau - \tau_d)} \left[\exp(-\frac{t}{\tau}) - \exp(-\frac{t}{\tau_d}) \right]$$

where $\tau=L/R$. From the interaction of this current with the toroidal field (B=8 T), negligible forces (~60 N) result applied to the short sides of each surface. Even by allowing a rapid plasma motion, these forces increase only by a factor 1.5.

In order to take into account more realistic cases, the maximum torque that the rotation mechanism can withstand (~600 Nm) was used to get a maximum allowable angle of 20° between the poloidal field and the limiter large face (BFGC in Fig. 4).

CONCLUSIONS

A pump limiter will be installed at the beginning of 1990 in the high density high field FTU machine. Experimental work will be principally devoted to the control of the plasma density in ohmic discharges and to the study of plasma edge related phenomena.

REFERENCES

[1] R.W. Conn: J. Nucl. Materials **128&129**, 407 (1984)
[2] V. Pericoli-Ridolfini: Plasma Phys. Control. Fusion **27**, 4, 493 (1985)
[3] E. Cupini et al.: NET Report 9 EUR XII+324/9 (1983)
[4] W.D. Turner et al.: Report ORNL/CSD/TM-15 (1977)
[5] C. Ferro et al.: Proc. 12th European Conf. on Controlled Fusion and Plasma Physics, Budapest 9F, 2, 555 (1955)
[6] L.C. Emerson et al.: J. Vacuum Science Techn. **A2**, 4, 1583 (1984)
[7] L.C. Emerson et al.: J. Nucl. Materials 122&123, 1156 (1984)
[8] D.W. Weissenburger et al.: Fusion Techn. 10, 448 (1986)

LOW-FREQUENCY FLUCTUATIONS AND FLUCTUATION-INDUCED TRANSPORT IN THE ASDEX EDGE PLASMA AND IN A LOW-PRESSURE DISCHARGE

M.Krämer*, A.Carlson, ASDEX-Team,
*Institut für Experimentalphysik II, Ruhr-Universität, D-4630 Bochum,
Max-Planck-Institut für Plasmaphysik, EURATOM association, D-8046 Garching,
Fed. Rep. Germany

Introduction Low-frequency turbulence is considered as a main cause of particle transport in a magnetized plasma, in particular, in the edge plasma of tokamaks. To gain more insight in the physical nature of the low-frequency turbulence and the anomalous transport, it is useful to compare this plasma with a plasma of much simpler properties (homogeneous magnetic field, no currents etc.). Hence, the low-frequency density and potential fluctuations and the transport induced by these fluctuations were studied both at the plasma edge of the ASDEX-tokamak and on the plasma of a low-pressure (weakly collisional) linear discharge which is dominated by anomalous cross-field transport as well.

Experimental details On ASDEX (**A**), the investigations were performed during ohmically heated divertor (double null) deuterium discharges in the plateau region at $t \approx 1.5s$. The probe signals were taken approximately $4cm$ outside the separatrix ($r' = 4cm, n = (2-3) \times 10^{12} cm^{-3}$, $L_n = (1/n\, dn/dr)^{-1} \approx 2cm$) for different combinations of the toroidal magnetic field and plasma current ($B_t = 1.69, 2.17, 2.61T$ and $I_p = 250, 320, 384kA$). In addition, a radial fluctuation profile was measured under standard conditions ($B_t = 2.17T$, $I_p = 320kA$). Correlation analysis of paired probe signals is applied to measure both the fluctuation spectra and the transport spectra. An array of four Langmuir probes (probe tips Mo, $r_p = 0.3mm$, $L_p = 1.5mm$, distance $\Delta x = 3mm$) is used to detect the density and the potential fluctuations. Accordingly, two probes are biased in the ion saturation regime and two at the floating potential. The probes are arranged such that both the poloidal (azimuthal) and the radial wavenumber spectra can be measured.

The low-pressure discharge (**D** ; $r_D \approx 9cm$, $L_D \approx 2m$) is generated in a homogeneous magnetic field $B = 0.08 - 0.21T$ using RF power pulses ($f = 27MHz$, $P_{RF} \leq 400W$) launched to the plasma by a ring antenna in the lower-hybrid regime. The fluctuation signals were taken in the outer region of the plasma ($p \approx 3mTorr$ hydrogen, $n_e \leq 10^{11} cm^{-3}$, $T_e \leq 10eV$). Here, the floating probes are replaced by capacitive probes which have a better frequency response. The four probes are aligned in the plane perpendicular to the magnetic field, and the probe tips (Wo, $r_p = 0.05mm$, $L_p = 5mm$, $\Delta x = 4mm$) are oriented in B-direction.

Correlation analysis is applied to analyze the fluctuation signals. The spectral density $S(k,\omega)$ for the density and the potential fluctuations, $\tilde{n}$ and $\tilde{\phi}$, is computed in a statistical manner (Beall et al.[1]), where k represents the wave vector component (here, k_r and k_θ) defined by two probe tips. By proper normalization of $S(k,\omega)$, we obtain the spectral distribution function whose first and second moment yield the mean wavenumber $\overline{k}(\omega)$ (which can be interpreted as "statistical" dispersion of the turbulence) and the variance $\sigma_k^2(\omega)$ (σ_k = wavenumber spectral width).

The transport, owing to the $\mathbf{E} \times \mathbf{B}$ -convection of the particles in the field of the fluctuations, is estimated from the correlation between density and potential fluctuations, where the phase angle α between the two quantities plays the dominant role. The transport spectrum can be written as $T(\omega) = 1/2\, k_\theta \tilde{n}\tilde{\phi} sin(\alpha) \gamma_{\tilde{n}\tilde{\phi}}/B$ (Powers^2) where the coherency $\gamma_{\tilde{n}\tilde{\phi}}$ and the other quantities are functions of ω.

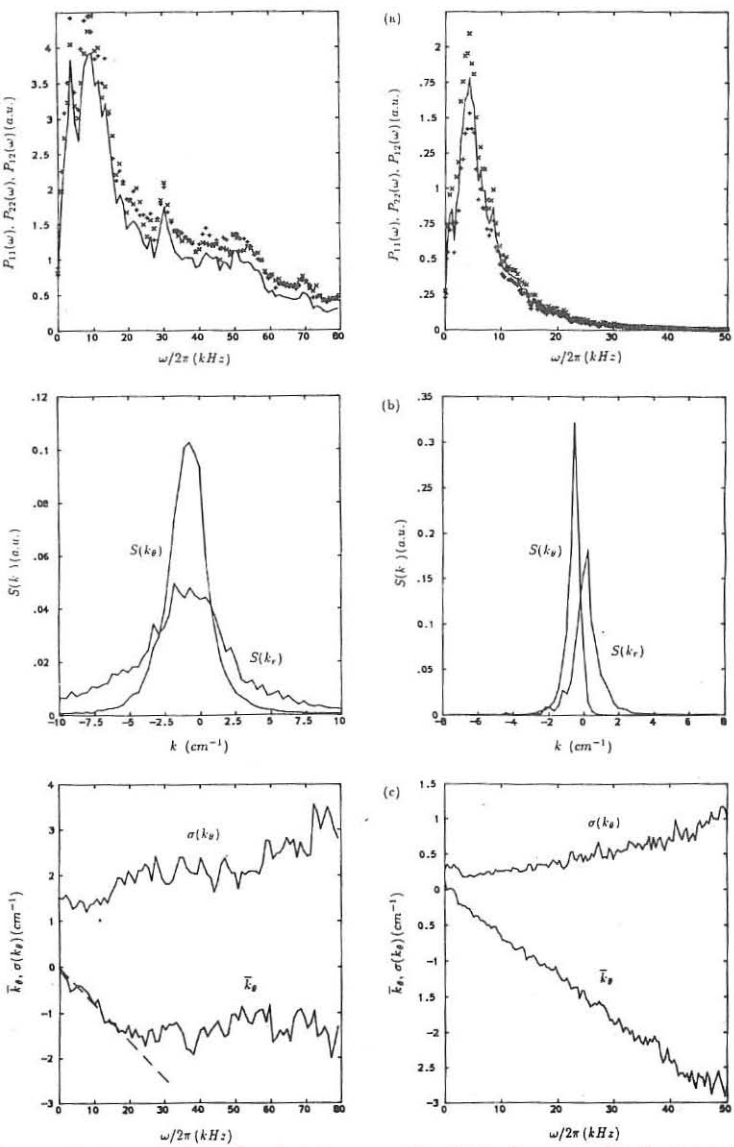

FIG.1 (a) Auto-power (×, +) and cross-power (θ, solid line) spectra, (b) Radial and poloidal wavenumber spectra. (c) Mean poloidal wavenumber and spectral width (A(left): #25525, $B_t = 2.61T$, $I_p = 384kA$; D(right): $r = 6.5cm$, $L_n = 2.2cm$, $B = 0.132T$, $T_e = 5eV$)

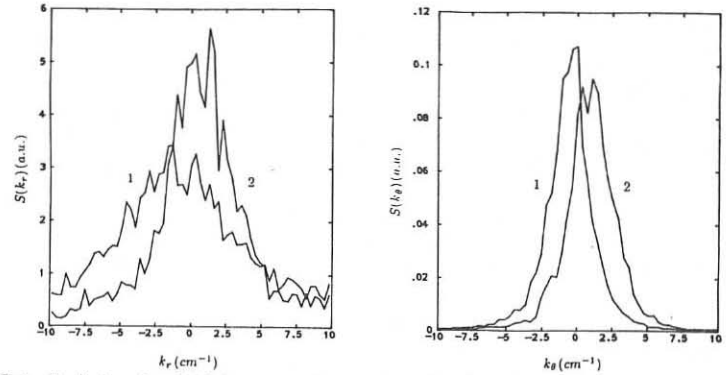

FIG.2 Radial and poloidal wavenumber spectra for $r_1' = 3.5cm$ and $r_2' = 3.0cm$ in A (shots #25572, and #25573, $B_t = 2.17T$, $I_p = 320kA$)

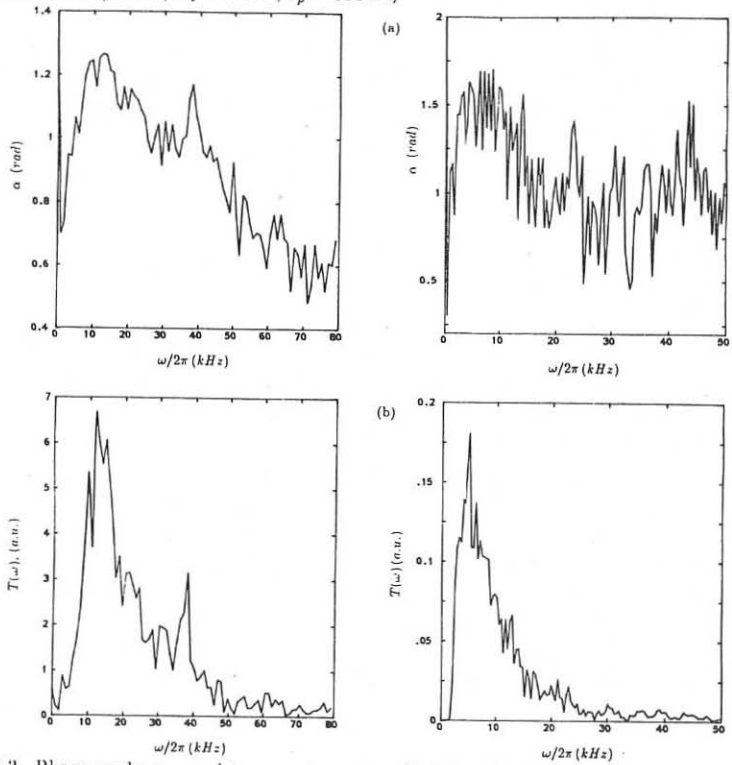

FIG.3 Phase angle $\alpha_{\tilde{n}\tilde{\phi}}$ and transport spectra (A(left), D(right) ; same data as in FIG.1)

Characterization of the fluctuations The power spectra (FIG.1a) show pronounced maxima at $f = 5-10kHz$ in A and $f = 2-5kHz$ in D. The (frequency integrated) wavenumber spectra (FIG.1b) depict much broader spectra in A than in D. However, in both cases, the coherence length is smaller in radial direction than in poloidal direction (A: $\sigma(k_r) = 3.5-5.0cm^{-1}$, $\sigma(k_\theta) = 1.8-2.7cm^{-1}$, B :$\sigma(k_r) = 1.7-2.0cm^{-1}$, $\sigma(k_\theta) = 0.3-0.4cm^{-1}$). Correspondingly, the spectral index q is smaller in A ($q_r = 1.1-2.5$, $q_\theta = 2.2-3.6$) than in D ($q_r = 2.4-3.0$, $q_\theta = 4.4-5.6$) In both experiments,the fluctuation level $\tilde{n}/n$ is nearly constant over all shots. In D, $\tilde{n}/n$ increases monotonically with ρ_s/L_n as various drift wave theories predict (Wakatani and Hasegawa[5]), whereas, in A, $\tilde{n}/n$ is nearly constant although ρ_s/L_n varies by a factor 3. (Mean values for $\tilde{n}/n(A) = 0.21 \approx 15\rho_s/L_n$, $\tilde{n}/n(D) = 0.32 \approx 4.4\rho_s/L_n$). The observed $\tilde{n}/n$ is in both experiments about twice larger than the 'mixing length' level $1/k_\perp L_n$ ($k_\perp \approx \sigma(k_r)$ from $S(k_r)$).

Poloidal phase velocity Evaluating the dispersion curves (Fig.1c), we found that the observed poloidal phase velocities are in ion diamagnetic direction (as was already observed on TEXT[3] and CALTECH[4]). This observation can be described by a superposition of the electron drift velocity v_{De} and the $\mathbf{E} \times \mathbf{B}$-velocity due to the constant electric field in radial direction: $v_{ph} = \omega/k_\theta = (T_e/eL_n - E_r)/B$. Calculating the profiles of the mean density and the mean floating potential during the fast movement of the probe, taking into account the relation $\phi_p = \phi_f + ln(m_i/m_e)T_e/2e$ between plasma and floating potential, and assuming $T_e = 20eV$ and $L_n \approx L_{Te}$ (taken from comparable shots), it turns out that the $\mathbf{E} \times \mathbf{B}$-velocity predominates over v_{De}, and rough agreement with the observed phase velocities ($v_{ph,min} = 5 \times 10^4 cm$ for $B_t = 2.61T$, $I_p = 250kA$ and $v_{ph,max} = 2.2 \times 10^5 cm$ for $B_t = 1.69T$, $I_p = 320kA$) is achieved. As on TEXT[3], the propagation velocity reverses when the probe is moved inward. From Fig.2, a sharp transition is observed, and the k_r-spectra broaden at the same position.

In D, the pronounced linearity of the dispersion is noteworthy. Also here, the turbulent waves travel in ion diamagnetic direction due to the sufficiently large electric fields causing $\mathbf{E} \times \mathbf{B}$-drift. However, this is observed from the lower-hybrid resonance cone (at $r \approx 4cm$) where the electric fields are large to the plasma edge with small electric fields. Hence, the fluctuations, particularly the azimuthal phase velocity, does not depend solely from the local plasma parameters.

Particle transport Typical transport spectra, computed from the $\tilde{n}$ and $\tilde{\phi}$ fluctuation signals are shown in Fig.3. In both experiments, the phase angle α takes values up to $90°$. The transport spectra have a similar shape as the $\tilde{n}$ and $\tilde{\phi}$ power spectra. However, when the probe approaches the zone where the phase velocity changes sign, the spectra become very broad. The total particle flux at $r' = 4cm$ is $\Gamma = 0.6 \times 10^{16} - 1.5 \times 10^{16} cm^{-2}s-1$ ($\overline{\Gamma} = 8.4 \times 10^{15} cm^{-2}s-1$). There is no systematic scaling with B_t and I_p. In particular, the diffusion coefficients calculated from Fick's law, do not scale as the Bohm coefficient $D_B = T_e/16eB$, but they have the same order of magnitude as D_B.

In D, the particle confinement is also determined by anomalous cross-field transport. However, the diffusion coefficients evaluated from the transport spectra are an order of magnitude smaller than D_B. In addition, no scaling with T_e and $1/B$ is observed.

[1] J.M.Beall, Y.C.Kim, and E.J.Powers, J.Appl.Phys. **53**, 3933(1982).
[2] E.J.Powers, Nucl. Fusion **14**, 749(1974).
[3] Ch.P.Ritz,R.B.Bengtson,S.J.Levinson, and E.J.Powers,Phys.Fluids,**27**,2956(1984).
[4] S.J.Zweben and R.W.Gould,Nucl.Fusion,**25**,171(1985).
[5] M.Wakatani and A.Hasegawa,Phys.Fluids, **27**,611(1984).

STRUCTURE OF TURBULENCE IN THE PLASMA EDGE OF THE TJ-I TOKAMAK

C. Hidalgo, M. A. Pedrosa, A. P. Navarro and E. Ascasibar

Asociación **EURATOM/CIEMAT,** 28040 MADRID, **SPAIN**

INTRODUCTION

In order to understand anomalous transport in tokamaks, much effort has been done both experimentally and theoretically in determining the role of fluctuations in particle and energy transport (1). Studies of edge turbulence in TEXT have shown that the particles fluxes driven by electrostatic fluctuations can give account of most of the particle transport at the plasma edge (2).

In the present work we have studied electrostatic and magnetic fluctuations in the edge region of the TJ-I tokamak. The particle flux resulting from electrostatic fluctuations have been estimated as well as its scaling with density and toroidal field. Magnetic fluctuations levels have been studied using magnetic coils.

EXPERIMENTAL

TJ-I is an ohmically heated Tokamak with a major radius of 30 cm and minor radius of 10 cm. In the TJ-I the vacuum chamber plays the role of a belt limiter. For these experiments the machine was operated at a plasma current of 35 kA, chord-average density ($0.5\text{-}2\text{x}10^{13}\text{cm}^{-3}$) and toroidal field (1.0-1.4 T). Plasma discharges last typically 30 ms. Measurements were taken during the flat top of the discharge.

An square array of four Langmuir probes (3x3mm) was used to determine density and potential fluctuations in the outer region of the equatorial plane. Langmuir probes, of radius 0.02 cm and 0.5 cm length, were working either polarized (-60 V) into the ion saturation regime to measure density fluctuations or without bias to measure floating potential fluctuations. The ion saturation current is given by, $I_s=(1/2)en_eA(T_e/m_i)^{1/2}$ where A is the probe exposed area (≈ 0.06 cm^2), n_e is the local electron density and T_e is the electron temperature ($\approx$ 10 eV). Data acquisition was carried out by means of a four channel CAMAC module with 8 kB of memory per channel at 500 kHz sampling rate. Conventional FFT was used for data analysis.

Electron temperature was measured supplying a swept voltage (-50, 10 V) to a single

Langmuir probe. Temperature fluctuations were considered negligible. Therefore, floating potential and ion saturation current fluctuations were assigned to space potential and density fluctuations respectively.

Magnetic probes (three coils place inside a shielded quartz tube) were used to measure radial ($\tilde{B}_r$) and poloidal ($\tilde{B}_\theta$) magnetic field fluctuation levels at the limiter radius in the top region of the plasma.

RESULTS AND DISCUSSION

Density and potential fluctuations show a turbulent nature with the fluctuation power confined basically below 100 kHz. Density fluctuation level was found to increase with plasma radius. In the proximity to limiter radius density fluctuation level was around (10-20) %. Electron temperature was in the range (5-15) eV. The frequency - wave number spectra $S(k,\omega)$ have been computed for density and potential fluctuations for toroidal and poloidal propagation (3). Typical $S(k,\omega)$ spectra are shown in Figure 1. For poloidal propagation the frequency spectra are broad for all wave numbers and with clear peaks displaced from zero in the electron drift direction; for toroidal propagation the wave-number spectra are narrow and confined around zero. Frequency spectra $S(\omega)$ and wave number spectra $S(k_\theta)$ decrease for large ω and k_θ with a dependence given by $S(\omega)\approx\omega^{-\alpha}$ ($\alpha\approx2$) and $S(k_\theta)\approx k^{-\beta}$ ($\beta\approx3$).

Fluctuations propagate with a velocity, $v(\omega)=\Sigma_k(\omega/k)S(k,\omega)/\Sigma_\omega S(k,\omega)$, basically constant for frequencies below 100 kHz, in the order of 10^5 cm s^{-1} in the electron diamagnetic drift direction.

An estimation of the particle flux due to electrostatic fluctuations can be made from the correlation between density and potential fluctuations (4):

$$\Gamma(\omega) = k(\omega)\,|\gamma_{n_\phi}(\omega)|\;\alpha_{n_\phi}(\omega)\,\tilde{n}\,\tilde{\phi}/B$$

where $k(\omega)$ is the poloidal wave number obtained from the pair of Langmuir probes with a

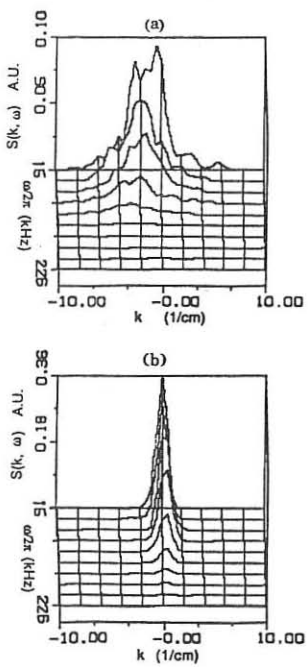

Figure 1. $S(k,\omega)$ spectra for potential fluctuation: (a) poloidal propagation and (b) toroidal propagation.

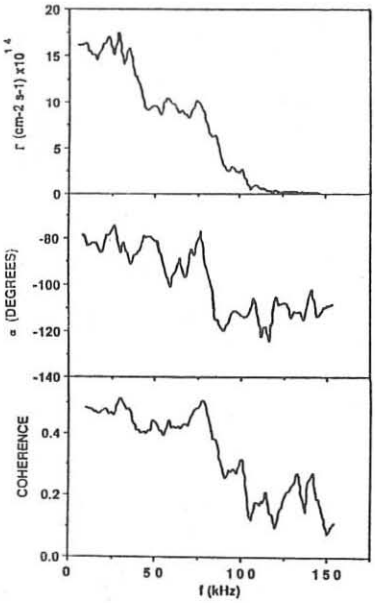

Figure 2. Spectrally resolved flux, phase angle and coherence between density and poloidal fluctuations.

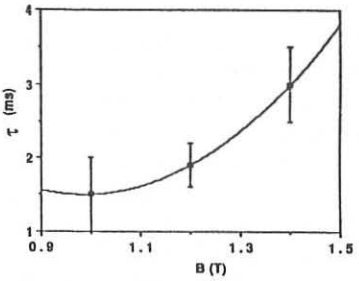

Figure 3. Scaling of the particle confinement time predicted from electrostatic fluctuations with toroidal field.

poloidal separation of 3 mm, and $\gamma_{n\phi}(\omega)$, $\alpha_{n\phi}(\omega)$ are the coherence and the phase angle between density (n) and potential fluctuations (ϕ) respectively. Typical frequency resolved particle flux $\Gamma(\omega)$ as well as $\gamma_{n\phi}(\omega)$ and $\alpha_{n\phi}(\omega)$ are shown in figure 2. The particle flux is mainly due to fluctuations with frequencies below 100 kHz.; phase angle between density and potential fluctuations is between 0.3π and 0.5π and coherence decreases at the higher frequencies. In order to deduce total particle fluxes, we have assumed poloidal and toroidal symmetries. With this hypothesis the particle confinement time inferred from electrostatic fluctuations is given by $\tau \approx n_e\, a/2\, \Gamma$, where n_e is the chord average electron density, a is the plasma radius and $\Gamma = \Sigma_\omega\, \Gamma(\omega) \approx 3\times10^{16} cm^{-2}s^{-1}$.

The particle confinement time scaling with toroidal field is shown in figure 3. It increases with increasing magnetic field in the range (1.0 -1.4) T. These measurements were performed with an average electron density of $1 \times 10^{13} cm^{-3}$. Particle confinement time inferred from electrostatic fluctuations is in accordance with the impurity confinement time measured by the laser ablation technique in TJ-I (5). It is remarkable that the particle confinement time due to electrostatic turbulence scale with magnetic field in the same way that the central impurity confinement time in TJ-I.

The particle confinement time also increases with increasing density in the range $(0.5\text{-}2.0)\times 10^{13} cm^{-3}$, keeping the magnetic field constant at 1.0 T. However the increas-

ing of the particle confinement time inferred from electrostatic fluctuations with density is in conflict with the observed decreasing in the impurity confinement time in TJ-I as density raises (5).

A broad spectrum of poloidal magnetic field fluctuations $\tilde{B}_\theta$ is shown in Figure 4. The spectrum of oscillations in the radial magnetic field presents similar characteristics to those observed in $\tilde{B}_\theta$. Both are roughly constant below 80 kHz and decrease at higher frequencies with a dependence given by $B \approx \omega^{-1.3}$. The observed fluctuation levels, $\tilde{B}_r/B$ and $\tilde{B}_\theta/B$, that increase as probe is inserted into the plasma, were in the range 10^{-4}-10^{-5}.

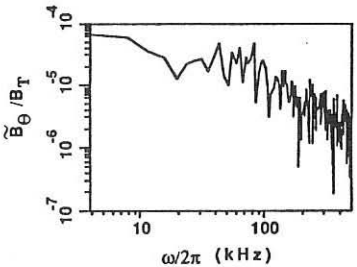

Figure 4. Frequency spectrum of poloidal magnetic fluctuations.

CONCLUSIONS

Electrostatic and magnetic fluctuations have been characterized by Langmuir and magnetic probes in the edge region of the TJ-I tokamak. The results show broadband turbulence with dominant frequencies below 100 kHz and density fluctuation levels $n/n \approx$ (10 -20%). Fluctuations propagate in the electron diamagnetic drift direction with a velocity of about 1×10^5cm s^{-1}. Poloidal and radial magnetic fluctuation levels were in the range 10^{-4}- 10^{-5} suggesting that magnetic fluctuations have a negligible influence on the confinement properties in TJ-I.

Assuming poloidal and toroidal symmetries, it was found that the particle confinement time due to electrostatic fluctuations is comparable to the central impurity confinement time in TJ-I. Whereas the scaling of the particle confinement time induced by electrostatic fluctuations with magnetic field is in good agreement to that observed in the central impurity confinement time, the scaling with density shows a disagreement.

REFERENCES

(1) P. Liewer, Nuclear Fusion 25, 543 (1985)
(2) A. J. Wootton et al. Plasma Physics and Controlled Fusion 30, 1479 (1988).
(3) J. M. Bell, Y. C. Kim, E. J. Powers, J. Applied Physics 53, 3933 (1982).
(4) E. J. Powers, Nuclear Fusion 14, 2857 (1974).
(5) B. Zurro, C. Pardo, F. Mompean, Plasma Physics and Controlled Fusion 30, 1767 (1988).

BOUNDARY LAYER CALCULATIONS FOR TOKAMAKS WITH TOROIDAL LIMITER

H. Gerhauser, H.A. Claaßen

Institut für Plasmaphysik, Kernforschungsanlage Jülich GmbH,
Association EURATOM-KFA, P.O. Box 1913, D-5170 Jülich, FRG

The calculations with the code SOLXY /1/ originally restricted to tokamaks with a poloidal limiter are now being modified to describe also the sol of a toroidal belt limiter like the ALT-II of TEXTOR. Preliminary considerations suggest that the experimentally observed asymmetries of the plasma profiles and fluxes on the ion and electron sides of ALT-II at the position $\theta = -45°$ may be traced back to the reaction of the limiter to the electric and pressure gradient drifts and electric currents producing strong oppositely directed effects on both sides.

The geometry of the TEXTOR boundary layer is shown schematically in Fig. 1 and specified by its width $44\ \text{cm} < r < 50\ \text{cm}$ at $\theta = \pm\pi/2$ (in the sketch extended by factor 3), separatrix radius $a = 46$ cm, major radius $R = R_0 + r\cos\theta$ with $R_0 = 175$ cm, main field $B \approx B_\phi = B_0 R_0/R$ with $B_0 = 2$ Tesla, and for $\beta(\text{pol}) \approx 1/2$ the poloidal field may to a very good approximation be taken as poloidally constant $B_\theta \approx \mu_0 I_p/2\pi r$. Typically $h_\theta = B_\theta/B \lesssim 0.1$, i.e. the magnetic field intersects the limiter at very oblique angles $\gtrsim 83°$.

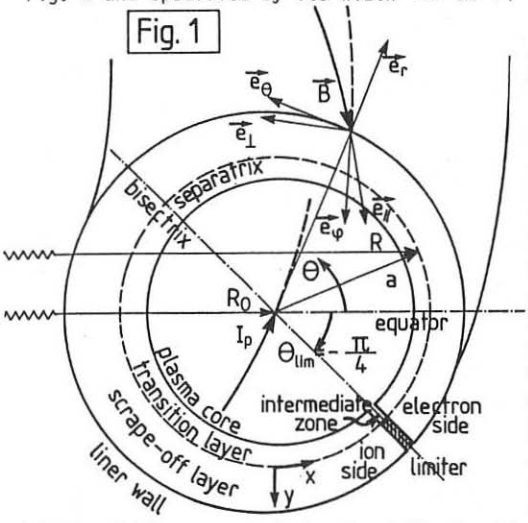

The excentric displacement of the circular flux surfaces by the Shafranov shift leads to a poloidal variation of the boundary layer width that is inversely proportional to R. This suggests the introduction of special boundary layer coordinates in the vicinity of the separatrix by the following line elements:

$$ds_\theta = r d\theta\,, \quad ds_\phi = R d\phi\,, \quad ds_y = dr = dy\, R_0/R \qquad (1)$$

Toroidal symmetry requires $\partial/\partial\phi \equiv 0$ so that $\partial/\partial s_\parallel = h_\theta \partial/r\partial\theta$ and $\partial/\partial s_\perp = h_\phi \partial/r\partial\theta \approx \partial/r\partial\theta$ for all vector components of plasma variables. The boundary layer being very narrow, we neglect $1/r$ compared to $\partial/\partial r$ throughout and replace finally r by a and $rd\theta$ by $dx = ad\theta$, e.g.

$$\nabla\cdot\vec{v} = \frac{\partial v_\theta}{r\partial\theta} + \frac{\partial v_r}{\partial r} + O\left(\frac{v_r}{r}\right) \longrightarrow \frac{\partial v_\theta}{\partial x} + \frac{R}{R_0}\frac{\partial v_r}{\partial y} \quad \text{with } R = R_0 + a\cos\theta \qquad (2)$$

Furthermore the smallness of h_θ allows the omission of terms of relative order h_θ^2. In this way the basic equations have been rewritten in the new coordinates and put into a form very similar to the poloidal limiter case while keeping all effects of toroidal geometry. The boundary layer is transformed to a rectangular x,y-integration domain covering the total connexion length from the e-side about 3 times around the torus ($q \approx 3$) to the i-side. The toroidal geometry causes the appearance of essential new terms in the equations related to the occurrence of large drift motions and electrical currents. Besides the radial diffusion we have an additional radial drift velocity v_{rd} of the same order, and both the projected parallel velocity $h_\theta v_\parallel$ and the perpendicular drift $v_\perp$ (poloidal rotation, equally of the same order and oriented in the $-\theta$ direction) contribute to the poloidal convection velocity $v_\theta = v_\perp + h_\theta v_\parallel$, for which the boundary condition at the limiter is $v_\theta \stackrel{!}{=} \pm h_\theta c_s = \mp h_\theta \sqrt{(T_e + T_i)/m_i}$. The main physical effect comes from the poloidal rotation being counteracted by the toroidally closed belt limiter, which builds up a pressure asymmetry with higher pressure on the e-side, so that a higher plasma flux towards the i-side is produced in agreement with ALT-II measurements.

We take into account the following elements of the stress tensor π:

$$\pi_{\parallel\parallel} = -\frac{4}{3}\eta_o\left(\frac{\partial v_\theta}{\partial x} - \Omega\right) = -\frac{4}{3}\eta_o\left(\frac{\partial v_\theta}{\partial x} - \frac{3}{2}\frac{\partial v_\perp}{\partial x} + \frac{3}{2}\frac{v_\theta - 2v_\perp}{R}\sin\theta\right)$$

$$\pi_{\perp\perp} = \pi_{rr} = -\pi_{\parallel\parallel}/2\,, \qquad \pi_{r\parallel} = \pi_{\parallel r} = -\eta^\perp \partial[(v_\theta - v_\perp)/h_\theta]/\partial r \tag{3}$$

The example of the parallel component of the equation of motion shows the structure of the transformed equations ($b = \pi_{\parallel\parallel}/2$):

$$\partial v_\theta/\partial t + \vec{v}\cdot\nabla\,(v_\theta - v_\perp) = (-\partial p/\partial x + k_\eta + k_R)\, h_\theta^2/mn + I_o \tag{4}$$

with $\quad \vec{v}\cdot\nabla = v_\theta\,\partial/\partial x + (-\overset{*}{D}{}^\perp\,\partial n/n\partial y + v_{rd}\,R/R_o)\,\partial/\partial y$

viscous friction $\quad k_\eta = \frac{\partial}{\partial x}\left[\frac{4}{3}\eta_o\left(\frac{\partial v_\theta}{\partial x} - \Omega\right)\right] + \frac{\partial}{\partial y}\left[\overset{*}{\eta}{}^\perp\,\partial(v_\theta - v_\perp)/\partial y\right]$

centrifugal force $\quad k_R = \left[3b - mn\,(v_\theta - v_\perp)^2/h_\theta^2\right](\sin\theta)/R$

transfer from neutrals $\quad I_o = (S_{p\theta} - mv_\theta\,S_n - S_{p\perp} + mv_\perp\,S_n)/mn$

rescaled coefficients $\quad \overset{*}{D}{}^\perp = D^\perp R^2/R_o^2\,, \qquad \overset{*}{\eta}{}^\perp = \eta^\perp R^2/R_o^2 h_\theta^2$

The new drift and curvature terms are readily identified. From the dominant terms of the radial and $\perp$ components of Ohm's law and the eq. of motion we derive the following drift velocities and equilibrium currents:

$$Bj_\perp = \partial(p - b)/\partial r\,, \qquad enBv_\perp = \partial(p_i - b)/\partial r + en\,\partial\Phi/\partial r$$

$$Bj_r = -\partial(p - b)/\partial x - \{3b + mn\,(v_\theta - v_\perp)^2/h_\theta^2\}(\sin\theta)/R + S_{p\perp} \tag{5}$$

$$enBv_{rd} = -\partial(p_i - b)/\partial x - en\,\partial\Phi/\partial x - \{\ldots\}(\sin\theta)/R + S_{p\perp}$$

For the numerical solution these may be kept constant during several (say 20) time steps of the code and then readjusted like the neutral sources, consequently $\partial v_\perp/\partial t$ is neglected in (4). The required electrostatic potential Φ is obtained by integration of the parallel Ohm's law

$$e\,\partial\Phi/\partial x = \partial p_e/n\partial x + 0.71\,\partial T_e/\partial x - ej_\parallel/h_\theta\sigma_\parallel \tag{6}$$

The parallel current density $j_\parallel = \tilde{j}_\parallel + j_{\parallel c}$ consists of two parts. The variable part $j_\parallel$ is determined from j_r, $j_\perp$ and the condition $\nabla \cdot \vec{j} = 0$ and is essentially $\sim \cos\theta$, i.e. $j_\parallel$ is the well known compensation current. However, the total poloidal current $j_\theta = j_\perp + h_\theta j_\parallel$ is interrupted by the belt limiter, which builds up a sheath potential asymmetry (in addition to the one resulting from T-asymmetry) and a new poloidally constant current $h_\theta j_{\parallel c}$ of order $enh_\theta c_s$ to be determined from the condition

$$\oint d\Phi = \int_{x_{es}}^{x_{is}} (\partial\Phi/\partial x)\, dx + \Delta\Phi_{es} - \Delta\Phi_{is} = 0 \qquad (7)$$

with

$$e\,\Delta\Phi = -T_e \ln\left[\sqrt{2\pi m_e (T_e + T_i)/T_e m_i}\,(1 - j_\theta/env_\theta)\right] \qquad (8)$$

being the sheath potential drop on the e-side (x_{es}) or i-side (x_{is}) of the ideally conducting limiter. Clearly the parallel conductivity $\sigma_\parallel$ must now play an important role. Thus we conclude that there is a variety of complex interlinked phenomena in the case of a toroidal limiter that did not show up in the poloidal case, and it seems that especially the drift and current effects have not been taken into due account by some of the elsewhere used computer codes. In our simplified model geometry we may easily investigate the relevance of the different physical effects.

At present (by mid of Dec. 88) we are switching the code SOLXY step by step from the poloidal to the toroidal limiter. First the integration domain was doubled, because the bisectrix dividing the domain into the halves of equal length is no longer a symmetry line. For the intermediate zone in front of the limiter head we now use parabolic interpolation to ensure continuous transition of T_e, T_i and v_θ from the i-side to the e-side. Then the poloidal projection ($v_\parallel \to v_\theta$, $ds_\parallel \to dx$, etc.) was performed, but still in cylindrical geometry. In this case the profiles remain symmetric with respect to the bisectrix, as shown for v_θ in plot 1. Remarkably there are only slight changes of the values of n, T_e, T_i with respect to the poloidal case, if the same total fluxes from the core to the boundary are assumed, as also experimentally observed with ALT-II. Next the toroidal curvature and the Shafranov shift were introduced via the terms with R^2/R_0^2 (plots 2 to 5). Since the particle and energy outflux enters the boundary layer preferentially near the outboard midplane ($\theta \approx 0$, narrower flux surfaces and larger toroidal circumference) we get higher $|v_\theta|$ on the limiter e-side than on the i-side and positive v_θ at the bisectrix. The n- and T-gradients are steeper near the i-side than near the e-side. The recycled neutrals are treated with a similar analytical model as in /1/, but the radial angular spread of the squeezed cos-like distribution of the emitted neutrals is now increased from ± 5° to ± 27°. Finally, since the ions impinging on the limiter are deflected in the magnetic sheath (angle of incidence about 60° instead of 83°), we assumed a correspondingly ($\approx$ 4x) increased poloidal projection of the neutral velocity. Plot 6 shows that then the neutrals are able to penetrate much deeper into the sol than in the poloidal case, so that the toroidal steepening of the plasma density profiles near the limiter results to be weaker. However, the radial decay length close to the limiter is always $\lesssim$1 cm, in agreement with ALT-II experimental profiles.

/1/ H. Gerhauser, H.A. Claaßen, Proc. Int. Workshop Augustusburg (GDR), April 1988, Contrib. Plasma Phys. 28 (1988), p. 359 (with D. Reiter), and Proc. 14. Contr. Fus. Plasma Phys. Madrid, June 1987, part II, p. 674.

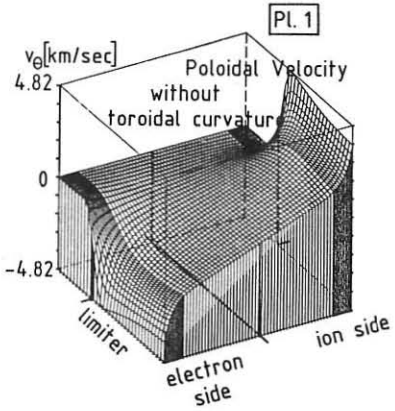
Pl. 1
v_Θ[km/sec]
4.82
Poloidal Velocity
without
toroidal curvature
0
-4.82
limiter
electron
side
ion side

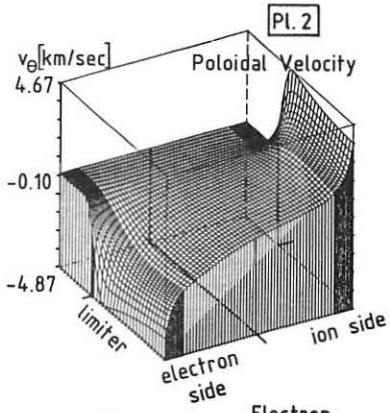
Pl. 2
v_Θ[km/sec]
4.67
Poloidal Velocity
-0.10
-4.87
limiter
electron
side
ion side

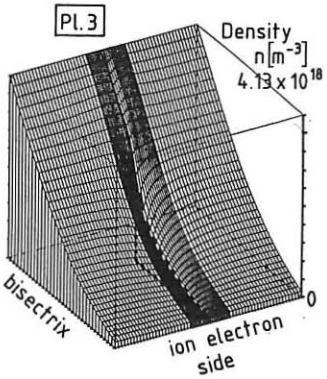
Pl. 3
Density
n[m^{-3}]
4.13 x 10^{18}
bisectrix
ion electron
side
0

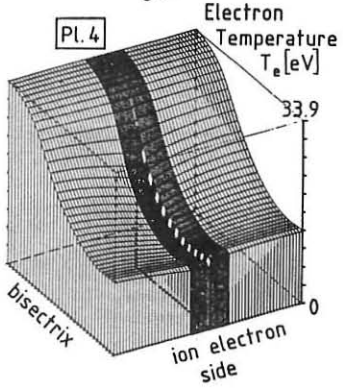
Pl. 4
Electron
Temperature
T_e[eV]
33.9
bisectrix
ion electron
side
0

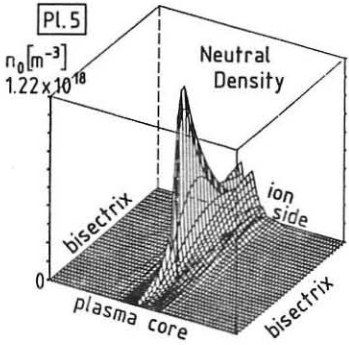
Pl. 5
n_0[m^{-3}]
1.22 x 10^{18}
Neutral
Density
bisectrix
ion
side
0
plasma core
bisectrix

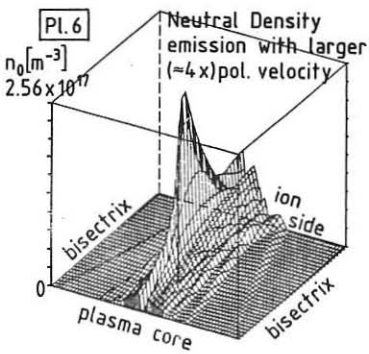
Pl. 6
Neutral Density
emission with larger
(≈4 x) pol. velocity
n_0[m^{-3}]
2.56 x 10^{17}
bisectrix
ion
side
0
plasma core
bisectrix

POLOIDAL ELECTRIC FIELD AND VARIATION OF RADIAL TRANSPORT DURING ICRF HEATING IN THE JET SCRAPE-OFF LAYER

S Clement°, J A Tagle, M Laux*, S K Erents+, M Bures
P C Stangeby$^{\Delta}$, J Vince and L de Kock

JET Joint Undertaking, Abingdon, Oxon OX14 3EA, UK
* Zentral Institut für Elektronenphysik, AdW der DDR, 1086 Berlin, DDR
° Association CIEMAT/EURATOM, Madrid, Spain
+ Culham Laboratory, Association UKAEA/EURATOM, Abingdon, Oxon, UK
Δ Institute for Aerospace Studies, University of Toronto, Canada

1. INTRODUCTION

The highly anomalous perpendicular transport in the plasma edge of a tokamak is generally attributed to plasma turbulence, primarily to density and electrostatic potential fluctuations. The edge transport could be modified by changing the geometry of objects in contact with the plasma (limiters, radio frequency antennae ...) and during additional heating experiments. Poloidal asymmetries in the scrape-off layer (SOL) in tokamaks using poloidal limiters (eg. ALCATOR-C) have been recently reported [1], indicating a poloidal asymmetry in cross-field transport. A poloidal ring limiter obstructs communications between different flux tubes in the SOL, thus permitting poloidal asymmetries in n_e and T_e to develop if $D_\perp$ is θ-dependent. When JET was operated with discrete limiters, equivalent to a single toroidal limiter at the outside mid-plane, little poloidal variation in the SOL plasma properties was observed [2]. Currently JET is operated with two complete toroidal belt limiters located approximately one meter above and below the outside mid-plane. This configuration breaks the SOL into two regions: the low field side SOL (LFS), between the limiters, and the rest of the SOL on the high field side (HFS). Differences on the scrape-off lengths in the two SOLs are reported here, indicating that cross-field transport is faster on the LFS-SOL, in agreement with observations made on ASDEX [3] and T-10 [4]. The cross-field transport will also be influenced by the presence of a poloidal electric field ($\vec{E}_\theta$) in the SOL plasmas, through $\vec{E}\times\vec{B}/B_z^2$ drifts. As a consequence the ions, accelerated by the field, will strike the surfaces of the limiters, wall and antennae and enhance the neutral and impurity influxes. These effects have been observed during ICRF heating in several tokamaks [5]. If $\vec{E}_\theta$ varies poloidally then this would also result in poloidal variation in transport. $\vec{E}_\theta$ was measured in the JET SOL using a triple Langmuir probe during ICRF heating. Strong radial drifts are deduced at the (single) observation point employed, which may also contribute to enhanced sputtering.

2. DENSITY SOL LENGTHS IN JET BELT LIMITER CONFIGURATION

In the discrete limiter configuration each flux tube traces out at least one complete poloidal transit, and any poloidal variation in $D_\perp$ would

not be expected to manifest itself as a variation in plasma properties, due to the rapid transport along $\vec{B}$. In contrast, in the belt limiter configuration, any poloidal variation in $D_\perp$ would be expected to manifest itself as different SOL lengths in the SOLs (LFS and HFS). Figure 1 shows a density profile measured with two fixed Langmuir probes on one of the ICRF antenna protection tile located in the LFS-SOL, and the density profile measured with a reciprocating probe (RCP) at the top of the vessel in the HFS. Also presented is the correction of the density profile from the RCP after the compression of field lines (~ 2.5) has been taken into account. Figure 2 shows the SOL length (λ_n) for discharges with $I_p = 3$ MA, $B_T = 3.4$ T and additional ICRF heating up to 17 MW. It can be seen that $\lambda_n^{LFS} > \lambda_n^{HFS}$ independently of the power applied. Although the connection length in the LFS-SOL is shorter than for the HFS-SOL, when the toroidal plasma geometry is taken into account, then one expects $\lambda_n^{LFS} \approx \lambda_n^{HFS}$, provided $D_\perp$ does not vary poloidally. Since the results show that, in fact, $\lambda_n^{LFS} > \lambda_n^{HFS}$, it is concluded that $D_\perp^{LFS} > D_\perp^{HFS}$. No strong variation with ICRF power was found except a slight flattening of profiles at high current and high power. The ion saturation current values (I_{sat}) at the Last Closed Flux Surface, LCFS, measured from RCP and antenna probes are shown in figure 3. Since the LCFS cannot be precisely determined at the RCP location, the difference of a factor of two in the I_{sat}^{LCFS} values is within experimental uncertainty. It is also found that edge temperatures are lower (LFS-SOL) for the belt limiter configuration than for the discrete limiters. Inference of average values of $D_\perp$ for the LCFS and HFS SOLs will be carried out taking into account the difference in the temperature and the geometries of the two SOLs; present results indicate that the plasma outflux is higher in the outer midplane.

3. EDGE POLOIDAL ELECTRIC FIELD DURING ICRF HEATING

During a number of discharges with RF in JET the three tips of a triple probe were allowed to float and very large differences of potential were measured between the tips during the RF pulse. The probe tips are located at the same radius, in different poloidal position (30 mm apart) and in different flux tubes [6]. The potentials between the tips range from 2V/cm during the ohmic part of the discharges up to around 40 V/cm during the RF pulse, and are interpreted as an electric field. Two dependent but not orthogonal components of the field give the strength as well as the orientation. Figure 4 shows the total electric field during a 5 MW RF heating discharge ($I_p = 3.1$ MA, $B_T = 3.4$ T) in D gas with ^{3}He (33 MHz) as a minority heating gas. The field is oriented downwards (angle $\sim -60°$) with respect to the plasma current. The voltage signals were measured at a low sampling rate (< 10 kHz) and without filtering. Rectifying effects on the probe tips during RF were found to be negligible in previous experiments at low RF powers ($\lesssim 4$ MW) [7]. Measurements were made with the probe located 10 mm behind the RF antenna protection tiles and 15 mm behind the LCFS. Owing to the change of plasma conditions in consecutive discharges, where the probe was moved radially, we could not measure any radial dependence of these potentials. However, for a fixed radial position, the variation of the electric field with RF power and different gas minority heating has been studied. Figure 5 shows

the electric field for a 3.1 MA, 3.4 T discharge in D with H minority (44 MHz). It is worth noting that the electric field is much lower in high power discharges H than for ^{3}He minority heating. The antenna configuration was dipole in both cases and the field dependence with total RF power and minority gas is shown in figure 6. The small field found during H minority heating is consistent with the more efficient wave damping when compared to the ^{3}He minority case. It agrees with the measurements of the oscillating magnetic fields in the plasma edge in JET [8]. The electric field was found to exist during ICRF, independently on whether the antenna closest to the probes was powered or not, implying a significant toroidal extent of the field. This field causes a radial drift of $E_\theta/B_\phi = 1500/3.4 \approx 400$ m/s which is comparable to the diffusive velocity $D_\perp/\lambda_n = 2.5/0.015 \approx 170$ m/s. Such drifts could therefore change the SOL particle balance locally, and strong local outflows may occur, implying enhanced ion sputtering and impurity production during ICRH.

REFERENCES

[1] B La Bombard and B Lipsshultz, Nuclear Fusion 27 (1987) 81-89.
[2] P C Stangeby, J A Tagle, S K Erents and C Lowry, Plasma Physics and Controlled Fusion, to be published.
[3] M Keilhacker and B Daybelge, Nuclear Fusion 21 (1981) 1497.
[4] V A Vershkov et al, J Nuclear Material 145-147 (1987) 611.
[5] R J Taylor et al, 9th IAEA Conference, Baltimore, Plasma Physics and Controlled Fusion (1982), Vol III, 251-256.
[6] M Laux and J A Tagle (to be published).
[7] S K Erents et al, J Nucl Mater 145-147 (1987) 231.
[8] M Bures et al, Bull American Physics Soc 33 No 10 (1988).

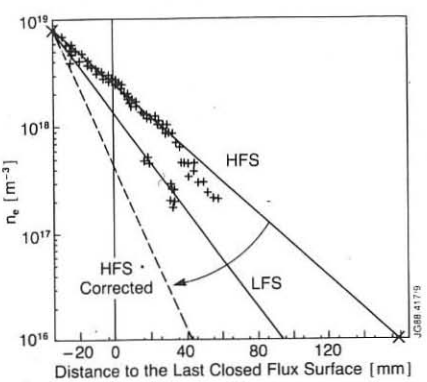

Fig 1: Density profile in the SOL at the HFS and the LFS.

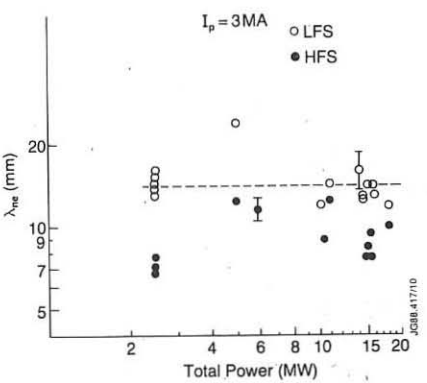

Fig 2: Density scrape-off SOL length vs total applied power for 3 MA discharges.

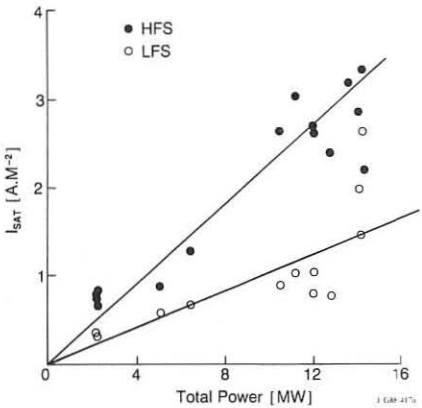

Fig 3: Ion saturation current at the LCFS vs total applied power in LFS and HFS.

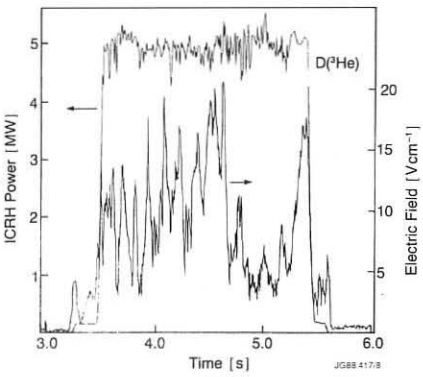

Fig 4: Electric field measured during ICRF heating, with ^{3}He as minority gas.

Fig 5: Same as Fig 4, but with H as minority gas.

Fig 6: Strength of the electric field vs ICRF power for ^{3}He and H minority gases.

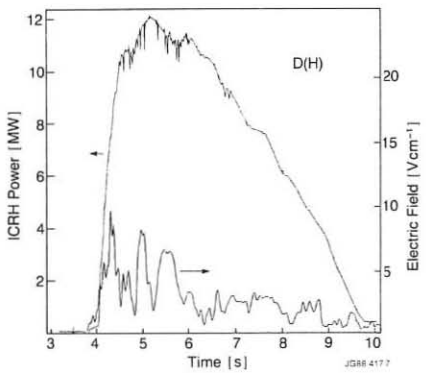

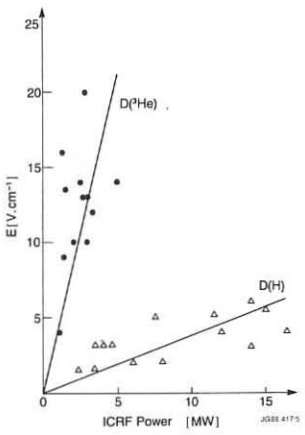

THE SCALING OF EDGE PARAMETERS IN JET WITH PLASMA INPUT POWER

* S K Erents, P J Harbour, S Clement, D D R Summers
* G M McCracken, J A Tagle and L de Kock

JET Joint Undertaking, Abingdon, Oxon, OX14 3EA, UK
* Culham Laboratory, Association UKAEA/EURATOM, Abingdon, Oxon, UK

1. Introduction

The scaling of edge parameters of density and temperature with central density and ohmic power in JET has been presented previously for the discrete limiter geometry (1) and more recently for the new belt limiter configuration, (2). However, the scaling with plasma current (I_p) is difficult to interpret because varying I_p does not only change the input power but also the safety factor qs and consequently the SOL thickness. The use of additional heating at constant current allows more direct observation of the effects of changing heating power.

In this paper we present data in which the plasma input power is increased by ICRH, (Pt < 20MW), using a 3MA target plasma, and compare data for different plasma currents using discrete and belt limiter geometries. Edge data is presented from Langmuir probes in tiles at the top of the torus, when the tokamak is operated in single null magnetic separatrix (divertor) mode, as well as for probes in the main plasma boundary to contrast these date with limiter data.

2. Diagnostics

Edge measurements are made using a reciprocating Langmuir probe at the top of the vessel, about half between X-point tile and upper belt limiter, which can cross the last closed flux surface (LCFS), defined by the limiters even in high power discharges. Details of the diagnostic are reported in (2). For measuring conditions at the target tiles during divertor operation, a poloidal array of 8 Langmuir probes, separated by -70mm, is used, (3).

3. Limiter Fluxes

For the discrete limiter configuration, it was found that the ion saturation current I_s at the LCFS was almost independent of central density $\langle \bar{N}_e \rangle$, but increased as the square of plasma current, I_p, (1). This result contrasts with belt limiter data, in which it is found that $I_s \alpha I_p$. The results are illustrated in figure 1. However, the total flux to the limiters $\Gamma = I_s.A_w$ (A_w = wetted are of limiter) in both configurations is similar in both scaling and magnitude, as might be expected since it should be determined by global plasma parameters. The fact that total flux Γ scaling is similar while the flux density I_s is different is because the two configurations have different wetted areas. For the discrete limiters $Aw = 2.8\ \lambda\ hw\ (m^2)$ where hw is the

wetted height. For the belt limiters Aw = 52 λ sinθ (m2) where θ is the angle the field lines make with the limiters. For both configurations, $\lambda \alpha 1/I_p$, but $\theta \alpha 1/qs$, ie $\theta \alpha I_p$. Hence for the belt limiters the wetted area is almost constant, (0.2 m²). An empirical scaling Γ = 2.4E21 I_p s-1 is found.

4. Densities and temperatures in limiter discharges

The problem of changing qs is eliminated when power is put in by means other than ohmic heating. Neutral beam heating results in a steep change in central density, and internal plasma energy, W, with Pt. This is not the case for ICRF heating in a well conditioned torus, when also a sufficiently long steady state is obtained, figure 2. For Pt = Pohm + Picrh > 5MW, $\langle \bar{N}e \rangle$ shows only a slow rise with Pt. The density at the LCFS Ne(a) on the other hand rises linearly with Pt. At low ICRH powers there is a rise in $\langle \bar{N}e \rangle$, and this is reflected in a fall in edge temperature $T_e(a)$. However, at higher powers Te(a) also rises with Pt. The low edge temperatures (< 90eV even at 20MW) and high edge densities, are indicative of rapid re-cycling in the edge - a feedback mechanism keeping edge temperatures low.

5. Edge temperature scaling with power to the edge

The global power balance/transport model (1) predicts the approximate scaling that $T_e(a) \alpha P_c^{0.66} / \langle \bar{N}_e \rangle^{1.7}$. Experimentally for belt limiter plasmas, edge temperatures scale as $T_e(a) \alpha \langle \bar{N}_e \rangle^{-\frac{1}{2}}$, (2) but are generally lower than those for discrete limiter operation reported in (1). To investigate the scaling of $T_e(a)$ with power to the edge, P_c = Pohm + Pirch - Prad, we plot $T_e(a)$. $\langle \bar{N}_e \rangle^{\frac{1}{2}}$ versus P_c, to eliminate changes in $\langle \bar{N}_e \rangle$. The results are shown in figure 3. A scaling of Te(a) α Pc $^{0.5}$ (fitted line) is obtained for the belt limiter data. The divertor (X-point tile) 3MA ohmic data is lower, and more scattered, however scaling with P_c is inconclusive. Agreement with the simple theory is very good for these constant q_s, (I_p = 3MA) belt limiter data.

6. Power to the divertor tiles

Total power to the divertor tiles has been plotted as a function of P_c for ohmic single null discharges in figure 4. Two data sets are illustrated, the upper when the separatrix was clearly on probe 5 of the 8 probes. The power SOL thickness λ_p refers to the outer (low field side) SOL. The inner SOL has shorter λ_p, and in general a much lower fraction of the total power falls on the tiles in this region. When the null is moved poloidally to the high field side of the torus, the separatrix falls close to probe 4 or even 3, and the total power to the tiles appears to fall, (lower data set). A small error (< factor 2) may exist in absolute values of P_t due to an uncertainty in the position of the separatrix, and the collecting area of the probes. Clearly, however, for both data sets there is a shortfall of a factor 2

or more in the power to the tiles. This is consistent with both discrete and belt limiter discharge data when only 40% of available power to the edge was accounted for. The SOL thickness (110 mm) agrees well with reciprocating probe data for divertor discharges when the field line compression is taken into account in moving ~1m poloidally round the torus.

7. Conclusions

1. Total particle fluxes to limiters are similar for both discrete and belt limiter configurations, and scale linearly with plasma current.

2. Both edge density and and temperature increase as power is input to the plasma by ICRH. The linear increase in edge density due to extra influx of neutrals directly released from the wall holds temperatures to < 90 eV even at 20MW input power.

3. A temperature scaling with power close to that predicted by global power balance/transport (1) is obtained when the plasma is heated by ICRH, ($T_e \propto P_c^{0.5}$).

4. Power to divertor tiles in divertor plasmas increases linearly with power to the edge, but only 50% of the power is accounted for, as in limiter discharges.

References

1. S K Erents, J A Tagle, G M McCracken, P C Stangeby and L de Kock, Nuclear Fusion 28 (1988) 1209

2. S K Erents, J A Tagle, G M McCracken, G Israel, H W Brinkschulte and L de Kock, 'The behaviour of the scrape-off layer in JET with toroidal belt limiters', J Nucl Mat 163-165 (1989 to be published.

3. P J Harbour et al, 'The behaviour of the scrape-off plasma during X-point discharges in JET with L- and H-modes'. J Nucl Mat 163-165 (1989) to be published.

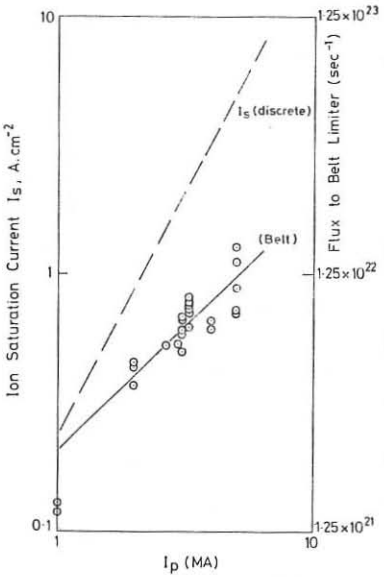

FIGURE 1. SCALING OF ION SATURATION CURRENT WITH PLASMA CURRENT FOR DISCRETE AND BELT LIMITERS.

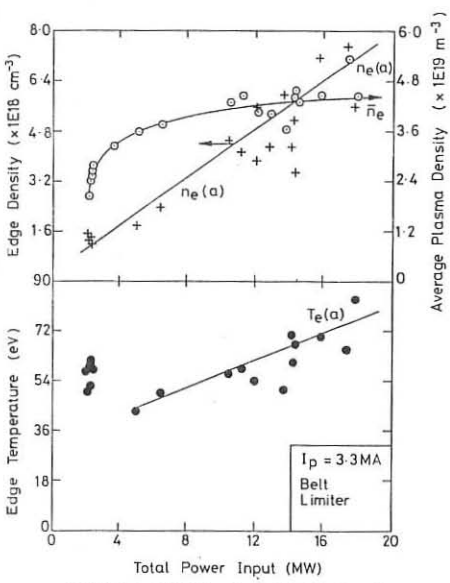

FIGURE 2. EFFECT OF ICRH POWER ON EDGE DENSITY AND TEMPERATURE.

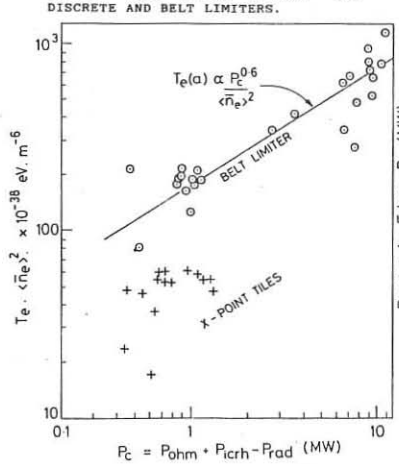

FIGURE 3. SCALING OF EDGE TEMPERATURE WITH POWER TO THE EDGE FOR LIMITER AND DIVERTOR (X-POINT) PLASMAS.

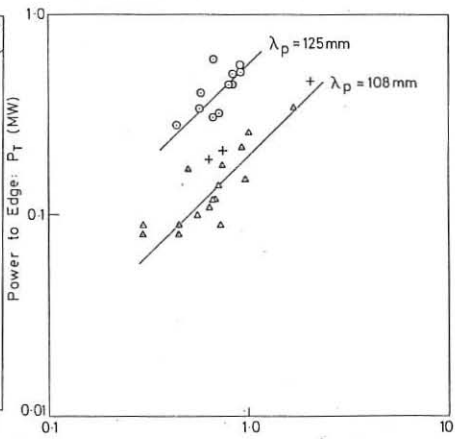

FIGURE 4. POWER SCALING TO DIVERTOR TILES DURING SINGLE NULL DIVERTOR OPERATION.

PLASMA SURFACE INTERACTIONS AT THE JET X-POINT TILES

A.P. Martinelli*, R. Behrisch*, J.P. Coad, and L. de Kock

JET Joint Undertaking, Abingdon, Oxon OX14 3EA, UK
*Max-Planck-Institut für Plasmaphysik, EURATOM Association
D-8046 Garching/München, FRG

Introduction

Operation with a magnetic divertor, which leads to a zero poloidal field inside the volume of the discharge vessel (the X-point) has led to substantial improvements in confinement time in JET. In this mode the diverted plasma is conducted to a large number of graphite tiles (X-point tiles) near the top of the vessel. The power handling capability of these tiles limits the maximum additional heating power to the discharge.

The study of the surface modifications of the X-point tiles of JET is therefore of interest both to correlate the magnetic configuration and plasma particle and energy fluxes with the surface modifications, and also to get information about the erosion and deposition at these wall areas.

Figure 1 shows the geometry of the X-point tiles and the separatrix in JET /1/. Two bands of graphite target tiles with scrape off layer impinging on the slope of the tiles are shown; the analysis of one such band of (four) tiles is described here.

Experimental and Results

The set of four carbon tiles with an area of (540 x 184 x sin70°) mm^2 were removed from the vessel wall close to the plasma X-point of Octant VIII b/c. A view of the tiles (as seen from below) and their relative position to Oct. I and VII as well as to the inner and outer wall are schematically shown in Fig. 2.

The tiles had been in use in the June 1987 to May 1988 experimental period of about 4300 discharges, of which ca. 1000 were X-point discharges, and they were removed in May 1988. Carbon strips as indicated in Fig. 2 were cut (about 2 mm thick, 8 mm wide) along the lines HH, KK (from 0 to 540 mm) and along LL, MM, NN, OO (from 0 to 184 mm). The tiles are ridged, so that for strips LL, MM, NN and OO the surface from 0-92 mm faces the electron-drift direction and from 92-184 mm faces the ion-drift direction with in each case the point at 92 mm being nearest the plasma centre. The strips were analysed each 5mm by nuclear reaction analysis (NRA) using the $^3He(D,p)\ ^4He$ reaction with 790 keV $^3He^+$-ions in order to determine deuterium collected in a surface layer of about 0.5 /um and by proton induced x-ray emission (PIXE) using 1.5 MeV H^+ to detect the metals (Ni, Cr, Fe) in a surface layer of about 8 /um.

The results of the NRA and PIXE analysis along line HH are shown in Fig. 3. The D concentration ranges from a maximum of about 10^{18} D/cm^2 down to a minimum of about 10^{17} D/cm^2 at coordinates between 80 and 240 mm, then reaches a value of about 6 10^{17} D/cm^2 from about 240 to 540 mm. The

metal (Ni, Cr, Fe) concentrations are lower, but they show a lateral distribution similar to the D deposition. This observation is similar to results of earlier analysis of limiters from JET /2,3/ and other plasma experiments /4/. The relative concentrations of Ni, Cr, Fe agree well with their concentration in Inconel.

Figure 4 shows the D and Ni, Cr, Fe concentrations along line MM (0 to 184 mm). The D and metal depositions are much lower from ca. 30 mm to the ridge at 92 mm, by factors of 10 to 20. The cut-off at ca. 30 mm probably represents the shadow cast by the next set of poloidal tiles at Octant VIII a/b. The D and metal depositions are also reduced on the electron-drift side of the tiles on slices NN and OO, but by smaller factors (ca. 2 and 12, respectively), whilst on slice LL there is only a slight decrease in the level. The results show strong erosion on the electron-drift side of the tiles, centred near the strip MM and tailing off away from this area (e.g. Fig. 3).

At several representative spots the depth profiles of the depositions have been measured by SIMS (Secondary Ion Mass Spectroscopy). These profiles show that the major part of the deposition is carbon with a D concentration of about 0.4 and a metal concentration in the range of 1 %. The deposited layers have a total thickness mostly 1.5 to 2 /um and up to 5 /um in the areas of large deposition. With the NRA only a layer of 0.5 /um is analysed, and the total deposition of D in the areas of large deposition is a factor 3 to 5 higher, as observed in the SIMS measurements.

A systematic SEM (Secondary Electron Microscopy) investigation of the cut strips shows layers of deposited material all over the strips. The deposited layers appear to have suffered erosion, to a larger extent in the dotted-region, where low deposition was measured, to a lesser extent in the hatched and cross-hatched regions with higher deposition as shown in Fig. 2.

Discussion

From the poloidal and toroidal strips of the analysed set of tiles an average value of about 3.3×10^{18} D/cm^2 for the D deposit can be attributed to these areas, and a D inventory D = 3×10^{21} per set of four X-point tiles.

Since there are 40 bands of X-point tiles they contribute 1.2×10^{23} D atoms to the total inventory, which is ca. 4 times more than reported for tiles exposed in June/August 1987 /5/, but perhaps to be expected after the vastly increased number of X-point discharges.

The much lower levels of D and metals (ca. 10^{17} D/cm^2 and 2×10^{16} metal atoms/cm^2) on sections of MM (Fig. 4) are consistent with an area where erosion dominates during X-point discharges, but where deposition may occur at other times as observed previously on limiters /2,3/ and the polished visual appearance of the tile in this region is consistent with this hypothesis. It appears, therefore, that the electron-side separatrix intersects the band of tiles in the neighbourhood of strip MM, so that NN and OO are deeper into the SOL and thus receive progressively lower flux of less energetic ions. The position of the separatrix is known to move by ca. 150 mm during a single X-point discharge, which agrees well with the width of the minimum in D along HH shown in Fig. 3. There will also have been some variation in X-point position from shot to shot and during the operational campaign.

At the separatrix strong erosion occurs. Away from the separatrix, i.e. on the ion-drift side of the tiles and in the area LL on the electron-drift side, deposition as the dominant mechanism is more evident. The deposition levels well away from the separatrix are similar to those observed on the sides of limiters, where deposition occurs (ca. 10^{18} D cm^{-2} and ca. 2×10^{17} Ni cm^{-2}) /2,3/.

By considering codeposition of C and D on the tile surface one finds on the average C = D/0.4 = $3.3\ 10^{18}/0.4 = 8.2 \times 10^{18}$ C/cm^2. This corresponds to an average thickness of about 1.4 /um (ca. 4000 monolayers of C), which is also close to the value observed by the SIMS measurements in the hatched and cross-hatched regions of Fig. 2.

Similarly, a deposit of carbon 2.5×10^{17} C/cm^2 can be calculated on the dotted area of low concentration in Fig. 2 (ca.100 monolayers of C or more). Evidence of erosion (or no erosion) of the graphite substrate at the dotted (or the other regions of Fig. 2) cannot be given, therefore, strictly speaking, the measured concentrations of D, Ni, Fe, Cr, and C cannot be considered as "net" deposition.

However, by extrapolating linearly the average carbon deposition C = 8.2×10^{18} C/cm^2 after 2×10^4 s (1000 discharges x 20 s) to a year operation, an average C deposition of about 1 mm thickness with local variations by a factor 10 is calculated on the surface of the tiles.

The following table summarizes some main results:

	D	C	Ni
Average Deposit/set of tiles (D/cm^2)	3.3×10^{18}	8.2×10^{18}	2.0×10^{17}
Total Deposit (D, C, Ni)	3.0×10^{21}	7.7×10^{21}	1.9×10^{20}
Average Deposit/sec (D/cm^2 s)	1.7×10^{14}	4.0×10^{14}	1.0×10^{13}

References

/1/ P.J.Harbour, L. de Kock, S.Clement, Procs. 15th Europ. Conf. Controlled Fusion and Plasma heating, Eds. S. Pesic, J. Jacquinot, Dubrovnik 1988, EPS, Geneva, 12 B, Part II, p. 655.

/2/ R.Behrisch, J.Ehrenberg, H.Bergsaker, J.P.Coad, L.de Kock, B.Emmoth, H.Kukral, A.P.Martinelli, G.M.McCracken, and J.W.Partridge, J. of Nucl. Mater. 145-147 731-735 (1987).

/3/ H.Bergsaker, R.Behrisch, J.P.Coad, J.Ehrenberg, B.Emmoth, S.K.Erents, G.M.McCracken, A.P.Martinelli and J.W.Partridge, J. of Nucl. Mater. 145-147 727-730 (1987).

/4/ TFR Group, A.P.Martinelli, R.Behrisch, and W.Englert,J. of Nucl. Mater. 145-147 681-685 (1987).

/5/ J.P.Coad, R.Behrisch, H.Bergsaker, J.Ehrenberg, B.Emmoth, J.Partridge, G.Saibene, R.Sartori, J.C.B.Simpson and W.M.Wang,, PSI Conf. Jülich, to be published in J. of Nucl. Mater. (1989).

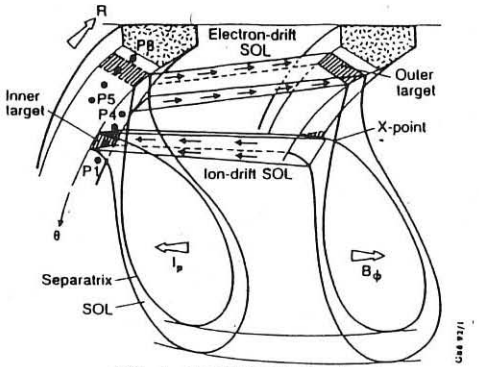

Fig. 1. Geometry of the X-point divertor in JET.

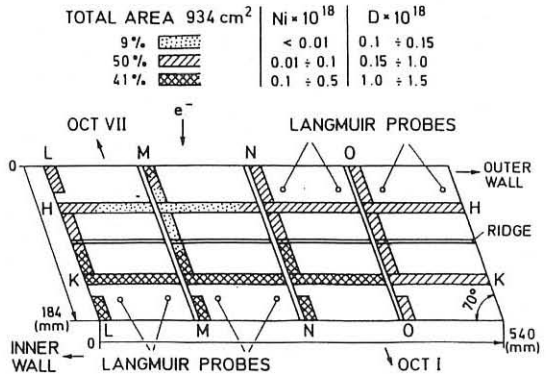

Fig. 2. Set of four plasma X-point carbon tiles of octant VIIIb/c of JET. Indicated are the strips analysed by NRA and PIXE as well as the analysis results.

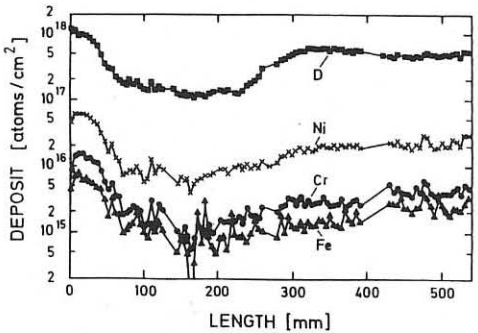

Fig. 3. NRA and PIXE analysis along line HH of the X-point carbon tiles.

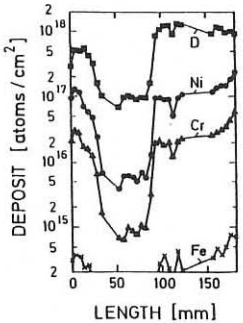

Fig. 4. NRA and PIXE analysis along line MM of the X-point carbon tiles.

DISTRIBUTION OF EROSION AND DEPOSITION ON THE JET BELT LIMITERS

G M McCracken*, R Behrisch**, J P Coad, D H J Goodall*, P Harbour, L de Kock, M A Pick, C S Pitcher+, J Roth**, P C Stangeby**,

JET Joint Undertaking, Abingdon, Oxon OX14 3EA, UK

* UKAEA Culham Laboratory, Abingdon, OX14 3DB, UK, (Culham/Euratom Association)
** Institute for Aerospace Studies, University of Toronto, Canada, M3H 5T6
+ Canadian Fusion Fuels Technology Project, Ontario, Canada
++ Max-Planck-Institut fur Plasmaphysik, 8046 Garching bei Munchen, FRG

1. Introduction

The distribution of erosion and deposition of limiter material is of importance both for extrapolating to the next generation of fusion machines and for understanding impurity transport in the boundary layers of present day tokamaks. Erosion patterns have previously been reported for the JET discrete graphite limiters used up to 1986 [1]. We have now made measurements on the belt limiters used in 1987-88. These measurements show that although the pattern of net erosion is qualitatively similar to the earlier results the new maximum erosion ($\sim$40μm) is reduced by about a factor 5, consistent with the larger limiter surface area.

2. Experimental Observations: Belt Limiters

The two toroidal belt limiters were installed in JET in 1987 on the low field side of the vacuum vessel, above and below the midplane [2]. These limiters consist of a large number of graphite tiles on water cooled inconel mounting plates. The physical dimension of a number of tiles were carefully measured before installation. Two tiles were removed in August 1987 after about two months operation, $\sim$ 470 discharges. A further 8 tiles were removed in May 1988 after $\sim$ 4000 discharges. They were then remeasured. The difference between two sets of measurements is plotted in fig 1 as a function of the distances along the centre-line of the tile. The erosion is 20-50μm, which compares with the much larger erosion of 150μm at the discrete limiter tiles exposed to 2800 discharges in 1986. The lower erosion rate is expected because the belt limiter area is about ten times larger than the discrete limiters, and the total particle outflux is similar. The tiles are mounted in adjacent pairs and generally reproducible results are obtained for each

pair. The pair exposed for only 2 months have erosion/deposition values less than 10μm. The tiles from the bottom limiter and from 2 toroidal positions on the top limiter have quantitatively similar results with erosion/deposition changes ∿ 20-40 μm. This indicates reasonable toroidal uniformity, consistent with Langmuir probe results [3]. A cross-check on the absolute deposition was carried out by sectioning the tiles. Typical results are also shown in fig 1. Where deposition is indicated by the physical measurements it is clearly observed in the sectioning; where erosion is indicated by the measurements no deposition can be seen. The results obtained for deposition show the erosion/deposition transition in good agreement with the mechanical measurements.

A series of depth profile measurements were then carried out using SIMS. Samples from different positions on the tile were measured to obtain the nickel, chromium, hydrogen and deuterium depth distribution. Some of the results are shown in fig 2. Nickel was the dominant metal with concentrations up to 10^{21} atoms cm^{-3} (1% of graphite density). Chromium and iron were present at levels ≤ 15% of the nickel. In the samples from the deposition region (fig 2, position A) the metal and hydrogen distributions extends into > 10μm. In the region E where net erosion was measured, the depth of the metals is < 2μm with a peak at 0.3μm. At positions M & P the depth of the metals is 3-4μm. The hydrogen and deuterium depth profiles show similar behaviour to the metals. One surprising result is that the amount of hydrogen in the surface is typically 10-20 times higher than the deuterium, despite the fact that plasma operation and glow discharge cleaning over most of the exposure period was in either deuterium or helium. Sample E, where there is net erosion is an exception. The hydrogen may be due to adsorption of water vapour by the deposited film on exposure to atmosphere.

3. Discussion

The experimental results were first compared with a simple analytical model which neglects ionization in the SOL [1]. The theoretical change in limiter dimension (Δh) has been plotted in fig 2 as a function of position on the tile. We have taken typical experimental values of the ion flux density ($2A/cm^2$) and electron temperature (50eV) at the LCFS and have assumed an exposure time of 5×10^4 seconds, corresponding roughly to the integrated duration of the plasma discharges. We have also taken the e-folding distances for the fuel and impurity particle fluxes to be equal (λ_Γ) and the electron temperature e-folding distance, $\lambda_T = 2\lambda_\Gamma$. It has been found that the distributions of net erosion/redeposition are insensitive to the value of λ_T, when $\lambda_T > \lambda_\Gamma$, which is always observed. Similarly, the predicted distributions are insensitive to the assumed temperature in the range 30 eV < T_e (a) < 100 eV, which encompasses most operating conditions in JET.

Reasonable agreement is obtained between the experimental curves and the theoretical results in fig 1, both in the relative shape of the

erosion pattern and the absolute level. One striking disagreement occurs in the region of the tangency point, where in the model the erosion/redeposition approaches a null since the field lines are parallel to the surface at this point. In contrast, the experimental results show significant net deposition in this region which may result from ionisation of impurities in the SOL. Net deposition near the LCFS for the belt limiters is also in contrast with those from the discrete limiter case, where there was net erosion at the limiter surface closest to the plasma [1]. To assess the effect of ionisation in the SOL we have used the Monte Carlo code, LIM [4]. Earlier calculations have shown that ionisation in the SOL becomes significant ($\geq$ 25% of total ionisation), when the edge density reaches a value $\approx 3 \times 10^{18}$ m^{-3}. This leads to redeposition near the LCFS where the ionisation rate is high [5]. The results are shown in fig 1. It is seen that net deposition does occur near the tangency point. The reason for the difference between the belt limiter results and the earlier discrete limiter data is probably the higher operating density associated with high power additional heating.

No direct measurements have yet been made of erosion and deposition on the divertor target plates. However, the spatial distribution of deuterium, hydrogen and metal concentrations on the plates has been studied by Martinelli [6]. Comparison of the results with present measurements indicates that there is net erosion at the ion and electron side separatrix with deposition elsewhere. A similar picture emerges from the recent β back-scattering measurements [7].

Conclusions

An erosion and redeposition pattern has been observed on the JET belt limiters. The effect is toroidally symmetric. The radial distribution is similar to that observed for the earlier discrete limiters, except that there is now some net deposition near the LCFS, where previously there was net erosion. This effect is probably due to the higher operating densities leading to ionisation in the SOL. The effect has been modelled with the Monte Carlo code LIM and moderately good agreement with the spatial distribution has been obtained.

References

[1] G M M McCracken, D H J Goodall, P C Stangeby et al. J Nucl Mat 163-165 (1989) to be published.
[2] K J Dietz. J Nucl Mat 155-157 (1988)8.
[3] Erents et al. J Nucl Mat 163-165 (1989) to be published.
[4] P C Stangeby, C Farrell and L Wood Contributions to Plasma Physics 28 (1988)501.
[5] G M McCracken, P C Stangeby and C S Pitcher. Contributions to Plasma Physics 28 (1988) 447
[6] A P Martinelli. 16th EPS Venice 1989
[7] B Mills and D Buchenauer. Private communication. December 1988.

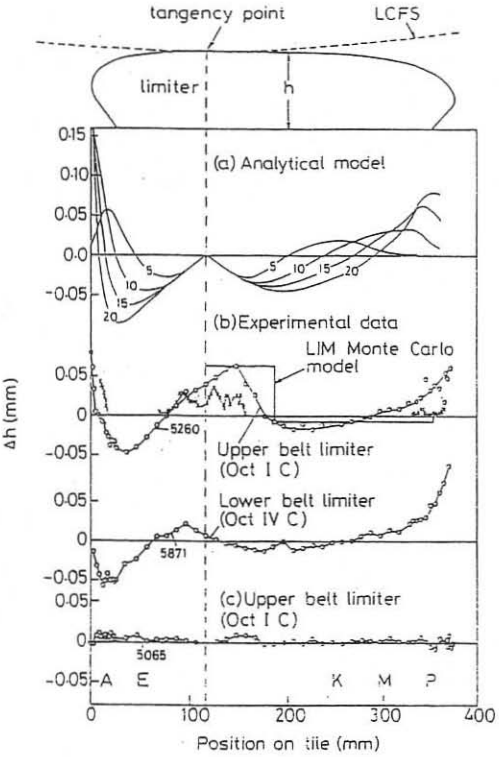

1a Calculated erosion of limiter tile using analytical model [1] which neglects ionisation in the SOL. Ion current density 2A cm^{-2} deuterons, Te(a) = 50 eV, exposure times 5 x 10^4s, for different λ_Γ and $\lambda_T = 2\lambda_\Gamma$.

b. Spatial distribution of erosion and redeposition on the JET belt limiter after exposure to ∿ 4000 discharges in 1987-88. Physical measurements °°°°°, measurements of deposition obtained by sectioning xxxx. Monte Carlo calculation using LIM code for $T_e(a)$ = 50eV λ_Γ = 20mm λ_T = 40mm $D_\perp = 1 m^2 s^{-1}$ $n_e(a) = 3 \times 10^{18} m^{-3}$

c. Distribution on belt limiter after 470 discharges; physical measurements.

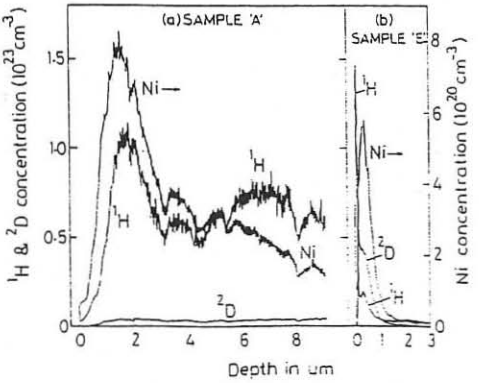

2. Depth distribution of nickel, hydrogen and deuterium measured on two samples; 'A' from a region of deposition; 'E' from an erosion region, see fig 1. The distributions were obtained by SIMS using a 15keV O^{2+} beam.

Observations of Impurity Charge State Distributions in the DITE Boundary using Plasma Ion Mass–Spectrometry

G. F. Matthews, P. C. Stangeby[†]

Culham Laboratory, UKAEA/Euratom Fusion Association,Oxon, U. K.
[†]Institute for Aerospace Studies, University of Toronto, Canada

1 Introduction

A plasma ion mass-spectrometer (PIMS) is being developed on DITE for in-situ real-time measurements of impurity ion mass-to-charge ratios in the scrape-off layer. The new instrument is based on the cycloidal motion of ions in crossed electric and magnetic fields which gives perfect velocity focusing for the components of the the ion velocity normal to the magnetic field [1] . Analysis of the trajectories shows that the focal length b, of such a device is given by

$$b = \frac{2\pi m_i}{ZeB^2} E \tag{1}$$

where m_i is the ion mass, Z the charge state, B the magnetic field and E the electric field. The perpendicular ion velocity does not enter into this expression at all and so all ions with the same mass to charge ratio are focused to the same line which lies parallel to the magnetic field. The perfect focusing property is important for tokamak applications since the plasma is a hot ion source.

2 Experiment

Figure 1 shows a schematic of the instrument. Ions from the plasma enter through a slit placed normal to the magnetic field. The electric field inside the probe is uniform and pulls ions onto the defining slit. An image of the defining slit is focused onto three collector wires. Mass-spectra are obtained by sweeping the electric field in the cavity. When correctly aligned with the magnetic field the instrument achieves a resolution of $R = (m_i/Z)/(\delta(m_i/Z)) \approx 20$.

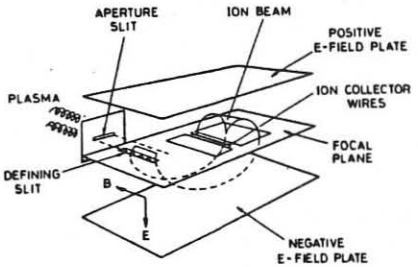

Figure 1: Schematic structure of the plasma ion mass-spectrometer.

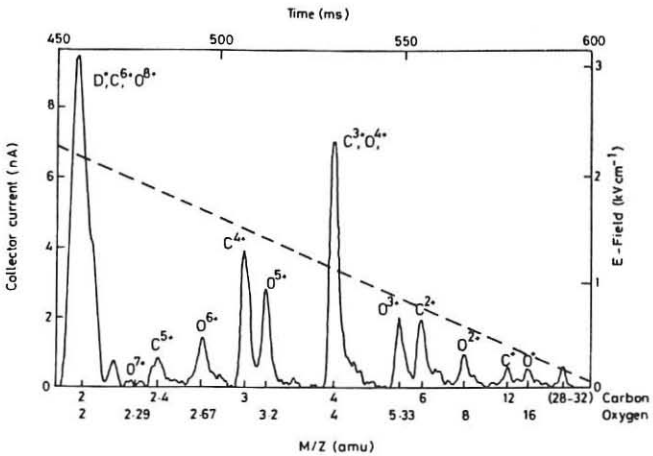

Figure 2: Mass-spectrum obtained in a $100kA$ deuterium discharge.

3 Results

Figure 2 shows a complete mass-spectrum obtained from a deuterium discharge with a plasma current of $100kA$, toroidal magnetic field of $2T$ and line average density of $\bar{n}_e = 2.3 \times 10^{19} m^{-3}$. The peaks in the mass-spectrum may almost all be identified as due to the various charge states of oxygen and carbon impurities. There are two points of ambiguity; one at $M/Z = 4$ where the C^{3+} and O^{4+} peaks overlap and again at $M/Z = 2$ where the D^+ peak overlaps with the fully stripped carbon and oxygen ions, C^{6+} and O^{8+}.

The problem of distinguishing the impurities from the working gas at certain charge states is worse in He discharges where the He^+ peak overlaps the C^{3+} and O^{4+} peaks. A mass-spectrum obtained in a $60kA$ He discharge is shown in figure 3, the He^{2+} peak which is off scale in this plot reaches a value of $100nA$.

The peak heights in the mass-spectrum are proportional to the current carried by particular charge states and so to calculate the fluxes these must be divided by the ionic charge of the contributing ion. Figure 4 shows the the flux in each charge state as a percentage of the total flux of each ion species as measured by PIMS.

4 Discussion

A two-dimensional Monte-Carlo code has been developed by Stangeby [2] (LIM) which models the ionisation and transport of impurities with a realistic limiter geometry in a specified target plasma. The predicted charge state ratios are shown in figure 5 alongside those measured. Two sources are considered: first a limiter source (Lim.) of physically sputtered neutrals and secondly a wall source of monoenergetic neutrals at $1eV$ (Wall). Either source fits the

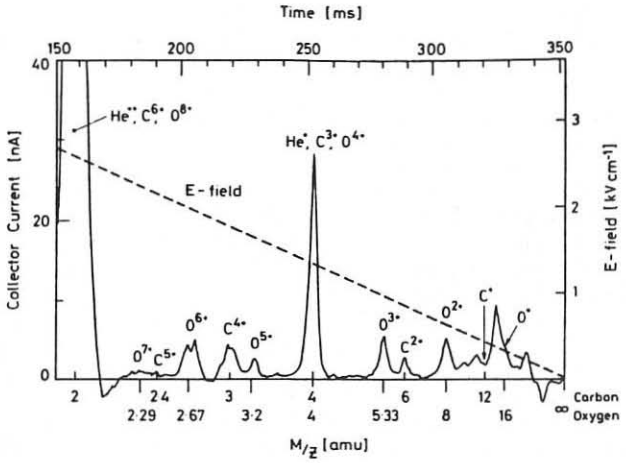

Figure 3: Mass-spectrum obtained in a $60kA$ helium discharge.

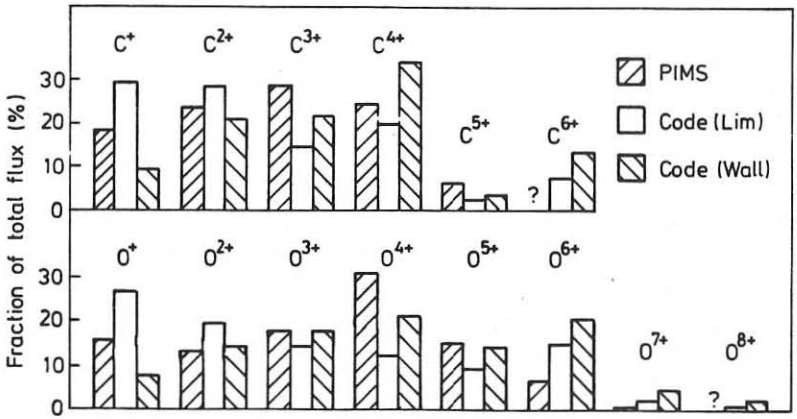

Figure 4: Charge states of carbon and oxygen measured with PIMS and predicted by the LIM code for a wall source (Wall) and limiter source (Lim.).

experimental data well. By contrast, assuming a limiter sublimation source of carbon (average neutral energy 0.1eV) gave poor agreement, e.g. $\sim$ 75% of the ions were singly charged.

A striking result is that the charge state distribution in the edge is far from coronal equilibrium. At typical DITE edge temperatures of 20eV the carbon would be almost entirely C^{4+} for coronal equilibrium [3]. Another clear feature of the charge state distributions is that the C^{4+} flux is 5 to 10 times greater than that of C^{5+}, and similarly the O^{6+} flux substantially exceeds that of O^{7+}. These large ratios arise from the fact that the C^{4+} and O^{6+} ions are in a helium-like configuration and have high ionisation potentials. For example, the ionisation potential of C^{3+} is only $64eV$ while that for C^{4+} is $392eV$ and for C^{5+} is $490eV$. The step in ionisation potential is associated with a corresponding step in ionisation rate coefficient. In DITE the central electron temperature in these discharges was around $600eV$ which means that the volume of plasma hot enough to ionise the C^{4+} within one impurity confinement time is relatively small. Also, once in the C^{5+} state the step to C^{6+} is not great.

The main uncertainty associated with the PIMS spectrum is the transmission characteristics of the instrument, which depend on the forward velocity distribution of the ions. This is not a problem when comparing the ratios of neighbouring peaks in the spectrum because the transmission is expected to be a relatively weak function of M/Z. An unambiguous comparison of the total fluxes of carbon and oxygen is also possible, since both impurities exhibit a similar dispersion of charge states and so the uncertainties in the transmission function will cancel out. These fluxes are equal to within about 5% which is unlikely to be a coincidence. The explanation is that the main impurity production process in DITE is chemical sputtering by oxygen leading to the production of CO with a yield of unity. Only a few percent oxygen are required for the oxygen chemical sputtering to dominate over deuteron sputtering because the edge electron temperature is $10 - 20eV$ under these conditions in DITE, leading to a physical sputtering yield of around 0.01. The unquantified variation of the instrumental transmission with the M/Z ratio makes the comparison of the total carbon and oxygen fluxes to the deuteron flux inconclusive.

5 Conclusions

Preliminary results from plasma ion mass-spectrometry of the DITE scrape-off layer show that the impurity spectrum is dominated by carbon and oxygen. Similar fluxes are observed in each charge state up to the helium-like ion state and a substantially lower flux in the hydrogen-like state. The observed charge state distributions are not in coronal equilibrium but are well modeled by the LIM impurity transport code. Also, the stoichiometry of the carbon and oxygen which is observed gives a clear indication that oxygen chemical sputtering is the dominant impurity production process during deuterium discharges in DITE.

References

[1] W.Bleakney and J.A.Hipple, Phys. Rev., **56** (1938) 521-529

[2] P.C.Stangeby et al, 14^{th} Euro. Conf. on Contr. Fusion and Plasma Physics, Madrid 22–26 June 1987 II 714

[3] P.G.Carolan and V.A.Piotrowicz, Plasma Physics, **25** (1983) 1065

EDGE ION TEMPERATURE AND SHEATH POTENTIAL MEASUREMENTS DURING OHMIC HEATING IN THE DITE TOKAMAK

R. A. Pitts[†], *G. M. McCracken, G. F. Matthews and S. J. Fielding*

Culham Laboratory, Abingdon, Oxon OX14 3DB, U. K. (UKAEA/Euratom Fusion Association)

[†] Royal Holloway and Bedford New College, University of London, U. K.

1 Introduction

Using the technique of retarding field energy analysis, we have measured the sheath potential fall and the component of the fuel ion temperature parallel to the toroidal magnetic field as a function of line averaged central density, working gas and radial position in the DITE plasma boundary. In this paper we present experimental evidence for significant deviations from equipartition ($T_i \neq T_e$) in the edge plasma in the case of helium as the working gas and, regardless of the plasma species, for a reduction in the sheath potential compared with the conventional theoretical values of $3kT_e/e$. The implications for the calculation of sputtering yields at limiter and divertor plate surfaces are considered.

2 Experiment

Measurements are made with the probe [1] operating in the ion energy analyser mode. Ions enter the probe through small, radially separated, defining apertures and are subject to retarding electric fields. Application of a ramped positive voltage to a high transparency grid yields a collected current which depends on the ion velocity distribution along the magnetic field. The probe entrance slits are electrically isolated and so may be used as simple Langmuir probes to measure the local electron temperature. Additional T_e measurements are provided by Langmuir probes embedded in the surfaces of the DITE pumped limiter located $\sim 200°$ toroidally from the energy analyser and connected to it along the magnetic field ($\sim 4.2m$).

3 Results

Experiments are performed in hydrogen, deuterium and helium ohmic discharges, each with $I_p = 100kA, B_T = 2.1T$ and with varying line average central density, $\overline{n}_e$. The probe enters the torus from the top of the machine at poloidal angle $\theta = 81°$ with respect to the outside midplane. The entrance aperture dimensions have been varied from $(5 \rightarrow 100\mu m) \times (3 \rightarrow 7mm)$. Measurements indicate that sheath potential data obtained using slit widths of $w \geq 25\mu m$ are unreliable and results for the case of $w = 5\mu m$ only will be presented here. This does not apply to ion temperature data, which are considered accurate as long as $w \leq 100\mu m$. These dimensions should be compared with the Debye length in the edge plasma, which for these experiments ranges from $\lambda_D = 14 \rightarrow 170\mu m$.

In almost all cases studied the collected ion current characteristics are found to be consistent with a displaced Maxwellian distribution of velocities. The magnitude of the displacement is interpreted as the sheath potential fall between plasma and probe, V_s and, if the presheath is ignored, the ion temperature may be obtained by fitting the exponential tail of each characteristic. Since the probe and associated electronics use the torus potential as reference, each value of V_s is a measurement of the plasma potential with respect to the torus potential and not the local floating potential.

In figs. 1 and 2 we illustrate the radial variation of T_i, T_e and V_s in deuterium and helium for fixed values of line average density; $\overline{n}_e = 1.3 \times 10^{19} m^{-3}$ (deuterium), $2.6 \times 10^{19} m^{-3}$ (helium). Although not shown, the local floating potential is relatively constant at between $-5 \rightarrow -10$ volts across the range of minor radius. The helium data are calculated assuming all the collected current to comprise He^{2+} ions.

In deuterium the edge electron and ion temperatures are comparable, with the measured sheath potential and electron temperature remaining flat with increasing radius. The ion temperature declines with radius but with no convincing exponential trend. In helium the ion temperature is considerably higher than for deuterium and hydrogen whilst the electron temperature and sheath potential are again comparable and of the same magnitude as the deuterium data. There is an exponential decrease with radius for the ion temperature with $\lambda_{T_i} = 4.4cm$. Fig. 3 shows the results for a density scan in helium, where in this case the sheath potential data have been adjusted using floating potential measurements so that the values may be compared with theoretical predictions (section 4). The ion temperature decreases markedly as the density rises, with T_i approaching T_e only at the highest densities. The electron temperature also decreases with density as previously observed with the impurity control limiter [2]. Once more V_s and T_e are comparable.

4 Discussion

One important feature of our results is the large difference between the ion temperatures in deuterium and helium discharges. The assumption that He^{2+} ions are the majority species is valid if the outflux of He^{2+} from the core plasma into the probe flux tube dominates the recycled fluxes of He^{+} from the limiter and, to a lesser extent, from the probe itself. Simple calculations assuming a cosine distribution for the recycled helium atoms and including the geometry of the pump limiter and the probe, suggest that the flux of He^{+} ions at the probe is as little as 1% of the He^{2+} flux from the plasma core. Nevertheless, our data necessarily represent an upper limit on T_i for these experiments. Under these assumptions, values for the helium fuel ion temperature of $\sim 60eV$ near the limiter radius at $\overline{n}_e = 2.6 \times 10^{19} m^{-3}$ are in good agreement with earlier measurements of the perpendicular impurity ion temperature [1]. This is an indication that the fuel and impurity ions are in thermal equilibrium and that $T_{i_\parallel} \sim T_{i_\perp}$ for these edge conditions.

Considering the measurements of sheath potential, simple theory [3] leads to the expression

$$V_s = \frac{T_e}{2} log_e \left\{ \frac{2\pi m_e}{m_i} (Z_i + \frac{T_i}{T_e})(1 - \gamma_e)^{-2} \right\} \quad (1)$$

where T_i, T_e are in eV, Z_i is the ion charge and γ_e the secondary electron emission coefficient. In fig. 4 the experimental values for V_s from fig. 3 are shown together with those calculated

using eqn. (1) with $\gamma_e = 0$ and $T_i = T_e$ as is commonly assumed in plasma edge modelling. Evidently theory overestimates V_s by up to a factor 2. This is probably due to the neglect of γ_e which, from the data of fig. 4, must take values close to 1 for theory and experiment to be in accord. Unfortunately, experimental data for secondary electron emission at low primary electron energy are scarce. Calculations using the available data extrapolated to low energies, indicate values of $\gamma_e \sim 0.3 \rightarrow 0.5$ for a graphite coated tungsten surface and the range $T_e = 30 \rightarrow 10eV$ for the data in fig. 4 [4].

To a first approximation the impact energy of ions incident on limiter is given by the sum of the thermal energy and that gained by acceleration through the sheath potential drop

$$\frac{E}{e} = 2T_i + Z_i V_s \qquad T_i, T_e \; in \; eV \tag{2}$$

Using eqn. (2) the sputtering yields for He^{2+} ions on carbon evaluated with an empirical relation due to Bohdansky [5] have been calculated using both the experimental values for V_s and T_i and the theoretical values for V_s and E assuming $T_i = T_e$. The results are also shown in fig. 4 from which it is clear that the yields are approximately equal except at high densities – two incorrect assumptions have cancelled to give the same result.

5 Conclusions

Measurements have been made of the ion temperature and sheath potential in the DITE plasma boundary for a range of operating conditions. In hydrogen and deuterium discharges the ion and electron temperatures are found to be comparable near the limiter radius. In helium, assuming He^{2+} ions to be the majority species, the ion temperatures are higher for equivalent radial positions, being in the range 2–2.5 T_e near the limiter. Both T_e and T_i are observed to decrease with increasing central density with $T_i = T_e$ being satisfied only at the highest density. Under all conditions studied, the sheath potentials are found to be only marginally higher than the local electron temperature. Calculations show that sputtering yields evaluated on the basis of simple theory for the sheath voltage and under the assumption that $T_i = T_e$ in the boundary, are close to those obtained using experimental data in the case of helium discharges.

References

[1] R. A. Pitts et al, Proc. 8^{th} Int. Conf. on Plasma Surface Interactions (Jülich 1988), to be published in J. Nuc. Mater. **163–165**

[2] G. F. Matthews et al, 14^{th} Euro. Conf. on Contr. Fusion and Plasma Phys., Madrid 22–26 June 1987 **II** 762

[3] P. C. Stangeby, Phys. Fluids **27** (3) (1984) 682

[4] G. F. Matthews et al, J. Nuc. Mater., **145–147** (1987) 225

[5] J. Bohdansky, Nucl Fus. Special Issue (1984) 61

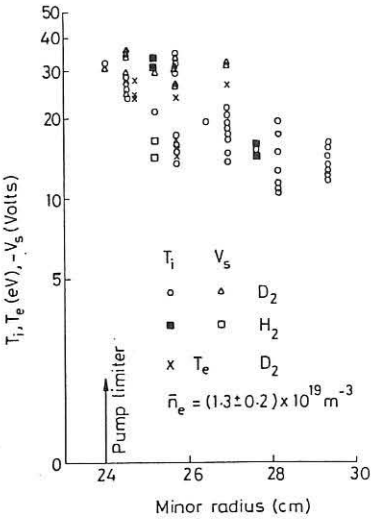

Fig. 1 Radial variation of T_i, V_s and T_e in deuterium discharges

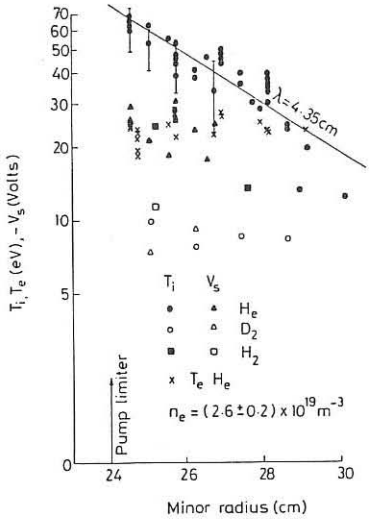

Fig. 2 Radial variation of T_i, V_s and T_e in helium discharges

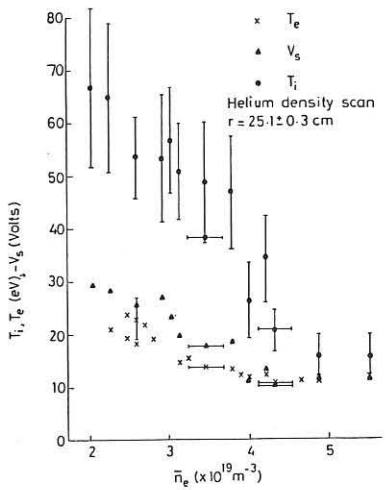

Fig. 3 Dependence on line average central density of T_i, V_s and T_e for helium discharges

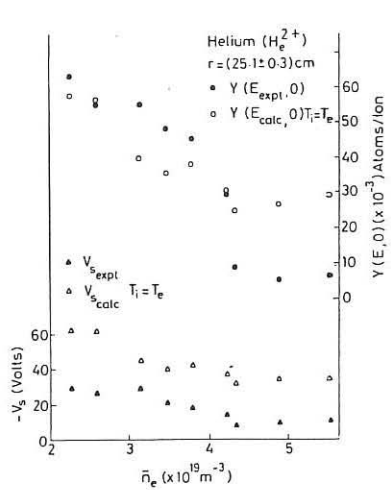

Fig. 4 Experimental and calculated values for V_s and sputtering yields for the data of Fig. 3

PUMP LIMITER WITH GAS-PUFFING FROM DIVERTOR REGION IN JFT-2M TOKAMAK

S.Sengoku, A.Aikawa, K.Hoshino, S.Kasai, T.Kawakami, H.Kawashima, T.Kondoh,*
H.Maeda, T.Matsuda, Y.Miura, M.Mori, I.Nakazawa,** C.R.Neufeld,*** K.Odajima,
H.Ogawa, T.Ogawa, H.Ohtsuka, T.Shoji, N.Suzuki, H.Tamai, Y.Uesugi, T.Yamamoto,
T.Yamauchi, K.Hasegawa, A.Honda, I.Ishibori, Y.Kashiwa, M.Kazawa, K.Kikuchi,
H.Okano, E.Sato, T.Shibata, T.Shiina, K.Suzuki, T.Tani, T.Tokutake and S.Uno

Department of Thermonuclear Fusion Research,
Japan Atomic Energy Research Institute,
Tokai, Naka, Ibaraki 319-11, Japan
* On leave from University of Tsukuba, Ibaraki, Japan
** On leave from Mitsubishi Electric Co., Tokyo, Japan
*** On leave from Hydro-Quebec, Varennes, Quebec, Canada

A dense and cold divertor plasma is obtained with a pump limiter in JFT-2M tokamak. In an Ohmic phase, the divertor plasma density builds up only when a gas-puff is terminated. It is shown that a very dense and cold divertor plasma ($\sim 4\times10^{13}$ cm^{-3}, $\sim$10 eV) is compatible with a beam heated H-mode discharge.

INTRODUCTION: Formation of the dense and cold divertor plasma establilshed in Doublet-III /1,2/ and ASDEX /3/ is favorable for minimizing erosion due to sputtering of the divertor plate. When such a plasma is formed with an open divertor geometry, however, particle recycling or gas pressure at the main plasma periphery increases at the same time ("neutral back flow" from the divertor region)./4/ As is systematically studied in Ref.5, the energy confinement time is degraded when the edge neutrals build up.

A pump limiter is employed aiming to prevent the neutral back flow in JFT-2M open divertor operations. Detailed descriptions of the pump limiter and the tokamak are given in Refs. 5 and 6. The pump limiter is located close to the divertor null-point, outside the separatrix (Fig.1). A gas-puff outlet is located between the separatrixes intersecting the divertor plate. This location of puff is appropriate for a future reactor, since the material that suffers energetic charge-exchanged particles due to gas puffing should be exchangeable for maintenance. The divertor plate is considered to be an exchangeable module. In this report, another puff located at the bottom of the torus is used as a referece.

REDUCTION OF EDGE GAS PRESSURE BY THE PUMP LIMITER: The neutral gas pressure at the main plasma periphery P_{D_2} measured by a residual gas analyzer RGA is considerably decreased by the pump limiter PL with gas-puff from the divertor region (Fig.2). The edge electron temperature of the main plasma T_e^{edge} inferred from electron cyclotron emission ECE is relatively high with the pump limiter at higher density.

FORMATION OF THE DENSE AND COLD DIVERTOR PLASMA: In Ohmic phase, the dense and cold divertor plasma was not observed to the extent of the allowable gas-feed rate which does not give any deleterious effects on the main plasma. Electron density at the divertor plate n_e^d does not build up during the gas puffing (Figs.3, 4). This n_e^d is relatively low without PL presumably due to the low T_e^{edge} as shown in Fig.5.

After the reduction or termination of the gas-puff, the T_e^{edge} increases, the divertor plasma density builds up from 0.6×10^{13} cm^{-3} to 2×10^{13} cm^{-3} and the electron temperature near the divertor plate at the density peak T_e^d cools down from 17 eV to 10 eV; the line-averaged electron density of the main plasma of $\bar{n}_e = 4\times10^{13}$ cm^{-3} in either puff case [Figs.4-a) and b)]. This implies that the ionization mean-free-path (~20 cm) is too long due to low T_e^{edge} during the gas-puffing as shown in Fig.5 compared to the length of divertor channel (~7 cm). This can be also responsible to the small differene between the both gas-puffing case.

In a beam-heating phase , T_e^{edge} is two times higher than that of in Fig.5 even though a strong gas-puff Q_H is introduced during the beam. The power flow to the divertor channel is supposed to be large in this case. The gas-feed rate of up to 20 Torrl/s is compatible for switching on an H-mode with the pump limiter. The buildup of n_e^d is very strong and T_e^d is below 10 eV with the injected beam power of 1.7 MW as shown in Fig.6 for the case with the bottom gas-puff. The line-averaged electron density of the main plasma at t = 0.8 sec is about 6×10^{13} cm^{-3}. The discharge becomes L-mode when Q_H of about 30 Torrl/s is introduced.

CONCLUSIONS: The combination of a pump limiter and a gas-puff from the divertor region is examined. The pump limiter reduces the

edge neutral pressure and the edge cooling due to a cold gas-puff in the high density regime. In an Ohmic discharge, a dense and cold divertor plasma is formed only when the gas-puff is terminated, since the main plasma edge is cooled by the gas-puff. In the beam-heating phase, however, very dense and cold divertor plasma is obtained as to be compatible with an H-mode discharges. High edge temperature is necesarry in order to realize a dense and cold divertor plasma.

ACKNOWLEDGEMENTS: The authors are grateful to Drs. S. Mori, M. Yoshikawa and M. Tanaka for their continuous encouragement.

/1/ M. Shimada et al., Nucl. Fusion **22** (1982) 643.
/2/ S. Sengoku et al., Nucl. Fusion **24** (1984) 415.
/3/ Y. Shimomura et al., Nucl. Fusion **23** (1983) 869.
/4/ S. Sengoku et al., in Proc. 10th Int. Conf. on Plasma Phys. Controlled Nucl. Fusion Res., London, 1984 (IAEA, Vienna, 1985), Vol.1, p. 405.
/5/ S. Sengoku et al., J. Nucl. Mater., **145-147** (1987) 556.
/6/ S. Sengoku et al., presented at the 8th Int. Conf. on "Plasma-Surface Interactions in Fusion Devices", Jülich, May, 1988, paper 192.

Figure captions

Fig.1 Cross section of the JFT-2M with a divertor separatrix. The location of pump limiter, Langmuir probe array and gas-puff outlet are also shown.

Fig.2 The neutral pressure P_{D_2} and electron temperature T_e^{edge} at the main plasma edge for the cases with and without the pump limiter PL as functions of the central line-averaged electron density $\bar{n}_e$.

Fig.3 The temporal evolution of the profile of electron density at the divertor plate n_e^s. The locations of separatrixes intersecting the divertor plate are shown by arrows. The probe position is measured from the high field side. The gas-puff is terminated at t=0.803 sec.

Fig.4 The temporal evolutions of 1) n_e^s and the electron temperature near the divertor plate T_e^s at the density peak, 2) $\bar{n}_e$, T_e^{edge} and the gas-feed rate Q for the cases with gas-puff a) from the divertor region and b) from the bottom of the torus. For comparison, n_e^s without the pump limiter are shown with broken lines.

Fig.5 The comparison between the time-traced T_e^{edge} with and without the pump limiter as functions of the density.

Fig.6 The dependece of gas-feed rate during 1.7 MW neutral-beam heating Q_H on the formation of the dense and cold divertor plasma. Discharges get into the H-mode are laveled with ⟨H⟩, other with ⟨L⟩.

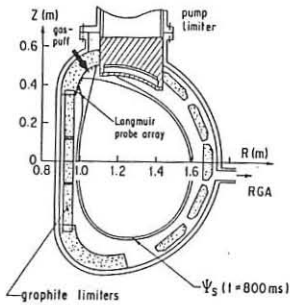

Fig.1

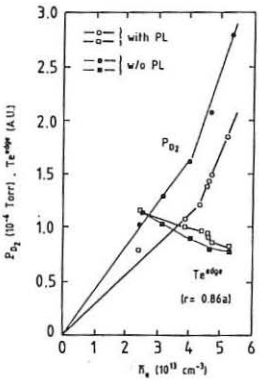

Fig.2

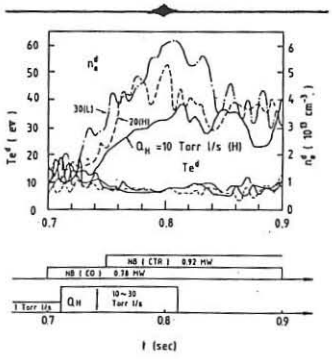

Fig.6

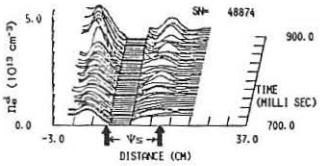

Fig.3

a)

b)

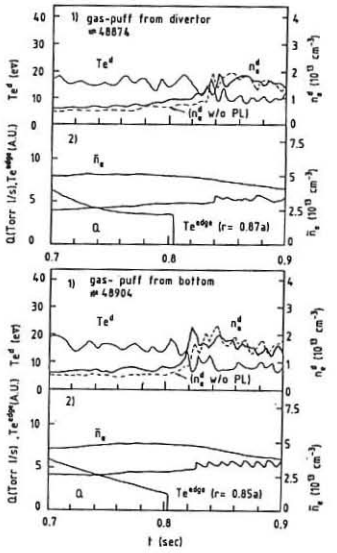

Fig.4

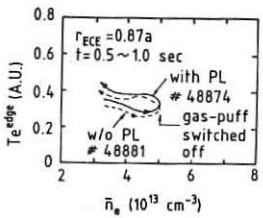

Fig.5

GAS BALANCE MEASUREMENTS AT JET

R. Sartori, G. Saibene, J.L. Hemmerich, M.A. Pick

JET Joint Undertaking, Abingdon, Oxon OX14 3EA, England.

1. Introduction

The inventory of gas in the walls of the JET machine is of concern for future operation, in particular during the DT phase. A diagnostic system which allows one to quantify the amount of gas released after each JET discharge as well as over a longer period has been operated since December 1987. Gas balance calculations have been carried out by comparing the amount of gas released to the total number of molecules fuelled into the plasma as cold gas, pellets and neutral beams. In addition, all the gas released during a period of operation, ranging from a few discharges to a few days, was collected and chemically analysed.

2. Experimental set-up and procedure

The experimental data presented were collected over a period of 9 months of JET operation. The in-vessel configuration was as described in [1]. The experimental set-up is shown in Fig. 1. During the measurements the main roughing pumps are disconnected (VA closed) and replaced by the helium cryopump CR. At the start of a discharge VB is closed. During the discharge gas is pumped from the vessel by the main turbo pumps and the pressure in V_1, measured by the capacitive gauge 2 , increases. After 600 seconds VB opens and the gas is collected in CR. Subsequently CR is heated and the collected gas is transferred to the reservoir R. Samples are taken to be chemically analysed by gas chromatography. The number of molecules collected after one shot or a series of shots is calculated from the pressure increase in the calibrated volumes V_1 and R respectively. The chemical composition of the collected gas is used to determine a correction factor for the number of deuterium molecules in the gas collected.

Deuterium (and/or He) is introduced into JET either as cold gas (initial puff followed by a density feedback system control inlet), as pellets or as neutral beams [2]. We estimate the error of the amount of gas input to be ± 5% (± 10% for pellet fuelled discharges). The error on the output measurements is estimated to be ≤ 5%.

3. Results

Data were collected for more than 500 discharges in a wide range of operational conditions. Fig. 2 shows the ratio P between the number of molecules released within 600 s after the discharge and the total number injected N_i, as a function of N_i, for successful plasma shots only. All these discharges have deuterium as main input gas. For a typical input of $N_i \geq 3 \times 10^{21}$ molecules only a fraction of N_i varying from 10% to 40% is recovered within 600 s. In fact a variation of an order of magnitude in the total input results in only a factor of two variation in the total output. Values above 50% are normally observed only for very low density shots. These results are in good agreement with gas balance measurements

for ohmic shots with deuterium in TFTR [3].

The percentage of gas recovered (Fig. 2) decreases with increasing input indicating that the total amount of deuterium trapped in the walls increases with the number of molecules injected. The fraction of gas released is independent of whether the shot is ohmic, additionally heated and/or pellet fuelled. The increase in the fraction released observed in TFTR after NB heated discharges is not found in JET. The fraction of deuterium released shows no significant dependence on plasma current (from 3 to 7 MA), current flat-top duration (1-10s), total power (up to 20 MW) or plasma configuration. Measurements carried out in JET operating at higher wall temperature (350°C versus 300°C) showed only a marginally higher recovery. After a He-cleaning pulse (i.e. a very low density, long current flat-top He discharge) the percentage of gas recovered varies from ~ 100% up to 900% of the input. Assuming that all the He is recovered, an average value of 0.8×10^{21} molecules of deuterium are released after such a discharge. Under these conditions at least 10 He discharges would be required to recover all the gas trapped in the walls during a high density deuterium shot (input ~ 10×10^{21} molecules). However, other experiments in JET show a decreasing in the deuterium release rate over a sequence of cleaning shots [4]. The amount of deuterium recovered after a plasma shot ending in a disruption varies from 2×10^{21} to 1×10^{22} molecules, i.e. up to 10 times the release measured after a shot with soft landing. The percentage of gas recovered varies from 50% to 500% of the deuterium injected, being around 80% for most of the disruptions. The total number of molecules recovered is always greater than the plasma inventory at the time t_D of the disruption. No clear relationship has been found between the measured fractional release and the plasma current or power at the time t_D. This could indicate that the induced outgassing depends on the dynamics of each particular disruption, including in particular the local power deposition.

Taking account of the deuterium released during a whole day of operation (not only during the first 600 s after each shot), the average amount of gas recovered is ~<50%. We measured the long term outgassing of the vessel for 8-12 hrs after the last shot of the day with the wall and the limiters remaining at operation temperature. The decreasing deuterium release rate R was determined as a function of time. This further outgassing, however, contributes to the overall gas balance only by a few percent. The main impurities detected in the collected gas are hydrocarbons of various orders, the most abundant being CD_4 (~ 2% of the molecules); the relative amounts are fairly constant for different JET operating conditions. The resulting average correction on the total number of deuterium molecules is around +8%. With this correction the amount of deuterium that is left in the vessel walls is estimated to be around 40% of the input. This result is in good agreement with preliminary in-vessel deuterium retention measurements for the 1987 campaign [5].

Further understanding in the wall pumping phenomena during a plasma discharge can be gained by relating the fuelling and outgassing characteristics of a discharge to the actual plasma inventory. The fuelling efficiency F, the fraction of input gas which ends up in the plasma, is defined as the ratio between the plasma electron inventory I (corrected for Z_{eff}) and the gas input N_{io}. Both quantities are taken at time t_o, defined as the time when the fuelling due to density feedback

stops. For $N_{io} > 2 \times 10^{21}$ molecules, F varies from 10% to 60% (Fig. 3). A large fraction of the input gas molecules is therefore already lost in the early phase of the discharge during or at the end of the density ramp-up, which is in many cases coincident with the end of the current ramp-up. In particular for ohmic shots with no fuelling after the density ramp-up the number of molecules recovered is equal or slightly less than the maximum inventory (Fig. 4). For additionally heated or pellet fuelled discharges the ramp-up pumping does not account for all the gas lost, since in this case the recovery is lower than the maximum inventory. For all but pellet fuelled discharges, where there is a large additional fuelling, this early pumping does, however, represent the major contribution to the total wall pumping. F is, similar to the percentage recovered, a decreasing function of N_{io} [6].

4. Conclusions

Particle balance measurements on a shot-by-shot basis show a high deuterium retention in the JET vessel walls. The fraction of input gas trapped into the walls at 600 s varies from 60% to 90% of the injected deuterium, the latter value being the most representative for high density shots. On this basis a direct prediction of the tritium inventory during the future DT operation can be done. Correcting for hydrocarbon content and taking into account overnight outgassing, it is shown that still up to 70% of the input gas is likely to be trapped in the walls. For example, for 100 high density plasma discharges requiring a total fuelling of 7.5 g of tritium, the maximum total tritium retention would be around 4.9 g. However, it has to be pointed out that this estimate does not take into account any physical or chemical process (e.g. thermal outgassing, He glow discharge cleaning) which could be exploited to enhance tritium release.

For ohmic shots the trapping of deuterium by the walls takes place mostly during the density ramp-up. Two phenomena are likely to contribute to the deuterium trapping into the JET walls: prompt implantation and co-deposition. Co-deposition of deuterium-rich carbon layers is related to the sputtering of carbon during the plasma discharge. This phenomenon, although it cannot account for the large early pumping observed, is likely to contribute to the 'further pumping'. The same considerations apply in general to additionally heated discharges. For pellet fuelled shots a stronger further pumping is observed. A more detailed analysis of the observed effects will be published.

References

[1] M. Pick et al, Proc. of 12th Symp. on Fusion Engineering, Monterey (CA) 1987, p. 137

[2] B.J. Green, Spring College on Plasma Physics, Trieste (Italy) 1987 (JET-R(87)06)

[3] K.L. Wilson, H.F. Dylla, Joint Report SAND88-8212 and PPPL-2523, October 1988

[4] G. McCracken, private communication

[5] M.P. Coad et al, 8th PSI, Jülich May 1988. To be published in J. Nucl. Mat.

[6] J. Ehrenberg, 8th PSI, Jülich May 1988. To be published in J. Nucl. Mat.

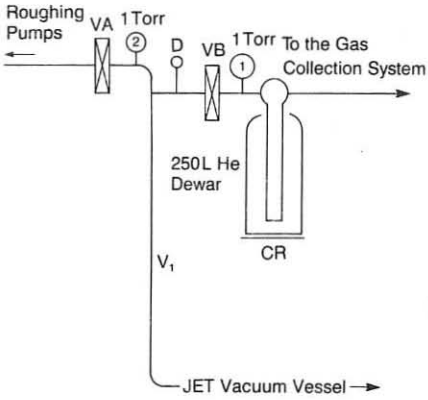

Fig. 1: Experimental set-up

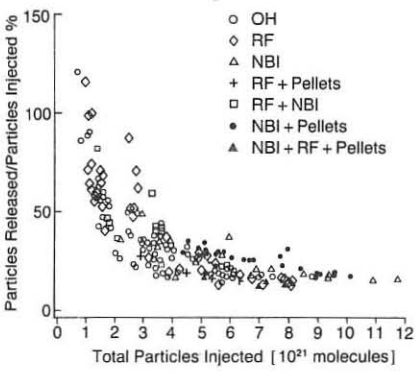

Fig. 2: The fraction of gas released P in 600 s after the end of a discharge as a function of the number of molecules injected N_i

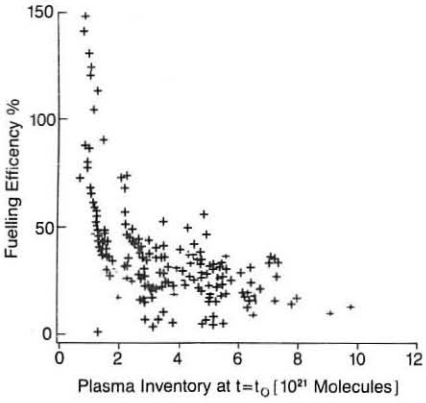

Fig. 3: The fuelling efficiency F as a function of the number of molecules injected N_{io}, for the same set of data as Fig. 1.

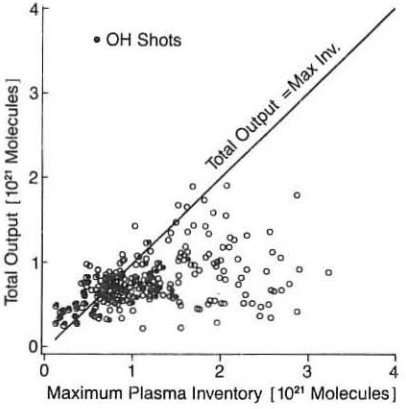

Fig. 4: The total output as a function of the maximum plasma inventory, for the same set of data as Fig. 1.

EDGE BROAD-BAND FLUCTUATIONS AND PARTICLE TRANSPORT DURING ECRH IN DITE

P.Mantica*, S.Cirant*, J.Hugill, G.F.Matthews, R.A.Pitts#, G.Vayakis°

Culham Laboratory, UKAEA/Euratom Fusion Association, OXON, U.K.

* Istituto di Fisica del Plasma, Associazione Euratom/ENEA-CNR, Milano, Italy
# Royal Holloway and Bedford New College, University of London
° Dept. of Engineering Science, University of Oxford

Within the framework of the experimental investigation of a possible relation between microturbulence and anomalous transport /1,2/, the purpose of this work is to compare the role of edge broad-band magnetic field, density and electric field fluctuations in determining particle transport. Particular attention will be paid to the strong deterioration of particle confinement observed in ECR heated plasmas /3/.

During ECRH experiments on the DITE tokamak, with a=24 cm, R=120 cm, 60 GHz, X-mode from high-field side, P_{ECRH} up to 200 kW for 200 ms, 1st and 2nd harmonic resonance /4/, the following edge diagnostics have been used to measure high frequency fluctuations up to 250 kHz and particle transport in the plasma boundary:

- arrays of Mirnov probes, to determine the poloidal and toroidal structure of poloidal magnetic field fluctuations, $\widetilde{B}_\theta$,
- poloidal and radial pick-up coils mounted on a reciprocating drive, to measure radial profiles of $\widetilde{B}_\theta$ and $\widetilde{B}_r$ in the scrape-off layer (SOL),
- a 4-pin Langmuir probe mounted on a reciprocating drive, to measure radial profiles of electric field $\widetilde{E}_\theta$ or potential $\widetilde{\Phi}$ and density $\widetilde{n}$ fluctuations in the SOL,
- a set of fixed Langmuir probes flush with the surfaces of the main limiters, to measure the total particle outflow from the plasma.

Ohmic magnetic fluctuation levels of the order of $\widetilde{B}_\theta/B_T \sim 10^{-5}$ at the limiter are observed, with a pronounced inverse dependence on plasma density. Correlation measurements suggest that they are generated by filamentary perturbations of the current density lying along the field lines in the plasma periphery /5/. Radial profiles in the SOL (Fig.1a) provide an estimate of their poloidal scale-length of about 3-5 cm, or equivalently an average poloidal number m~15-20.

The injection of EC power causes an increase in the magnetic fluctuation level of 30% to 200%. A reduction in the filament size is also observed. The increase in $\widetilde{B}_\theta$ is larger at low density (Fig.2a) and for resonance positions displaced from the centre /5/ and is closely related to the increase in D_α emission and particle outflow due to the deterioration of particle confinement during ECRH. The latter can be estimated (Fig.3) from the plasma density together with measurements of the total ion saturation current using the limiter Langmuir probes and under the reasonable assumptions that particles are singly charged and that any ionization sources in the

SOL do not contribute significantly to the flow.

From the reciprocating Langmuir probe measurements, ohmic fluctuation levels $\tilde{n}/n$ ~ 0.3 and $e\tilde{\Phi}/kT_e$ ~0.5 are obtained under the assumption $\tilde{T}_e/T_e \ll 1$. Most of the power is concentrated below 100 kHz. Radial profiles (Fig.1 b,c) show that the Boltzmann relation is not satisfied in the SOL, i.e. $\tilde{n}/n \neq e\tilde{\Phi}/kT_e$. The normalized density fluctuations also show an inverse dependence on density (Fig.2b). Typical ohmic cross-coherence between density and electric field fluctuations is γ_{nE} ~.5, with a cross-phase $\alpha_{nE}(\omega)$ lying between -60° and +60°. Fig.4 shows a typical cross-field particle flux spectrum, calculated according to

$$\Gamma_e = \langle \tilde{E}_\theta \tilde{n}_e \rangle / B_\Phi = \tilde{n}_{e\ rms}\ \tilde{E}_{\theta\ rms}\ \gamma_{nE} / B_\Phi \qquad (1)$$

ECRH causes an increase of 30% to 100% in the fluctuation levels and although the cross-coherence between $\tilde{n}$ and $\tilde{E}_\theta$ decreases to γ_{nE} ~.25, a net increase in the driven particle outflow is observed. The cross-field particle flux induced by electric field and density fluctuations is compared to the global parallel flow to the limiters in Fig.5. One can see that fluctuation induced transport can account for a substantial part, if not all, of the measured particle flux. The fact that the fluctuation induced flux is actually larger than the global one is mainly due to combined probe area calibration errors (±50%), toroidal and poloidal asymmetries and the neglect of temperature fluctuations. More importantly, the increase of flux during ECRH is completely accounted for in a self-consistent manner by the electric field and densiy fluctuation increase. On the other hand, estimates according to weak turbulence models of the contribution to particle transport of magnetic fluctuations are 3 orders of magnitude below the measured transport.

Power balance calculations for hydrogen discharges at $\bar{n}_e \sim 2 \times 10^{19}$ m^{-3} and assuming $T_i = T_e$ at the limiter /6/ show that convective heat loss due to electric field and density fluctuations can account for at most 50% of the non-radiative heat loss, whilst the magnetic conduction term is negligible. However, direct measurements of temperature fluctuations are needed to check whether they can account for the missing power.

The fact that magnetic fluctuations are systematically related to the increase of particle transport indicates that they might be driven by the density fluctuations according to pressure balance

$$\tilde{B}_\theta/B_0 = G\ \tilde{B}_{||}/B_0 = G\ \beta/2\ \tilde{p}/p_0 \qquad (2)$$

where G is an unknown factor between1 and 10, B_0 and p_0 the steady-state field and pressure and β the edge beta In fact, within the large uncertainties associated with edge temperature measurements, the experimental values of $\tilde{B}_\theta/B_0$ and $\beta/2\ \tilde{n}/n$ lie in the same order of magnitude. More importantly, the increase of magnetic fluctuations during ECRH is well accounted for by the increase in $\tilde{n}/n$ and edge beta.

Further evidence for a connection between the two kinds of fluctuations comes from measurements in the presence of modulated EC power. Similar behaviour of amplitude and phase delay with respect to the RF power as a function of resonance position is observed for magnetic and density fluctuations and particle outflow (Fig.6). Moreover, the maximum delay, minimum amplitude behaviour for central resonance indicates that the observed boundary response is not due to direct

interaction of the RF with the boundary plasma, but rather to propagation to the edge of the effect of plasma-wave interaction at the resonance location. In fact, the observed edge response time appears to be consistent with the heat pulse diffusion time measured by ECE and SX-ray diagnostics /7/. It is also to be noted that considerable up-down asymmetries in the phase delays have been observed by all edge diagnostics.

/1/ P.C.Liewer, Nucl.Fus., Vol.25, No.5 (1985), p.543

/2/ A.J.Wootton et al., Pl.Phys. and Contr.Fus., Vol.30, No.11 (1988), p.1479

/3/ S.Cirant et al., accepted for publication in Pl.Phys. and Contr.Fus.

/4/ M.Ashraf et al., Proc. of 12th IAEA Conf. on Pl.Phys. and Contr.Nucl.Fus. Res., IAEA-CN-50/E-I-3, Nice, October 1988.

/5/ P.Mantica et al., Proc. of 15th EPS Conf. on Contr.Fus. and Pl.Heat., Dubrovnik, May 1988, Vol. 12B, part II, p.815.

/6/ R.A.Pitts et al., P4E6 this conference.

/7/ M.Ashraf et al., Proc. of 12th IAEA Conf. on Pl.Phys. and Contr.Nucl.Fus. Res., IAEA-CN-50/A-V-2.1, Nice, October 1988.

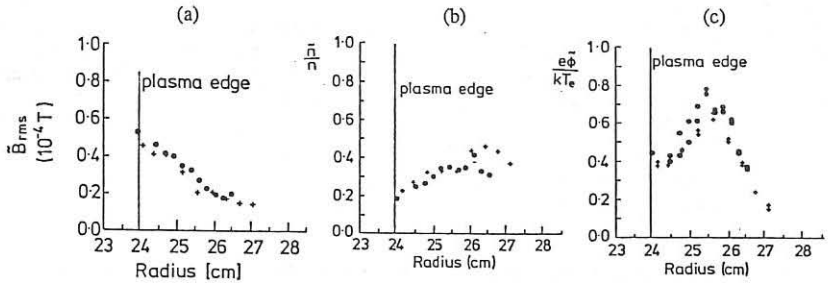

Fig.1 : Radial profiles in the SOL of (a) $\widetilde{B}_r$, (b) $\widetilde{n}/n$, (c) $e\widetilde{\Phi}/kT_e$ (shot 34553).

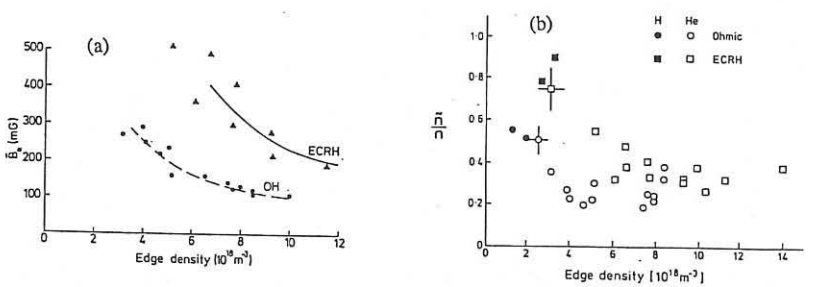

Fig.2: Magnetic field (a) and normalized density (b) fluctuations vs. edge density in ohmic and ECRH regimes.

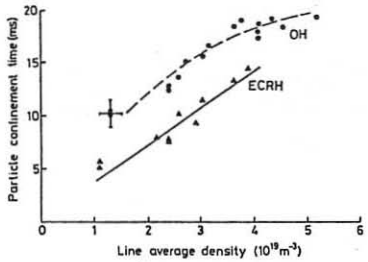

Fig.3: Particle confinement time vs. density in ohmic and ECRH regimes.

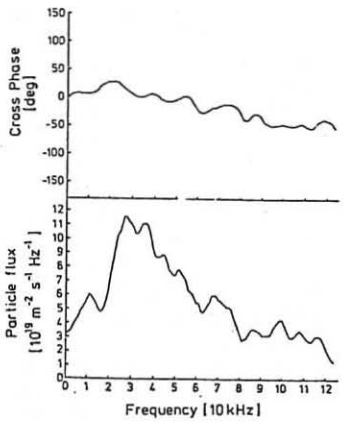

Fig.4: Measured phase between electric field and density fluctuations and associated particle flux spectrum (shot 34337).

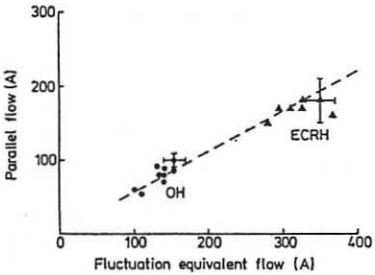

Fig.5: Comparison between total parallel flow to the limiters and fluctuation induced cross-field flux in ohmic and ECRH regimes.

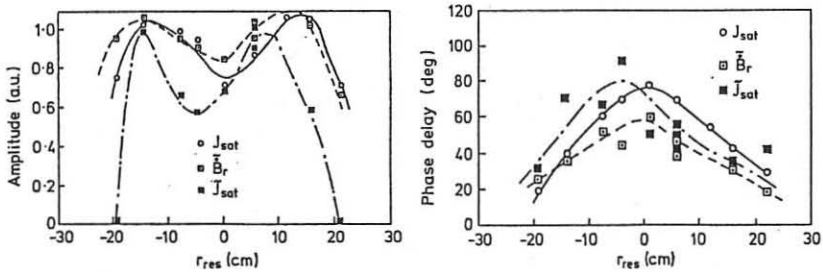

Fig.6: Amplitude and phase with respect to EC power of the stationary ion saturation current, fluctuating radial magnetic field and fluctuating ion saturation current as a function of resonance position.

RECYCLING OF H,D, AND He-ATOMS AT STEEL AND CARBON LIMITERS

P. Bogen, D. Rusbüldt and U. Samm
Institut für Plasmaphysik der Kernforschungsanlage Jülich GmbH,
Ass. EURATOM-KFA, D-5170 Jülich, Germany

Abstract

In the TEXTOR tokamak, the Doppler broadening of spectral lines, emitted by the recycling atoms in front of a limiter, have been measured to derive the distribution of their radial velocity component. When the carbon limiter is replaced by a steel limiter, the line profile changes in accord with the increased particle reflection coefficient of steel.

Introduction

Ions hitting the limiter are normally neutralized and then either directly reflected with a fraction of their incoming ion energy or they are first adsorbed and, at a later time, desorbed with low energies. By observation of the Doppler broadened H- and He-line profiles, the relative contribution of reflected and desorbed particles has been estimated /1, 2/. In the first experiments, a test limiter made of steel has been used. The experiments described here had the aim to study the influence of the test limiter materials on the velocity distribution. Steel and carbon limiters have been investigated, since they have particle- and energy-reflection coefficients, which are considerably different /3/.

Principles

Ions arriving at the limiter gain energy in addition to their thermal value by the acceleration in the plasma sheath potential, which is approximately given by

$$U = (kT_e/e)\ \ln(4\pi\, m_e/m_i)^{1/2} \qquad (1)$$

More refined models /4/ give for the total ion energy about 9 kT_e for He^{++} ions in a helium plasma and 4.8 kT_e for H^+ ions in a hydrogen plasma. With T_e = 20 eV, ion energies in the range of 100 eV are expected.

In comparing the reflection of light ions from graphite and steel, simple arguments from collision theory may give some guidance for the interpretation. In a collision with a 180° scattering angle, the maximum energy change ΔE is

$$\Delta E/E = 1 - \{(m_1 - m_2)/(m_1 + m_2)\}^2 \qquad (2)$$

In this case, He-ions loose 75 % of their energy by a collision with a C-atom, but H-ions loose only 7 % by a collision with a Fe-atom.

Particle reflection coefficients are often discussed by comparing values of different elements at the same Thomas-Fermi energy ε, which is related to the energy E by /3/

$$\varepsilon/E = \frac{m_2}{m_1 + m_2}\, 0.032/Z_1 Z_2 \left(Z_1^{2/3} + Z_2^{2/3}\right)^{1/2} \qquad (3)$$

where m_1, Z_1 and m_2, Z_2 are the masses and nuclear charges of the incoming and the target atoms, respectively.

From eq. (3) follows, that the energy of the light ions in Thomas-Fermi units is about a factor of five higher for a collision with C-atoms than for a collision with Fe-atoms. Since the reflection coefficient decreases with increasing ε, it follows, that the reflection coefficient of carbon is considerably lower.

Experimental

TEXTOR shots with 340 kA plasma current, 2 T toroidal field and various mean electron densities n_e have been investigated. The experimental set-up for the limiter observation has already been described in reference /2/. The H- and the He- (6678 Å) line profiles have been observed in radial direction, the spectral resolution was better than 0.2 Å. Light reflected by the limiter surface has been eliminated by a light dump consisting of a triangular groove in the limiter (see fig. 1).

For a quantitative comparison of the profiles observed with steel and graphite limiter, the profiles have either been normalized to equal peaks or to equal integrals $\int J_\lambda d\lambda$ corresponding to a normalization of $\int f(v_r)dv_r$ (v_r = radial velocity). In the case of the hydrogen isotopes, the proportionality between J_λ and $f(v_r)$ is somewhat perturbed by molecular H_α-emission due to dissociative excitation of H_2 and H_2^+ /1/.

Results

In fig. 2, the profiles of the He-line 6678.15 Å observed in front of a steel or a graphite limiter are shown. The profiles are normalized to equal integrals $\int J_\lambda d\lambda$. With the measured T_e = 17 eV, the profiles observed with steel limiter extend to more than 100 eV whereas the profile observed with the graphite limiter extends only to about 1/3 of this value in accord with eq. 2.

It is obviously difficult, to set an exact limit in fig. 2 for a classification into desorbed and reflected particles. As a first step, we take the peak height to compare the number of desorbed atoms. Assuming for the Fe-limiter 50 % desorbed and 50 % reflected He-atoms, we then obtain 70 % desorbed and 30 % reflected He-atoms for the C-limiter, a result in accord with code calculations /3/.

With increasing n_e (see fig. 3), the number of reflected atoms increases. This result, already shown in /2/ for a steel limiter, is a consequence of the reduction of T_e in the plasma edge. At reduced energy, the particle reflection coefficient increases.

Results from H_2 and D_2 discharges are shown in fig. 4 and 5. In contrast to the He-line, the H_α-line extends to wavelengths corresponding to rather high energies also with C-limiter, although somewhat less than with Fe-limiter. The line wings are less intensive with C-limiter than with Fe-limiter as expected.

In the case of the hydrogen isotopes, the line wings are not only emitted by reflected particles, but also by fast charge exchange particles. The strong reduction of the wing intensity, when the steel is exchanged by a graphite limiter, already indicates that the contribution of charge exchange particles is not high. This is confirmed by Monte-Carlo calculations using a 1-D code. Fig. 6 shows a computed H_α-profile for the case that only H_2-molecules leave the limiter. Only a low wing intensity from charge exchange is indicated. A comparison with the measured profile implies that more than 33 % of the incoming ions are reflected in the atomic state.

Bibliography

/1/ U. Samm et al., J. Nucl. Mater. (1989) in press
/2/ P. Bogen, D. Rusbüldt and U. Samm, J. Nucl. Mater. (1989) in press
/3/ R. Behrisch and W. Eckstein, p. 413 ff in:
Physics of plasma-wall interactions in controlled fusion" ed. by D.E. Post and R. Behrisch, Plenum Press, New York, 1986
/4/ G. Emmert et al. Phys. Fluids 23, 803 (1980)

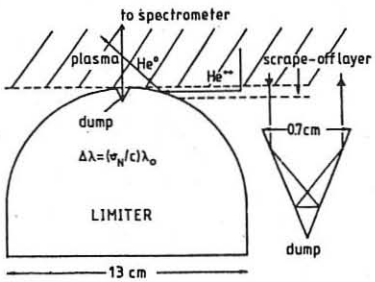

Fig. 1: Experimental arrangement

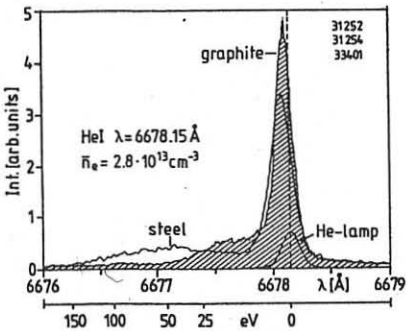

Fig. 2: He-line profiles with graphite- and steel-limiter

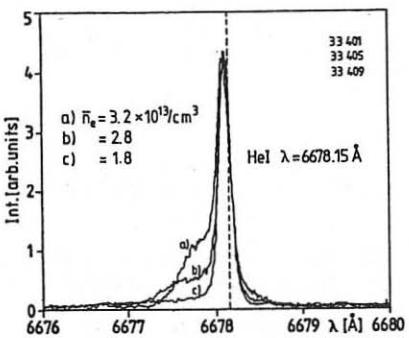

Fig. 3: He-line profiles with graphite limiter at different $\bar{n}_e$

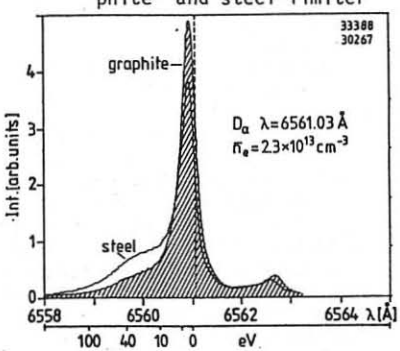

Fig. 4: D_α-profile with graphite- and steel-limiter

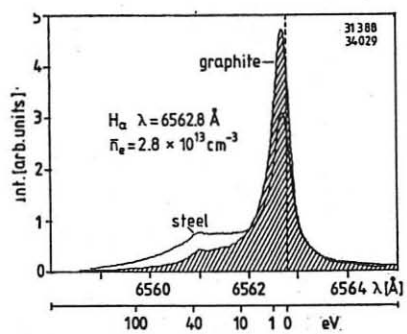

Fig. 5: H_α-profile with graphite- and steel-limiter

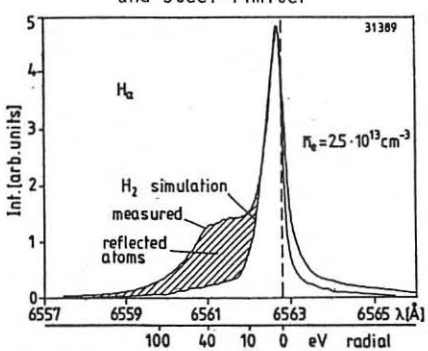

Fig. 6: Calculated and experimental H_α-profiles

2D TRANSPORT THEORY FOR TRACE IMPURITIES IN A HYDROGEN SCRAPE-OFF PLASMA FLOW AND ITS APPLICATION IN THE COLLISION-DOMINATED LIMIT

H.A. Claaßen, H. Gerhauser, D. Reiter

Institut für Plasmaphysik, Kernforschungsanlage Jülich GmbH,
Association EURATOM-KFA, P.O. Box 1913, D-5170 Jülich, FRG

The starting point is the kinetic equation (in cylindrical geometry)

$$\left.\frac{\partial a}{\partial t}\right|_{\vec{x},v_\parallel} - \frac{1}{\rho}\left.\frac{\partial}{\partial \rho}\left(\rho D_\perp \frac{\partial a}{\partial \rho}\right)\right|_{\zeta,v_\parallel,t} + v_\parallel \left.\frac{\partial a}{\partial \zeta}\right|_{\zeta,v_\parallel,t} + \left.\frac{ZeE_\parallel}{M}\frac{\partial a}{\partial v_\parallel}\right|_{\rho,v_\parallel,t} = \left.\frac{\partial_s a}{\partial t}\right|_{\vec{x},t} + Q(\vec{x},v_\parallel,t) - \nu_I a$$

for the distribution function $a(\vec{x}, v_\parallel, t) = 2\pi \int_0^{+\infty} dv_\perp v_\perp \bar{f}(\vec{x}, v_\parallel, v_\perp, t)$

where $\bar{f}(\vec{x}, v_\parallel, v_\perp, t)$ is the guiding-centre distribution function of impurity ions with charge Ze and mass M. The vector $\vec{x}$ stands for (ρ,ζ).

$$D_\perp = \int_{-\infty}^{t} d\tau \left\langle \vec{\varepsilon}\,[\vec{x}, v_\parallel, t] \cdot \vec{\varepsilon}\,[\vec{x}(\tau), v_\parallel(\tau), \tau] \right\rangle / B^2[\vec{x}(\tau)]$$

is the cross-field (Bohm-like) diffusion coefficient due to low frequency long wavelength electromagnetic field fluctuations $\delta\vec{e}$, $\delta\vec{b}$ producing the effective electric field $\vec{\varepsilon} = \delta\vec{e} \times \vec{B}/B + v_\parallel \delta\vec{b}$ (assuming $\vec{B}\cdot\delta\vec{e} = 0 = \vec{B}\cdot\delta\vec{b}$, $|1/\partial \ln a/\partial t| \gg$ correlation time $\gg 1/\Omega$, $|1/\partial \ln a/\partial\zeta| \gg$ correlation length $\gg v_T/\Omega$ with $\Omega = ZeB/M$, and neglecting cross-correlations between the different vector components of $\vec{\varepsilon}$). The integration is performed along the unperturbed ion motion along the magnetic field $\vec{B}$ and $\langle \ldots \rangle$ denotes a time average with respect to the fluctuations /1/.

The rhs of the kinetic equation describes Coulomb collisions with the hydrogen ions and electrons (which are involved in the thermodiffusion effect) as well as electron impact ionization, recombination, and charge-exchange. The latter give rise to the source and loss terms Q and $-\nu_I a$ coupling neighbouring ionization levels. The Fokker-Planck operator

$$\left.\frac{\partial_s a}{\partial t}\right|_{\vec{x},t} = \nu_C \left(v_T^2 \frac{\partial^2 a}{\partial v_\parallel^2} + \left[\alpha\,(v_\parallel - V_\parallel) - \beta v_T\right] \frac{\partial a}{\partial v_\parallel} + \alpha\, a \right)$$

describes the Brownian motion of the impurity ions in a hydrogen plasma having electron and ion temperatures $T_{e,i}$ and a centre-of-mass velocity $\simeq V_{\parallel i}$ along $\vec{B}$. The operator is formulated in a reference frame moving with the convection velocity $V_\parallel$ of the impurity ions under consideration. This form is adequate for all situations, in which $v_T \ll v_{Ti}$ (the thermal velocity of the hydrogen ions) and applies in particular to the case $V_\parallel \simeq V_{\parallel i} = 0\ (v_{Ti})$.

The collision coefficients α and β are integrals over the hydrogen ion (respectively electron) distribution function /2/ to be formulated here in a reference frame moving with $V_\parallel$. In case of a weakly disturbed Maxwel-

lian f_i^{sM} shifted with respect to the ion flow velocity $V_{\parallel i}$ we have

$$f_i = f_i^{sM}\,(1 + \Psi_i) \quad \text{with} \quad |\Psi_i| \ll 1.$$

We set $$\Psi_i \sim \frac{4}{5}\,\frac{(v_{\parallel i} - V_{\parallel i})}{p_i v_{Ti}^2}\left(h_{\parallel i}(c_i^2 - \frac{5}{2}) + \frac{2}{7}\,\frac{r_{\parallel i}}{v_{Ti}^2}\,(c_i^4 - 7c_i^2 + \frac{35}{4})\right)$$

with $$c_i^2 \equiv \frac{(v_{\parallel i} - V_{\parallel i})^2 + v_{\perp i}^2}{v_{Ti}^2} \quad \text{and} \quad \frac{\left|h_{\parallel i},\, r_{\parallel i}/v_{Ti}^2\right|}{p_i v_{Ti}} \ll 1$$

corresponding to the first two nonvanishing vector terms ($\sim \vec{v}_i - \vec{V}_i$) in Grad's Hermite polynomial expansion /3/ yielding the same accuracy in the longitudinal diffusion and heat transfer coefficients as Braginski's Sonine polynomial expansion /4/. $h_{\parallel i}$ is the heat flux along $\vec{B}$. With $r_{\parallel i} = 0$ we recover Grad's 13 moment approximation. A shifted Maxwellian form of f_i generally leads to complicated expressions for α and β. It is only on the condition $|V_{\parallel i} - V_{\parallel}|/v_{Ti} \ll 1$ that α and β can be simplified by

$$\alpha = \frac{2T}{T_i} \quad \text{and} \quad \beta = 2\sqrt{\frac{M\,T}{m_i T_i}}\left(\frac{V_{\parallel i} - V_{\parallel}}{v_{Ti}} - \frac{3}{5}\,\frac{h_{\parallel i}}{p_i v_{Ti}} + \frac{3}{7}\,\frac{r_{\parallel i}}{p_i v_{Ti}^3}\right)$$

These formulae apply in particular to regions far from a limiter or divertor target (where $|V_{\parallel i}| \ll v_{Ti}$ and only wall sources are relevant) and to higher charge states in the near target region (where $|V_{\parallel i} - V_{\parallel}|/v_{Ti} \ll 1$ is possible in spite of $|V_{\parallel i}/v_{Ti}| \leq 1$).

Inserting these formulae into the collisional momentum transfer term we have

$$\int_{-\infty}^{+\infty} dv_{\parallel} v_{\parallel} \left(\frac{\partial_s a}{\partial \tau}\right)_{\parallel}^{\vec{x},t} = \alpha \nu_C (n V_{\parallel i} - \Gamma_{\parallel}) - \frac{3}{5}\,\alpha \nu_C\,\frac{n}{p_i}\left(h_{\parallel i} - \frac{5}{7}\,\frac{r_{\parallel i}}{v_{Ti}^2}\right)$$

where $$-\frac{3}{5}\,\alpha \nu_C\Big|_{zi}\,\frac{n}{p_i}\left(h_{\parallel i} - \frac{5}{7}\,\frac{r_{\parallel i}}{v_{Ti}^2}\right) \simeq 2.21\,\frac{nZ^2}{M}\,\frac{\partial\,(kT_i)}{\partial \zeta}$$

describes the thermodiffusion effect due to a hydrogen ion temperature gradient $\parallel \vec{B}$. The thermodiffusion coefficient given here has the same accuracy as Braginski's formula for the longitudinal heat conductivity of the ions. For $r_{\parallel i} = 0$ the factor $15/8\sqrt{2}$ (2.65 instead of 2.21) is obtained, which is identical to that given by Chapman /5/ when going to the limit $m_i/M \to 0$. In an analogous way we arrive at the thermodiffusion flux

$$-\frac{3}{5}\,\alpha \nu_C\Big|_{ze}\,\frac{n}{p_e}\left(h_{\parallel e} - \frac{5}{7}\,\frac{r_{\parallel e}}{v_{Te}^2}\right) \simeq 0.71\,\frac{nZ^2}{M}\,\frac{\partial\,(kT_e)}{\partial \zeta}$$

due to an electron temperature gradient $\parallel \vec{B}$. Here the factor 0.71 arises instead of 0.80 for $r_{\parallel e} = 0$.

The kinetic equation for $a\,(\vec{x}, v_{\parallel}, t)$ is difficult to solve exactly. An approximate solution can be constructed by a moment method. The crucial step is the choice of appropriate basis functions to form the moment equations. In the present case we expand $a\,(\vec{x}, v_{\parallel}, t)$ into eigenfunctions of

the operator

$$v_{\parallel} \left.\frac{\partial}{\partial \zeta}\right|_{\rho, v_{\parallel}, t} - c_{\parallel} \left.\frac{\partial}{\partial \zeta}\right|_{\rho, c_{\parallel}, t} - \left(\left.\frac{\partial_s}{\partial \tau_{\parallel}}\right|_{\vec{x},t} - \frac{ZeE_{\parallel}}{M} \left.\frac{\partial}{\partial v_{\parallel}}\right|_{\vec{x},t} \right), \quad c_{\parallel} = v_{\parallel} - V_{\parallel}$$

separating the convection term $c_{\parallel} (\partial/\partial\zeta)_{c_{\parallel}}$ with respect to the reference frame moving with $V_{\parallel}$. The hope is that the series expansion rapidly converges in this reference frame so that only the lowest order expansion coefficients are needed to get a sufficiently accurate solution. The expansion coefficients are calculated from a set of moment equations, which result from substitution of the series expansions into the kinetic equation. In particular we set

$$\begin{pmatrix} a \\ Q \end{pmatrix} (\vec{x}, v_{\parallel}, t) = \sum_{m=0}^{\infty} \begin{pmatrix} A_m \\ Q_m \end{pmatrix} (\vec{x}, t) \frac{\chi^{m+1}}{\sqrt{\pi}} H_m(\xi) \exp(-\xi^2)$$

where $H_m(\xi)$ are Hermite polynomials in the variable $\xi = \chi (v_{\parallel} - V_{\parallel})$ depending on the charge state z. The convection velocity $V_{\parallel}$ and the distribution coefficient χ can be found from the auxiliary conditions

$$V_{\parallel} \frac{\partial V_{\parallel}}{\partial \zeta} = \beta \nu_C v_T + \frac{ZeE_{\parallel}}{M} \quad \text{and} \quad \frac{1}{\chi} \frac{\partial \chi}{\partial \zeta} = \frac{2\nu_C v_T^2}{V_{\parallel}} \left(\frac{\alpha}{2v_T^2} - \chi^2 \right) + \frac{1}{V_{\parallel}} \frac{\partial V_{\parallel}}{\partial \zeta}$$

for the existence of the eigenvalue equation

$$\left(-v_{\parallel} \left.\frac{\partial}{\partial \zeta}\right|_{\rho, v_{\parallel}, t} + c_{\parallel} \left.\frac{\partial}{\partial \zeta}\right|_{\rho, c_{\parallel}, t} + \left.\frac{\partial_s}{\partial \tau_{\parallel}}\right|_{\vec{x},t} - \frac{ZeE_{\parallel}}{M} \left.\frac{\partial}{\partial v_{\parallel}}\right|_{\vec{x},t} + \lambda_m \nu_C \right) \chi^{m+1} H_m(\xi) \exp(-\xi^2) = 0$$

with the eigenvalues $\lambda_m \nu_C = m \alpha \nu_C + (m+1) \dfrac{\partial V_{\parallel}}{\partial \zeta}$

presupposing that the hydrogen plasma parameters are stationary. The coefficient χ can be found from the integral representation

$$\frac{1}{\chi^2(\zeta)} = \frac{1}{\chi^2(0)} \exp\left(-2 \int_0^{\zeta} F(\tau)\, d\tau \right) + \int_0^{\zeta} G(\eta) \exp\left(-2 \int_0^{\zeta} F(\tau)\, d\tau \right) d\eta$$

with $$F(\zeta) = \frac{\partial \ln V_{\parallel}}{\partial \zeta} + \frac{\alpha \nu_C}{V_{\parallel}} \quad \text{and} \quad G(\zeta) = \frac{4kT_i}{M} \frac{\alpha \nu_C}{V_{\parallel}}$$

For $\dfrac{\partial \chi}{\partial \zeta}(0) = 0$ we have $\chi^2(0) = \left(1 + \dfrac{1}{\alpha \nu_C} \dfrac{\partial V_{\parallel}}{\partial \zeta} \right) / (2kT_i/M) \Big|_{\zeta = 0}$

$\chi(\zeta)$ can be evaluated once $V_{\parallel}(\zeta)$ is known. Unfortunately, the differential equation for $V_{\parallel}$ does not have a general analytical solution and has to be solved numerically for arbitrary hydrogen plasma profiles along $\vec{B}$. There are two simple cases, where $V_{\parallel}$ can be given analytically: a) For plasma parameters being constant along $\vec{B}$ we have $V_{\parallel} = V_{\parallel i} + ZeE_{\parallel}/M\alpha\nu_C$ and $\chi^2 = M/2kT_i$. b) For a linear variation $V_{\parallel i} = V_i \zeta$ and $E_{\parallel} = E \zeta$ we have $V_{\parallel} = V \zeta$ and $\chi^2 = \beta/2v_T$ with $V = (1/2)\, \alpha\nu_C(-1 + \sqrt{1+4\beta\, v_T/\alpha^2 \nu_C})$ and $\beta = (\alpha\nu_C V_i + ZeE/M)/v_T \nu_C$ in agreement with the formulae in ref. /2/. With the knowledge of $\chi(\zeta)$ and $V_{\parallel}(\zeta)$ the expansion coefficients A_m

can be calculated from the moment equations

$$\frac{\partial A_m}{\partial t} - \frac{1}{\rho}\frac{\partial}{\partial \rho}\left(\rho D_\perp \frac{\partial A_m}{\partial \rho}\right) + V_\parallel \frac{\partial A_m}{\partial \zeta} + (\nu_I + \lambda_m \nu_C) A_m = Q_m - (m+1)\frac{\partial A_{m+1}}{\partial \zeta} + R_m$$

with the recursion term (δ_{mr} being Kronecker symbols)

$$R_m = (1 - \delta_{mo})\left(\sqrt{\frac{\Lambda_v}{\rho}}\frac{\partial}{\partial \rho}\left(A_{m-1}\sqrt{\rho\,\Lambda_v}\right) - \chi^{m-1}\frac{\partial}{\partial \zeta}\left(\frac{A_{m+1}}{2\chi^{m+1}}\right)\right) +$$

$$+ (1 - \sum_{r=o}^{1}\delta_{mr})\left(-\sqrt{\frac{\Lambda_\chi}{\rho}}\frac{\partial}{\partial \rho}\left(A_{m-2}\sqrt{\rho\Lambda_\chi}\right) + \frac{\Lambda_v^2}{4D_\perp}A_{m-2}\right) +$$

$$+ (1 - \sum_{r=o}^{2}\delta_{mr})\,\Lambda_{\chi v}\,A_{m-3} + (1 - \sum_{r=o}^{3}\delta_{mr})\frac{\Lambda_\chi^2}{4D_\perp}A_{m-4}$$

where $\Lambda_\chi \equiv \frac{D_\perp}{\chi^3}\frac{\partial \chi}{\partial \rho}$, $\Lambda_v \equiv 2D_\perp \frac{\partial V_\parallel}{\partial \rho}$ and $\Lambda_{\chi v} \equiv \frac{1}{\chi^3}\left(\frac{1}{4\chi^2}\frac{\partial \chi}{\partial \zeta} - D_\perp \frac{\partial \chi}{\partial \rho}\frac{\partial V_\parallel}{\partial \rho}\right)$

Truncating (in a collision-dominated situation) the transport hierarchy at m=1 and setting $A_2 = 0$ we have

$$\frac{\partial A_o}{\partial t} - \frac{1}{\rho}\frac{\partial}{\partial \rho}\left(\rho D_\perp \frac{\partial A_o}{\partial \rho}\right) + \frac{\partial}{\partial \zeta}(V_\parallel A_o + A_1) = Q_o - \nu_I A_o$$

$$(\nu_I + \lambda_1 \nu_C) A_1 = Q_1 + \sqrt{\frac{\Lambda_v}{\rho}}\frac{\partial}{\partial \rho}\left(A_o\sqrt{\rho\Lambda_v}\right) - \frac{\partial}{\partial \zeta}\left(\frac{A_o}{2\chi^2}\right)$$

A_o, $V_\parallel A_o$ and A_1 denote, respectively, the density as well as the convective and diffusive part of the parallel particle flux $\Gamma_\parallel$. $MA_o/2\chi^2$ is (for $A_2 = 0$) the impurity ion pressure due to the thermal motion $\sigma_{\parallel B}$.

The above couple of transport equations is closed by the auxiliary conditions for $V_\parallel$ and χ and yields to first order approximation the density distribution of trace impurities in a streaming hydrogen plasma background. The decisive difference between our procedure and that commonly used (see, for instance, ref. /6/) is the splitting of the centre-of-mass velocity into a convective and a diffusive part, the former being independently calculated from one of the auxiliary conditions, which can be readily solved for simple plasma profiles. The outlined transport theory is presently applied to the numerical computation of 2d density and line radiation profiles of C^{z+} in a hydrogen scrape-off plasma, using a Monte-Carlo calculation of the C^+ sources.

/1/ A.V. Gurevich et al., Nuclear Fusion 27 (3), 453 (1987).
/2/ H.A. Claaßen, H. Repp, Nuclear Fusion 21 (5), 589 (1981).
/3/ H. Grad, J. Pure & Appl. Math. 2, 324 (1949), Phys. Fluids 6, 147 (1963); V.M. Zhdanov, P.N. Yushmanov, ZPMT 4, 24 (1980)
/4/ S.I. Braginski, Reviews of Plasma Physics 1, 205 (1965).
/5/ S. Chapman, Proc. Phys. Soc. 72, 353 (1958).
/6/ J. Neuhauser et al., Rpt. IPP 1/216 (1983).

POWER DEPOSITION ON TOROIDAL LIMITERS IN TEXTOR

J.G. Watkins[1], K.H. Finken[2], K.H. Dippel[2], R.T. McGrath[1], R. Moyer[3], the NI Team[2], and the TEXTOR Team[2]

[1] Sandia National Laboratories, Albuquerque, NM, USA
[2] Kernforschungsanlage Jülich GmBH, Association KFA -Euratom
[3] University of California, Los Angeles, USA

Abstract

Power deposition measurements have been carried out on the ALT-II toroidal belt pump limiter and the inner bumper limiter in TEXTOR for Ohmic, neutral beam and RF heated discharges. Two infrared cameras and the ALT-II thermocouple array indicate that λ_E remains unchanged (7 mm) in the presence of beams but increases to 10 mm with ICRH. The heating distribution is less uniform on the bumper limiter than on ALT-II, which explains the differences seen in graphite surface pumping.

TEXTOR has two toroidal graphite limiter systems: the ALT-II toroidal belt pump limiter system (45° below the outer midplane) and the inner wall bumper limiter. Through the use of two infrared cameras and the thermocouple array on ALT-II, measurements of the power deposition on these limiters have been performed. The thermocouple array allows a toroidal extrapolation of the more detailed surface deposition pattern obtained with the infrared systems for the ALT-II belt. The bumper limiter power deposition is observed over a representative selection of tiles at two toroidal locations. These measurements have been carried out for Ohmic, RF and NBI heated discharges with up to 2.8 MW of auxiliary heating power. Typical TEXTOR parameters for these experiments are given in table I.

Table I.

R = 1750 mm	V_{loop} (OH/NBI) = 1.2/0.7 V
a = 450 mm	P_{OH} = 500 kW
B_T = 2.0 T	P_{NBI} = 2.4 MW
n_o = 1 - 5 x 10^{19} m^{-3}	P_{RF} = 2.8 MW
I_p = 340 kA	

For Ohmic discharges up to 500kW, the power deposited on the ALT-II belt limiter varies from a few percent up to 50%. The distribution of power over the 8 adjustable limiter blade segments can be made very uniform (±5%). The highest limiter power deposition occurs for low density (~1 x 10^{19} m^{-3}) and low Z_{eff} (fresh carbonisation or boronisation). This is consistent with theoretical predictions [1]. The power scrape-off length (λ_E) is determined from the IR data through a two dimensional thermal model using 2DPEP [2] and verified with a 3D thermal model using PATRAN and ABAQUS. The typical Ohmic value of 7 mm is consistent with other boundary measurements such as from the scanning double Langmuir probe [3].

For the case of auxilliary heating with co, counter and combined neutral beam injection, λ_E remains unchanged (7 mm), although the fraction of power seen on the limiter was observed to be as high as 70%. The higher fraction is consistent with lower radiation levels. The measurement of λ_E is again consistent with boundary measurements of n_i, T_e, and Γ_i from the scanning probe. A comparison between Ohmic and NBI surface temperature measurements is seen in figure 1. In the case of RF heating, λ_E increases to 10 mm.

For the inner bumper limiter, the power deposition is much less uniform. Although carefully aligned to within 0.5 mm during installation, strong edge heating of about 20% of the observed tiles occurs during plasma operation. A typical infrared pattern is shown in figure 2. The pattern we predict with our 3DHF code for a perfectly aligned IBL panel in a magnetic field with a 7 mm power scrape-off is shown in figure 3. This pattern shows nonuniformity in the heat flux deposition because of 1) the toroidal flatness of each IBL panel and 2) the plasma minor radius is smaller than the design radius. With a 2 mm misalignment on one edge of the panel, the predicted heat flux maximum is more than 6 times higher.

The edge heating effect we observe is due to small misalignments and tends to explain the enhancement in surface pumping of the graphite on the inner bumper limiter over that of ALT-II. These observations are similar to wall pumping behavior on JET [4]. The maximum surface temperature rise during a plasma discharge is more than 2.5 times higher on the inner bumper limiter. This leads to a lower hydrogen saturation level [5] on the graphite surface at the end of a discharge and leaves the surface somewhat depleted at the beginning of the next discharge. In our case, the surface pumping effect saturates quickly (< 1 second) which is consistent with the surface depletion explanation. Another effect, codeposition[6], is also enhanced by localization of the surface heat flux and may be occurring here but this effect does not saturate and may be more important for explaining the JET results.

References

1) J. Lingertat et.al., Plasma Phys. Vol. 29, 10A, 1365 (1987)
2) K.H. Finken et.al., Proc. of the 8th Int. Conf. on Plasma Surface Interactions in Controlled Fusion Devices, Jülich, FRG (1988).
3) R. Moyer et.al., this conference.
4) S. Cohen et.al., Plasma Phys. Vol. 29, 10A, 1205 (1987)
5) R. Causey, Proc. of the 8th Int. Conf. on Plasma Surface Interactions in Controlled Fusion Devices, Jülich, FRG (1988)
6) W. Hsu, R. Causey, J. Vac. Sci. and Technol. A5 (6) (1987)

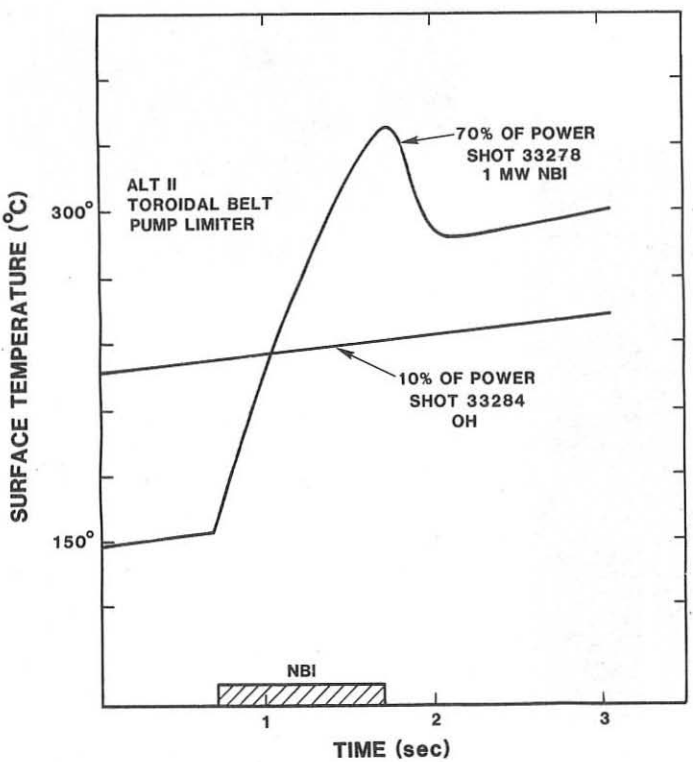

Figure 1

Figure 2

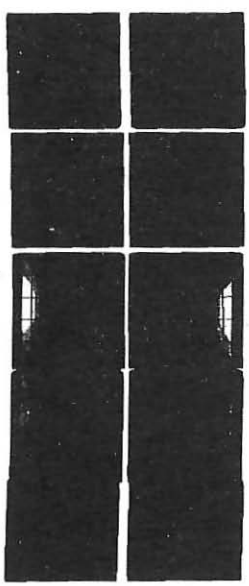

Figure 3

Figure 2 (above) is an infrared view of the inner bumper limiter. One can see two panels and part of a third. This is a total of about 27 tiles.

Figure 3 (left) is a computer generated view of a single inner bumper limiter panel. Heat flux is applied with a magnetic field model using a 7 mm scrape-off length for the power. The highest heat flux predicted for the Ohmic case (when everything is properly aligned) is 55 W/sq.cm.

FIRST RESULTS FROM LYMAN-ALPHA FLUORESCENCE MEASUREMENTS IN THE PLASMA BOUNDARY OF A TOKAMAK

Ph. Mertens, P. Bogen

Institut für Plasmaphysik, Assoc. Euratom-KFA Jülich, D-5170 JÜLICH

Abstract: A laser-induced fluorescence experiment in the vacuum UV has been set up to measure the atomic density and velocity distribution of deuterium in the plasma boundary of a tokamak. A dye laser has been used, the frequency of which has been tripled in a phase matched gas mixture (krypton-argon). Signal to noise ratios better than 30 have been obtained at L_α. This allows the determination of the energy distributions in the few eV range. The resulting profiles correspond to atomic energies which indicate that molecular dissociation processes are involved in the first place.

Introduction

The knowledge of the densities and fluxes of neutral particles in the plasma boundary of a fusion device is very important for the understanding of the physical processes underlying the recycling phenomena. So much the more so when it comes to the hydrogen and its isotopes. So far, detailed information on the density and velocity distribution of atomic hydrogen near the wall of a tokamak has been mainly collected from spectroscopic data of the H_α-line. This method has a number of drawbacks: the intensities are integrated over the line of sight, the excitation is caused by electron impact on atoms and molecules (dissociative excitation), the evaluation of fluxes requires an estimate of T_e and n_e and the application of a complicated collisional-radiative excitation model.

Some of these drawbacks can be avoided by measuring hydrogen densities and velocity distributions with L_α-fluorescence. By this method, only H-atoms in the n=1 state are excited. Velocities are deduced from the Doppler-broadening of the line profiles; densities, on the other side, can be obtained from spectrally integrated fluorescence intensities. First experiments were carried out on the tokamak TEXTOR to explore the applicability of this method in the fusion research.

Principle

The observed fluorescence volume in our scheme is illuminated by the frequency tripled radiation of a pulsed dye laser. In contrast to most laser-induced fluorescence experiments in the visible or near UV, the spectral power density of the available L_α-radiation doesn't excite the atoms to be detected up to the saturation level, i.e. induced emission effects can be neglected. The fluorescence signal is then not only proportional to

the atomic density, but also to the incident third harmonic power. The cross-section relevant to this process (resonant excitation of the fluorescence) is given by /1/

$$\sigma_F = \frac{1}{4\pi\varepsilon_0} \frac{e^2}{mc^2} \pi \lambda_0^2 \; f \; L(\lambda-\lambda_0)$$

where λ_0 is the wavelength of the atom at rest, f the oscillator strength and $L(\lambda-\lambda_0)$ the normalized line shape function. The broadened profiles allow an estimation of the atomic velocities from the wavelength shift by means of the Doppler relation :

$$\lambda-\lambda_0 = v\,\lambda_0/c$$

The influence of the magnetic field has been eliminated by polarizing the laser to drive only the π-components of the Zeeman triplet. Their splitting of about 0,5 pm is negligible in comparison to the measured line width, which amounts to more than 5 pm.

Experimental arrangement

The experimental apparatus which we have recently described elsewhere /2/ in connection with laboratory experiments was slightly modified to cope with the much longer optical path (ca. 8 m) from the laser system down to the tokamak (fig.1). The main source consists of an excimer-pumped dye laser, the wavelength of which is tuned by tilting the grating or through a pressure variation in the oscillator chamber. The remote

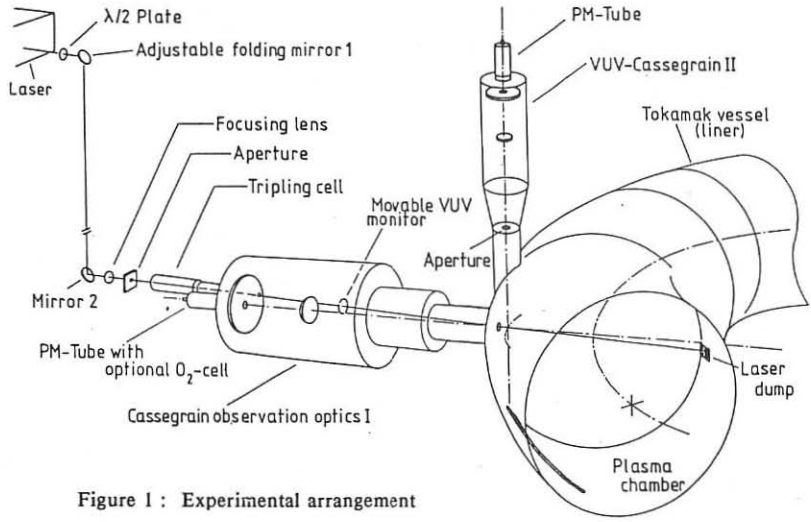

Figure 1 : Experimental arrangement

tripling cell is filled with mixtures of krypton and argon to produce the VUV-radiation at L_α (121.6 nm, 150 W in 4 ns pulses). This VUV-light illuminates a fluorescence volume of about 1.5 cm diameter and about 10 cm length. A Cassegrain system images this fluorescence volume in the plasma boundary to a KBr photomultiplier. A second -similar- telescope is now installed to observe the plasma perpendicularly to the incident laser beam with higher spatial resolution (1 cm). An optional oxygen cell can be used as L_α-filter in front of the multiplier /3/, but it was normally not needed. The fluorescence signals are displayed on a fast digitizer (500 MHz bandwidth); the time-resolved pulses corresponding to the laser shots are stored in sequence by a local computer in synchronisation with the TEXTOR timing system. With a laser repetition rate of 5-10 Hz, this corresponds to about 30 laser shots per plasma discharge.

First results and discussion

Typical fluorescence pulses recorded during the flat top of a tokamak discharge are shown in fig. 2. According to the laser repetition rate, these single pulses are 100 ms apart. The time scale between the vertical markers is expanded to 100 ns in order to show the time-resolved pulses, as an additional clue to their atomic origin. Although the signal to noise ratio exceeds 40 around the maximum of the spectral profile, it of course becomes much worse on the wings. This picture was taken near the line centre, so that the signal reproducibility can also be appreciated, under steady discharge conditions.

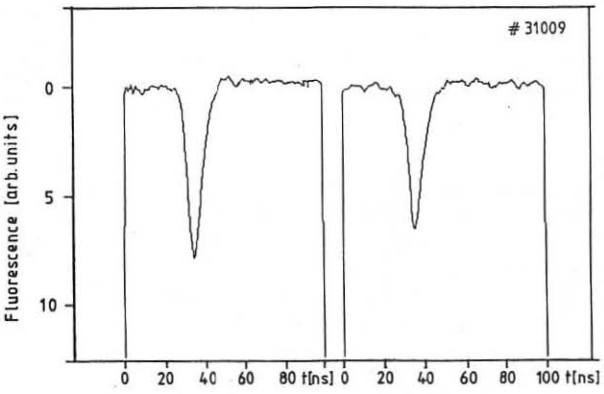

Figure 2. Fluorescence pulses recorded during the flat top of a tokamak discharge (2 laser shots).

The whole sequence of a tokamak shot has been recorded in fig. 3, along with the plasma current, and with the electron density near the centre. In addition to the stable current plateau, the ignition of the discharge shows up through a larger signal. An average value over ten to twelve laser shots can be computed for a given laser wavelength, which isn't modified during the discharge. Spectral scans have been performed this way, by gathering results from different plasma shots. Pressure scanning will be improved in a near future so as to be implemented as a means of getting a similar scan within a single discharge. The resulting spectral profiles look like the one in fig. 4. The indicated error

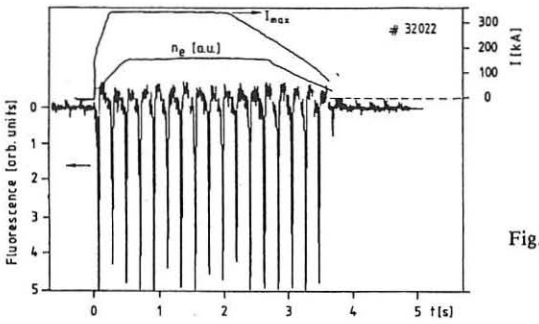

Fig.3 Fluorescence signal during TEXTOR shot # 32022 (laser rep. rate 5 Hz)

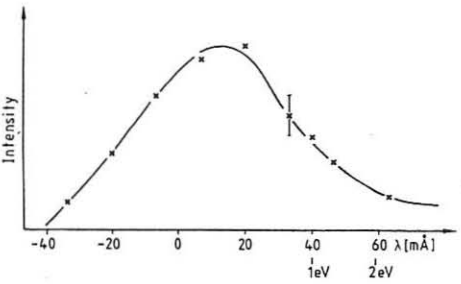

Fig.4 Spectral profile taken over several TEXTOR shots (n_e = 2.4 10^{13} cm^{-3}, I_p = 250 kA)

bar accounts not only for the inaccuracy of the diagnostic, but also for the (larger) unreproducibility of different plasma discharges. The half width of the red wing in this profile (emitted by atoms flowing towards the laser) corresponds to an energy of about 1 eV, indicating a molecular origin, i.e. molecules leaving the wall and being dissociated in the plasma boundary. The line is asymmetrical since atoms flowing into the plasma have a shorter lifetime than those flowing out of it.

Conclusion

In spite of the background radiation, our first attempt to detect atomic deuterium in the boundary of a tokamak with laser-induced fluorescence at L_α has led to satisfying signal to noise ratios, at least in the line centre, corroborating the feasibility of the method. The recorded spectral profiles originate mainly from neutral particles flowing out of the plasma. In the low energy range (a few electron-volts), the profiles indicate that these atoms are the products of dissociated deuterium molecules.

We thank Professor E. Hintz for his strong support and Dr. M. Korten and Mr. B. Becks (from the TEXTOR data acquisition group) for their help in the start-up phase.

/1/ A. Unsöld, *Physik der Sternatmosphären*, Springer (1955)
/2/ Ph. Mertens, P. Bogen, Appl. Phys. **A43**, 197-204 (1987)
/3/ J.A.R. Samson, *Techniques of Vacuum Ultraviolet Spectroscopy*, Wiley (1967)

SPECTROSCOPIC DETERMINATION OF MOLECULAR FLUXES AND THE BREAKUP OF CARBON CONTAINING MOLECULES IN PISCES-A

A.Pospieszczyk[1)], J.Hogan[2)], Y.Ra, Y.Hirooka, R.W.Conn, D.Goebel, B.LaBombard, R.E.Nygren

Institute of Plasma and Fusion Research, UCLA, Los Angeles, USA*
*Work supported by U.S. DOE Contract No. DE-FG03-86ER52134
1) IPP der KFA Jülich GmbH, Association EURATOM-KFA, Fed.Rep.of Germany
2) ORNL, Oak Ridge, Tenneessee, USA

1. Introduction

In present day tokamaks carbon is one of the most widely used materials for limiters and wall coatings. Therefore it is important to know to which extent carbon containing molecules like CH_4 or CO play a role in the fueling and impurity release during a discharge. Emission spectroscopy offers a method to determine the strength and the nature of the molecular particle sources. It can also be used in order to study the breakup processes of the molecular species on their way from the source through the plasma. Unfortunately, there is presently not much information for a plasma with parameters close to that of a tokamak boundary layer concerning observable lines or bands with reasonable intensities, which could be used for absolute flux measurements of the interesting molecules and their radicals in the plasma edge of a tokamak.

2. Experiment and computer model

We have used the PISCES-A facility at UCLA for the production of a representative plasma with parameters close to that of a tokamak boundary layer. Details of PISCES-A operation and its construction can be found in the references /1//2//3/. Steady state plasmas with densities in the range of 10^{11} to 10^{13} cm^{-3} and electron temperatures up to 30 eV are readily achieved. A uniform axial magnetic field constrains a 100 cm length plasma to a cylindrical shape of 6 to 10 cm diameter. Fig.1 shows the experimental set-up schematically.

Carbon containing molecules (CH_4, C_2H_2, C_2H_4, CO, and CO_2) were introduced via a gas injection system through a slit aperture into a helium plasma. A helium plasma was chosen in order to avoid possible interference with molecular band emission from the background gas. The absolute amount of the introduced molecular flux was determined by the upstream pressure, measured by a baratron, and the conductivity of the pipe. For the spectrographic recordings of the emission a camera was attached to an optical spectrometer (1.33m monochromator with a grating of 1200 groves/mm). The plasma was focussed onto the entrance slit in such a way that simultaneous information about spectral and spatial distribution of the emission could be obtained. Spectrograms of each gases were taken for two different plasma conditions: High T_e ($\approx$30 eV), low n_e ($\approx$ 1×10^{12}/ cm^3), and low T_e ($\approx$10 eV), high n_e ($\approx$ $5\times10^{12}/cm^3$) in order to simulate two cases of a tokamak boundary plasma. The discharge parameters were measured by a Langmuir probe in front of the nozzle. A complete spatial scanning of the plasma was also possible by a fast moving probe.

For quantitative results the molecular band intensities were absolutely measured via a PMT and an optical multichannel analyser (OMA) attached to the spectro-

meter. Three plasma temperature regimes were chosen for the experiments: hot (≈30 eV), medium (≈25 eV), and low (≈10 eV).

For a spatial recording of the penetration of the molecules and their radicals through the plasma, the OMA in front of the exit slit was rotated by 90^0. The experimental results for CH_4 are compared with calculations from the ORNL Monte Carlo Code. This code has a 3D geometry, and solves the complete breakup process using rates collated by /4/.

3. Results

Fig.2 shows two representative examples of the spectra obtained. The gas enters the plasma through the nozzle from the bottom. Each spectrogram shows 10 cm of the gas flow through the plasma. Penetration depths of about 2 cm can be qualitatively derived. Fig. 2a (C_2H_2-injection) displays the main features of a hydrocarbon spectrum in the visible spectral range. The bands of CH, CH_2, and C_2 as well as the atomic lines of hydrogen and carbon can be identified. Fig. 2b is an example for a CO-gas injection showing strong CO-bands between 6000 and 6500 Å. These CO-bands and the CH(D), $CH(D)^+$ bands around 4300Å were already seen on TEXTOR spectra from the main limiter /5/ indicating that - beside hydrocarbons - carbonoxides seem to play a mayor role in the transport of carbon and oxygen.

In order to calibrate the intensity of several bands and lines, the number of emitted photons at these wavelengths for known molecular fluxes was measured as a function of electron temperature. The measured ratio of the molecular decay rate to the respective photon intensity is shown in Fig.3a for the CH-band and in Fig.3b for H_α in the case of CH_4. It should be noted that for spectral lines from atoms and ions this ratio is generally a monotonously growing function of T_e in the range between 1eV and 200eV (see e.g./6/). However, in the case of molecules there can be a minimum, which is the result of a necessary dissociation process. A fortunate conclusion of this behavior is that this ratio can then be treated as relatively constant. The boxes in Fig.3a are derived from excitation cross sections measured by /7/ and decay rates from /4/. They agree well with our experimental values. Fig.4 shows the respective rates for CO gas injection. One should note that the CO band emission has to behave like those for atoms.

Fig 5. shows a comparison of the measured penetration depth for CH and hydrogen in the case of CH_4-injection with computer calculated values based on /4/. Considering the tentative nature of the rate coefficients used, the agreement between the model and the experimental data is fairly good. Plasma effects (e.g. the trapping of ions in front of the nozzle), which have been neglected in the calculations, could be the determining factor in the spatial dependence of the ionized species and account for the discrepancies. Therefore similar experiments will be performed in TEXTOR in order to test the validity of these measurements for a real plasma boundary layer.

4. References

/1/ D.M.Goebel, G.A.Campbell, R.W.Conn. J.Nucl.Mat. **121**(1984) 277
/2/ D.M.Goebel, and R.W.Conn, J.Nucl.Mat. **128&129** (1984)249
/3/ D.M.Goebel, Y.Hirooka, T.A.Sketchley, Rev.Sci.Instr. **56**(1985)1717
/4/ A.B.Ehrhardt and W.D.Langer, Report PPPL-2477, Princeton Univ., 1987
/5/ A.Pospieszczyk, H.L.Bay, P.Bogen, H.Hartwig, E.Hintz, L.Könen, G.G.Ross, D.Rusbüldt, U.Samm, and B.Schweer J.Nucl.Mater. **145-147** (1987), 574
/6/ M.F.Stamp, K.H.Behringer, M.J.Forrest, P.D.Morgan, H.P.Summers, Proc. 14th Europ. Conf. Contr. Fus. Plasma Phys., Budapest (Hungary), 1985, Vol.II, 539
/7/ G.R.Möhlmann and F.J.de Heer, Chemical Physics, **19** (1977), 233

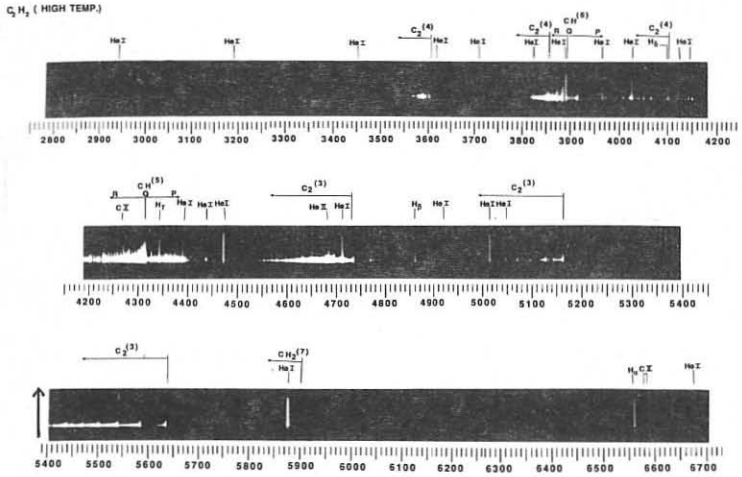

Fig.2a: Spectrum of a discharge with C_2H_2 - injection (T_e = 30 eV)

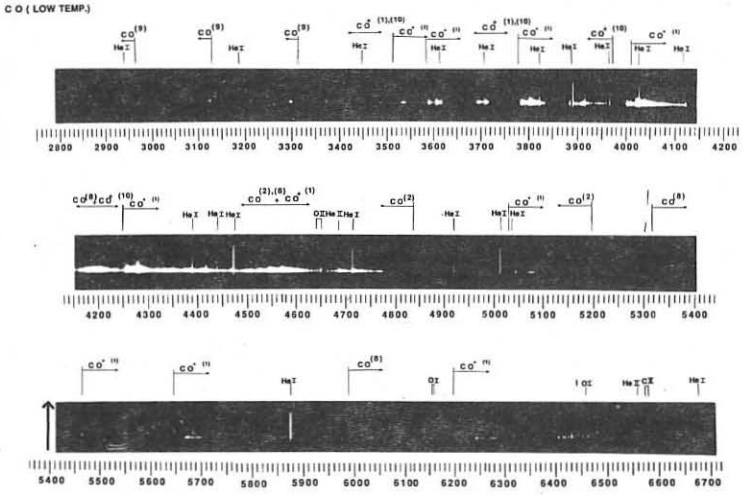

Fig.2b: Spectrum of a discharge with CO - injection (T_e = 10 eV)

Identification table for Fig.2a,b

(1) Comet tail system, $A^2\Pi - X^2\Sigma$
(2) Ångström system, $B^1\Sigma - A^1\Pi$
(3) Swan system, $A^3\Pi_g - X'^3\Pi_u$
(4) Deslandres-d'Azambuja system, $c^1\Pi_g - b^1\Pi_u$
(5) 4300 Å system, $A^2\Delta - X^2\Pi$
(6) 3900 Å system, $B^2\Sigma - X^2\Pi$
(7) Methylene radical,
(8) The Triplet Bands, $d^3\Delta - a^3\Pi$
(9) Third Positive Bands, $b^3\Sigma - a^3\Pi$
(10) Baldet-Johnson system, $B^2\Sigma - A^2\Pi$

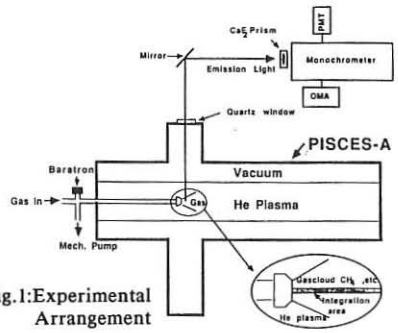

Fig.1: Experimental Arrangement

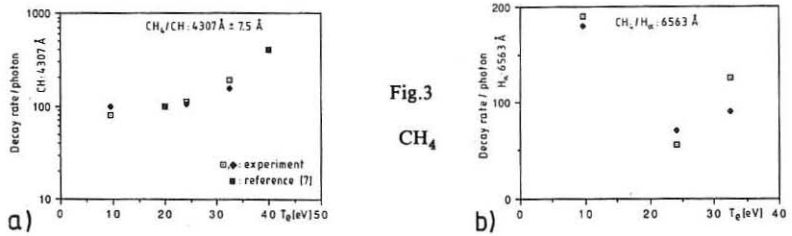

Fig.3 CH_4

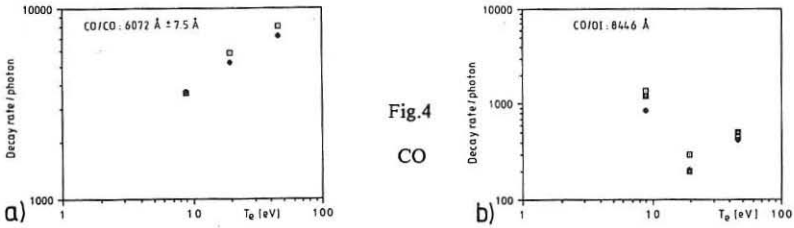

Fig.4 CO

Molecular decay rates per photon vs T_e for CH_4 and CO

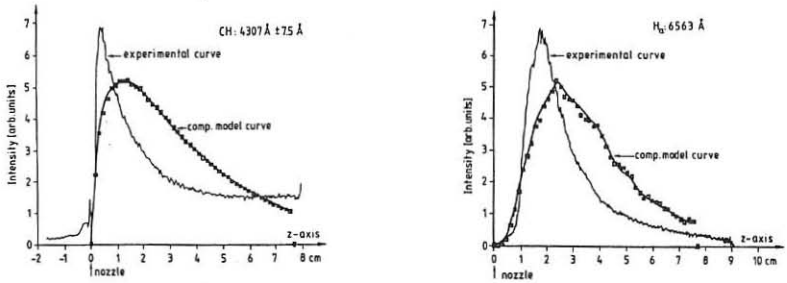

Fig.5: Axial penetration profiles for CH_4 - injection

FIRST RESULTS ON PLASMA-EDGE PROPERTIES WITH NEUTRAL BEAM HEATING IN TEXTOR

U. Samm, P. Bogen, H. Hartwig, E. Hintz, K. Höthker, Y.T. Lie,
A. Pospieszczyk, D. Rusbüldt, B. Schweer

Institut für Plasmaphysik
KFA Jülich GmbH, Ass. EURATOM-KFA

Abstract

The significant impact of neutral beam heating (NBI) on plasma boundary parameters in TEXTOR, namely a strong increase of n_e and T_e, is demonstrated. The heat flux to the limiter increases more than proportional to the heating power (factor >17) due to enhanced energy transport in the center and due to a change of power sharing by reducing the fraction of radiation from light impurities and increasing the fraction of convective energy flow at the separatrix. The probability for trapping injected H atoms in the wall-limiter system is estimated from spectroscopic measurements.

1. Introduction

Additional heating with neutral beam injection started in TEXTOR in September 1988. Co- and counter-injection beams, each having about 1.2 MW of power and a duration of up to 3 s, are available. The central electron temperature is increased significantly with NBI [1]. Even more pronounced variations are achieved at the plasma boundary. A first study of the impact of NBI on plasma boundary properties in TEXTOR has been performed in a series of discharges in deuterium with co-injection of hydrogen with 0.5 s duration and 1.2 MW of power, the results of which are described in the following.

2. Experiment

The data presented in this paper refer to the flat top phase of ohmic discharges with I_P=340 kA, B_T=2 T, a minor radius of a=46 cm defined by the toroidal and poloidal graphite limiters and a major radius of R=175 cm. The wall is carbonized. The neutral beam heating system is described elsewhere [1].

The comprehensive edge diagnostics in TEXTOR are used to determine particle fluxes at limiter and wall (emission spectroscopy, H_α, D_α, CI, OI; resolved in time, space and wavelength), heat fluxes to the limiter (ir-thermography) and electron-density profiles $n_e(r)$ (thermal Lithium beam, electric probes). Additional information is provided by HCN-interferometry, and bolometry.

3. Results

The flux of recycling deuterium at the limiter increases with NBI by about a factor of 4.8, exhibiting a strong oscillation with a signal modulation of about 15% (D_α-measurement, Fig. 1) synchronous to the sawtooth modulation of T_e in the center. The heat flux to the limiter increases by about a factor of 17, leading to a rise of the surface temperature by more than 250 K (ir-thermography, Fig. 2). The heatflux can reach values of 8 kW/cm^2 through a plane oriented perpendicular to the

fieldlines. We can estimate the change of T_e and n_e at the limiter edge by using the relation for the particle flux $\Gamma \propto n_e T_e^{1/2}$, and for the heat flux $Q \propto n_e T_e^{3/2}$. Thus, the measured Γ and Q result in an increase of n_e and T_e by a factor of about 2.5 and 3.5 respectively. The variation of n_e is consistent with the measurements of the line averaged density at r=40 cm (HCN-interferometer, Fig. 1) and of the n_e-profiles inside the scrape-off-layer (thermal Lithium beam, Fig. 3).

Because the central n_e and T_e values increase much less (factors 1.1 and 1.4) than those at the boundary, a significant broadening of profiles is evident indicating increased transport. Consequently, the confinement times decrease. The particle confinement time τ_P is reduced by about a factor of 3 from 100 ms to 35 ms as can be calculated from Γ and the total number of particles N_{tot}. Similar values (35 ms/80 ms) are obtained for the characteristic times of the deuterium flux to become stationary after the switch on/off of NBI (Fig. 4).

The total power loss going to the limiter P_{conv} increases more than proportional to the heating power when NBI is switched on. This is linked, according to the relation $P_{heat}=P_{rad}+P_{conv}$, to a reduction of the radiation level P_{rad}/P_{heat} : typically from 65% to 30%, or at high densities (ohmic plasma "detached", NBI plasma "attached" [2]) from 95% to 45% (Fig. 5). Thus, the energy loss with NBI goes preferentially via convective transport to the limiters and may be explained on the one hand by increased transport in the center, as is evident from the reduction of energy confinement time τ_E (factor of about 2.5) [1], and on the other hand by the strongly increased T_e at the boundary, leading to a reduction of the ratio of photons/ionizations of the impurities (C and O) and thus to a change of power sharing between limiter and wall by reducing the radiating fraction [3].

The line radiation from impurity atoms OI and CI measured at the limiter is shown in Fig. 6. With NBI the intensity increases by a factor of about 1.9 for OI and 2.2 for CI and the ratios of intensities OI/D_α and CI/D_α decrease by factors of 2.1 and 1.8 respectively. These intensities are proportional to the particle fluxes O and C and to the relative fluxes O/D and C/D from the limiter provided T_e is constant. Since T_e increases strongly with NBI the numbers have to be corrected in order to get the variation of fluxes. So far, a precise calculation is not possible due to a lack of knowledge about the T_e-profiles, but we estimate that the relative influx of impurities is roughly the same for the ohmic and the NBI phase of the discharge. Obviously the C flux increases slightly more than the O flux (factor 1.15), thus indicating that the coupling of the two fluxes, as is normally observed and is explained by chemical erosion via CO-formation [4], is altered by an increasing contribution from physical sputtering of C. But it appears that even a moderate increase of impurity fluxes can be compensated by improved screening due to the enhanced plasma-temperature and density at the separatrix in the case of NBI.

Because H is injected into a D plasma it is possible to distinguish between injected and intrinsic particles. From the simultaneous measurement of the H_α and D_α line shapes at a test-limiter with a high resolution scanning spectrometer [5] it is possible to determine the evolution of the concentration of H in D and to deduce the probability for hydrogen trapping in the limiter-wall system. The ratio H/D increases during NBI, as is shown in Fig. 7, from ≈0.11 before NBI to ≈0.23 at the end of NBI, thus the ratio increases by ≈0.12 due to NBI. In 0.5 s of NBI 1.1 10^{20} H particles are injected. The D filling before NBI is 1.6 10^{20} particles and at the end of NBI the total number of ions is 2.1 10^{20}. Without any trapping, i.e. recycling R=1, the H/D

ratio is expected to rise by ≈0.68 or with 100% trapping and τ_p=50 ms, i.e. R=0, by ≈0.07. The measured value ≈0.12 lies between those for R=1 and R=0 indicating that a significant fraction of H is trapped. We estimate that this fraction amounts to about 65% of the injected particles. These numbers should serve as an example of the method. Under different conditions the trapping of H may vary. For example in a series of NBI discharges the H/D ratio increases steadily due to an accumulation of hydrogen in the wall. This enhanced H concentration may cause serious problems for the combined application of NBI and ICRH in the minority heating regime.

Conclusion

The application of NBI opens a new parameter regime for the investigation of plasma-wall interaction in TEXTOR by providing values at the limiter edge as high as T_e≈100 eV, n_e≈1.·10^{13}cm^{-3} and Q≈10 kW/cm^2 (//B).

Acknowledgement

We would like to thank the NBI- and the TEXTOR-team for the excellent experimental conditions and J. Schlüter and H. Soltwisch for providing valuable data.

References

[1] H. Conrads et.al., this conference
[2] U. Samm et.al., Plasma Physics and Controlled Fusion, Vol.29, No. 10A, p.1321-1332 (1987)
[3] U. Samm et.al., this conference, "isotopic effects ..."
[4] V. Philipps, E. Vietzke and M. Erdweg, in Proceedings of the 8th International Conference on Plasma Surface Interactions in Controlled Fusion Devices, Jülich 1988
[5] P. Bogen, D. Rusbüldt and U. Samm, in Proceedings of the 8th International Conference on Plasma Surface Interactions in Controlled Fusion Devices, Jülich 1988 and
P. Bogen et.al., this conference

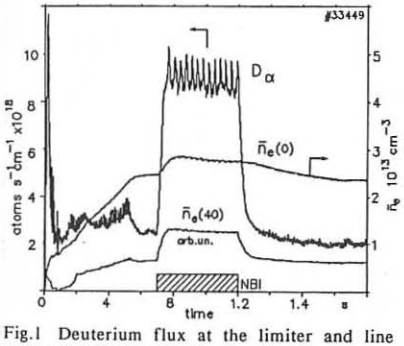

Fig.1 Deuterium flux at the limiter and line averaged densities at r=0 cm and r=40 cm

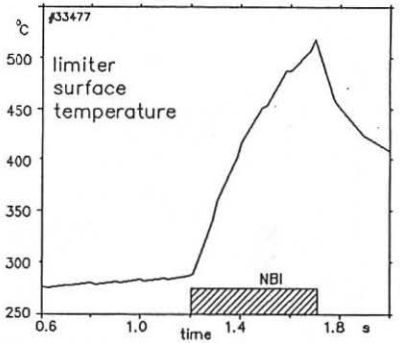

Fig.2 limiter surface temperature measured by infrared thermography; max heatflux 8 kW/cm^2 parallel to magn. field

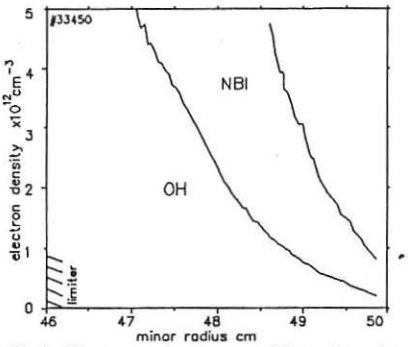

Fig.3 Electron density profiles in the scrape-off-layer measured with a thermal Lithium-beam

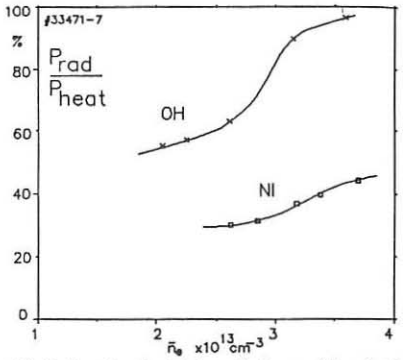

Fig.5 Level of total radiation with ohmic and NBI heating as a function of the line averaged electron density during flat top

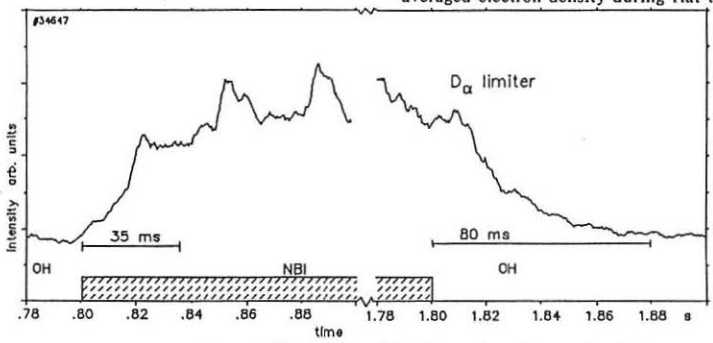

Fig.4 NBI-switch-on/off behavior of the Deuterium flux at the limiter

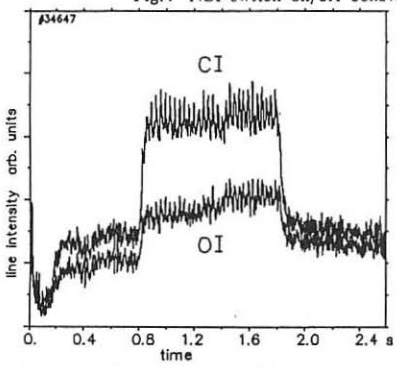

Fig.6 Intensity of impurity line radiation at the limiter

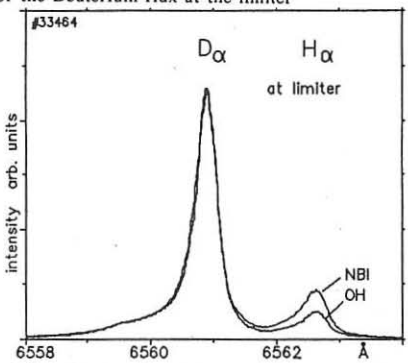

Fig.7 H_α-D_α-line profiles at the limiter; peak normalized (NBI: H injection in D)

ISOTOPIC EFFECTS ON PLASMA EDGE PROPERTIES

U. Samm, P. Bogen, H. Hartwig, E. Hintz, K. Höthker, Y.T. Lie,
A. Pospieszczyk, D. Rusbüldt, B. Schweer

Institut für Plasmaphysik
KFA Jülich GmbH, Ass. EURATOM-KFA

Abstract

Electron-densities, -temperatures, particle and heat fluxes at the plasma boundary of a limiter tokamak with hydrogen filling are compared with those in deuterium and the relation between central profiles, radiation and penetration of neutrals is studied. The data demonstrate increasing transport with decreasing ion mass and indicate a possible scaling of transport with the thermal velocity of the ions.

1. Introduction

Significant differences in the transport properties of hydrogen (H) and deuterium (D) plasmas have been reported from tokamak experiments. Generally, the energy transport in H is found to be faster than in D leading to a profound difference in energy confinement times τ_E [1]. Similar observations are made in particle transport studies. The longer particle confinement time τ_P in D is linked with peaked density profiles. From a transport analysis in ASDEX under certain conditions the relations $v/D_\perp \propto A_i^{-1/2}$ and $\chi \propto A_i^{-1/2}$ have been found [2], where v denotes the inward drift velocity, $D_\perp$ the diffusion coefficient, A_i the ion mass number and χ the electron heat conductivity. In the scrape-off-layer measurements of the cross field diffusion coefficient $D_\perp$ gave values for H being about a factor of 1.5 larger than those for D [3].

The dependence of transport on A_i is not understood, even the sign of the exponent of the mass dependence cannot be explained so far. But progress in transport theories can only be achieved by improving the database of well diagnosed discharges in H and D. In TEXTOR a series of experiments has been devoted to this task with particular emphasis on the determination of plasma edge properties.

2. Experiment

TEXTOR has been specially prepared for operation in H and D by carbonizing the wall with either CH_4 or CD_4 [4] in order to assure identical conditions and to keep the concentration of the "wrong" mass as low as possible (<2%). The data presented in this paper refer to the flat top phase of ohmic discharges with I_P=340 kA, B_T=2 T, a minor radius of a=46 cm defined by the toroidal graphite limiter and a major radius of R=175 cm.

Comprehensive plasma edge diagnostics are applied : e.g. emission spectroscopy (H_α, D_α, OI, CI) resolved in time, space and wavelength, ir-thermography, atomic probing beams (thermal Lithium, laser ablation of Li/C) and electric probes [5]. Additional information is provided by HCN-interferometry, Thomson-scattering and bolometry.

3. Results

It is impossible to change A_i without varying other important plasma parameters. Therefore, one has to select a specific parameter which has to be kept constant for comparing isotopes. We present our results in two different ways : 1) The total number of particles N_{tot} is kept constant in the medium density range $\bar{n}_e \approx 2.3 \cdot 10^{13} cm^{-3}$, at the onset of the τ_E saturation regime; note that $\bar{n}_e$ differs then by about 8% between H and D. 2) The variation of parameters with $\bar{n}_e$ is determined (density scan).

1. N_{tot}=const

The n_e- and T_e-profiles in the plasma center are much broader in H than in D, as can be seen from the HCN-interferometer and Thomson-scattering data in Fig.1a,b. The n_e and T_e values at the limiter radius r=a vary opposite to those in the center, as is already indicated by the central profiles and becomes evident from the measurements at the plasma edge (atomic Li/C beam [6]) displayed in Fig.2a,b. The ratios of these values are given in table 1.

	r=a edge	r=0 center
n_e	1.4	0.87
T_e	1.7	0.7
$\sqrt{A_i T_e}$	0.9	0.6
$\sqrt{T_e/A_i}$	1.8	1.2

Table 1 - ratio of hydrogen over deuterium values for N_{tot}=const

The broader profiles in H with enhanced n_e and T_e at the boundary have the following consequences : 1) The particle recycling at the limiter is larger (H_α/D_α factor 2). Thus, τ_P is about a factor of 2 lower in H. 2) With a reduction of the total energy content by a factor of 1.2 and an increase of the loop voltage by a factor of 1.15 τ_E is about a factor of 1.4 lower in H, whereby the enhanced energy transport accounts for about half of the increase of the convective heat flux measured at the limiter (total increase factor 2-3). The other half is due to reduced radiation from the light impurities C and O at the boundary region: typical values are $P_{rad}/P_{heat} \approx 60\%$ in D and 30% in H (see Fig.3b). The decrease of radiation is mainly due to the reduction of the ratio of photons/ionizations, as it is the case in an diffusive ionization equilibrium - typical for light impurities - for increasing T_e with steepening profiles at the plasma boundary. The relative impurity fluxes from the limiter C/H(D) and O/H(D) are about equal in H and D (about 2% each). 3) The penetration depth of neutral H atoms is slightly smaller than for D atoms, as is indicated in Fig.3c by the location of the $H_\alpha(D_\alpha)$ peak radiation (CCD-camera) relative to the inner bumper limiter (r=48.5 cm). This is in contrast to the expectations based on the assumption that $n_e(a)$ and $T_e(a)$ are the same in H and D plasmas.

2. density scan

In H the plasma parameters are much more sensitive to the variation of $\bar{n}_e$. With rising $\bar{n}_e$ the density profile broadens slightly in H - except close to the $\bar{n}_e$-limit - but steepens in D as shown by the profile parameter $\bar{n}_e(40)/\bar{n}_e(0)$ in Fig.3a and by the different slopes of the rise of $n_e(a)$ in Fig.2a. Te(a) decreases, as generally observed in ohmic discharges, but with different slopes in H and D,

such that beyond a critical density the values in H can become equal or even lower than those in D (Fig.2b). At these low $T_e(a)$ values of about 10 eV the plasma becomes "detached", a condition which is usually defined in TEXTOR[7] by the strongly increased penetration depth of neutrals (Fig.3c). Concurrently $n_e(a)$ starts to decrease (Fig.2a). In H a dramatic increase of P_{rad} is observed (Fig.3b). For both isotopes the radiation appears to behave according to the change of $T_e(a)$ which is, to a certain approximation, proportional to the ratio of ionizations/photons for carbon and oxygen. The density limit in terms of $\bar{n}_e$ is slightly lower for H but in terms of N_{tot} it is nearly the same.

4. Discussion

The data presented in this paper should provide a basis for further testing and developing transport models. In order to give some hints of characteristic parameters which might dominate the transport, the change of the Larmor radius $r_L \propto \sqrt{A_i T_i}$ and of the thermal velocity $v_i \propto \sqrt{T_i/A_i}$ (assumption $T_e=T_i$) are included in table 1. The data suggest that the transport might scale with v_i. This would be expected e.g. in an ergodic type of transport with $D_\perp \propto \Delta^2/T$, where Δ is a characteristic radial step width of the magnetic fieldlines and T is the time of flight of the ions for a toroidal loop. Provided Δ is constant we get the relation $D_\perp \propto v_i$. A similar scaling for the convective energy transport is suggested by Rogister [8] based on the theory of drift waves.

For the changeover from H-D plasmas to D-T plasmas isotopic effects may play an important role; we expect improved confinement as well as enhanced radiation cooling.

Acknowledgement

We wish to thank G. Fuchs, E. Graffmann, J. Schlüter, H. Soltwisch and the TEXTOR team for providing valuable experimental data and H. Kever and A. Rogister for discussions on the theoretical background.

references

[1] H. Murmann, F. Wagner, et.al., Proceedings of the 15th European Conference on Controlled Fusion and Plasma Physics (1988), Dubrovnik
[2] O. Gruber, et.al., Proceedings of the 15th European Conference on Controlled Fusion and Plasma Physics (1988), Dubrovnik and IPP Report AR/1986, Garching
[3] F. Wagner, Nucl. Fusion, 25, (1985) 525
[4] J. Winter, J. of Nucl. Mater. 145-147 (1987) 131-144
[5] P. Bogen and E. Hintz, in "Physics of Plasma-Wall Interactions in Controlled Fusion", Plenum Press, New York, 1986, Eds. D.E. Post and R. Behrisch
[6] A. Pospieszczyk and G. Ross, Proceedings of the 8th International Conference on Plasma-Surface-Interactions in Controlled Fusion Devices (1988), Jülich
[7] U. Samm, R. Weynants, this conference
[8] A. Rogister, private communication

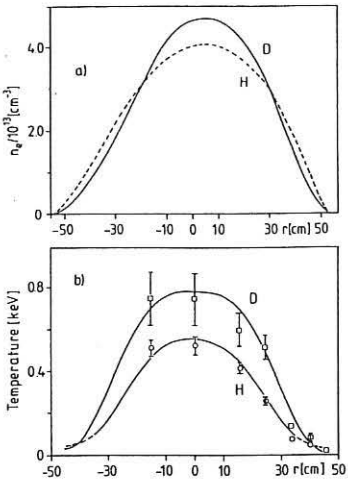

Fig.1 a) central electron-density and b) -temperature profiles

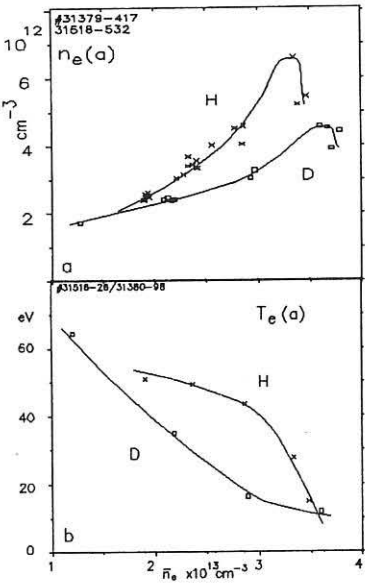

Fig.2 variation with $\bar{n}_e$ of a) edge electron-density and b) -temperature

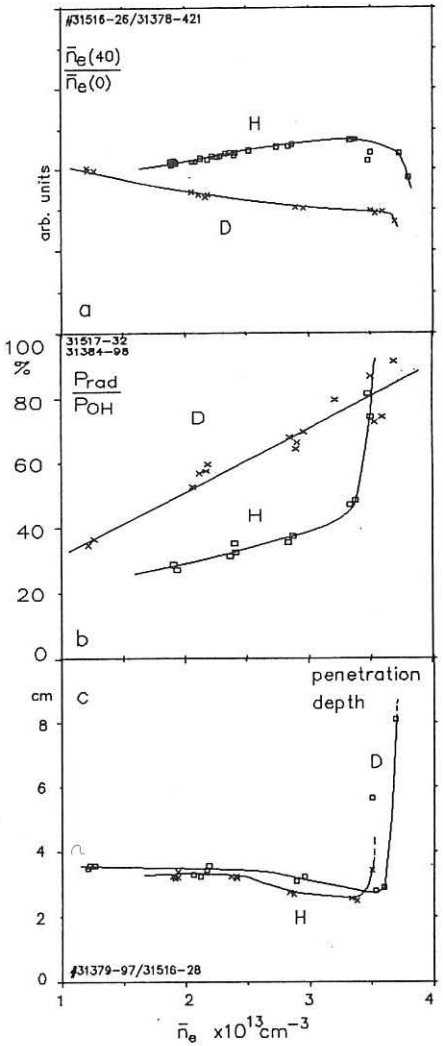

Fig.3 variation with $\bar{n}_e$ of a) profile parameter, b) total radiation and c) location of $H_\alpha(D_\alpha)$ peak radiation relative to inner limiter (r=48.5cm)

REDEPOSITION STUDIES IN THE BORONIZED TEXTOR

P. Wienhold[1], B.Emmoth[3], H.Bergsåker[3], J.v.Seggern[2], H.G.Esser[1], J.Winter[1]

[1]IPP, [2]IGV, KFA Jülich GmbH, Ass.EURATOM/KFA, P.B. 1913, 5170 Jülich, FRG
[3]MSI, Ass. EURATOM-NFR, S-10405 Stockholm, Sweden

1. Introduction

Redeposition studies in TEXTOR with carbonized inner walls have shown that the material which is collected on targets in the srape-off layer (SOL) is identical with the carbonization layer itself, i.e. amorphous deuterium rich carbon (a-C:D) with a D/C-ratio of about 0.4 /1/. The stationary recycling of the carbon back to the wall and limiters where it is eroded is a desired goal. Fluxes higher than 2 x 10^{16} C/cm^2s have been observed in the SOL under those conditions corresponding to a carbon concentration of about 1 % in the plasma /2/. C (accompanied by O) is the major impurity and mainly due to chemical erosion at wall and limiters /3/. A boronization was performed at 5.3.88 to the TEXTOR inner wall in order to reduce further the impurity concentrations. All limiters (graphite) and the liner (inconel) were covered with an amorphous boron containing carbon layer (a-C/B:H) of 30 - 80 nm thickness /4/. The B/C-ratio ranged between 1/2 and 1/1. Such layers were expected to show a reduced chemical erosion by about a factor of 10 /5/. The Stockholm-TEXTOR probe systems has joined the new situation and has collected particles in the SOL in time resolved and integrated manner /6/. This paper addresses time integrated exposures carried out at 15.3.88, i.e. about 200 discharges after the boronization. The study of the probable changes of the structure of the deposit and of the C and O fluxes to the collector and their comparison to previous results were the major aims beside the observation of the B deposition.

2. Experimental situation at TEXTOR

During all exposures, the plamsa radius a = 44 cm was defined by the toroidal limiter system ALT II (poloidal angle Θ = -45° below equatorial plane). The poloidal limiters were withdrawn to r = 50 cm which is also the radial position of the poloidal graphite shields of the ICRH-antennae (AL). ALT I was dismounted. Liner (r = 55 cm) and limiters were at about 160 °C and boronized with H as hydrogen constituent. Exposures were made during 28 discharges (32202-32243) in deuterium with I_p = 337 kA, B_T = 2.0 T and the average duration of 2.6s. $\bar{n}_e$ ranged between 2.3 and 3.3 x 10^{13} cm^{-3} for most of the exposures. 3 discharges ended disruptively.

Plane Ta-targets mounted on a housing were inserted horizontally (Θ = 0°) into the SOL by means of the Stockholm-TEXTOR probe system. At electron drift side they reach a radial position which is 1.2 cm closer to the plasma than on ion drift side. The surface area (8 x 6 cm^2) of the targets was oriented perpendicular to the toroidal direction. Slits of 5 mm width along the center line allowed particles to reach a cyclindrical graphite target inside the housing. By rotating this cylinder between shots, integrations over selected discharges could be made while the outer

Ta-plates were exposed to 28 discharges. The field line distance on electron drift side to ALT II was about 40 m, except for radial positions $r > 50$ cm where AL shadowed the target in a distance of 2.5 m. On ion drift side the connection length (to ALT II) was even shorter: 1.4 m. After the exposure the targets were disassembled for analysis. C, B, D and O areal densities have been determined by ion beam analysis in MSI, Stockholm. The first results are reported here and discussed with observations made with other techniques (AES, interference fringe analysis).

3. Results and dicussion

Fig. 1 shows the areal densities of carbon (squares), boron (dots) and deuterium (triangles) measured on the Ta-target which was exposed on the electron drift side for 72.8s in deuterium. The analysis is made parallel to the center line at a poloidal angle $\Theta = -0.7°$. Obviously, the element ratios are rather independend of the radial position. The ratio $B/C = 0.23 \pm 0.03$ is confirmed by AES analysis on samples taken from this target and is in agreement with observations made in-situ at another location of TEXTOR /10/. The fraction of boron is much lower than in the original boronization layer where we found values between 0.5 and 1.0. Depth profiling with AES showed up the homogeneity of the deposit.

B is exceeded by D (except at the target tip), and the ratio D/C ranges between 0.3 and 0.5 as usual for amorphous carbon deposits /1, 2/. The reduction at $r < 47$ cm is likely due to effusion during a strong temperature excursuion of the target tip after one of the disruptions. The amorphous character of the deposit is also indicated by the appearence of interference colours. This lead us to apply the colour-thickness relation which has been found for a-C:H /7/. The estimated thicknesses are marked as crosses in the figure and related to the right hand scale. This scale is set up by using the relation 6.3×10^{17} C/cm^2 $\hat{=}$ 100 nm which was found to be valid for amourphous carbon deposits growing in a carbonized surrounding. The agreement between the two independently determined carbon profiles demonstrates the applicability of this "quick test" for redeposited material in a boronized machine. It is not surprising because the total boron fraction in the layer is about 13 % only.

The deposition rate of carbon has decreased to, e.g. 1.2×10^{16} cm^{-2}s^{-1} at $r = 46.5$ cm from 2.1×10^{16} cm^{-2}s^{-1} found after a carbonization. It agrees well with the spectroscopical observations /8/, but is less than expected and shows that carbon erosion is still dominant. The carbon profile in general decays down steeply towards $r = 50$ cm which is the radial position of the antenna limiter and levels off in its shadow. This is the same behaviour as observed in the carbonized TEXTOR /2/. It could be understood in terms of a model where carbon is eroded chemically from the carbonized wall, but mostly recycled and redeposited thereon (and on the target collectors). This model suggests lower deposition rates on the ion drift side because of the shorter connection length to the limiter. This is again observed here, but not shown in the figure: on the ion drift side target about half as much carbon is detected than on the electron drift side.

Carbon eroded from the limiters can also reach the collector plates by diffusion out of the plasma when the field line distance is long enough ($L > 12$ m). This is the case on the electron drift side for $r < 50$

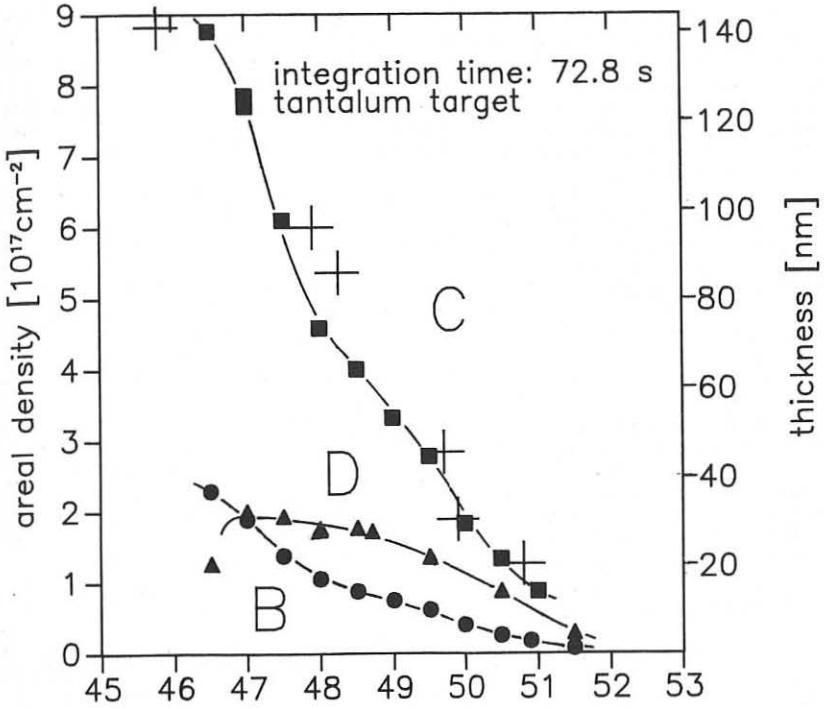

fig.1. distance from plasma center [cm]

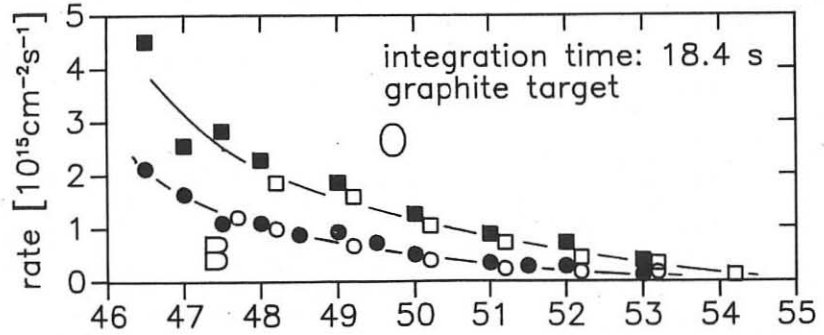

fig.2. distance from plasma center [cm]

cm. The decay length seems to be larger (~ 2.5 cm) as found in the carbonized machine (~ 1.5 cm) and would correspond to a diffusion constant of about 5 x 10^3 cm^2s^{-1}. Boron is most probably liberated from the limiters (see discussion in /6/). The collected amount increases with increasing temperature T_e. There is indication that boron diffuses into the graphite matrix /4/, in particular under thermal impact. This would explain that lower boron concentrations are achieved on the limiter surface and hence in the reformed layers.

Fig. 2 shows deposition rates of oxygen (squares) and boron (circles) as they were deduced from the graphite sample. The integration time here was 18.4s corresponding to 7 discharges with $\bar{n}_e$ = 2.8 x $10^{13}cm^{-3}$ each. The profiles found on the electron drift side (full signs) and on the ion drift side (open signs) are almost equal within the statistical error. Because the oxygen is collected mainly by implantation into the graphite target /9/ its amount does not correspond to the fraction in the deposition layer.

Deposition rates of ~ 3 x 10^{15} O/cm^2s at, e.g. r = 47.5 cm indicate the dramatic reduction of the oxygen impurity flux in SOL by factors between 15 and 20 after the boronization. Exposures on graphite targets made when the machine was carbonized yielded values between 4 - 6.2 x 10^{16} $cm^{-2}s^{-1}$ at r = 47.5 cm at almost identical discharge conditions /9/. The drastic reduction is in agreement with the observed decrease of the OVI line intensity and corresponds to the CO and CO_2 decay measured with the sniffer probe /4/. Operation of TEXTOR could be achieved with improved density control and heating of the plasma and Z_{eff} values of 1.2.

4. Conclusions

The collector probe meausrements show that after a boronization of TEXTOR the oxygen impurity flux in the SOL is reduced significantly (factor 15 - 20) while the carbon erosion still dominates (reduction factor ~ 2). The carbon is recycled to the wall elements and forms back the amorphous hydrogenated layer as in the carbonized machine. The boronization has improved the plasma performance without losing the beneficial recycling of the wall material. But, the degradation of the boron content in the redeposits may indicate a slow transition back to the less beneficial conditions in carbonized machines. Since this is likely due to a diffusion loss of boron into the graphite matrix of the limiters it would be of interest using a boron doped graphite as limiter material.

References

/1/ P. Wienhold, et al., 14th EPS Conf., June 1987, Madrid, Vol. II, 782
/2/ P. Wienhold, F. Waelbroeck et al., J.Nucl.Mat.163-165(1988), in print
/3/ E. Vietzke, V. Philipps, et al., J. Nucl.Mat. 163-165(1988), in print
/4/ J. Winter, H.G. Esser, et al., J. Nucl. Mat. 163-165 (1988), in print
/5/ S. Vepřek, S. Rambert, et al., J. Nucl. Mat. 163-165 (1988), in print
/6/ H. Bergsåker, B. Emmoth, P. Wienhold, M. Rubel, this conference
/7/ P. Wienhold, U. Littmark, E-MRS Sym. Proc. Vol. XVII, 441 (June 87)
/8/ U. Samm, P. Bogen, et al., J. Nucl. Mat. 163-165 (1988), in print
/9/ M. Rubel, F. Waelbroeck, et al., to appear in J. Nucl. Mat., 1989
/10/ T. Banno, private communication

PARTICLE EXHAUST DURING NEUTRAL BEAM HEATING WITH THE TOROIDAL BELT PUMP LIMITER ALT-II IN TEXTOR:

R.A. Moyer[1], K.H. Dippel[2], R.P. Doerner[1], K.H. Finken[2], D. Gray[1*], K. Nakamura[3], J.G.Watkins[4], R.W. Conn[1], W.J. Corbett[1], A. Hardtke[2], the NI team[2], and the TEXTOR team[2]

[1]Institute of Plasma and Fusion Research, and Department of Mechanical, Aerospace, and Nuclear Engineering, University of California, Los Angeles, CA 90024, U.S.A.* *
[2]Institut für Plasmaphysik, Kernforschungsanlage Jülich, Association EURATOM-KFA, D-5170 Jülich, Federal Republic of Germany
[3]Plasma Engineering Laboratory, Naka Fusion Research Establishment, JAERI, Naka-machi, Japan
[4]Sandia National Laboratories, Albuquerque, New Mexico 87185, U.S.A. * *

Abstract

Particle collection, removal, and exhaust by the toroidal belt pump limiter ALT-II have been measured in deuterium discharges with co-, counter-, and balanced injection of 48 keV neutral hydrogen particles. Particle collection increases from 50–80 A to 150–320 A during 1.2 MW of co- or counter-injection or 2.4 MW of balanced injection. The removal rate for pumping at two of the eight blades (3 of 15 scoops) reaches 2.7 Torr–l/s with a removal efficiency of nearly 45%. Extrapolating these results to a full belt with 15 scoops and eight pumps yields 140 amps of removal. This compares favorably with the maximum injectable current of 50 A and suggests that ALT-II with full pumping can provide sufficient exhaust during NI heating.

Introduction:

The Advanced Limiter Test-II (ALT-II) is an eight segment, toroidal belt pump limiter located 45° below the outer midplane in the TEXTOR tokamak.[1] Previous experiments have measured the particle collection, removal, and exhaust efficiencies in Ohmic discharges and in discharges with up to 2.5 MW of ICR auxiliary heating.[2] The effects of poloidal asymmetries in particle flows and scrape-off lengths and of modifications to SOL profiles during high power ICR heating have been determined.[3]

In this paper, we report results on particle collection, removal, and exhaust by the pump limiter in deuterium discharges with 1.2 MW co- or counter-injection and 2.4 MW of balanced injection. Measurements of particle collection in the 15 localized particle collection scoops are presented first. Removal rate measurements and removal and exhaust efficiencies, extrapolated to eight operational pumping stations (mid-1989), are presented next. Conclusions are summarized in the final section.

Particle Collection during Neutral Particle Injection (NI):

Particle exhaust has been measured in deuterium discharges with co-, counter-, and balanced injection of 48 keV neutral hydrogen particles. The current collected by an electrostatic probe biased to collect ion saturation current in an ion drift direction particle collection scoop ("flux probe") is plotted versus time for typical co-, counter- and balanced injection discharges in Figure 1. This flux probe integrates the current into the scoop in the

radial direction to account for profile effects. For 1.2 MW of co- or counter-injection, the particle flux into all ALT scoops increases by a factor of 2.5–3.5. The increase is systematically larger for counter-injection by 10-20% under comparable machine conditions. During 2.4 MW of balanced injection with comparable machine conditions, the flux increases 4–5 times. Particle flow asymmetries in the Ohmic phase, if present, are maintained throughout the NI pulse in all three injection schemes. The total particle collection during NI heating increases with the line average central density achieved during the NI pulse from 150 to 320 A, compared to 50–80 A in Ohmic discharges, as shown in Figure 2a.

Langmuir probe measurements in the scoops show that the particle flux increase results nearly entirely from a density increase (Figure 3). Typical electron temperature rises in the scoops are less than 25% and often are zero. Scanning double probe flux and density profiles taken along the outer midplane indicate that the tangency point flux rises from 1–2 A/cm^2 in the Ohmic phase to 5–10 A/cm^2 during neutral injection, in agreement with increases in particle fluxes to the limiters measured with D_α monitors.[4] The tangency point density rises from $1–2 \times 10^{12}$ /cm^3 to $8–20 \times 10^{12}$ /cm^3. The flux and density e-folding lengths decrease by about 10–20% during neutral injection.

Behavior of the SOL T_e profile is more difficult to determine. In the past, it has been observed that the T_e profile in Ohmic discharges decreases rapidly from its tangency point value in the first 0.5 cm of the SOL. Beyond the first 0.5–1 cm, the T_e profile is quite flat ($\lambda \approx$ 4–6 cm), and obtaining accurate estimates of the tangency point T_e requires SOL profile information to within 0.5 cm of the limiter radius. This is not possible due to the power flux to the probe (> 3 kW) in the last 0.5 cm that heats the probe to emission. Estimates of the T_e rise at the tangency point from spectroscopic measurements[4] give a factor of 3.5. One centimeter deep in the SOL, scanning probe measurements indicate that the T_e rises by about a factor 2 from 20–25 eV to 40–50 eV. This result is consistent with the Langmuir probe T_e measurements in the scoops (2.8 cm beyond limiter radius) shown in Figure 3 since the e-folding length beyond the first 0.5 cm also shortens substantially (4–6 cm to 2–3 cm) during NI heating with the result that the T_e at the radius of the scoop Langmuir probes is nearly unchanged by the NI heating.

Particle Removal and Exhaust:

Substantial pressure rises (5–7×) are seen at the unpumped scoops during the NI pulse. At the pumped blades, the removal rate increases roughly in proportion to the flux. These increases are compared with the flux increases of the previous section in Figure 4. Removal rates in excess of 2 Torr-l/s for the three pumped scoops are easily obtained (Figure 2b). To date, the record removal rate and efficiency, obtained with 1.2 MW of 48 keV neutral hydrogen co-injected into a high density deuterium discharge (3.7×10^{13} cm^{-3}) are 2.7 Torr–l/s and 45% respectively. This exceeds previous record values, obtained with 2.5 MW of ICR heating, of 1.2 Torr-l/s and 30%. Such high density discharges have not yet been attempted with the higher power level of balanced injection where one would presumably obtain even higher removal rates. Several balanced injection data points, obtained on a different day with a line average density of 3.0×10^{13} cm^3, are also plotted in Figure 2b for comparison. Extrapolating these results to a belt with 15 scoops and eight pumps yields a removal rate of 140 amps. This compares favorably with the maximum injectable current of 50 A and suggests that ALT-II with full pumping will provide sufficient exhaust during NI heating to permit density control.

Scanning probe particle flux profiles in the SOL have been used to estimate the total core efflux, the global particle confinement time τ_p, and the exhaust efficiency. This technique suffers from the limitation that poloidal variations in the SOL flux profile are neglected. The measurements are made along the outer midplane where the e-folding lengths are known to be longer than along either the top or bottom central chord. These calculations might therefore overestimate the core efflux and hence underestimate the global particle confinement time and represent a lower limit.

The global particle confinement time decreases from 100–150 ms in Ohmic discharges (depending upon the line average density), to 25–35 ms during NI heating. The database is presently too limited to permit detailed variations among the three injection schemes to be determined. The resulting exhaust efficiency (removal rate/core efflux) is 5–10%.

Conclusions:

Measurements of the particle collection, removal, and exhaust by the ALT-II pump limiter during 1.2–2.4 MW of NI heating indicate that the toroidal belt pump limiter system is capable of handling the exhaust requirements during high power NI heating if the pumping system is completed at the remaining six unpumped blades. This will occur in mid-1989. Improvements in the exhaust and removal efficiencies by a factor of 2 may be achieved by reducing the blade thickness.[3] To date, no systematic variations in the SOL profiles obtained from the scanning probe among the three injection schemes has been observed. Differences in particle collection and removal may be attributed to the overall NI power level and confinement degradation. Future NI experiments will include deuterium injection, measurement of the helium removal rate for ALT-II, and efforts to improve confinement while using ALT-II as the main TEXTOR limiter system.

References:

[1]Conn, R.W., *et al.*, J. Nucl. Mat., **121** (1984) 350.
[2]Goebel, D., *et al.*, Proc. 8th Int. Conf. Plasma Surface Interactions in Controlled Fusion Devices, Jülich, FRG 1988.
[3]Dippel, K.H., *et al.*, Proc. 12th Int. Conf. on Plasma Physics and Controlled Nuclear Fusion Research, IAEA, Nice, France, Paper CN-50/A-7-10.
[4]Samm, U., *et al.*, this conference, paper P 8 E 6.
*This work was performed under appointment to the Magnetic Fusion Science Fellowship Program which is administered for the U.S.D.O.E. by Oak Ridge Associated Universities.
**This work supported in part by the U.S. D.O.E.

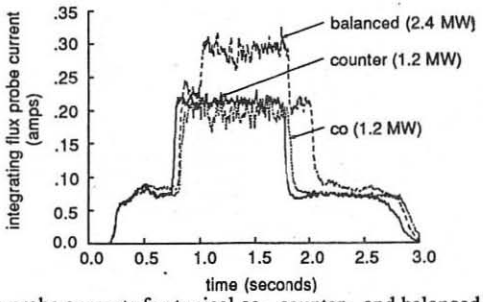

Figure 1: Flux probe currents for typical co-, counter-, and balanced injection discharges.

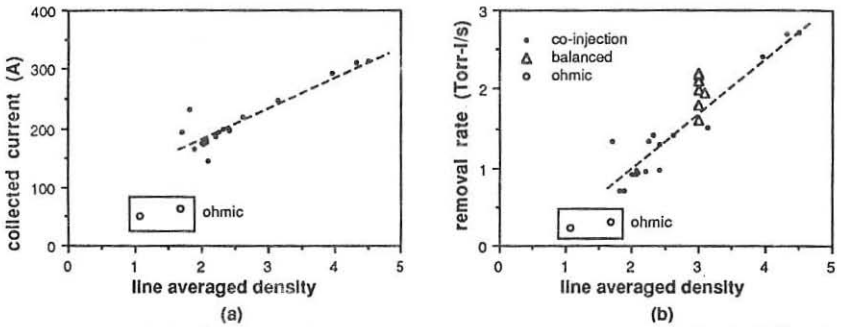

Figure 2: (a) Total current collected by ALT-II versus line average density ($\times 10^{13}/cm^3$). (b) Removal rate by pumps at two blades (3 of 15 scoops) versus line average density ($\times 10^{13}/cm^3$).

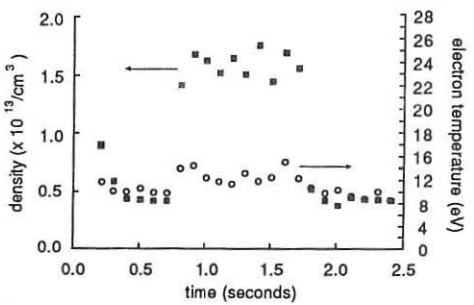

Figure 3: Variation of ion density and electron temperature in the particle collection scoop.

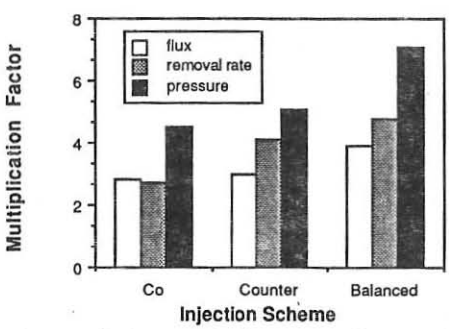

Figure 4: Comparison of the increase in flux, removal rate, and neutral pressure in the unpumped scoops during co-, counter-, and balanced injection.

SPECTROSCOPIC STUDIES OF PLASMA SURFACE INTERACTIONS IN TORE SUPRA

C.C.Klepper*, W.R.Hess, T.Fall, J.T.Hogan*
A.Grosman, D.Guilhem

Asso. EUR-CEA CEN-Cadarache,F-13108 Saint Paul-Lez-Durance,France
* Permanent adress: ORNL, Oak Ridge, Tenn., U.S.A.

1. Introduction.

Tore Supra (1) is a large tokamak (R=238 cm, a=75 cm) with superconducting coils.This tokamak is designed for quasi-steady-state operation and therefore the properties of the edge plasma and its interactions with edge components are of primary interest. All surfaces in contact with the plasma are of graphite construction

In its first year of operation only a small number of reproducible shots have been obtained. However, these shots are representative of plasmas in the ohmic phase of the machine and deserve to be studied before the next phase of operation with additional heating.In the initial experiments the plasma was leaning on the inner axisymmetric graphite wall, which covers about +-45° poloidally. To simplify particle control, the working gas in these discharges was helium. Past studies of particle confinement times in tokamaks have involved hydrogen, and the collisional-radiative model of Johnson and Hinnov (2) has been employed to relate the measured intensity of H-lines to the ground state population n(1). The electron source n(1)neSeff is then calculated using an effective rate coefficient Seff. In this study the model is extended to helium by including the work of Drawin et al (3,4). For the first Tore-Supra discharges only one line of sight was available. The spatial distributions are modeled by a 3D neutral transport code which is coupled to a 2D equilibrium code. In a previous study this code was benchmarked to experimental results by modeling complete spatial ionization profiles from TEXT (5).

2. Experimental setup:

A 0.64 m Czerny-Turner spectrometer equipped with an Optical Multichannel Analyzer (OMA) and a grating with 2400 gr/mm (dispersion=0.14 A/pixel) is used. Due to the fused silica lenses of the telescope (f/2;f=50 cm) and the silica fibers (PCS-1000;d=1mm) the spectral range available extends from 300 to 800 nm. Each fiber views a chord through the plasma of about 6 cm in width. Nine radial views are achieved. They scan the bottom half of the poloidal cross-section.

The first is slightly above the horizontal midplane, and the last is just outside the last closed magnetic surface. This system is absolutely calibrated by means of a tungsten filament lamp and a Lambertian diffuser plate,both calibrated against standard sources. For the calibration, the diffuser plate was placed inside the tokamak at the actual center of the plasma chord observed.

3. Experimental results:

In this paper we study some typical discharges during the early phase of TS operation. Figures 1 and 2 show plasma current (Ip), line-averaged density (ne), loop-voltage (Vp) and a typical Halpha signal. During the current plateau (Ip=600 kA) a gas injection is used to raise the density from 1.5 to 2.1x10E13 (cm-3).The radius of the plasma is maintained constant at 70cm with the plasma limited by the inside carbon wall. The continuum signal given by the OMA in the range of 520nm is used to calculate an averaged Zeff. The initial value of Zeff=3 (+50 -10%) before gas puffing drops to 2.5 and remains at this value until the end of the current plateau. This calculation uses only the Te-profile obtained with the ECE system, and the absolute value of Te(o) was derived from the transport code (MAKOKOT). This leads to the large error bar quoted above. We have verified spectroscopically that no heavy impurities contributed to the Zeff measurement presented here. The dominant contribution to the Zeff are carbon, oxygen, and hydrogen.

4. Method of analysis:

Neutral impurity influxes are calculated from measurements of absolute intensities of neutral or weakly ionized ions. For hydrogen the model of Johnson and Hinnov (2) has been used. The carbon influx was derived from a simple model using the ratio of ionization to excitation coefficient JET (6). Drawin extended the collisional-radiative model to HeI and HeII. We used the effective ionization rate coefficient Seff compiled by Bell and al. (7). We find (fig.3) that the ratio of ionization events per photon, unlike the case of hydrogen, is strongly dependent on the electron temperature. Since we did not dispose of an electron temperature profile we have assumed an electron temperature corresponding to half the ionization potential of the considered ion i.e. 7eV for H, 12eV for HeI and CII, and 25eV for HeII.

Neutral transport modeling is used to relate the locally measured flux to the poloidally averaged flux. In these calculations,

an axisymmetric equilibrium is coupled with a 3D Monte-Carlo code (5) to estimate the relative poloidal distributions of HeI and HeII. HeI is assumed incident from the inner limiter, emitted uniformly in the toroidal direction. An incident energy (typical of reflected particles) of 30eV is assumed. The calculation uses ionization rates published by Janev and Langer (8) and neglects Helium charge exchange. Ionized Helium is assumed to move on a flux surface, subject to random cross-field diffusion (D=1M2/s). The HeI distribution is localised near the limiter, while HeII exists in a poloidal shell. Temperature and density profiles will affect the quantitative results. The predicted local brightness in the model is integrated along the same chord as used experimentally.

5. Results and discussion.

The particle confinement time has been computed for the typical early Tore-Supra discharge. The ionization source used in the computation includes contribution of not only the working gas He, but also of H which is always present due to desorption from the graphite surfaces. The measured local sources and their ratios to the modeled poloidally weighted sources are shown in the table (shot 570 fig.1,2 and shot 511):

SPECIES	ne(10^{13})	LAMBDA(nm)	LOCAL SOURCE	WEIGHTING FACTOR
H	2.	656.3	4.4 10^{15} cm-3s-1	6.3
HeI	1.	388.9	5.0 10^{14} "	2.4
HeII	2.	656.0	4.0 10^{15} "	>1.0
CII	2.	657.8	0.8 10^{14} "	-

The viewing chord used for this measurement had a normal radius of 44cm. For the neutrals, the source comes primarily from the inner carbon limiter. For the Tp calculation, the HeII was not modeled, but it can be assumed that its emission is poloidally symmetric due to the high ionization potential (54eV), and hence the weighting factor is assumed to be close to 1.0.

Analysis of the partial pressures of the recombined gas, right after the end of the discharge has been achieved with an absolutely calibrated quadrupole mass spectrometer. This analysis shows a 9% ratio of H to He atoms. This should be compared with 18% ratio measured from recycling neutrals.

In the computation of Tp the absence of the HeII contribution to the source is overcome with the approximation that 2 electrons are contributing for each He atom. Using only the neutrals, a total

ionization source of $1.6*10^{21}$ particles/s is found and a particle confinement time of 127ms is computed. An uncertainty of +-100% is estimated primarily due to the sensitivity of these calculations to the edge electron temperature. This value for Tp is reasonable for a low density, low current He plasma.

Acknowledgements: This work is part of the CEA-FRANCE/DOE-USA Collaboration and is partially supported under U.S. DOE contract No ACO5-84OR21400. The authors wish to thank Dr Drawin and Dr M.H. Achard for many helpfull discussions.

References:

1 P. Deschamps et al., J. Nucl. Mat., 128 et 129, 38(1984)
2 L. Johnson and E. Hinnov, J. Quant. Spect. Rad. T. 13, 333(1973)
3 H.W. Drawin,F. Emard,Report EUR-CEA-FC-534, Fontenay-Roses(1970)
4 H.W. Drawin, F. Emard, Physica 85 C 333 (1977)
5 J. Hogan, J. Nucl. Mat., 111-112, 413 (1982)
6 JET-P(85)31 Jet-Report-APS Nov(1985)
7 K.L. Bell and al. J. Phys. Chemi. Ref. Data, Vol12, No4 (1983)
8 R. Janev and W. Langer, Springer Verlag, (1987)

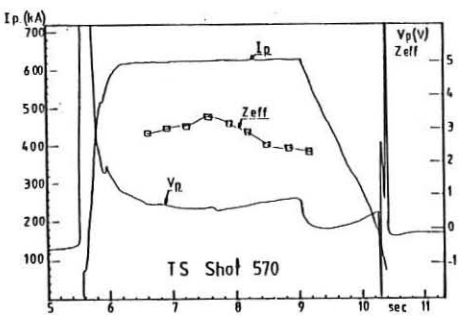

fig. 1

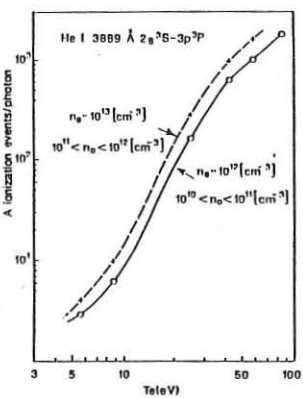

fig. 3

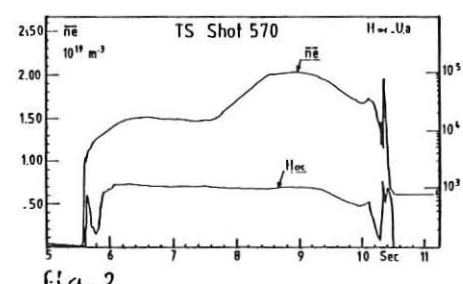

fig. 2

Ergodic Divertor Experiments on Tore Supra

T. E. EVANS[◊], A. GROSMAN, H. CAPES, A. SAMAIN, Ph. GHENDRIH

Departement De Recherches Sur La Fusion Controlee
Association EURATOM-CEA
CEN-Cadarache, St. Paul-Lez-Durance, France

1. INTRODUCTION AND DESCRIPTION OF THE EXPERIMENTAL HARDWARE The ergodic divertor (ed) configuration is expected to provide substantial benefits in terms of controlling edge parameters and impurity concentrations in high temperature fusion plasmas. Although previous ed experiments [1,2] have provided stimulating results the Tore Supra ed program is uniquely positioned to yield significantly new physics with which to advance our understanding of plasma surface interactions and their relationship to the overall confinement properties of tokamaks plasmas. Tore Supra is a relatively large machine (i.e., R_o= 2.37 m, a= 0.8 m, B_T = 4.5 T) with a long plasma pulse and high power auxiliary heating. The ed coils are mounted inside the vacuum vessel (6 coils equally spaced toroidally) and are equipped with neutralizer plates attached to pumping channels with getter pumps for exhausting particles [3] and heat. By matching the angle of the field lines on the resonant surface they create a magnetic island structure centered at higher poloidal mode numbers than in previous experiments. An ed layer, consisting of several overlapping island chains, is produced within a well localized radial interval ≈ 10 cm at the edge. These elements provide flexibility for modifying the boundary conditions and interactions with a variety of plasma facing components (pump limiters, RF couplers,...). In addition to edge studies, the ergodic layer provides an opportunity for MHD and equilibrium experiments (due to modifications in the current profile and boundary conditions) and for runaway electron confinement experiments.

The technical specifications for the ed coils have been described by Lipa et al., [4]. The key physics points are that the coils produce a relatively broad toroidal (n) and poloidal (m) Fourier mode spectrum (e.g., a full poloidal width at half maximum of ±0.15 m_o, where m_o is the fundamental poloidal mode number) and can be phased such that m/n resonant surfaces occur at several q values between 1.33 and 8. The width of the ergodic layer as well as the degree of stochasticity in the layer can be varied by changing either the ed current or the radial position of the m_o/n_o resonant surface with respect to the coils. The overlap or Chirikov (δ_c) parameter may be varied from 0 to approximately 1.7-2.0 with a maximum ed coil current of 45 kA.

2. THEORETICAL HARDWARE AND BACKGROUND MODELS Plasma effects in the ergodic layer are calculated in terms of the usual magnetic diffusion coefficient ($D_M=L_c\sum_{m,n}\delta(m-n/q)(b_{m,n}/B_T)^2$, where $b_{m,n}$ is the resonant part of the imposed perturbation field and L_c is the correlation length) with a quasilinear model. Such calculations have been validated via a 3-D variational method [5]. Additional analytic and numerical ed models, including several types of field line tracing/mapping codes, and a modified Grad-Shafranov (G-S) equation are used to guide the experiments. These are briefly discussed here with respect to their implications on various aspects of the experimental program. In particular, the numerical codes are used to evaluate the vacuum magnetic field structure in the ergodic layer as a function of the coil current, direction, and magnitude for various plasma q(r) profiles while the modified G-S equation is used for MHD stability and equilibrium studies with an ergodic layer. The line tracing and mapping codes give us a surface image of the magnetic patterns on the walls and plasma facing components. This provides an important link between data obtained with visual and infrared imaging diagnostics and the 3 dimensional field structure in the ergodic layer.

The field line tracing codes are also used to evaluate the spectral properties of the ed coils and to study the size, orientation, and relative coherence of island chains on each resonant surface as well as for the computation of exact field line trajectories to any boundary point. For instance, in one case, a tracing code, has been used to follow field lines started at the r=74.45 cm surface for a distance of 200 meters. The result show that, given 400 initial points, 36% hit the midplane pump limiter. Of this, about 4% enter the limiter throat, 31% hit the leading edge of the limiter blade, and 1% hit the face of the limiter positioned at r=74.5 cm [6].

Global MHD stability and equilibrium properties are also an important consideration for the planning of the ed experiments, especially with respect to ideal kink modes and resistive tearing modes as the current profile is reconfigured during the formation of the ergodic layer. A modified Grad-Shafranov model, in which an exponential term is used to include changes in the boundary conditions, is employed to study discharge equilibrium properties with ed layer effects included. This equation is known to exhibit bifurcated solutions [7] indicating that the introduction of the ed layer may trigger a switch between two possible current profiles. If these solutions prove to be stable, we may find that one profile is highly peaked (giving a q significantly less than 1 on axis) while the other is relatively flat similar to those observed during L and H-mode discharges. In addition, the model may be used to determine a parametric condition for the loss of toroidal equilibrium. A stability parameter applicable to the ed geometry includes changes in the effective plasma radius with the introduction of the ergodic layer.

3. ERGODIC DIVERTOR PARTICLE CONFINEMENT TIME MODEL An essential part of the ed experiments is to determine the effects of stochastic fields on the behavior of heat and particle transport (especially impurities) to the machine walls and plasma facing components. Thus an experimental figure of merit $\Xi = \delta_c/\tau_p^{ed}$, where τ_p^{ed} the ed layer particle confinement time:

$$\tau_p^{ed} = \frac{N^{ed}}{\frac{2S_a\Delta}{a^2}\int_b^a \mathbb{S}\, x\, dx} \approx \frac{N^{ed}}{\frac{2S_a\Delta}{a}\int_b^a \mathbb{S}\, dx},$$

provides a useful measure for quantifying the ergodic divertor performance. In this form τ_p^{ed} is easily evaluated when it is known the source term, $\mathbb{S} = n_o n_e \langle\sigma v_e\rangle_{ion}$, is localized within the ed layer. Under this assumption the $H\alpha$ (λ = 6563 Å line) intensity ($I\alpha$) provides a direct measure of $\int_b^a \mathbb{S}\, dx$ where $I\alpha$ is simply expressed as the ratio of $\langle\sigma v_e\rangle_{exc}$ to $\langle\sigma v_e\rangle_{ion}$ times $\Gamma_o B_{32}(4\pi)^{-1}$ and B_{32} is the branching ratio from the excited state to either the n_2 or n_1 ground state. N^{ed} (the number of particles in the ed layer) is determined by density profile measurements. The source localization assumption is justified if the density and temperature in the ed layer are high enough that the ionization mean free path (λ_o) of the neutral flux from the walls satisfies $\lambda_o < \Delta$ where Δ=a-b is the width of the ed layer. For low ed layer density or temperature the denominator may be replaced with an expression of the form $S_a\,[\bar{R}\Gamma_a + \Gamma_{ext}][1 - (S_b/S_a)\,\exp\{-\int_b^a (n_e\langle\sigma v_e\rangle_{ion}/v_o)\,dx\}$, where Γ_{ext} is an externally imposed flux and $\bar{R}$ is the recycling coefficient. The exponential attenuation factor depends, in the slab approximation, primarily on the electron density profile across the ed layer (located with its outside edge at r=a) and the ratio of the surface areas (S_b,S_a) on each side of the cylindrical ed layer. Thus it is necessary to measure the n_e profile and the neutral particle flux, $\Gamma_o = \bar{R}\Gamma_a$, through surface r=a to obtain τ_p^{ed}. The same approach may be developed for impurity transport studies and correlated with perturbation experiments such as: gas and metal impurity injections experiments. Gas puff, laser blow-off, or pellet injection hardware on Tore Supra provide the tools for these experiments. Finally, this approach can be used to quantify runaway electron confinement with an ed layer. The high energy electrons provide a method of isolating parallel transport properties from perpendicular transport more typical of the heavy ions.

4. IMPURITY TRANSPORT AND CONTROL The dynamics and production of impurities with an ed layer is a key technical questions to be

addressed in the Tore Supra experiments. Initially experiments will study transport, using the models described above. The second goal is to study production. Therefore, it is essential that we test the hypothesis that a cold, high density layer, forming near the wall, will radiate strongly and cool the outflowing plasma particles before they hit the facing components. If achieved, this will reduce sputtering losses from the walls and lower the concentration of high-Z impurity throughout discharge. Diagnostics designed specifically for these studies have been implemented on Tore Supra. Finally, the drag effect [5] is believed to be important for sweeping impurities out of the discharge and will be studied in detail. The ed layer model given in section 3 and a heat transport model as in ref. [5] are used to develop a physical understanding of impurity transport and production. These will ultimately be linked to more complicated models for impurity transport and production with an ergodic layer but first experimental data must be acquired and the basic models tested.

5. SUMMARY The Tore Supra ergodic divertor program will concentrate on particle confinement and impurity control experiments during a first series of experiments. Numerical and analytical models are producing results which are useful for guiding the experiments and which will be used to analyze the measurements. There are a wide variety of heat and particle transport experiments underway and MHD studies will follow shortly. The results from these programs will provide a more complete assessment of ergodic divertor benefits for high temperature, long pulse fusion reactor plasmas and will yield new physical insight into the complex domain of plasma surface interactions.

6. ACKNOWLEDGEMENTS The Tore Supra ergodic divertor program is part of the CEA-FRANCE/DOE-USA Collaboration and is partially supported under U.S. DoE Contract No. DE-AC03-84ER51044

References

[1] McCool, S. C., et al., "Electron Thermal Confinement Studies With Applied Resonant Fields on TEXT", to appear in Nucl. Fusion.
[2] Ohyabu, N., and deGrassie, J. S., Nucl. Fusion 27 (1987) 2171.
[3] Ghendrih, Ph., et al., "Edge Plasma Control: Particle Channelling in Tore Supra Pump Limiter and Ergodic Divertor", to appear in J. Nucl. Mater.
[4] Lipa, M., et al., Proceedings of the 15th Symposium on Fusion Technology, Utrecht, The Netherlands, September 19-23, 1988.
[5] Samain, A., et al., J. Nucl. Mater. 111-112 (1982) 408.
[6] This calculation was carried out by LaHaye and Bard using a newly developed, high efficiency, field line tracing algorithm.
[7] Hsu, J. A. and Chu, M. S., Phys. Fluids 30 (4) 1221; and Marder, B. and Weitzner, H., Plasma Physics 12 (1970) 435.

◊Permanent address: General Atomics, P.O. Box 85608, San Diego, Ca., U.S.A.

THERMODESORPTION OF GRAPHITE EXPOSED TO A DEUTERIUM PLASMA

E. Gauthier, J. Bardon, J.P. Palmari and A. Grosman*

CRMC2-CNRS - Campus de Luminy - Case 913
13288 Marseille Cedex 9, France

*C.E.N. Cadarache - Association Euratom-CEA sur la fusion
13118 Saint Paul-lez-Durance

1. INTRODUCTION

It became more and more evident during the last years that the total gas balance in the fusion machines was largely dependent on the recycling properties of the graphite which is the principal component of the inner wall.

Numerous studies, reviewed e.g. in [1,2], have been done to increase the physical understanding of phenomena like retention, detrapping and diffusion of the hydrogen isotopes, which controls the recycling behaviour of the graphite.

If the graphite implanted by energetic ion beam has been extensively studied, less work was made on thermally exposed graphite [3-5] and very little information is available for low energy high density plasma exposure typical of the inner wall conditions in the Tokamaks.

Therefore, we describe in this paper the first results that we have obtained by implanting pyrolytic and polycrystalline samples of graphite with a Deuterium plasma source. The density of the plasma was 5.10^{12} cm^{-3} and the electronic temperature was T_e = 15 eV. After the plasma exposure, the samples were analysed by thermodesorption with different heating rates.

The thermodesorption spectra show a rather complex structure with peak desorption at lower temperature than those obtained by the authors (see e.g. [6] and ref. therein) which used energetic ion beam implant but comparable to the experiments [5] made with graphite thermally exposed to hydrogen isotopes.

The last part of the paper gives the results of the comparison between the experimental data and numerical simulation of detrapping processes and diffusion processes.

We show that the principal features of our desorption data can be explained as well by diffusion processes as by detrapping and recombination mechanism, with in the two cases activation energies between 0.2 and 1.5 eV.

2. EXPERIMENTAL

The experimental set-up will be described elsewhere with more details. It involves one plasma source and one thermodesorption device.The graphite sample can be moved without breaking of vacuum from the plasma source to the analysis apparatus.

2.1. Plasma source

It is a duopigatron source [7] with an anticathode made of polycrystalline graphite. The electronic temperature was set at 15 eV and the density is 5.10^{12} cm^{-3}.

In these conditions, the electrically floating sample is implanted by Deuterium ions of about 45 eV and with a flux of $\simeq 10^{18}$ s^{-1}.

The plasma density and temperature have been measured by a double Langmuir probe at different positions and checked by the value of the sheath potential between the anode and the anticathode. We have also verified the results by the ratio of H_α and H_γ lines.

2.2. Thermodesorption apparatus

The analysis vessel has a base pressure of 1.10^{-10} torr. Thermodesorption spectra are

recorded from a quadrupole mass spectrometer. The sample is heated by electronic bombardment on the side not exposed to the plasma. Temperature is measured by a thermocouple inserted inside the sample. The heating ramp, numerically driven, is perfectly rectilinear and his rate may be changed from 0 to 2.5 Kelvin s^{-1}.

The temperatures obtained were checked by an infrared pyrometer. In thermodesorption experiments, the temperature uniformity across the sample is essential. It was inspected by Infrared Camera and color analysis did not show noticeable temperature variation.

2.3. Samples

The samples were made with Carbone-Lorraine 5890PT (as used for the Tore Supra first wall) and pyrolytic graphite from Union Carbide. Dimensions are 11x11x2 mm. They are mounted on a molybdenum support. The plasma exposure is done by an aperture of 9 mm diameter in the anticathode.

Two series of experiments were made. The first one with the sample directly screwed onto the support ; the second one with the sample electrically and thermally isolated from the support by little ceramic pieces.We have verified that for the second serie, the support did not degas during thermodesorption experiment by implanting a sample as usual and replacing it by another identical sample which had not been exposed to the plasma. Then, we proceeded a thermodesorption experiment during which the D_2 signal remained negligible. This fact rules out any influence of the support on the thermodesorption spectra.

3. RESULTS

A typical desorption spectrum is shown in Fig. 1 giving evidence for four peaks at less.

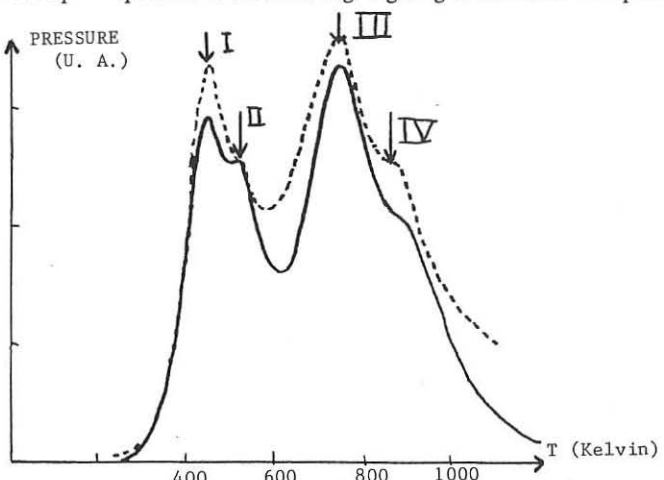

Fig.1 - - - Experimental desorption spectrum . Heating rate 1.5 Kelvin s^{-1}
——Numerical simulation of diffusion mechanism . Desorption energies : 1.3 , 1.05 , 0.73 , 0.60 eV . $I^2/D_0=10^{-6}$ s^{-1} . See text below .

Preliminary experiments with exposure time to the plasma from 0.4 s to 12 s have not shown differences in the amount of implanted Deuterium. That is coherent with the well-established [1] fact that graphite retains all the non reflected hydrogen until the saturation concentration is reached. However the observed height of the first peak is lower when a same fluence is obtained by one shot than by some shots separated by time intervals.

We suppose that the higher temperature rise of the sample for higher times of

continuous exposure is the reason for this lowering of this first peak at 420 Kelvin. This was confirmed by an identical lowering of the first peak when the initial temperature of the sample was 100 Kelvin above room temperature.

Series of desorption were made at heating rates of 0.5, 1, 1.5 and 2.5 Kelvin s^{-1}. The spectra are reproducible and the estimated positions of peaks are given in Table 1.

Heating rate	I	II	III	IV
0.5	410	480	690	820
1	430	500	720	840
1.5	444	510	750	860
2.5		520	765	895

Table I: Peak Temperatures(Kelvin) for different heating rates

As expected, the peak positions are shifted to higher temperatures when the heating rate is increased.

The experiments done with pyrolytic graphite have given the same results for the peak positions and the general features of the spectra with a lower first peak, due to a temperature rise during the bombardment more important for the less conducting pyrolytic graphite along the c axis.

4.DISCUSSION

With high energetic ion beam exposition [6], the thermodesorption spectra show structures with peak temperatures around 1100 Kelvin ; these structures are sometimes washed by the high rate of temperature rise. These experiments were, in most cases, interpreted by second order detrapping processes.

Our results are more similar to those of Atsumi and al. [5], where the interaction between graphite and deuterium was obtained by high temperature high pressure exposition of the graphite to the gas. They obtained structured spectra with peaks in the same range of temperature as our results. They have supposed that bulk and pore diffusion processes were the dominant mechanism of the desorption.

We have done two series of numerical simulation ; the first with a second order process (detrapping and recombination), the other one with a diffusion model.

In the first case, the pressure P(t) is given by

$$P(t) = \propto n^2(t) \exp(-E_d / kT(t)) \qquad (1)$$

where n is the number of implanted species, Ed the detrapping energy of activation, T the temperature and $\propto$ a coefficient proportional to the preexponential term of the detrapping process and dependent on the pumping rate and geometrical features of the device.

Then, if v is the heating rate, the peak temperature T_p is given by the relation

$$\frac{E_d}{kT_p^2} - \frac{2\,n(T_p)}{v} \propto \exp\left(-\frac{E_d}{kT_p}\right) = 0 \qquad (2)$$

which needs simple numerical computation to be solved.

In fact, thanks to the minor variation of $n(T_p)$ versus v, numerical trials gave same results for the peak temperature variation versus the heating rate with first and second order processes. We can therefore use the well-known first order result where the slope of the quantity Log T_p^2/v versus $1/T_p$ gives the activation energy. If the curves thus obtained are straight lines, it is a presumption of validity for the model. These curves are shown in Fig. 2 for the four peaks that we obtained.

Therefore Fig. 2 shows that our results can be explained by a detrapping model of first or second order with low activation energies of 0.7 eV, 0.51 eV, 0.43 eV, 0.25 eV.

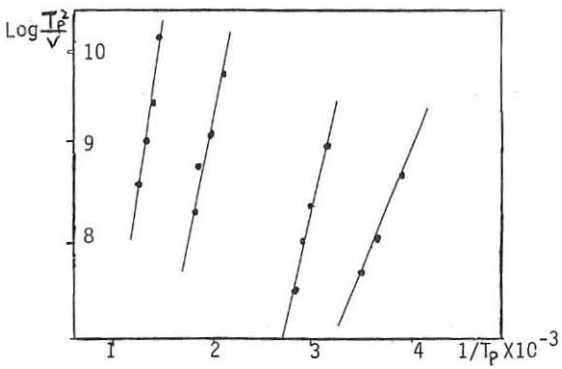

Fig.2 • Experimental and —— simulated values of Log T_p^2 / V for a detrapping mechanism of 0.7 , 0.5 , 0.43 , 0.25 eV activation energies . Heating rate in Kelvin min^{-1}.

We have also simulated a diffusion process with a simple model of an initial implanted slab of uniform concentration between x = 0 and x = l in a semi-infinite solid x>0.Such a simple initial concentration gives a good approximation of the experimental distribution observed by Causey and al.[3] in the low temperature exposure case. During the desorption, the surface concentration is set to zero.

The solution of this model is almost analytic(8), including only numerical computation for the change of time scale(9) to $I = \int_0^t D(t)\,dt$ and gives

$$P(t) = \frac{\alpha n_0 D}{4\sqrt{I}} \left(1 - \exp\left(-\frac{l^2}{4I}\right)\right)$$

Our results can be adequately described by such a model with activation energies of 1.3 eV, 1.05 eV, 0.73 eV, 0.60 eV and D_0= 1. $cm^2\ s^{-1}$ for an implantation length of 30 μm which compares with the results of Causey and al.(3).

Numerical simulation gives peaks with a tail at the left side for second order desorption and at the rightside for the diffusion mechanism, but the overlapping of the peaks prevents the use of the form of the spectra to take conclusions.

In conclusion, independent measurements of the diffusion coefficients seems to be necessary for a choice of one mechanism. We are actually working on preliminary results of incoherent quasielastic neutron scattering experiments and we hope that we shall obtain at less an upper limit for the diffusion coefficient.

BIBLIOGRAPHY

1 K.L. Wilson, W.L. Hsu; J. Nucl. Mater. 145-147 (1987) 121
2 W. Möller; J. Nucl. Mater. Proc. of 8th PSI , In press.
3 R. A. Causey, M.I.Baskes, K.L. Wilson; J.Vac.Sci. Technol.A 4, 3 (1986) 1189
4 H.D. Röhrig, P.G. Fischer, R. Hecker; J. Am. Ceram. Soc. 59 (1976) 316
5 H. Atsumi, S. Tokura, M. Miyake; J. Nucl. Mater. 155-157 (1988) 241
6 J. Roth, J. Bohdansky; Appl. Phys. Lett. 51, 13 (1987) 964
7 J.P. Grandchamp;Thesis, Paris Orsay 1982
8 H.S. Carslaw,J.C. Jaeger; Conduction of Heat in Solids,Oxford Clarendon Press,1959 p.59
9 J. Crank;The Mathematics of Diffusion, Oxford Clarendon Press, 1956 p.14

MAGNETIC FIELD STRUTURE AND TRANSPORT INDUCED BY THE ERGODIC DIVERTOR OF TORE SUPRA

A. Samain, Ph. Ghendrih, A. Grosman, H. Capes, T. Evans, J.P. Morera

Association EURATOM-CEA pour la Fusion Contrôlée
CEN Cadarache, F-13108 Saint Paul lez Durance, Cédex, France

Introduction

The problem of extracting large power fluxes at the edge of tokamak plasmas with tolerable production of impurities, as well as of improving the plasma pumping efficiency, may be alleviated if the plasma interacts with the wall with a large density, small temperature. Such a configuration should be obtained by magnetic connection between the hot plasma and the wall, if the parallel energy flux induces a temperature decrease along the flux lines, while the pressure nT tends to remain constant. This is achieved with axisymmetric divertors [1,2]. On Tore Supra, we have planned to test that possibility with the ergodic divertor [3], where the magnetic connection is due to a resonant magnetic pertubation which creates a stochastic layer between the hot plasma and the wall. The aim of this paper is to present the expected transport performances of the implemented device in the framework of the quasilinear theory.

Magnetic topology

The coils creating the magnetic pertubation consists of 6 identical modules 60° apart in the toroidal direction (fig.1). To take account of the toroidal effects, it is convenient to change the coordinates from the usual r, θ, φ, R, to a system r', θ', φ', R', where $\pi r'^2 B_0$ is the toroidal flux labelling each unperturbed magnetic surface, θ' and φ' being the intrinsic poloidal and toroidal coordinates which exhibit a constant $\nabla_{/\!/}$, and finally where the average length along flux lines per toroidal rotation is 2πR'. The perturbation of the trajectory of the flux lines, and generally of pure $v_{/\!/}$ particles, by a vector potential $\delta A_{/\!/}(r',\theta',\varphi')$ is then calculated as in the cylindrical case. This statement holds when an electric potential perturbation $U(r',\theta',\varphi')$ is present.

Fourier analysis of $\delta A_{/\!/}$ in θ', φ' produces a spectrum $\tilde{A}_{/\!/}(M,N)$. The wave number M along θ' is distributed in an interval 24 ± 5 at the plasma edge r'= 0.8m (M = 10 ± 2 at r'= 0.6m). The wave number N along φ' takes values : N=6, 12 or N=3, 9 according to whether parallel or opposit voltages are applied to successive modules. The predominant resonance occurs for q_{edge} = M/N = 4 (N=6) or 2.66 (N=9). For the case q_{edge} = 4 and N=6 the position of the resonance surfaces M/N = 24/6, 23/6, etc., are shown on fig.1. Figure 1 also displays the Chirikov parameter $2\delta_{isl}/d_{isl}$ where

$\delta_{isl} = (8\,\tilde{A}_{/\!/}(M,N)\ qR'/(B_o r' dq/qdr'))^{1/2}$ is half the island width, and d_{isl} is the radial distance between successive island chains. The island chains strongly overlap within the 0.1 m edge layer, the number of resonant surfaces being ~ 5, which is large enough to ensure a stochastic diffusion of the field lines. The quasilinear diffusion coefficient of the flux lines $D_{QL} = \sum_M 2\pi qR' \left| (M/r')(\tilde{A}_{/\!/}(M,N)/B_o) \right|^{1/2}$, on a given resonance surface M, is corrected to account for weak overlapping in the plasma core, yielding the effective value of the diffusion coefficient, D_{QLC}, shown on fig.2. Note the strong decrease towards the plasma center.

Heat conduction

A radial pertubation of the magnetic field allows a radial transport of energy through the parallel motion of the electrons. When the ergodic divertor is activated, the thermal diffusion coefficient χ_{erg} thus combines the stochastic transport process (D_{QLC}) and the parallel transport. In the plasma core, the latter is collisionless, and thus $\chi_{erg} = D_{QLC} \frac{3}{\sqrt{\pi}} n (2T/m_e)^{1/2}$. It is here essential that D_{QLC} vanishes towards the center so that the ergodic heat transport does not prevail over the actual turbulent heat transport ($\chi/n \sim 1\ m^2/s$). In the ergodic layer at temperature $\leqslant 100$ eV, a collisional regime applies. The heat conduction is then $\chi_{erg} = D_{QLC} (\chi_{/\!/}/qR)\ h$, where $\chi_{/\!/} = 2.10^{22} T_{ev}^{5/2} m^{-1} s^{-1}$, and where h is a correcting factor depending on $\mathrm{Log}(\chi_{/\!/}/\chi_{\perp})$ [4]. Values of $h = 0.3 \div 2$ are expected from 3D calculations [3]. The energy fluxe $\Phi_E \sim 0.1 \div 0.3$ MW/m^2 escaping from the plasma core should thus sustain a strong thermal gradient, $dT/dr \sim -\Phi_E/\chi_{erg}$, which is necessary to achieve a density accumulation at constant pressure.

Plasma convection

The ergodic layer will maintain a constant pression profile provided the radial convection has the form $\Gamma_{erg} = -D_{erg} \partial(nT)/T\partial r'$ with a large enough stochastic diffusion coefficient D_{erg}, namely $D_{erg} \gg D_{\perp}$, $D_{\perp}$ being the diffusion coefficient due to microturbulence. This is the case when the ED acts alone and the relation holds with $D_{erg} \sim D_{QLC}$. However when a self consistent electric field, i.e. a radial component $-\partial \bar{U}/\partial r'$ and a fluctuating component $-\vec{\nabla}(\delta U)$ is taken into account, the transverse electric drift motion contributes to Γ_{erg} and one expects the particle flux induced by the ergodic field lines to be modified. Since constant pressure is at the crux of the effects expected from the ergodic divertor it is important to characterize this change. The electric potential is such that there is no parallel electric current $J_{/\!/}$ carried by electrons, thus using the Braginskii coefficient β_o:

$$\rho J_{/\!/} e/T = -(\nabla_{/\!/} n)/n - e\,(\nabla_{/\!/} U)/T - \alpha\,(\nabla_{/\!/} T)/T = 0 \;;\; \alpha = 1 + \beta_e = 1.7 \div 2.5 \quad (3)$$

This expression is split into fluctuating ($\tilde{n}$, etc.) and non-fluctuating ($\bar{n}$, etc.) parts. In the quasilinear framework the plasma continuity and dynamical equation along the field lines are linearized and one obtains for each Fourier mode (M,N) :

$$-2nT\left[ik_{/\!/}\left(\frac{\tilde{n}}{n}+\frac{\tilde{T}}{T}\right)+ i\frac{k_\theta \tilde{A}}{B_o}\left(\frac{\partial \bar{n}}{n\partial r'}+\frac{\partial \bar{T}}{T\partial r'}\right)\right] - im_i n k_\theta \frac{\partial \bar{U}}{B_o \partial r'}\tilde{V}_{/\!/} - m_i n\,\gamma_v \tilde{V}_{/\!/} = 0 \quad (2a)$$

$$-ink_{/\!/}\tilde{V}_{/\!/} - i\frac{k_\theta}{B_o}\left(\frac{\partial \bar{U}}{\partial r'}\tilde{n} - \frac{\partial \bar{n}}{\partial r'}\tilde{U}\right) - \gamma_n \tilde{n} = 0 \quad (2b)$$

where $k_\theta = M/r'$, $k_{/\!/} = (N + M/q)/R'$, where m_i is the ion mass, and where the tilde symbols now means the Fourier components (M,N). The coefficients γ_v, γ_n are positive and reflect viscosity and density damping at small scale. They are assumed small. The quasilinear radial flux $\Gamma_{erg} = \langle n \frac{\delta B}{B} v_{/\!/} + \frac{\delta E \times B}{B^2} \delta n \rangle_{\theta,\varphi}$ is obtained from (3a,3b) in the form :

$$\Gamma_{erg} = -\sum_{M,N} \frac{ik_\theta n}{B_o}\left(\tilde{A}^*_{/\!/}\tilde{v}_{/\!/} - \tilde{U}^*\tilde{n}/n\right) + c.c. = -D_{erg}\frac{\partial(\bar{n}\,\bar{T})}{T\partial r'} \quad (3)$$

$$D_{erg} = \sum_{M,N,\xi=\pm 1} \pi V_i \delta(k_{/\!/} + \xi k^*_{/\!/}) \left|\left(k_{/\!/}\tilde{T}/(\partial \bar{T}/\partial r')\right) + \left(k_\theta \tilde{A}_{/\!/}/B_o\right)\right|^2 |\alpha\eta/(\alpha\eta+1)|^{1/2} \quad (4)$$

$\eta = \partial_r \mathrm{Log}(\bar{T})/\partial_r \mathrm{Log}(\bar{n}) \sim -1$; $k^*_{/\!/} = k_\theta \rho_i |\alpha\eta(\alpha\eta+1)|^{1/2} \partial \bar{n}/(n\partial r')$; $V_i = (2T/m_i)^{1/2}$
Equation (4) implies a dependence of Γ_{erg} on the pressure gradient. The perturbation $k_{/\!/}\tilde{T} + k_\theta(\tilde{A}_{/\!/}/B_o)\partial \bar{T}/\partial r'$ which drives the resonances is the derivative $\nabla_{/\!/} T$ along the stochastic flux lines. Neglecting $k_{/\!/}\tilde{T}$ yields $D_{erg} \sim D_{QL}$. However the actual values of $\nabla_{/\!/} T$ experience an attenuation and a radial localization on the resonant surfaces, which involve $\mathrm{Log}(\chi_{/\!/}/\chi_\perp)$.

Conclusion

We have performed a comprehensive quasilinear analysis of transport in stochastic fields, including the electric pertubation, which will be tested by the ergodic divertor experiments on Tore Supra.

References

[1] M. Keilhacker, Sov. J. Plasma. Physica, 9 (1983) 55.
[2] N. Ohyabu, J. Nucl. Fusion 24 (1984) 415.
[3] A. Samain, et al., J. Nucl. Mat., 128-129 (1984) 395.
[4] A.B. Rechester, M.N. Rosenbluth, Phys. Rev. Lett., 40 (1978) 38.

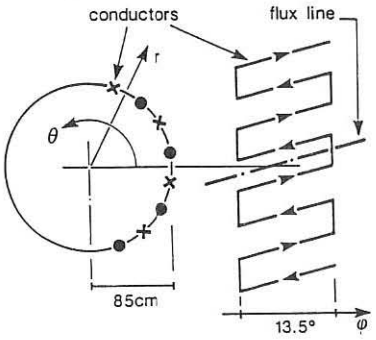

Figure 1 : Geometry of a coil module.

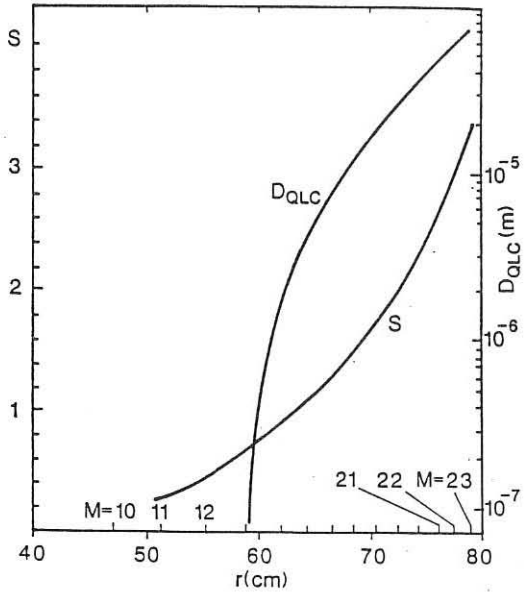

Figure 2 : Radial position of resonant magnetic surfaces M (N = 6, $q_{edge} = 4$), Chirikov parameter S, and quasilinear diffusion coefficient of flux lines D_{QLC} corrected to take account of small island overlapping towards the center.

NEUTRAL CONFINEMENT IN PUMP LIMITER WITH A THROAT

Ph. Ghendrih, A. Grosman, A. Samain, H. Capes, J.P. Morera

Association EURATOM-CEA sur la Fusion Contrôlée, CEN Cadarache,
F-13108 Saint Paul lez Durance, Cédex, France

1 Introduction

In quasi-steady tokomak operation, active control of recycling is achieved by pumping a fraction of the plasma outflux with pump limiters. In order to optimize the efficiency of this apparatus one can either act on the properties of the plasma SOL, or one can improve the particle collection with the help of the throat leading from the nozzle to the neutralizer plate [1,2,3]. This reduces the amount of escaping neutrals owing to plasma-neutral-sidewall interaction. In this paper, we derive the characteristic lengths of this effect, and we compute the neutral density build-up of pump limiters with a long throat (for a large ratio length L over the transverse dimension a).

2 Geometrical effect of the throat on neutral outflux

The basic throat effect is to reduce the amount of neutrals escaping from the pump limiter without bouncing on the sidewall. This effect depends on the ratio of the transverse velocity (thermal velocity v) to the parallel velocity u and on the ratio of the distance to the sidewall a_w over the distance to the nozzle d=L-x. For shifted Maxwellian distributions the probability P_G to reach the nozzle on a ballistic trajectory is :

$$P_G(u/v,a_w,d)=\frac{1}{2}\left[1+\mathrm{erf}\left(\frac{u}{v}\right)-\frac{\exp-\left((u/v)^2\dfrac{a_w^2/d^2}{1+a_w^2/d^2}\right)}{\left(1+a_w^2/d^2\right)^{1/2}}\left(1+\mathrm{erf}\left(\frac{u/v}{1+a_w^2/d^2}\right)\right)\right] \quad (1)$$

For current values of u/v, only the neutrals with a birth point close to the nozzle have to be considered, fig.1. One can then assume that $a_w \sim a/2$ and $u \sim 0$ for neutrals resulting from charge exchange (vanishing plasma average velocity at the nozzle) and that $a_w \sim a$ and $u \sim V_s$ (V_s is the sound velocity) for neutrals undergoing neutral-sidewall interaction. The flux of neutrals in the state of ballistic flight to the nozzle is then :

$$\Gamma_{bal}=\int_0^L dx\ \left(n_p\langle\sigma v\rangle_{CX}P_G(u/v\sim 0,a/2,L-x)+\nu_b P_G(V_s/v,a,L-x)\right)n_N(x) \quad (2)$$

where $n_p \langle\sigma v\rangle_{CX}$ is the rate of charge exchange, and where ν_b is the frequency of neutral-sidewall interaction. One finds that the neutrals on ballistic trajectories are created at a distance $\lesssim 2a$ from the nozzle. Hence Γ_{bal} can be neglected when the neutral density is vanishing at $x \lesssim L-2a$, i.e. when the plugging regime, described below, is reached on distances smaller than L-2a.

3 Plugging length, effect of plasma-neutral interaction

We are interested in the plugging regime where the neutral flux exhibits an exponential decay from the neutralizer to the nozzle with an e-folding length, the plugging length L_B, smaller than the throat length L. This length L_B has been derived precisely but assuming no neutral pumping [3]. A simple interpretation of this expression is that the neutrals experience a random walk process with a step L_s defined by the distance covered before a momentum change, i.e. $L_s^{-1}=L_{CX}^{-1}+L_p^{-1}$, where L_{CX} is the charge exchange mean free path and where L_p is the characteristic length of momentum (p) loss on the sidewall $L_p \sim p/\partial_x p$. The number of steps before ionization is L_I/L_s where L_I is the ionization mean free path. The plugging length $\tilde{L}_B$ is thus :

$$\tilde{L}_B^2=(L_I/L_s)L_s^2 \quad ; \quad \tilde{L}_B=(L_I L_p)^{1/2}(1+L_p/L_{CX})^{-1/2} \qquad (3)$$

To incorporate the effect of neutral pumping in the vicinity of the neutralizer we consider the continuity and mechanical equations :

$$n_N(x)u_N(x) + n_p(x)u_p(x) = P\, n_p(x=0)u_p(x=0) \; ; \; \partial_x(n_N u_N) = -\, n_p n_N \langle\sigma v\rangle_I \qquad (4a)$$

$$\frac{1}{m}\partial_x(n_N T_N + m n_N u_N^2) = -\, n_N n_p \langle\sigma v\rangle_I u_N + n_N n_p \langle\sigma v\rangle_{CX}(u_p-u_N) - n_N u_N (T_N/m)^{1/2}/L_p \qquad (4b)$$

where P is the pumped fraction of the plasma flux reaching the neutralizer plate. This set of equations accepts a solution with an exponential decay of the neutral density $\exp(-x/L_B)$ while the neutral temperature T_N and average velocity u_N, the plasma density n_p, temperature T_p, and average velocity u_p are constant. One thus obtains the following decay law and the plugging length :

$$\partial_{x^2} n_N - \partial_x n_N \frac{P}{L_{CX}}\left(\frac{2T_p}{T_N}\right)^{1/2}\left(\frac{n_p(x=0)}{n_p(x=L)}\right) - n_N \frac{(1+L_p/L_{CX})}{L_I L_p} = 0 \qquad (5a)$$

$$L_B^{-1} = -\, L_{XP}^{-1} + \left(\tilde{L}_B^{-2} + L_{XP}^{-2}\right)^{1/2} \; ; \; L_{XP} = \frac{2L_{CX}}{P(2T_p/T_N)^{1/2}(n_p(x=0)/n_p(x=L))} \qquad (5b)$$

This expression reduces to (3) when P=0 and increases with the pumping coefficient P. This increase is a consequence of the larger momentum exchange between neutrals and plasma due to the unbalanced particle

fluxes. Furthermore the plugging length depends on the plasma density decrease along the throat, which induces a nonlinear dependence on the pumping coefficient. The temperature T_N is derived from a balance between the energy gain by charge exchange and the energy loss on the sidewall hence $T_N/T_p \sim L_E/L_{CX}$, where L_E is the characteristic length of energy loss due to neutral-sidewall interaction ($L_E \sim L_p \sim a$ is the smallest length scale). At first order in P, one then finds taking $n_p(0)/n_p(L) \sim 1/3$ [3] :

$$L_B = \tilde{L}_B \left(1 + \frac{P}{3\sqrt{2}} \left(\frac{L_p L_I}{L_E L_{CX}} \right)^{1/2} \right) \qquad (6)$$

4 Neutral density build-up

The neutral density build-up at the neutralizer, derived in [3], can be interpreted in terms of a balance between the pressure gradient and the momentum loss on the sidewalls.

$$\partial_x (n_N T_N) \sim \frac{n_N(0) T_N(0)}{L_B} \sim \frac{m\, n_N(0) u_N(0)}{\tau} \quad ; \quad n_N(0) u_N(0) \sim n_p(0) u_p(0) \qquad (7)$$

The time scale of neutral momentum loss is $\tau = L_p/(T_N/m)^{1/2}$, which yields the approximate value of the neutral density at the neutralizer plate :

$$n_N(0) \sim \frac{\sqrt{2}}{3} \left(\frac{L_I L_E}{L_{CX} L_p} \right)^{1/2} \frac{T_p}{T_N(0)} \, Q \Big/ \left(\gamma T_p (T_p/m)^{1/2} \right) \qquad (8)$$

Here the SOL is determined by the plasma temperature and the available energy flux $Q \sim \gamma\, n_p (T_p/m)^{1/2} T_p$. The compression for both open and closed configuration are displayed on fig.2. Two domains of improved efficiency of closed configuration with respect to open configuration are found : one at low temperature $T_p \lesssim 10$ eV, yielding the highest neutral build-up and one at high temperature $T_p \gtrsim 100$ eV.

5 Conclusion

In this paper we show that pump limiters with a long throat can be operated in the plugging regime which strongly enhances the neutral density build-up, especially at low plasma SOL temperature. The efficiency of the apparatus should thus be increased in cold and dense edge plasmas.

References :

[1] R. W. Conn, J. Nucl. Mat., 128-129, (1984) 407.

[2] Ph. Ghendrih, A. Samain, A. Grosman et al., "Edge PLasma Control : Particle channeling in Tore Supra Pump Limiter and Ergodic Divertor", 8th Conf. on PSI in Cont. Fus. Devices, Jülich 1988, to be published in J. Nucl. Mat.

[3] Ph. Ghendrih, A. Grosman, A. Samain et al., "Plugging Regime in the Pump Limiter Throat", to be published in Nucl. Fusion.

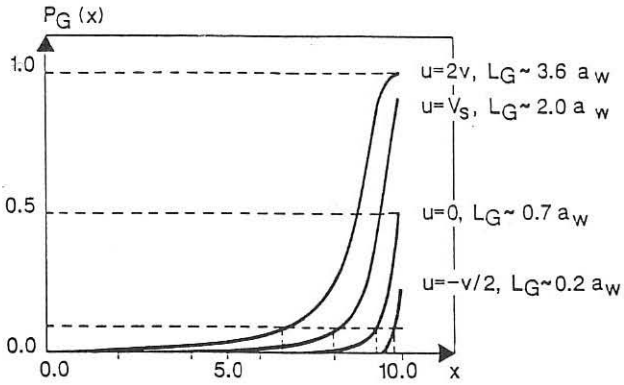

Figure 1 : The escape probability via ballistic trajectories to the nozzle for neutrals created at x with average velocity u and thermal velocity v. L_G is the characteristic length such that $P_G(L-L_G)=0.1$ ($L = 10\ a_w$)

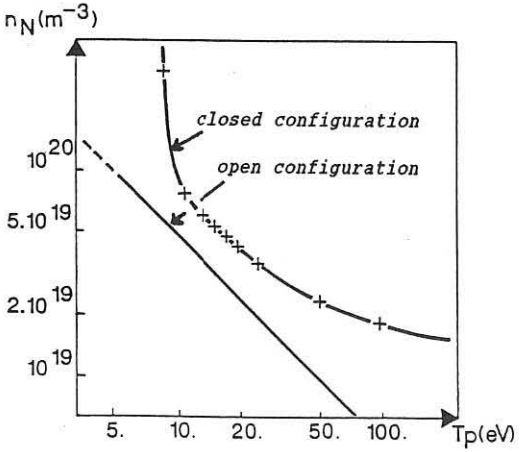

Figure 2 : Neutral density at the neutralizer plate at given heat flux flowing to the limiter, here $Q=10MW/m^2$, as a function of the plasma SOL temperature.

BORON FLUXES IN THE SCRAPE-OFF LAYER OF TEXTOR FOLLOWING BORONIZATION.

H. Bergsåker, B. Emmoth, P. Wienhold* and M. Rubel**.

Manne Siegbahn Institute of Physics, S-104 05 Stockholm, Sweden. * Institut für Plasmaphysik, KFA, POB 1913, D-5170 Jülich, FRG. ** Space Research Centre, Polish Academy of Sciences, 01-237 Warszawa, Poland.

1. Introduction

The Stockholm-TEXTOR probe has previously been used to study fluxes of metal impurity ions in the scrape-off layer at TEXTOR with various conditions of operation (with poloidal or toroidal limiters, with all-metal machine, carbonized walls and all-carbon machine, i.e. with graphite limiters and carbonized walls). The carbon redeposition at surfaces in the scrape-off layer has also been studied, and attempts have been made to distinguish the contribution of molecular species arriving from the wall to the amount of carbon in the SOL /1/.

In spring 1988, TEXTOR was operated with liner and limiters covered with a plasma deposited layer of boron carbide /2/. The objective of these experiments was to reduce impurity release by chemical erosion /3/, and to achieve gettering of oxygen by boron.

This paper reports on the flux of boron in the scrape-off layer shortly after boronization, and how it scales with main plasma parameters. The experimental procedure is described in some detail, and its capacity is assessed.

2. Experimental

TEXTOR was boronized on the 7:th of March 1988, and the collector probe was operated following this conditioning on the 8:th, 9:th 10:th and 15:th of March. The probe consists of a rotatable cylindrical collector which is contained in a housing with slit apertures. Ions which enter through the apertures stick to the collector surface, and the cylinder is removed afterwards and brought to an accelerator laboratory for ion beam analysis. The areal density of boron at the probe surface is determined using the $^{11}B(p,\alpha)^{8}Be$ nuclear reaction /4/. The sticking probability for medium-Z metal ions impinging on low-Z surfaces has been shown to be very high. The sticking of boron ions, e.g. at graphite surfaces remains to be investigated separately; it will be implicitly assumed below that this probability is close to unity. Any re-erosion of deposited material will also be neglected, since the collection takes place at least 20 mm outside the last closed flux surface. More information about the nature of the deposited layers is given in /5/.

The sensitivity of the collector probe method in terms of detectable boron fluxes can be estimated in the following way: The probe should not be too large if it is not to disturb the plasma in an unacceptable way. The Stockholm-TEXTOR probe carries collector cylinders with 24 mm radius. The slit aperture has to be wide enough to allow gyrating ions to go through with high probability of transmission /6/and to be

compatible with the spatial resolution of the analysis technique. Typically, the slit width 2 mm is used. The requirement that at least one 4 s discharge should be recorded on a full rotation with 2 mm wide slit aperture implies that the time resolution, or exposure time is $\tau > 0.05$ s. The probe can also be kept fixed and collect boron throughout one or more complete discharges, but usually it is difficult to have more than $\simeq 10$ identical shots. Consequently $\tau \leq 40$ s. The cross section of the $^{11}B(p,\alpha)^8Be$ reaction is about 100 mb/sr at 660 keV p /4/, and α-particles are detected, with essentially no background, using a particle detector with $\simeq 9$ μm mylar foil in front of it to protect from backscattered protons. The detector solid angle is typically $\Omega \approx 10^{-2}$ sr. No significant thermal or ion induced release of boron was observed when graphite or thin Al foil collectors were analysed with 6 $\mu A/cm^2$ proton beam. With 180 nA proton beam on a 2 mm wide spot, and the given solid angle and cross section, the areal density $\Phi_B \cdot \tau = 2.5 \cdot 10^{15}$ B/cm^2 can be detected in 3 minutes analysis time per point, with 5 % statistical accuracy. With time resolution $\tau = 0.05$ s the flux density $\Phi_B = 5 \cdot 10^{16}$ cm^{-2} s^{-1} can be detected in this way, while if $\tau = 40$ s, then $\Phi_B = 6 \cdot 10^{13}$ cm^{-2} s^{-1} can be measured accurately.

On the 8:th of March the probe was exposed to 18 of the shots 32017 - 32053, in a time-resolved way but with all 18 shots overlaid on the same collector area.The toroidal limiter ALT II was used at minor radius 460 mm. On the 9:th the probe was exposed to shots 32079, 32080, 32083, 32084, 32108 and to the eight overlaid shots 32123-32130. The toroidal limiter was still used at a=460. On the 10:th the probe was exposed to shots 32144 and 32147, with ICRF heating. This time the poloidal limiters were used to define the plasma edge at a=460. On the 15:th the probe was exposed to shots 32209, 32215, 32219, to eight shots from 32224 to 32232, and to 14 other shots between 32202 and 32241. TEXTOR was operated with ALT II at a=440 mm. The probe was also exposed to shot 32243, with ALT II at 460. The probe was operated with time resolution/exposure time rangeing from $\tau = 0.27$ s to $\tau = 34$ s. The collector material was graphite, except 8/3 when it was Al foil.

3. Results and discussion

Figure 1 shows two examples of the time dependence of boron fluxes in the scrape-off layer. Shot 32080 is an ohmic discharge. The boron flux levels off during flat top but starts increasing again during current ramp down. In shot 32144 the boron flux increases drastically during the ICRH pulse, but then drops quickly off again, though with a short time delay, when RF heating is finished. Figure 2 shows typical examples of radial distributions. The distributions are piecewise exponential. On the ion drift side the e-folding length was very constant, $\lambda_i = 18.9 \pm 2.3$ mm. The connection length on that side to the toroidal belt limiter is 1.4 m. Assuming $T_e \approx 20$ eV, a diffusion constant

$$D_\perp = 2\frac{\lambda^2}{L} \cdot \sqrt{\frac{2kT_e}{m}} \approx 10 \quad m^2/s$$

can be derived. The connection length on the electron drift side is much larger, approximately 40 m, and the e-folding length is often larger on this side: 70 – 120 mm, close to the plasma edge. Usually a breakpoint is observed in the radial distribution on the electron drift side, corresponding to shadowing from secondary limiters or the antenna

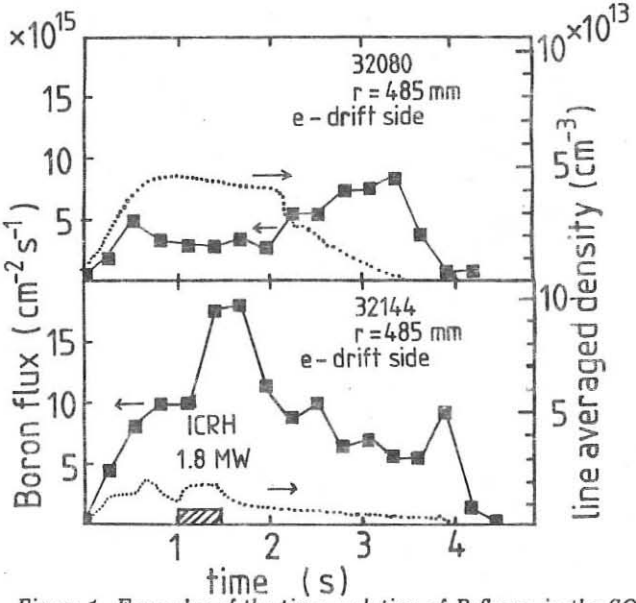

Figure 1. Examples of the time evolution of B-fluxes in the SOL.

protection limiters. There is a tendency for the λ on the electron drift side to decrease during ICRH in shots 32144 and 32147. This is unexpected, since the scrape-off width in tokamaks is usually found to increase with auxilliary heating power. For comparison from shot to shot, the fluxes are extrapolated to a reference point 20 mm outside the last closed flux surface during ohmic flat top. In all cases this point is only shadowed by one limiter, usually the ALT II. No obvious decrease from day to day after the boronization was observed, but the fluxes at the reference point clearly increased with decreasing central electron density, as shown in figure 3. Roughly $\Phi_B(a+20) \propto n_e(0)^{-1}$.

A similar behaviour of impurity fluxes with the central density has been observed earlier for metal impurities /7 /, and has been attributed to the energy dependence of physical sputtering at the limiters. It also agrees with spectroscopic observations /2/. Taken alone, the fact that the impurity content in the plasma, or the influx of impurities, increases with decreasing plasma density (and consequently with increasing edge electron temperature) is not sufficient to conclude anything about the primary source of impurities. It is conceivable that such a dependence may also occur as a result of changes in transport properties of the scrape-off layer, such as improved screening of impurities coming from the wall due to increased density in the SOL. The present investigation of fluxes far out in the scrape-off layer excludes this second possibility and suggests that boron is released mainly by physical sputtering at the limiters, in the same way as metal impurities.

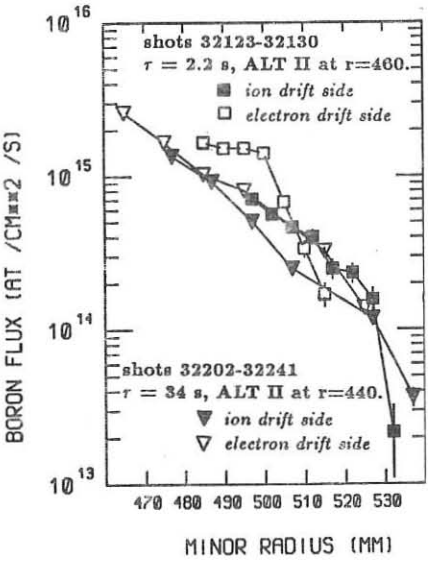

Figure 2. Radial distributions.

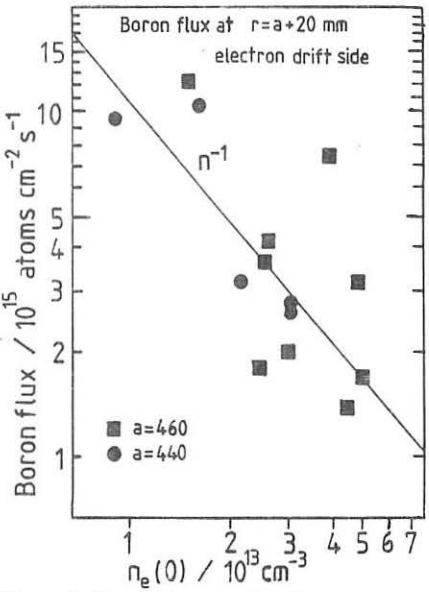

Figure 3. Boron flux vs. density.

As a conclusion, it appears that boron fluxes in the scrape-off layer can be conveniently and sensitively studied with surface probes. The essential problems of sticking and reerosion of boron at graphite surfaces have not been adressed here. They deserve further investigation, and experiments to this end are being prepared.

Boron deposition rates in the scrape-off layer during the week following boronization increased with decreasing central plasma density, similar to metals. This is probably due to the energy dependence of physical sputtering at the limiters. The dependence was roughly $\Phi_B = const. \cdot n_e(0)^{-1}$ in the range $1\text{–}5 \cdot 10^{13}$ cm^{-3}.

References

/1/ P. Wienhold et al. P. 14-th Eur.Conf.Cont.Fus.Plasm.Phys. Madrid 1987 p. 782.
/2/ J. Winter, H.G. Esser, L. Könen et al. To be pub. J.Nucl.Mater.
/3/ S. Veprek, S. Rambert, M. Heintze et al. To be pub. J.Nucl.Mater.
/4/ E. Ligeon and A. Bontemps, J. Rad. Chem. 12(1972)335.
/5/ P. Wienhold, B. Emmoth, H. Bergsåker et al., These proc.
/6/ H. Sätherblom, Nucl. Inst. Meth. A252(1986)107.
/7/ H. Sätherblom, H. Bergsåker, M. Braun et al., Physica Scripta 38(1988)150.

LOW-FREQUENCY FLUCTUATIONS OF THE EDGE PLASMA DENSITY AND POTENTIAL UNDER ICR HEATING IN THE URAGAN-3 TORSATRON

V.V.Chechkin, L.I.Grigor'eva, N.I.Nazarov, I.B.Pinos, V.V.Plyusnin, A.F.Shtan', S.I.Solodovchenko, V.S.Taran, A.Yu.Voloshko

Kharkov Institute of Physics and Technology, the Ukrainian SSR Academy of Sciences, 310108 Kharkov, USSR

Introduction. A high level of low-frequency (LF), $\omega \ll \omega_{Bi}$, density and potential fluctuations together with the violation of the electron response adiabaticity in their behaviour in the edge plasma of many tokamaks [1] suggest that some other (i.e., not associated with the pressure gradient) free energy sources sustaining the fluctuations may exist. Particularly, if RF fields are used to heat the plasma, then LF oscillations can arise due to the parametric decay of the pump waves [2]. Some instabilities of this kind have recently been observed for $\omega_0 = 2\omega_{Bi}$ RF heating of the plasma in the ASDEX [3] and TEXTOR [4] tokamaks. In this connection, it is of interest to analyse some characteristics of the LF electrostatic fluctuations which are observed in the edge plasma during plasma production and heating under ICR conditions in the URAGAN-3 (U-3)torsatron.

Experimental conditions. The U-3 machine (Fig.1) is an $l = 3$ torsatron with 9 periods of the helical magnetic field. $R = 100$ cm; the inner radius of the helical winding casings (1,2,3) is 19 cm; the average radius of the outmost closed magnetic surface is $\bar{a} \simeq 9$ cm; $\iota(0) = 0.18$; $\iota(\bar{a}) = 0.4$. The hydrogen plasma [$\bar{n} \sim (2\text{-}4)\times10^{12}$cm^{-3}; $T_i(0) \sim 600\text{-}900$ eV; $T_e(0) \sim 250$eV] was produced by an RF discharge with ion cyclotron wave excitation at $\omega_0/2\pi = 5.25$ MHz, $\omega_0/\omega_{Bi}(0) \simeq 0.8$. An RF power of $\lesssim 300$ kW in the $\lesssim 50$ ms pulse was coupled to the plasma via one of the two frame-like antennae without the Faraday shield (K-1 and K-2 in Fig.1). The antennae were installed at a minor radius $r = 16$ cm on the low field side. The edge plasma density ($r \gtrsim 10$ cm) was several units 10^{11}cm^{-3}, $T_e \sim 40$ eV. LF fluctuations were detected by capacitive and Langmuir probes which were introduced into the plasma in the lower half-circle of the torus cross-section (4) (see Fig.1,b). A set of electrostatic analysers (I-V in Fig.1,b) was used to detect a charged particle flux onto a surface intersected by the divertor magnetic flux. All probe signals were subjected by correlation analysis.

Experimental results and discussion. The plasma generation and heating are accompanied by intense density ($\tilde{n}/n \gtrsim 0.1$) and potential ($e\tilde{\Phi}/T_e \sim 1$) fluctuations in the edge plasma in the frequency range from several units to ~100kHz (Figs.2 and 3). The fluctuation amplitude distribution in the torus cross section (4) at a steady stage of the discharge is given in Fig.4. Radial distributions of the plasma density and its fluctuations as measured along the major radius near the cross section (4) are shown in Fig.5. The intensity peaks of the fluctuations fall into the section regions between the outmost flux surface and helical winding casings, where the steepest radial drop in the density occurs. Reasoning from the data in Figs.2-5, the fluctuations observed should be treated as an evolution of density gradient driven drift waves. The intensity peaks in the spectrum (Fig.3) correspond within the accuracy of the probe signal processing to the azimuthal mode numbers $m = 3,6,9,\ldots$. The lowest frequency excited ($m = 1$) lies within 3.0-4.5kHz for various samples and is close to the $\omega^* = (1/\bar{a})(cT_e/eB)(d\ln n/dr)$ value estimated from Figs.4 and 5. The highest fluctuation intensity (10-30 kHz) belongs to the $m = 3;6$ modes. The lowest parallel wave number $k_\parallel$ of the fluctuations was estimated from cross-phase spectra of the probe signals with the rotational transform taken into account. The $k_\parallel$ value is $\sim 0{,}06$ rad/cm and ~ 0.4 rad/cm for the lower and upper limits of the fluctuation frequency range respectively. From ion energy measurements by the retarding potential technique it follows that the ion temperature of the edge plasma is $\gtrsim 100$ eV. Thus, $\omega < k_\parallel v_{Ti}$ throughout the fluctuation frequency domain, i.e. a strong ion Landau damping should take place. The increasing fluctuation level with RF power and a fast drop of this level ($t < 100\,\mu s$, see Fig.2) after the RF pulse is off, indicate that some waves at ω_0 could act as an energy source which sustains the fluctuations. During the RF discharge, coherent potential oscillations at ω_0 and harmonics were invariably detected in the edge plasma [5] (Fig.6). These oscillations experienced a noise-amplitude modulation (Fig.7). It follows from Fig.7 that the modulation correlates with the local LF potential fluctuations. This means that the spectrum of the high-frequency (HF) potential should involve narrow single peaks at ω_0 and harmonics, and also side band spectra $(\omega_0 \pm \omega)$, $(2\omega_0 \pm \omega, \ldots$, attached to each peak, the ω frequencies forming a spectrum similar to that shown in Fig.3. Such a spectral picture is the evidence of a parametric decay of HF pumping waves with the excitation of drift-like oscillations in the LF region. It follows from Fig.7, that in the course of modulation the minima of the HF signal always correspond to the maxima of the LF noise and vice versa. This is the indication of the energy pumping from the HF domain to the LF one and back, which is also characteristic of a parametric interaction.

In view of the relation $\omega < k_{\parallel} v_{Ti}$ found experimentally the LF oscillations in terms of survey [2] (and the papers cited there) can be identified as "low-frequency ion quasimodes", which cannot exist without pumping.

As it follows from ion energy measurements, the parametric wave interaction leads to an appreciable ion heating in the edge plasma. This, in turn, should give rise to the RF power absorption in the edge plasma. Estimations, based on the edge plasma energy content calculations with the temperature decay time taken into account show that power losses are comparable with the total RF power input.

An important consequence of the parametric process in the edge plasma should be an additional impurity release. It has been demonstrated recently [5] , that the ion flux arising in the divertor magnetic flux region during the RF pulse hits the antenna and causes the erosion of its surface. As it follows from the ion flux measurements (see Fig.2,c), the fluctuating component forms an essential part of the total ion flux ($\sim 10^{17}$ ions/cm^2.s). Moreover, the ion flux fluctuations are time-correlated with the local plasma potential, i.e., the fluctuating component of the ion flux is caused by the plasma potential fluctuations.

References

1. Liewer,P.C., Nucl.Fusion 25 (1985) 543.
2. Liu,C.S. and Tripathi,V.K., Phys.Reports 130 (1986) 145.
3. Noterdaeme,J.M., Brambilla,M., Gernhardt, J., et al., in Controlled Fusion and Plasma Heating (Proc.15th Eur. Conf., Dubrovnik, May 16-20, 1988), Pt.2, p.162.
4. Nieuwenhove, R.Van, Oost,G.Van, Beuken,J.M., et al., Ibid., p.778.
5. Grigor'eva L.I., Konovalov,V.G., Nazarov,N.I., et al., Rep.A-30, PSI-VIII, Jülich, 1988.

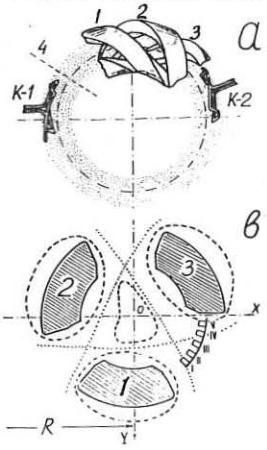

Fig.1. a - schematic view of the U-3 machine;
b - torus cross section (4) with the analysers I-V installed.

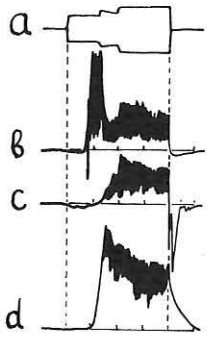

Fig.2. a-RF antenna voltage; b-plasma potential; c-analyser current; d-ion saturation current.
5 ms/div.

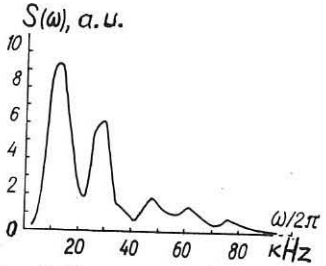

Fig.3. Power spectrum of the potential fluctuations.

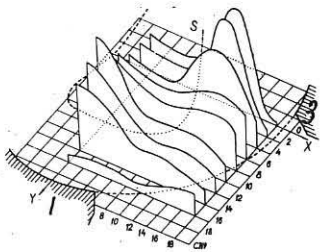

Fig.4. Potential fluctuation distribution in cross-section (4). Vertically values proportional to $d\tilde{\Phi}/dt$ are plotted.

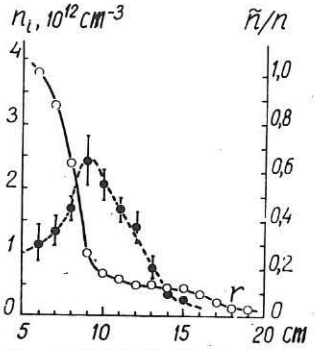

Fig.5. Radial distributions of density (o) and its fluctuations (•).

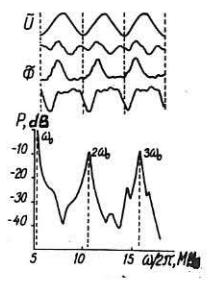

Fig.6. Antenna voltage ($\tilde{U}$) and plasma potential ($\tilde{\Phi}$, 1-20MHz) taken at three different locations of the capacitive probe; power spectrum of the potential oscillations (Langmuir probe, 5-20MHz).

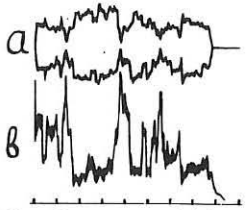

Fig.7. a-capacitive probe signal (1-20MHz); b-capacitive probe signal (0-60 kHz). The probe spacing is 1 cm. 0.25 ms/div.

ON THE MARFE ARISING THRESHOLD AND DENSITY LIMIT IN A TOKAMAR

Tokar' M.Z.

Institute for High Temperatures of the USSR Academy of Sciences, Moscow, USSR

Introduction. Radiation of light impurities can substantially influence on the heat balance of a tokamak edge plasma, leading to the states with Marfe and detached plasma, provoking the disruption instability.

In the papers /1-3/ devoted to the explanation of these phenomena the consideration was based on the analysis of the local heat balance. In the present paper we consider another approach, which permits to obtaine the results comparable with experimental data.

The peripheral region heat balance. In a tokamak with a limiter we can distinguish a peripheral region inside the last closed magnetic surface touching the limiter. In this region the ionization of the neutrals recycling from the limiter and liner takes place. It's width is of the order of the depth of the neutral penetration into the plasma: $l_* \approx 2/n_o \sigma_*$, where $\sigma_* = \sqrt{k_i(k_i+k_c)}/v_i$, $k_{i,c}$ are the ionization and charge-exchange constants, v_i is the ion thermal velocity, n_o is the plasma density at the periphery boundary with core of the discharge; n_o is close to the tokamak mean density $\bar{n}$ /4/. In the peripheral region the convection gives a significant contribution into the heat transport and the plasma temperature T changes weakly across this region. If there are impurities in the edge plasma the heat balance of the peripheral region can be written in the form:

$$q_o = \bar{Q}_I \cdot l_* + \gamma_o \Gamma_s T \qquad (1)$$

where q_o is the heat flux density into the periphery, $\bar{Q}_I = \xi_I n_o^2 L_I/4$ is the impurity radiation power averaged over the periphery width, ξ_I is the impurity concentration, L_I is the radiative cooling rate.

The second term in the right hand side of Eq.(1) is the heat flux transfered to the limiter and liner by the charged particles. If the SOL is transparent for the recycling neutrals the plasma particle flux Γ_s into the SOL can be estimated as $\bar{D}_\perp \cdot n_o/l_*$. Here $\bar{D}_\perp$ is characteristic diffusivity in the peripheral region. For the Alcator scaling - $D_\perp = A/n$, $A \approx 10^{17}$ cm^{-1}s^{-1} - one has:

$$\Gamma_s \approx A \sigma_* n_o$$

From Eq.(1) we obtaine the equation for T:

$$F(T) \equiv \frac{\xi_I L_I(T)}{2\sigma_*} + \gamma_o A \sigma_* T = \frac{q_o}{n_o} \equiv p \qquad (2)$$

The cooling rate L_I has a strong maximum near some plasma temperature T_m, which depends on the impurity species /5/. L_I in corona equilibrium can be approximated by the following formulas:

$$L_I = \exp\,(-2{,}64\ \ln^2 T + 9{,}44\ \ln T - 23\ )$$

in the carbon impurity case and

$$L_I = \exp\,(-1{,}71\ \ln^2 T + 9{,}94\ \ln T - 28.8\ )$$

in the oxygen case, where T is expressed in eV, L_I - in eV cm^3/s.

The dependences of F on T are shown on Fig.1. Calculations have been done for $\gamma_o = 7{,}5$; $\xi_I = 1\%$. Let's analyse the evolution of the peripheral plasma with p change. If the initial mean density in the discharge is sufficiently low and p exceeds the maximum value of F than with n_o increase and p decrease the edge temperature changes along the AB portion of the curve F(T). With attaining of critical value p_c corresponded to F minimum value the cooling instability takes place and the discharge periphery develops into the state C where the heat balance is determined by the impurity radiation.

As it's known the heat and particle losses in a tokamak have a poloidal asymmetric character: they are more intensive at the outer edge than at the inner one. To take this fact into account we assume $q_o = \bar{q}_o \cdot f(\theta)$, $A = \bar{A} \cdot f(\theta)$, where $\bar{q}_o$, $\bar{A}$ are q_o, A magnitudes averaged over the poloidal angle θ and f decreases with θ increase. In such a case one has instead of Eq.(2) the following equation:

$$F(T,\theta) \equiv \frac{L_I(T)\xi_I}{2\sigma_* f(\theta)} + \gamma_o \bar{A} \sigma_* T = \frac{\bar{q}_o}{n_o} \equiv \bar{p} \qquad (3)$$

As analysis shows the minimum value of F increases with f decrease. Hence with p diminution the condition for the plasma transition into the state with strong radiation is fulfiled first of all for the inner edge.

The change of f may be considered as the change of the impurity concentration and it is natural that for larger ξ_I the cooling instability develops at lower n_o. But with taking into account the real nonlinear dependence $L_I(T)$ we obtained much more weaker dependence of the critical value of $p-p_c$ - on ξ_I than it follows from the results of Ref. /2,3/. The dependence of p_c on ξ_I is shown on Fig.2 for f = 0,2, which is typical for the inner edge.

According to Ref./6/ Marfe - the inner edge region of the cold dense plasma with strong radiation - arises when the

parameter $\rho = a^2 n/I_p$ (a is the plasma minor radius, I_p is the discharge current) exceeds a critical value ρ_c changing for many devices in a narrow range: $\rho_c = 0{,}4 \div 0{,}7 \cdot 10^{12}$ A^{-1}cm^{-1}. This fact agrees with the weak dependence of p_c on impurity concentration. In an ohmical discharge one has:

$$\rho = \frac{V \alpha_q}{4\pi R/a \alpha_n} p^{-1} \qquad (4)$$

where V is the loop voltage, α_q is the part of power put into discharge, which is transported into the periphery by the plasma conduction, $\alpha_n = n_o/\bar{n}$.

The values in Eq.(4) are approximately the same for different tokamaks. Assuming their typical magnitudes: $R/a = 3$ $\alpha_q = \alpha_n = 0{,}75$, $V = 1$V we obtaine that with the change of the oxygen content in the discharge in the range 0,2% ÷ 2% ρ_c must change in the interval: $0{,}39 \div 0{,}55 \cdot 10^{12}$ A^{-1}cm^{-1}.

The state with radiative periphery and the plasma density limit. If the mean density in the discharge is sufficiently high that is the condition $\bar{p} < \bar{p}_c(\theta = 0)$ holds the peripheral region as a whole must transit into the state with stong radiation. We assume the radiative zone minor radius is a_* and it's width Δ_* is much smaller than a_*. Then the heat balance in the zone can be discribed by the equation:

$$dq_\perp / dy = - n^2 \xi_I L_I(T) \qquad (5)$$

where $y = r - a_*$, $q_\perp = - \varkappa_\perp dT/dy$, $y=0$ corresponds to the radiative zone boundary with hot core, $y = \Delta_*$ - to the boundary with cold periphery that is $T_+ = T(y=0) > T_M$, $T_- = T(y=\Delta_*) < T_M$, $L(T_+)$, $L(T_-) \ll L_I(T_M)$, $q_\perp (y=\Delta_*) \ll q_\perp (y=0) = q_o$.

Let's multiphy the both sides of Eq.(5) on $q_\perp$ and integrate over the radiative layer width:

$$q_o^2 = 2 n_b^2 \xi_I \varkappa_\perp \cdot g \qquad (6)$$

where n_b is the plasma density at the radius with $T = T_m$, $g = \int_{T_-}^{T_+} L_I(T) dT$; $g \approx 3.5 \cdot 10^{-6}$ eV^{2}cm^3/s for carbon, and $g \approx 1{,}7 \cdot 10^{-5}$ eV^{2}cm^3/s for oxygen.

In an ohmic discharge $q_o = I_p V/4\pi^2 a_* R$ and we obtaine from Eq.(6):

$$a_* = \frac{I_p V}{4\pi^2 \sqrt{2 \xi_I \varkappa_\perp g}\, R n_b}$$

Thus with the plasma density rise the radiative layer radius diminishes and the value of safety factor $q_* = 5 B_o a_*^2 / R I_p$ at it's boundary changes as follows:

$$q_* = \frac{5 B_o I_p V^2}{32 \pi^4 \xi_I \varkappa_\perp g R^3 n_b^2}$$

When q_* reduces down to 2 the large MHD instabilities are developed and the discharge disruption takes place. Hence the value

$$n_b^{max} = \frac{V}{8\pi^2 R}\sqrt{\frac{5B_o I_p}{\xi_I \alpha_\perp g R}} \qquad (7)$$

may be considered as a plasma limit density at the tokamak discharge periphery.

Fig.3 shows the dependence of the limit mean density on the plasma current calculated for TEXTOR device (n_b=0,75n, B_o=2T, an impurity is oxygen with 0,5% concentration, $\alpha_\perp$ = =5·$10^{17}$$cm^{-1}s^{-1}$). The experimental data /7/ are also shown here.

References

1. Sringer T.E. Cont.Fusion Plasma Phys.Proc. 12th Europ. Conf. Budapest. 1985. Vol.9F, Part 1, 86-89.
2. Neuhauser J., Schneider W., Wunderlich R. Ibid, Part 2, P.476-479.
3. Neuhauser J. e.a. Nucl.Fusion 1986, Vol.26, No.12,1679-1692.
4. Stangeby P.C. J.Nucl.Mater. 1987, Vol.145-147, 105-116.
5. Post D.E. e.a. Rep. PPPL-1352, 1977.
6. Samm V. e.a. Rep. Rep. Jül - 2123, 1987.
7. Castracane J. e.a. Nucl.Fusion. 1987, Vol.27, No.11, 1921-1925.

Fig.1. The dependences of functions F on the edge plasma temperature for carbon (1) and oxygen (2) impurities.

Fig.2. The dependence of the critical value $\bar{p}_c$ for inner tokamak edge on the impurity concentration: 1 - carbon, 2 - oxygen.

Fig.3. The dependence of the limit density on the plasma current in TEXTOR: ____ theory, * - experimental data /7/.

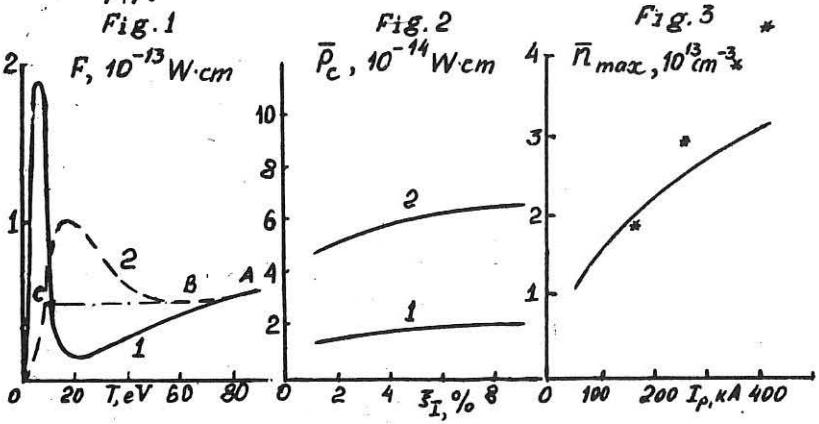

ORIGIN OF EDGE TURBULENCE IN TOKAMAKS

A.V. Nedospasov

Institute for High Temperatures of the USSR Academy of Sciences, Moscow, USSR

It has been shown in Ref. /1/ that the plasma at the outer edge of a tokamak is unstable against the interchange perturbations. The development of instability results in the edge turbulence with the plasma diffusivity of Bohm order, that depends on the poloidal angle.

During the plasma motion across the magnetic field the mechanical work converts into the electric energy. According to the equations of the plasma equilibrium and Ohm's law the power released in a volume unit is equal to

$$\bar{v}\cdot\bar{\nabla}p = -j^2/\sigma + jE \qquad (1)$$

The plasma diffusion in a straight magnetif field and Pfirsch-Schlüter convection give the well known examples of this equality. In the tokamak SOL the work done by the current flowing through the potential sheats near limiter surfaces prevails over Joule dissipation. The sheaths play a role of a load in MHD-generator. Under assumptions of Refs. /2,3/ that the plasma potential and density are constant along the lines of force segments between the circular poloidal limiter sides and a net current from the plasma is equal to zero the following identity holds:

$$e\Lambda V_s \int n\left(\frac{\partial\varphi}{\partial r}\sin\theta_0 + \frac{\partial\varphi}{r\partial\theta}\cos\theta_0\right)dS = 2\int j_\parallel \varphi dS \qquad (2)$$

$$e\varphi/T_e = -\ln\left[1+\Lambda\left(\frac{\partial u}{\partial r}\sin\theta_0 + \frac{\partial u}{r\partial\theta_0}\cos\theta_0\right)\right] \qquad (2a)$$

Here $\Lambda = 2(T_e+T_i)cq\sin\pi/q\,kV_sB$, $u=\ln n$, V_s is the ion sound velocity, θ_0 is the poloidal angle of the line of force

segment middle, T_e, T_i = const. The integration is taken over the whole SOL cross section. Pfirsch-Schlüter longitudinal current being in the right hand side equals:

$$j_{\parallel} = e V_s \Lambda \left(\frac{\partial n}{\partial z} \sin\theta_0 + \frac{\partial n}{\partial \theta_0} \frac{\cos\theta_0}{z} \right)$$

The work that is done in some point dissipates in the layer and brings to the plasma compression in the other points.

Under conditions of strong turbulence the dissipation of the electric power pulsations must take place locally in the vicinity of the order of correlation length. The connection with far remote regions and the limiter surfaces is manifested through the existance of the time averaged density and potential gradients. Hence for an approximative determination of the turbulence spectrum one may demand the locality of the energy balance for a single wave and consider the equality

$$n \left(\frac{\partial \varphi}{\partial z} \sin\theta_0 + \frac{\partial \varphi}{\partial \theta_0} \frac{\cos\theta_0}{z} \right) = \varphi \left(\frac{\partial n}{\partial z} \sin\theta_0 + \frac{\partial n}{\partial \theta_0} \frac{\cos\theta_0}{z} \right) \qquad (3)$$

as an equation for the wave amplitude under an assumption that there is't energy exchange between different waves.

The solution is chosen in the form: $n = n_0 +$

$$+ \tilde{n} \exp(i k_z z + i m\theta - i\omega t) + \tilde{n}^* \exp(i\omega t - i k_z z - i m\theta)$$

where $n, \tilde{n}, \tilde{n}^* \sim \exp(-z/d)$, $\tilde{n}, \tilde{n}^*$ are the complex conjugated amplitudes of the oscilations. For Bohm diffusion $d \approx 3\Lambda \ll a$. Assuming

$$k_z a \gg 1, \quad k_\theta a = m \gg 1, \quad \left| \frac{\partial n}{\partial z} \sin\theta \right| \gg \left| \frac{\partial n}{\partial \theta} \frac{\cos\theta}{z} \right|$$

, substituting the expansion into a series of (2a) into Eq.(3) one can obtain after time-averaging: $\Lambda^2 (k_z \sin\theta_0 + k_\theta \cos\theta_0)^2 \frac{\tilde{n}\tilde{n}^*}{n^2} \approx \frac{1}{4} \div \frac{1}{6}$

As it follos from this result the characteristic scale of the wave length is determined by $\Lambda = 2\pi\rho_i \sin\pi/q$ and does't depend on device dimensions. With $k_\perp \rho_i \sim 0.1$ $\tilde{n}^2/n^2$ is of unity order and with smaller wave lengths $\tilde{n}^2/n^2 \sim k_\perp^{-2}$. For larger values of $(\tilde{n}/n)^2$ the power losses $\varphi_{j_\parallel}$ in the layer exceeds the energy release and such a fluctuation must be damped. Eq.(3) corresponds to the equality of the time-averaged increment to zero.

Given estimates are in agreement with known experimental fact. Firstly, the turbulence spectrum and level in the SOL are approximately the same for small and large tokamaks. Secondly, in the experiments /4/ for large k_θ $/\tilde{n}^2/$ is proportianal to k_θ^{-q} where $2{,}5 \leq q \leq 3$. The more rapid decrease of the amplitude square with k_θ increase than proportionally to $k_\perp^{-2}$ can be explained by the wave energy exchange. Our theoretical ideas on the edge turbulence nature are in agreement with the experimental fact that the plasma flux onto the wall is larger at the outer detour of a torus than at the inner one.

References

1. Kolesnikov V.K., Nedospasov A.V. Sov.Phys.Dokl. 1987, Vol.32, N 6, P. 478-479.
2. Motley R.W. // Nucl.Fusion 1981, V.21, P. 1541-1548.
3. Nedospasov A.V., Petrov V.G., Fidel'man // Nucl.Fusion, 1985, V.25, N 1, P. 21-27.
4. Liewer P.C. // Nucl.Fusion, 1985, V.25, N 5, P.543-621.
5. Levinson F.G., Beall J.M., Pawers I.Y., Bengston R.D.// Nucl.Fusion. 1984, V.24, P. 527.

EDGE PLASMA MEASUREMENTS BY ELECTRIC PROBES ON MT-1 TOKAMAK

J. S. Bakos; B. Kardon; L. Koltai

Central Research Institute for Physics
H-1525 Budapest, P.O.Box 49, Hungary

Introduction

In order to have a better knowledge about the scrape off layer of the MT-1 tokamak investigations have been carried out by Mach-number probes in the limiter shadow region and by Penning manometer in the limiter chamber. In the experiments the behaviour of the Penning manometer signal and the ion saturation current drawn by the electrodes of the Mach-number probe have been studied at different plasma parameters.

Experiment

The MT-1 tokamak is a small scale device with major radius of $0.4m$, minor radius of $0.1m$, plasma current $< 30kA$, duration of the discharge $= 8ms$, average electron density $1 - 3 \times 10^{19}m^{-3}$, toroidal magnetic induction of $1T$.

A poloidal limiter with the radius of $0.09m$ and a passive pump limiter 54° toroidally from the poloidal limiter was installed on MT-1 tokamak on the top side (Fig. 1/a.) The radius of the pump limiter can be changed in the range of $65mm \leq a \leq 95mm$, while it covers 46° – 70° sector poloidally. This limiter contains four Langmuir probes and a Penning type manometer inside the limiter chamber $35mm$ outward the entrance slot to measure the neutral density and pressure enhancement at the plasma edge region. (Fig. 1/b.) The manometer was calibrated in situ in tokamak with a known gas pressure without discharge. The time evolution of the signal from Penning manometer has the same character as in tokamak PDX. [1]

Two Mach-number probes similar to that described by G. Proudfoot [2], were placed at different positions. (Fig. 1/a. 1/c.) One of them is situated on the top toroidally 72° away from the pump limiter. Further this probe will be called 'upper probe'. The other Mach-number probe is placed in the same poloidal cross section as the pump limiter but 15° away from the outher midplane (poloidally 75° away from the pump limiter). Further we shall refer to this probe as 'lateral probe'.

Biasing the electrodes of the Mach-number probes at $-150V$ relative to the vacuum chamber they were used in ion saturation mode. For the evaluations the average value of the ion saturation current in the stable phase of the discharge (4–6 ms) has been considered. During this time the ion saturation current fluctuates practically around a constant value. We followed the same way in evaluating the Penning signal.

In the experiments dependences of the signal of the Mach-number probes and Penning manometer on bulk plasma parameters and the direction of plasma current have been investigated. Clockwise plasma current direction will be called positive. The dependence of Mach-number probe signal on probe position has also been studied.

Results and Conclusions

Characteristic ion saturation current profiles can be seen on Fig. 2. Noticeable that changing the plasma current direction the asymmetry at the upper probe turnes i.e. at positive plasma current direction the ion side electrode and at negative plasma current direction the electron side electrode collects more ion saturation current. (Fig. 2/a. 2/b.) However on the lateral probe the ion side electrode draws more ion saturation current in both plasma current direction. The distance between the pump limiter and the upper probe along a flux tube in electron side direction is $0.5m$ in ion side direction $9.5m$ if the plasma current is positive ($q \approx 4$). In case of opposite plasma current these distances are changed.

Assuming Bohm diffusion and taking into consideration the given geometry the natural collection length of the probe is $L_{\parallel a} = 5.4m$ [3]. Due to the vicinity of the pump limiter the shadow zone of the probe cannot be developed to that extent determined by the cross field diffusion and parallel convection at positive plasma current on the electron side and at negative plasma current on the ion side. This can be responsible for the behaviour of the upper probe signals described above.

The lateral probe, however, 'sees' the pump limiter at a distance of 2.5m on the ion side and of 7.5m on the electron side at both plasma current directions. In spite of this fact the ion side electrode draws allways more current than that of electron side. (Fig. 2/c. 2/d.) Thus the cross diffusion coefficient calculated from the Bohm formula is not large enough to describe this effect. Assuming the natural collection length of the probe to be less than 2.5 m the cross field diffusion coefficient $D_\perp \geq 2.2\frac{m^2}{s}$. It is also worth to be noticed that in spite of theoretical considerations the above mentioned profiles do not show exponential character.

During the experiments it came to light that the ratio of the ion saturation currents of the ion and electron side of the upper probe ($\alpha = I_{sat.,ion}/I_{sat.,el.}$) does not depend on the average bulk electron density at positive plasma current. At opposite plasma current $\alpha < 1$ and slightly decreasing function of the average electron density in the range of $10^{19}m^{-3} \leq n_e \leq 3\times10^{19}m^{-3}$. Studying the dependence of the same quantity on the plasma current $\alpha < 1$ was found for both plasma current directions. It was observed that α increases with increasing I_p for negative plasma current direction only.

The pressure variation with limiter radius was measured by Penning manometer in order to derive the electron temperature in this region. The pressure enhancement in the pump limiter is proportional to n_eT_e, the ion saturation current collected by a Langmuir probe is proporional to $n_eT_e^{1/2}$. From these two measured values it is possible to calculate the electron temperature. On the other hand one can estimate the average electron temperature from the resistivity using the Spitzer formula. Fig. 3. shows the electron temperature against the limiter radius calculated by different methods. If we suppose the same temperature profile at different limiter radii then the electron temperature calculated from the Spitzer formula could be compared with the values derived from the Penning-Langmuir probe measurements. Both curves show a fairly good agreement with decreasing character.

Fig. 4. shows the pressure in the limiter chamber against the averaged electron density measured by microwave interferometer and the plasma current at different current directions. A saturation can be observed on the $P - (n_e)$ diagram. There are

lot of possible explanations of this saturation effect. One of the most probably ones is connected to the pressure equilibrium in the exhaust chamber, where the Penning manometer situates. For a solid explanation further examinations are needed.

References

[1] H. F. Dilla; J. Vac. Sci. Technol. 20 (1982) 119.

[2] G. Proudfoot, P. J. Harbour; J. Nucl. Mat. 111 – 112 (1982) 87.

[3] P. C. Stangeby; J. Phys. D 18 (1985) 1547.

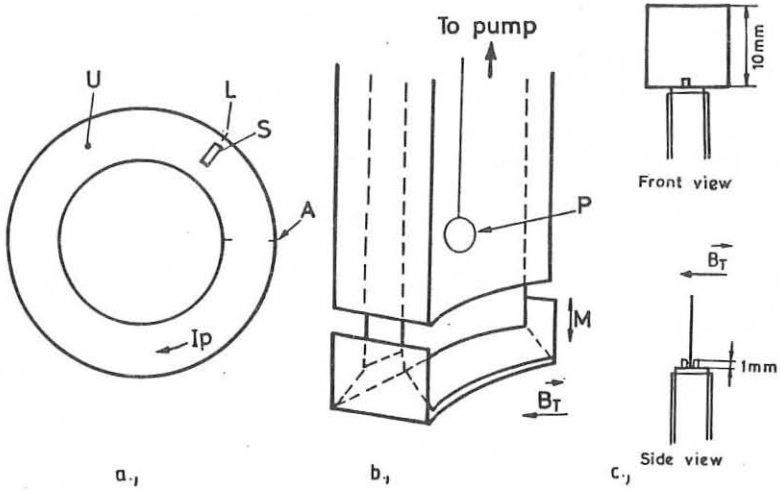

Fig. 1. —a. Scheme of the tokamak, top view. A: poloidal limiter; S: pump limiter; U, L : upper and lateral Mach number probes respectively. — b. sketch of the pump limiter. M: changeable entrance slot; P: Penning manometer — c. tip of the Mach number probe.

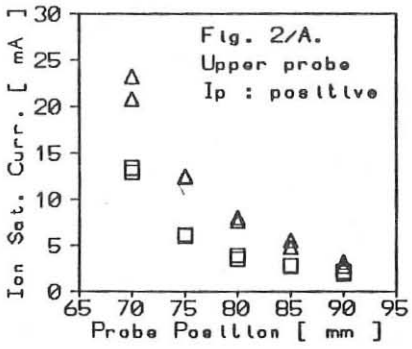

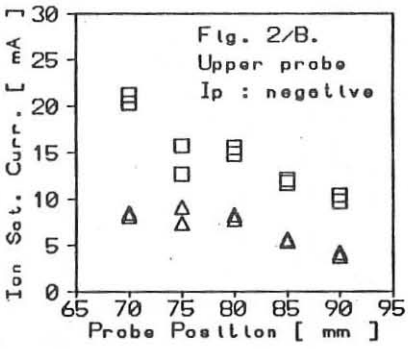

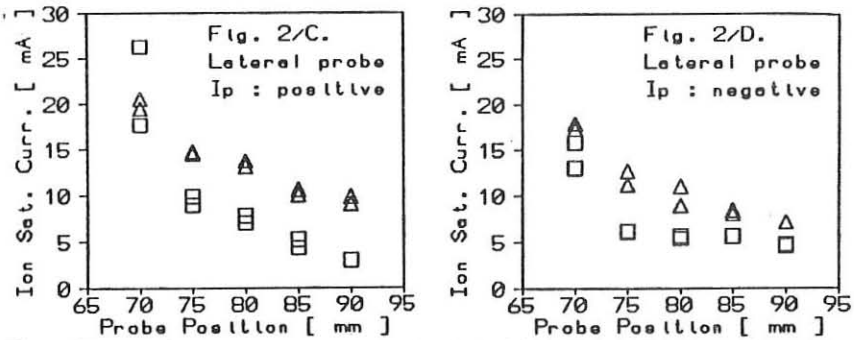

Fig. 2. Plot of the ion saturation current collected by different Mach number probes versus probe position. □ electron side; Δ ion side.

Fig. 3.
Electron temperature data vs limiter radius
□ Penning–Langmuir method
Δ Spitzer formula

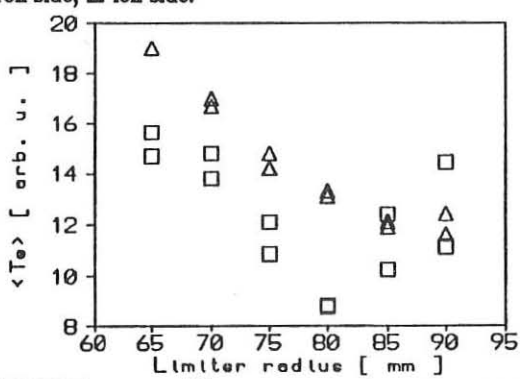

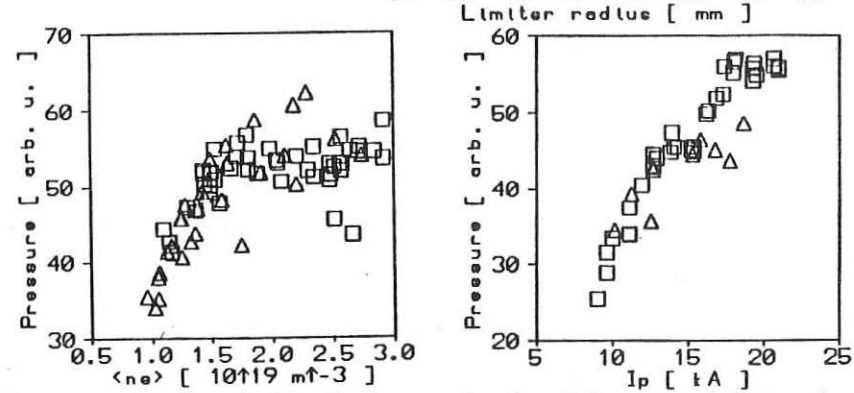

Fig. 4. Pressure in the limiter chamber as a function of line averaged electron density (left) and plasma current (right). □ positive plasma current; Δ negative plasma current.

MODIFICATIONS OF EDGE PLASMA AND PARTICLE TRANSPORT BY ERGODIC MAGNETIC LIMITER IN HYBTOK-II

M.Miyake, Y.Shen, and S.Takamura
Department of Electrical Engineering
Faculty of Engineering, Nagoya University
Nagoya 464-01, Japan

1. Introduction

It has been recognized that the tokamak edge plasma has important roles not only in the impurity control and particle exhaust but also in the core confinement characteristics. A stochastic magnetic field is one of effective means for tokamak edge modifications. This is known as a concept of ergodic magnetic limiter (EML). In addition the electron transport along the stochastic magnetic field is considered as one of important candidates for anomalous transport in tokamaks.

We have investigated the effects of EML from the following many aspects: a. Detection of modified magnetic field structure by electron beam probing[1]; b. Stochastic properties of magnetic field lines[1,2,5,6]; c. Relations between structures of magnetic field and electric potential[1,2]; d. Demonstration of wall lapping plasma by rotating helical magnetic field[2,4]; e. Structural properties of edge plasma parameters and transport[1,2,4]; f. Preliminary result on hydrogen recycling[4]; and g. Potential control associated by energetic electrons generated by lower hybrid waves[3].

In this conference, hydrogen recycling due to edge transport modifications, changes in edge plasma structure, and the impurity behavior are discussed.

2.Modifications of Particle Transport at the Edge.

A resonant helical magnetic field was applied on the HYBTOK-II (R=0.4cm, a_p=0.11m, B_t=0.4T, I_p~15kA) tokamak plasma with local helical coils(m/n=6/2). The magnetic field structure has already been well studied, taking into account of exact shape of local helical coils and tokamak equilibrium field[5,6]. A stochastic magnetic field enhances the plasma transport at the edge, that is, the plasma contact with the chanber wall. This increases the hydrogen recycling as shown in Fig.1. A computed tomography imaging of Lyα emissions through the tangential port confirms the increase in hydrogen spectral line as shown in Fig.2.

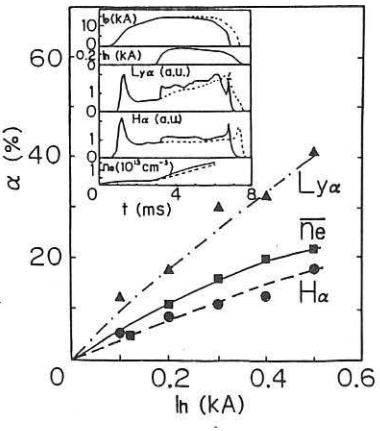

Fig.1 Recycling properties. Increase in $H\alpha$ and $Ly\alpha$ emissions and line-averaged electron density as a function of helical coil current. Insertion shows the traces of these quantities. The value at t=5ms are plotted.

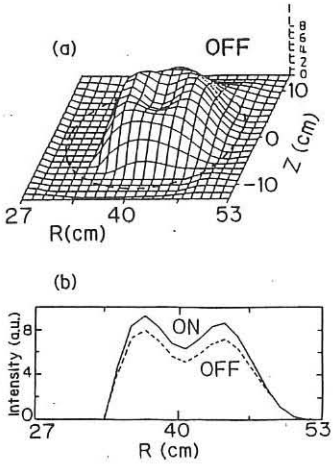

Fig.2 Emission profile of $Ly\alpha$ line on the poloidal plane at t=6ms. (a) Ih=0. Dotted line show the location of Mo Limiter. (b)One dimensional profiles in the equatorial plane (Z=0) for Ih=0.3kA (solid line) and Ih=0 (broken line).

An array of Langmuir probes is installed at the scrape off layer(SOL) and movable on a poloidal plane. Typical result on the profile of plasma parameters are shown in Fig.3 for the equatorial plane. There, we have an increased electron density and a decreased electron temperature. However, such a tendency is not uniform along the poloidal circumference. The reduction of electron temperature was not observed at the locations where the electron density decreases. Therefore the poloidal modulations of plasma parameters will be a common feature of EML, which is also able to be inferred from the structure of magnetic field very close to the wall. Nevertherless this observation is a preliminary demonstration of low temperture, high density buffer plasma expected in the EML concept. As shown in Fig.3 the radial profile of electron density was flattened by the application of EML. This means that the transport across the main magnetic fieled in SOL increased. The cross-field diffusion coefficient was estimated numerically using a simplified assumption. This is the alternative representation of the reason for the increase in hydrogen recycling.

In order to study more about the poloidal variation of plasma parameters, an array composed of 32 Langmuir probes is set on a poloidal plane. The ion saturation currents at the limiter radius are plotted in Fig.4 for a weak and a strong helical field, normalizing by that without helical perturbations. The edge density does not change or somewhat increase for a weak perturbation, while a strong helical field enhances the spatial modulation. It seems that the magnetic field structure affects such a poloidal modulation.

Concerning intrinsic impurities, the line emissions from light impurities were enhanced by EML, while those from metal impurities were suppressed in the core plasma. The difference is discussed in terms that the range of penetra-

tions of impurity atoms is inside the ergodic magnetic layer or not. These impurity behaviors are argued by referring the magnetic field structure.

References
1.S.Takamura et al., Phys. Fluids 30(1987)144.
2.S.Takamura et al., Nucl. Fusion 28(1988)183.
3.S.Takamura at al., Plasma Phys. Controlled Fusion 30(1988)615.
4.S.Takamura at al., Proc. of 8th PSI Conf. Jülich(1988), to be published in J. Nucl. Mater.
5.S.Takamura at al., Proc. of International Workshop on Plasma Edge Theory in Fusion Devices, Augustusburg(1988), Contrib. Plasma Phys., Berlin 28(1988)393.
6.T.Tamakoshi et al., Trans. IEE Japan 108A(1988)572

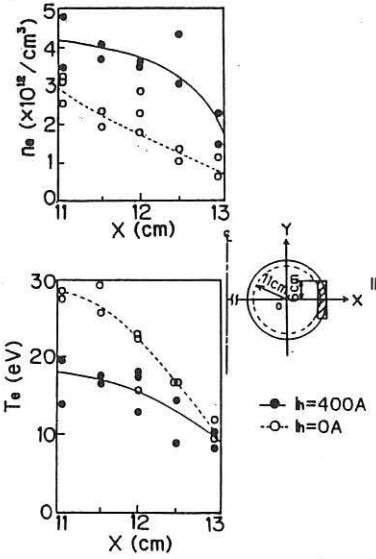

Fig.3 Radial profiles of electron density and temperature on the equatorial plane in SOL at t=5.5ms. Solid circles indicate values with Ih=0.4kA, while open ones without helical perturbation. $\overline{n_e}$=9.5→ 11.0× 10^{12}cm^{-3}.

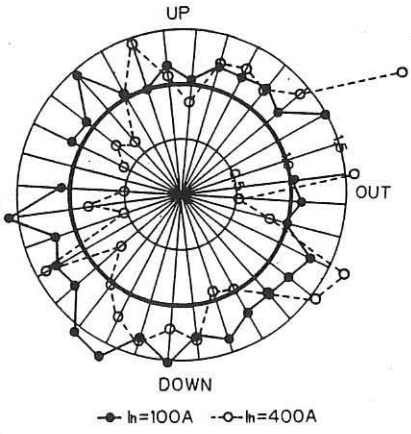

Fig.4 Distributions of ion saturation current along the poloidal direction. These are normalized by those without helical perturbation. Each point is the value for four discharge shots.

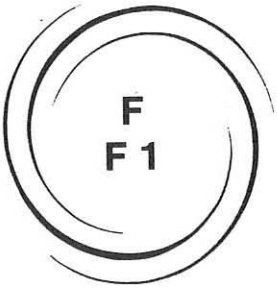

PLASMA HEATING AND CURRENT DRIVE

ION CYCLOTRON RESONANCE HEATING (ICRH)

EVIDENCE OF GLOBAL MODE EXCITATION IN THE TEXTOR TOKAMAK

P. Descamps*, T. Delvigne, F. Durodié, R. Koch, A. M. Messiaen+, P.E. Vandenplas, R.R.Weynants+

Laboratoire de Physique des Plasmas - Laboratorium voor plasmafysica
Association "Euratom-Etat belge" - Associatie "Euratom-Belgische Staat"
Ecole Royale Militaire - B 1040 Brussels -Koninklijke Militaire School

1) Introduction : Cavity modes have been observed experimentaly and studied in several tokamaks [1,2,3,4]; their excitation in TEXTOR is studied during the ICRH experiments with the new antenna system [5] (four antennae grouped in pairs and located in the LFS of the torus). Cavity modes may become visible on the loading resistance, depending on the minority concentration in an (H)-D plasma; their effect on the plasma wall interaction is discussed.

2) Theoretical models : The theoretical study of cavity modes is made using a cold cylindrical model and a slab model: i) in the cylindrical model [1], an inhomogeneous plasma containing *a single ion species* is surrounded by a conducting shell. A finite length antenna located in the vacuum layer between the plasma and the wall is described by a surface current distribution expanded in $e^{i(n\theta+k_{//}z)}$ space harmonics. ii)the slab model [6] is used to describe a plasma containing *several ion species* in an inhomogeneous magnetic field; the inhomogeneous plasma slab is limited by two metallic walls. The waves emitted by a finite length antenna placed along one wall can be reflected on the other wall or on the cut-off, near the ion-ion hybrid resonance; this leads to the build-up of stationary waves. Damping at the fundamental and second harmonic of the ion cyclotron frequency is included in the slab model using the hot dielectric tensor elements [6].

The value of the resonant densities, obtained from the cylindrical model for $n=0,\pm1$ and from the slab model for $k_y=0$ are represented in function of $k_{//}$ for different values of the radial wave number m, which indicates the order of the radial solution (fig.1). The slab model gives qualitatively the same resonance behaviour than the cylindrical one and provides futhermore information on the damping when the minority concentration is varied.

An antenna pair excites a $k_{//}$ spectrum which depends principally on its geometry; as seen from (fig.1), resonances characterised by different poloidal, toroidal and radial wave number are simultanously excited and contribute to the loading resistance [7].

3) Experimental evidence of cavity modes : The specific resistance R of one antenna of the pair is deduced from the incident and reflected voltage in the transmission line and from the voltage pattern measured using capacitive probes [5]. For the two antennae of a pair *fed in phase* (0 configuration), the evolution of R with the integrated central chord density $\bar{n}_{e0}$ shows several resonance peaks (fig.2.a). No correlation exists between these peaks and $\bar{n}_{e40}$, the integrated line density measured at r=40 cm, near the limiter position.

---

* EEC grantee at the Institut für Plasmaphysik, Jülich, F.R. Germany

+ Research Director at the NFSR, Belgium.

This suggests that the variations on R are indeed due to cavity modes excitation and not to a change in edge density.

4) Comparison between theory and experiment.

4.1) Study of a (H)-D discharge poor in H : The loading resistance R is computed for a pure Deuterium plasma as function of $\bar{n}_{eo}$ (fig. 2.b); the resonant density values are in good agreement with the experimental ones and the shape of the resonances(a fast rise followed by a slow decay) is well described by the slab model. The study of the real part of the radiated power spectrum $P(k_{//})$ (with $R \propto \int Re(P(k_{//}))\, dk_{//}$)helps us to understand the asymmetry of the peak(fig. 3). For fixed values of m and n, the resonance condition is only satisfied for $\bar{n}_{eo} > (\bar{n}_{eo})_{min}$ associated with $k_{//}=0$(fig. 1). When the density is increased, this condition is satisfied for greater values of $k_{//}$ for which the radiated power becomes lower.

4.2)Effect of H concentration in a (H)-D fuelling mixture . Experimentally, the resonances are only well observed when the H concentration is small (≈ 1%) or above 10% . Between these values (which correponds to the best heating conditions), the resonances are strongly damped. This is seen on fig. 2.a and can be explained theoretically by two mechanisms: i) an additionnal damping is associated with the ion-ion hybrid resonance; ii) reflection at the cut-off near the ion-ion hybrid resonance increases with the minority concentration due to a larger separation between cut-off and resonance. The loading resistance computed using the slab model for different H concentration in a (H)-D plasma follows qualitatively the experimental curves(fig.2.b) but the experimental Q of the resonance is always less than the values predicted by the slab model.

4.3)Effect of the toroidal field : For a sufficiently high concentration of minority in the plasma, a change in the toroidal field which modifies the ion-ion hybrid resonance layer position must change the resonant density value.The loading resistance measured for a (H)-He^3 plasma and at two different value of the toroidal field (B_T=1.9-2.1T) is well described by the slab model if we take a H concentration near its estimated value (fig.4).

5) Effect of the antennae phasing on the detection of cavity modes : During operation with the antennae fed out of phase (π configuration), no resonant behaviour has been observed on R. The loading resistances computed for antennae fed in phase (excited $k_{//}$ domain: $0\ m^{-1} < |\ k_{//}\ | < 5\ m^{-1}$) and out of phase ($3m^{-1} < |\ k_{//}\ | < 10\ m^{-1}$) [7] shows that the resonances associated to the eigenmodes are less apparent for the π configuration than for the 0 configuration (fig.5). However, the eigenmode are still present on the $k_{//}$ power spectrum in the π configuration (fig .3). The major differences between the two spectra are: a) more peaks contribute to the π spectrum since for high $k_{//}$, the resonant density is more dependent on the $k_{//}$ value (fig.1); b) the sharp peak appearing when the density crosses one of the resonant densities at $k_{//} \cong 0$ (fig.1) is not excited in the π configuration. For these reasons, a scan in density will give for the π configuration an approximatively flat resistance curve as the peaks in the spectrum simply shift from low to high $k_{//}$, always reproducing the same kind of resistance pattern.

6) Effect of global modes excitation on the heating efficiency and impurity production : The analysis of the D_α spectroscopic signal at different times corresponding to a peak or valley on the loading curve gives information about the correlation between gas release and global modes excitation (fig 6). The change in RF power coupled to the plama due to a change in loading resistance is negligible(< 5%). The intensity of the spectral line D_α, caracteristic of the particle flux leaving the wall is flat ,which proves that the global modes exitation do not change fundamentaly the plasma-wall interaction. Parameters giving information about heating efficiency (ion temperature deduced from neutron measurement or slope of the sawtheeth on ECE measurement) are also

examined. No net correlation exists between these signals and the peaks existing on the loading curve.

7) Conclusions : During operation with the best heating conditions, cavity modes were generally not observed on TEXTOR; nevertheless, they were observed with the antennae fed in phase and for a not optimized (H)-D mixture. For the antennae fed out of phase, no resonant behaviour has been observed ; even if cavity modes are still present, we have shown that they don't influence the loading resistance. No net positive or negative influence of global modes on the heating efficiency or plasma-wall interaction has been detected.

References :

[1] A.M. Messiaen et al-Joint Varenna Int. Symp. on Heating in Toroidal Plasmas, Grenoble, 2,1978,229.
[2] J. Adam et al-5th IAEA Int. Conf. on Cont. Fusion and plasma Physics,Tokyo, 1,1975,65.
[3] J. Adam, J. Jacquinot-EUR-CEA-FC 886 report, 1977.
[4] L. Mc Carthy et al-15th Conference on Controlled Fusion and Plasma Heating, Dubrovnik(CAVTAT), 12b, part I, 1988, 717.
[5] F Durodié et al -15th Symposium on Fusion Technology, Utrecht, 1988, to be published
[6] R. Koch et al- internal report n° 87, LPP ERM/KMS, Brussels, 1988.
[7] A.M. Messiaen et al- to be published in Plasma Physics.

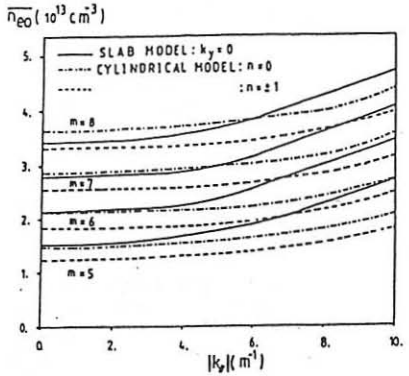

Fig. 1: Resonant densities computed as a function of $k_{//}$ for different values of the radial wave number m. The toroidal wave number is defined as $k_{//} = k/R$ (k=1, 2, ...). A parabolic density profile is choosen with a vacuum layer of 7 cm in the edge .

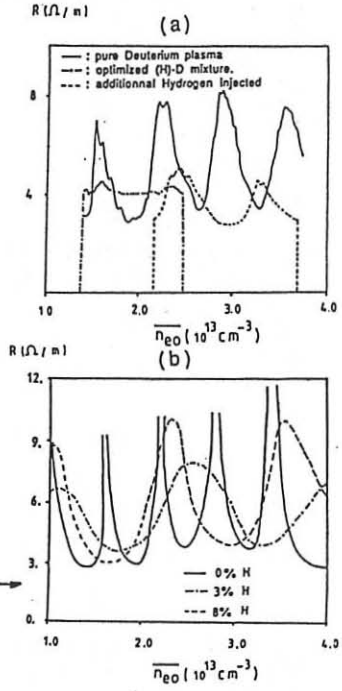

Fig. 2 : Evolution of the loading resistance of one antenna (0 configuration) in function of $\overline{n_{eo}}$ for different minority concentration in an (H)-D plasma.
a) experimental measurements
b) values computed with the slab model.

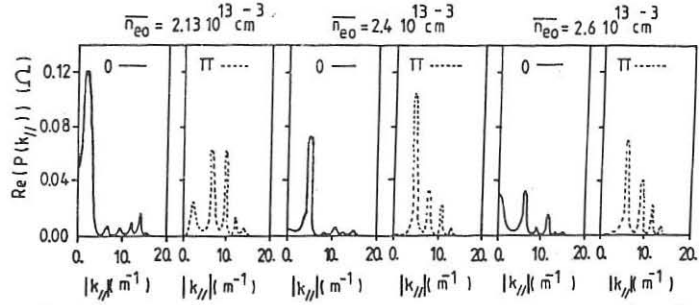

Fig.3 : Radiated k// power sprectrum computed for different $\overline{n_{eo}}$ values.

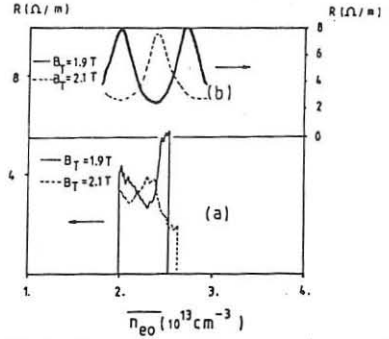

Fig.4 : Comparison between the experimental evolution (a) and the theoretical evolution (b) of R with $\overline{n_{eo}}$ for different values of the toroidal field; 8% H in a (H)-^{3}He plasma.

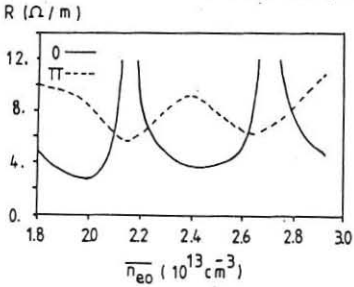

Fig.5 : Loading resistance computed in function of $\overline{n_{eo}}$ for the antennae fed in phase and out of phase.

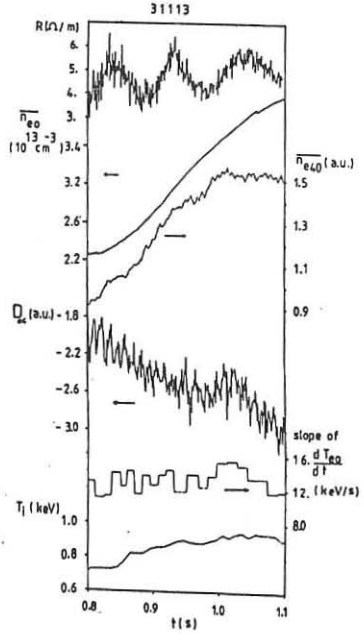

fig.6 : Evolution of the signals characteristic of the plasma-wall interaction and heating efficiency during cavity modes excitation.

MINORITY DISTRIBUTION FUNCTION EVOLUTION DURING ICRH MODULATION EXPERIMENTS

M.P. EVRARD*

Laboratoire de Physique des plasmas-Laboratorium voor Plasmafysica
Association "Euratom-Etat Belge"-Associatie "Euratom-Belgische Staat"
Ecole Royale Militaire- B 1040 Brussels- Koninklijke Militaire School

1 *Introduction*

During the last campaign of operations, RF power modulation experiments have been performed at JET during sawtooth-free periods (monster). Those experiments aim at determining the RF power deposition profile ,avoiding altogether the difficulties linked to the sawteeth as described in [1]. Preliminary results on power deposition profile in monsters have already been published [2]. In this paper we analyse how the minority ions transmit the modulated RF power to electrons, a vital ingredient in the subsequent analysis of the electron temperature evolution.

The experiments for which this analysis is developed are characterised by a high level of average RF power ($<P_{RF}> \approx$ 6-10 MW) on which is superposed a square wave modulation ($\pm\Delta P$, $\Delta P \approx$ 2 MW) at a frequency of 4 or 5 Hz . The heating of the minority is described in the framework of a Fokker-Planck equation which includes Coulomb collisions and a quasi-linear perpendicular velocity diffusion induced by the RF [3]. At the high RF power level attained in JET, the minority distribution has fully developed a high energy tail, and all the RF power eventually ends up in the electrons [4] ,indicating that collisions between minority and majority ions can be safely neglected.

Furthermore for ions with an energy lesser than several MeV, the approximation $|v_{||}|, v_{\perp} << v_{the}$ is still valid , and the operator representing minority-electron collisions is then separable in $v_{||}, v_{\perp}$. Assuming azimuthal symmetry ($\frac{\partial f}{\partial \theta} = 0$), the Fokker-Planck equation finally reads

$$\frac{\partial f}{\partial t} = \frac{1}{t_s}\left(\frac{\partial}{\partial v_{||}} v_{||} + \frac{1/2\, m_e\, v_{the}^2}{m} \frac{\partial^2}{\partial v_{||}^2}\right) f$$

$$+ \frac{1}{t_s}\left(\frac{1}{v_{\perp}} \frac{\partial}{\partial v_{\perp}} v_{\perp}^2 + \frac{1/2\, m_e\, v_{the}^2}{m} \frac{1}{v_{\perp}} \frac{\partial}{\partial v_{\perp}} v_{\perp} \frac{\partial}{\partial v_{\perp}}\right) f \qquad (1)$$

$$+ \frac{P_{RF}(t)}{2m} \frac{1}{v_{\perp}} \frac{\partial}{\partial v_{\perp}} v_{\perp} \frac{\partial}{\partial v_{\perp}} f$$

where t_s is the Spitzer time as defined in [3,p749] ,and $P_{RF}(t)$ is a power per particle (in eV/s) . Alternatively , this means that the distribution function is

---

* Part of this work has been done while at JET in relation with contract JJ7/9007

normalised to unity (and not to the density). In the quasi-linear RF diffusion term we have also neglected a $J_0^2(\frac{k_\perp v_\perp}{\omega_{ci}})$ factor, where J_0 is a Bessel function, on the ground that $\frac{k_\perp v_\perp}{\omega_{ci}} \approx \frac{v_\perp}{v_A} \leq 1$ in the perpendicular velocity range of interest. In particular , it means that no FLR effects are present in this model. An isotropic model including the effects of majority ions in the TEXTOR context is presented in [6].

2 *Solution of the Fokker-Planck equation*

The first step in the resolution of eqn (1) is to separate the $v_{||}$ part which is trivial and whose solution is obviously a 1D-Maxwellian with a temperature $kT_{||} = kT_e = 1/2\ m_e\ v_{the}^2$. Now, the remaining (perpendicular) part has the form

$$\frac{\partial f_\perp(v_\perp,t)}{\partial t} = [\ a(t)\ \ L_1(v_\perp) + b(t)\ \ L_2(v_\perp)\ ] f_\perp(v_\perp,t) = L_\perp f_\perp(v_\perp,t) \qquad (2)$$

with $L_1 = \frac{1}{v_\perp}\frac{\partial}{\partial v_\perp} v_\perp^2$ and $L_2 = \frac{1}{v_\perp}\frac{\partial}{\partial v_\perp} v_\perp \frac{\partial}{\partial v_\perp}$, a and b are (possibly) functions of time but don't depend on $v_\perp$. To be able to compute $f_\perp(v_\perp,t)$ for any initial distribution , we need to know the Green function $U(t,t_0)$ solution of eqn(2) in terms of which $f_\perp(v_\perp,t) = U(t,t_0)\, f_\perp(v_\perp,t_0)$. The operator $L_\perp$ being time dependent , the Green function is to be formally written as a time-ordered exponential $U(t,t_0) = T\ \exp\{ \int_{t_0}^{t} du\ L_\perp\ (u) \}$, not a very tractable expression . Instead , we will follow the method described in [5] and represent $U(t,t_0)$ as a product of operator

$$U(t,t_0) = \exp(\beta(t)\ L_2)\ \exp(\alpha(t)\ L_1) \qquad (3)$$

where α and β are two unknown functions of t to be determined from a(t),b(t). This will be possible simply only when the commutators of the operators involved (here L_1 and L_2) obey certain relations (see [5]) The lack of space does not allow to go into details here, but the calculations present no difficulty. When the Green function is obtained, it is a simple matter to make it operate on the initial distribution $f_\perp(v_\perp,t_0)$,chosen to be a maxwellian with a temperature $T_{\perp 0}$. The final result, as can be easily checked by replacement into eqn(1) is

$$f(v_\perp, v_{||}, t) = \sqrt{\frac{m}{2\pi k T_{||}}}\ \exp\left(-\frac{1/2 m v_{||}^2}{k T_{||}}\right) \frac{m}{2\pi k T_\perp(t)}\ \exp\left(-\frac{1/2 m v_\perp^2}{k T_\perp(t)}\right) \quad (4a)$$

with $kT_{||} = kT_e = 1/2\ m_e\ v_{the}^2$ and

$$\frac{d}{dt} kT_\perp(t) = -\frac{kT_\perp(t) - kT_e}{\tau} + P_{RF}(t) \quad (4b)$$

where $\tau = t_s/2$ is the energy slowing-down time . Equations (4a) and (4b) which show that the minority distribution function maintains its maxwellian character but with a time-dependent perpendicular temperature, are our main result. Unfortunately this result depends crucially on the hypothesis made and cannot be extended simply. For instance , considering the Bessel function factor $J_0^2(\frac{k_\perp v_\perp}{\omega_{ci}})$ would modify the commutation relations between the different parts of $L_\perp$ in such a way to make the method inapplicable. Including the collisions with majority ions to extend the results towards lower level of average RF power, would even spoil the separability of the Fokker-Planck equation. Nevertheless, our assumptions are general enough for our result to be useful in the analysis of rf power modulation experiments on monsters. As an application we show in Fig.1 the instantaneous power transferred to electrons (the first term in the RHS of eqn(4b)) resulting from a sine-wave modulation switched on at t=0 : $P_{RF}(t) = P_0 + \Delta P \sin \omega t\ \theta(t)$ .The increasing delay and decreasing amplitude as the determining parameter $\omega\tau$ increases are clearly seen. The curves are asymptotic in the sense that all the transients have been allowed to die out and are not present in Fig.1

3 *Conclusions*

Under rather mild and realistic assumptions we have shown that during RF modulation experiments with a high average power level the minority distribution function is bi-Maxwellian with $kT_{||} = kT_e$ and the perpendicular temperature $kT_\perp(t)$ a solution of a very simple differential equation of first order whose inhomogenous term is $P_{RF}(t)$

REFERENCES

[1] D.J. GAMBIER, M.P. EVRARD, *et al.* ,submitted to Nuclear Fusion

[2] F. TIBONE, M.P. EVRARD ,*et al.* , 15th Eur. Conf. on Controlled Fusion and Plasma Heating (Dubrovnik 1988) vol 12B , part II ,p709

[3] T.H. STIX , Nucl. Fus. 15 (1975) 737

[4] M.P. EVRARD, 14th Eur. Conf. on Controlled Fusion and Plasma Heating (Madrid 1987) vol 11D , part III ,p809

[5] F. WOLF , Journ. Math. Phys. 29 ,n°2 (1988) 305

[6] D. LEBEAU ,*et al.* ,this conference

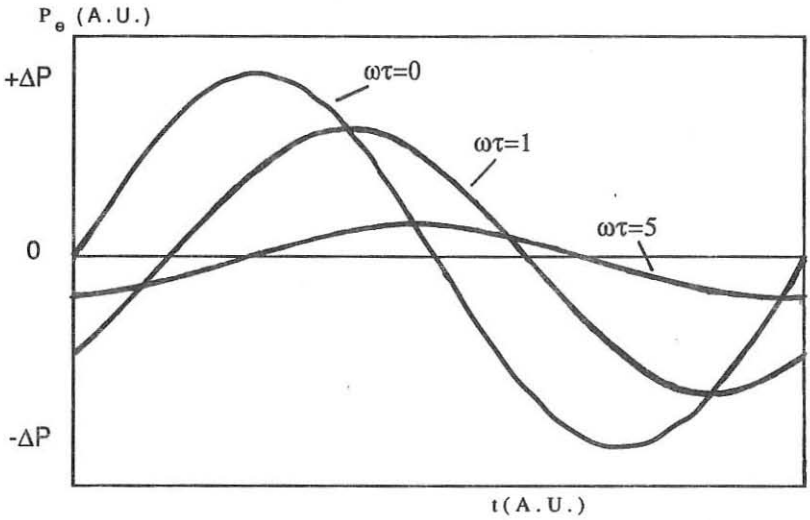

Fig.1 Power transmitted to electrons in response to a sine wave modulation superposed to a high level of steady RF power for different value of ωτ . The curve labeled with ωτ =0 is also $\Delta P_{RF}(t) = \Delta P \sin \omega t$

RF POWER DENSITY EVALUATION BY MEANS OF RF MODULATION ON TEXTOR

D. Lebeau, R. Koch, A.M. Messiaen*, P.E. Vandenplas, R.R. Weynants*

Laboratoire de Physique des Plasmas - Laboratorium voor Plasmafysica
Association "Euratom-Etat belge" - Associatie "Euratom-Belgische Staat"
Ecole Royale Militaire - B 1040 Brussels - Koninklijke Militaire School

ABSTRACT

In order to analyse RF amplitude modulation experiments on TEXTOR [1,8], we develop a realistic three species model for the energy transfer during RF heating. We solve the stationary and the non-stationary behaviour of the quasi-linear isotropic Fokker-Planck equation with a global minority confinement time and find the existence of many characteristic times including fast ones for the ion slowing down. We take care of the sawtooth and the density modulation and apply our model to the experimental data. The mean and the modulated power going to minority ions are differently distributed between background species.

ENERGY TRANSFER SCHEME

The RF power is given to the electrons via mode conversion (p_{mc}) and to minority ions via minority heating (p_{min}). These ions transfer their energy to the electrons ($p_{min,e}$) and the majority ions ($p_{min,i}$). Defining equipartition time between background species τ_{ei}, confinement times for the three species τ_e, τ_i, τ_{min} [4] and ohmic density power p_{oh}, the energy transfer is modeled by:

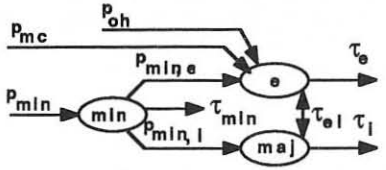

* Research director at the NFSR, Belgium

$$\frac{dE_e}{dt}=p_{oh}+p_{min,e}+p_{mc}-\frac{E_e-E_i}{\tau_{ei}}-\frac{E_e}{\tau_e} \qquad \left(E_e=\tfrac{3}{2}nkT_e\right)$$

$$\frac{dE_i}{dt}=\frac{E_e-E_i}{\tau_{ei}}-\frac{E_i}{\tau_i}+p_{min,i} \qquad \left(E_i=\tfrac{3}{2}nkT_i\right)$$

$$\frac{dE_{min}}{dt}=-\frac{E_{min}}{\tau_{min}}-p_{min,e}-p_{min,i}+p_{min} \qquad (1)$$

Using Spitzer conductivity and neglecting the small effect of the density modulation, we have: $\tilde{p}_{oh} \approx -\tilde{E}_e/\tau_x$ with $\tau_x = 3E_e/2p_{oh}$

We linearize the two first equations in the modulated quantities (~) having an $j\omega t$ dependence :

$$\tilde{E}_e=\frac{\left(\tilde{p}_{min,e}+\tilde{p}_{mc}\right)\left(j\omega+\tau_B^{-1}\right)+\tilde{p}_{min,i}\tau_{ei}^{-1}}{\left(j\omega+\tau_A^{-1}\right)\left(j\omega+\tau_B^{-1}\right)-\tau_{ei}^{-2}} \qquad (2)$$

$$\tilde{E}_i=\frac{\left(\tilde{p}_{min,e}+\tilde{p}_{mc}\right)\tau_{ei}^{-1}+\tilde{p}_{min,i}\left(j\omega+\tau_A^{-1}\right)}{\left(j\omega+\tau_A^{-1}\right)\left(j\omega+\tau_B^{-1}\right)-\tau_{ei}^{-2}}$$

$$\tau_A^{-1}=\tau_e^{-1}+\tau_{ei}^{-1}+\tau_x^{-1} \quad (3a) \qquad \tau_B^{-1}=\tau_i^{-1}+\tau_{ei}^{-1} \quad (3b)$$

POWER GOING FROM MINORITY IONS TO BACKGROUND SPECIES

The perturbed behaviour of eq. 1 is studied using the distribution function of minority ions **f**(v) obeying the isotropic quasi-linear Fokker-Planck equation [2,7]:

$$\frac{df}{dt}=\mathbf{L}f$$

$$\mathbf{L}=\frac{1}{v^2}\frac{d}{dv}\left[v^2(D+H)\frac{d}{dv}+v^2F\right]+\frac{1}{v^2}\frac{d}{dv}\left[\frac{v^3}{2\tau_{min}}\right]$$

D,H,F are the diffusion, the minority heating and the friction coefficients. Losses introduced by the last term [6] are consistent with particle and energy conservation. If we neglect the collisions

with majority ions (hypothesis 1) and if we use the approximate form of the Chandrasekhar function (hypothesis 2) [3], D is a constant and $F=v/t_{s,e}$ where $t_{s,e}$ is the electron slowing down time [2,p749]. In addition, if we neglect finite Larmor radius effects, H is proportional to the RF power and independant of v. Eigenfunctions and eigenvalues of the L operator are:[10,p101]

$$f_n = \frac{f_{sta}}{v\sqrt{D+H}} \exp(-x^2) H_{2n-1}(x) \qquad n = 0,1,...$$

$$x = v\left(2t_{s,e}^{-1}+\tau_{min}^{-1}\right)^{-1}(D+H)^{-1} \quad \lambda_n = n\left(2t_{s,e}^{-1}+\tau_{min}^{-1}\right) \quad (5)$$

H_n is a Hermite polynome of order n.

The loss term modifies strongly the stationary distribution function f_{sta} and the effective temperature T_{eff} [2,p751]. For typical condition, $t_{s,e}$ is 40 ms and a τ_{min} of 100ms or 50ms will give a T_{eff} 17% or 29% less that the one expected:

$$f_{sta} \rightarrow \left(f_{sta,\tau_{min}=\infty}\right)^{1+\frac{t_{s,e}}{2\tau_{min}}}$$

$$T_{eff} = \left(T_{eff,\tau_{min}=\infty}\right)\left(1+\frac{t_{s,e}}{2\tau_{min}}\right)^{-1}$$

An anisotropic study related to JET experiments is done in [5]. On TEXTOR, minority ions do interact with the majority ions and the first hypothesis is not valid. We use the previously derived functions to form a basis in order to calculate by diagonalisation the eigenfunctions of the complete operator. Fig 1 shows the evolution of the eigenvalues vs the RF power. For high RF power density, the analytical solutions (5) are recovered.

The sinusoidal modulation of the RF power is introduced as a perturbed operator Q:

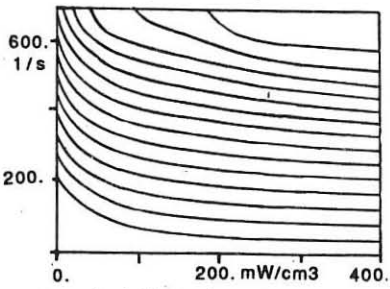

fig.1 Eigenvalues vs p_{min}

$$\frac{df}{dt} = \mathbf{L}f + \mathbf{Q}f\cos(\omega t) \qquad Q = \frac{1}{v^2}\frac{d}{dv}\left(v^2\tilde{H}\frac{d}{dv}\right)$$

The eigenfunction expansion gives:

$$f = \sum_{n=0} a_n f_n$$

$$\frac{d}{dt}\begin{bmatrix}a_0\\a_1\\...\end{bmatrix} = \begin{bmatrix}\lambda_{0,0} & ...\\ 0 & \lambda_1 ...\\ ... & ...\end{bmatrix}\begin{bmatrix}a_0\\a_1\\...\end{bmatrix} + \begin{bmatrix}q_{0,0}q_{0,1} & ...\\ q_{1,0}q_{1,1} & ...\\ ... & ...\end{bmatrix}\begin{bmatrix}a_0\\a_1\\...\end{bmatrix}\cos(\omega t)$$

Because of particle conservation, a_0 is constant. In case of small modulation, the power going from minority ions to background species is:

$$\tilde{p}_{min,i(e)} = \sum_{n=1} \frac{\pi_{min,i(e)_n} a_0 q_{0,n}}{j\omega + \lambda_n} \quad (4)$$

where $\pi_{min,i(e)_n}$ is the power density transferred to majority ions (electrons) for the mode n. Under conditions where majority ions and electrons are heated, many eigenfunctions participate with their own characteristic times (fig 2) and, so, we renounce our earlier treatment of eq.1 [8]:

$$j\omega E_{min} = -\frac{E_{min}}{\tau_{min}} - \frac{E_{min}}{\tau_{min,e}} - \frac{E_{min}}{\tau_{min,i}} + p_{min}$$

In addition, some eigenfunctions with very small characteristic time exist (fig.2). This is an evidence of the existence in the heating process of an ion slowing down time:

$$t_{s,i} \approx t_{s,e}\sqrt{\frac{m_e}{m_i}}$$

$t_{s,i(e)}$ are defined for $v_{min} < v_{th,i(e)}$. For a typical deuterium plasma in TEXTOR, $t_{s,e}$ and $t_{s,i}$ are 40ms and .7ms.

MODULATION EXPERIMENTS

The shots which will be analysed have been performed under the following conditions:

P_{rf}=1.MW, $|\tilde{P}_{rf}|$=0.35MW, $\omega/2\pi$: 5→26Hz antennae π phasing [8], pulse length:1.5s, $n_{eo}=4\,10^{13}cm^{-3}$, T_{eo}=1.4keV, T_{io}=1keV, 5% of H in D, sawtooth (ST) frequency: ≈50Hz.

Density and ST period modulation

The modulation induces parasitic effects on the density and on the ST behaviour. The recycling modulation of the wall, in phase with the RF power, produces a density modulation (fig.3 d,e). This periodic

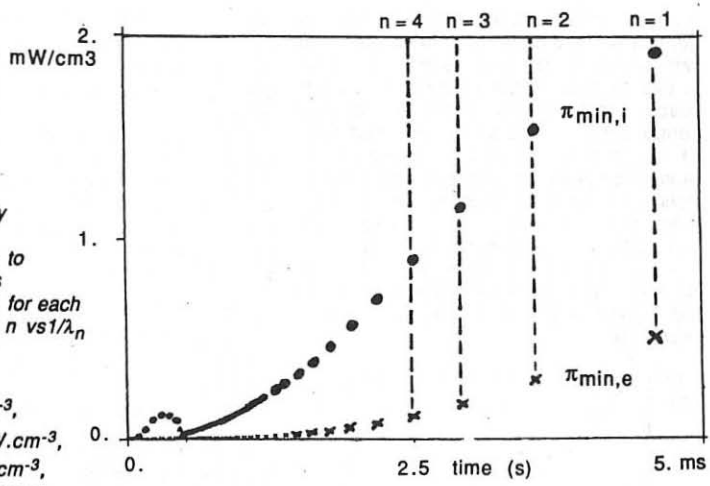

fig.2
Power density going from minority ions to majority ions and electrons for each eigenfunction n vs $1/\lambda_n$ (T_i=.8keV, T_e=1.keV, neo=10^{13}.cm^{-3}, $|\tilde{p}_{min}|$=10mW.cm^{-3}, p_{min}=10mW.cm^{-3}, 50 base functions).

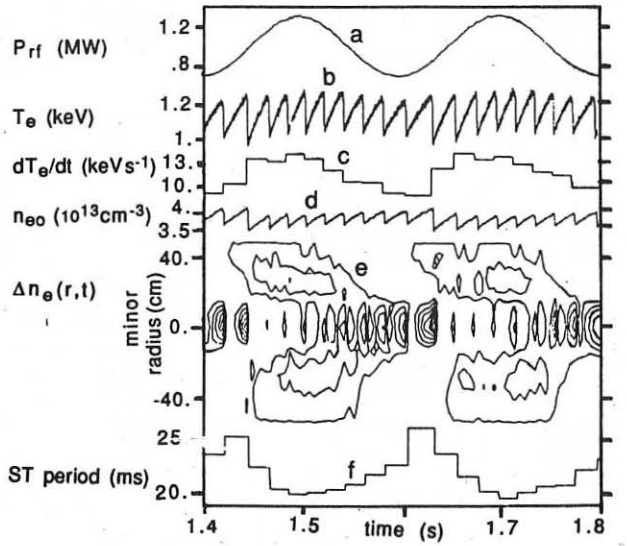

fig.3
Time evolution of
a/ the RF power
b/ the central electron temperature
c/ the slope of the central electron temperature during the sawteeth,
d/ the central density
e/ the profile of density variation (Contour plots of density variation. Positive steps of 5.10^{11}cm^{-3})
f/ the sawteeth period (shot 32455, fmod=5Hz, P_{rf}=1MW, $\tilde{P}_{rf}$=0.35MW)

particle influx creates a density rearrangement which progresses towards the center with a velocity of about 2.5 m/s. In addition to this, as soon as the modulation frequency reaches 10 Hz, the horizontal position control system is too slow and a modulation of the plasma position is observed. RF modulation produces also a change in the ST period. As seen on fig.3f, the ST is longer when the flux of particles arriving in the q=1 surface is maximum. As soon as the modulation frequency increases, particles do not have the time to reach the center in one RF period and the ST period variation decreases:

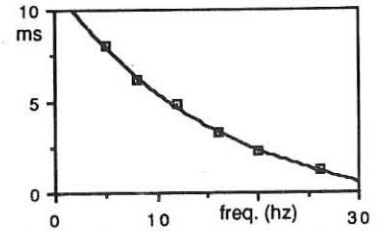

fig.4 Total variation of the sawteeth period for a peak to peak modulation of 0.7MW

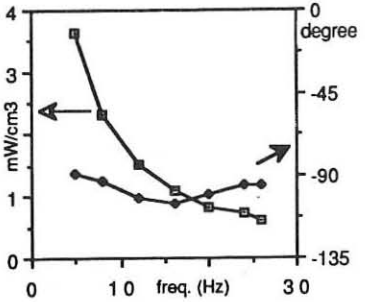

fig.5 Central electron energy. amplitude (for 1MW RF) and phase

Furthermore, when one harmonic of the RF modulation frequency is near the ST frequency, we observe a locking of the ST on the RF modulation frequency.

Central electron energy modulation

We construct numerically the central electron energy ($3/2 n_e k T_e$) to take into account the modulated density and we subtract the ST crashes to avoid the parasitic effect of the ST period modulation [9]. Modulated data are obtained by numeric filtering (fig.5). Because of the high central energy confinement during the ST rise, τ_e and τ_i are neglected in eq 3a and 3b. A fit of modulated central electron energy with our model (eq 2 and 4) gives the following power density:

	Prf=1MW	$\lvert\tilde{P}_{rf}\rvert$=0.35MW
pmin,i	140	20
pmin,e	70	57
pmc	75	26 mW/cm3

The RF modulation affects the existing minority tail which yields his energy mainly to the electrons. This explains the difference between the repartitions of the mean and the modulated power to the background species.

THANKS

The authors thank D.W.Faulconer and M.Jadoul for helpful discussions.

REFERENCES

[1] P.E. Vandenplas et al.,11th int Conf. on Plasma Phys. and Controll. Nucl. Fusion Res., IAEA, Kyoto, 1986, Vol.I, 485-493
[2] T.H. Stix, Nucl. Fus.,15 (1975) 737
[3] M.P. Evrard, Proc. 14th Europ. Conf. on Controll. Fusion and Plasma Phys., Madrid 1987, ECA. Vol 11D, part III, p809
[4] R.R. Weynants et al., this conference
[5] M.P. Evrard, this conference
[6] M.R. O'Brein, M. Cox, D.S.H. Start, computer phys. com., 40 (1986) 123
[7] R. Gianella et al., Nucl. Fus., 28 (1988) 193
[8] R.R. Weynants et al.,12th int Conf. on Plasma Phys. and Controll.Nucl.Fusion Res., IAEA,Nice,1988, paper IAEA-CN-50/E-2-1
[9] R. Koch et al., report n °87, LPP, ERM-KMS, Brussels, 1988
[10]H.Risken, The Fokker-Planck equation, Springer-Verlag, 1984

OBSERVATION OF A LOCALIZED RF ELECTRIC FIELD STRUCTURE IN THE SCRAPE-OFF LAYER DURING ICRF ON TEXTOR AND ASDEX.

R. Van Nieuwenhove, G. Van Oost, R. Koch, P.E. Vandenplas

Laboratoire de Physique des Plasmas, Laboratorium voor Plasmafysica, Association Euratom-Etat Belge, Associatie Euratom-Belgische Staat, Ecole Royale Militaire, B-1040 Brussels, Koninklijke Militaire School, Belgium

J.-M. Noterdaeme

Max-Planck-Institut für Plasmaphysik, Euratom Association D-8046 Garching, Federal Republic of Germany

Abstract. Radial RF electric field profiles, measured with fast drive probes in the SOL of TEXTOR and ASDEX during ICRF, revealed strong radial variations of the poloidal RF electric field. The electric field structure is found to be independent of plasma density, toroidal magnetic field and plasma current, thereby excluding surface waves or global modes as possible explanations.

Experimental set-ups. On TEXTOR, the measurements were performed by means of a fast drive double probe system [1], normally used to characterize the scrape off layer (SOL) density and temperature profiles during the ALT-II toroidal belt pump limiter operation. The scanning probe is located in the horizontal midplane of TEXTOR, at a distance of about 0.87 m toroidally away from ICRF antenna pair 1 (A1). A second ICRF antenna pair (A2) is located 180 ° away from A1. A description of the ICRF antenna system is given in [2]. The pneumatically driven double probe scans a distance of 15 cm, moving from behind the TEXTOR liner to near the ALT-II limiter tangency point in about 0.1 s. The double probe consists of two wires, each 0.63 mm in diameter and 3.0 mm long, separated by 2 mm in the poloidal direction. To measure the RF electric field at the generator frequency (29 MHz), the differential probe signal was first filtered by a bandpass filter with a flat frequency response in the range 25-35 MHz and then rectified by a linear RF detector. The RF fields measured in this way are not calibrated; the voltage $|V_m|$ measured over the terminating resistance R_T (50 Ω) of the coaxial measuring cable depends on the internal impedance R_p of the probe [3], since $|V_m| = |V_{RF}|\, R_T/(R_T + R_p)$ where $|V_{RF}|$ is the amplitude of the RF voltage in the plasma. Neglecting displacement currents through the sheath, which surrounds the probe tips, R_p is given by [3], $R_p = T_e/I_i$, where T_e is the electron temperature expressed in eV and I_i (A) is the ion saturation current to the probe. In the present situation, it turns out that $R_p \gg R_T$ and thus $|V_m| = |V_{RF}|\, / R_p = |V_{RF}|\, I_i / T_e$. Since I_i is proportional to $n_e\sqrt{T_e}$, where n_e is the electron density, one obtains $|V_m| \sim |V_{RF}|\, n_e/\sqrt{T_e}$. Except very close to the ALT-II limiter tangency point the electron temperature profile in the SOL was found [1] to be much flatter than the electron density profile, so that we can write $|V_m| \sim |V_{RF}|\, n_e$.

On ASDEX, the RF field profiles were also measured by a pneumatically driven fast drive probe system which scans a distance of 8 cm in about 200 ms. The probe manipulator is located in the horizontal midplane of ASDEX, at a distance of 1 m toroidally away from one ICRF antenna (labeled 'SO'). A second antenna pair (labeled 'NW') is located 180 ° away from the antenna SO. A description of the (cooled) ICRF antenna system is given in [4]. Two electrical dipole antennas, and two single-turn magnetic loop antennas were mounted on the head of the probe manipulator. For each pair, the two antennas were oriented perpendicularly to each other. These RF probes have a toroidal (z) (or poloidal (y)) extension of 37 mm, a radial extension of about 20 mm, and a thickness of 4 mm. In contrast to the measurements on TEXTOR, the measured RF amplitude $|V_m|$ was made independently of the plasma density and temperature in the SOL. This was accomplished by placing resistors (250 Ω) in series with each tip of the electrical dipoles at a distance of only 2 cm behind the probe tips.

Using typical SOL plasma parameters, an internal impedance R_p on the order of 8 Ω (thus significantly lower than on TEXTOR due to the much larger probe area) is obtained, which is much smaller than the external (2 × 250 Ω) series resistors. The measured RF amplitude can therefore be considered as essentially independent of R_p. The RF probe signals were filtered by a bandpass filter with a flat frequency response in the range 50-70 MHz to select only the generator frequency (67 MHz).

Measurements. The measurements on TEXTOR were performed in four different gas mixtures; ^3He-(H), ^4He-(H), H and D-(H). The Radial Profile of the Electric field (RPE) for the ^3He -(H) mixture is shown in Fig.1. The position of the peaks in $|E_y|$ was found to be completely independent of the toroidal magnetic field B_T and of the line-averaged density $\bar{n}_{e0}$, for B_T between 1.8 and 2.1 T and $\bar{n}_{e0}$ between 2. 10^{13} cm^{-3} and 3. 10^{13} cm^{-3}. The decreasing amplitude of $|E_y|$ towards the wall can be attributed to the density dependent sensitivity of the RF electric dipole, as explained before. Note also that the radial position of the large peaks in $|E_y|$ seems to correspond to the radial position (r = 47 cm) of the most protuding part of the antenna protection limiters.
For the ^4He-(H) case, nearly the same electric field structure as compared to the ^3He-(H) case was observed. The position of the peaks in $|E_y|$ was the same as in the previous case (for the same antenna position). The plasma conditions were similar to those of the ^3He case, except for the plasma current. The structure in $|E_y|$ was found even for the lowest RF power (50 kW).
In pure hydrogen, the observed RPE is different as compared to the previous cases (Fig.2). The position 47.2 cm of the innermost peak corresponds again to the radial position of the most protuding part of the antenna protection limiters. The RPE was again found to be independent of B_T, $\bar{n}_e$ and the plasma current I_p.
The RPE in the case of D-(H) is shown in Fig.3. The ICRF antenna limiter was in this case positioned at r = 46 cm, which is also the radius where the RPE shows a sharp transition.
The measurements on ASDEX were performed in the second harmonic heating scenario in pure hydrogen and using the double null magnetic configuration. Neutral injection power was applied simultaneously with the ICRF heating pulse. An example of the observed RPE is shown in Fig.4, when only antenna NW was excited. This antenna is nearly at the diametrically opposite side of the torus. $|E_y|$ shows a sharp transition at r = 215.3 cm, while no transition is seen on the toroidal magnetic field component $|B_z|$. The position of the antenna protection limiter is at r = 212 cm, which is close to the radial position of the sharp transition in $|E_y|$, when one considers the radial extension (2 cm) of the electric dipole.
Measurements of the floating potential in the divertor of ASDEX have shown[6] previously a strong negative dip in the scrape off layer at the last flux surface entering the divertor (which is also the surface directly in front of the antenna).

Discussion. Since the sensitivity of the RF probes on TEXTOR depends on the electron density and temperature, strong radial variations in these quantities could, in principle, give rise to the observed RPE. When the scanning probe diagnostic was operated in the double Langmuir probe mode however, such strong variations of n_e and T_e were not observed; this fact and the ASDEX measurements therefore exclude such an explanation. A theoretical interpretation based on global or surface modes can also be excluded because the presence of such modes can cause only much more gradual radial wave amplitude variations and because their characteristics are strongly dependent on all plasma parameters. One might also think of resonance cones [7], to explain the two peaks in the ^3He-(H) and the ^4He -(H) case. This possibility can also be ruled out because (i) resonance cones depend strongly on the plasma density (ii) the "ion-branch" cones exist only for $\omega < \omega_{ci}$, whereas in most of the experiments ω was larger than ω_{ci}.
From previous measurements on TEXTOR [8] it is known that due to the sheath rectification effect at the ICRF antenna, a large dc current is generated between the ICRF antenna frame (box, screen, protection limiters) and the wall (liner). This dc current flows primarily along the magnetic field lines and results in a radially localized dc current layer in the SOL. The negative dip in the floating potential[6] in the divertor of ASDEX could also be related to this dc current layer. This dc current, according to sheath theory results from the RF current flowing in the same direction. Evidence for the existence of such toroidal RF currents generated by RF electric antennas has already been found on the CALTECH tokamak[9]. The link between the $|E_y|$ field structure and this RF current, as well as the apparent correlation between the radial position of the sharp transition in $|E_y|$ and the antenna position have to be further investigated.

Acknowledgements.
The authors like to thank Dr. D.M. Goebel and W.J. Corbett of the ALT-II group on TEXTOR for the use of their fast drive probe and the ASDEX and ICRH groups (Garching) for making the RF probe measurements on ASDEX possible.

References

1. Goebel,D., et al., J. Nucl. Mater. 162-164 (1989) (Proc. PSI-8).
2. Van Oost,G., et al., Fusion Technology, 12, 449-475, 1987.
3. Chen,F., Research Report IPPJ-750, Nov. 1985, Institute of Plasma Physics, Nagoya University.
4. J.-M. Noterdaeme et al., Fusion Technology (14 th Symp., Avignon,1986) Pergamon Press, Oxford 1986, Vol. 1, 795.
5. Van Nieuwenhove,R., Koch,R., Van Oost,G., et al., Europh. Conf. Abstracts, 14 th Eur. Conf. on Contr. Fusion and Pl. Phys., Vol. 11D, III, 928 (1987).
6. J.-M. Noterdaeme et al., Contr. Fusion and Plasma Phys. 14 th Eur. Conf., Madrid, Europh. Conf. Abstracts, Vol.11D, II, 678 (1987)
7. Fisher,R.K. and Gould,R.W., Phys. Fluids, 14, 1971.
8. Van Nieuwenhove,R. and Van Oost,G., J. Nucl. Mat., 162-164 (1989) (Proc. PSI-8).
9. Greene,G.J., Int. Conf. on Plasma Phys., Lausanne, 1984, p.5-9.

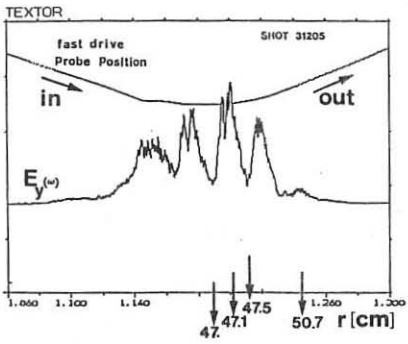

FIG. 1. Radial, uncalibrated profile of $|E_y|$ measured on TEXTOR in a $^3He(H)$ discharge, with 300 kW on A1 and 300 kW on A2 ; ALT-II limiter at 46 cm ; $B_T = 2.1\,T$, $I_p = 340\,kA$, $\bar{n}_{e0} = 2.0\,10^{13}\,cm^{-3}$, H concentration = 5 %.

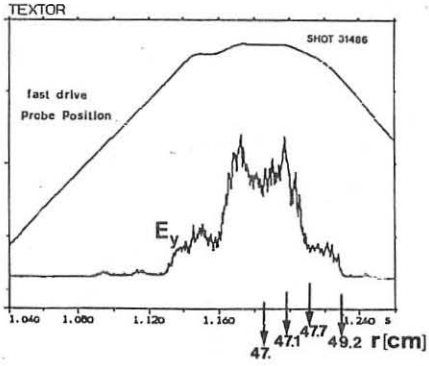

FIG. 2. Radial, uncalibrated profile of $|E_y|$ measured on TEXTOR in a H discharge, with 80 kW on A1 ; ALT-II limiter at r = 46 cm, antenna limiters at 47 cm, $B_T = 2.5\,T$, $I_p = 460\,kA$, $\bar{n}_{e0} = 3.7\,10^{13}\,cm^{-3}$.

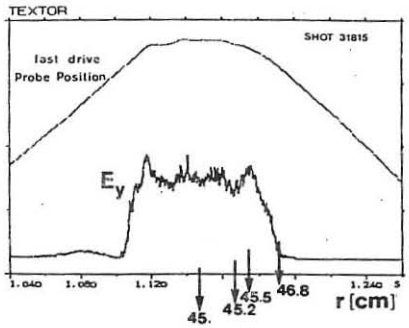

FIG. 3. Radial, uncalibrated profile of $|E_y|$ measured on TEXTOR in a D(H) discharge, with 400 kW on A1 and 400 kW on A2 ; ALT-II limiter at r = 44 cm, antenna limiters at r = 46 cm, $B_T = 2.0\,T$ $I_p = 337\,kA$, $\bar{n}_{e0} = 2.85\,10^{13}\,cm^{-3}$. H concentration = 6 %.

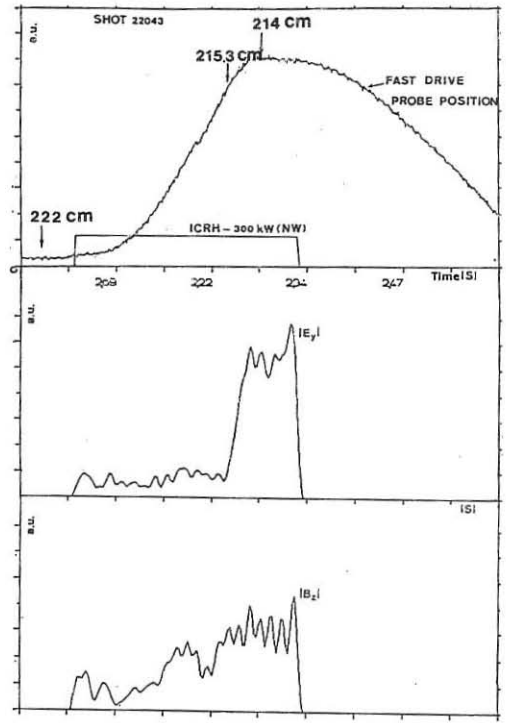

FIG. 4. Radial profiles of $|E_y|$ and $|B_z|$ measured on ASDEX in a H discharge, with 300 kW on antenna NW ; $B_T = 2.26\,T$, $I_p = 320\,kA$, $\bar{n}_{e0} = 3.0\,10^{13}\,cm^{-3}$, Neutral Injection power : 1.0 MW. Antenna limiters at r = 212 cm.

ION BERNSTEIN WAVE HEATING OF HIGH DENSITY PLASMAS WITH WAVEGUIDE ANTENNAS

A. Cardinali, R. Cesario, F. De Marco, M. Ono*

Associazione EURATOM-ENEA sulla Fusione, C. R. E. Frascati,
C.P. 65 - 00044 - Frascati, Rome, Italy

INTRODUCTION

Ion heating by an externally launched Ion Bernstein Wave (IBW) has assumed great consideration in recent years [1,2]. This frequency is in the range of ion cyclotron frequency and the energy transfer occurs via ion Landau damping near the harmonic resonance of ion cyclotron frequency (n = 2,5). Sources with high power levels are available in this range of frequencies and the coupling of the power to the plasma can be obtained by a waveguide antenna for avoiding the disadvantages of an antenna coil placed inside the vacuum vessel. This fact makes the IBW a very attractive technique for ion heating in tokamak-like reactor devices. The waveguide coupler is high and narrow and can fit between the toroidal coils of the tokamak. In the IBW range of frequencies, the waveguide structure can be much simpler than that for lower hybrid coupling and waves with $n_\parallel < 1$ could be coupled to the plasma.

In particular an experiment with a waveguide coupler is planned on FTU with a frequency of 433 MHz and a power of 1.5 MW. This frequency corresponds to the fourth harmonics of hydrogen near the plasma centre for a magnetic field B_0~8 Tesla on the axis.

THE DISPERSION RELATION

In order to study the propagation and the absorption of the externally launched IBW, we have used the complete electrostatic dispersion relation in a slab geometry:

$$\varepsilon_{xx} n_\perp^2 + \varepsilon_{zz} n_\parallel^2 = 0 \qquad (1)$$

where

$$\varepsilon_{xx} = 1 + \sum_a \frac{\omega_{pa}^2}{\omega^2} \sum_{-\infty}^{+\infty} \frac{n^2}{\lambda_a} I_n(\lambda_a) e^{-\lambda a} x_{0a} Z(x_{na})$$

$$\varepsilon_{zz} = 1 + 2 \sum_a \frac{\omega_{pa}^2}{\omega^2} \sum_{-\infty}^{+\infty} I_n(\lambda_a) e^{-\lambda a} x_{na} (1 + x_{na} Z(x_{na})) \qquad (2)$$

$$\lambda_a = \frac{k_\perp^2 V_{tha}^2}{2\Omega_a^2}, \qquad x_{na} = \frac{\omega - n\Omega_a}{k_\parallel V_{tha}} \tag{3}$$

and $Z(x_{na})$ and $I_n(\lambda_a)$ are the plasma dispersion function and the modified Bessel function respectively.

The electrostatic approximation seems to be justified here because of the very high value of $n_\perp$ everywhere inside the plasma. The only critical point is the very edge of the plasma where the lower hybrid resonance layer takes place ($\omega_{LH} \sim \omega_{IBW} \sim \omega_{pi}$).

This layer, as we will see later, is easily overcome by the wave which propagates freely towards the harmonic resonance. Equation (1) is solved in the complex plane for $n_\perp$ in all the slab domain. Our numerical method for finding the complex roots of Eq. (1) is based on the Newton formula of approximation on the complex plane and needs an initial guess to start.

The calculation is repeated at each point x in the plasma. As $n_\perp$ is a complex quantity, we can have information on the characteristics of propagation of the radio-frequency (real part of $n_\perp$ vs x) and on the wave absorption (imaginary part of $n_\perp$ vs x). In the numerical treatment of Eq. (1), we have taken up to the hundreth harmonics of the ion species ($n = \pm 100$) in the series of Eqs. (2). This was necessary because, owing to the high value of λ_i ($1 < \lambda_i < 10$) for the ion species, the series of Eqs. (2) does not converge rapidly as in the case of electrons where $\lambda_i \ll 1$. In Fig. (1a,b) we show a run of

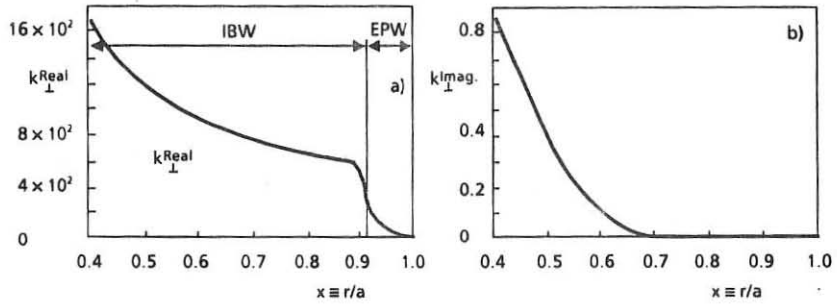

Fig. 1 - a) Real part of $k_\perp$ vs x (normalized slab length) for FTU typical plasma parameters: a = 31 cm, R_0 = 93,5 cm, B_0 = 7,8 Tesla, n(O) = $3.5 \cdot 10^{14}$ cm^{-3}, Te(O) = Ti(O) = 1.5 keV, $n_\parallel$ = 5, hydrogen plasma and density and temperatures parabolic profiles; b) Imaginary part of $k_\perp$ vs x for the same parameter as in Fig 1a

our code for FTU plasma parameters. The real part of $n_\perp$ vs x gives the characteristics of propagation of the IB wave. It is possible to recognize at the very edge of the plasma the LHW resonance layer. In this region the mode transformation process occurs [3]. This is a process where a wave (EPW) excited at the plasma boundary goes into another type of wave (IBW) without singularities in the transition region.

The imaginary part of $n_\perp$ gives the rate of absorption of the wave by the plasma which becomes relevant when the wave approaches the harmonic resonance.

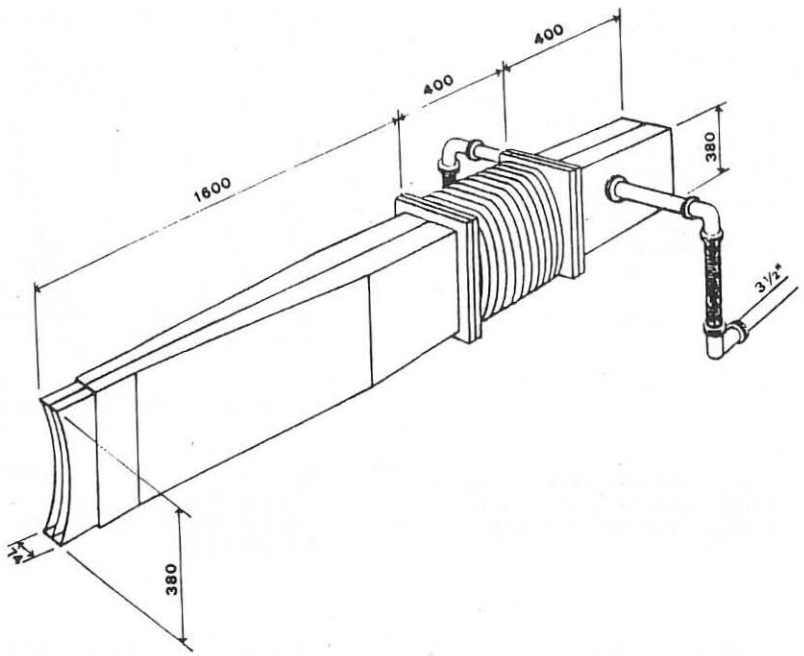

Fig. 2- IBW antenna: side view outline

IBW WAVEGUIDE COUPLING

The waveguide coupling coefficient is evaluated by the calculation of the reflection coefficient associated with the whole launched spectrum of a double waveguide antenna (Fig. 2): this is in order to have a good coupling to the plasma and to enhance the power handling capability.

The reflection coefficient is calculated by a modified version of the Brambilla code where the plasma surface impedance is calculated by using a slab model with a multistep plasma density profile [4].

Figure 3 shows a plot of the rf power spectrum vs the parallel refraction index for the two phasing conditions 0-0 and 0-π. Figure 4 shows the reflection coefficient vs the value of the plasma density at the mouth of the antenna for two phasing conditions of the grill. It is possible to observe two regions of the density where the reflection coefficient is low: one region around the value which corresponds to the LHW resonance just in front of the grill, and the other where the position of the grill is beyond the lower hybrid resonance. In this last case, a direct coupling of the IBW is expected to occur and very low values of the reflection coefficients are obtained for both the phasing conditions considered.

CONCLUSIONS

The IBW seems to be particularly indicated for tokamak-like reactor devices because, owing to the dimensions of these devices, the power carried by the wave can be coupled to the plasma by a waveguide antenna which can fit between the toroidal coils of the tokamak.

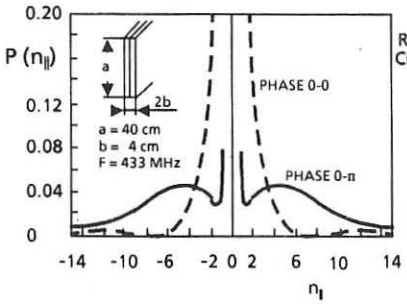

Fig. 3 - RF power spectrum vs the parallel refractive index for a double waveguide antenna suitable for the port of FTU

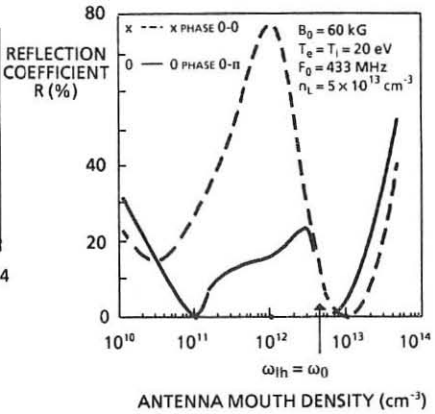

Fig. 4 - Plot of the reflection coefficient vs the plasma density value at the mouth of the antenna calculated by the IBW coupling code

Calculations on the propagation, absorption and coupling have been presented for FTU which seems to be very well indicated for an IBW heating experiment by a waveguide coupler with f = 433 MHz and P = 1.5 MW.

The ions of a hydrogen plasma would be directly heated at the fourth ion-cyclotron harmonics near the plasma centre.

REFERENCES AND FOOTNOTE

* Princeton University Plasma Physics Laboratory,P.O. Box 451, Princeton, NJ 08544 USA

[1] J.D. Moody, M. Porkolab, et al.: Phys. Rev. Lett **60**, 298 (1988)
[2] M. Ono, et al., Phys. Rev. Lett **60**, 294 (1988)
[3] M. Ono, K.L. Wong, G.A. Wurden: Phys. Fluids **26**, 298 (1983)
[4] J. Stevens, M.Ono, R. Horton, J.R. Wilson: Nucl. Fusion **21**, 1259 (1981)

STUDIES OF RF PLASMA PRODUCTION AND HEATING IN THE URAGAN-3 TORSATRON

Zaleskij Yu.G., Nazarov N.I., Plyusnin V.V., Shvets O.M.

Kharkov Institute of Physics and Technology,
the Ukrainian SSR Academy of Sciences, 310108 Kharkov, USSR

Introduction. In earlier experiments on ICRF plasma heating in the Uragan-2 stellarator [1] an effect of anomalously fast heating of hydrogen and deuterium ions during time much less then Coulomb time of energy exchange was revealed. As was shown in [2], such fast heating may be due to plasma particle scattering off turbulent pulsations of electric fields arising as a result of small scale instabilities [3] and parametric phenomena [4] in the plasma. The experimental proof of the existence of nonlinear phenomena during interaction of electromagnetic fields with plasma was obtained for the first time by the absorption line broadening in the $\omega \sim \omega_{ci}$ range [5] and by observation of low hybrid oscillations during the RF plasma heating on the Uragan-1 stellarator [6]. Recent measurements of RF oscillations spectra [7,8] have shown the existence of parametric phenomena in the edge plasma during ICRF heating experiments.

This paper describes the experimental results of investigations of wave processes during RF plasma production and heating by ion cyclotron (Alfven) waves (ICW(AW)) in the Uragan-3 torsatron [9].

Experimental results. The investigations were performed in the Uragan-3 torsatron ($R = 100$ cm, $B_o \leq 1.0$ T, $P_{RF} \leq 1.0$ MW), the plasma production with parameters $n_e \simeq 2 \div 4 \cdot 10^{12}$ cm^{-3}, $T_i \simeq 1$ keV, $T_e \simeq 0.3$ keV, was provided by using 0.4 MW of RF power. The measurements of spectrum of excited RF oscillations were performed for the study of wave processes in two regimes:

1. $B_o \simeq 0.7$ T, $f_o = 8.5$ MHz, $P_o \simeq 8 \cdot 10^{-6}$ Torr
2. $B_o \simeq 0.44$ T, $f_o = 5.2$ MHz, $P_o \simeq 1.2 \cdot 10^{-5}$ Torr

The change of working gas pressure is connected with the intention to keep the main plasma parameters constant after changing the value of the confining magnetic field. Both regimes corresponded to the frequency range $\Omega \equiv \omega_o / \omega_{ci} \simeq 0.8$. The longitudinal wavelength spectrum of ICW(AW) ($\lambda_{\parallel}$) was determined by RF current distribution in the antenna.

The measurements were performed by using moving probes: an RF magnetic probe (MRFP) and a single electric one (ERFP) located side by side in the equatorial plane on the opposite side of the torus with respect to the antenna. The measurements of electric RF oscillations in the plasma were performed by using ERFP, its bias being fixed close the plasma potential V_p . The amplitude of the radial component ($\tilde{H}_r$) of ICW(AW) in the plasma was measured by using MRFP.

The processes of plasma production and its density attaining a steady level during the RF voltage being applied to the antenna are presented in Fig.1. The evolution of the ICW (AW) magnetic field ($\tilde{H}_r$) and the electric RF oscillation ($\tilde{U}_{ep}$) detected signals is presented here too. In the initial stage of RF plasma production ($\bar{n}_e \simeq 10^6 \div 10^{10} cm^{-3}$) there are only electric RF oscillations. The spectrum of these oscillations (Fig.2) has a large number of harmonics of the pumping frequency f_0 . The analysis of the experimental conditions and the spectrum of the RF oscillations at this plasma production stage shows that RF oscillations with frequencies nf_0 ($n=2$, 3 ...) cannot be generated by the RF power source. Simultaneously with the RF oscillations low frequency fluctuations of the plasma density and potential V_p were observed in the 1 ÷ 100 kHz frequency band. These experimental facts show essentially nonlinear character of the processes described. Intense harmonics of the pumping frequency may be due to parametric instabilities of a low density plasma on electrostatic branch of AW [10] or due to nonlinear effects which develop near the antenna. These phenomena strongly influence the absorption of RF energy in the plasma and working gas ionization.

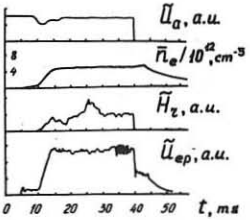

Fig.1. Plasma parameter evolution during RF discharge.

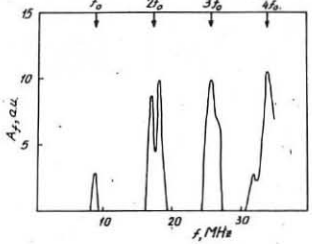

Fig.2. RF oscillation spectrum at the initial stage of plasma production.

At the density $\bar{n}_e \simeq 5 \cdot 10^{10} cm^{-3}$ the MRFP registers the appearance of RF oscillations (Fig.1) which are caused by ICW (AW) excitation. At the same time the ERFP registers a sharp increase of the RF electric oscillations simultaneously with the appearance of ICW(AW) $\tilde{H}_r$-component. The temporal evolution of the phase of these oscillations with the accuracy of $\pi/2$ correlates with the evolution of the $\tilde{H}_r$-component

phase with respect to the RF current phase in the antenna when the plasma density increases. Thus RF electric oscillations registered by ERFP at the pumping frequency are due to the electric field of ICW(AW). Apart from the pumping frequency f_0 and its harmonics the ERFP registers the oscillations with the frequencies $f_n = \frac{n}{2} f_{ci}$ (n=1,2,3...) at the stationary stage of the RF discharge. The important experimental result is the existence of these RF electric oscillations in the decaying plasma during a long time ($t \geq 5$ ms) after the RF generator is switched off.

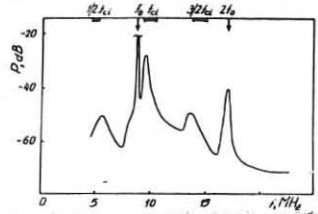

Fig.3.RF oscillation spectrum on the stationary stage of RF discharge (regime 1)

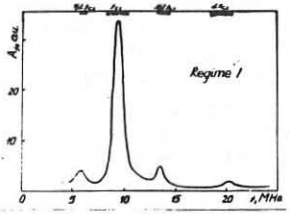

Fig.4.RF oscillation spectrum in the decaying plasma (regime 1)

The RF oscillation spectrum in the decaying plasma (Fig.4) is similar to that at the active stage of the RF discharge excluding the harmonics of the pumping frequency. This fact reveals a similar nature of these oscillations. It follows from the measurement that only electrostatic (potential) oscillations exist in the decaying plasma. The time of RF oscillations existence in the decaying plasma is comparable to the plasma energy lifetime. The comparison of RF oscillation spectra obtained in the regimes 1 (Fig.4) and 2 (Fig.5) shows the essential weakening of $2 f_{ci}$ oscillations when the confining magnetic field increases. The considerable broadening of RF oscillation spectrum and the shifting of it to higher frequencies as compared with the value of local ion cyclotron frequency at the probe localization were observed.

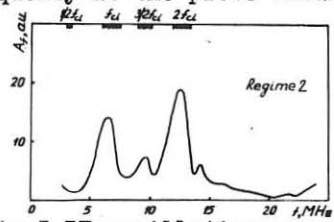

Fig.5.RF oscillation spectrum in the decaying plasma (regime 2).

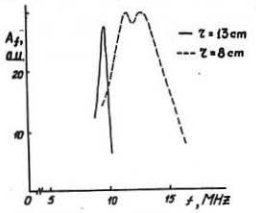

Fig.6.RF oscillation spectrum in the decaying plasma for two values of radial location of ERFP.

The oscillations on $f_n = \frac{n}{2} f_{ci}$ (n=1,2...) arise as a result of the RF instability of a plasma with hot ions. The presence of intence oscillations at ion cyclotron frequencies leads to a considerable increase in the effective collision frequency and to fast plasma heating.

Conclusions. The experimental results evidence strong nonlinear phenomena arising during RF plasma production and heating in the Uragan-3 torsatron. The arise of intense oscillations at the harmonics of ion cyclotron frequency leads to the increase of the effective collision frequency and to the fast plasma heating. The development of parametric instabilities at the initial stage of the RF discharge strongly influences neutral gas ionization and dense plasma production.

The authors are indebted to K.N.Stepanov for useful discussions and S.S.Kalinichenko for preparing the experiments and performing the measurements.

References

1. O.M.Shvets, S.S.Kalinichenko, Nazarov N.I. et al. Pis'ma v ZhETF, 1981, v.34, N10, p.533 (in Russian).
2. K.N.Stepanov. Fizika Plasmy, 1983, v.9, N1, p.45(in Russ.).
3. V.L.Sizonenko, K.N.Stepanov. Pis'ma s ZhETF, 1968, v.8, p.592 (in Russian).
4. A.B.Kitsenko, K.N.Stepanov. ZhETF, 1975, v.64, p.1606 (in Russian).
5. A.V.Dubovoi, O.M.Shvets, S.S.Ovchinnikov. Atomnaya Energiya, 1960, v.8, p.316 (in Russian).
6. N.F.Perepelkin, O.M.Shvets, M.P.Vasil'ev et al. In: Proc. of the 7th Europ.Conf. on Contr.Fus. and Plasma Physics, Lausanne, 1975, v.1, p.146.
7. R.Van Nieuwenhove, G.Van Oost, J.-M.Beuken et al.In:Proc. of the 15th Europ.Conf.on Contr.Fus. and Plasma Heating, Dubrovnik, 1988, v.12B,pt 2, p.778.
8. R.Van Nieuwenhove, G.Van Oost, J.-M.Noterdaeme, M.Brambilla et al. Report IPP III/129, January, 1988.
9. O.M.Shvets, I.A.Dikij, Kalinichenko S.S. et al. Nucl. Fusion, 1986, v.26, N1, p.23.
10. A.F.Korzh, K.N.Stepanov. Fizika Plazmy, 1987, v.13, N3, p.291 (in Russian).

A METHOD TO STUDY ELECTRON HEATING DURING ICRH

L.-G. Eriksson* and T. Hellsten

JET Joint Undertaking, Abingdon, Oxon., OX14 3EA, UK.
*Chalmers University of Technology, S-41296 Göteborg, Sweden.

INTRODUCTION - Collisionless absorption of ICRF waves occurs either by ion cyclotron absorption or by electron Landau (ELD) and transit damping (TTMP). Both ion cyclotron absorption, and direct electron absorption results in electron heating. Electron heating by minority ions occurs after a high energy tail of the resonating ions has been formed i.e. typically after 0.2-1s in present JET experiments. Electron heating through ELD, and TTMP, takes place on the timescale given by electron-electron collisions which is typically of the order of ms. This difference in the timescales can be used to separate the two damping mechanisms. This can be done by measuring the time derivatives of the electron temperature after sawtooth crashes during ramp-up and ramp-down of the RF-power.

After a sawtooth crash, the electron temperature profile becomes almost flat in the centre and hence resulting in a small energy conduction The electron energy balance equation can therefore be approximated by

$$\frac{d}{dt}\left(\frac{3}{2} nkT_e\right) = \eta j^2 - \frac{1}{\tau_{ie}} nk(T_e - T_i) - P_{rad} + P_{RFD} + P_{RFI} \qquad (1)$$

where η denotes the resistivity, j the current density, τ_{ie} the energy transfer time between ions and electrons, P_{rad} the radiation losses, P_{RFD} the direct RF-power density going to the electrons and P_{RFI} the power density due to power transfer from the heated minority ions.

The l.h.s. of Eq. (1) can be obtained from the experiment by measuring the slope of the electron temperature, vs time, after a sawtooth crash and from the electron density. The electron temperature is measured by the 12-channel grating polychromator [1], which measures the temperature at 12 positions. The density is measured with a 2mm microwave interferometer [2]. The main contributions to the r.h.s. of Eq. (1) comes from the ohmic and the RF-heating terms. Thus, if direct heating dominates over indirect heating, and the ohmic heating stays roughly constant, one would expect to see a linear relation between the coupled power and the electron heating after sawtooth crashes during power ramps. The power density due to direct electron heating by ICRH can then be obtained from the slope of the curve of the local electron heating (i.e. l.h.s. of Eq. (1)) vs the coupled power. Hence, the power deposition can be found by measuring this slope for different radii. If indirect heating dominates, the local heating becomes a nonlinear function of coupled power. In particular, the indirect heating should be delayed by the order

of a slowing down time for ion electron collisions, t_s. To get a qualitative understanding of the indirect heating, we study the following simplified Fokker-Planck equation

$$\frac{\partial f}{\partial t} = Q_{RF}(f) + \frac{1}{v^2}\frac{\partial}{\partial v}\left[\frac{v^3 f}{t_s}\right] + \frac{f}{t_1} \qquad (2)$$

where f is the distribution function, Q_{RF} is the RF-operator [3], and t_1 is an equivalent loss time. Multiplying by $\frac{1}{2}mv^2$ and integrating yields

$$W_f = \exp\left[-\int_o^t \left(\frac{2}{t_s} + \frac{1}{t_1}\right)dt'\right]\left\{\int_o^t p_{RF}(t)\,\exp\left[\int_o^t \left(\frac{2}{t_s} + \frac{1}{t_1}\right)dt''\right]\,dt' + W_f(t=0)\right\} \qquad (4)$$

where W_f is the energy of the resonating ions. The indirect electron heating is then obtained as $p_e = 2W_f/t_s$. It is possible to obtain some insight into the indirect heating by taking the experimental data for the electron temperature and the coupled power and integrate Eq. (4) numerically using different t_1 to model losses during a sawtooth crash.

ANALYSIS OF EXPERIMENT - A series of ICRH experiments were performed in ^{4}He-plasmas with ^{3}He as the minority species. The RF-frequency was equal to 33.9MHz chosen such that the cyclotron resonance of ^{3}He passed close to the magnetic axis. Toroidal dipole phasing of the antennae was used, which peaks the spectrum around toroidal mode numbers n ≈ 30. The axial electron density was about $n_e(0) \approx 4\text{-}4.5\times10^{13}$ cm^{-3}, $B_o \approx 3.4$T, $T_e \approx$ 5-10keV, $T_i \approx$ 4-8keV and $Z_{eff} \approx$ 4-4.5. The filling pressure of the minority ions, ^{3}He, varied between 5-120mbar.

The discharges #13683, 13684, 13687 and 13692 all showed a linear relation between the electron heating, p_e, and the coupled power, P_{RF}, indicating that direct electron heating dominated. The direct RF-power deposition profiles are shown in Fig.1. For the lower filling pressures (15-30mbar, 30mbar corresponds to $n_{^3He}/n_e \approx 0.05$) the deposition profiles are broad and almost identical whereas the 120mbar discharge gave a more peaked profile.

We have compared the measured power deposition profiles for direct electron heating with profiles calculated with a modified version of the LION code, which includes ELD and TTMP [4]. Two calculated power deposition profiles due to TTMP and ELD are shown in Fig.1, with $n_{^3He}/n_e$ = 0.025 and 0.05. The power deposition has been obtained by approximating the coupling spectrum with six toroidal modes. There is a rough agreement between the calculated and measured deposition profiles. Both show broad profiles which become more peaked at higher minority concentration.

Fig.2 shows p_e, P_{RF}, for discharges #13684, 13688 and 13689. Only the discharge with the lowest filling pressure (5mbar) gives a nonlinear relation between p_e and P_{RF} consistent with indirect electron heating. Discharge #13689, with filling pressure 60mbar, shows a non-linear relation between p_e and P_{RF} which is different from what one would expect from indirect heating. As mentioned before, discharge #13684, (30mbar), gives a linear relation between p_e and P_{RF} consistent with dominating direct electron heating.

Further information can be obtained by studying the energy content of

the minority ions. For indirect electron heating the energy content of the minority ions should be large whereas it is expected to be small for direct electron heating. The energy content in the perpendicular minority ion tail, W_f, can be obtained as: $W_f = 3/4(\delta W_{DIA} - \delta W_{MHD})$, where W_{DIA} and W_{MHD} measures the plasma energy content based on the diamagnetic effect and equilibrium calculations, respectively ($W_{DIA} = 3/2\ W_\perp$, $W_{MHD} = 3/4\ W_\perp + 3/2\ W_{||}$). Fig.3 shows the estimated fast ion energy contents for discharge #13688, (8mbar) and 13692, (120mbar), the fast ion energy content increases only significantly for discharge #13688, which is in agreement with the analysis above. Both discharges #13688 and 13692 gave rise to sawtooth-free periods, whereas the discharges in the 15-30mbar range did not. Thus, it appears to be possible to create sawtooth-free periods with both dominating indirect electron heating or with dominating direct electron heating.

We now analyse discharge #7220 in which hydrogen minority heating in a deuterium was performed, $n_H/n_D \approx 0.03$. It was dominated by indirect electron heating. A prominent feature of this discharge is the hysteresis effect seen when the coupled power is ramped up and down, Fig. 4. A numerical solution of Eq. (5) using the experimental data for the electron temperature, RF-power etc. is also shown in Fig. 4. The theoretical curve has been normalised at $P_{RF} = 4.38$MW. The qualitative features, i.e. the shape of the curves, are in good agreement. It is interesting to note that the shape of the theoretical curve is almost unchanged if one assumes losses up to 50% of the fast ion energy content during a sawtooth crash. It is therefore difficult to determine the fast ion losses from this analysis.

DISCUSSIONS - For intermediate minority concentrations with the dipole phasing of the antennae a broad power deposition profile is obtained for the direct electron heating. Due to the large toroidal mode number no linear mode conversion should take place. TTMP and ELD are then the most likely absorption mechanisms. For the highest concentration of minority ions the direct deposition profile becomes more peaked. Comparison between the power deposition profile due to TTMP and ELD as calculated with the LION-code shows rough agreement with the measured profiles. Sawtooth-free periods were obtained for both the high and low minority concentrations, but not for the intermediate concentrations.

When indirect electron heating dominates, the electron heating increases on the time scale of high energy ions slowing down on electrons. Theoretical calculations of the electron heating are in good qualitative agreement with the measured values. The results indicate that indirect electron heating dominates for low minority concentrations and that a non-negligible part of the ions are being confined near the centre after sawtooth crashes.

ACKNOWLEDGEMENTS - The authors wish to thank the ECE-group for providing the measurements of the electron temperature. They are also grateful to Drs. D.J. Campbell and D.F. Düchs for valuable discussions concerning the manuscript.

REFERENCES

[1] Tubbing, B.J.D. et al., in Contr. Fusion and Plasma Physics, Proc. 12th European Conf, Budapest 1985, 9F-I (1985) 215.
[2] Fessey, J.A. et al., J. Phys. E: Sci. Instrum. 20 (1987) 169.
[3] Stix, T., Nucl. Fusion 15 (1975) 737.
[4] Llobet, X. et al., Proc. Joint Varenna-Lausanne Int. Workshop on "Theory of Fusion Plasmas", Chexbres, 1988.

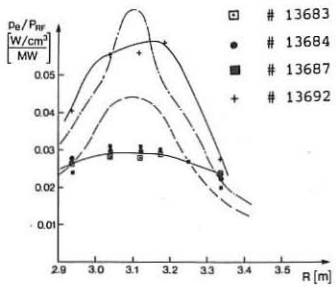

Fig. 1: Measured and calculated direct electron heating profiles calculated for
$n_{^3He}/n_e = 0.025$ (- - -),
$n_{^3He}/n_e = 0.05$ (-.-.-)

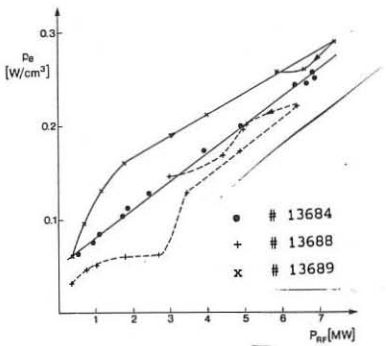

Fig. 2: The increase of the electron energy after a sawtooth crash, p_e vs coupled RF-power. The arrows show the time sequence.

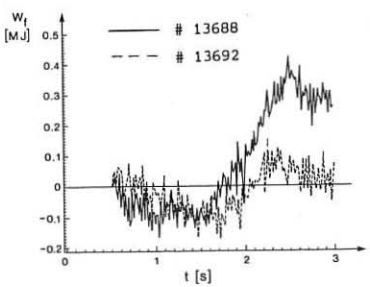

Fig. 3: Fast ion energy content. The RF-power is ramped during t = 2s to t = 3s and then reaches a flat top.

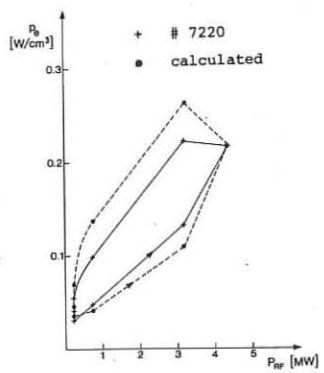

Fig. 4: The increase of electron energy after a sawtooth crash.

ICRF MINORITY HEATING COMBINED WITH COUNTER NEUTRAL INJECTION IN ASDEX

F.Ryter, M.Brambilla, A.Eberhagen, O.Gehre, R.Nolte, J.-M.Noterdaeme, F.Wesner,
ICRH-Group, ASDEX-Group, NI-Group

Max-Planck-Institut für Plasmaphysik,Euratom Association,
D-8046 Garching,Fed. Rep. Germany

Introduction:

As reported in ref /1/, counter-injection in the ASDEX tokamak is able to induce density profile peaking and a subsequent improvement of both the energy and particle confinement. We discusse here is the application of ion cyclotron hydrogen minority heating (33.5 MHz) combined with D^0 counter-injection to ASDEX deuterium plasmas containing a low percentage of hydrogen. The resonance layer was in the plasma center. The vacuum vessel was carbonised to handle the high impurity production due to ctr-NI.

1. Phenomenology of ICRH+ctr-NI discharges:

Figure 1 shows the time evolution of two discharges from an ICRH power scan (0.25-2.0 MW) combined with P_{NI}=1 MW ctr-NI (launched powers). As usual with ctr-NI, the discharges are not stationary. The line density increases monotonically, the plasma energy W_p reaches a maximum after which the impurity accumulation induces a rapid decrease of $T_e(0)$ and W_p, and the discharges end in a disruption, as discussed in ref /2/. The peaking factor $Q_n=n_e(0)/\langle n_e\rangle$ increases as soon as the injection starts, decreases suddenly when the ICRH begins, due to a strong density increase at the plasma edge, and then increases up to about 1.8 at which time W_p reaches a maximum. For ICRH powers larger than ≈1 MW, an intermediate maximum is observed for Q_n, W_p and $T_e(0)$. When the plasma center is not strongly dominated by the radiation losses, W_p and $T_e(0)$ follow the time behaviour of Q_n. In contast to the cases with ctr-NI alone in which $T_e(0)$ remains constant or even decreases along the shot, with ICRH $T_e(0)$ increases despite the density increase. The soft X-ray emission from the central chord shows the strong radiation increase of the plasma center due to impurity accumulation towards the end of the discharge when the sawteeth disappear. The sawtooth behaviour clearly depends on the ICRH power. At low power the sawteeth tend to stabilise early in the heating pulse and the period is erratic. As the ICRH power is increased, the period evolves smoothly and increases with Q_n and $T_e(0)$ or decreases when they decrease. The possible mechanism for the sawtooth

behaviour is discussed in a companion paper /3/. Figure 2 shows n_e, Q_n and $T_e(0)$ values measured at the when W_p is maximum (W_{max}), and immediately before the disruption plotted versus the total deposited heating power ($P_{tot}= P'_{OH} + \alpha_{NI}P_{NI} + \alpha_{IC}P_{IC}$), where $\alpha_{NI}=0.59$ and $\alpha_{IC}=0.7$ are the estimated absorption coefficients for ctr-NI and ICRH respectively. The values of Q_n and n_e at W_{max} are almost independent of P_{IC}. The difference between $T_e(0)$ at W_{max} and at the disruption reflects the radiation losses due to impurity accumulation. At high power the clear decrease of Q_n prior to the disruption is due to an edge density increase.

As discussed in ref /1/, the peaking occurence is sensitive to the edge plasma and the role of the ICRH in peaking mechanisms is unclear. We observed, particularly with a fresh carbonisation for which the recycling is high, that ICRH can prevent the density peaking. This suggests that an apropiate ICRH power combined with ctr-NI could control the peaking effects. Obviously the density peaking results from the balance between the Ctr-NI influence which increases with P_{NI} and an opposing ICRH effect. For instance, with a new carbonisation and P_{IC}=1.6MW, peaking did not occur with P_{NI}=1MW but occurred with P_{NI}=1.6MW. The ICRH edge density increase certainly plays a role. However the electron density and temperature near the separatrix in cases with and without peaking were not measurably different. Appropriate conditioning of the wall and of the antennas would improve the combination ctr-NI+ICRH.

2. Heating and confinement properties:

The heating properties of the series described in §1 are illustrated in figure 3. The maximum plasma energy follows the off-set linear scaling law as already observed with co-NI (see Fig. 4 and ref /4/). The incremental confinement time is about 37 ms. The same behaviour is found for the electron temperature and electron plasma energy which contributes about 70% of the total plasma energy. The radiation in the center increases more strongly with the power than in the co-NI case. W_{max} is determined by th opposing effects of the confinement improvement related to the density peaking and the radiation increase in the central part of the plasma. The ICRH contribution to the radiation in the center is around 0.8 Wcm^{-3} for 1 MW deposited ICRH power, which is to be compared with 1.3 Wcm^{-3}, the theoretical estimate of the absorbed power density in the center (for 1 MW). The radiation and RF power deposition profiles in the central part of the plasma (not shown here) have a comparable shape with a width of about r=10 cm.

Ctr-NI+ICRH and co-NI+ICRH are compared in figure 4 for various NI and ICRH powers in different series: Co1=co-NI+ICRH fresh carbonisation, Co2=co-NI+ICRH older carbonisation, Ctr1=ctr-NI+ICRH fresh carbonisation, Ctr2=ctr-NI+ICRH older carbonisation. The values of W_{max} for each ctr-NI discharge and W_p in the stationary phase for the co-NI discharges are plotted versus P_{tot}, (α_{NI}=0.85 for co-NI). No ctr-NI+ICRH dischargehas yet reached the highest plasma energy values obtained in Co1.However, all the ctr-NI+ICRH discharges lie within the range of the Co2 discharges. The Ctr1 discharges showed no clear peaking ($Qn\approx1.6$). The peaking factor for Co1 and Co2 lies at ≈1.5.

The co-NI+ICRH discharges have comparable hollow radiation profiles for which the central radiation is low. Therefore radiation effects cannot explain the difference between series Co1 and Co2. The difference is probably due to edge and wall conditions and/or to better RF absorption due to a more favourable hydrogen concentration. In contrast, the radiation plays an important role for ctr-NI discharges and in comparing the intrinsic confinement properties of co-NI+ICRH and ctr-NI+ICRH discharges it is important to take the central radiation into account. For this purpose, we correct the deposited power by substracting from it the radiation power inside a volume of a given radius, both for the co-NI and ctr-NI cases.The Ctr2 plot $W_p=f(P_{tot})$ becomes equal to or somewhat better than the Co1 one when r is taken in the range $15cm \leq r < 39cm$. For r=15cm, the correction is 15% and 3% of Ptot for the ctr-NI and co-NI cases respectively. This indicates that the confinement of Ctr2 and Co1 is comparable. It must however be stressed that the plasma energy is clearly correlated with the peaking factor for the ctr-NI+ICRH discharges. Indeed, figure 1 shows that W_p improves when Q_n increases. The RF absorption coefficent, a parameter which could play a role, is measured with an uncertainty of $\approx$20% which is not sufficiently precise to allow a difference between co-NI and ctr-NI casesto be detected. The NI absorption is well documented but a decrease could come from RF coupling to injected ions which would enhance orbit losses and contribute to losses of both the NI and ICRH power. It is however doubtful that this could be more than 20% of the NI-power.

3. Conclusion

The combination of ICRH minority heating with D^0 counter injection is able to produce peaked density discharges in which the confinement increases with the peaking factor. ICRH clearly heats the plasma center where the electron temperature reaches high values despite the high density and prevents an early radiation collapse of the discharges. The discharges follow the off-set linear scaling law, as previoulsy observed for co-NI+ICRH for which comparable values of the incremental confinement time are measured. The results could certainly be improved by a conditioning method of the wall and antennas which would reduce the impurity production and the recycling.

Acknowledgement

The authors wish to thank the operation teams of the ICRH, ASDEX and NI groups.

References:

/1/ G.Fussmann at al., 12th IAEA Conf. Plasma Phys. Contr. Fus., Nice 1988
/2/ A.Stäbler et al., this conference.
/3/ R.Nolte at al., this conference.
/4/ J.-M.Noterdaeme et al., 12th IAEA Conf. Plasma Phys. Contr. Fus., Nice 1988

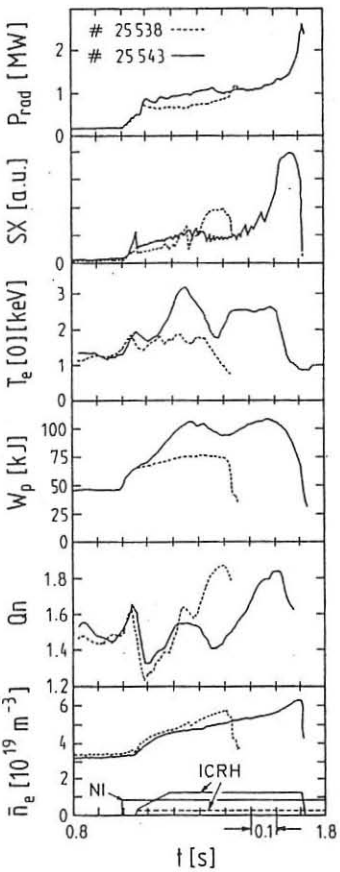

Fig.1 Time evolution of discharges with P_{NI}=1MW, P_{IC}=0.25Mw broken line, P_{IC}=1.7MW solid line. $\bar{n}_e$= line averaged density , W_p= plasma energy, Qn= density peaking factor, Te(0)=central electron temperature from laser scattering, probably somewhat over-estimated by the fit extrapolation, SX= line integrated central soft X ray signal, P_{rad}= volume averaged plasma radiation

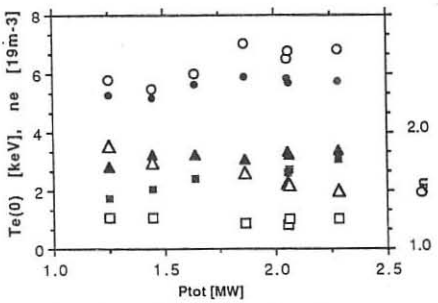

Fig.2 Q_n (triangles), n_e (circles), $T_e(0)$ (squares) at plasma energy maximum (closed symbols), before the disruption (open symbols), versus total power.

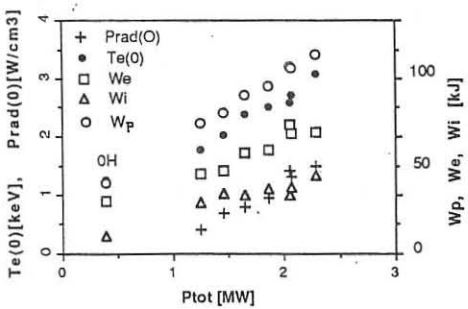

Fig.3 W_p, electron plasma energy We, Wi = Wp-We, central radiation power $P_{rad}(0)$, at W_{max} , versus total deposited heating power.

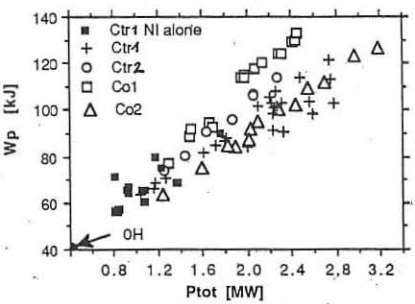

Fig.4 Plasma energy versus total deposited heating power for co-NI+ICRH and ctr-NI+ICRH discharges.

ANALYSIS OF THE LOADING RESISTANCE FOR ICRF HEATING EXPERIMENTS IN ASDEX

Y. Ogawa*, F. Hofmeister, J.-M. Noterdaeme, F. Ryter,
F. Wesner, J. Bäumler, W. Becker, F. Braun, R. Fritsch,
A.B. Murphy, S. Puri, H. Wedler, ASDEX-, NI-, Pellet-Teams

Max-Planck-Institut für Plasmaphysik, EURATOM Association,
D-8046 Garching, FRG.
* Institute of Plasma Physics, Nagoya Univ., Nagoya, 464-01, Japan

Introduction

Long-pulse high-power ICRF heating experiments have been conducted in the H-minority (10% H, f=33.5MHz) and second harmonic ($2\Omega_{CH}$,f=67MHz) regimes with two low-field-side antennas, in combination with NI and repetitive pellet refueling [1]. In three particular cases the loading resistance has been compared with theory, using a global wave code with a slab geometry [2]. 1) In H-minority heating experiments, H-phases lasting for up to 0.5 sec have been achieved in combination with NI. At the L-H transition the loading resistance decreases sharply. But, during the H-phase, the increasing density induces a variation of the loading resistance. Due to the presence of eigenmodes the pre-transition value can be recovered. 2) In long pulse $2\Omega_{CH}$ heating experiments, a slowly changing isotope concentration (H concentration; from 70% to 85%) is accompanied by a gradual decrease of the loading resistance. 3) In $2\Omega_{CH}$ heating experiments with repetitive pellet refueling, in which two confinement phases have been identified, it has been observed that the temporal behaviour of the loading resistance is also quite different for the two phases.

II. H-Minority Heating Experiments

In H-minority (10% H) heating experiments, H-phases lasting for up to have been achieved in combination with NI. The L-H transition induces a sudden decrease of the loading resistance (Fig. 1), which corresponds to a decrease of the density in the SoL. However, the loading resistance does not stay at the reduced level during the H-phase, but changes on a long time scale (0.2 sec) with many spikes due to ELMs. The slow variation is not correlated with the plasma position. Despite the fact that the density rises monotonically during the H-phase, the loading resistance has revealed maximum/minimum values. This is interpreted in terms of eigenmode effects.

Indeed, to understand this slow variation during the H-phase, we have calculated the loading resistance summed up for various toroidal mode numbers $n(=k_{\parallel}R_0)$ with the global wave code, as a function of density (Fig. 2). Peaks of the loading resistance correspond to eigenmodes standing between two cut-off layers of the fast wave (i.e., at the two-ion hybrid layer and at the plasma edge). The experimental loading resistance [3] during the H-phase is also plotted as a function of the density. The spacing of the peaks and the amplitude of the variation are in agreement with the loading

resistance calculated for $n \geq 16$. Therefore, we conclude that the slow variation of the loading resistance during the H-phase indicates the existence of the eigenmode. This is the first clear evidence of eigenmodes in ASDEX. Note that the theory predicts the disappearance of the eigenmode, if the percentage of hydrogen is reduced below 5%.

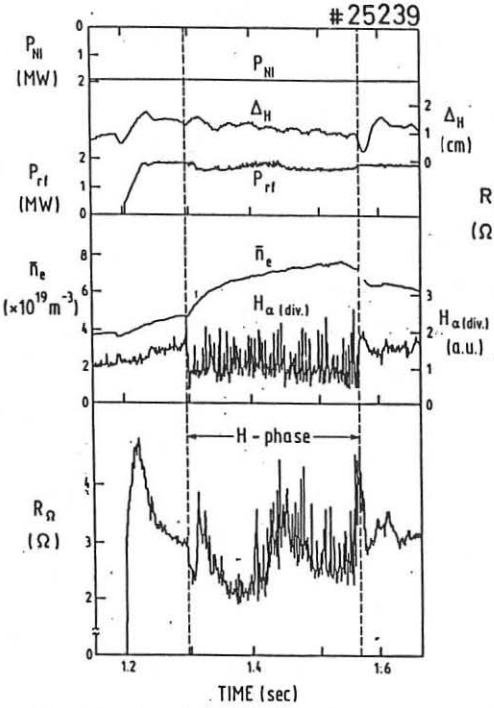

Fig. 1 H-mode discharge in 10% H-minority heating experiments.

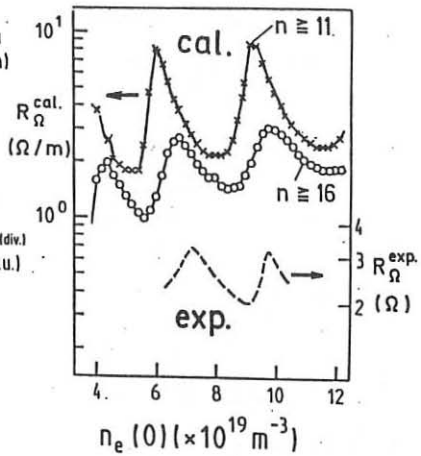

Fig. 2 The loading resistance calculated with a global wave code is plotted as a function of the central density $n_e(0)$ for various sums of the toroidal mode numbers $n(=k_\parallel R_0)$. The experimental data shown in Fig. 1 are also plotted.

III. Second Harmonic Heating Experiments

III.1 Long pulse discharge

Figure 3 shows a typical long pulse discharge for $2\Omega_{CH}$ heating experiments, where NI was used only at the beginning of the ICRF pulse. Let us first discuss the beneficial role of the NI(either H^0 or D^0). The loading resistance has been calculated as a function of the hydrogen temperature $T_H(0)$. The loading resistance increases monotonically with $T_H(0)$ below 1 *keV*, and saturates at $T_H(0)>1$ *keV*. Since the ion temperature in the ohmic phase is 0.6-0.7 *keV* in ASDEX plasmas and increases with NI pre-heating above 1 *keV*, the achieved better loading could be one reason why NI at the beginning of the rf pulse is beneficial for rf operation.

After the turn-off of NI, the gradual decrease of the loading resistance has been observed on a long time scale (1 sec), accompanied by a slowly changing isotope concentration (the H concentration increases from 70% to 85%). Other parameters are constant. From the computer code we found indeed that, as the H concentration is increased from 50% to 100%, the loading resistance decreases slightly, in agreement with the experimental observations. This can be understood in terms of the difference in the cut-off density for the fast wave between deuterium D and hydrogen H; i.e., $n_H(cut\text{-}off)/n_D(cut\text{-}off)=(\omega+\Omega_{CH})/(\omega+\Omega_{CD})=1.2$ for all various toroidal mode numbers $n(=k_\varphi R_0)$. Figure 4 shows the positions of the cut-off for H and D ions. When D is replaced by H, the position of the cut-off for the fast wave moves about 0.33 cm away from the antenna, giving a slight deterioration of the antenna-plasma coupling.

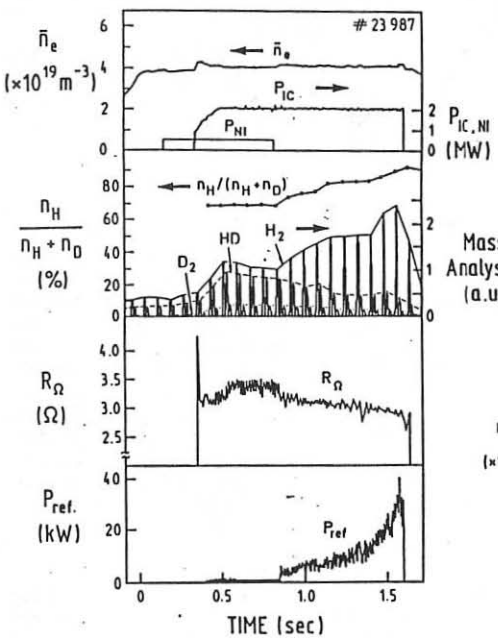

Fig. 3 Long pulse discharge for $2\Omega_{CH}$ heating, with the help of the NI at the beginning of the rf pulse.

The gradual decrease of the loading resistance experimentally observed could thus be explained by the increase of the cut-off density for H enriched plasmas, although the role of eigenmodes or changes in the SoL can not be excluded.

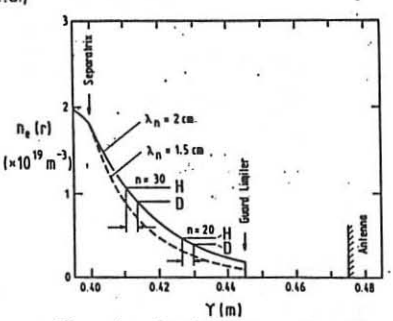

Fig. 4 Positions of the cut-off densities for the fast wave at the SoL for H and D ions.

III.2 Repetitive Pellet Refueling

In $2\Omega_{CH}$ heating experiment refueled by repetitive pellet injection, two confinement phases (phase I and II) have been observed [1]. The improved confinement phase (phase II) is characterized by a peaked density profile, accompanied by a deeper penetration of the pellet. Figure 5 shows the

loading resistance of the two antennas (called SO and NW) for the two phases. Synchronized to the pellet injection, a large positive spike has been observed clearly only on the signal of the SO antenna in phase I. Since the pellet injector is toroidally only 45° away from the SO antenna, but 135° from the NW antenna, this spike could be an indication of a strong perturbation transiently produced rather locally by the pellet in the boundary.

The temporal behaviour of the loading resistance after the pellet injection is quite different for the two phases. In phase I, the signal is characterized by a quick recovery(~15ms) followed by a gradual decrease, and in phase II the loading resistance is staying at the reduced level for a relatively long time. The plasma position seems to bear no clear correlation with it, as shown in Fig. 5. The time scales of these gradual changes seem to be corresponding not to those of SoL parameters, but to those of the bulk plasma(e.g., the changes of the density profile, H temperature and its high energy tail, and so on). Further work is in progress.

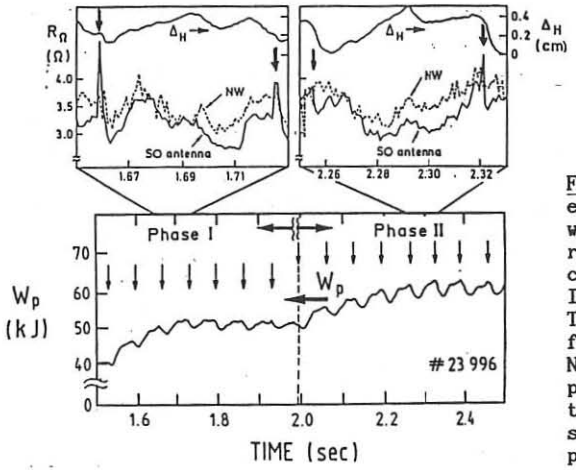

Fig. 5 $2\Omega_{CH}$ heating experiment in combination with repetitive pellet refueling, where two confinement phases (I and II) have been identified. The loading resistance for two antennas (SO and NW) and the plasma position Δ_H are shown for the two phases. Arrows show the times at which pellets are injected.

Acknowledgements

The authors wish to thank the members of the technical and operation teams of ASDEX, the ion cyclotron heating, the neutral beam injection and the pellet groups. One of the authors(Y.O.) acknowledges the members of Technology, ASDEX and W-VII groups for their hospitality. Computations are performed using the CRAY-computer in the Computer Center of the Max-Planck-Institut für Plasmaphysik.

References

[1] Noterdaeme, J.-M., *et al.*, 12th Int. Conf. on Contr. Fusion and Plasma Physics, Nice 1988, IAEA-CN-50/E-2-2.

[2] Fukuyama, A., *et al.*, Comp. Phys. Rep. 4 (1986) 137.

[3] Hofmeister, F., *et al.*, Proc. 14th Symp. of Fusion Technology (1986, Avignon), CEC, vol. 1, 801.

ENERGY GAIN OF PLASMA IONS IN A STRONG HIGH FREQUENCY ELECTRIC FIELD BETWEEN TWO TARGET PLATES

R. Chodura, J. Neuhauser

IPP Garching, EURATOM-Association, D-8046 Garching, Fed. Rep. of Germany

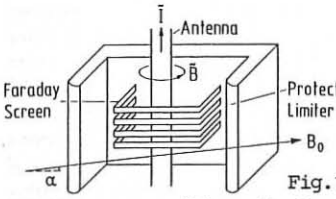

Fig. 1

Introduction. In the past RF-heating at ion cyclotron frequency has proved to be a promising method of plasma heating. Nevertheless, this method suffers from being connected with strong impurity production due to sputtering in the antenna region. The origin of the high energy sputtering ions is not quite clear. We discuss a possible mechanism for creating such high energy plasma ions and show some reults of a numerical model on this phenomenon.

Figure 1 gives a schematic view of an ion cyclotron wave antenna. A high frequency current flows through central conductor loop $\tilde{I}$. The loop is shielded by a Faraday screen of metallic strips which suppress electric field components parallel to the strip direction (and keeps plasma out of the antenna interior). The antenna is protected by a lateral limiter. The current loop is oriented poloidally, the Faraday strips either purely toroidal or nearly toroidal along the main magnetic field B_o (exact parallelism being very unlikely in practice).

Due to the finite inclination α of the magnetic field B_o relative to the toroidal direction, the poloidal RF current $\tilde{I}$ induces a magnetic RF flux through an area bounded by a contour which runs along a magnetic field line nearby to the antenna from a conducting wall to another (e.g. between Faraday strips, antenna limiters or vessel walls) and returns back through the conducting material. Thus, the magnetic RF flux produces a voltage along the magnetic field in the plasma between two material walls. This voltage can be estimated to be of the order of $10^2 - 10^3\ V$ for usual antenna currents of several hundred amperes, i.e. much larger than the plasma sheath potential of $\sim 3T_e/e$ in the antenna vicinity. We are mainly interested in this electric field effects along magnetic field lines rather than the details of launching the fast magnetosonic wave. Therefore we ignore magnetic field oscillations in the following study and replace the induced RF voltage along field lines between material walls by a given potential difference.

Model. In order to study the plasma response to the applied RF voltage, in particular the ion energy gain, an 1D electrostatic Monte-Carlo particle code [1] was used.

The code depends on one spatial coordinate perpendicular to the boundary targets (assumed as infinitely extended plates). The two target plates are assumed to be totally absorbing, the plasma to be collisionless. The loss of plasma particles and energy to the targets is replaced by an ambipolar particle and heat source flux. Between the two target plates a prescribed voltage is applied. The code calculates the spatial distributions of potential, current, density, etc. as well as the local velocity distributions of plasma ions and electrons, in particular at the target plates.

Results. Calculations were done for a prescribed potential difference ϕ between the two target plates at x=0, $\phi(0) = 0$ and x=L, $\phi(L,t) = \phi_o \cos \omega t$. Self-inductance in the circuit was ignored. In the following ϕ_o was chosen as $e\phi_o/T_o = 10$, where T_o is the temperature of ions and electrons entering the system at x=L/2 $\pm d$. The system length L was 160, d=5, in units of Debye lengths with temperature T_o and density $n_o = \Gamma_o/2C_o$. Γ_o is the ambipolar source flux along B_o of ions and electrons entering the system, $C_o = (T_o/m_i)^{1/2}$ the ion sound speed. Of course, the ratio of system length L to Debye length is not realistic but should not change the qualitative behaviour. The magnetic field B_o is assumed to strike the target plates under an angle of $\psi = 60°$ to the normal, and to have a magnitude such that $\omega_{ci}(B_o) = 0.1\omega_{Pi}(n_o)$. In order to save computing time the ion mass ratio was reduced to $m_i/m_e = 100$ (which diminishes the potential jump in the electrostatic sheaths).

Figure 2 shows profiles of potential ϕ and ion and electron fluxes Γ_{ix} and Γ_{ex} at two time steps a quarter period $\pi/2\omega$ apart as functions of the coordinate x perpendicular to the target plates for three different frequencies ω of the applied voltage $\phi(L,t)$. At the small frequency, $\omega/\omega_{Pi} = 0.1$, the potential changes only little within the plasma but exhibits a sharp drop alternatingly at one or the other plate. Electrons coming from the source cannot overcome this potential drop and move to the opposite plate. Ions flow towards both plates but prefer that with the potential drop. The density profile stays nearly constant, only the distribution in the sheaths adjacent to the plates differ. This result is similar to that expected from static Langmuir characteristics.

At the higher frequency, $\omega/\omega_{Pi} = 1$, the potential gradient within the plasma has increased. Additional to the electrons coming from the source, also the displaced electrons from the electrostatic sheaths at the plates, $n\lambda_D\omega$, contribute appreciably to the electron flux, giving rise to the sharp changes of Γ_e at the plates.

At the still higher frequency $\omega/\omega_{Pi} = 5$, i.e. for $\omega >> C_s/\lambda_D$ with C_s the sound speed, even the electrons no more can follow the externally applied potential changes. The potential now drops nearly completely within the plasma, only a small, thermal potential drop across the sheaths at the target plates remains. Ions and electrons now flow ambipolarly and symmetrically to both plates.

Figure 3 shows for the same frequencies as Fig. 2 the time history of the potential $\phi(L)$ across the 2 plates, the potential at the midplane in the plasma $\phi(L/2)$, the ion and electron fluxes Γ_{ix} and Γ_{ex} and the energy fluxes Q_{ix} and Q_{ex} per ion and per electron carried to one target plate. The plasma potential in the midplane essentially stays positive even during the half cycle of negative external potential as was found also experimentally in [2]. The fluxes are strongly oscillating for $\omega < \omega_{Pi}$ and become nearly stationary for $\omega >> \omega_{Pi}$.

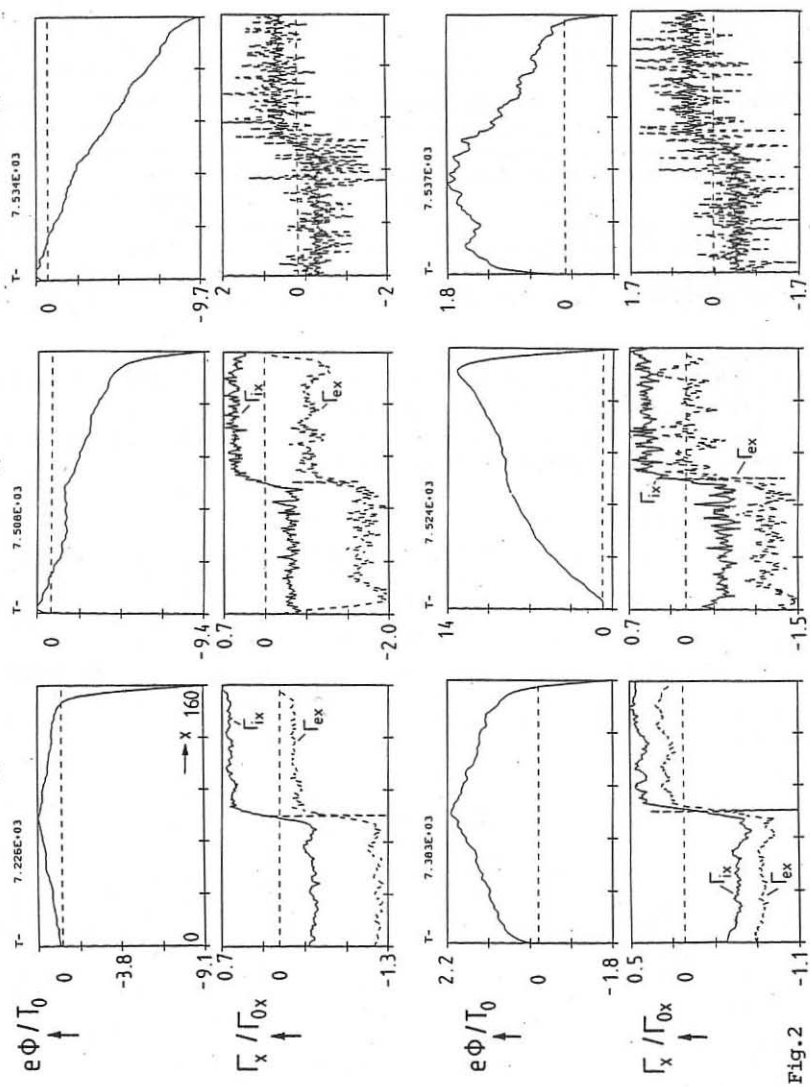
ω = 0.1ω_pi
ω = ω_pi
ω = 5ω_pi
eΦ/T_0
Γ_x /Γ_0x
T- 7.226E-03
T- 7.508E-03
T- 7.534E-03
T- 7.303E-03
T- 7.524E-03
T- 7.537E-03
x 160
Γ_ix
Γ_ex

Fig.2

Conclusions. The results clearly show that at least for $\omega \lesssim \omega_{Pi}$ (and hence for a typical Alfven and ion cyclotron range of frequencies) there is a significant nonresonant ion acceleration by sheath rectification of the induced electric field parallel to magnetic field lines. As a consequence significant sputtering is to be expected wherever these field lines intersect material walls, e.g. at the antenna screen, the antenna limiters or even at more remote structures, depending on the actual antenna and wave field distribution in the edge region. Assuming a sputtering coefficient in the percent range, a total ion flux of a few times $10^{20}\ s^{-1}$ into the antenna region is required in ASDEX to explain typical impurity influxes during ICRH [3]. This is only a small fraction of the total recycling flux and hence quite realistic. From the basic process it is clear that antenna optimization (Faraday shield, dipol antenna, etc.) minimizing the induced field along field lines intersecting material walls could significantly reduce the impurity inflow.

References.

[1] R. Chodura, Phys. Fluids **25**, 1628 (1982); J. Nucl. Mat. **111&112**, 420 (1982).

[2] L.I. Grigor'eva et al., J. Nucl. Mat. **128&129**, 317 (1984).

[3] J. Roth, G. Janeschitz et al., Impurity production and transport in the divertor tokamak ASDEX, submitted to Nuclear Fusion.

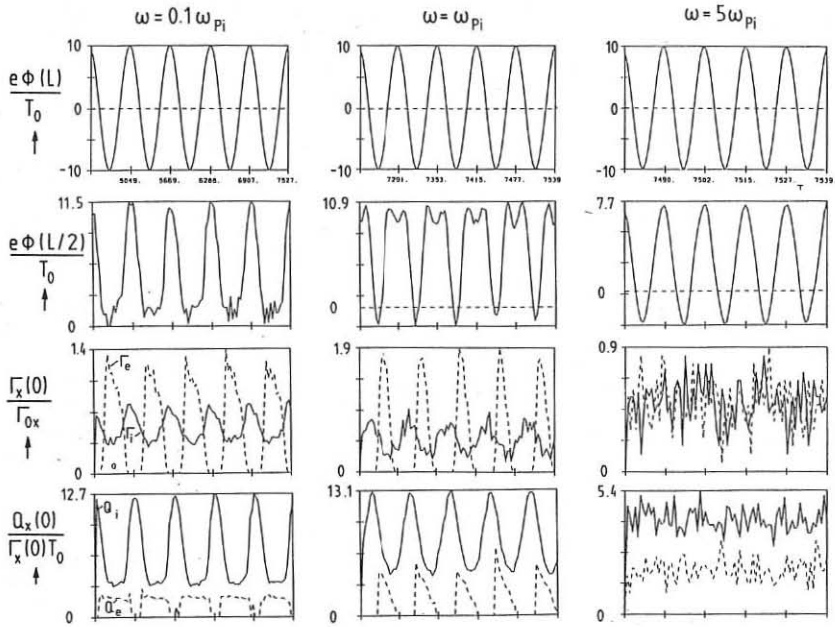

Fig.3

EVALUATION OF AN ICRF WAVEGUIDE LAUNCHER INCORPORATING A POLARIZATION ROTATOR

A. B. Murphy

Max–Planck–Institut für Plasmaphysik, D–8046 Garching, Fed. Rep. Germany.

Waveguides are potentially attractive wave launchers for plasma heating in the ion cyclotron range of frequencies. A conventional vacuum waveguide cannot, however, be used to launch the fast wave in a toroidal device, owing to the relatively low frequencies used, and the need to position the launcher between toroidal field coils. In this paper I evaluate an alternative waveguide design, illustrated in Fig. 1, which has been proposed by Vdovin [1; see also 2] for the ITER device. The waveguide is dimensioned with $a > c/(2f) \gg b$, where f is the excitation frequency and c the speed of light, so that only the $\mathrm{TE}_{1,0}$ mode propagates. This mode is excited by a horizontal coupling probe. A wire grid oriented at an angle ψ to the vertical wall rotates the wave polarization from $\pi/2$ to $\pi/2 - \psi$, through excitation of a large evanescent $\mathrm{TE}_{0,1}$ component. A horizontal Faraday screen at the waveguide mouth acts as an analyzer, reflecting the remaining $\mathrm{TE}_{1,0}$ component, and allowing the $\mathrm{TE}_{0,1}$ component to be coupled to the plasma. I first analyze separately the coupling from the waveguide to a large plasma through the Faraday screen, and the reflection and transmission of waveguide modes by the grid. I then consider the combined effect of these discontinuities, and coupling from a transmission line to the waveguide through the coupling probe.

WAVEGUIDE–PLASMA COUPLING

I describe the fields $\vec{E}^w$ and $\vec{H}^w$ in the waveguide as a sum of $\mathrm{TE}_{m,n}$ modes (denoting (m,n) by the subscript l). For example,

$$E_y^w = U(y,z) \sum_l G_l(y,z)[A_l \exp(-j\beta_l x) + B_l \exp(j\beta_l x)] \tag{1}$$

where $\beta_l = \sqrt{\omega^2/c^2 - (m\pi/a)^2 - (n\pi/b)^2}$, $G_l(y,z) = \cos(m\pi y/a)\sin(n\pi z/b)$, $U(y,z) = 1$ if $0 < y < a$ and $0 < z < b$, 0 otherwise. I approximate the plasma by a straight cylinder (with r, θ, z coordinate system) periodic in $z = 2\pi R$, where R is the major radius of the torus. The plasma fields $\vec{E}^p$ and $\vec{H}^p$ may be Fourier analyzed to give, for example, $E_\theta^p = \frac{1}{4\pi^2} \sum_\mu \sum_\nu E_{\theta\ \mu,\nu}^p(r) e^{j\mu\theta} e^{j\nu z/R}$. The boundary conditions at the vessel wall (i.e., at $x = 0$, $r = r_w$): $E_\theta^p(r_w) = E_y^w(0)$ and $U(r_w\theta, z) H_z^p(r_w) = H_z^w(0)$, and the orthogonality of the waveguide modes, give

$$A_q - B_q = \sum_l L_{ql}(A_l + B_l), \quad L_{ql} = \left(\pi^2 abr_w R D_q^w\right)^{-1} \sum_\mu \sum_\nu G_{q\ \mu,\nu}^* Y_{\mu,\nu}^p G_{l\ \mu,\nu}$$

$$\text{and} \quad G_{l\ \mu,\nu} = \int_0^a dy \int_0^b dz\, G_l(y,z)\, e^{-j\mu\theta} e^{-j\nu z/R}. \tag{2}$$

$D_q^w = \beta_q/(\mu_o\omega)$ is the waveguide admittance of the mode q, the asterisk denotes complex conjugate. Note that this expression differs from that given by Lam *et al.* [3], who mistakenly excluded the $U(r_w\theta, z)$ factor from the H_z boundary condition. The plasma edge admittance $Y^p_{\mu,\nu} = H^p_{z\ \mu,\nu}/E^p_{\theta\ \mu,\nu}$ is calculated for a plasma of proposed ITER parameters ($B = 5$ T, $R = 5.8$ m, $r_w = 2.4$ m) using the method of Theilhaber and Jacquinot [4]. All power is assumed to be absorbed in a central region of constant density $n_{eo} = 1 \times 10^{20}$ m^{-3}, which is surrounded by a parabolic region of width 1.4 m, and an edge region of width r_e in which the density decays exponentially from $0.1n_{eo}$ to $0.01n_{eo}$ at the wall. I use $f = 76$ MHz (twice the deuteron cyclotron frequency). The reflection coefficients $\Gamma_{lq} = K_q B_q/(K_l A_l)$, where K_l and K_q are constants used to give the waveguide fields the same normalization as defined in the next section, may be found using Eqn. (2).

Fig. 2 shows the power reflection coefficient $|\Gamma_{(0,1)(0,1)}|^2$ of the $TE_{0,1}$ mode calculated for different waveguide dimensions and plasma–wall separations, using up to 20 TE modes. For $0.05 \lesssim b/a \lesssim 0.1$, excellent transmission to the plasma occurs for a wide range of r_e (less than 1% of the input power is reflected as other modes in this range of b/a). The $TE_{1,0}$ mode is fully reflected with a phase reversal due to horizontal orientation of the Faraday shield.

POLARIZATION ROTATING GRID

I approximate the grid as N parallel, infinitely thin, perfectly conducting wires. Following Collin [5], the transverse waveguide fields $\vec{E}_l^T$ and $\vec{H}_l^T$ of mode l are normalized so that $\int_0^a \int_0^b \vec{E}_l^T \times \vec{H}_q^T \cdot \hat{x}\, dy\, dz = \delta_{lq}$, where δ_{lq} is the Kronecker delta. The amplitude of the scattered field of mode q due to an incident field of mode l is

$$S_{lq} = -\frac{1}{2} \sum_{k=1}^{N} \int I_l(L_k)\,(\sin\psi\,\hat{y} + \cos\psi\,\hat{z}) \cdot \vec{E}_q^T\, dL_k \qquad (3)$$

where $I_l(L_k)$ is the current excited along the kth wire by mode l (proportional to $\vec{E}_l^T(L_k)$) and the integral is along the wire. The corresponding reflection and transmission coefficients are $R_{lq} = S_{lq}$ and $T_{lq} = \delta_{lq} + S_{lq}$ respectively.

Fig. 3 shows the dependence of the transmission amplitude coefficients $T_{(1,0)q}$ on ψ for an incident $TE_{1,0}$ wave. The amplitude of the transmitted $TE_{0,1}$ mode is maximum at $\psi \sim 20°$. The corresponding value of ψ increases with both a and b, and is independent of N for $N \gtrsim 20$. $T_{(1,0)q} = 0$ for modes $q = (m, n)$ when $m + n$ is even.

GRID–PLASMA SYSTEM

The calculation of the combined effect of the polarization rotating grid and the waveguide–plasma boundary requires consideration of the scattering coefficients of both propagating and evanescent modes at both discontinuities, and the propagation coefficients of the modes. The resultant matrices for the reflection coefficient from the

grid $[\mathcal{R}_{(1,0)q}]$ and incident field on the Faraday shield $[\mathcal{A}_{(1,0)q}]$ due to the $TE_{1,0}$ mode incident on the grid are

$$[\mathcal{R}_{(1,0)q}] = [R_{(1,0)q}] + \sum_{S=0}^{\infty} [T_{(1,0)q}p_q]\,[\Gamma_{lq}p_q]\,([R_{lq}p_q]\,[\Gamma_{lq}p_q])^S\,[T_{lq}]$$
$$[\mathcal{A}_{(1,0)q}] = \sum_{S=0}^{\infty} [T_{(1,0)q}p_q]\,([\Gamma_{lq}p_q]\,[R_{lq}p_q])^S \tag{4}$$

where $p_q = \exp(-\gamma_q l_g)$, $\gamma_q = j\beta_q$ for propagating modes and $|\beta_q|$ for evanescent modes, and l_g is the grid–Faraday shield separation. The power transmitted to the plasma can then be calculated from $[\mathcal{A}_{(1,0)q}]$ and $[\Gamma_{lq}]$ using energy conservation.

Fig. 4 shows the l_g dependence of the fraction of the the incident power transmitted to the plasma for different values of a, b and ψ. This fraction is far lower than would be expected from separate consideration of the values of T_{lq}, R_{lq}, Γ_{lq} and p_q. This is because, after both the first and subsequent reflections from the Faraday shield, the $TE_{1,0}$ mode reaches the grid almost exactly out of phase with the initial incident mode, and the thereby reflected $TE_{0,1}$ component is thus also out of phase with the initially transmitted $TE_{0,1}$ component. The cancellation is most complete when the $TE_{0,1}$ and $TE_{1,0}$ components excited by the initial scattering of the incident $TE_{1,0}$ by the grid are of equal amplitude, which unfortunately occurs at the same ψ at which the excitation of the $TE_{0,1}$ mode is strongest (see Fig. 3). The cancellation effect can be reduced by increasing the phase shift undergone by the $TE_{1,0}$ mode in travelling between the grid and Faraday shield (by increasing l_g or a) or by decreasing the ratio $T_{(1,0)(1,0)}/T_{(1,0)(0,1)}$ (by increasing ψ). Note that increasing l_g increases the effect of the $TE_{0,1}$ mode's evanescence; this can be countered by increasing b. The efficacy of these measures can be seen in Fig. 4. In all cases, however, only a very small proportion of the power initially incident on the grid is transmitted to the plasma. It may be possible to improve this situation through the interposition of a horizontal inductive element between the grid and the Faraday shield. This would change the phase of the $TE_{1,0}$ mode, without affecting the $TE_{0,1}$ mode.

COUPLING TO THE WAVEGUIDE THROUGH THE COUPLING PROBE

Expressions for the coupling from a transmission line to a waveguide via shorted ($d = b$) and open-ended ($d < b$) cylindrical coupling probes (see Fig. 1) have been calculated by Collin [5] and Lam *et al.* [3]. Using these expressions, I find that it is possible to match a 50 Ω transmission line to the waveguide using an open-ended probe, despite the large reflection coefficient of the $TE_{1,0}$ mode from the grid–plasma system. For example, in the case with the best coupling to the plasma of those shown in Fig. 4, for which the $TE_{1,0}$ amplitude reflection coefficient is $-0.990+j0.086$, matching can be achieved using $t = 0.06$ m, $d = 0.18$ m, $l = 3.22$ m and $l_p = 2.78$ m. The standing wave ratio in the waveguide would, however, be extremely high, leading to substantial losses in the waveguide walls, and possibly to breakdown problems at high power. Without modification, the waveguide would thus be unsuitable as a high power ICRF launcher.

REFERENCES

[1] Vdovin V. L., ITER Current Drive and Heating Meeting, Paper 29, Garching, 1988.
[2] Wilhelm R., to be published in *Fusion Eng. and Design.*
[3] Lam N. T. *et al.*, *IEEE Trans. Plasma Science* **14** (1986), 271.
[4] Theilhaber K. and Jacquinot J., *Nucl. Fusion* **24** (1984), 541.
[5] Collin R. E., *Field Theory of Guided Waves*, McGraw-Hill, New York (1960).

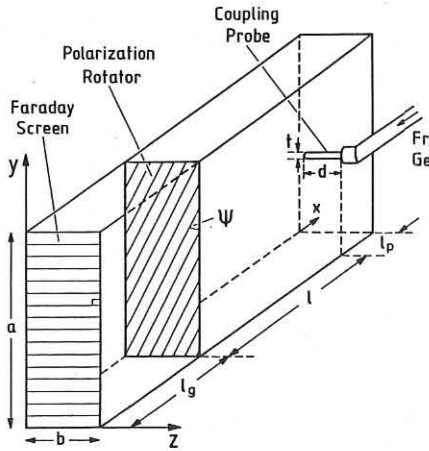

Fig. 1—The waveguide launcher.

Fig. 2—b/a dependence of the power reflection coefficient of the $TE_{0,1}$ mode from the waveguide–plasma boundary.

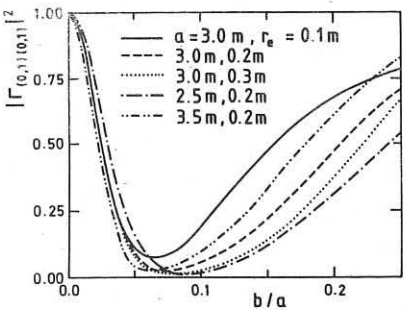

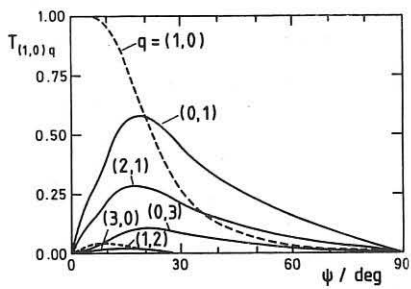

Fig. 3—ψ dependence of the transmission amplitude coefficients of different transmitted modes q, for a $TE_{1,0}$ mode incident on the polarization rotating grid, with $a = 3.0$ m, $b = 0.3$ m, $N = 51$.

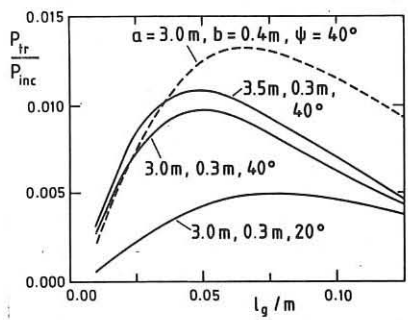

Fig. 4—l_g dependence of the ratio of power transmitted to the plasma to power incident on the grid, for the combined grid–plasma system.

NONLINEAR ION CYCLOTRON RESONANCE FOR TWO INTERACTING LOW-FREQUENCY WAVES IN A PLASMA

A.B.Kitsenko, K.N.Stepanov

Institute of Physics and Technology, the Ukrainian SSR Academy of Sciences, 310108 Kharkov, USSR

"Slow" short wavelength waves (SW) i.e. ion Bernstein modes (IBW) and "kinetic" Alfven wave (KAW) are used for plasma heating and current drive [1,2]. In some problems e.g. for creating two-component fusion regime or ion current drive it is necessary to provide the preferential absorption of large amplitude SW's by a certain ion species [2]. Solution to such a problem may encounter certain difficulties [2], e.g. the appearance of the opacity region for SW in the cyclotron resonance zone of the ion group being heated or a strong Cherenkov absorption by electrons. It is shown in the present report that if one uses two large amplitude SW's with different frequencies $\omega(\vec{k})$ and $\tilde{\omega}(\vec{\tilde{k}})$ then ion cyclotron absorption of these waves may be accomplished by ions resonating with the beat wave,

$$\Omega = \omega(\vec{k}) + \tilde{\omega}(\vec{\tilde{k}}) - (k_\parallel + \tilde{k}_\parallel) v_\parallel - n\omega_{ci} \approx 0, \qquad (1)$$

where $n = 0, \pm 1, \pm 2, \ldots$, ω_{ci} is the ion cyclotron frequency, $\vec{k}$ and $\vec{\tilde{k}}$ are wave vectors of the first and second waves. Using the resonance (1) offers new possibilities for plasma heating and current drive.

Nonlinear ion cyclotron damping of one pumping wave ($\omega(\vec{k}) \approx \tilde{\omega}(\vec{\tilde{k}})$, $\vec{k} \approx \vec{\tilde{k}}$), theoretically predicted in papers [3,4] was discovered experimentally for $n = 1,3,5$ in several devices [1,5]. In [3] for a general case of nonpotential waves there was determined the part of nonlinear cyclotron damping that is connected with nonlinear effects of resonant particle movements in electric and magnetic fields of the wave (nonlinearity enters the wave phase) and the influence of beat wave fields on the movement of these particles was neglected, the beat fields being connected with the nonlinearity of the plasma itself. In [4] the nonlinear cyclotron damping of ion Bernstein wave is determined with the account of both these effects ($n = 3,5,\ldots$).

The damping of interacting waves with spectral intensity $I(\vec{k})$ is defined by the kinetic equation

$$\frac{\partial I(\vec{k})}{\partial t} + v_{gx} \frac{\partial I(\vec{k})}{\partial x} - \frac{\partial \omega(\vec{k})}{\partial x} \frac{\partial I(\vec{k})}{\partial k_x} = 2\gamma_L(\vec{k}) I(\vec{k}) + 2\gamma_{NL}(\vec{k}) I(\vec{k}), \qquad (2)$$

where $\gamma_L(\vec{k})$ is the linear damping rate, $\vec{v}_g$ is the group velocity. The nonlinear damping rate is equal to

$$\gamma_{NL}(\vec{k}) = \frac{8\pi^3 e^4 k_\perp^2}{\partial \mathrm{Re}\,\varepsilon/\partial\omega\; k^2 m_i^2 \omega_{ci}^4} \int d\vec{\tilde{k}}\, \tilde{k}_\perp^2 I(\vec{\tilde{k}}) \left[\frac{q(\psi,\tilde{\psi}) q(-\psi,-\tilde{\psi})}{\Delta} - h \right], \quad (3)$$

where

$$q(\psi,\tilde{\psi}) = \int v_\perp dv_\perp dv_\parallel g\, \delta(\Omega) J_n(a') Q(\psi,\tilde{\psi}), \quad \Delta = \int v_\perp dv_\perp dv_\parallel g\, \delta(\Omega) J_n^2(a'),$$

$$h = \int v_\perp dv_\perp dv_\parallel g\, \delta(\Omega) Q(\psi,\tilde{\psi}) Q(-\psi,-\tilde{\psi}), \quad g = -\left(\frac{n\omega_{ci}}{v_\perp} \frac{\partial f_0}{\partial v_\perp} + k_\parallel' \frac{\partial f_0}{\partial v_\parallel} \right),$$

$$Q(\psi,\tilde{\psi}) = \sum_{j=-\infty}^{\infty} J_j(a) e^{ij\psi} J_{n-j}(\tilde{a}) e^{i(n-j)\tilde{\psi}} \left[\frac{\cos(\tilde{\psi}-\psi)}{(1-b)^2 - 1} + i \frac{\sin(\tilde{\psi}-\psi)}{(1-b)^2 (1-b)} + \frac{k_\parallel \tilde{k}_\parallel}{k_\perp \tilde{k}_\perp (1-b)^2} \right].$$

Here ψ and $\tilde{\psi}$ are the azimuth angles of wave vectors $\vec{k}$ and $\vec{\tilde{k}}$, $a = k_\perp v_\perp / \omega_{ci}$, $b = (\omega - k_\parallel v_\parallel)/\omega_{ci}$, $\vec{k}' = \vec{k} + \vec{\tilde{k}}$, $f_0(v_\perp, v_\parallel)$ is the resonant ion distribution function, $\varepsilon(\omega)$ is the linear permeability of potential waves. The intensity $I(\vec{k})$ is defined according to the relation

$$\langle \varphi(\vec{k},\omega) \varphi^*(\vec{\tilde{k}},\tilde{\omega}) \rangle = I(\vec{k}) \delta(\omega - \omega(\vec{k})) \delta(\omega - \tilde{\omega}) \delta(\vec{k} - \vec{\tilde{k}}), \quad (4)$$

where $\varphi(\vec{r},t) = \int d\vec{k} d\omega\, \varphi(\vec{k},\omega) \exp[i(\vec{k}\vec{r} - \omega t)]$ is the wave potential, $\vec{E}(\vec{r},t) = -\nabla\varphi(\vec{r},t)$, $\langle \dots \rangle$ is the symbol of statistical averaging.

For the plasma with Maxwellian distribution of ions for $|k_\parallel|, |\tilde{k}_\parallel| \ll k_\perp, \tilde{k}_\perp$

$$\gamma_{NL}(\vec{k}) = -\int d\vec{\tilde{k}}\, I(\vec{\tilde{k}}) \frac{n\omega_{ci}}{\sqrt{2}|k_\parallel'| v_{Ti}} \frac{\omega_{pi}^4}{\omega_{ci}^4} \frac{\exp(-z_n'^2)}{4\sqrt{\pi}\, n_e \varkappa T_i} \frac{\tilde{k}_\perp^2 |V|}{\partial \mathrm{Re}\,\varepsilon/\partial\omega}, \quad (5)$$

where

$$|V| = \int \eta d\eta\, e^{-\frac{1}{2}\varkappa^2} |Q(\psi,\tilde{\psi})|^2 - \left| \int \eta d\eta\, e^{-\frac{1}{2}\varkappa^2} J_n(a) Q(\psi,\tilde{\psi}) \right|^2 \left[\int \eta d\eta\, e^{-\frac{1}{2}\varkappa^2} J_n^2(a) \right]^{-1},$$

$$v_\perp = v_{Ti}\eta, \quad v_{Ti} = \sqrt{\varkappa T_i / m_i}, \quad z_n' = (\omega - n\omega_{ci})/\sqrt{2} k_\parallel' v_{Ti}, \quad \omega' = \omega + \tilde{\omega}.$$

Let us present the asymptotic expression for the factor $|V|$. In the case of one pumping wave ($\vec{k} \approx \vec{\tilde{k}}$, $\omega \approx \tilde{\omega}$) one has

$$|V| \simeq \rho^{2|n|+4} 2^{|n|+8} \left[|n|! (|n|+1)(|n|+2)^2 (|n|+4)^2 \right]^{-1}, \quad (\rho \ll 1); \quad (6)$$

$$|V| \simeq \exp(-\xi) \left[\frac{2}{\rho^2} - \sqrt{\frac{\pi}{2}} \frac{1}{\rho^3} - \frac{2}{\rho^2} \xi \exp(\xi) E_1(\xi) \right], \quad (\rho \gg 1); \quad (7)$$

where $\xi = n^2/(8\rho^2)$, $E_1(\xi) = \int_\xi^\infty dy \exp(-y)/y$, $\rho = k_\perp v_{Ti}/\omega_{ci}$.

Comparison with the numerical results [6] shows that the expression (7) for the case n=3 and n=5 differs from the exact value at $\rho \sim 2 \div 4$, where $|V|$ has a maximum, by 50%.

For two pumping waves at $\rho, \tilde{\rho} \gg 1$ and n=1

$$|V| \simeq \frac{1}{2\rho\tilde{\rho}} \left[2(1 + u\cos\varkappa) + \sin^2\varkappa \ln(4\rho\tilde{\rho}\sin^2\varkappa) + \delta \left[\sin^2\varkappa / \sqrt{\pi} - \right. \right. \quad (8)$$

$$\left. \left. - \frac{1}{2} \sin^2\varkappa \ln(u^2 - 1) + (\cos^2\varkappa - u^2) \ln\left[(u + \cos\varkappa)^2 / (u^2 - 1) \right] - \sqrt{2\pi}\, \rho'/(\rho\tilde{\rho})^2 \right],$$

where

$$\varkappa = \varphi - \psi, \quad u = (\rho^2 + \tilde{\rho}^2)/(2\rho\tilde{\rho}), \quad \tilde{\rho} = \tilde{k}_\perp v_{Ti}/\omega_{ci}, \quad \rho' = k_\perp' v_{Ti}/\omega_{ci}, \quad \delta = -\int_0^\infty e^{-y^2} \ln y\, dy \simeq 0.87.$$

For two narrow packets of interacting waves,

$$I(\vec{k}) = \mathcal{I}_\alpha [\delta(\vec{k}-\vec{k}_\alpha)+\delta(\vec{k}+\vec{k}_\alpha)] + \mathcal{I}_\beta [\delta(\vec{k}-\vec{k}_\beta)+\delta(\vec{k}+\vec{k}_\beta)], \quad (9)$$

from Eq.(3) there follow two nonlinear equations for $\mathcal{I}_\alpha$ and $\mathcal{I}_\beta$. These equations coincide with equations for amplitudes A_α and A_β of two waves with initial phases fixed,

$$\varphi(\vec{r},t) = A_\alpha \exp[i(\vec{k}_\alpha\vec{r}-\omega_\alpha t)] + A_\beta \exp[i(\vec{k}_\beta\vec{r}-\omega_\beta t)] + \text{compl. conj.}, \quad (10)$$

one only should change $\mathcal{I}_{\alpha,\beta} \to |A_{\alpha,\beta}|^2$. In a steady case for $\gamma_L(\vec{k})=0$ these equations have the form

$$\frac{d|A_\alpha|^2}{dx} = -\mathcal{Q}_{\alpha\beta} \exp(-z_n'^2)|A_\alpha|^2|A_\beta|^2, \quad \frac{d|A_\beta|^2}{dx} = -\mathcal{Q}_{\beta\alpha} \exp(-z_n'^2)|A_\alpha|^2|A_\beta|^2 \quad (11)$$

where

$$\mathcal{Q}_{\alpha\beta} = \frac{n\omega_{ci}}{2\sqrt{2\pi}|k_{\parallel}'|v_{Ti}} \frac{\omega_{pi}^4}{\omega_{ci}^4} \frac{k_{\alpha\beta}^2 |V(\vec{k}=\vec{k}_\alpha, \vec{k}'=\vec{k}_\beta)|}{n_0 x T_i} \left(v_{g\alpha}\frac{\partial \Re e\,\varepsilon}{\partial\omega_\alpha}\right)^{-1}, \quad z_n' = \frac{\omega_\alpha+\omega_\beta-n\omega_{ci}}{\sqrt{2}\,k_{\parallel}'v_{Ti}}.$$

The interaction of two waves occurs in a narrow region where $|z_n'| \lesssim 1$. Assuming that in this region ω_{ci} changes linearly with x, $z_n' = (n\omega_{ci}(0)/\sqrt{2}k_{\parallel}'v_{Ti})(x/R)$ where $R=(d\ln\omega_{ci}/dx)^{-1}$, and that the coefficients $\mathcal{Q}_{\alpha\beta}$ and $\mathcal{Q}_{\beta\alpha}$ do not depend on x we obtain that

$$\mathcal{Q}_{\beta\alpha}|A_\alpha(x)|^2 - \mathcal{Q}_{\alpha\beta}|A_\beta(x)|^2 = \text{const}. \quad (12)$$

Assuming that both waves are incident on the resonant layer from the side $x<0$ ($v_{gx}>0$) one obtains from (11) taking (12) into account:

$$\left|\frac{A_\alpha(x)}{A_\alpha(-\infty)}\right|^2 = \frac{1-\delta}{1-\delta\exp[-\tau(x)(1-\delta)]}, \quad \left|\frac{A_\beta(x)}{A_\beta(-\infty)}\right|^2 = \frac{(1-\delta)\exp[-\tau(x)(1-\delta)]}{1-\delta\exp[-\tau(x)(1-\delta)]} \quad (13)$$

where

$$\tau(x) = \mathcal{Q}_{\beta\alpha}|A_\alpha(-\infty)|^2 \int_{-\infty}^{x} \exp(-z_n'^2)\,dx, \quad \delta = (\mathcal{Q}_{\alpha\beta}|A_\beta(-\infty)|^2)/(\mathcal{Q}_{\beta\alpha}|A_\alpha(-\infty)|^2).$$

The relation (13) for $x=+\infty$ determines the damping of waves for one path through the layer. Evidently, the absorption will be noticeable at $\tau(\infty) \gtrsim 1$. If the amplitude of one wave considerably exceeds that of another one then at $\tau(\infty) \gg 1$ the small amplitude wave will be totally absorbed whereas the damping of the large amplitude wave will be small. The damping of both waves will be the strongest if $\delta \to 1$ and $|1-\delta|\,\tau(\infty) \ll 1$

$$|A_\alpha(\infty)/A_\alpha(-\infty)|^2 = |A_\beta(\infty)/A_\beta(-\infty)|^2 = [1+\tau(\infty)]^{-1} \quad (14)$$

where

$$\tau(\infty) = \frac{R}{2\sqrt{\pi}} \frac{\omega_{pi}^4}{\omega_{ci}^4} k_{\alpha\beta}^2 |V(\vec{k}=\vec{k}_\alpha, \vec{k}'=\vec{k}_\beta)||A_\beta(-\infty)|^2 \left(n_0 x T_i v_{g\alpha}\frac{\partial \Re e\,\varepsilon}{\partial\omega_\alpha}\right)^{-1}.$$

Evidently, the damping of both waves is complete if $\tau(\infty) \gg 1$.

For IBW with $\rho, \beta \sim 1$, $\omega_{\alpha,\beta} \sim \omega_{ci}$ one has $v_g \lesssim v_{Ti}$ and the condition $\tau(\infty) \sim 1$ determines the "threshold" value

of the specific power flux

$$\mathcal{S}_{th} \sim \frac{v_{Ti}^2 n_e \varkappa T_i}{2\sqrt{\pi}\,|V|\,R\omega}\,\zeta^2, \quad \left(\zeta = \left|\frac{\omega_{ci}^2}{\omega_{pi}^2}\frac{v_g}{v_{Ti}}\,\omega\frac{\partial k_{\parallel}\varepsilon}{\partial\omega}\right| \lesssim 1\right). \quad (15)$$

For devices with parameters of ITER the values of $\mathcal{S}_{thr}$ are not large, $\mathcal{S}_{th} \sim 1$ kW/cm^2.

If waves 1 and 2 are KAW's ($|\omega_{d,\beta}| < \omega_{ci}$) then only condition $|\omega_\alpha| + |\omega_\beta| = \omega_{ci}$ can be fulfilled. If one of the interacting waves is KAW and another one is IBW or both waves are IBW's then for them the conditions $|\omega_\alpha| \pm |\omega_\beta| \approx n\omega_{ci}$ at $n=1,2,\ldots$ may be fulfilled. For these waves the conditions are possible when the resonance (1) takes place in the central part of the discharge.

In conclusion we note that the obtained expressions for γ_{NL} at $n=0$ determine the nonlinear Landau damping. When using waves weakly absorbed in the linear approximation with $\omega/k_\parallel \gg v_{Ti}$ then strong absorption of both waves travelling in opposite directions may be provided if the beat wave with the differential frequency $|\omega_\alpha| - |\omega_\beta|$ possesses low phase velocity $|(|\omega_\alpha| - |\omega_\beta|)/(k_{\parallel\alpha} + k_{\parallel\beta})| \sim v_{Ti}$.

References

1. M.Ono. See Course and Workshop on Applications of RF waves to tokamak plasmas. Edited by S.Bernabei, U.Gasparino and E.Sindoni, vol.1, 1985, p.197.
2. A.V.Longinov et al. 11th Intern.Conf. on Plasma Physics and Controlled Nuclear Fusion Research (Kyoto, Japan, 1986) vol.2, IAEA, Vienna, 1986, p.205.
3. A.B.Kitsenko et al. ZhETF, v.67, N5(11), p.1726,1974 (In Russian).
4. M.Porkolab. Phys.Rev.Lett., 1985, vol.54, N5, p.434.
5. I.A.Dikij et al. 15th Europ.Conf. on Cotrolled Fusion and Plasma Physics (Dubrovnik, 1987), vol.11, p.734.
6. M.Porkolab et al. 11th Intern.Conf. on Plasma Physics and Controlled Nuclear Fusion Research (Kyoto, 1986) vol.1, IAEA, Vienna, 1987, p.509.

EXCITATION OF SLOW ICRF WAVES IN THE PLASMA WITH DIELECTRIC SLOWING DOWN STRUCTURES OR CORRUGATED METAL SURFACES

Longinov A.V., Lukinov V.A.

Kharkov Institute of Physics and Technology,
the Ukrainian SSR Academy of Sciences, 310108 Kharkov, USSR

1. Introduction. The possibility of using slow kinetic waves (SW(k)) in the $\omega \gtrsim \omega_{ci}$ frequency range (ion Bernstein waves) for plasma heating, current drive or creation of two-component regime of thermonuclear burning is determined mostly by the solution to the problem of coupling high RF-power to the plasma. Using "surface wave" antennae considered in papers [1,2] is one of the effective methods of SW(k) excitation. This report considers the possibility of improving the characteristics of such antennae with the help of slowing-down systems based on dielectrics or corrugated metal surfaces (CMS). For the first time using dielectrics for excitation the fast as well as slow electromagnetic waves (SW(E)) was considered in [3], whereas using CMS for LH wave excitation was considered in [4]. In contrast to previous work this report deals with the case when the density on the plasma edge fulfille the condition $\omega < (\omega_{pi}^2 + \omega_{ci}^2)^{1/2}$ and surface SW(E) may exist [1,2].

2. Description of the model. Fig.1 shows the scheme of the antenna system. The analysis is performed with the account of finite width of the slot δ using the theory described in [1,2] for the waves with $k_y = 0$. The excitating field on the slot is assumed to be homogeneous $E_z(z) = \text{const}$. Such approximation in the case when $\delta \gtrsim d$ may be valid, in particular, in the presence of additional plates located in the slot and enabling one to diminish the maximum gradients of the electric field. The CMS is described approximately as a medium with anisotropic conductivity ($\varepsilon_1 = \infty$, $\varepsilon_2 = \varepsilon_3 = 1$) what is strictly valid at $\delta_0 \ll d$.

Dispersion equation for surface SW(E)'s in the presence of slowing-down system has the following form:

$$\varepsilon_0 \kappa_n' (a + b\,\mathrm{th}\,\kappa_n' d) + \kappa_n (b + a\,\mathrm{th}\,\kappa_n' d)\,\mathrm{th}\,\kappa_n h = 0 , \qquad (1)$$

where

$a = N_{\perp 1} N_{\perp 2} (N_{\perp 1}^2 - N_{\perp 2}^2)$, $b = i\kappa_n' \varepsilon_3 [N_{\perp 2}(\varepsilon_3 - N_{\perp 2}^2) - N_{\perp 1}(\varepsilon_3 - N_{\perp 1}^2)]$, $N_\parallel = \mathrm{Re}\,N_\parallel + i\,\mathrm{Im}\,N_\parallel$.

$N_{\perp 1}$ and $N_{\perp 2}$ are refractive indices for SW(E) and SW(k), respectively, $\kappa_n' = \omega/c\,(N_\parallel^2 - 1)^{1/2}$, $\kappa_n = \omega/c\,(N_\parallel^2 - \varepsilon_0)^{1/2}$ for the case of dielectrics with the dielectric constant ε_0 and

$\kappa_n = i\omega/c$ and $\varepsilon_o = 1$ for a CMS.

Eq.(1) determines the value of longitudinal slowing-down ($Re N_{\parallel}$) of surface SW(E)'s. Propagating along the magnetic field the surface SW(E) is damped due to SW(k) excitation in the plasma. The damping length ℓ' may be determined as follows: $\ell' = c/\omega / Im N_{\parallel}$.

3. Discussion of the results.

The calculations were performed for the homogeneous d-plasma with the following parameters: $B_o = 4$ T, $\omega/\omega_{ci} = 1.95$, $n_e = n_i = 4 \cdot 10^{11}$ cm^{-3}, $T_i = T_e = 200$ eV. In Fig.2 there are depicted the $Re N_{\parallel}$ and $Im N_{\parallel}$ dependences of surface waves on the d dimension for systems with a dielectric ($\varepsilon_o = 3$) and a CMS ($h = 5$ cm). Here are also shown, for comparison, the curves for the vacuum gap ($\varepsilon_o = 1$).

In systems with a dielectric or a CMS ℓ' becomes considerably less than for the vacuum gap case. Especially, important role play the slowing-down system for the lowered T_i values and high n_e values on the plasma boundary when ℓ' increases strongly and its value may become inadmissible (Curves 2 and 3 in Fig.2). Strong increase in $Im N_{\parallel}$ on growing $Re N_{\parallel}$ is due to a stronger coupling between SW(E) and SW(k) for bigger $Re N_{\parallel}$ values (this fact was noted in [5] for current excitation systems).

Fig.3 shows the dependences of the active (Z_a) and reactive (Z_p) parts of the slot impedance and also of the antenna efficiency $\eta = P_p / P_o$ (P_p is the power coupled to the plasma, P_o is the power of Ohmic losses in the antenna, the material is stainless steel) on d dimension for a slowing-down system with a dielectric ($\varepsilon_o = 3$, $\delta = 2$ cm, $\ell = 3\lambda_v = 6\pi c/\omega$). The broken lines show the Z_a and η dependences for the vacuum gap ($\varepsilon_o = 1$). As is seen from Fig.3 due to smaller ℓ''s in the presence of a dielectric the range of small gaps d in which the radiation regime with a preferentially active impedance ($\ell' << \ell$) is realized widens approximately 3 times in comparison with the vacuum gap case. This is also the reason for the considerable increase in efficiency η .

Fig.4 shows the spectrum of SW(k)'s excited in the plasma in the presence of dielectric ($d = 1.1$ cm, $\ell = 3\lambda_v$): a) $\varepsilon_o = 3$ and b) $\varepsilon_o = 10$. "a" case corresponds to the resonance of the surface SW(E) with $Re N_{\parallel} = 2.5$ when $Z_p = 0$ and the power flux into the plasma has a maximum at the given potential difference across the slot. "b" case realizes the radiation regime of the surface SW(E) what the spectrum form shows. Thus the transition to the radiation regime may be accomplished by the choice of sufficiently small values of the gap d or by using the slowing-down system. Fig.5 shows the impedance versus d dependences illustrating the features of antenna systems with a CMS. Here the results of calculations are given for $\ell = 3\lambda_v$: $h = 5$ cm, $\delta = 2$ cm (broken line); $h = 15$ cm and three values of the slot width: $\delta = 10$ cm (curves 1), $\delta = 2$ cm (curves 2), $\delta = 0.6$ cm

(curves 3). The increase in the CMS depth h leads to widening the area of d-values where the antenna operates in the radiation regime of the surface SW(E) with a relatively weak Z_a versus d dependence. The characteristic peculiarity of the antenna system with a CMS consist in that by due choice of the slot width one may provide practically purely active character of the slot impedance in the wide range of spacing values (curve 2). For small slot width δ (curve 3) the reactive part of impedance Z_p is capacitive in nature whereas for large δ's the character is inductive.

Fig.6 shows the $|E_x|$ field distribution in the plasma and in the dielectric ($\varepsilon_o=10$, $d=1.1$cm) when spacing between slots of the antenna system is $\ell = 1.5\,\lambda_V = 7.5$ m ($\ell' \ll \ell$). The surface SW(E) in the dielectric excites SW(k) in the plasma in the form of two "cones" propagating in opposite directions from the slot area. The E_x field amplitude corresponds to the radiation power of each antenna $P = 2$MW/m (per unit length along the slot in y-direction). The strong diminishing of the field amplitude in the plasma ($E_x^{max} \approx 3$ kV/cm) as well as especially in a dielectric ($E_x^{max} = 1$ kV/cm) compared with the case $\varepsilon_o=1$ (see [2]) is due, first of all, to higher $\mathrm{Re}\,N_{||}$ values of the surface SW(E).

4. Conclusions. Using dielectrics or CMS allows one to increase the slowing-down of the surface SW(E) excited by the slot what increases sharply the SW(k) excitation efficiency and diminishes the damping length of the surface wave. Apart from the diminishing the longitudinal dimensions of the radiating surface one also achieves the diminishing of electric fields in the slot area. Using a dielectric also provides the gap without plasma near the first wall i.e. the condition necessary for the surface wave existence. The antenna systems suggested may be used for SW(k) excitation in the plasma with high RF-power fluxes in the $\omega \gtrsim \omega_{ci}$ frequency range for powerful heating regimes, current drive and the realization of the two-component regime of thermonuclear burning.

References

1. Longinov A.V. ZhTF, 1972, v.42, N8, p.1591 (in Russian).
2. Longinov A.V., Lukinov V.A. In: Contr.Fusion and Plasma Heating (Proc. 15th Europ.Conf.Dubrovnik, 1988) vol.2. Europ.Phys.Soc. (1988) 742.
3. Longinov A.V., Stepanov K.N. Preprint KhFTI 72-1, 2, Kharkov, 1972 (In Russian).
4. Golant V.E., Sov.Phys.- Techn.Phys. 16 (1972) 1980.
5. Sy W.M-C. et al. Nucl.Fus. 25 (1985) 795.

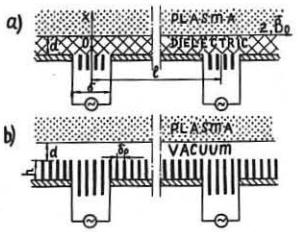

Fig.1 Antenna system scheme.

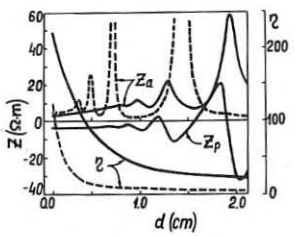

Fig.3 Real(Z_a)and imaginary (Z_p)parts of the antenna impedance and also efficiency versus d for $\varepsilon_o=3$ and $\varepsilon_o=1$ (the broken lines).

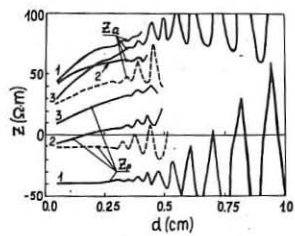

Fig.5 Real(Z_a) and imaginary (Z_p)parts of the antenna impedance versus d in the presence of a corrugated surface.

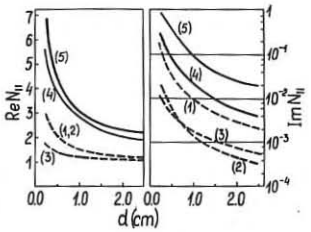

Fig.2 $ReN_{||}$ and $ImN_{||}$ versus d for the surface SW(E). Curve 1- $\varepsilon_o=1, n_e=4\cdot10^{11}$ cm^{-3}, T_i =200eV; Curve 2- $\varepsilon_o=1$, $n_e=4\cdot10^{11}$ cm^{-3}, T_i=50 eV; Curve 3- $\varepsilon_o=1$, $n_e=1{,}6\cdot10^{12}$ cm^{-3}, T_i=200 eV; Curve 4-corrugated surface, h=5 cm; Curve 5-dielectric, $\varepsilon_o=3$. Curves 4,5 - $n_e=4\cdot10^{11}$cm^{-3}, $T_i=200$eV.

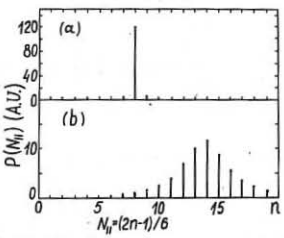

Fig.4 Radiation power spectrum at d=1.1cm; a)dielectric with $\varepsilon_o=3$, b)dielectric with $\varepsilon_o=10$.

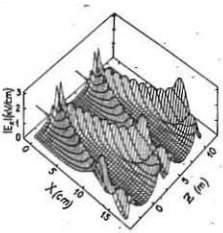

Fig.6 $|E_x|$ field distribution at the plasma periphery. Arrows point the location of the slots.

THE EFFECT OF THE PERIPHERAL PLASMA INHOMOGENEITY, DENSITY AND TEMPERATURE ON THE EXCITATION OF SLOW ICRF WAVES

Longinov A.V., Lukinov V.A., Pavlov S.S.

Kharkov Institute of Physics and Technology,
the Ukrainian SSR Academy of Sciences, 310108 Kharkov, USSR

Introduction. In papers [1,2] in the "homogeneous plasma with sharp boundary" approximation the possibility of using surface electromagnetic waves for effective excitation of slow kinetic waves (SW(K)) in plasmas in $\omega \gtrsim \omega_{ci}$ (ion Bernstein waves) frequency range was shown. In present report this possibility is investigated for the inhomogeneous plasma case for the example of a slot antenna [1,2].

Description of the model. The analysis was performed on the basis of the antenna [1] theory with following additions: Maxwell equations in the vacuum gap were solved with the account of the E- and H-waves and in the plasma the slow electromagnetic (SW(E)), the fast one (FW) and SW(K) were accounted for. To obtain solutions in the plasma for separate modes of Fourier development the numerical model was used that had been employed earlier for investigating FW excitation [3]. For generality the calculations were performed accounting for the condition of radiation into the half-space deep in the plasma (in the calculations it was on the distance 5 cm from the plasma boundary).

Plasma density and its gradient on the plasma column boundary are most important parameters from the point of view of SW excitation, three particular cases being considered (see Fig.1). Regime A: $n_e(0)=3n_{LH}$, where n_{LH} is the density corresponding to the lower hybrid resonance (LHR) condition ($\varepsilon_1=0$), $\nabla n_e = 5\cdot10^{11}$ cm^{-4}. Regime B: $n_e(0)=0{,}5\ n_{LH}$, $\nabla n_e = 5\cdot10^{11}$ cm^{-4}. Regime C: $n_e(0)=0{,}5\ n_{LH}$, $\nabla n_e = 2{,}4\cdot10^{10}$ cm^{-4}. Fig.2 illustrates the qualitative behaviour of $N_\perp^2$ for these regimes and the nature of SW(K) excitation.

In regime A the electromagnetic wave incident on the "plasma vacuum" boundary excites the nonpropagating ($N_\perp^2 < 0$) SW(E) in the plasma what provides the possibility for the existence of natural surface SW(E). SW(K) propagating into the plasma core is excited due to coupling with SW(E) due to the density inhomogeneity at the boundary as well as in the area close to the boundary. For the current system of excitation this case has been considered in [4]. Note that in homogeneous plasmas with a sharp boundary [2,5] the coupling between SW(E) and SW(K) is effected only at the plasma boundary.

In regime C at the plasma boundary the propagating ($N_\perp^2 > 0$) SW(E) is excited directly and approaching the LHR zone converted into SW(K). Regime B is intermediate, i.e. because of

the strong inhomogeneity in LHR zone(when the geometric optics approximation fails) SW(K) is excited not only due to conversion but also due to the coupling with the nonpropagating SW(E) (in regime C such a coupling is considerably weakened).

The calculations were performed for the deuterium plasma with parameters: $B_0=4T$, $T_e(x)=0.5\ T_i(x)$, $T_i(0)=50$ eV, $\nabla T_i=20$eV/cm, $\omega=1,95\ \omega_{cd}(0)$, the spacing between the adjacent slots system being L=15,7 m.

Discussion of the results. In Fig.3(regime B) and 4(regime C) there are shown the field components E_z ("excitating"field), E_x and E_y, the specific power D_e absorbed by electrons, the electromagnetic P_E and kinetic P_K fluxes of RF power in the plasma for a separate mode with $N_\parallel=2$(close to the natural surface wave). Regime C is characterized by the relatively weak swelling of the E_x field in the LHR zone. The E_y behaviour characterizing FW excitation points out that FW generation occurs in the space between the plasma boundary and LHR point. The proximity of this space to the vacuum chamber wall leads to the extremely weak FW excitation(the effect of mirror currents). Oscillations of the $|E_y|$ field in the region $n>n_{LH}$ characterize the presence of the travelling SW(K). The value of the kinetic flux is also essential in the SW(E) propagation region(at the point $n=n_{LH}$, $P_K \approx P_E$). The (collisional)dissipation on electrons is concentrated mainly in the SW(E)propagation region where E_z is larger and T_e is lower. The role of ion damping is negligible for this mode. In regime B the effect of the field swelling in the region $n \sim n_{LH}$ manifests itself considerably stronger. In spite of the small dimensions of the SW(E) propagation region in this regime($\Delta x \sim 0.5$ cm) it plays an important role in SW(K) excitation and swelling of E_x field.

In Fig.5 the spectral density fluxes of waves into the plasma are given. The spectrum in regime A is characteristic for the excitation of the surface SW(E) with $N_\parallel^{sw}=2,1$, which propagating along the magnetic field is damped due to SW(K) excitation in the plasma. The damping length ℓ' may be determined from the spectrum halfwidth $\Delta N_\parallel$: $\ell' = c/\omega/\Delta N_\parallel$. In this case $\ell' \ll L$. This regime is close to the homogeneous plasma case as regards the $N_\parallel^{sw}$ and $\Delta N_\parallel$ values.

As is seen from Fig.5 in cases B and C the regime is realized which may be interpreted as the excitation of the natural surface wave in spite of the existence of SW(E) propagation region. The $N_\parallel^{sw}$ value corresponding to the harmonic with maximum intensity is lower ($N_\parallel^{sw}=1.5$ in regime B and $N_\parallel^{sw}=0.8$ in regime C) and the essential asymmetry of the spectrum manifests itself. However, one may use the $\Delta N_\parallel$ value to estimate the damping length ℓ' of the surface SW(E) in this case too. It is seen that in regimes B and C ℓ' is sharply diminished as compared with regime A.

In Figs.6(A),7(B),8(C) the distribution of $|E_x|$ field in plasma and in the vacuum gap is shown. The field amplitude

corresponds to the power P_0 =10 MW/m coupled to the plasma through one slot(over the unit length along y direction). In contrast to regime A,in regimes B and C $|E_x|$ has a maximum between the plasma boundary and the LHR point. The strong damping of the surface SW(E) in regimes B and C leads to the field localization near the slot on the relatively small length ~ 1,2 m(B) and ~ 2 m(C). At the same time in regime C the field swelling region because of LHR appears to be strongly elongated over Z axis. The displacement of the wave packet (of the"cone" characterizing the SW(K) propagation)along Z axis is stronger in regime C than in regime B because of the smaller density of the plasma. It follows from Figs.6-8 that in regimes B and C the considerably smaller values of E_x field may be achieved in the plasma as well as in vacuum keeping constant the RF power fluxes through the unit area. This is extremely important for diminishing the incoming impurities as well as the probability of nonlinear phenomena to occur.

In conclusion let us discuss the main parameters obtained in calculations and given in Table 1 . All three regimes are characterized by a very small part of RF power (P_{FW}) coupled to FW . The power(P_{ei}) absorbed by electrons and ions(collisional,Cherenkov and cyclotron damping) in the peripheral area(of 5 cm thickness) is also low.

The ohmic losses of RF power in the antenna(stainless steel conductivity) are most essential though they are also comparatively low especially in small ℓ' regimes. Therefore the efficiency defined as SW(K) power to applied power ratio is rather high. The impedance of the antenna in all regimes remains mainly active what as was already noted [1,2] is one of the most important advantages of such antenna systems.

Conclusions. The results presented illustrate the possibility of effective excitation of SW(K) with high specific fluxes in the inhomogeneous plasma when using even relatively simple antennae with high effeciency what is necessary for powerful regimes of plasma heating and current drive and also the possibility of realizing two-component regime of thermonuclear burning using the direct excitation of slow waves [6] .

References.

1. Longinov A.V. Zh.TF,1972,v.42,N8,p.1591(in Russian)
2. Longinov A.V., Lukinov V.A. in:Contr.Fus.and Plasma Heating(15 the Europ.Conf.,Dubrovnik,1988),v.2,p.742
3. Longinov A.V. et al.in:Proc.12th Europ.Conf.on Contr.Fus. and Plasma Phys.(Budapest,1985),part 2,p.132
4. Sy W.N.-C. et al.,Nucl.Fusion 25(1985)795
5. Brambilla M., Nucl.Fusion 28(1988)549
6. Longinov A.V., Pavlov S.S., Stepanov K.N. Vopr.Atomnoj Nauki i Tekhniki,Ser.:Termoyaderni Sintez(1987),v.2.p.3 (In Russian)

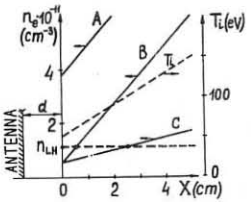

Fig.1

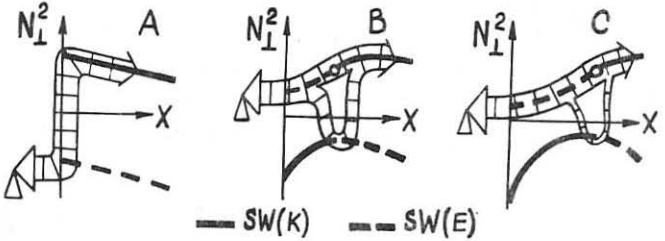

Fig.2

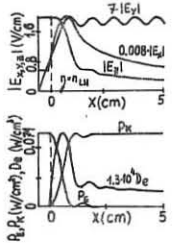

Fig.3

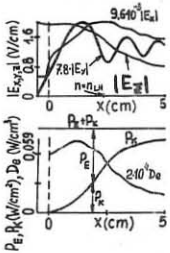

Fig.4

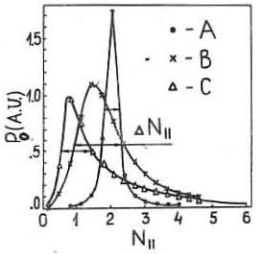

Fig.5

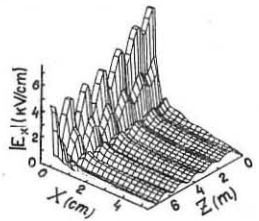

Fig.6

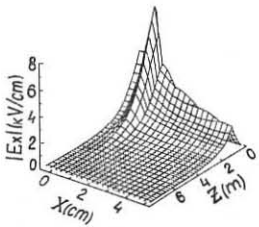

Fig.7

The slot arranged at z=0 and x=-0.5 cm (L=15.7 m)

P_0=10 MW/M , $P_0 = P_{SW} + P_{FW} + P_{BL} + P_W$

REGIME	P_{FW}/P_0 (%)	P_{ei}/P_0 (%)	P_W/P_0 (%)	EFF (%)	max$\lvert E_x^{PL}\rvert$ (KV/CM)	Z (Ω·M)	$N_\parallel^{SW}$	ℓ' (M)	max$\lvert E_x^{VAC}\rvert$ (KV/CM)
A	0.06	0.151	11.8	88.0	3.3	6.1-i1.6	2.1	7.5	7.2
B	0.01	0.071	1.9	98.0	8.0	8.7-i5.5	~1.5	~1.2	4.6
C	0.015	0.149	1.1	98.7	6.8	15.3-i5.	~0.8	~2.	3.8

Table 1

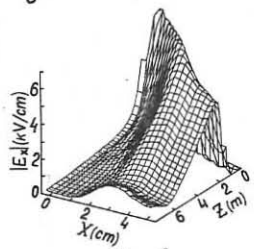

Fig.8

STABILIZATION OF MODULATIONAL INSTABILITY AT ION-ION HYBRID RESONANCE BY NON-UNIFORM PUMP FIELD.

T.A.Davydova, V.M.Lashkin

Institute for Nuclear Reseach of the Ukrainian Academy of Sciences, Kiev 28, USSR

It is now an established fact that one of the most principal mechanism of RF power absorption under ion cyclotron range of frequency plasma heating of a Tokamak is the conversion of the fast magnetosonic wave into the strong damping plasma wave near the ion-ion hybrid resonance point $\omega_{ii}=\left(\frac{\omega_{p1}^2\omega_{c2}^2+\omega_{p2}^2\omega_{c1}^2}{\omega_{p1}^2+\omega_{p2}^2}\right)^{1/2}$ /1/.

Pump field amplitude increases considerably in the resonance domain /2/ and therefore one could expect the rising of the parametric instabilities which can be additional (turbulent) mechanism of RF power absorption. The parametric instabilities can lead also to formation of "fast tails" on the particle distributinn function. This can influence both on the process of anomalous transport and the process of linear conversion.

In the present work, the modulational instability at ω_{ii} is studied for the case of the non-uniform pump field forming due to the linear conversion in the vicinity of the ion-ion hybrid resonance.

Let's consider the plasma in a slab geometry. Uniform magnetic field is directed along the z-axis and plasma density decreases mono tonically along the x-axis. The field

formed due to the linear conversion near the ion-ion hybrid resonance point is almost electrostatic and directed along the x-axis. It's amplitude has the following form /2/

$$E_0(x)=\begin{cases} F_0\sqrt{\pi}\left(\frac{x}{\Delta}\right)^{-1/4}\exp\left[i\frac{\pi}{2}+i\frac{2}{3}\left(\frac{x}{\Delta}\right)^{3/2}\right], & \text{for } x\gg\Delta \\ F_0\,G\left(\frac{x}{\Delta}\right), & \text{for } |x|<\Delta \end{cases} \qquad (1)$$

where $\Delta=\left(R^2L\right)^{1/3}$, L -the density inhomogeneity scale, $R^2=\left|-\frac{2}{\omega_{ii}\varepsilon'(\omega_0)}\sum_i\frac{3v_{Ti}^2\omega_{pi}^2}{(\omega_{ii}^2-\omega_{ci}^2)(\omega_{ii}^2-4\omega_{ci}^2)}\right|$, $\varepsilon'(\omega_0)=2\omega_{ii}\sum_i\frac{\omega_{pi}^2}{(\omega_{ii}^2-\omega_{ci}^2)^2}$ & $G(v)$ is the Airy function, F_0 is the maximum field amplitude in the resonance domain, $i=1,2$ -denotes of ion species.

For the case of uniform pump field $\vec{E}=\vec{E}_0\sin\omega_0 t$ (for $\omega\ll\omega_0$) the dispersion equation may be written as /3/

$$1+\sum_{\sigma,\eta}\sum_{\xi=+,-}\frac{J_1^2(\mu)}{2\varepsilon\varepsilon_\xi}\left[(\varkappa_\sigma-\varkappa_\sigma^\xi)(\varkappa_\eta-\varkappa_\eta^\xi)+\varepsilon\varkappa_\sigma^\xi\varkappa_\eta^\xi\right]=0 \qquad (2)$$

where $\varkappa_\sigma=\varkappa_\sigma(\omega)$ -partial permittivities of particles of kind σ, $\varkappa_\sigma^\pm=\varkappa_\sigma(\omega\pm\omega_0)$, $\varepsilon=1+\sum\varkappa_\sigma$, $\varepsilon_\xi=1+\sum_\sigma\varkappa_\sigma^\xi$, $\mu=|\mu_\sigma-\mu_\eta|$, $\mu_\sigma=\left|\frac{e_\sigma}{m_\sigma}\right|\left[\left(\frac{K_z E_{0z}}{\omega_0^2}+\frac{\vec{K}_\perp\cdot\vec{E}_{0\perp}}{\omega_0^2-\omega_{c\sigma}^2}\right)^2+\frac{\omega_{c\sigma}^2\left(\vec{B}_0\cdot[\vec{K}\times\vec{E}]\right)^2}{B_0^2\omega_0^2(\omega_0^2-\omega_{c\sigma}^2)^2}\right]^{1/2}$, $J_1(\mu)$ -Bessel function

The relative motion of the different species of ions plays the main role for the exiting of the instability at $\omega_0=\omega_{ii}$. We consider the modulational (purely growing) instability with $|\varepsilon|\gg1$. In that case the eq. (2) may be presented in the form

$$1-2J_1^2(\mu)\frac{\varkappa_1^2(\omega_0)\,\delta}{\varepsilon'(\omega_0)(\omega^2-\delta^2)}=0 \qquad (3)$$

where the "frequency mismatch" $\delta=-\frac{1}{2}\omega_{ii}K^2R^2<0$ (for D+H plasma).

The case $\mu\ll1$ (and $J_1^2(\mu)\approx\frac{\mu^2}{4}$) was studied in our previous work /4/. It had been shown that in such case $K_y\gg(\delta x)_{loc}^{-1}$ ($(\delta x)_{loc}$ -the width of the localization domain of the unstable mode in the non-uniform pump field) and $(\delta x)_{loc}^{-1}$ has the singularity for the finite value of the pump field.

In the present report, the case of sufficiently strong pump field with $\mu \lesssim 1$ (and $\gamma_1^2 \approx \frac{\mu^2}{4} - \frac{\mu^4}{16}$) is studied. It make possible to remove the singularity and to study the case $K_y \ll K_x$. To simplify the problem one can set $K_y = 0$. Then, we have the following expression for the growth rate

$$\gamma = \frac{\omega_0}{2} \left\{ \left[\alpha^2 \left(1 - \frac{\alpha^2}{4\beta} \xi^2 \right) - 1 \right]^{1/2} \right. \qquad (4)$$

The growth rate is at maximum at $\xi_{opt} = \frac{1}{\alpha^2} \left(\frac{8\beta(\alpha^2-1)}{3} \right)^{1/2}$ and it has the form $\gamma_m = \frac{4\omega_0 \beta (\alpha^2-1)^{3/2}}{3\sqrt{3}\,\alpha^4}$, $\beta = \frac{\omega_{p1}^2 \omega_{p2}^2}{4\omega_0^2(\omega_{p1}^2+\omega_{p2}^2)}$

where $\alpha^2 = \frac{A \varepsilon_1^2(\omega_0) E_0^2}{\varepsilon'(\omega_0)\omega_0 R^2}$, $A = \left(\sum_i (-1)^i \frac{e_i}{m_i(\omega_0^2 - \omega_{ci}^2)} \right)^2$, $\xi = K_x R$,

The dependence of the growth rate γ on the wave number for the case of uniform pump field is presented on Fig.1.

Let's consider the non-uniform pump field described by (1). The field may be approximated as follows $E_0^2(x) = E_0^2\left(1 - \frac{x^2}{\Delta^2}\right)$ in the domain $|x| \ll \Delta$. Then, from eq.(3) one can obtain the differential equation of 2th order for the field perturbation Ψ in ξ-space

$$\frac{d^2\Psi}{d\xi^2} + \frac{\Delta^2}{R^2} \cdot \frac{(\alpha^2-1)\xi^4 - (\alpha^4/4\beta)\xi^6 - 4(\gamma/\omega_0)^2}{\alpha^2 \xi^4 \left(1 - \frac{\alpha^2}{4\beta}\xi^2\right)} \Psi = 0 \qquad (5)$$

Setting $\gamma = 0$ in (5) one can determined the threshold of the instability of n-th mode. By using WKB method one find the following relation for threshold values α_n

$$\frac{4\sqrt{\beta}\,\Delta}{R\,\alpha_n} \left[E(p) - (1-p^2) K(p) \right] = \pi \left(n + \frac{1}{2} \right) \qquad (6)$$

where $p^2 = (\alpha_n^2 - 1)/\alpha_n^2$, K and E -the complete elliptic integrals of the first and second order respectively. The dependence of the threshold value α_n on the pump scale non-uniformity R/Δ is presented on Fig.2. In the cases $\alpha_n \gtrsim 1$ and $\alpha_n \gg 1$ may be written analytical expression

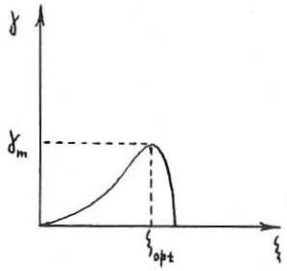

Fig.1

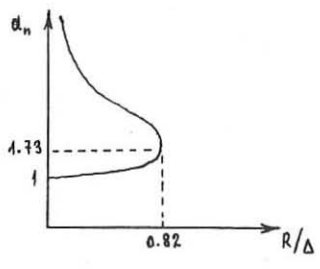

Fig.2

in the form $$d_n^2 = 1 + \frac{(2n+1)\,R}{4\,\Delta\,\sqrt{3}} \quad , \text{for} \quad d_n \gtrsim 1 \qquad (7)$$

and $$d_n = \frac{4\sqrt{3}\,\Delta}{\pi\,R\,(n+1/2)} \quad , \text{for} \quad d_n \gg 1 \qquad (8)$$

By using the expansion of "pseudopotential" in (5) in the vicinity of ξ_{opt} one can obtain for the instability threshold

$$\gamma_n = \frac{4\,\omega_0\,s\,(d^2-1)^{3/2}}{3\sqrt{3}\;d^4}\left[1 - \frac{d^3\,(n+1/2)\,R}{2\sqrt{3}\,(d^2-1)\,\Delta}\right]^{1/2} \qquad (9)$$

The width of the localization domain of the unstable mode is $< \Delta$ .One can see that (9) for $\Delta \to \infty$ give us the growth rate for uniform pump,and the threshold values obtained from (9) are coinciding with (7),(8).

For JET we have $d \sim 3 \div 4$,and this threshold can be exceeded in modern experiments on RF plasma heating in tokamaks.

REFERENCES

1.D.G.Swanson. Phys.Fluids, 28 , p.2645 , (1985) .
2.D.L.Grekov,K.N.Stepanov. Ukr.fiz.jurn. ,25, p.1281,(1980).
3.M.Ono,M.Porkolab,P.Chang. Phys.Fluids, 23 ,p.1654, (1980).
4.T.A.Davydova,V.M.Lashkin.Proc. 15th Europ. Conf. on Cont. Fusion and Plasma Heating (Yugoslavia),12B, p.730,(1988).

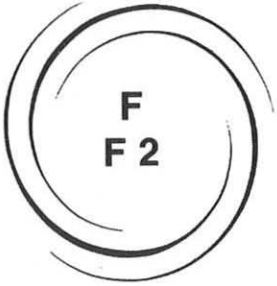

PLASMA HEATING AND CURRENT DRIVE

ELECTRON CYCLOTRON RESONANCE HEATING (ECRH)

RAY TRACING WITH NON-MAXWELLIAN ELECTRON DISTRIBUTION FUNCTIONS. A CASE EXAMPLE: HELIAC TJ-II

C. Alejaldre, F. Castejón and M.J. Taboada

Asociación EURATOM/CIEMAT para Fusión
28040 Madrid
Spain

I. Introduction

Recent ECH experiments on stellarators and tokamaks show the existence of a superthermal tail in the electron distribution function and at the same time a disagreement between the linear theory of microwave absorption and the experimental values is usually reported[1]. The ray-tracing code RAYS originally developed at Oak Ridge National Laboratory[2] has been adapted to the geometry of the TJ-II flexible heliac (R_0 = 1.5 m., B_0 = 1T.) and to account for the effect upon microwave power absorption of a superthermal tail in the electron distribution function, a new absorption module that takes into account the existence of a superthermal tail has been added. Then, an study has been conducted to

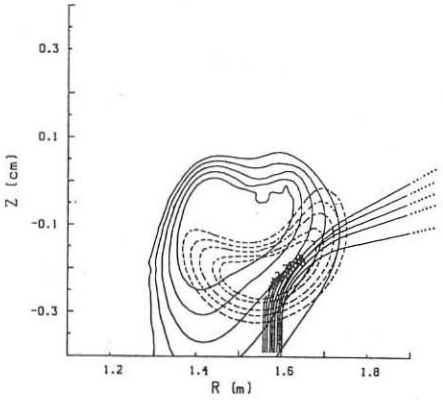

Figure 1
Ray-tracing in TJ-II. f=53.2 GHz., ϕ=16..875°

determine the optimum launching position, including the more realistic simulation module, and the influence upon profile deposition and power absorption of the tail distribution, for waves propagating in the first (28 GHz.) and near second harmonic (53.2 GHz) of the electron cyclotron frequency.

II. The absorption module

We simulate the electron distribution function by adding a drifted maxwellian to a bulk maxwellian:

$$f(p_\perp, p_\parallel) = \eta\, f_b(p_\perp, p_\parallel) + (1-\eta)\, f_t(p_\perp, p_\parallel) \qquad (1)$$

where,

$$f_b(p_\perp, p_\parallel) = \left(\frac{\mu_b}{2\pi}\right)^{3/2} (mc)^{-3} \exp\left[-\frac{\mu_t}{2(mc)^2}\left(p_\perp^2 + p_\parallel^2\right)\right] \qquad (2)$$

is the bulk, weakly relativistic, distribution function and

$$f_t(p_\perp, p_\parallel) = \left(\frac{\mu_t}{2\pi}\right)^{3/2} (mc)^{-3} \exp\left[-\frac{\mu_t}{2(mc)^2}\left(p_\perp^2 + (p_\parallel - p_0)^2\right)\right], \qquad (3)$$

a drifted maxwellian, with

$$\mu_{b,t} = \frac{mc^2}{T_{b,t}} \qquad (4),$$

and $\parallel$, $\perp$ indicate parallel and perpendicular to the static magnetic field, respectively, v_{th} is the thermal velocity and γ is the Lorentz factor. The free parameters used in the tail description, i.e., tail population (η), tail temperature (T_t) and

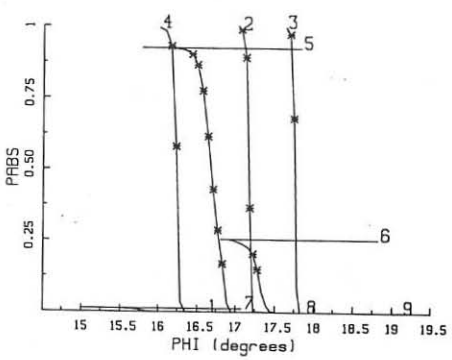

Figure 2
Fractional power absorbed in one-pass. f= 53.2 GHz.
$n_e(0)=1.5\times10^{13}$ cm^{-3}, $T_e(0)$=1keV

drift momentum(p_0) are taken in this study to be consistent with either the directly measured values , $\eta \approx 0.001$, $T_t \approx 10$ keV, or the residual currents observed (≈1kA) during ECRH at the Wendelstein VII-A stellarator[3] . This simple model to simulate the distribution function presents the advantage that allows to calculate the dielectric tensor for a current carrying distribution function analytically, with all the computational advantages associated with analytical methods. Due to the linearity in the calculation of the mobility tensor, for a distribution function like (1) the tensor $\varepsilon(\vec{N})$ can be written[9,11]: $\varepsilon(\vec{N}) = I - \mu\left(\frac{\omega_p}{\omega}\right)^2 \left[(1-\eta)D_b(\vec{N}) + \eta D_t(\vec{N})\right]$ (5)

where $\mathbf{D_b}$ is the tensor for a weakly relativistic maxwellian distribution function and $\mathbf{D_t}$ can be obtained, essentially, changing $N_{||}$ by $N_{||}$-p_0/mc . Details are shown in ref.4,5.

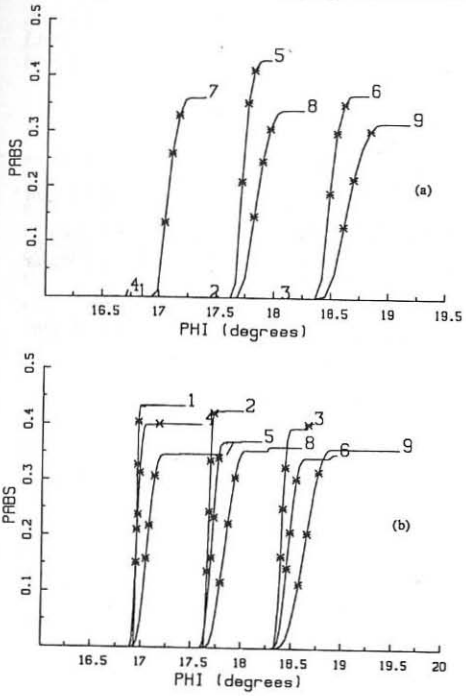

Figure 3

Fractional power absorbed in one pass for waves propagating at 28 GHz. using the non-maxwellian model (a) and the pure maxwellian case (b)

III Ray-tracing

Nine rays, located in a 3x3 rectangular array of ≈ 5x5 cm. to simulate a five cm. radius beam, are launched into the plasma. All figures in the paper are shown at the toroidal angle $\phi = 16.875^a$, chosen to be the illuminating point after this study. The plasma parameters are : $n_e(0) = 1.5 \times 10^{13}$ cm^{-3} , $T_e(0) = .8$ keV and a parabolic profile is assumed for both magnitudes. Figure 1 shows the

rays trajectories for a plasma with a 10 keV tail temperature and a microwave frequency of 53.2 GHz. It is observed that the region of absorption increases sensibly with respect to the pure maxwellian case in agreement with experimental observations, no appreciable difference can be observed in the absolute value of the absorbed power in the second harmonic, figure 2, since in both cases 100% of the power emitted is absorbed, even before the rays abandon the plasma. Figure 3 shows a degradation in power with an increasing value of the tail population for propagation in the first harmonic, 28 GHz that depending on the ray direction can be of significance.

REFERENCES

1. L.M.Kovrizhnykh, IAEA meeting, Nice, France, October 1988
2. R. C. Goldfinger and D. B. Batchelor, Nucl. Fusion **27** , 31 (1987)
3. V. Erckmann and VII-A team, *Proceedings of the 6th Topical Conference on Radiofrequency and Plasma Heating*, New York, 1985 (AIP, 1985), p. 198
   U. Gasparino, M. Massberg, M. Tutter, WVII-A team, E. Räuchle, ECRH group, *Proceedings of the14th European Conference on Controlled Fusion and Plasma Physics* , Madrid, 1987 (EPS, 1987), part III, p. 818
4. C. Alejaldre , Nucl. Fusion **28**, 849 (1988)
5. C. Alejaldre and F. Castejon, *Microwave Absorption on Stellarators with a non-Maxwellian Electron Distribution Function*, Submitted for publication

UP-SHIFTED AND DOWN-SHIFTED ELECTRON CYCLOTRON INTERACTION WITH A SUPRATHERMAL ELECTRON TAIL

D. Farina and R. Pozzoli*

Istituto di Fisica del Plasma, CNR,
EURATOM-ENEA-CNR ASSOCIATION, Milano, Italy

*Dipartimento di Fisica, Università di Milano, Milano, Italy

Abstract - EC power absorption and current drive are computed for a model electron tail produced by LHCD. The up-shifted and down-shifted resonance condition are compared. The latter case is shown to be suitable for optimization of both processes.

The main application of the interaction of electron cyclotron (EC) waves with suprathermal electrons is related to the problem of non inductive current drive in toroidal plasmas. We are interested in determining the optimal conditions for the EC wave interaction with a suprathermal tail and explicitly refer to the LHCD regime, which is characterized by an extended asymmetric electron tail in the parallel momentum $p_\parallel$. The distribution function f is written as $f = f_0 + f_1$ where f_0 represents the thermal bulk and f_1 the suprathermal tail. We assume that f_1 is flat with respect to $u_\parallel$ in the interval $u_1 < u_\parallel < u_2$ and Maxwellian with respect to $u_\perp$, characterized by a temperature $T_\perp$:

$$f_1 = \frac{n_1}{u_2 - u_1} \frac{\mu_\perp}{2\pi} \exp\left(-\frac{\mu_\perp}{2} u_\perp^2\right) \chi_{1,2}(u_\parallel) \tag{1}$$

where $\mathbf{u} = \mathbf{p}/mc$, $\chi_{1,2}$ is the characteristic function relevant to the interval u_1 , u_2 and $\mu_\perp = mc^2/T_\perp$.

Two different interation schemes can occur, depending on the injected $N_\parallel$ and on the ratio $Y = \Omega/\omega$, between the cyclotron frequency $\Omega = eB/mc$ and the injected wave frequency ω /1/. From the EC resonance condition for the first cyclotron harmonic $\gamma - N_\parallel u_\parallel - Y = 0$, in case of EC wave oblique injection in the same direction of the electron drift ($N_\parallel > 0$) the interaction occurs when $\omega > \Omega$ ($Y < 1$): up-shifted resonance (USR), while in the opposite case ($N_\parallel < 0$) mainly when $\omega < \Omega$, ($Y > 1$): down-shifted resonance (DSR).

From the energy balance equation and from the relativistic expression of the dielectric tensor, the absorption coefficient can be written:

$$\alpha = \frac{\omega}{c} \int d\mathbf{u}\, P(\mathbf{u}) \tag{2}$$

where the normalized single particle absorption efficiency $P(\mathbf{u})$ is given by $P(\mathbf{u}) = -\pi X/n\, u_\perp^2 T_1 \hat{L} f\, \delta(\gamma - N_\parallel u_\parallel - Y)$ with $X = (\omega_{pe}/\omega)^2$, $T_1 = |\theta_1|^2/|\mathbf{s}|$, being s the nor-

malized Poynting vector, the polarization term given by $|\theta_1|^2 \simeq |e_x - ie_y + N_\perp/Y\ e_\parallel u_\parallel|^2/4$, where $N_\perp$ is the perpendicular refractive index, **e** the polarization vector, and $\hat{L}f = [(\gamma - N_\parallel u_\parallel)/u_\perp\ \partial f/\partial u_\perp + N_\parallel \partial f/\partial u_\parallel]/\gamma$.
The EC driven current density J can be written as:

$$J = J_o \int d\mathbf{u}\ P(\mathbf{u})\ \eta(\mathbf{u}) \tag{3}$$

where $J_o = e/(mcv_c)\ \omega/c\ P_o/\sigma$, being $v_c = \omega_{pe}^4 \ln\Lambda/(2\pi nc^3)$ the collision frequency, P_o the local incident power, σ the local beam cross section and η the normalized current drive efficiency for single particle, given by $\eta(\mathbf{u}) = \gamma\ \hat{L}\ \chi$ where $\chi(\mathbf{u})$ is the normalized response function for the current /2/.
Being interested in the interaction of EC waves with suprathermal electrons, we exclude from our analysis the values of Y close to 1, where interaction with thermal electrons occurs. Since we assume $n_1/n_0 \ll 1$, the function f_1 only enters the expressions (2) and (3), while the propagation and the polarization in the same expression are computed by means of the function f_0 .

The absorption coefficient can be computed analytically, by inserting f_1 given by (1) in the expression (2). In order to have a physical insight of the mechanism which determines the different behaviours of the USR and DSR schemes, it is convenient first to consider in more detail the following integral which is proportional to the contribution to α coming from that part of T_1 independent of $u_\parallel$:

$$I = \frac{\mu_\perp{}^2}{4} \int_{u_{\parallel -}}^{u_{\parallel +}} du_\parallel\ u_\perp^2(u_\parallel) \exp(-\mu_\perp u_\perp^2/2)\ \chi_{1,2} = \int_{-1}^{1} dt\ \phi(t)\ \chi_{1,2} \tag{4}$$

where $u_\perp^2(u_\parallel) = (1 - N_\parallel^2)(u_{\parallel +} - u_\parallel)(u_\parallel - u_{\parallel -})$ is the resonant $u_\perp^2$, being $u_{\parallel \pm} = (N_\parallel Y \pm \Delta)/(1 - N_\parallel^2)$ the extrema of the resonant curve, with $\Delta^2 = Y^2 - 1 - N_\parallel^2$, and $\phi(t) = \Lambda^4 \Delta^3 (1 - t^2) \exp(-s^2(1 - t^2))$, with the parameter $s^2 = \mu_\perp/2\ \Delta^2/(1 - N_\parallel^2) = \Lambda^2\Delta^2$ and $\Lambda^2 = \mu_\perp/[2(1 - N_\parallel^2)]$.
We analyze the behaviour of the function $\phi(t)$ which represents the relative weight of the different resonant electrons taking part in the absorption process. For $s < 1$, ϕ exhibits a flat maximum in $t = 0$. In this case most of the resonant electrons contribute to the power absorption. When $s > 1$ the point $t = 0$ corresponds to a relative minimum, while maxima occur at $|t| = \sqrt{1 - 1/s^2}$. For increasing s, the maximum shifts towards $|t| = 1$, the function ϕ peaking at the maxima and becoming exponentially small in the region around $t = 0$. Therefore, for $s \gg 1$ the absorption is due to electrons with $u_\parallel$ close to $u_{\parallel \pm}$ (see Fig.1).
We note that for fixed $N_\parallel$ the limit $s \to 0$ corresponds to $T_\perp \to \infty$ $(\Lambda \to 0)$, or to $Y \to Y_0$ ($\Delta \to 0$) and the limit $s \to \infty$ corresponds to $T_\perp \to 0$ $(\Lambda \to \infty)$ or $Y \gg \sqrt{1 - N_\parallel^2}$ $(\Delta \gtrsim 1)$. For parameters of physical interest, the former case can occur only in USR, while the latter case is mostly verified in case of DSR or in the USR case at low perpendicular temperature.
Keeping $\chi_{1,2} = 1$ and performing the integral over t , the function I can be written as:

$$I = -\Lambda\left[2s + (1 + 2s^2)\, Z_R(s)\right] \tag{5}$$

where Z_R is the real part of the plasma dispersion function. The integral I is a function of the two independent parameters Δ and Λ . It is convenient to analyze its behaviour as a function of the parameter s for fixed $N_\parallel^2$, varying alternatively Λ (i.e. $T_\perp$) at Δ (i.e. Y) con-

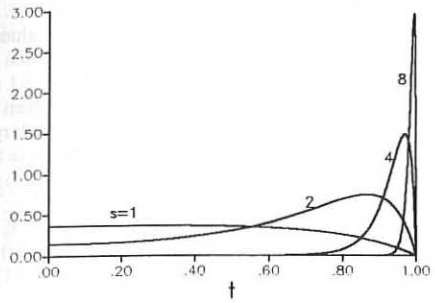

Figure 1. : Function ϕ/Λ versus t for different s values.

stant (curve a of Fig.2) or Δ at constant Λ (curve b of Fig.2). The expansion of I for $s \ll 1$ is $I \simeq 2s^4/\Delta$, while its asymptotic expansion for $s \gg 1$ is $I \simeq 2/\Delta\ (1 + 1/s^2)$. I exhibits a maximum at $s = 1.88$ when Δ is kept constant (curve a) and at $s = 1.51$ for constant Λ (curve b).

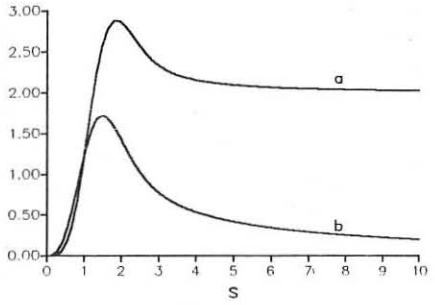

Figure 2. : Functions $I\,\Delta$ (curve a) and I/Λ (curve b) versus s.

The behaviour discussed above actually occurs when $\chi_{1,2}$ can be assumed equal to 1, i.e. only when the whole resonant curve belongs to the suprathermal tail. The behaviour of $\chi_{1,2}(t)$ vs t depends strictly on $N_\parallel$, Y , u_1 , u_2 as it has been widely analyzed in Ref.1. In the DSR case $\chi_{1,2}(t) \neq 0$ only for positive t, while in the USR case $\chi_{1,2}$ can be different from zero in the whole t –range, depending on the $N_\parallel$ and Y values. In the general case the truncation of the integral I due to the function $\chi_{1,2}$ has to be taken into account, leading to a reduction of the I value, when this effect is considered. However, when $s \gg 1$ (in practice $s > 4$), the absorption is strongly localized near $u_\parallel = u_{\parallel\pm}$: as a consequence $I \simeq 2/\Delta$ when both $u_{\parallel-}$ and $u_{\parallel+}$ belong to the tail (USR case) and $I \simeq 1/\Delta$ when only one of the extrema belongs to it, this latter case generally applying to the DSR condition.

Curve a of Fig.2 can describe the variation of I with the perpendicular temperature of the tail. We find that in USR conditions the absorption can be critically dependent on $T_\perp$ and

can decrease or increase with it, while is almost independent of $T_\perp$ in DSR conditions. In fact, when $T_\perp$ is decreased (keeping Y and $N_\parallel^2$ constant) starting from very high values in the USR case the absorption increases, reaching a maximum value for $s \simeq 2$ and then decreases to the asymptotic value $2/\Delta$. For the DSR case, for condition of interest $s \gg 1$ and $I \simeq 1/\Delta$. When $N_\parallel^2$ and $T_\perp$ are kept constant while Y is varied, the comparison between the USR and the DSR cases can be investigated by means of the curve b of Fig.2. The largest value of the absorption coefficient α can be reached in USR conditions for $s \simeq 1.5$. Note that the two resonance conditions are characterized by different Δ values, Δ being much larger in the DSR case.
When polarization effects, described by the term T_1 , are taken into account, the $u_\parallel$ dependence of $|\theta_1|^2$ and the Y dependence of $\mathbf{s}$, $e_x - ie_y$ and $N_\perp$ produce variation of the α profile versus Y , without substantially affecting the relative scaling of the USR and DSR cases.

Concerning the driven current (Eq.3), it is found that the USR condition is more suitable for current drive because both of the behaviour of the absorbed power $P(\mathbf{u})$, already discussed, and of the larger value of the CD efficiency $\eta(\mathbf{u})$, with respect to the DSR case. In fact, we observe that η is larger for $N_\parallel > 0$ than for $N_\parallel < 0$ (see Fig.3); moreover, in USR conditions trapping effects are negligible and the contributions coming from $u_{\parallel -}$ and $u_{\parallel +}$ sum up (contrary to the DSR case).

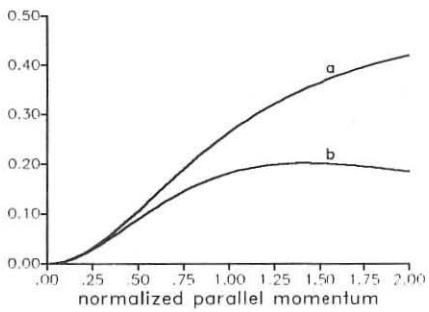

Figure 3. : Current drive efficiency for single particle $\eta(\mathbf{u}) = N_\parallel G(u) + u_\parallel dG/dy$ vs $u_\parallel$ for $u_\perp = 0$ being $G(u) = \chi(\mathbf{u})/u_\parallel$. Curve a correspond to $N_\parallel = 0.5$ and curve b to $N_\parallel = -0.5$.

In conclusion, we have shown that in the EC wave interaction with a suprathermal tail the DSR and USR conditions are characterized by different locations of the resonant electrons in momentum space, the USR being more efficient with respect to both power absorption and current generation. The DSR interaction is almost insensitive to variation of $T_\perp$, while the USR depends on it. The obtained results mainly depend on the gross characteristics of the distribution function describing the suprathermal tail, such as its parallel and perpendicular energies, while are weakly dependent on its detailed structure.

References

/1/ D. Farina, R. Pozzoli, Proc. "Theory of Fusion Plasmas", Lausanne 1988, in press;
/2/ C. F. F. Karney, N. J. Fisch, Physics of Fluids, **28**, 116 (1985);

NON LINEAR DYNAMICS OF FREE ELECTRON LASER RADIATION IN A MAGNETIZED PLASMA

A. Cardinali(+), A.V. Khinich(*), M. Lontano,
E.I. Rakova(*), A.M. Sergeev(*)

Istituto di Fisica del Plasma, EURATOM-ENEA-CNR Association, Milano, Italy
(+)CRE, EURATOM-ENEA Association, Frascati, Italy
(*)Institute of Applied Physics, Soviet Academy of Sciences, Gorky, USSR

Introduction

The self similar structure of the field amplitude and the density perturbation during the process of non linear self-focusing of high power electromagnetic (EM) radiation, polarized in the ordinary mode (OM), has been described in detail in a previous paper /1/ with particular reference to the MTX project/2/, where a free electron laser (FEL) source will be used for electron cyclotron resonant heating (ECRH) of a tokamak plasma. Here we present the results of numerical computations /3/ describing the dynamical evolution, in time and space, of a Gaussian beam of EM radiation within the "aberrationless" approximation which allows to follow the dynamics of the axial part of the wave beam along its trajectory in the medium.

Formulation of the problem

In ref. 1 it has been sown that the equations for the complex amplitude of the high frequency (HF) electric field E and for the non linear plasma density perturbation δn are:

$$-i\frac{\partial E}{\partial x}+\frac{\partial^2 E}{\partial y^2}+\frac{\partial^2 E}{\partial z^2}-nE=0\,, \tag{1}$$

$$\frac{\partial^2 n}{\partial t^2}=\frac{\partial^2 |E|^2}{\partial z^2}\,, \tag{2}$$

where dimensionless variables have been introduced according to the following transformations:

$$\frac{z}{z_0}\longrightarrow z;\quad \frac{y}{z_0}\left(1-\frac{\omega_{pe}^2}{\omega^2}\right)^{1/2}\longrightarrow y;\quad \frac{x}{2kz_0^2}\left(1-\frac{\omega_{pe}^2}{\omega^2}\right)\longrightarrow x;$$

$$Ez_0\left(\frac{c}{8p}\right)^{1/2}\longrightarrow E;\qquad \frac{z_0^2\,\omega_{pe}^2}{c^2\left(1-\frac{\omega_{pe}^2}{\omega^2}\right)}\frac{\delta n}{n}\longrightarrow n; \tag{3}$$

$$\frac{\omega_{pe} e t}{\omega z_o}\left[\frac{2P}{Mmc^3\left(1-\frac{\omega_{pe}^2}{\omega^2}\right)}\right]^{1/2} \longrightarrow t$$

Here ω and ω_{pe} are the injected wave and electron plasma frequencies, respectively, e, m, M are the unitary charge, the electron and ion masses, P is the injected power, z_o is the transverse half-dimension of the beam and k the wavevector. We refer to EM waves, polarized in the OM, and propagating along the x direction, almost perpendicular to the external magnetic field $\underline{B}_o = B_o \underline{e}_z$.

"Aberrationless" approach

When a Gaussian beam is incident, the most part of the wave energy is concentrated around its axis; we can then simplify the system of eqs.(1) and (2) using the so called "aberrationless" approach /4/; we represent the field amplitude and the density perturbation with the following functions:

$$E = \frac{1}{\sqrt{2a(x,t)b(x,t)}} \exp\left(-\frac{z^2}{2a^2} - \frac{y^2}{2b^2} + i\alpha + i\beta z^2 + i\gamma y^2\right) \quad (4)$$

$$n = -n_o(x,t)\exp\left[-\frac{z^2}{c^2(x,t)} - \frac{y^2}{d^2(x,t)}\right], \quad (5)$$

where a(x,t) and b(x,t), c(x,t) and d(x,t) are the characteristic transverse dimensions of the wave beam and of the density perturbation, respectively; β and γ describe the curvature of the wavefront and α is the phase shift. Introducing the expressions (4) and (5) in eqs. (1) and (2) and expanding in power of the small parameters y^2 and z^2, we obtain the set of differential equations:

$$\frac{\partial^2 a}{\partial \zeta^2} = \frac{1}{a^3} - fa, \qquad \frac{\partial^2 f}{\partial t^2} = \frac{3}{a^5 b},$$

$$\frac{\partial^2 b}{\partial \zeta^2} = \frac{1}{b^3} - gb, \qquad \frac{\partial^2 g}{\partial t^2} = \frac{1}{a^3 b^3}, \quad (6)$$

where $\zeta = 2x$, $f = n_o/c^2$, $g = n_o/d^2$. In the limit $a \longrightarrow 0$ the system (6) has the following asymptotic solution:

$$a \sim \frac{3^{1/4}}{\sqrt{20}}\left(-\frac{\zeta + \int^t u\,dt'}{u}\right), \qquad b \sim a\sqrt{3},$$

$$f = \frac{1}{a^4}, \qquad g = \frac{1}{b^4}, \quad (7)$$

corresponding to a field distribution in the form of a "running focus": the focal point travels at an arbitrary velocity u(t) toward the incoming radiation and the half-apex angle of the cone surface near the singularity increases as it slows down. In principle the function u(t) can be found solving the system, eqs. (1) and (2), with the appropriate boundary conditions; however, by means of numerical computations, we can determine the focus velocity within our approximation.

Results and conclusions

The system (6) has been solved numerically starting, at t = 0, with an ordinary diffractive structure $a = b = (1 + \zeta^2)^{1/2}$ for the wave beam and in the absence of plasma perturbations. In Fig. 1 the functions $a(\zeta)$ and $b(\zeta)$ are plotted versus ζ, at different times. It is shown that the initially divergent pattern of wave beam (a) evolves towards a convergent structure (b,c,d) inevitably followed by the singularity formation (e,f).

The self-focusing of the radiation can prevent the direct transmission of EM energy to the region of EC resonance or decrease the efficiency of EC damping. To avoid this effect, the experimental parameters should be chosen suitably in order to reduce the duration of the single FEL pulse to values smaller than the time of singularity formation:

$$\tau_u < t_F \sim \frac{\omega z_o}{e\,\omega_{pe}} \left[\frac{Mmc^3 (1 - \omega_{pe}^2/\omega^2)}{2P} \right]^{1/2} . \qquad (8)$$

Eq. (8) can be written in the form

$$\tau_u < \frac{\omega^2 z_o^2 Mmc^3}{2e^2 \omega_{pe}^2 W} \left(1 - \frac{\omega_{pe}^2}{\omega^2} \right) \sim \frac{1}{W} , \qquad (9)$$

where $W = P \cdot \tau_u$ is the energy of the FEL pulse.

Therefore to prevent the appearance of the non linear effects discussed here the pulse of EM radiation, for a fixed injected energy and beam size, has to be shortened.

References

/1/ A. Cardinali, M. Lontano, A.M. Sergeev, Proc. 15th Europ. Conf. Contr. Fus. and Plasma Heat., edited by S. Pesic and J. Jacquinot (EPS, Dubrovnik, 1988), vol. 3, p. 976; also accepted for publication in The Physics of Fluids;

/2/ K.I. Thomassen, **Free Electron Laser Experiments in Alcator-C**, Lawrence Livermore National Laboratory, Livermore, USA, LLL-PROP-00202, 1986;

/3/ A. Cardinali, A.V. Khimich, M. Lontano, E.I. Rakova, A.M. Sergeev, Istituto di Fisica del Plasma, EURATOM-ENEA-CNR Association, internal report FP 88/16, October 1988; submitted to Physics Letters A;

/4/ A.V. Petrischev, V.I. Talanov, Kvantovaja Elektronika, 6, 35 (1971), in Russian.

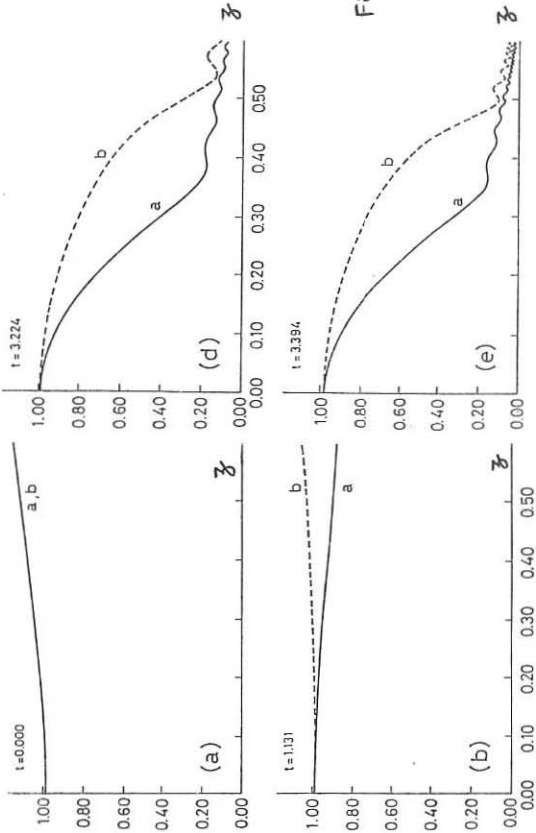
t=0.000
a,b
(a)
t=1.131
b
a
(b)
t=2.828
b
a
(c)
t=3.224
b
a
(d)
t=3.394
b
a
(e)
t=3.691
b
a
(f)
1.00
0.80
0.60
0.40
0.20
0.00
0.10
0.20
0.30
0.40
0.50
ξ

Fig. 1

LOCALIZED HEATING AND ENHANCED VELOCITY DIFFUSION BY ECRH IN THE GAMMA 10 TANDEM MIRROR

T.Saito, Y.Kiwamoto, T.Kariya, A.Kurihara, I.Katanuma, K.Ishii, T.Cho and S.Miyoshi

Plasma Research Center, University of Tsukuba
Tsukuba City, Ibaraki 305 Japan

Introduction

Electron cyclotron resonance heating(ECRH) in a tandem mirror has a specific role for confinement and heating of a plasma and hence it requires a special heating configuration to meet the expected role/1/. Experiments of ECRH have been done in axisymmetric end mirror cells of the GAMMA 10 tandem mirror/2,3/. Heating power(28 GHz, 140 kW max.) is injected in a beam shape onto each of the surfaces of the fundamental(1.0 T) and the second harmonic(0.5 T) resonance as shown in Fig. 1. It is spatially restricted within a region of the mirror field for localized heating and for energy control of hot electrons/4/. As a consequence, the cyclotron resonance condition

$$\omega - k_{//}v_{//} - n\omega_{ce}/\gamma = 0 \qquad (1)$$

is satisfied by electrons in a limited domain of the velocity space, in which electrons are strongly diffused. The domain reaches the loss cone boundary at energies which are determined from the heating configuration. ECRH in a mirror field may thereby leads enhanced velocity diffusion to be observed in an electron flux in the loss cone, which can be measured at an end of the machine/5/. This mechanism of velocity diffusion is significant to the potential formation in a tandem mirror/6/. We describe measurement of the microwave propagation which proves the localized heating and observation of the electron axial flux which indicates enhanced velocity diffusion of electrons peculiar to mirror ECRH.

Measurement of Microwave Propagation

The measurement of propagation of the fundamental(plug) heating power has been done and the power deposition in a restricted area has been found /6/. Here, we describe the measurement of propagation of the second harmonic(barrier) heating power and show the absorption of the power is almost attributed to the one-pass absorption of the beam component.

An array of open-ended waveguides is installed as shown in Fig. 1. and it is used to measure the two dimensional distribution of the transmitted power through a plasma. The end cell region is enclosed with an inner wall of stainless steel the diameter of which is large enough for the microwave beam to be nearly freely propagated. Cavity fields are measured at cardinal points in the inner wall and at openings on it. A typical distribution of the transmitted power is shown in Fig. 2. The line density of

a plasma is about 1 x 10^{13} cm^{-2}, which is well below the cutoff density. Open circles represent the transmitted power in the vacuum and closed ones does that through the plasma. The transmission coefficient is about 40%. The transmitted power belongs to the cavity field power and a part of it is absorbed by the plasma after reflection off the wall. The remainder escapes through the openings. The power density of the cavity field is very low compared to that of the beam component. Thus the fraction of the cavity field power to the total absorbed power is low. The one-pass absorption coefficient of the beam component is obtained from a self-consistent analysis of the microwave power flow based on the wave field measurement and it shares about 80% of the total absorbed power. Intended localized heating is realized. This is significant to the temperature control of hot electrons because most of electrons are heated by the microwave with a definite value of $k_{//}$ in the limited region of the mirror field.

Observation of Axial Electron Flux

Electrons which interact with the electric field of the injected microwave under the resonance condition Eq. (1) diffuse in the velocity space along heating characteristics which reach the loss cone boundary. Thus warm($E \leq 10$ keV) and hot($E \geq 10$ keV) electrons heated by ECRH are lost to the end of the machine. Figure 3 shows the warm electron current measured at the end together with the line density and the potentials. On application of the plug ECRH the plasma potential ascends and the floating potential V_{ep} of the end plate immediately descends below the ground potential. The end plate is connected to the ground through a high resistance R (1 MΩ). Since the plug ECRH drives a high axial electron flux, the potential of each position varies to keep the charge neutrality of the plasma. The warm electron energy is measured with a multi-grid electrostatic energy analyzer installed behind the end plate. Figure 4 is a logarithmic plot of the electron current flowing into a collector of the analyzer as a function of the bias voltage applied to an electron repeller grid. The electron flux is composed of two components; a lower temperature component and a higher temperature one. Although values of these temperatures depend on the experimental condition, drive of such a high axial flux of warm electrons with two components is a specific feature of the plug ECRH.

Secondary electrons are emitted with a high coefficient δ when an energetic electron hits the end plate of stainless steel and hence the secondary electrons play an essential role in the charge neutrality of a plasma. The net current flowing into the end plate is calculated with the energy distribution of warm electrons obtained from the plot in Fig. 4 by

$$I_{net} \propto \int_{V_{ep}}^{\infty} \{1 - \delta(E)\} f(E) dE \ .$$

The value thus calculated is nearly equal to the measured net current V_{ep}/R. The analysis shows that more than 90% of the primary current returns to the plasma as the secondary current.

The electron flux has much information about the heating mechanism of ECRH and it gives a valuable data base for the theoretical study. We have measured hot electron axial flux which is produced by the barrier ECRH/5/. An energy spectrum of end loss hot electrons has a remarkable feature; a

peak at an energy of about 100 keV. This peak has been attributed to velocity diffusion along heating characteristics associated with the third harmonic resonance. A narrow zone in which electrons strongly diffuse reaches the loss cone boundary and the peak is clearly observed in the spectrum. However, the peak disappears and the spectrum is flattened when plug ECRH is superposed on the barrier ECRH as shown in Fig. 5. Since the heating power of the plug ECRH is localized in a region of the higher field side of the resonance surface the maximum of $|\omega - \omega_{ce}|$ determines the muximum energy of electrons which have pitch angles near the loss cone and resonate with the wave field of the beam component. The energy E_m of about 10 ∿ 20 keV thus determined well accounts for the high flux of warm electrons. The zone in which electrons with energies higher than E_m resonate with the plug ECRH does not directly reach the loss boundary and electrons are strongly diffused in this zone. A bounce-averaged quasi-linear diffusion model gives a qualitative picture consistent with the observations. Energy spectra to be observed at the end calculated with a Fokker-Planck code are similar to measured ones/7/.

References

/1/ B.W.Stallard, IEEE Trans. Plasma Sci. PS-12 (1984) 134.
/2/ M.Inutake et al., Phys. Rev. Lett. 55 (1985) 939.
/3/ Y.Kiwamoto et al., Phys. Fluids 29 (1986) 2781.
/4/ B.W.Stallard et al., Nucl. Fusion 23 (1983) 213.
/5/ T.Saito et al., Phys. Rev. Lett. 59 (1987) 2748.
/6/ T.Kariya et al. Phys. Fluids 31 (1988) 1815.
/7/ I.Katanuma et al., Phys. Fluids 30 (1987) 1142.

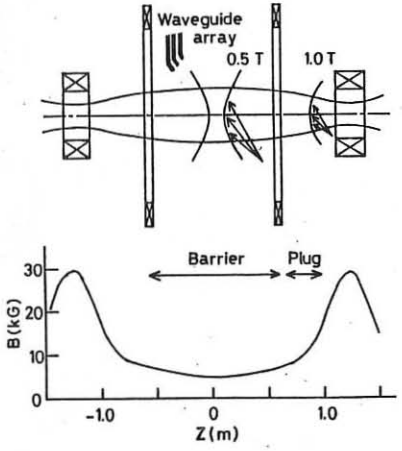

Fig. 1 Heating configuration of ECRH.

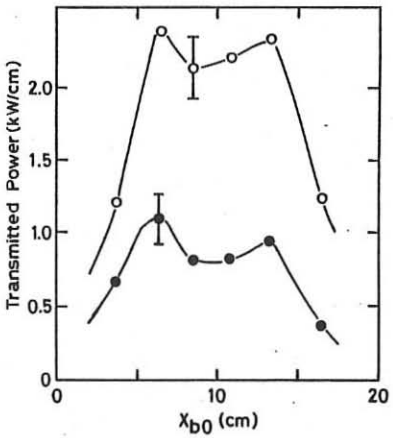

Fig. 2 Spatial distribution of transmitted power.

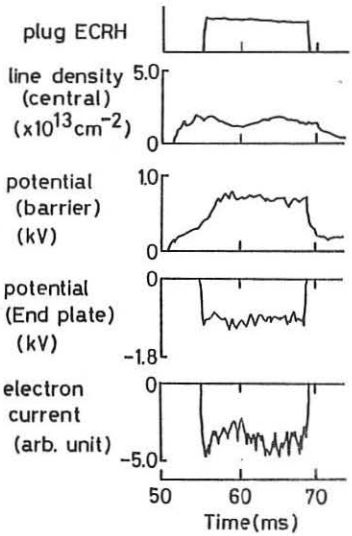

Fig. 3 Warm electron current measured at the end of the machine together with the line density at the central cell and the potentials.

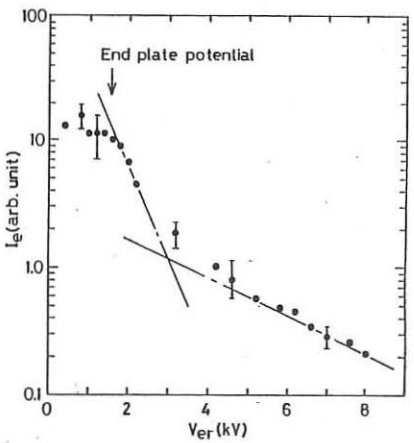

Fig. 4 Energy distribution of the warm electrons measured with an muti-grid energy analyzer.

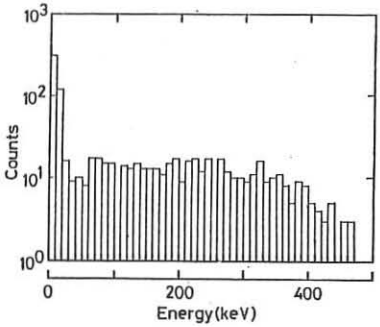

Fig. 5 Energy spectrum of hot electrons measured at the end. Both the plug and barrier ECRH are turned on.

Density Modulation During Modulated ECRH in DITE

C M Bishop, J W Connor, M Cox, N Deliyanakis ♣,
J Hugill, D C Robinson, M Ashraf, H W Lean, P Mantica ◇,
W Millar, B J Parham, R A Pitts ♠, A Simonetto△, and G Vayakis ♣

UKAEA/EURATOM Fusion Association,
Culham Laboratory, Abingdon, OX14 3DB, UK

△Attached under a Euratom Fellowship
♠Royal Holloway and Bedford New College, University of London
♣University of Oxford
◇IFP-CNR, Milano

INTRODUCTION

The effective thermal diffusivity, χ_{eff}, deduced from thermal wave propagation often differs from values derived from power balance (χ_{eff}^{PB}). For example, on DITE [1,2] the values (χ_{eff}^{MOD}) deduced from modulated heating studies using fundamental cyclotron absorption are somewhat higher than χ_{eff}^{PB} . Furthermore χ_e^{MOD} depends only weakly on $\bar{n}_e$ in contrast to χ_{eff}^{PB} which falls with $\bar{n}_e$. A possible explanation of such discrepancies between χ_{eff}^{MOD} and χ_{eff}^{PB} is that modulation of the density caused by the modulated heating, which is not taken into account in the analysis, may affect the propagation of the thermal wave. This paper assesses the magnitude of the density modulation produced by modulated ECRH and the extent to which the experimental results can be reconciled with theory.

ORIGIN AND IMPACT OF DENSITY MODULATIONS

Modulated ECR heating may give rise to modulation of the observed plasma density in a number of ways: Firstly, the density will change due to the equilibrium response to pressure modulations. These shifts also complicate the analysis of ECE and vertically viewing SXR diagnostics of the thermal wave [1]. Secondly, changes in recycling due to column shifts, direct edge absorption of ECR waves or the influence of the thermal wave propagating from the centre will affect the neutral particle source and, to some extent, the density profile. Such density sources give rise to terms in the heat transport equation formally equivalent to heat sources. Such effects will be significant only towards the plasma edge except at very low $\bar{n}_e$. Thirdly, changes in density transport and pinch terms in the plasma or coupling of heat and particle transport (due to off-diagonal terms in the transport matrix) generate density perturbations even in the absence of density source

terms [3]. In this case analysis of the temperature wave gives a 'hybrid' rather than purely thermal transport coefficient.

THEORY OF COUPLED TRANSPORT

The evolution equations for density and pressure can be written as

$$\frac{\partial n}{\partial t} + \nabla.\Gamma = S_n \;\; ; \;\; \frac{3}{2}\frac{\partial (nT)}{\partial t} + \nabla.Q = S_p \tag{1}$$

where $S_{n,p}$ are sources and $\Gamma(Q)$ the particle (heat) flux. It is usually assumed in both thermal wave and power balance transport analyses that Q is driven only by temperature gradients. In general, however, theoretical expressions for Q from both (neo)classical and anomalous transport models show that heat fluxes are also driven by density gradients (and, similarly, density fluxes are driven by temperature gradients). For example, in neoclassical theory if $T_i = T_e$ and ion temperature gradient and electric field (pinch) terms are neglected

$$\Gamma = -f(r)n[K_{11}A' + K_{12}T'/T] \tag{2}$$

$$Q = -f(r)nT[K_{12}A' + K_{22}T'/T] \tag{3}$$

where $A' = n'/n - 3T'/2T$ and $f(r)K_{ij}$ is the transport matrix. The off-diagonal terms in the transport matrix lead to a local modulated heat source at $r = \xi$ ($\tilde{S}_p = \delta(r-\xi)e^{i\omega t}/2\pi\xi$) driving n as well as T perturbations even in the absence of modulated density sources ($\tilde{S}_n(r,t) = 0$) since

$$K_{11} \,||\, \frac{n'}{n} \,||\, + (K_{12} - \frac{3}{2}K_{11}) \,||\, \frac{T'}{T} \,||\, = \; 0 \tag{4}$$

$$K_{12} \,||\, \frac{n'}{n} \,||\, + (K_{22} - \frac{3}{2}K_{12}) \,||\, \frac{T'}{T} \,||\, = \; \frac{e^{i\omega t}}{2\pi} \tag{5}$$

Here $||\quad||$ denotes the change in the function at $r = \xi$. This can only be satisfied if both T'/T and n'/n have non-zero oscillating components. Analytic solution of these equations is only possible if they are linearised ($\tilde{n}/n, \tilde{T}/T \ll 1$) and the scale length of the modulated components is assumed short compared with other length scales. Far away from the heat deposition region the eigenvector of the linearised transport matrix ($M_{11} = K_{11}, M_{12} = K_{12} - 3K_{11}/2, M_{21} = 2K_{21}/3 - K_{11}, M_{22} = 2K_{22}/3 - 2K_{12} + 3K_{11}/2$) with the largest eigenvalue, λ_+, dominates and the normalised ratio of density to temperature perturbation is $C = \tilde{n}T/(\tilde{T}n) = M_{12}/(\lambda_+ - M_{11})$. In the near field (which is more relevant to experiment), C depends somewhat on assumptions concerning $f(r)$ and the source profiles. Table I compares the far field values with the near field values, for the sources described above, assuming $f(r) = cr^{-2}$ for various transport models. The absolute magnitude of $\tilde{n}_e$ is largest at $r = \xi$. (The DTE mode model is a linearisation

of Horton's results [4].) Also shown is the ratio of χ_{eff}^{MOD} obtained in the far field of the thermal wave to χ_{eff}^{PB} assuming $\eta_e = n_e T_e'/n_e' T_e = 2$. Note that, with the above assumptions, only in the collisionless case is the ratio significantly different from unity. The effects of non-linearities, different $f(r)$ and sources of finite extent have yet to be explored.

Table 1

Model	$C = \tilde{n}T/n\tilde{T}$		Matrix Elements				Eigenvalues		$\frac{\chi_{eff}^{MOD}}{\chi_{eff}^{PB}}$
	Near Field	Far Field	M_{11}	M_{12}	M_{21}	M_{22}	λ_+	λ_-	
Collisionless neoclassical	0.19	-1.67	1.04	-0.36	-0.24	0.86	1.26	0.64	1.70
Collisional neoclassical	-0.08	0.32	0.33	0.06	0.04	0.51	0.52	0.32	0.99
Anomalous DTE Mode	-0.18	0.48	26.0	6.0	50.0	14.0	38.33	1.67	0.98

EXPERIMENTAL RESULTS

Transport studies performed on DITE have used modulated (at $\omega/2\pi = 143$ or 333Hz) 60GHz ECR heating utilising both fundamental ($B_\phi \simeq 2T$) and second harmonic ($B_\phi \simeq 1T$) resonance absorption. The data discussed in this paper are from the experimental campaigns reported in refs [1,2] to which we refer for details. The plasma density was diagnosed by a 5 chord 2 mm interferometer system viewing the plasma vertically. The line averaged nature of the density diagnostic means that short wavelength density modulations would escape detection. The line-average density, $\bar{n}_e$, ranged from $1-5\times10^{19}m^{-3}$ in fundamental and from $0.6-0.8\times10^{19}m^{-3}$ in second harmonic heating discharges. The major radial location of the plasma column was measured magnetically. Although feedback control was used, radial oscillations occurred as a result of modulation of the plasma pressure on a time-scale similar to the response time of the feed-back system. An example of the density modulations in a low density discharge is shown in Fig. 1. It is necessary to distinguish between fundamental and second harmonic results and between helium discharges and hydrogen/deuterium discharges. Table 2 shows the relative line-averaged density modulation ($\tilde{\bar{n}}_e/\bar{n}_e$) for a central and an outer chord for the various conditions studied. In many helium discharges no $\tilde{\bar{n}}_e$ is observable above the noise level ($\lesssim 0.2\%$ on the central chord, $\lesssim 0.6\%$ on the outer chords). The relative modulation of SXR emission and ECE temperature ranged up to $\sim 20-25\%$ for all heating and gas combinations. The larger $\tilde{\bar{n}}_e/\bar{n}_e$ during second harmonic heating was due in part to the larger column position modulation ($\mid \Delta\tilde{R}_0 \mid \lesssim 3mm$) than in fundamental heating discharges ($\mid \Delta\tilde{R}_0 \mid \lesssim 1.5mm$). However, at low density a significant residual density modulation remains which is partly localised in the periphery of the plasma but also in the power deposition region with

opposite sign. However, the transport driven $\tilde{n}_e$ is smaller than theoretical predictions (especially in helium discharges) indicating that the off-diagonal elements of the transport matrix are also small for the full range of density used ($0.6 - 5 \times 10^{19} m^{-3}$).

Table 2

	Gas	Relative $\bar{n}_e$ Modulation	
		Central Chord	Outer Chord
Fundamental	H/D	$\lesssim 1\%$	$\lesssim 3\%$
	He	$\lesssim 0.3\%$	$\lesssim 1\%$
Second Harmonic	H/D	$\lesssim 2\%$	$\lesssim 7\%$

References

[1] J Hugill et al, Proc. of the 15th EPS Conf., Dubrovnik, (1988), Vol 12B, Part II, p807.
[2] M Ashraf et al, 12th IAEA Int. Conf., Nice, (1988), Paper IAEA-CN-50/A-5-2-1.
[3] M Hossain et al, Phys. Rev. Lett. 58 (1987) 487.
[4] W Horton, Phys. Fluids 19 (1976) 711.

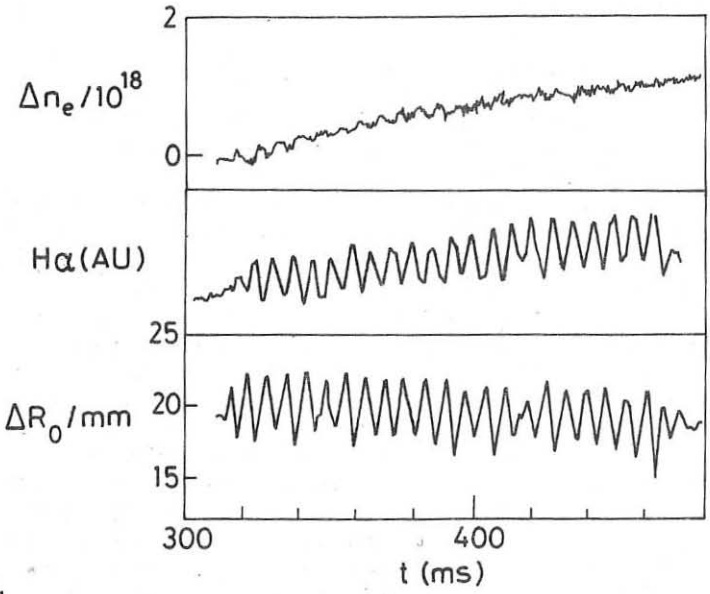

Fig. 1
The change in electron density, H_α emission and plasma position during modulated second harmonic heating ($\bar{n}_e = 0.8 \times 10^{19} m^{-3}$).

OBLIQUE ORDINARY WAVE PROPAGATION AND ABSORPTION AT THE ELECTRON CYCLOTRON SECOND HARMONIC IN A WAVE-DYNAMICAL APPROACH

V. Petrillo, C. Maroli, C. Riccardi and G. Lampis*

Dipartimento di Fisica del Plasma dell'Università degli Studi,
Via Celoria, 16, Milano
* Istituto di Fisica del Plasma, Associazione EURATOM-ENEA-CNR,
Via Bassini, 15, Milano

We study the oblique injection of ordinary (O) waves with frequency near to the second harmonic of the EC frequency (SHEC) into a tokamak plasma /1,2,3/. We use both the W.K.B technique and the dynamical approach. A similar phenomenon has been investigated in the range of the fundamental EC frequency /4,5,6/. Slab geometry is used.

Three kinds of cold cut-offs (CO) can be present inside the plasma, in correspondence to the solution of the equations:

$X(x)=1$; $X(x)=(1-n_{\parallel}^2)(1+Y(x))$; $X(x)=(1-n_{\parallel}^2)(1-Y(x))$

Here $X=(\omega_{pe}/\omega)^2$ and $Y=\omega_{ce}/\omega$, $\omega_{pe}(x)=\omega_{pe}(0)(1-x)^{\alpha}$.

If the injected frequency ω is taken equal to $2\omega_{ce}(0)$, Y assumes the form $Y(x)=0.5/(1+x/R)$. The coordinate x is adimensioned to the minor plasma radius a, and $R=R_o/a$ with R_o major plasma radius.

The $X(x)=1$ CO is always carried by the O mode, while the $X(x)=(1-n_{\parallel}^2)(1-Y(x))$ i.e. the low-n CO, is always carried by (X) the branch.

The high density CO: $X(x)=(1-n_{\parallel}^2)(1+Y(x))$ (high-n CO) can be carried by each one of these two fundamental modes, depending on the parameters.

In Fig. 1, the curves representing the appearence, at the centre of the plasma, of these CO points, are given in the plane $(X(0),n_{\parallel})$. Line OAP refers to the $X(0)=1$ CO, and curve CAD to the high-n CO. Curve EBF represents the locus of the points where the determinant Δ of the algebraic dispersion equation vanishes at $x=0$ /6/. This condition can be written as:

$$Y(0)^2(1-n_{\parallel}^2)^2+4(1-X(0))n_{\parallel}^2=0$$

In all the region of the $(X(0),n_{\parallel})$ plane, to the right of the EF curve, two conversion points between the O and the X branches are present.

When the condition $\Delta=0$ is verified for $n_{\perp}^2=0$, the high-n CO changes branch. In the EBL region, the CO point to the right of the SHEC resonance ($x>0$) is on the O mode, and, in the sector limited by the EB and BI branches, also the CO point to the left of $\omega=2\omega_{ce}$ ($x<0$) is on the O wave.

From the edge, the O wave propagates up to the point corresponding to

the first root of the equation $X(x)=1$. Between this point and the first root of $X(x)=(1-n_{\parallel}^2)(1+Y(x))$, an evanescent layer exists.

When $(1-n_{\parallel}^2)(1+Y(x_*))=1$, with x_* given by $X(x_*)=1$, the width of this evanescent layer goes to zero and the wave tunnels. This fact occurs along the lines GA and AH in Fig. 1, respectively for the CO region to the left and to the right of the resonance layer where $\omega = 2\,\omega_{ce}$.

If conversion between O and X modes occurs, strong absorption happens (NH part of the AH curve in Fig. 1). If conversion does not occur, the O wave is transmitted through the slab. (AN part of the AH curve).

In Fig. 2 the complex quantity $n_{\perp}$, solution of the complete classical dispersion relation /7/, is presented as a function of x for $X(0)=1.5$, $n_{\parallel}=0.6$, and $\mu=(c/v_{te})^2=500$. The magnetic field is taken $\underline{B}(x)=\underline{B}(0)/(1+x/R)$. From the outer (low $\underline{B}$ field) side (in this Fig. 2 at the right edge), the O wave propagates up to the high-n CO (point x_1), then an evanescent layer partially reflects the wave. After the $X(x)=1$ CO (point x_2), the O mode meets the conversion point with the X mode (point G). This last branch, contrarily to what happens in the cold model, crosses, towards the right, the UH resonance with increasing refractive index $n_{\perp}$. In this region the X wave is transformed into the quasi electrostatic Q wave. The Q mode, reaches point C where is converted into a backward, strongly damped Bernstein (B) wave. In the opposite side injection, (high $\underline{B}$ side), the O mode is cut off at x_3. The evanescent layer existing there is very thin. The O mode rises, after such layer, reaching the O-X conversion point F. The X mode existing there has a conversion point (D) into a Q wave. Therefore, for the high $\underline{B}$ field wave launching, no connection between X and B waves occurs and, then, no excitation of B modes happens.

As described in /6,8/ we reduced into a differential form the integrodifferential equations obtained from the Vlasov linearized equation and the Maxwell system. The set of equations at the SHEC, is deduced in /8/ under the conditions: $\lambda_o/R_o \ll 1$; $\mu \gg 1$; $\lambda_o\sqrt{\mu}/(2\pi R_o) \lesssim 1$

None of this conditions involves the injection angle θ, so the system is valid for arbitrary obliquity. We have fixed the resonance condition at $x=0$ $(Y(0)=0.5)$, and chosen $w=\omega a/c=100$. The other parameters are varied widely. The electron temperature profile is constant.

Fig. 3 shows the transmission (T), reflection (R), and absorption (A) coefficients as functions of the injection angle $\theta=\sin^{-1}(n_{\parallel})$ for $\mu=500$ and various values of $X(0)>1$. The injection, is from the outer side.

(R) is always large, except in an angular range centered around the critical angle $\theta_c=\sin^{-1}(Y(0)/(1+Y(0)))^{1/2}$, (Fig. 1, AH line). Outside this θ window the wave is reflected before reaching the absorption or conversion regions.

In correspondence to the critical angle θ_c the O wave is transmitted through the CO and, depending on the density and temperature, its

absorption varies. In this case, if $X \approx 1$, the system has the parameters near to the AN part of the AH curve in Fig. 1. There, the O-X conversion does not occur, and, therefore, the O mode is transmitted (Figs. 3a, 3b).

Crossing towards the right side, the $\Delta = 0$ (EBF) curve (in Fig. 1), the O-X conversion takes place, so, for $X(0) \gtrsim 1.1$ (Figs. 3c, 3d, 3e, 3f), (T) globally decreases, and strong absorption takes place around ϑ_c.
In Fig. 4 the real part of the x-component of the electric field E_x and the time-averaged Poynting vector x-component $\langle P_x \rangle$ are presented as functions of x, for $\vartheta = 35°$, $\mu = 500$ and for various values of X(0).

Short wavelenght modes appear, in correspondence with the situations where absorption takes place, for $X(0) \gtrsim 1.1$. In particular, in the cases of large densities (Figs. 4c, 4d, 4e), the presence of three different wave modes (O, Q and B) is clearly recognizable.

References

/1/ M. Bornatici, R. Cano, O. De Barbieri and F. Engelmann: Nucl. Fusion, 23,1153, (1983).
/2/ S. Pesic: The Physics of Fluids, 31,115, (1988).
/3/ J.Y. Hsu, V.S. Chan and F.Z. McClain: The Physics of Fluids, 26,3300, (1983).
/4/ J. Preinhaelter and V. Kopeky: J. of Plasma Physics, 10,1, (1973).
/5/ F.R. Hansen, J.P. Lynov, C. Maroli and V. Petrillo: J. of Plasma Physics, 39,319, (1988).
/6/ V. Petrillo, C. Maroli and G. Lampis: Il Nuovo Cimento, 9D,1073,1089, (1987).
/7/ J.J. Schuss and J.C. Hosea: The Physics of Fluids, 18,727, (1975).
/8/ V. Petrillo, G. Lampis, C. Maroli and C. Riccardi: to be published.

Figure Captions

Fig. 1 Curves giving, in the $(n_{\parallel} X(0))$ plane, the CO layers, the conversion layers, and the conditions for critical angle. Cold dispersion relation for R=3 and Y(0)=0.5.

Fig. 2 Re $n_\perp$ (——) and Im $n_\perp$ (----) vs x, as given by the classic Vlasov dispersion relation for: $X(0)=1.5$, $\mu = 500$, $n_{\parallel} = 0.6$ and R=3. The O, X, Q and B modes are represented.

Fig. 3 (R), (T) and (A) coefficients vs ϑ, for the OM outer side injection; $\mu = 500$, R=3 and: a) X(0)=1; b) X(0)=1.05; c) X(0)=1.1; d) X(0)=1.15; e) X(0)=1.2 and f) X(0)=1.5.

Fig. 4 Re E_x and $\langle P_x \rangle$ vs x for OM outer side injection; $\vartheta = 35°$, $\mu = 500$, R=3 and a) X(0)=1.01; b) X(0)=1.05; c) X(0)=1.08; d) X(0)=1.15 and e) X(0)=1.5.

Fig. 1

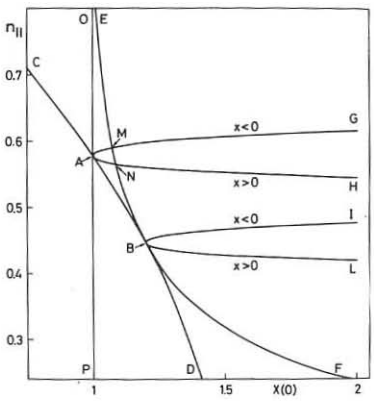

Fig. 2

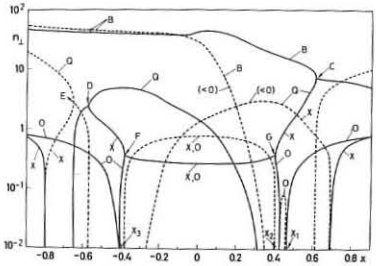

Fig. 3

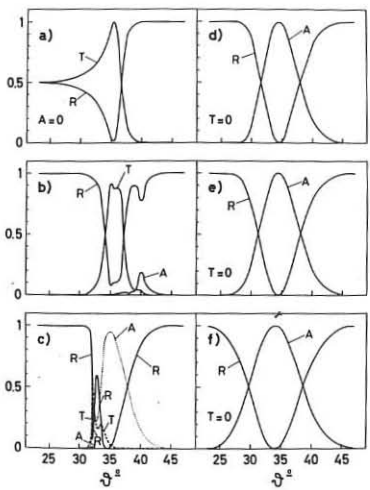

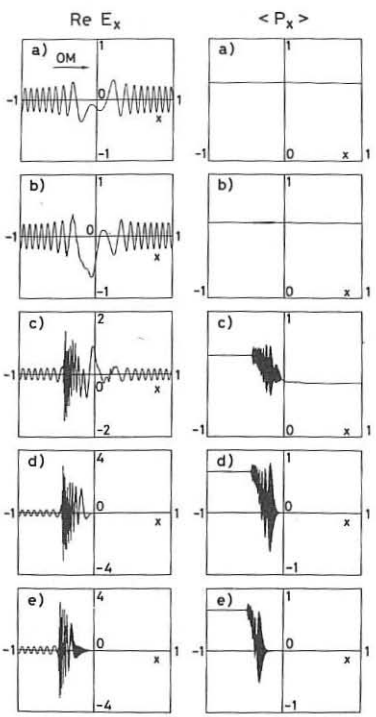

ECRH AS A RESEARCH TOOL ON RTP

R.W. Polman, F.M.A. Smits, P. Manintveld,
A.A.M. Oomens, F.C. Schüller, A.G.A. Verhoeven.

FOM Institute for Plasma Physics 'Rijnhuizen', Association EURATOM-FOM,
P.O. Box 1207, 3430 BE Nieuwegein, The Netherlands.

Introduction.

The energy confinement degradation with additional heating and the strong coupling between energy and particle confinement are notorious issues in current tokamak research. The true nature of the mechanisms causing the losses, however, has still to be determined. Those unknown mechanisms appear not to be affected by the plasma size in the sense that scaling laws exist, which cover small as well as large tokamaks [1]. Furthermore, global confinement is strongly influenced by anomalous transport in the boundary region. The power, density, and current dependence of the anomaly seems to be common for ECRH, NBI and ICRH, i.e. independent of the heating method [2,3]. Detailed transport studies in any tokamak large enough to avoid domination by atomic effects and equipped with a flexible system for powerful, localized, and programmable heating, along with an adequate diagnostic system, could contribute relevantly to the understanding of fundamental transport mechanisms in fusion relevant tokamak plasmas. RTP, the new Rijnhuizen Tokamak Project has come into operation early 1989 and will be dedicated to such studies. The stainless steel vacuum vessel with dimensions of $R_0 = .72$ m and $b = .23$ m has a carbon limiter allowing a minor radius up to $a = .185$ m. The maximum toroidal field is 2.5 T, $I_p \leq 200$ kA, the discharge duration is 250 ms, and the electron density will be in the range of $4 \cdot 10^{18}$ m^{-3} to $1 \cdot 10^{20}$ m^{-3}. RTP is the former Grenoble tokamak PETULA adapted to its new task [4]. A 60 GHz, 600kW Electron Cyclotron Resonance Heating (ECRH) system will be used for strong auxiliary heating.

Research programme for RTP.

The experimental work on transport mechanisms in tokamaks will focus on determining as accurate as possible the radial and poloidal structure of the plasma equilibrium and of the spectra of the fluctuations that can be expected to cause turbulent transport of particles and energy. In addition to the examination of steady state conditions of plasmas with Ohmic and intense additional heating, a large effort will be made to study the evolution of relevant plasma parameters in time and space for transient states, generated as a response to well-defined perturbations such as modulation of local heating, current, and gas puffing, and by pellet injection. Theoretical transport models will be compared with the experimental findings.

ECRH for RTP.

On RTP the additional heating power will be supplied by an ECRH system consisting of three 60 GHz, 200 kW, 100 ms gyrotrons. The almost optical propagation of the waves, localized absorption of wave power, direct electron heating, and the possibility of selective interaction in velocity space advance ECRH to be the best heating method for RTP. Localized, controllable power deposition is a must for the physics programme, and direct electron heating is highly appropriate as electrons are expected to be the main cause of anomalous transport.

The highest single-pass absorption will be obtained for waves propagating in fundamental O- or X-mode ($B = 2.14$ T), or in 2nd harmonic X-mode ($B = 1.07$ T). For fundamental O-mode in a 1 keV RTP-size plasma with central resonance, the single-pass absorbed power fraction is ≤ 0.65. Almost full absorption ($> .95$) occurs for high T_e (≥ 3 keV). The cut-off density of the waves is $n_{co} = 4.47 \cdot 10^{19}$ m^{-3}. Diffraction effects become considerable for $n_e > 3 \cdot 10^{19}$ m^{-3}. Second harmonic X-mode would show almost complete absorption ($> .99$) for a 1 keV plasma, but the cut-off density is halved to $2.23 \cdot 10^{19}$ m^{-3}, while target plasmas may not be as good as those of normal operation at 2.2 T. The first harmonic X-mode shows better

ECRH access to the torus. The power will be launched both from the LFS through ports in the equatorial plane via two outside launchers, and from HFS through top ports via two top-port launchers (fig.4). The LFS launcher (I) and top-port launcher (II) will be connected permanently to a gyrotron. The third gyrotron will be connected to either a top-port (IIIa) or to a LFS launcher (IIIb). The HFS launchers consist of bent corrugated (II and IIIa, HE_{11}-mode) waveguides with a 27.8 mm diameter and a rotatable focussing mirror at the end of the bend. The LFS launchers will be open-ended smooth (I, TE_{11}-mode) and corrugated (IIIb,HE_{11}-mode) waveguides with a 63.5 mm diameter radiating linearly polarized EC-power to couple to the 1st harmonic O-mode or 2nd harmonic X-mode. For the opposite torus wall three options are considered: a mode converting mirror, a smooth mirror or an absorber material which would make the study of single pass effects possible. A problem is the availability of suited absorber materials.

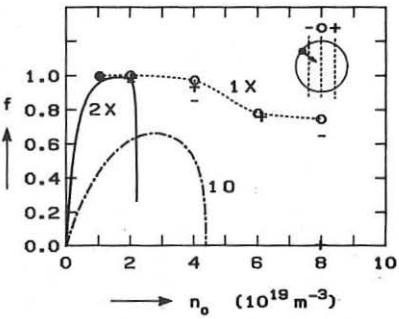

Fig. 3. Single pass absorption f of a ray launched from HFS (1X) (θ=125°,ϕ=-45°) for central resonance (o) and resonance +a/2 (+) and -a/2 (-) displaced. The values for O-mode (1O) and 2nd harmonic X-mode (2X) are also given (perpendicular LFS launch).

For all three gyrotrons it will be possible to modulate the RF output power. Square wave modulation with a frequency up to 100 kHz can be achieved for modulation depths up to 100%; modulation frequencies up to 300 kHz will be possible for 50% modulation depth. More sophisticated pulse shaping will be controlled by means of a micro processor. The deposition features in combination with the modulation possibility offer a wide variety of possible steady state or transient transport studies. Studies in the field of MHD control and profile control, and experiments affecting electron velocity distributions will be possible.

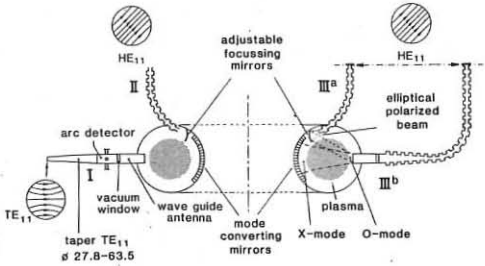

Fig. 4. The launching possibilities.

Elliptical polarizers.

For optimum oblique X-mode HFS launch, adjustable elliptical polarization of the waves is required. Two approaches are under study. In the first the elliptical polarization is produced by a waveguide polarizer. This polarizer principally consists of a circular waveguide which is gradually squeezed to an ellipse in the middle. At both ends, its cross-section is circular again. A sine-squared function is used for the squeeze distance to get a 90° phase difference between the field components perpendicular and parallel to the squeeze direction after passing through the polarizer. All elliptic polarizations between circular and linear can be produced by rotating the polarizer with respect to the incoming TE_{11} signal. By rotating both the TE_{01}-TE_{11} converter and the polarizer, the orientation of the ellipse can be adjusted. See [6] and the references therein. In this way, the radiation can be launched via a smooth focussing mirror.

The second approach to obtain the required elliptic polarization is to launch linearly polarized waves from a transmission line in HE_{11} mode onto a corrugated mirror. The linear polarization is converted to elliptical polarization upon reflection from the mirror. The ellipticity and the orientation of the ellipse can be varied by rotating the

absorption in an extended density range: up to $8.9 \cdot 10^{19}$ m^{-3}. However, the power must be launched obliquely to the magnetic field from the high field side (HFS) to reach the gyro-resonance regions directly, and to obtain high single-pass absorption. Due to down shifted resonance effects the absorption region along the ray is less localized than in the case of perpendicular O-mode launch from the low-field side (LFS), which is a few mm in depth. Nevertheless, the localization of energy deposition using HFS launching can remain satisfactory by employing grazing incidence on the flux surfaces. Ray paths and damping characteristics were obtained with the ray tracing code TORAY [5]. Density and temperature profiles were modelled with parabolas and squared parabolas, and using a modest pedestal. Fig.1 shows an example of ray tracing results for central electron density $n_e(0) = 2 \cdot 10^{19}$ m^{-3}, $T_e(0) = 1$ keV, and $B_T = 2.14$ T (central heating). The lines are projections of the ray trajectories on the poloidal plane. The angle ϕ between the projection of the ray on the equatorial plane and the major radius is -45°, while the angle between the ray and the vertical direction, θ, is varied from 95° to 175° with a 10° interval, which is thought to be characteristic for the beam width.

Fig. 1. manifests a simple tool to control the energy deposition: by varying θ, the energy can be deposited on chosen flux surfaces without changing the magnetic field, so on-axis and off-axis heating effects can be compared for the same target plasma. Further it would be possible to deposit energy at different flux surfaces simultaneously, using two or more gyrotrons. This is an important feature for transport studies.

Fig. 2 gives the absorbed power fraction, f, and the radial span within which the intensity in the ray drops from 90% to 10% of its initial value as a function of the angle θ. This spanwidth gives a measure of the localization of the power deposition.

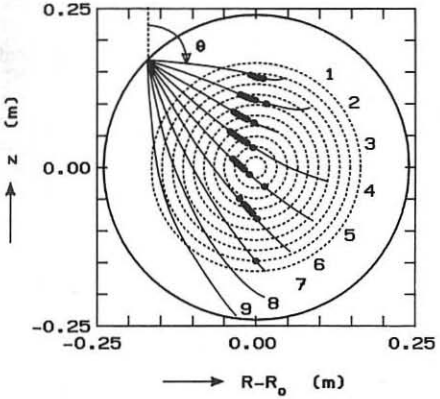

Fig. 1. Ray tracing results for HFS launch; 1st harmonic X-mode, $95° \leq \theta \leq 175°$, $\phi = -45°$, $T_e(0) = 1$ keV, $n_e(0) = 2 \cdot 10^{19}$ m^{-3}, $B_T = 2.14$ T. The crosses indicate where the power is deposited.

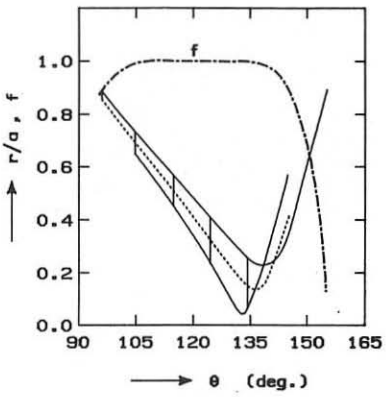

Fig. 2. The absorbed power fraction f and the span of the band within which the intensity drops from 90% to 10% of its initial value as a function of θ, for the case of Fig. 1.

Fig. 3 shows for a ray injected under $\theta = 125°$ and $\phi = -45°$ the absorbed power fraction as a function of the central density for three values of B. A high single pass absorption for $n_e = 1 - 8 \cdot 10^{19}$ m^{-3} is found for various magnetic fields and a wide range of injection angles. Comparison with fundamental O-mode and 2nd harmonic X-mode launching shows the superior properties of the HFS fundamental X-mode injection scheme for RTP.

Four ports at two toroidal positions which are about 180° apart, are available for the

polarization direction of the incident wave and by rotating the direction of the grooves in the plane of the mirror by an angle η. If τ is the phase shift of the electric field component perpendicular to the grooves with respect to the field component parallel to the grooves after reflection on the mirror, the ellipticity that can be produced which is closest to 1 equals $\mathrm{tg}(\tau/2)$. In order to achieve arbitrary ellipses, τ must therefore equal 90° for all angles of incidence. However, since τ is a (complicated) function of the angles of incidence, the groove parameters can only be chosen such that τ is close to 90° for all angles η and reflection angle ζ. At RTP, ζ satisfies $22° \leq \zeta \leq 46°$ whereas η can be chosen arbitrarily. Since τ is symmetric in η every 90°, measurements and calculations were performed for $0° \leq \eta \leq 90°$. For a mirror with groove width 2 mm, period 2.5 mm, and depth 0.9 mm, the results are shown in fig. 5. Crosses indicate measurements, while calculations are given by solid lines. The accuracy of the groove depth appeared to be about 0.05 mm. This introduces a systematic error of ±5° which explains the deviation between measurements and calculations. Work is in progress at mirrors with an accuracy of 0.01 mm.

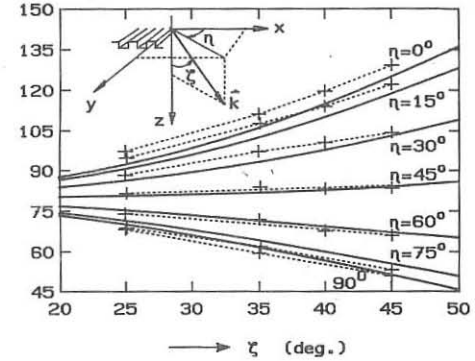

Fig. 5. The phase shift τ between the field components perpendicular and parallel to the grooves after reflection on the mirror as a function of η and ζ.

The required polarization direction of the wave incident on the mirror,and the required rotation angle η of the grooves can be calculated from τ [7]. For RTP, τ must lie between 60° and 120°. From the measurements one observes that for most values of η and ζ, τ lies within that range. Moreover, groove parameters have been found for which $60° < \tau < 120°$. In conclusion: at low power, the corrugated mirror is an adequate instrument to produce the elliptical polarized waves that will excite the X-mode in the RTP plasma. At high power, arc breakdown across the grooves caused by sharp edges may distort the reflection characteristics Therefore, in the near future, measurements will be performed on mirrors with rounded ribs.

Acknowledgement.

This work was performed under the Euratom-FOM association agreement with financial support from NWO and Euratom.

References.

[1] Goldston, R.J., Plasma Physics and Controlled Fusion 26 (1984) 87-103.
[2] Burrel, K.H. et al., Proc. of the 10th IAEA Conf. on Plasma Physics and Controlled Nuclear Fusion, London (1984), Vol 1, 131-139.
[3] Cordey, J.G. et al., Proc. of the 11th IAEA Conf. on Plasma Physics and Controlled Nuclear Fusion, Kyoto (1986), Vol 1, 99-110.
[4] Kruyt, O.G. et al., Proc. of the 15th Symp. on Fusion Technology, Utrecht (1988), paper A03, to be published.
[5] Kritz, A.H. et al., Proc. of the 3rd Int. Symp. on Heating in Toroidal Plasmas, Grenoble (1982), Vol 2, 707-723.
[6] Manintveld, P. et al., Proc. of the 15th Symp. on Fusion Technology, Utrecht (1988), paper B05, to be published.
[7] Smits, F.M.A., to be published.

NONLINEAR EFFECTS AT ELECTRON CYCLOTRON HEATING OF A TOROIDAL PLASMA BY FEL RADIATION

A.G.Litvak, A.M.Sergeev, E.V.Suvorov,
M.D.Tokman, and I.V.Khazanov

Institute of Applied Physics, Academy of Sciences of the USSR
46 Uljanov Str., 603600 Gorky, USSR

Nonlinear effects at ECRH of a plasma in tokamaks by means of FEL radiation are analysed briefly. We shall classify nonlinear phenomena by "the place of action" and distinguish in the general problem two independent issues:
1) parametric and self-focusing processes along the wave propagation path towards the ECR region in a plasma;
2) nonlinear effects in the ECR region.

1. The role of parametric processes at ECRH of a plasma by powerful radiation was considered in [1] as applied to experiments to be carried out on the Alcator C installation. The estimates obtained in this work show that the most dangerous process in the heating by an extraordinary wave at the fundamental is stimulated backscattering by ions. A decay into two electron Bernstein modes may play a significant role in the heating by an extraordinary wave at the second EC harmonic. Consider also two other dangerous parametric processes. One of them is related to the stimulated ordinary-wave scattering into upper hybrid oscillations while the other one to the extraordinary wave decay into the second harmonic of an electron Bernstein mode and into lower hybrid oscillations. Estimates based on [2] show that such instabilities may develop not worse than the instabilities considered in [1]. Omitting details we shall present equations for the growth rate γ and the gain K in both processes:

$$\gamma \simeq \frac{\omega_0}{10\pi}\,\frac{\omega_{pe}^2}{\omega_0^2}\,\frac{v_\sim^2}{v_{Te}^2}\,, \qquad \Gamma = \frac{\gamma}{\omega_0}\,\kappa L_n \qquad \kappa\rho_e = 0{,}3 \qquad (1)$$

$$\gamma = \omega_{pi}\,\frac{v_\sim}{v_{Te}}\,, \qquad \Gamma = \frac{\gamma^2}{2\omega_{pi}^2}\,\frac{L_n}{\rho_e}\,, \qquad \kappa\rho_e \simeq 0{,}3 \qquad (2)$$

Here the gain is $K = \exp\Gamma$, ρ_e is the Larmor electron radius, and L_n is the characteristic plasma scale.

For the evaluation of the role of self-focusing we need, first of all, to compare the source power with a so-called critical self-focusing power that, in the case of transverse

(with respect to the magnetic field) propagation of the gaussian-shape wave packet, can be represented in the form 3

$$P_{cr} = \frac{c}{4\beta} \frac{a_z}{a_y} \left(1 + \alpha \frac{a_y^2}{a_z^2}\right). \qquad (3)$$

Here $a_{z,y}$ are the longitudinal (along $\vec{B}_0$) and the transverse sizes of the wave beam at the plasma edge. The diffraction α and the nonlinear β parameters for the ordinary wave have the form

$$\alpha = 1 - \frac{\omega_{pe}^2}{\omega^2}, \qquad \beta = \frac{\omega_{pe}^2}{\omega^2} \frac{e^2}{4mc^2(T_e + 3T_i)} \qquad (4)$$

The value of P_{cr} in Alcator C experiments is to be $(1\text{-}2)10^8$W which is much smaller than the peak power in a FEL pulse. Estimates of the time and space scales of filamentation instabilities prove this effect to be possible in the Alcator C tokamak. A nonstationary theory of FEL radiation self-focusing in a toroidal plasma was developed in [4].

2. A relativistic cyclotron frequency shift is one of the main nonlinear effects accompanying cyclotron acceleration of electrons by electromagnetic waves. Essentially nonlinear regimes of electron acceleration, in which the particles acquire the energy that is much higher than the initial value, are most interesting for experiments using FEL. This case is analysed in [1,5] for an ordinary mode. Consider electron acceleration by an extraordinary wave.

Under ECRH conditions the relativistic electron motion is described by the relations similar to the equation of an anharmonic oscillator excited by an external harmonic force. The energy accumulation of the particle transiting through the ECR region is similar to the effect (known in the theory of oscillations) of a stepwise variation of forced oscillations as a result of adiabatically slow frequency or amplitude variation of the driving force. Let, for example, the electrons transit through the aperture of the microwave beam propagated across the toroidal magnetic field that can be assumed to be constant along the particle trajectory. The corresponding analysis [6] shows that the particle energy variation is irreversible in the region where

$$\omega < \omega_B^0 < \omega \left[1 + \left(E_{max}^{(+)} / H_0\right)^{2/3}\right]. \qquad (5)$$

Here $\omega_B^0 = eB_0/mc$ is a nonrelativistic cyclotron frequency and $E_{max}^{(+)}$ is the value of the maximum resonance field component of the beam. As the particle transits through the micro-

wave beam, the maximum energy accumulation amounts to $3\,mc^2 \times (E^{(+)}_{max}/B_0)^{2/3}$ and the criterion of realization of a nonlinear regime has a form $2\omega_a/v_{\parallel} >> (B_0/E^{(+)}_{max})^{2/3}$ where

a is the microwave beam radius.

The relation between the resonance component $E^{(+)}$ of the microwave field and the root-mean-square intensity $E^{(0)}$ depends on plasma density: the depression effect for this component in a sufficiently dense plasma is well known. Analysis of a nonlinear dispersion equation reveals the relation between the characteristic energy $\langle \mathcal{E} \rangle$ of accelerated particles, and the parameter $q = \omega_{pe}^2/\omega^2$ describing the plasma density [6]:

$$\langle \mathcal{E} \rangle = mc^2 \begin{cases} (E^{(0)}/B_0)^{2/3}, & q \leqslant (E^{(0)}/B_0)^{2/3} \\ (E^{(0)}/B_0)^2/2q, & (E^{(0)}/B_0)^{2/3} << q << 1 \\ (E^{(0)}/B_0)^2 & 1 << q \end{cases} \qquad (6)$$

The particles in the field of an ordinary wave are accelerated up to the energy [1,5]

$$\langle \mathcal{E} \rangle = (mc^2)^{2/3} \langle \mathcal{E}_{\parallel} \rangle^{1/3} (E^{(0)}/B_0)^{2/3} \qquad (7)$$

Comparison of (6) and (7) shows that particle acceleration in the field of an ordinary wave may be simulated by the acceleration in a low-density plasma using an extraordinary mode with decreased radiation power.

References

1. K.I.Thomassen (Sci. Ed.), Livermore, USA, LLL-PROP-00202--1986.
2. A.G.Litvak and V.Yu.Trakhtengerts, ZhETF, 1972,v.62,p.228.
3. A.G.Litvak and A.M.Sergeev, in: High-Frequency Plasma Heating, Inst.Appl.Phys.,Acad.Sci.USSR,Gorky, 1983, p.324.
4. M.Lontano and A.M.Sergeev, Preprint N 88/1, Inst.Plasma Phys., Milan, Italy.
5. W.M.Newis et al., Phys.Rev.Lett., 1987, v.59, p.60.
6. E.V.Suvorov and M.D.Tokman, Fizika Plazmy, 1988, v.14, p.950.

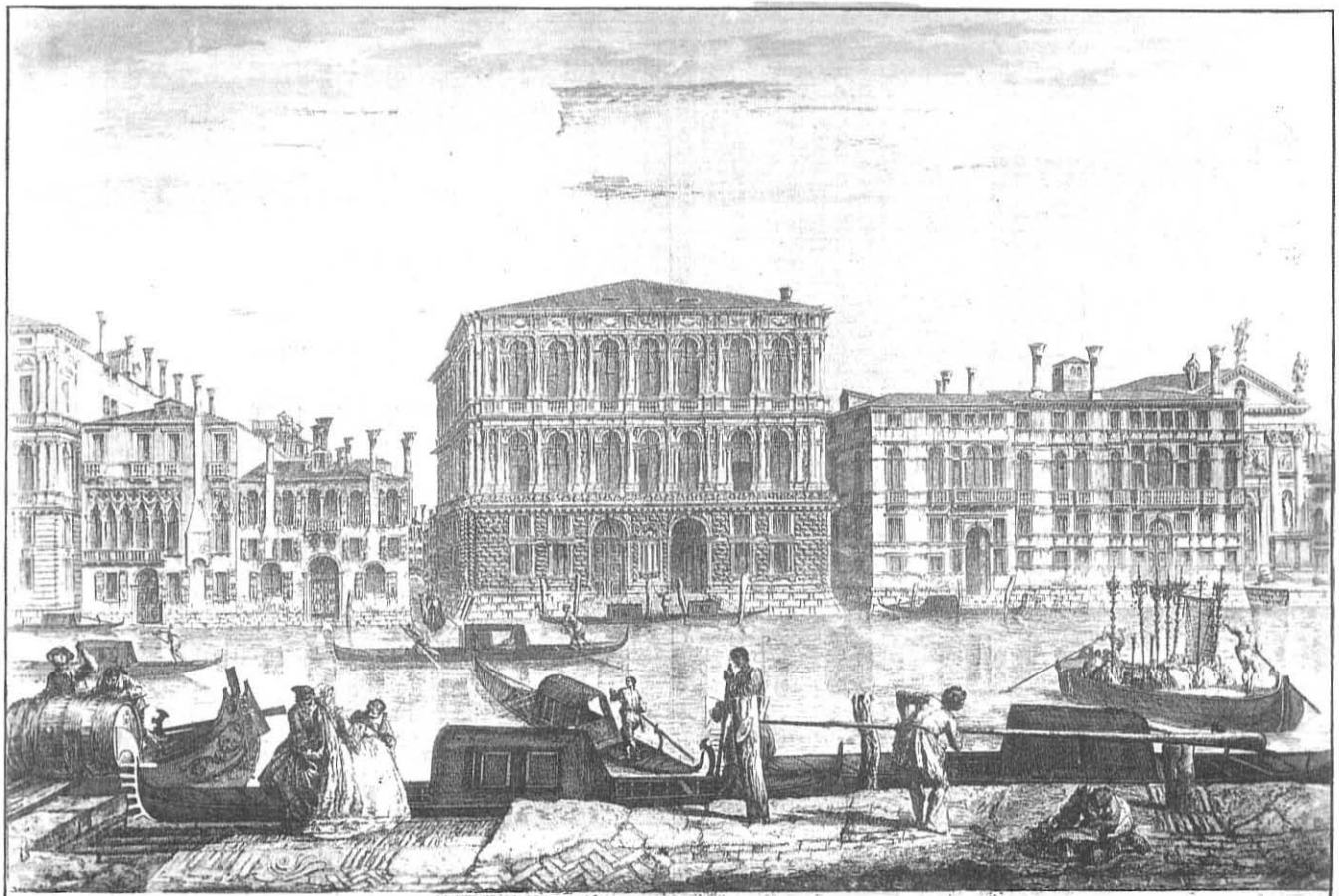

Pisaurorum Familiæ Ædes ad Canalis magni marginem, una cum D: Eustachij templo dextrorsum, et sinistrorsum cum parte Corneliorum ædis

OBLIQUE PROPAGATION OF ELECTRON CYCLOTRON WAVES IN RELATIVISTIC PLASMAS

F. Moser and E. Räuchle

Institut für Plasmaforschung der Universität Stuttgart
7000 Stuttgart 80, Pfaffenwaldring 31
Fed. Rep. of Germany

Abstract:
The propagation of electromagnetic waves in homogeneous, anisotropic, weakly relativistic, magnetized plasmas is investigated theoretically. Appropriate forms of the dielectric tensor are used to calculate phase velocity, damping and polarization for ordinary and extraordinary modes. The waves are assumed to propagate oblique to the external magnetic field for resonant and nonresonant frequencies. Electron distribution functions with anisotropic temperatures and drift motion of the electrons parallel to the magnetic field as well as relativistic loss-cone distribution functions are considered. Numerical results are shown for data which are of interest for electron cyclotron heating near the electron cyclotron harmonics.

1) Introduction

The investigation of the dispersion and absorption of electromagnetic waves in magnetized plasmas for frequencies close to the electron cyclotron frequency or its harmonics is of great interest in fusion physics. The plasma dielectric tensor is of fundamental importance for the theoretical treatment of the propagation of electromagnetic waves in plasmas. General expressions in terms of the distribution functions of the charged particles may be found in [1], [2], [3].

In this work we use the dielectric tensor in the form given by Shkarofsky [2], Tsai et al. [4] and Orefice [5].

2) The dielectric tensor

In the derivation of the dielectric tensor ε_{ij} electrons are considered only.

We consider two appropriate forms of distribution functions:

A) For an electron distribution function defined by

$$F(p_\perp, p_\parallel) = \frac{1}{\pi^{3/2}\cdot\alpha_\parallel \alpha_\perp^2 \cdot m_o^3} \cdot \exp\left(-\frac{(p_\parallel - p_o)^2}{m_o^2\cdot\alpha_\parallel^2} - \frac{p_\perp^2}{m_o^2\cdot\alpha_\perp^2}\right) \qquad (1)$$

Tsai et al. [4] derived ε_{ij} for the case of quasi-perpendicular propagation of the fundamental mode near $\omega = \omega_{ce}$ within the weakly relativistic approximation. ω_{ce} is the electron cyclotron frequency, $\alpha_{\perp,\parallel}^2 = 2\,V_{t\perp,\parallel}^2$, $V_t = (kT_e/m_e)^{1/2}$ the electron thermal velocity, m_o the electron rest mass, the

indices $\perp$ and $\parallel$ refer to the direction perpendicular and parallel to the external magnetic field.

An extension to higher harmonics is given in [6].

B) In this case an electron distribution function of the form

$$f(p_\perp, p_\parallel) = w_1 \cdot f_1(p_\perp, p_\parallel) + w_2 \cdot f_2(p_\perp, p_\parallel) \tag{2}$$

with

$$f_1(p_\perp, p_\parallel) = \frac{1}{m!}\left(\frac{\mu_1}{2}\right)^m \cdot p_\perp^{2m} \cdot \left(\frac{\mu_1}{2\pi}\right)^{3/2} \cdot \exp\left[-\frac{1}{2}\mu_1(p_\perp^2 + p_\parallel^2)\right] \tag{3}$$

(= loss-cone type distribution)

and

$$f_2(p_\perp, p_\parallel) = \left(\frac{\mu_2}{2\pi}\right)^{3/2} \cdot \exp\left[-\frac{1}{2}\mu_2(p_\perp^2 + (p_\parallel - p_o)^2\right] \tag{4}$$

(= drifting Maxwellian distribution)

is considered.

Due to Orefice [5] the dielectric tensor is given within the weakly relativistic theory for arbitrary angles of propagation and all harmonics:

$$\varepsilon_{ij} = \delta_{ij} + \left(\frac{\omega_{po}}{\omega}\right)^2 \cdot \left\{ \tilde{H}_{ij}\left[\frac{L_1(f)}{p_\perp}\right] - \Gamma_{ij}\left(w_1 + \frac{w_2}{\gamma_o}\right) \right\} \tag{5}$$

w_1 and w_2 are the weights of the distribution functions f_1 and f_2 with $w_1 + w_2 = 1$, m is the index of the loss-cone-type distribution, $\mu_{1/2} = m_o c^2/T_{1/2}$ with $T_{1/2}$ the electron temperatures, $\bar{p}$ the electron momentum in $m_o c$ units, ω_{po} the electron plasma frequency, $\Gamma_{ij} = \delta_{i3} \cdot \delta_{3j}$ and $\gamma_o = (1+p_o^2)^{1/2}$. The operator $\tilde{H}_{ij}$ is given in [5] and can be expressed by the Shkarofsky-functions $\tilde{F}_{q+1/2}(s)$ [7] which can be reduced to the plasma dispersion function by a recursion relation [8].

This relationship is used here to investigate numerically the dispersion relation for electro-magnetic waves with propagation oblique to the magnetic field. Results given here concern the quasiperpendicular case ($k_\parallel \approx 0$) and nearly resonant frequencies (A).

3) Numerical results

The dispersion relation $\mathrm{Det}|\Lambda_{ij}| = 0$ (6)

with $\Lambda_{ij} = n^2 \cdot (\bar{k}_i \cdot \bar{k}_j - \delta_{ij}) + \varepsilon_{ij}(\bar{k}, \omega)$ (7)

$$\left(\bar{k}_i = \frac{k_i}{|\bar{k}|}\right)$$

is solved numerically [6] in addition with the equation of polarization. Typical cases are shown in the following figures.

As shown in Fig. 1 the drift parallel to the magnetic field strongly influences the damping rate.

The longitudinal electrical field component enrceases with encreasing drift velocity for the ordinary wave (Fig. 2). There is a maximum damping at the normalized drift velocity $\bar{V}_{de} = 0.11$. The damping rate is also encreased with encreasing temperature anisotropy which has no influence on the polarization (Fig. 3).

Figure captions

Fig. 1: Damping rate $n_i = \mathrm{Im}(n)$ of the extraordinary wave versus the electron drift velocity $\bar{V}_{de} = V_{de}/c$ and angle of propagation θ.
(parameters: $\omega = \omega_{ce}$, $\omega_{pe}^2/\omega^2 = 0.8$, $Te_{\parallel} = Te_{\perp} = 1\,\mathrm{keV}$)

Fig. 2: Ordinary wave: Refraction index $n = (n_r, n_i)$ and polarization $|E_x|$, $|E_z|$ of the fundametal mode versus the electron drift velocity $\bar{V}_{de} = V_{de}/c$.
(parameters: $\omega = \omega_{ce}$, $T_{e_{\parallel}} = T_{e_{\perp}}$ 1 keV, $\theta = 89°$, $\omega_{pe}^2/\omega^2 = 0.8$)

Fig. 3: Ordinary wave: Refraction index $n = (n_r, n_i)$ and polarization $|E_x|$, $|E_z|$ of the fundamental mode versus the temperature anisotropy $\mu = T_{e_{\perp}} / T_{e_{\parallel}}$.
(parameter: $\omega = \omega_{ce}$, $\theta = 89°$, $\omega_{pe}^2/\omega^2 = 0.8$, $\bar{V}_{de} = 0$)

References:

[1] B.A. Trubnikow in Plasma Physics and the Problems of Controlled Thermonuclear Reactions, edited by M.A. Leontovich (Pergamon, New York, 1959), Vol. III, p. 122.
[2] I.P. Shkarofsky, Phys. Fluids 9, (1966) 561.
[3] M. Bornatici et al., Nucl. Fusion 23, (1983) 1153.
[4] S.T. Tsai et al., Phys. Fluids 24, (1981) 2186.
[5] A. Orefice, J. Plasma Physics 39, (1988) 61.
[6] F. Moser et al., Proc. 15th Europ. Conf. on Contr. Fus. and Plasma Heating, Dubrovnik, 1988, Vol. II, 870.
[7] A. Airoldi and A. Orefice, J. Plasma Physics 27, (1982) 515.
[8] A. Orefice, J. Plasma Physics 34, (1985) 319.

Fig. 1

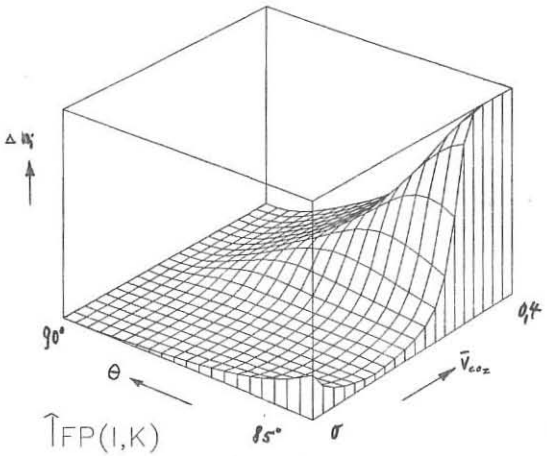

Fig. 2

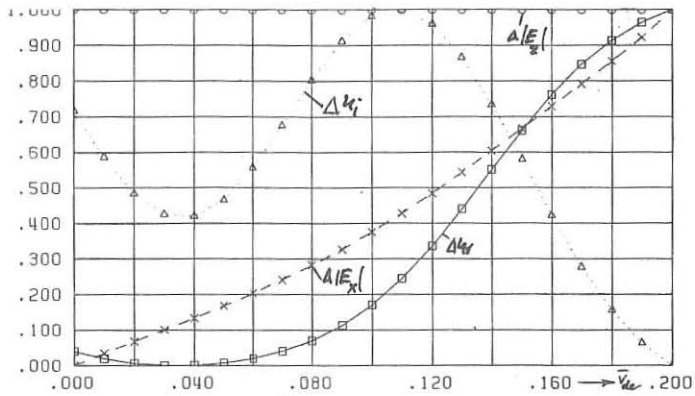

Fig. 3

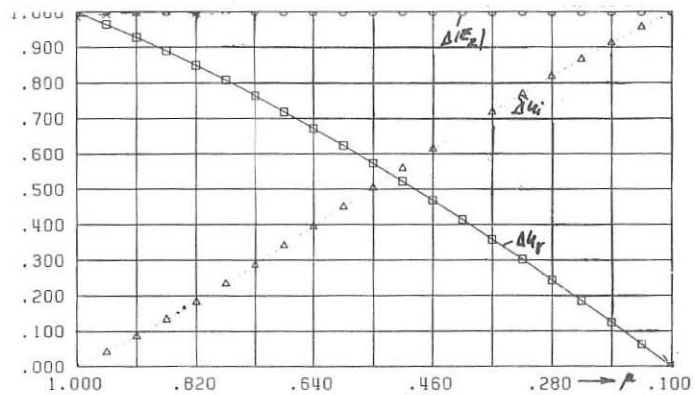

CALCULATION OF ENERGY DEPOSITION PROFILES AT ELECTRON-CYCLOTRON HEATING IN T-10 AND ITER

O.B.Smolyakova and E.V.Suvorov

Institute of Applied Physics, Academy of Sciences of the USSR
46 Uljanov Str., 603600 Gorky, USSR

At present ECRH is considered to be a reliable method of plasma heating up to fusion temperature. It is used as the main heating technique in the T-10 tokamak; large-scale ECRH experiments are also being planned on the D-IIID and T-15 installations, besides, EC waves are now discussed as the main candidates for plasma heating and current drive in the international tokamak reactor ITER. An advantage of the EC method of plasma heating in toroidal systems is the possibility to provide any desirable energy deposition profile (EDP) which, within the concept of "profile consistency" [1], may be used for initiating regimes with improved energy confinement.

In this paper results of theoretical calculations of EDP are presented for the experimental conditions in T-10 [2], as well as for plasma parameters typical of ITER. A low field side injection of a quasi-optical beam of ordinary waves at the fundamental is considered. A microwave beam is approximated by a discrete set of geometrical-optics rays with a gaussian distribution of R.F. power over the transverse aperture and a uniform angle divergence. The parameters chosen for R.F. beams (divergence $\pm 3^\circ$ with respect to both angular coordinates and the diameter of the cross-section of about 8 cm at the $1/e$ power level) correspond approximately to those of the launching system in T-10. The energy deposition in some region of the plasma column from the i-th ray is defined as

$$\Delta P = \int_{\Delta \ell_i} d\ell \, P_{oi} \exp(-\tau_i(\ell)) \frac{d\tau_i}{d\ell} \qquad (1)$$

where $\Delta \ell_i$ is the part of the ray trajectory in this region, P_{oi} is the initial power of the i-th ray and τ_i is the optical depth of the i-th ray from the injection point to the point with the ℓ-coordinate. Below, the energy deposition is assumed to be uniformly distributed over magnetic surfaces that are simulated as a set of concentric circles in the minor cross-section of the torus for T-10 and as a set of D-shaped curves with the elongation $b/a = 2$ and triangularity $\delta = 0.4$ for ITER (a set of model D-shaped magnetic surfaces used here is shown in Fig.1). The radial density and temper-

ature profiles are given in the form

$$n_e = n_0 \left(1 - \frac{r^2}{a^2}\right)^q \quad , \quad T_e = T_0 \left(1 - \frac{r^2}{a^2}\right)^p \qquad (2)$$

where the r -coordinate denotes the "number" of the magnetic surface and a is the effective minor radius of a plasma.

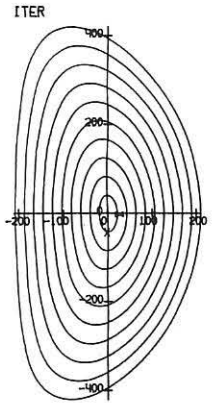

Fig.1

Only the toroidal component of the magnetic field is taken into account.

Ray tracing calculations use expressions for the refractive index of an ordinary wave in a cold plasma. The cyclotron absorption coefficient is calculated in a weakly relativistic approximation for the radiation with a linear polarization corresponding to the transverse propagation of an ordinary wave, nevertheless both the relativistic dependence of gyrofrequency and the Doppler shift are taken into account in the resonance condition

$$\frac{2\mathrm{Im}\,k}{k} = \frac{\sqrt{\pi}\,\omega_p^2}{\omega_H \omega} \cdot \frac{2}{15} S^3 \left(5x^2 + S^2\right) \exp\left(-z - 2x^2\right) \qquad (3)$$

where $z = \frac{2(\omega_H - \omega)}{\omega_H \beta_T^2}$, $x = \frac{2n_\parallel}{\beta_T} \frac{\omega}{\omega_H}$, $S = \sqrt{x^2 + z}$,

ω_H and ω_p are the cyclotron and the plasma frequencies, ω is the radiation frequency, $n_\parallel = ck_\parallel/\omega$ is the longitudinal (with respect to the magnetic field) refractive index, and $\beta_T = V_T/c$.

EDP in T-10 was calculated for the experimental conditions under which plasma heating was produced with three gyrotrons operating at the frequency corresponding to cyclotron resonance in the center of the plasma column. The best fitting for experimental n_e and T_e profiles is provided by eq.(2) with $n_0 = 6.3\ 10^{13}\mathrm{cm}^{-3}$, $T_0 = 1.04$ keV, $p = 3.5$, and $q = 3.0$. The calculated EDP for this case is shown in Fig.2(A). It is quite different from the experimental profile presented in Fig.2(B). Profiles more close to the real ones can be obtained assuming that the radiation pattern has side lobes. Figure 3 shows the EDP calculated

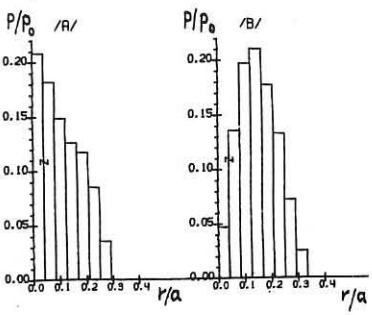

Fig.2

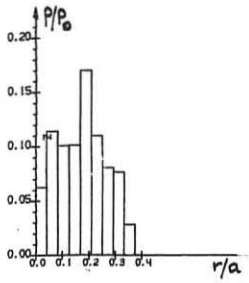

Fig.3

for the case when each gyrotron has, besides the major lobe, two side lobes spaced in the vertical plane $\pm 4^{\circ}$ apart from the central axis and having the beamwidth 3° and the energy content about 50 % of the total one.

Numerical simulation of ECH for ITER was performed for the regime with the electron temperature T_0 =15 keV in the center, the central density n_0 = =5 10^{13}cm^{-3} and the magnetic field intensity B =5 T at the plasma column axis. The major radius R was taken to be equal to 5.8 m and the minor one r = =2.1 m. The ray refraction is negligibly small for such parameters and the energy deposition of every R.F. beam is strictly localized. EDP are presented for the cases of equatorial launching at ω/ω_H =0.86 (Fig.4) and non-central launching at a height h =1 m from the equatorial plane at the fundamental (Fig.5).

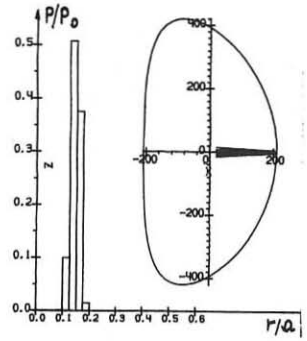

Fig.4

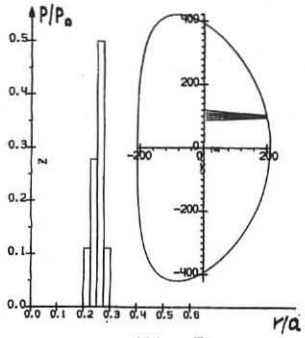

Fig.5

Figures 6 and 7 show combined EDP when a great number of gyrotrons is used for heating with a specified EDP shaping. Figure 6 presents a profile due to single-frequency heating with horizontal launching of radiation from 51 gyrotrons vertically spaced from each other by 20 cm; the corresponding number of units (beginning from the equatorial plane) is: 1,1,2,2,3,3,4,4,4,5,4,4,4,4,3,3. The EDP in Fig.7 corresponds to multifrequency heating with equatorial launching of radiation from all gyrotrons, their number being 0;2;3;5;2;7;7;11; 5;4;4;4; (54) at frequencies ω/ω_H =1;0.98;0.96;0.94;0.93; 0.92;0.90;0.88;0.86;0.85;0.84;0.82, respectively.

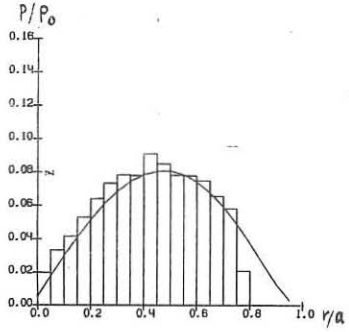

Fig.6

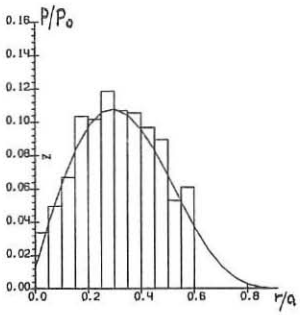

Fig.7

The integral profiles are assembled to be similar to those for ohmic heating for the temperature distribution (2) with $q = 1$ (Fig.6) and $q = 3$ (Fig.7).

References

1. V.V.Alikaev et al. Fizika Plazmy,1988, v.13, N 1,p.3-19.
2. V.V.Alikaev et al. Fizika Plazmy,1988, v.14, N 9,p.1027-1046.

ELECTRON CYCLOTRON HEATING STUDIES OF THE COMPACT IGNITION TOKAMAK(CIT)

M. Porkolab, P. T. Bonoli, R. Englade and R. Myer
PLASMA FUSION CENTER, MIT, Cambridge, MA 02139 USA
G. R. Smith, LLNL, Livermore, CA 94550 USA
A. H. Kritz, Hunter College, CUNY, New York, NY 10021 USA

I. Introduction

The Compact Ignition Tokamak (CIT) operating scenario calls for ramping the toroidal magnetic field from B_T = 7.0 (8.0) to 10.0 Tesla in a few seconds, followed by a burn cycle and a ramp-down cycle. Simultaneously, the plasma must be heated from an initial low beta equilibrium ($\bar{\beta} \simeq 0.44\%$ at 7.0 to 8.0 Tesla) to a final burn equilibrium ($\bar{\beta} = 2.8\%$) having 10.0 Tesla on the magnetic axis [1]. Since the toroidal plasma current will be ramped at the same time and since the available time for flat-top magnetic field must be reserved for the burn cycle, it is imperative that densification and heating be carried out as the magnetic field is ramped.

Here we examine an approach which is applicable to ECR heating. The frequency remains constant, while the angle of injection is varied by simply rotating a reflecting mirror placed in the path of the incident microwave beam. The rotating mirror permits one to launch waves with sufficiently high $N_\parallel$ so that the Doppler broadened resonance of particles on the magnetic axis with f = 280 GHz and B_T = 7.0 - 8.0 Tesla can provide adequate absorption [2]. As the resonance layer moves toward the magnetic axis the beam is swept toward perpendicular to reduce the Doppler width and avoid heating the plasma edge. At B_T = 10.0 Tesla the beam will be at normal incidence with strong absorption immediately on the high field side of the resonance (relativistic regime) [3]. We envisage using the ordinary mode (O-mode, $\vec{E}_{RF} \parallel \vec{B}$) of polarization which is accessible from the outside (low-field side) of the torus provided the density is such that $\omega_{pe} \leq \omega \approx \omega_{ce}$ (max). Considering f = 280 GHz for central heating at $B(0) = 10.0T$, the maximum cutoff density is at $n_{crit} \approx 9.7 \times 10^{20}\mathrm{m}^{-3}$ which is above the maximum central density in CIT. We note that recent advances in source technology (gyrotrons and FELs) make ECR heating of CIT at 280 GHz a viable option. Equilibration of temperature between electrons and ions (τ_{EQ}) is expected to be significantly shorter than typical energy confinement times, τ_E. For example, at $n_e \approx 2.0 \times 10^{20}\mathrm{m}^{-3}$, T_e = 5 keV, $Z_{eff} \approx 1.5$, we estimate $\tau_{EQ} \approx 30$ msec, while at $n_e(0) \approx 8 \times 10^{20}\mathrm{m}^{-3}, T_e \approx T_i \approx 20$ keV, $\tau_{EQ} \approx 60$ msec, both significantly shorter than the expected energy confinement time.

II. Ray Tracing Results

Here we study single pass absorption of waves in equilibria representative of the CIT plasma. In terms of a normalized poloidal flux ψ, the temperature and density profiles are taken to be $T_e(\psi) = T_e(0)[1-\psi]$ and $n_e(\psi) = n_e(0)[1-\psi]$. The ray tracing and absorption simulation was performed using the Toroidal Ray Tracing, Current Drive and Heating Code (TORCH) developed by Smith and Kritz[4]. We first present the results of ray tracing calculations for the nonresonant magnetic field of B(0) = 7.5T in the Doppler regime.

In Figures 1 (a,b) we show cases of wave penetration and absorption for B_T = 7.5 T, $\theta = 30°$, $T_e(0)$ =5, 10 keV and $n_e(0)$ = (2.2 and 1) $\times 10^{20}\mathrm{m}^{-3}$, respectively. The large dots shown in these figures represent the locations where the power in each ray decreases by 20%. We find 100% single pass absorption for $T_e(0) \geq 5.0$ keV, with absorption peaking at

r/a $\simeq$ 0.3 at $T_e(0) = 5.0$ keV, and r/a $\gtrsim$ 0.2 at $T_e \gtrsim$ 10 keV. Notice that the half width of the absorption layer is typically $\Delta r \simeq 10$ cm. We find that relativistic effects (which are included in this code) shift the absorption toward the cyclotron resonance layer by amounts $\Delta r \gtrsim 10$ cm.

Since the width of the particle resonance and the location of maximum absorption in the Doppler regime is directly proportional to $N_\parallel$, the power deposition profile can be controlled by changing the incident wave propagation angle. We find that for the 7.5 Tesla case, the optimum angle is approximately 30° to the normal. For $B_T = 7.0$ T, the absorption shifts far to the high field side of the plasma column, whereas for $B_T > 7.5$ T, the absorption shifts toward the low field side. In order to keep the absorption close to the magnetic axis as the beta and magnetic fields are increasing during the ramp-up, we find that the angle must be swept toward normal incidence at $B_T = 10.0$ Tesla. This ensures wave penetration to the center at full field and beta (relativistic regime, $N_\parallel < (T_e/m_e c^2)^{\frac{1}{2}}$) [3]. While strong off-axis absorption may be appropriate in a burning plasma for controlling MHD activity, in the low beta regime central heating may be preferable. Typical results of power deposition at $B_T = 10$ T, $\theta = 10°$, $T_e = 10$ keV are shown in Figure 1(c). As we see, central wave penetration and absorption occurs at $\theta \leq 10°$. For normal incidence ($\theta = 0$), complete wave absorption results in a few centimeter radial distance beyond the cyclotron resonance layer. This gives us confidence that these waves can penetrate to the core of even a burning plasma ($n_e(0) \gtrsim 8 \times 10^{20}\mathrm{m}^{-3}$, $T_e(0) \simeq 20$ keV), and be absorbed near the center.

The efficiency of coupling to the O-mode at the edge of the plasma as a function of the angle of incidence has been calculated, and the result is

$$\frac{P_O}{P_T} = \frac{1}{4}\left(1 + \frac{\sin^2\theta}{\eta}\right)^2 + \frac{\cos^2\theta}{\beta\eta^2}, \tag{1}$$

where $\beta = \omega_{ce}^2/\omega^2$ and $\eta = (\sin^4\theta + 4\cos^2\theta/\beta)^{\frac{1}{2}}$. For nonresonant heating ($B_T \geq 7$ T, $\theta \leq 30°$), Eq. 1 predicts that at least 68% of the power injected will couple to the O-mode at the edge.

We have also examined the importance of scattering of EC rays by low frequency density fluctuations [5], and find that for $< \delta n_e/n_e > \gtrsim 0.1$, scattering is not important.

III. Transport Code Simulations

A version of the combined equilibrium and transport code BALDUR1-1/2D originally developed by G. Bateman [6] has been used to simulate some important aspects of the ECH heating scenario for CIT. In our initial investigations, we have held constant the total plasma current, toroidal field, and parabolic particle density profile, and followed the time evolution of the electron and ion temperature distributions. We have assumed that the electron heat flux can be written as $q_e = -\mathrm{M}\kappa_e \nabla T_e - (\mathrm{M}-1)\alpha_T \kappa_e T_e \nabla \mathrm{V}/\mathrm{V}(a)$ (conduction and inward heat pinch), with $\kappa_e = [\mathrm{CI}(\rho)\mathrm{V}^2(\mathrm{a})\mathrm{A}^{-3/2}/T_e(\rho)|\nabla V|^2][1 + \gamma_0(1 - P_{OH}/P_{TOT})^2 < \beta_p >]$ [7, 8]. Here ρ is a flux surface label, I_ρ is the current within ρ, A is the total cross-sectional area, $\mathrm{V} = \mathrm{V}(\rho)$ is the volume within ρ, $\rho = \mathrm{a}$ designates the plasma boundary, and α_T describes a "canonical" profile shape $T_e \propto \exp(-\alpha_T \mathrm{V}/\mathrm{V}(a))$ which the transport model seeks to enforce. The constant C is chosen to fit low density Ohmic experiments, and $\gamma_0 \simeq 5(10)$ reproduces H-(L-) mode experimental results with auxiliary heating. We have taken $\alpha_T = 3.33$ and $\mathrm{M} = 3$. Ion thermal transport is assumed to be 0.5 times that of the electrons in addition to a neoclassical contribution. ECH absorption per unit volume by electrons is represented by the form $\mathrm{P}(\rho) = \mathrm{P}_0 \exp[-(x - x_0)^2/225]$, where $x(\rho)$ is the half-width in cm of a flux surface in the

meridian plane, x_0 designates the location of maximum absorption, and P_0 is proportional to the total power launched in the O-mode.

In Figure 2(a) we show the time development of the central temperatures when 10 MW of ECH is input for 3 seconds into an ohmic target plasma with B_T = 7.5 T, I_p = 8 MA, Z_{eff} = 1.5, and $n_e(0) = 2.2 \times 10^{20}\mathrm{m}^{-3}$. In agreement with ray tracing results, maximum absorption is taken one third of the way out from the magnetic axis. Here we have assumed H-mode (auxiliary) confinement and no sawteeth. Figure 2(b) illustrates the same case with a sawtooth repetition time of 0.3 sec. The plasma does not ignite because of the low density used in the simulations. For L-mode confinement and no sawteeth, T_e and T_i saturate at 14 keV and 12 keV, respectively. Shifting the location of maximum absorption to the magnetic axis results in a 40% enhancement of central electron temperatures, but the ion temperatures remain similar for the above cases. Neglecting the inward pinch term in the heat transport model ($M \rightarrow 1$) has little effect for the off-axis cases, but enhances electron and ion temperatures by 100% and 50% respectively for on-axis heating.

We have also investigated the behavior of a high density ($n_e(0) = 6.6 \times 10^{20}\mathrm{m}^{-3}$) CIT plasma with B_T = 10 T, I_p = 10 MA, and Z_{eff} = 1.5 when ECH absorption peaks at the magnetic axis. For the case of 10 MW input power, H-mode confinement, 1.5 sec. pulse length, and no sawteeth (Figure 3(a)), ignition occurs with $< \beta > = 1.3\%$ and τ_E = 0.9 sec. Sawteeth with a 0.3 sec. repetition time prevent ignition at the 10 MW power level, but not at 17 MW. Lowering the power to 5 MW, ignition conditions are again achieved after a 3 sec. RF pulse length with H-mode confinement and no sawteeth (Figure 3(b)). Finally, using L-mode confinement, ignition is obtained with 17 MW of input power applied for 3 sec. (τ_E = 0.6 sec., $< \beta > = 2.2\%$). For a flatter density profile ($n(\psi)/n(0) \simeq (1-\psi)^{1/2}$), $n(0) = 6.6 \times 10^{20}\mathrm{m}^{-3}$, and L-mode confinement, $P_{RF} \approx 25$ MW is required for ignition within 3 sec. at $< \beta > = 2.8\%$, and τ_E = 0.6 sec. We note that under the above conditions $\tau_{Kaye} \leq 0.44$ sec., $\tau_{Goldston} \leq 0.27$ sec., and ignition would not occur.

Figure Captions

Fig. 1. ECH ray trajectories. Each dot represents 20% power absorption. a) B_T = 7.5 T, θ =30°, T_e = 5 keV; b) B_T = 7.5 T, θ = 30°, T_e = 10 keV; c) B_T = 10 T, θ =10°, T_e = 10 keV.

Fig. 2. CIT discharge evolution for $n_e(0) = 2.2 \times 10^{20}\mathrm{m}^{-3}$. P_{RF} = 10 MW, deposited at r_0/a = 0.3, Δt_{RF} = 3 sec., H-mode confinement a) without sawteeth; b) with sawteeth, τ_{saw} = 0.3 sec.

Fig. 3. CIT discharge evolution for $n_e(0) = 6.6 \times 10^{20}\mathrm{m}^{-3}$, on-axis deposition, H-mode confinement, no sawteeth; a) P_{RF} = 10 MW, Δt_{RF} = 1.5 sec.; b) P_{RF} = 5 MW, Δt_{RF} = 3 sec.

References

[1] R. Parker, et al., paper IAEA-CN-50/J-I-1, presented at the 12th Int. Conf. on Plasma Physics and Contr. Nuclear Fusion Research, Nice, France, October 12-19, 1988.

[2] R. Myer, M. Porkolab, G. R. Smith, A. H. Kritz, MIT PFC/JA-89-2 (1989).

[3] M. Bornatici, R. Cano, O. DeBarbieri, and F. Engelmann, Nuclear Fusion **23**, (1983) 1153.

[4] G. R. Smith, W. Nevins, R. Cohen, A. Kritz, Bull. Am. Phys. Soc. **31**, (1986) 1516.

[5] E. Ott, B. Hui, K. R. Chu, Phys. Fluids, **23**, (1980) 1031.

[6] G. Bateman, Spring College on Plasma Physics, Trieste, Italy (1985).

[7] B. Coppi, Fizica Plazmy **11**, (1985) 83. Also: MIT Report PTP-85-16 (1985).

[8] R. Englade, MIT Report PTP-87-12 (1987).

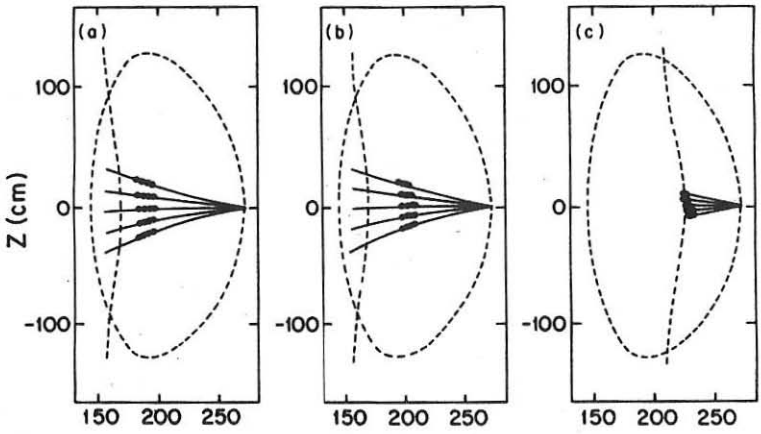

Fig. 1

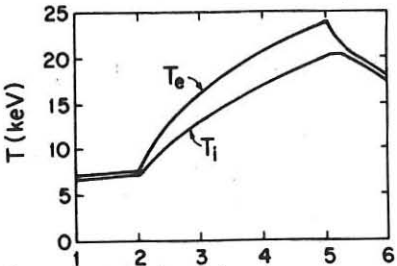

Fig. 2(a)

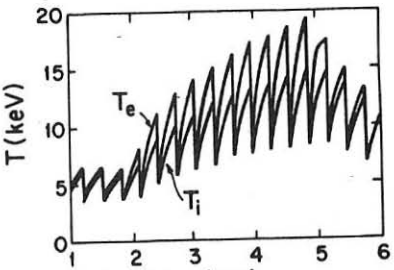

Fig. 2(b)

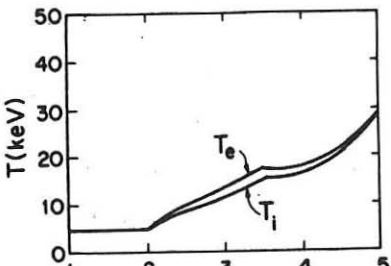

Fig. 3(a)

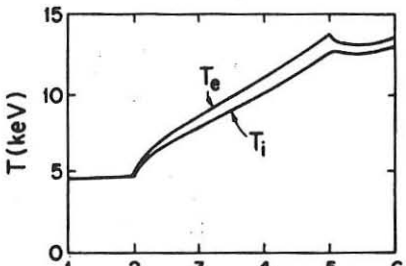

Fig. 3(b)

NONLINEAR INTERACTION OF INTENSE ELECTRON CYCLOTRON WAVE PULSES WITH A PLASMA

Roberto Pozzoli* **and Dario Ronzio**

Dipartimento di Fisica, Università di Milano, Milano, Italy

* also *Istituto di Fisica del Plasma C.N.R., Milano, Italy*

Abstract

Starting from the Hamiltonian formulation of the motion equation, the conditions for effective electron interaction in a single crossing of the radiation beam are determined, for the ordinary mode in perpendicular propagation. The electron energy gain is estimated, and the deformation of the electron distribution is computed under adiabaticity conditions.

Non linear interaction regimes are foreseen to occur in *ECRH* experiments, like *MTX*, where intense microwave pulses are used. An analysis of the relevant power absorption mechanism and the computation of the resulting strong deformation of the electron distribution function have been performed in Refs.1,2 . An extensive analytical treatment for the case of perpendicular energy gain larger than the thermal energy is given in Ref.3 . Here we consider the motion equation, determine the condition for energy exchange between the electrons and the electromagnetic field, and estimate the modification induced on the electron distribution. The analysis is limited to the ordinary mode near the fundamental frequency, in perpendicular propagation.

We refer to a pulse with a $g(z)$ profile ($0 \leq g(z) \leq 1$) along the magnetic field $\vec{B}_o = B_o \hat{e}_x : \vec{E} = \hat{e}_x E_o g sin(ky - \omega t)$. A relevant time independent Hamiltonian is

$$h(\vartheta, J; z, P_x) = \gamma_o (1+2J)^{\frac{1}{2}} \left(1 - \frac{agP_x}{\gamma_o} \frac{\sqrt{J/2}}{1+2J} \cos\vartheta \right) - \gamma_o^2 \nu J \qquad (1)$$

where h is normalized to mc^2, momenta to mc, length to c/Ω (being $\Omega = eB_o/mc$), $\nu = \omega/\Omega$, $\gamma_o^2 = 1 + P_x^2$, $a = NE_o/B_o$, with $N = ck/\omega$, $J = \left((y - P_z)^2 + P_y^2\right)/2\gamma_o^2$, with P_x constant of motion, $\vartheta = \arctan\left((y - P_z)/P_y\right) + \nu(NP_x - t)$, with t normalized on Ω^{-1}.

In initial and final conditions, when the particle enters or leaves the radiation beam, $g = 0$ and the unperturbed h becomes $h = \gamma_o (1+2J)^{\frac{1}{2}} - \gamma_o^2 \nu J$.

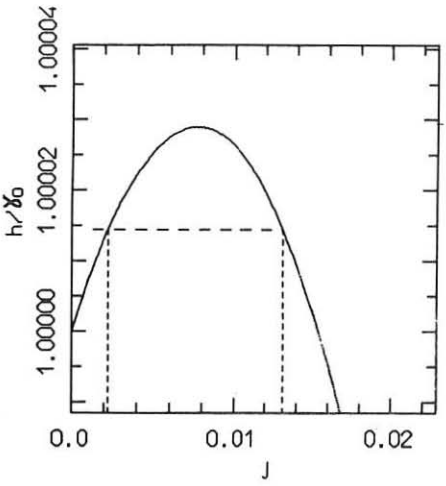

Fig. 1 Unperturbed Hamiltonian h vs J for a fixed $\gamma_o = 1.0024$. The dotted line shows two different J values pertaining to the same h.

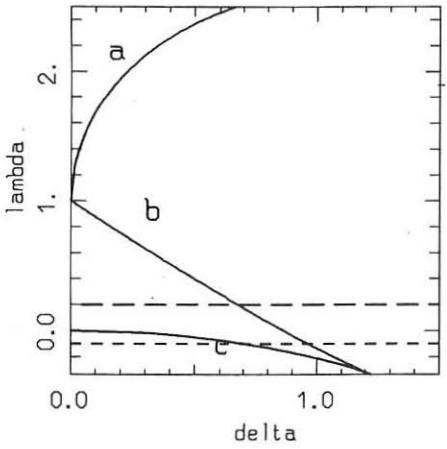

Fig. 2 Location of the critical points in the (ϑ, λ) plane. Curve a corresponds to the elliptic point in $\vartheta = \pi$, curve b to the hyperbolic point in $\vartheta = 0$, curve c to the elliptic point in $\vartheta = 0$. The motion is characterized by constant λ (dotted lines).

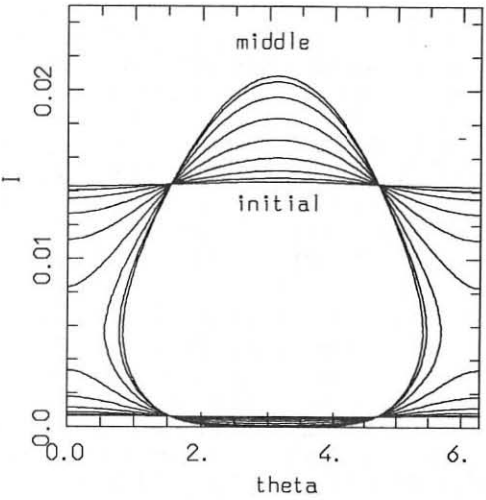

Fig. 3 Motion trajectories in the (ϑ, J) plane for a case with $0 \leq \lambda \leq 1$, at different z , from the initial z value, corresponding to $g = 0$, to the z value in the centre of the beam, corresponding to $g = 1$. The parameter δ_{max} is larger than δ_c.

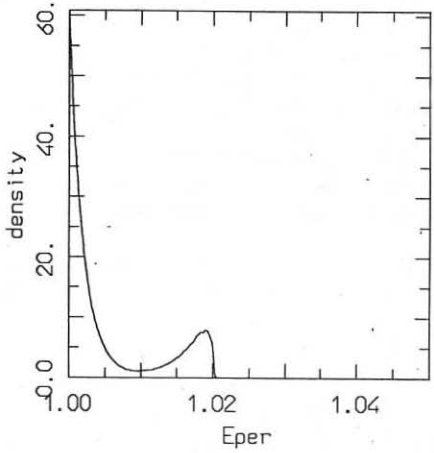

Fig. 4 Rappresentation of the electron distribution function versus the perpendicular γ at constant P_z after the interaction with the radiation beam. The initial distribution is assumed Maxwellian.

The plot of the unperturbed h vs J for fixed γ_o is shown in Fig.1. Assuming that γ_o remains almost constant during the motion, due to the smallness of a and of dg/dz, the interaction process can lead to a variation of the particle energy only when different J values correspond to the same h. Putting $b = \nu\gamma_o$ and $d = h\nu$, this gives the parameter range of interest $b \leq 1$ and $J \leq 2(1-b)/b^2$, with the corresponding d in the range $b \leq d \leq (1+b^2)/2$. When an effective interaction occurs the variation of J is given by $\Delta J = \pm 2\sqrt{1-2d+b^2}/b^2$, with the two signs corresponding to an initial J smaller or larger than $(1-d)/b^2$. The actual occurrence of such variation strictly depends on a, which gives a necessary conditions for it, and on the motion adiabaticity. This dependence can be investigated looking at the critical points of the (ϑ, J) trajectories, as follows.

Introducing the parameters $\delta = \frac{agP_z}{\sqrt{2}\gamma_o(1-b)}$ and $\lambda = \frac{2(d-b)}{(1-b)^2}$, the location of the critical points in the (δ, λ) plane is shown in Fig.2 . For constant λ, the increase of δ from zero to δ_{max} corresponds to the particle motion across the beam to the point of maximum r.f. field; the decrease of δ back to zero corresponds to the subsequent particle motion from the centre of the beam to the outside.

Let us consider the case $0 \leq \lambda \leq 1$, which corresponds to the mentioned conditions where two values of J pertain to the same h. If $\delta_{max} \leq \delta_c$ (with δ_c corresponding to the hyperbolic critical point in $\vartheta = 0$), then the initially open orbits of the (ϑ, J) motion remain always open, since a connection between them is not allowed, and $\Delta J = 0$. If $\delta_{max} \geq \delta_c$, the initially open orbit becomes closed, when $\delta \geq \delta_c$, and, as δ is decreased, can merge in the open orbit with the J value different from the initial. In this case $\Delta J \neq 0$. When $\lambda \leq 0$, for a given h only one value of J is initially possible; the elliptic point and the subsequent hyperbolic point can be reached if δ_{max} is larger enough, but ΔJ should be zero.

The motion trajectories in the (ϑ, J) plane for the cases $0 \leq \lambda \leq 1$ are shown in Fig.3 at different z values corresponding to g from zero to one. The chosen δ_{max} allows the crossing of the critical point.

The deformation of the electron distribution can be easily investigated under the adiabaticity condition. For this case, when $0 \leq \lambda \leq 1$ and $\delta_{max} \geq \delta_c$, and the initial distribution is a Maxwellian in J, the final electron distribution function, for a fixed P_z, is shown if Fig.4 .

In conclusion we have determined the condition of effective interaction $\delta_{max} \geq \delta_c$, the possible value of ΔJ, and the deformation of the electron distribution under adiabatic conditions.

References:

1. W.M.Nevins, T.D.Rognlien and B.I.Cohen *Phys.Rev.Lett.* **59**, 60 (1987)
2. B.I.Cohen, R.H.Cohen, W.M.Nevins, T.D.Rognlien, P.T.Bonoli and M.Porkolab *Proc. "Theory of Fusion Plasmas"*, Lausanne 1988, *in press*
3. I.A.Kotelnikov and G.V.Stupakov, *to be published*

ELECTRON CYCLOTRON RESONANCE HEATING AND CURRENT DRIVE AT LARGE $N_{||}$ IN TOKAMAKS

A G Miller

University of St Andrews
North Haugh, St Andrews, Fife KY16 9SS, Scotland

1. Introduction

Electron Cyclotron Resonance Heating of fusion plasmas has received much attention over recent years. With the advent of high power high frequency power sources such as the gyrotron and more recently the free electron laser there has been a growing interest in nonlinear heating. The nth harmonic resonance condition is $\omega - k_{||}V_{||} - n\Omega/\gamma = 0$, where γ is the relativistic energy in units of mc^2. Increases in γ usually cause electrons to go out of resonance and prevent efficient heating. Any heating scheme in which γ changes but the resonance condition continues to be satisfied owing to changes in other quantities is called autoresonance: various methods have been studied for years. Golovanivsky[1] has studied magnetic means, viz adiabatically increasing the magnetic field and hence Ω while Nevins et al[2] have experimented with increases in $N_{||}$ and have also looked at trapping in phase space. It has been shown that Cyclotron Resonance Masers (CRMs) can have particularly good emission efficiencies by achieving doppler shifted autoresonance for beams with $N_{||} = 1$[4] (the so-called Carm effect). The inverse i.e. absorption can be used in heating plasmas, an effect which was first studied in the context of solar physics by Davydovskii[3]. However there are a number of problems in achieving this for a tokamak geometry as such a scheme could work only at the first harmonic with right handed circularly polarized (RHCP) waves propagating close to parallel to the background magnetic field. In section 2 a condition for autoresonance to take place is derived. In section 3 the ordinary linear theory proposed by O'Brien is modified, and it is shown that the modified theory gives rise to non-diffusive heating. Section 4 gives a comparison of this theory with numerical experiment, and section 5 discusses feasibility of the idea.

2. The Auto Resonance Condition

From gyro-averaged equations (ref 5) at the first harmonic the phase of the particle with respect to the wave, φ, obeys

$$d\varphi/dt = \omega - k_{||}V_{||} - \Omega/\gamma + e/2m\, E_{eff}\sin(\varphi)/U_p$$
$$= 0 \text{ for autoresonance.}$$

A number of disturbing influences can upset autoresonance, and are treated here as small perturbations:

To leading order in 1/G, 1/R,F, near $N_{||} = 1$

$$d\varphi/dt = F\omega + \Omega_o z/\gamma G - k_{\parallel o} V_{po}{}^2 \Omega_o z/(2\gamma\Omega G V_\parallel) + e/2mE_{eff}\sin(\varphi)/U_p - 2\delta(N_\parallel)U_\parallel\omega/c + k_{\parallel o}V_\parallel z(z_o - z/2)/R^2 \quad (1)$$

where

R is the tokamak major radius
G is a linear gradient scale in Ω such that $|\Omega| = |\Omega_o|(1+z/G)$ (assuming that $|B| = |B_o|(1+x/R)$ and dx/dz = constant where x is the distance into the tokamak)
$F = (\omega - K_\parallel V_\parallel - \Omega/\gamma)/\omega$ is a measure of the frequency mismatch,
E_{eff} is the effective electric field, $E(1-k_\parallel V_\parallel/\omega)$,
$\delta(N_\parallel) = 1 + N_\parallel - F$
Z is the distance along the path of the particle and
Z_o is the centre of the beam.

For large tokamaks the effect of the toroidal geometry will be small and so the last term in (1) is ignored. The effect of ignoring this term is demonstrated in section 4.

For good heating the electron must have $\cos(\varphi) < 0$ throughout heating i.e. $|d\varphi/dt|_t \leq \pi/2$.

This will require an extremely small frequency mismatch $-|F| \ll 1$.

3. Heating and Diffusion

In the model used here the approach of refs (5) and (6) is followed.

$$\Delta\mu = U_p|K|\cos(\vartheta)/2 + |K|^2/8 \quad \text{where} \quad \mu = U_p{}^2/2 \text{ ref(5)} \quad (2)$$

$$K = \int (eE_{eff}(0)/m)/V_\parallel \exp(i\int^t(-\Omega/\gamma - k_\parallel V_\parallel + \omega)dt' - z^2/L^2 - \alpha z)dz$$

for a Gaussian beam of form $E_{eff}(0)\exp(-z^2/L^2 - \alpha z)$. α the free damping parameter, and L the effective Guassian width, depend on the angle of propagation into the plasma.

The linear theory is suited very well to autoresonance because of the constancy of phase. $\int^t(-\Omega/\gamma - K_\parallel V_\parallel + \omega)dt'$ can be replaced by $(F\omega + \Omega_o z/2\gamma G - 2\delta(N_\parallel)U_\parallel\omega/c)z/V_\parallel$ and the integral reduces to

$$|K| = \sqrt{(\pi/W)}/V_\parallel \exp(-(F\omega + \Omega_o z/2\gamma G - 2\delta(N_\parallel)U_\parallel\omega/c)z/V_\parallel) \text{ where}$$

$W^2 = 1/L^4 + (\Omega_t/2V_\parallel)^2$ and

$\Omega_t = \Omega_o(1 + F\omega V_p{}^2\Omega_o/(V_\parallel{}^2\gamma\Omega^2 G))/G$.

Unfortunately, if the condition

$$|\Delta V_\parallel/V_\parallel| = |\gamma k_\parallel (eE_{eff}L)^2/(8V_{\parallel o}{}^3 m^2\Omega)| \ll 1 \quad (3)$$

is not satisfied we can no longer assume $V_\parallel$ is constant over the transit of the beam because at large $N_\parallel$ ECRH increases $V_\parallel$ as well as V_p.

Hence $V_\parallel$ must be replaced by the averaged value

$$V_\parallel = V_{\parallel o} + 1/3\ \Delta V_\parallel$$

as a first approximation. This is good if $dE_{eff}/dz = 0$ (i.e. square beam) and the changes in $V_\parallel$ are mainly due to heating rather than magnetic effects, but it can also be used as a crude approximation for some Gaussian beams. The change in $V_\parallel$ owing to ECRH means that the heating is no longer

diffusive.

4. Comparisons with Numerical Experiment

Comparisons have been made of the above theory with the so-called SPEECH codes developed by A W Taylor[5]. The code uses gyro-averaged equations for particle motion to evaluate heating. A comparison between theory and numerical experiment is given in Table 1. The plasma has been assumed isotropic so that $N_{||} \times R_{beam}$ = constant where R_{beam} = distance of beam from centre of tokamak - the geometric optics approximation. $K_{||}$ changes through a change in R_{beam} during interaction with the electron. This change is non-negligible even in large devices and causes deterioration in heating only when the power input is high.
The columns represent:

(a) theory without change in $k_{||}$, or change in $U_{||}$,

(b) theory without change in $k_{||}$ but with change in $U_{||}$,

(c) numerical results without change in $k_{||}$,

(d) numerical results with change in $k_{||}$.

Illustrative tokamak and particle parameters were used in the calculations. The quantities recorded are $\langle\mu\rangle_{final}/\mu_{initial}$ where the average is taken over initial phase. The results show that even in the limit of very high heating the modified theory is very accurate.

Table 1

E_{eff} Vm^{-1}	(a)	(b)	(c)	(d)
$3*10^2$	7.0	5.3	5.4	5.2
10	78	20	20	19
$3*10^3$	700	50	50	44

5. Accessibility

The proposed heating scheme uses RHCP waves and heats at the first harmonic. Inside launch is unable to provide $N_{||} \approx 1$ and outside launch access is impossible because the low density cut-off occurs before the cyclotron resonance. The preferred heating scheme involves heating highly doppler-shifted particles outside the low-field cutoff. In this case $|\Delta V_{||}/V_{||}| << 1$, heating is diffusive and ordinary linear theory is accurate.

6. Conclusion

ECRH can be used to drive small numbers of particles to high energies using doppler-shifted autoresonance, by heating highly doppler-shifted particles outside the low-field cutoff. Current drive calculations using this scheme are being considered.

7. Acknowledgements

I would like to acknowledge the financial assistance of an SERC CASE studentship with the UKAEA Culham Laboratory and guidance of my supervisors Dr R A Cairns and Dr C N Lashmore-Davies. I would also like to thank Mr M R O'Brien of Culham Laboratory for helpful suggestions and for his help in running the SPEECH codes, and last but not least, Dr A W Taylor for his permission to use and modify the SPEECH codes.

References

1. K S Golovanivsky, Soviet J.P.P. 11 171 (1985).
2. W M Nevins, T D Rognlien and B I Cohen, Phys. Rev. Lett. 59 60 (1987).
3. A T Lin, Int. J. Electronics 57 1097 (1984).
4. V Ya Davydovskii, Sov. Phys. JETP 16 629 (1963).
5. A W Taylor, R A Cairns and M R O'Brien, Plasma Physics and Controlled Fusion 30 1039 (1988).
6. M R O'Brien, M Cox and D F H Start, Nucl. Fus. 26 1625 (1986).

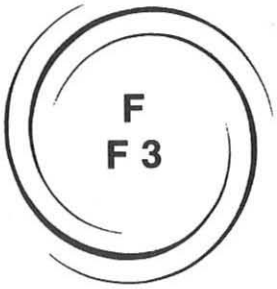

PLASMA HEATING AND CURRENT DRIVE

LOWER HYBRID HEATING (LHH)

VARIATIONAL DESCRIPTION OF LOWER HYBRID WAVE PROPAGATION AND ABSORPTION IN TOKAMAKS

D. Moreau, Y. Peysson, J.M. Rax, A. Samain, J.C. Dumas*

Association EURATOM-CEA sur la Fusion Contrôlée
Centre d'Etudes Nucléaires de Cadarache
13108 Saint-Paul-lez-Durance Cedex, France
*CISI Ingénierie, C.E.N. Cadarache, 13108 Saint-Paul-lez-Durance Cedex, France

ABSTRACT :

A variational approach to a global solution of the lower-hybrid wave propagation and absorption in tokamaks is presented. It is based on the use of trial functions which are locally solutions of the homogeneous problem ("eikonal trial functions"). Preliminary results in circular cylindrical geometry are reported, showing the radial power deposition profiles for various toroidal wavenumbers excited by the r.f. source.

1- INTRODUCTION

Variational techniques provide an efficient scheme to describe both propagation and absorption of electromagnetic waves in tokamak plasmas. Such a scheme has been successfully implemented for the ion cyclotron frequency range but, due to the large number of degrees of freedom of the wave field, an extension to higher frequencies seems prohibitive.

This paper describes a method for attempting a full wave description of r.f. fields in the lower hybrid frequency range, in order to study current generation and profile control via Landau absorption. The basic idea is to use eikonal trial functions which locally satisfy the cold dispersion relation. This allows to use a mesh larger than the wavelength and reduces the number of unknowns.

2-VARIATIONAL PRINCIPLE AND TRIAL FUNCTIONS

Since mode conversion between the cold propagation branches occurs commonly in lower hybrid current drive experiments, it is important to start with a full wave equation which describes both the electron plasma wave and the whistler wave, ie from a vectorial wave equation which takes into account the electromagnetic and the electrostatic components of the fields. As opposed to the magnetosonic case, this leads us to use the three components of the electric field as our variables rather than to perform a reduced description in terms of two components of the vector potential.

Maxwell's equations are equivalent to finding the extremum of the following form :

$$L(\mathbf{E},\mathbf{E}^*) = \int dr[(\nabla\times\mathbf{E}(r)).(\nabla\times\mathbf{E}^*(r)) - \frac{\omega^2}{c^2}\mathbf{E}^*(r).\mathbf{K}(r).\mathbf{E}(r) - \frac{4i\pi\omega}{c^2}\mathbf{E}^*(r).\mathbf{J}_a(r)] \qquad (1)$$

for all variations $\delta\mathbf{E}^*(\mathbf{r})$ subject to the condition $n\times\delta\mathbf{E}^*(r) = \mathbf{0}$ on the metallic boundary.

Because of the small wavelengths involved in the problem, performing a discretization of the variational form on a scale length which is smaller than the wavelength would require a prohibitive processing time. As a consequence we must use trial functions which can approximate the solution over several wavelengths. In practice we divide the plasma in a number of radial cells whose width is a given fraction η of the inhomogeneity scale length, ie such that

$$\eta = \text{Max}\,(\frac{\Delta n_e}{n_e}, \frac{\Delta r}{r}) \quad . \qquad (2)$$

The simplest functions which can approximate both the analytic behaviour of the fields near the singularity at r = 0 ("whispering gallery" effect), and the propagative nature of the wave away from the magnetic axis, are of the form r^λ where $\lambda = \alpha + i\,\beta$. λ is a complex number which can take four values λ_i (i=1,4) to be determined from the local wave equation.

In each cell the λ_i's (i=1,4) are the eigenvalues associated with a 4x4 matrix and they physically correspond to the slow and fast waves propagating both inward and outward. Associated with each of these four values, there is a polarization vector for the electric field $\mathbf{E}_i$ and the trial function in a particular radial cell can be written:

$$\mathbf{E}(r,t) = \sum_{i=1}^{4} \alpha_i\, \mathbf{E}_i\, r^{\lambda_i}\, \exp(\,i\,n\,\phi + i\,m\,\theta - i\,\omega\,t\,) \qquad (3)$$

where r, θ, $\phi = z/R_0$ are the cylindrical coordinates, R_0 being the major radius of the torus, n and m are toroidal and poloidal wavenumbers respectively, and ω is the pulsation of the r.f. field. In this paper we restrict ourselves to the cylindrical approximation of the tokamak so that n and m are integers which can be specified together with the frequency of the r.f. source.

3-PRINCIPAL BOUNDARY CONDITIONS AND LAGRANGE MULTIPLIERS

Having chosen the trial functions described above, the variational form (1) has a matrix representation :

$$L(\mathbf{E},\mathbf{E}^*) = \mathbf{X}^+.\mathbf{A}.\mathbf{X} - \mathbf{X}^+.\mathbf{S} \qquad (4)$$

where $\mathbf{X}$ is the vector whose components are the α_i's (eq.2). $\mathbf{A}$ is a square matrix of dimension 4N - 2, N being the total number of cells, (in the central cell two unphysical solutions for λ_i must be eliminated).

Our choice for the trial functions entails that A is diagonal by blocks of dimension 4x4, as cells are completely decoupled. Therefore, for the problem to be well-posed, it is obvious that some continuity constraints have to be imposed to supplement the extremum principle.

In fact it can be shown that, imposing the continuity of the tangential components of the electric field at the border of each cell is both necessary and sufficient for the uniqueness of the solution, provided that there is some dissipation (even infinitesimal) at every point in the volume considered. Such boundary conditions are usually called principal boundary conditions as opposed to the natural boundary conditions (continuity of $\nabla \times \mathbf{E}$) which are automatically satisfied when the variational form is extremum [1].

The constraints inherent to the principal boundary conditions can be written :

$$\mathbf{B} \,.\, \mathbf{X} = 0 \tag{5}$$

with our notations, where **B** is a large rectangular matrix. We therefore introduce a set of Lagrange multipliers, the vector Λ, and look for a vector **X** which, for a particular choice of Λ, satisfies simultaneously

$$\mathbf{B} \,.\, \mathbf{X} = 0 \tag{6}$$

and

$$\delta \mathbf{X}^{+} \,.\, (\mathbf{A} \,.\, \mathbf{X} \; - \; \mathbf{S} \; + \; \mathbf{B}^{+} \,.\, \Lambda) \; = \; 0 \tag{7}$$

with no restriction on the variation $\delta \mathbf{X}^{+}$.

If uniqueness is assessed (absorption at every point), it can be shown that **A** is regular and that $\mathbf{B} \,.\, \mathbf{A}^{-1} \,.\, \mathbf{B}^{+}$) is also regular. Then it is straightforward to write the solution as :

$$\mathbf{X} \; = \; \mathbf{A}^{-1} \,.\, [\, \mathbf{S} \; - \; \mathbf{B}^{+} \,.\, (\, \mathbf{B} \,.\, \mathbf{A}^{-1} \,.\, \mathbf{B}^{+} \,)^{-1} \,.\, (\, \mathbf{B} \,.\, \mathbf{A}^{-1} \,.\, \mathbf{S} \,)] \; . \tag{8}$$

4-POWER DEPOSITION PROFILES IN CYLINDRICAL GEOMETRY

As first results, we present some radial deposition profiles which were obtained assuming parabolic dependences for the ion and electron densities $n_i(r)$, $n_e(r)$, the electron temperature $T_e(r)$, and the safety factor $q(r)$. Both the collisional absorption and the resonant Landau damping of the waves are taken into account by including the corresponding anti-hermitian component into the local dielectric tensor. In these calculations the plasma parameters on axis are $n_e(0) = 5 \times 10^{19}$ m^{-3}, $T_e(0) = 5$ keV, $q(0) = 1$, and at the edge $q(a) = 3$. The toroidal magnetic intensity is 3.4 T, the frequency 3.7 GHz and the major and minor radii of the tokamak, $R_0 = 3$ m and $a = 1$ m respectively. The poloidal mode number was fixed at $m = 10$. Various toroidal mode numbers ranging from $n = 450$ to $n = 850$ have been selected thus showing the influence of the parallel wavenumber on the power deposition (fig. 1). In addition, we have considered two distinct values of the discretization parameter, $\eta = 0.1$ and $\eta = 0.05$, corresponding to 86 and 171 radial cells respectively (figs. 2, 3 and 4). In both cases, the central cell has a fixed radius of 1 mm and the outer one which extends itself from the antenna layer ($r = 0.96$ m) to the edge is also fixed.

In cases of weak absorption (n = 450) the Bessel-like structure of the wave appears clearly near the centre (fig.5). The discontinuous character of the density profile shows up by giving rise to local resonances (figs.3 and 4) in some particular cells whose width matches the wavelength of the field. These resonances have a precise physical origin and therefore it seems possible to avoid them by going to a finer mesh when the damping is too weak. The stability of this variational scheme requires further investigation and will be reported later.

REFERENCES

[1]- G.I.Marchuk, 'Methods of numerical mathematics', Springer-Verlag (Berlin,1978)

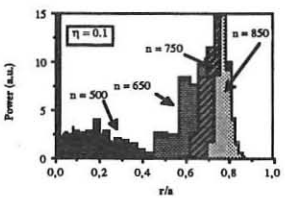

figure 1

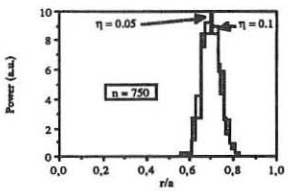

figure 2

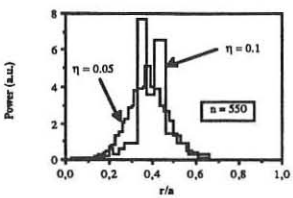

figure 3

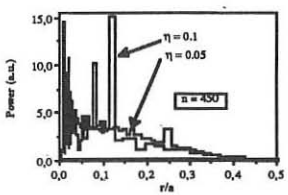

figure 4

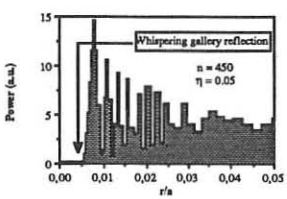

figure 5

ABSORPTION OF LH WAVES BY FUSION-GENERATED α-PARTICLES

E. Barbato, F. Santini

Associazione EURATOM-ENEA sulla Fusione, C. R. E. Frascati,
C.P. 65 - 00044 - Frascati, Rome, Italy

INTRODUCTION

The α-particle population in an ignited plasma could deteriorate the current drive efficiency of lower hybrid (LH) waves in a steady state reactor. In fact, due to the high energy production, α-particles may interact with the LH waves and reduce the absorption by electrons. This effect is absent if the frequency is high enough (10 GHz for ITER like parameters). Nevertheless, the technical difficulties of using such a high frequency necessitate investigating whether the absorption by α-particles may be negligible for ITER parameters at relatively lower frequencies also. This problem has been examined [1] by using only linear Landau damping. Since the quasilinear diffusion can exceed the collisional drag, the complete equation for the α-distribution function (df) has been studied and is reported in this paper. The consequent wave absorption by α's is supplemented in a 1-D deposition code which includes wave propagation and absorption [2].

THE ABSORPTION MODEL

In order to investigate the wave absorption by α-particles, we first look for the df f_α as a solution of the steady state Fokker-Planck equation supplemented by the quasilinear diffusion term. In the absence of the latter, the solution is known to be $\propto (v_3+v_c^3)^{-1}$ up to the velocity v_s where α's are generated (see, for example, Refs. 1,3 for the definition of v_c and the slowing down time τ_s). This stationary solution is a consequence of the isotropic source at 3.5 MeV and of a sink term at low energy ($\ll m_\alpha v_c^2/2$).

In the presence of RF, the quasilinear diffusion term can exceed the collisional drag and accelerate the α-particles above v_s, thus generating a high energy flux which should be balanced by a proper sink at a velocity (say v_M) $> v_s$. The latter sink could be related to the large banana losses of energetic particles. Steady state solutions may be justified since τ_s and τ_{ql} (the quasilinear time) are low enough with respect to other typical times (i.e., confinement time, etc.) for ITER parameters.

The diffusion coefficient for α's due to RF in the direction perpendicular to the magnetic field is given by [4]

$$D = \frac{Z_\alpha^2 e^2}{2 m_\alpha} \int dk_\parallel \frac{|E_k|^2}{(v_\perp^2 k_\perp^2 - \omega^2)^{1/2}} \frac{\omega^2}{k_\perp^2 v_\perp^2} \qquad (1)$$

where $\int dk_\parallel |E_k|^2 = \bar{E}^2_{rms}$ is the square of the average wave field, $D=0$ for $v_\perp < v_{RIS} = \omega/k_{\perp max}$, with $k_{\perp max}$ related to $k_{\parallel max}$ in the spectrum via the dispersion relation. Instead

of using $v_\perp$ and $v_\parallel$, we rewrite the quasilinear Fokker-Planck equation in the coordinates $v=(v_\perp^2+v_\parallel^2)^{1/2}$ and $\mu=v_\parallel/v$. Following the same procedure used for ion cyclotron waves [5], we expand f_α in the power of μ, we average the equation on μ, and keeping only the lowest order we obtain

$$\frac{\partial f_\alpha}{\partial t} \simeq \frac{1}{v^2}\frac{d}{dv}\left(\frac{v^3+v_c^3}{\tau_s} f_\alpha + \frac{\pi}{2}\frac{D_0 v_s^3}{(v^2-v_{RIS}^2)^{1/2}}\frac{df_\alpha}{dv}\right) + S\,\delta(v-v_s) = 0 \qquad (2)$$

where a narrow $k_\parallel$-spectrum has been assumed, $D_0 v_s^3 = \omega v_{RIS} Z_\alpha^2 e^2 \bar{E}^2_{rms}/2m_\alpha^2 k_\perp^2$ and S is the α source. Equation (2) is integrated and solved once τ_s, S, v_{RIS}, D_0 are known and the fluxes in the low energy sink ϕ_0 and the high energy sink ϕ_M are given. The request for f_α to be continuous positive imposes a maximum velocity $v_M > v_s$, where the high energy sink is placed.

Instead of ϕ_0 and ϕ_M, we may use the α-density $n_\alpha = \int d^3 v\, f_\alpha$ as a free parameter and use the particle balance $\phi_0+\phi_M=Sv_s^2$. Finally, we are left with the above two relations and the three quantities n_α, ϕ_M/ϕ_0 and v_M which are shown in Fig. 1 for three values of $\pi D_0\tau_s/2v_s^2$. Here we take $T_e=20$ keV and $m_\alpha v_{RIS}^2/2 = 1500$ keV. For the case c and $\phi_M/\phi_0=0.5$, f_α is shown in Fig. 2 where the effect of the quasilinear diffusion is evident for $v>v_{RIS}$. In Fig. 3 the damping coefficient $\gamma \propto P_{RF}/\bar{E}^2_{rms}$ is shown for the same three cases of Fig. 1, the quasilinear absorption being less than the linear limit.

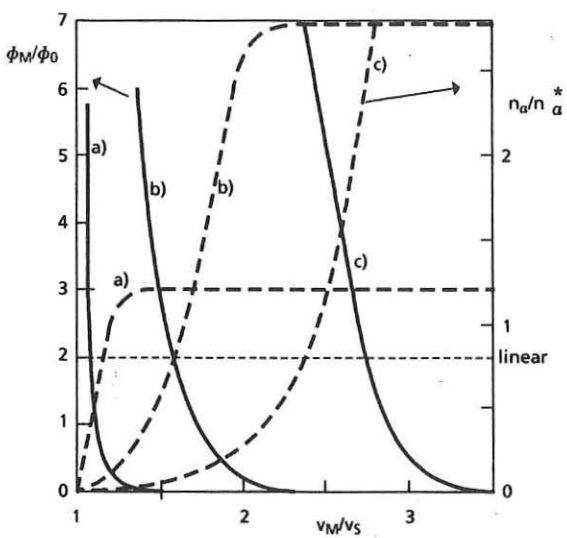

Fig. 1 - Dependence of the two-sink ratio ϕ_M/ϕ_0 and of the α density n_α/n_α^* ($n_\alpha^* = 4\pi v_s^2 S\tau_s$) with the maximum velocity v_M/v_s for $\pi D_0\tau_s/2v_s^2 = 0.1$ (a), = 1 (b), = 10 (c)

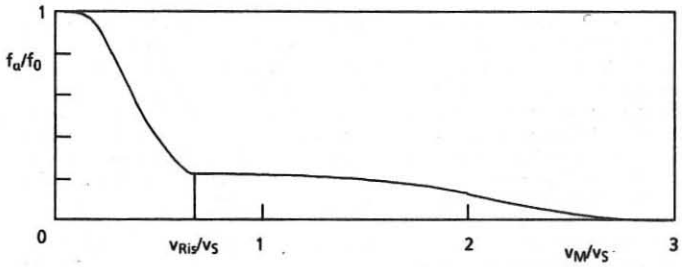

Fig. 2 - α distribution function for case c) and $\Phi_M/\Phi_0 = 0.5$, $v_M/v_s = 3$, $n_\alpha/n_\alpha{}^* = 6$

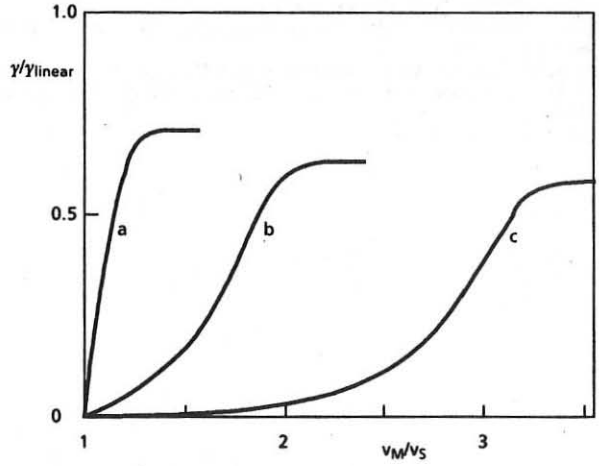

Fig. 3 - Ratio of γ-quasilinear to γ-linear as a function of v_M/v_s

DISCUSSIONS AND CONCLUSIONS

The results of the previous section can be summarized as follows: For the same value of the source S, the α-particle density obtained from the quasilinear calculation exceeds the density of the linear case; this is due to the RF acceleration which feeds the high energy tail up to v_M. Nevertheless, the associated damping rate γ results less than the linear γ.

In the homogeneous case, an important role is played by the density profile of the α-particles. They are generated according to the production rate $<\sigma v>_{DT}$ which has a spatial profile quite peaked at the plasma center. However a profile broadening may be induced if the banana orbits are thick enough. To take into account this effect, the

spatial profile of the source term S is taken for a D-T plasma to be of the type $S(r) = n_D n_T <\sigma v>_{DT} f(b,r)/4\pi v_s^2$, where the broadening factor f depends on the parameter $b = IA/10$ (I is the plasma current in MA and A the aspect ratio) related to the thickness of the banana orbit. When b is much larger than 1, f is a constant equal to 1.

The maximum velocity v_M can be related to several effects. If we consider only the orbit prompt losses, v_M depends on b again, namely, $v_M/v_s = b$, which for ITER plasma exceeds 1. Figure 1 indicates that for $v_M/v_s \geq 2$, the high energy sink plays no role ($\phi_M \simeq 0$), and n_α and γ reach the saturation values at least in cases a and b, which are more representative of the ITER parameters ($P_{RF} = 90$ MW).

This model has been included in a 1-D deposition code where ray tracing in a cylindrical plasma is considered, as well as wave energy and momentum absorption by electrons at the first pass. A numerical analysis is in progress for ITER plasma parameters and preliminary results indicate negligible α-particle absorption even at 6 GHz.

REFERENCES

[1] P.T. Bonoli, M. Porkolab: Nucl. Fusion 27, 1341 (1987)

[2] E. Barbato, V. Zanza: Proc. 13th Europ. Conf. on Contr. Fusion and Plasma Phys. (Schliersee 1986) 2, 449

[3] D. Anderson, H. Hamnen, M. Lisak: Phys. Fluids 25, 353 (1982)

[4] F. Santini: in Application of RF Waves to Tokamak Plasmas (course and Workshop, Varenna 1985) 1, 251

[5] T.H.S. Stix: ibidem, p. 24

PARAMETRIC DECAY OF LOWER HYBRID WAVES

A. Cardinali, R. Cesario, F. Paoletti

Associazione EURATOM-ENEA sulla Fusione, C. R. E. Frascati,
C.P. 65 - 00044 - Frascati, Rome, Italy

INTRODUCTION

A crucial feature of all the experiments concerning the lower hybrid current drive and heating of tokamaks is that there exists a strong density threshold beyond which the current cannot be driven if the r.f. power exceeds a certain value. It is possible that at higher operating densities the lower hybrid waves excite parametric instabilities well before reaching the centre, with the consequence that the current drive can be inhibited due to the fact that instead of going to the electrons in the tail distribution, the wave momentum and energy are diverted elsewhere.

During recent experiments, the reduction of the efficiency of the current drive or heating was associated with a typical activity of the r.f. probe signals observed when the plasma density and the r.f. power exceed the threshold value [1].

We are interested in studying the possible role of the parametric instabilities in the next lower hybrid current drive experiments on ASDEX. In this paper we present the results of the study of parametric instabilities obtained by solving the complete parametric dispersion relation numerically, considering for the typical plasma parameters a wide range of frequencies which involve different channels of instabilities.

PARAMETRIC DISPERSION RELATION AND DECAY INSTABILITIES

We consider the propagation, in a plasma magnetized by a static magnetic field B_0, of a lower hybrid pump wave (ω_0, k_0) with finite extent which decays into a low frequency mode (ω_1, k_1) and two high frequency sidebands $(\omega_1 \pm \omega_0, k_1 \pm k_0)$. The plasma is assumed locally homogeneous, i.e., $k_\perp \gg |\nabla n/n|, |\nabla T/T|$, where $k_\perp$ is the perpendicular (to B_0) wavevector of the waves involved and n and T are the plasma density and temperature. The parametric dispersion relation is

$$\varepsilon(\omega_1, k_1) = \frac{\mu^+}{\varepsilon(\omega_1+\omega_0, k_1+k_0)} + \frac{\mu^-}{\varepsilon(\omega_1-\omega_0, k_1-k_0)} \tag{1}$$

where $\varepsilon(\omega,\mathbf{k}) = 1 + \chi_i(\omega,\mathbf{k}) + \chi_e(\omega,\mathbf{k})$ is the dielectric function and χ_i, χ_e are the linear susceptibilities. For $\omega_{1R} < k_{1\parallel} v_{the}$, i.e., when the response of the electron in the parallel (to B_0) direction is adiabatic, we can assume [2]

$$\mu^\pm = \frac{\chi_e(\omega_1,k_1) - \varepsilon(\omega_1,k_1)}{4\,\omega_0^2 k_1^2 c_s^2 \varepsilon(\omega_1,k_1)} \omega_{pi}^4 \left[1 + \frac{\omega_1}{k_{1\parallel} v_{the}} Z\left(\frac{\omega_1}{k_{1\perp} v_{the}}\right)\right]^2 \sin^2\xi^\pm \frac{U^2}{c_s^2} \tag{2}$$

In this formula, Z is the Fried-Conte plasma dispersion function, ω_{pi} the ion plasma frequency, c_s the ion sound velocity, $U=E_0c/B_0$ the EXB drift velocity of electrons, and $\delta^{\pm} = \measuredangle\, k_{2,3\perp}, k_{0\perp}$ the angle between $k_{2,3\perp}$ and $k_{0\perp}$, as $k_{2,3}=k_1 \pm k_0$.

We have numerically solved Eq. (1) with respect to the complex frequency $\omega_1=\omega_{1R}+\gamma$. For a given numerical calculation, we assumed one of the plasma and r.f. parameters n, T, B_0, P_{RF}, $k_{0\parallel}$, $k_{2,3\parallel}$, $k_{2,3\perp}$, $k_{1\parallel}$, $k_{1\perp}$ as an independent variable, keeping the others fixed. The ASDEX deuterium plasma parameters are obtained using the density and temperature profiles modeled by the following functions of the radial (x) coordinate:

$$n(x) = n(0)\left[1-\left(\frac{x}{1.2a}\right)^3\right]^{2.5}, \quad T_e(x) = T_e(0)\left[1-\left(\frac{1}{1.1a}\right)^2\right]^{2.5} \tag{3}$$

where n(0), T(0) are the peak plasma density and temperature, a = 40 cm is the radius of the separatrix. These functions are plotted in Figs. 1a and 1b. These figures report the expected trends of the plasma parameters for $a<x<x_L$ where x_L is the liner radius, extrapolated by the Langmuir probe measurements. The magnetic field is described by $B=B_0\, x/R$ where $B_0=20$ kG.

We have examined the threshold due to the finite extent of the wave launcher and the finite width of the resonance cones [3]. For simplicity, the plasma is supposed locally homogeneous. For the case $\delta^-=90°$, so that $k_{2y}=k_{2\perp}$ and $k_{2x}=0$, the solution of Eq. (1) gives a sideband wave which propagates poloidally and away from the interaction region, never reaching the plasma centre. The spectral growth factor of the sideband wave due to the convective loss in the poloidal (y) and toroidal (z) directions are respectively $A_y=\gamma\, L_y/|v_{2y}|$, $A_z=\gamma\, L_z/|v_{2z}|$, where v_{2y}, v_{2z} are the poloidal and toroidal components of the group velocities of the sideband wave and L_y and L_z are the dimensions of the grill. The thresholds are set when both these values are of the order of 1 or more. Figure 2 shows the numerical solution of the parametric dispersion relation for the above-mentioned parameters. The frequency of the first sideband is separated by that of the pump wave by a value which is approximately the ion cyclotron frequency. We have verified that a sideband wave can grow and propagate only if its parallel refractive index is sufficiently small so that $n_{2\parallel} \sim k_{2\parallel}/\omega_0 < 8$, with $n_{0\parallel}=k_{OH}/\omega_0=2$ that of the pump.

We have evaluated the convective power threshold using in the expression of the amplification growth factor the values of the homogeneous growth rates which are

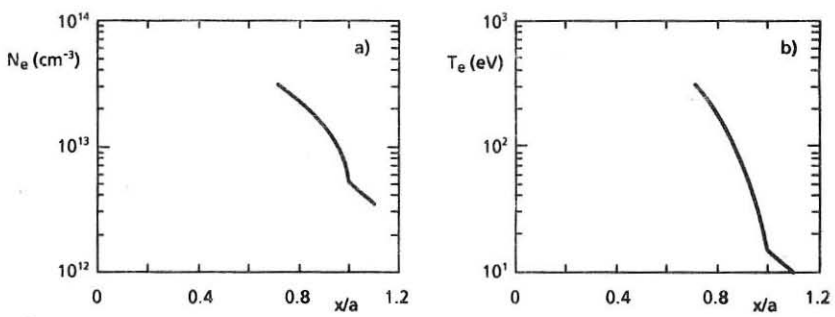

Fig. 1 - Plot of the density and temperature profiles assumed for the numerical calculations

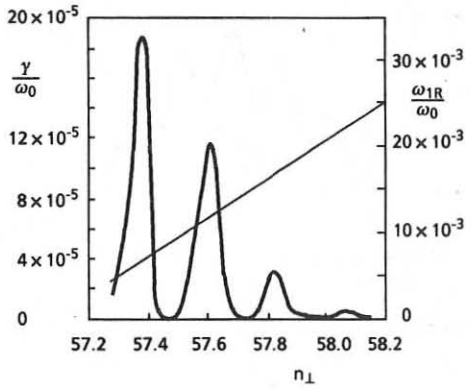

Fig. 2 - Numerical solution of the parametric dispersion relation at x = a, $n_e = 6 \cdot 10^{13}$ cm^{-3}, $T_e = 15$ eV, $P_{RF} = 10$ kW, B = 18 kG, $n_{0\parallel} = k_{0\parallel} c/\omega_0 = 2$, $n_{2\parallel} \simeq k_{2\parallel} c/\omega_0 = 7$, $\delta^- \equiv \measuredangle\, k_{0\perp}, k_{2\perp} = 90°$

obtained by the numerical solutions of Eq. (1) at different values of the r.f. power of the pump wave. The highest spatial amplifications and, consequently, the lowest convective thresholds are found for a r.f. power of about 200 kW and an electron density and temperature $n = 6 \times 10^{12}$ cm^{-3} and $T_e = 15$ eV which are the typical parameters expected at the position of the separatrix for $n = 4 \times 10^{13}$ cm^{-3}.

We also examined the solution of Eq. (1) by assuming some angle values $\delta^- < 90°$, so that $k_{2x} \neq 0$, which correspond to cases of instability with the sideband propagating almost parallel to the pump wave. The decay wave is assumed to propagate in the x-z plane and the spatial growth factor can be estimated by [4]: $A_x = \gamma\, \Delta x / |v_{2x}|$ where

$$\Delta x = \frac{L_z}{\left| \frac{v_{2z}}{v_{2x}} - \frac{v_{0z}}{v_{0x}} \right|}$$

is the maximum distance which the decay wave can travel in the x direction before leaving the pump resonance cone.

In considering the convective losses in all the directions, the threshold is found when the smallest growth factor between A_x, A_y, A_z reaches a value of the order of 1. We obtained the lowest power threshold of about 100 kW at a value of the angle $\delta^- = 60°$, where the condition for homogeneity $\Delta x \ll a$ is still satisfied. Moreover, we found that in this case also, the value of the parallel refractive index of the first sideband wave must be $n_{2\parallel} < 8$, with $n_{0\parallel} = 2$ that of the pump wave. In fact, the solution of Eq. (1) obtained for $n_{2\parallel} > 8$ does not satisfy the linear dispersion relation, so the sideband cannot propagate.

Finally, we considered the case of the parametric instability decay process where the first sideband acts as a pump wave. In this case we assumed $n_{0\parallel} = 7$ for the parallel refractive index of the new pump. The solutions for the homogeneous growth rate are shown in Fig. 3. Here the plasma parameters are the same as in Fig. 2 and $n_{2\parallel} \sim k_{2\parallel}/\omega_0 = 13$ and $\delta^- = 60°$. The r.f. power of the pump is 10 kW. We observe that in this case the maximum growth rate is reached for a sideband whose frequency is downshifted by that

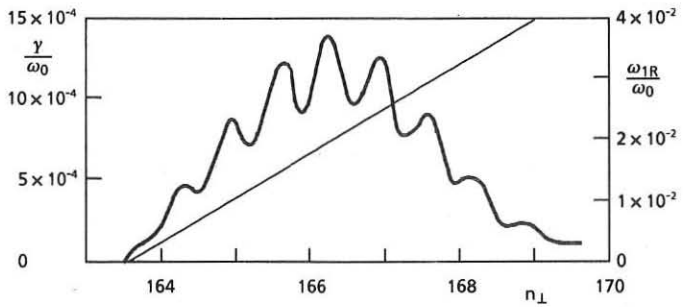

Fig. 3 - Numerical solution of Eq. (1) for $\delta = 60°$, $n_{2\parallel} = 13$, $n_{0\parallel} = 7$ and the other parameters as in Fig. 2

of the pump by approximately 4 ω_{ci}. The r.f. power threshold which could exceed the new pump in this cascading phenomenon is about 100 kW. For sligthly different values of the plasma and pump wave parameters, we have obtained solutions of Eq. (1) which give sidebands whose frequency shift is $|\omega_2 - \omega_0| \simeq \ell\, \omega_{ci}$, with $4 \leq \ell \leq 20$. These cascading processes are expected only if a strong power transfer from the launched wave to the first sideband occurs.

CONCLUSIONS

We have performed some preliminary calculations of the convective thresholds of parametric instability for the case of the ASDEX current drive experiment. We have found a threshold of the order of 100 kW which is in the range of the r.f. power which is to be injected into the plasma, so parametric instability can occur and can be responsible for a reduction of the current drive efficiency.

The power threshold of this phenomenon can be strongly increased by a modification of the density and temperature profiles near the separatrix radius which produces a slight increase of the temperature and a reduction of the density.

REFERENCES

[1] M. Porkolab, B. Lloyd, T.J. Schuss, Y. Takase, et al.: 4th Int. Symp. on Heating in Toroidal Plasmas (Rome, 21-28 March 1984) 1, 529
F. Leuterer, S. Söldner, K. Bernhardi, M. Brambilla, et al.: Proc. 10th Int. Conf. on Plasma Phys. and Nucl. Fusion (London, 1984) IAEA 1, 597
F. Alladio, et al.: 4th Int. Symp. on Heating in Toroidal Plasmas (Rome, 21-28 March 1984) 1, 546

[2] V.K. Tripathi, C.S. Liu: Phys. Reports 130, 143 (1986)

[3] M. Porkolab: Phys. of Fluids 20, 2058 (1977)

[4] E. Villalon, A. Bers: Nucl. Fusion 20, 243 (1980)

ABSORPTION OF LOWER HYBRID WAVES BY FUSION GENERATED ALPHA PARTICLES

M. Spada[a,*)] and M. Bornatici[a,b)]

a) Physics Department "A. Volta", University of Pavia, Pavia, Italy;
b) Physics Department, University of Ferrara, Ferrara, Italy;
*) Present address: The NET Team, c/o Max-Planck-Institut für Plasmaphysik, Garching bei München, Federal Republic of Germany.

The absorption by fusion generated alpha particles of lower hybrid waves obeying the dispersion relation $\omega = \omega_{pe}(1 + \omega_{pe}^2/\omega_{ce}^2)^{-1/2}\,(k_\parallel/k)$ is investigated, along with quasi-linear electron Landau damping, for the characteristic slowing-down distribution and the birth profile for the density of the alphas. For the limited parameter range considered for a NET-like device, the absorption by alpha particles is found not to be significant due to the poor penetration of the lower hybrid waves.

Introduction. The absorption of lower hybrid (LH) waves by α-particles in reactor grade plasmas has recently been evaluated for a fixed frequency, namely, $f = 4.6$ GHz,[1] as well as for varying frequencies (up to 8 GHz).[2,3] From these preliminary studies it appears that the α-absorption depends sensitively on the density profile of the alphas. More specifically, whereas for an α-density profile equal to the corresponding birth profile the absorption by the α's is found not to be significant,[1,3] a comparatively stronger absorption occurs when the α-density profile is taken to be the same as that of the electrons.[2]

Here we extend our previous investigation of the α-absorption[3] to account for both a finite width of the LH wave spectrum and the quasi-linear plateauing of the electron distribution function, the latter being evaluated on the basis of a simple Fokker-Planck model which allows to obtain analytical expressions for both the distribution of the resonant electrons and the corresponding quasi-linear parallel Landau damping.

Quasi-linear electron absorption. The power density dissipated per individual Fourier components in $N_\parallel$ is just the spatial rate of change of the (spectral) energy density flux $S_o(N_\parallel) \times \exp[-2\int dx\ (k_e'' + k_\alpha'')(x,N_\parallel)/\cos\theta(x)]$ so that for a spectrum of $N_\parallel$ the power density deposited into either electrons or alphas is

$$P_{e,\alpha}(r) = 2\int dN_\parallel \frac{k_{e,\alpha}''(r,N_\parallel)}{\cos\theta(r)} S_o(N_\parallel) \exp\left[-2\int_r^a dx \frac{(k_e'' + k_\alpha'')(x,N_\parallel)}{\cos\theta(x)}\right] \qquad (1)$$

with $S_o(N_\parallel)$ the (spectral) energy density flux at $r = a$. Considering a rectangular-like spectrum, one has $S_o(N_\parallel) = \mathcal{P}/\Sigma\,\Delta N_\parallel$ for $N_\parallel^{(min)} < N_\parallel < N_\parallel^{(min)} + \Delta N_\parallel$ and 0 otherwise, with Σ the area of the surface relevant to the deposition of the power $\mathcal{P}$ ($\Sigma = 4\pi^2 R_o r$ for a toroidal surface of major and (effective) minor radius R_o and r (> 0.4 a), respectively, and $\Sigma = 0.4 \times 4\pi^2 R_o a$ if $r < 0.4$ a, a being the tokamak minor radius); $\Delta N_\parallel$ is the width of the LH wave spectrum. The effective wave spatial damping is given by $k''/\cos\theta$, where $k'' \equiv \mathrm{Im}\,\underline{k}\cdot\hat{\underline{v}}_g$ is the imaginary part of $\underline{k}$ along the group velocity $\underline{v}_g$, and $\cos\theta \equiv v_{g\parallel}/v_g$ ($= (1 + \omega_{pe}^2/\omega_{ce}^2)^{1/2}\,\omega/\omega_{pe}$, with $v_{g\parallel}$ the perpendicular (to the magnetic field) component of the group velocity)

accounts for the fact that what is relevant is the wave absorption in the radial (perpendicular) direction (rather than along the group velocity).

The absorption of LH waves by the alphas, due to perpendicular unmagnetized Landau damping, has been evaluated and discussed in detail elsewhere[3] and the numerical results that follow are based on the model developed previously.[3]

As for the absorption by the electrons, the relevant mechanism is taken to be parallel electron Landau damping (ELD) and is evaluated on the basis of the distribution function $F(v_{||})$ that is the solution of the steady-state Fokker-Planck (FP) equation describing the balance between the collisional diffusion as well as drag and quasi-linear wave diffusion in (one-dimensional, $v_{||}$) velocity space (the distribution in $v_\perp$ is assumed to be Maxwellian). A first integration (with respect to $v_{||}$) of the FP equation yields

$$\frac{1}{F(v_{||})}\,\frac{dF(v_{||})}{dv_{||}} = -\,[1 + \frac{D(v_{||})}{D_c(v_{||})}]^{-1}\,\frac{v_{||}}{v_t^2} \qquad (2)$$

where $D_c \equiv (2 + Z_i)\, v_t^5\, \nu_o / v_{||}^3$ describes the diffusion connected with collisional scattering ($v_t^2 = T/m$; $\nu_o = \omega_{pe}^4\, \lambda_{ei}/4\pi n_e v_t^3$, λ_{ei} being the Coulomb logarithm). The coefficient $D(v_{||})$, describing the diffusion due to the LH waves, is evaluated under the assumption that neither the energy nor the shape of the wave spectrum are significantly affected by the absorption itself, i.e., $D(v_{||})$ is independent of $F(v_{||})$. More specifically, for the rectangular spectrum considered, it is $D(v_{||}) = A\,(1/v_{||}^2)\,(\mathcal{P}/\Sigma\,\Delta N_{||})$ for $c/(N_{||}^{(min)} + \Delta N_{||}) \,(\equiv v_{||}^{(min)}) \le v_{||} \le c/N_{||}^{(min)}$, and 0 otherwise, with $A \equiv 4\pi^2 (e/m)^2\,(\omega/\omega_{pe})^2\,(c/\omega)$. With such an approximation, Eq. (2) reduces to a 1.st order linear differential equation whose solution can be obtained analytically.[4] In particular,

$$F(v_{||}) = C(\Gamma)\,\left(\frac{v_{||}/v_t + \Gamma}{v_{||}^{(min)}/v_t + \Gamma}\right)^{\Gamma^2} \exp\{-[\frac{(v_{||}^{(min)})^2}{2\,v_t^2} + \frac{v_{||} - v_{||}^{(min)}}{v_t}\,\Gamma]\} \qquad (3)$$

in the resonant velocity range $v_{||}^{(min)} \le v_{||} \le c/N_{||}^{(min)}$, where $C(\Gamma)$ is a normalization constant such that $\int_{-\infty}^{\infty} dv_{||}\, F(v_{||}) = m/2\pi T$, and

$$\Gamma \equiv \frac{v_{||}}{v_t}\,\frac{D_c(v_{||})}{D(v_{||})} = (2 + Z_i)\, v_t^4\, \nu_o\, [A\,\frac{\mathcal{P}}{\Sigma\,\Delta N_{||}}]^{-1} \qquad (4)$$

From (3), it appears that i) $F(v_{||})$ tends to a constant (the plateau regime) as $\Gamma \to 0$, i.e., for $\mathcal{P}/\Delta N_{||} \to \infty$, so that, at fixed incident power, the plateau regime is favoured by narrowing the spectrum; ii) $F(v_{||})$ tends to a Maxwellian as $\Gamma \to \infty$, i.e., as $\mathcal{P}/\Delta N_{||} \to 0$ (this limit follows by noting that $[(x + \Gamma)/(y + \Gamma)]^{\Gamma^2} \cong \exp[(y^2 - x^2)/2 + (x - y)\Gamma]$ for $\Gamma \to \infty$); iii) $F(v_{||})$ yields a current due to its non-even $v_{||}$-dependence.

With (2) and (3) the (parallel) quasi-linear ELD k'' $\propto (dF/dv_{||})_{v_{||} = c/N_{||}}$ is

$$\frac{k_e''}{k_{e,lin}''} = \frac{C(\Gamma)}{C_M}\,\frac{N_{||} v_t \Gamma/c}{1 + N_{||} v_t \Gamma/c}\,\left(\frac{c/N_{||} v_t + \Gamma}{v_{||}^{(min)}/v_t + \Gamma}\right)^{\Gamma^2}$$

$$\times \exp\{-[\frac{1}{2 v_t^2}((v_{||}^{(min)})^2 - \frac{c^2}{N_{||}^2}) + \frac{c/N_{||} - v_{||}^{(min)}}{v_t}\Gamma]\} \qquad (5)$$

where $C_M \equiv [(2\pi)^{3/2} v_t^3]^{-1}$ and

$$k''_{e,lin} \cong \frac{1}{2}(\frac{\pi}{2})^{1/2} \frac{\omega}{cN_{||}^2}(\frac{mc^2}{T})^{3/2}(1 - \frac{\omega^2}{\omega_{pe}^2} - \frac{\omega^2}{\omega_{ce}^2})^{-1/2} \exp(-\frac{mc^2}{2N_{||}^2 T}) \qquad (6)$$

is the linear parallel ELD. The r.h.s. of (5) tends to 1 in the linear regime ($\Gamma \to \infty$), whereas it tends to 0 in the plateau regime ($\Gamma \to 0$).

Numerical analysis and discussion. The radial profile of the absorption is now evaluated numerically for a profile of the electron density and temperature given, respectively, by $n_e(r) = (n_{eo} - n_{ea})[1 - (r/a)^2]^{\gamma_n} + n_{ea}$, and $T_e(r) = (T_{eo} - T_{ea})[1 - (r/a)^2]^{\gamma_t} + T_{ea}$. For the numerical results that follow we take the profile indexes $\gamma_n = 0.5$ and $\gamma_t = 1$; the central and edge-density $n_{eo} = 10^{14}$ cm^{-3} and $n_{ea} = n_{eo}/10$, respectively; the edge-temperature $T_{ea} = 0.5$ keV, whereas the central temperature T_{eo} is either 30 keV or 15 keV; $Z_i = Z_{eff} = 1.3$. Furthermore, the major and minor radius are $R_o = 520$ cm and $a = 124$ cm, respectively, and the magnetic field is 60 kG. As for the LH parameters, we consider the frequency $f = 4.6$ GHz and a rectangular spectrum of width $\Delta N_{||} = 0.1$ and $N_{||}^{(min)} = 1.75$ ($> N_{||}^{(acc)}(r/a = 0)$). With reference to the quasi-linear effects on the electron distribution function, the tendency to form a plateau in the (narrow) resonant velocity range $(N_{||}^{(min)} + \Delta N_{||})^{-1} = 0.54 \leq v_{||}/c \leq (N_{||}^{(min)})^{-1} = 0.57$ is apparent in Fig. 1 where the (dimensionless) distribution $F(v_{||})/C(\Gamma)$, given by (3), is shown as a function of $v_{||}/c$, for $T_{eo} = 30$ keV, $r/a = 0.8$ and different values of the incident power. As for the (effective) quasi-linear spatial ELD, $2k_e''a/\cos\theta$ with k_e'' given by (5) and (6), this is shown in Fig. 2 as a function of the LH power, for $N_{||} = N_{||}^{(min)} + \Delta N_{||}/2$ (= 1.80), $T_{eo} = 30$ keV, and different radial positions. One can see the significant decrease of k_e'' with power as a result of the quasi-linear plateauing of the distribution function shown in Fig. 1. On the other hand, the drastic decrease of the damping as the temperature decreases is due to the exponential dependence of k_e'' on T, cf. (5).

The radial profile of $aP_{e,\alpha}(r)/(\mathcal{P}/\Sigma)$, with $P_{e,\alpha}(r)$ the absorbed power given by (1), is shown in Fig. 3 for $T_{eo} = 30$ keV and in Fig. 4 for $T_{eo} = 15$ keV, for different values of the LH power. The notable feature is that the power deposition occurs in the peripheral plasma region, the LH penetration improving somewhat as the power increases and/or the temperature decreases, in either case the ELD tending to be weaker.

As for the fraction of the injected LH power absorbed by the α-particles, i.e., the area subtended by the corresponding curve of the power deposition of Figs. 3 and 4, this is given in the following table for both $T_{eo} = 30$ keV and 15 keV.

$\mathcal{P}$ (MW)	$T_{eo} = 30$ keV	$T_{eo} = 15$ keV
5	2.0 %	3.3 %
30	5.3 %	8.2 %
60	8.3 %	12.6 %
100	11.7 %	17.5 %

Note that the power deposition to the alphas is greater for $T_{eo} = 15$ keV than for T_{eo}

= 30 keV, despite the fact that $n_\alpha(T_{eo} = 15\ keV) < n_\alpha(T_{eo} = 30\ keV)$. This results from the improved penetration of the LH waves at lower temperatures.

In conclusion, for the limited parameter range considered for a NET-like device, the LH absorption by the alphas is found not to be significant as a result of the poor penetration of the LH waves, due to the strong peripheral ELD.

Acknowledgements. Useful discussions with F. Engelmann, A. Nocentini and J.-G. Wégrowe are gratefully acknowledged. This work was supported by EURATOM and the Ministero della Pubblica Istruzione of Italy.

References.

1. P. T. Bonoli and M. Porkolab, Nucl. Fusion **27**, 1341 (1987).
2. E. Barbato and F. Santini, paper at "ITER Meeting on Assessment of Current Drive and Heating Issues", Garching, June (1988).
3. M. Spada and M. Bornatici, Proc. of the Joint Varenna-Lausanne Int. Workshop on Theory of Fusion Plasmas, Chexbres, Switzerland, 1988 (in the press).
4. J.-G. Wégrowe, Proc. of the 12th Eur. Conf. on Controlled Fusion and Plasma Physics, Budapest (1985), Vol. 9F Part II, p. 176.

Figure Captions.

Fig. 1 $F(v_{||})/C(\Gamma)$, given by Eq. (3), as a function of $v_{||}/c$ for T_{eo} = 30 keV and different values of the incident power.

Fig. 2 The effective spatial damping as a function of the incident LH power, at different radial positions.

Fig. 3 The profile of the radial power deposition $aP_{e,\alpha}(r)/(\mathcal{P}/\Sigma)$ to both electrons (full line) and α-particles (dashed line) for T_{eo} = 30 keV and different values of the incident LH power.

Fig. 4 The same as Fig. 3 for T_{eo} = 15 keV.

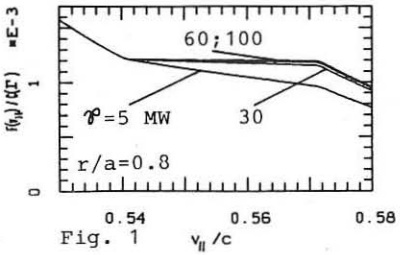

Fig. 1

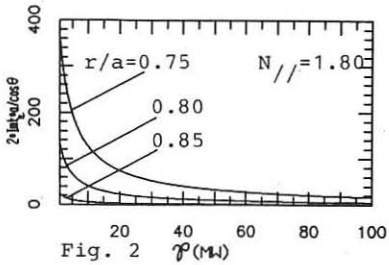

Fig. 2

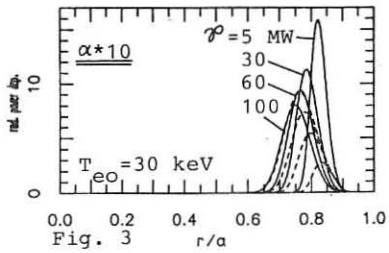

Fig. 3

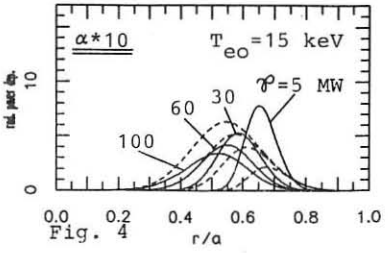

Fig. 4

TURBULENT CONDUCTIVITY OF PLASMAS DUE TO PARAMETRICALLY COUPLED LOWER HYBRID AND CONVECTIVE CELL MODES

V.N.Pavlenko and V.G.Panchenko
Institute for Nuclear Research of the Ukrainian Academy of Sciences, Kiev, USSR

P.K.Shukla
Faculty of Physics and Astronomy, Ruhr University Bochum, F.R.Germany

It is known that the parametric instability can lead to the enhanced plasma fluctuations exceeding the thermal noise level and to rapid transference of the electromagnetic wave energy from the pump wave to plasmas. In such situation the efficiency of the radio-frequency heating is defined in terms of the plasma turbulent conductivity $\sigma_{tur.}$ [1,2].

In this paper, the turbulent conductivity of a plasma is calculated under conditions such that the lower-hybrid pump wave amplitude exceeds the parametric instability excitation threshold. The latter is associated with the decay of the lower-hybrid pump into a daughter wave and the modified convective cell mode which plays an important role with regard to cross-field particle diffusion. It is shown that scattering of charged particles by suprathermal plasma fluctuations is a nonlinear mechanism for the stabilization of parametrically unstable waves and is the cause of the lower-hybrid wave dissipation in a magnetized plasma.

The modified convective cells are the oscillations in which the electron motion along the magnetic field lines are taken into account ($k_z \neq 0$). Keeping the ions two-dimensional and assuming the conditions $k_\perp^2 \rho_e^2 \ll 1$, $k_\perp \rho_i \ll (k_z/k)(m_i/m_e)^{1/2} \ll 1$ and $k v_{Ti} \ll \omega \ll \Omega_i, (k_z/k)\Omega_e$ to be fulfilled we can write the linear plasma susceptibilities in the form

$$\chi_e^0(\omega,\vec{k}) = -\left(\omega_{pe}^2/\omega^2\right)\left(k_z/k\right)^2 (\omega + i\nu_{ei})/\omega ,$$

$$\chi_i^0(\omega,\vec{k}) = \left(\omega_{pi}^2/\Omega_i^2\right)(\omega + i\mu_i k_\perp^2)/\omega \qquad (1)$$

where $\omega_{pe(i)}$ is the electron (ion) plasma frequency, Ω_i is the ion gyrofrequency, and ν_{ei} is the electron-ion collision frequency. Substituting the expressions (1) into the dispersion equation

$$1 + \chi_e^0(\omega, \vec{k}) + \chi_i^0(\omega, \vec{k}) = 0$$

one can obtain the frequency and the damping rate of the modified convective cell modes [3,4]

$$Re\,\omega \equiv \omega_c = \Omega_i \left(k_z/k\right)\left(m_i/m_e\right)^{1/2} \ll \Omega_i , \qquad (2)$$

$$Im\,\omega \equiv \gamma_c = -\frac{1}{2}\mu_i k_\perp^2 - \frac{1}{2}\nu_{ei} \approx -\frac{1}{2}\nu_{ei} \qquad (3)$$

where $\mu_i = 0{,}3\,\nu_i \rho_i^2$ is the ion gyroviscosity.

We can interested in electron-ion plasma immersed in the external magnetic field $\vec{B}_0 = B_0\vec{z}$ and subjected the influence of an RF pump field $\vec{E}(t) = E_0\vec{y}\cos\omega_0 t$ with frequency ω_0 which lies in the region $\Omega_i \ll \omega_0 \ll \Omega_e$. The expression for the elctric field fluctuation spectral density $\langle \delta\vec{E}\delta\vec{E}\rangle_{\omega,\vec{k}}$ in the magnetized plasma with the pump wave has been obtained in [2]. Let us consider the behaviour of the correlator $\langle \delta\vec{E}\delta\vec{E}\rangle_{\omega,\vec{k}}$ in the region near the decay instability threshold when

$$\omega_0 = \omega_{lk} + \omega_c , \qquad (4)$$

Here $\omega_{lk} = \omega_{pi}\left(1+\frac{\omega_{pe}^2}{\Omega_e^2}\right)^{-1/2}\left(1+\frac{k_z^2}{k^2}\frac{m_i}{m_e}\right)^{1/2}$ is the lower-hybrid frequency. The fluctuation spectral density has the form

$$\langle \delta\vec{E}\delta\vec{E}\rangle_{\vec{k}} = 2\pi T_e \frac{\left(\Omega_i^2/\omega_{pi}^2\right)}{\left(1 - E_0^2/E_{th}^2\right)}\left[1 + \frac{\mu^2}{16}\frac{\omega_c^2\,\omega_{pi}}{\gamma_{lk}\gamma_c\,\Omega_i^2}\right], \qquad (5)$$

where $\mu = \frac{k_\perp E_0 c}{\omega_0 B_0} \ll 1$, γ_{lk} and γ_c are the damping rates of the lower hybrid and the modified convective cell mode respectively, and

$$E_{th}^2 = 16\,\frac{\omega_0^2 B_0^2}{k_\perp^2 c^2}\,\frac{\Omega_i^2}{\omega_{pi}^2}\,\frac{\gamma_{lk}}{\omega_{lk}}\,\frac{\gamma_c}{\omega_c} . \qquad (6)$$

is the threshold electric field strength required for the excitation of the parametric instability. It can be seen from (5) that fluctuation level increases infinitely when $E_0 \to E_{th}$. We show that scattering of charged particles by suprathermal plasma fluctuations is a nonlinear mechanism of instability stabilization and is the cause of the RF pump wave power dissipation in the plasma. The mechanism of this scattering is physically similar to twin particle collisions and we can express the turbulent plasma conductivity $\sigma_{tur.}$ in terms of the effective collision frequency ν_{eff}.

$$\sigma_{tur.} = \frac{e^2 n}{m_e \omega_0^2} \nu_{eff}. \qquad (7)$$

On the other hand the conductivity of a plasma immersed in an RF pump field can be determined from the energy balance equation $\frac{1}{2}\sigma_{tur.} E_0^2 = \sum_a n_a \int d\vec{p} \left(\vec{P}^2/2m_a\right) \bar{I}_a(\vec{P})$ where $\bar{I}_a(\vec{P})$ is the collision integral of the charged particles. Following [2], we shall assume that the main contribution to the collision integral is made by the term associated with the particles turbulent diffusion. As a result one can find the connection between the effective collision frequency ν_{eff} and the spectral density of the turbulent fluctuations $\underbrace{\leq \delta\vec{E}\delta\vec{E}^* >_{\omega,\vec{k}}}_{< \delta\vec{E}\delta\vec{E}^* >_{\omega,\vec{k}}}$ in the region above threshold. The correlator is defined by the expression (5), in which the eigen frequencies of the plasma are taken to be $\omega_j' + i\nu_{eff}$ (ω_j' are the eigen frequencies of the plasma in the absence of an pump field). Finally, one obtains the nonlinear equation for Solving it we have

$$\nu_{eff.}(E_0) \approx \nu_c \frac{E_0^2}{E_{th.}^2(k_0)} \qquad (8)$$

where k_0 is the wave number determined from the decay condition (4).

With taking into account (7) the expression for $\sigma_{tur.}$ has the form

$$\sigma_{tur.} = \frac{1}{64\pi} \frac{k_{\perp 0}^2 c^2}{\omega_0^2 B_0^2} \frac{\omega_{pe}^2 \omega_{ek} \omega_c}{\Omega_i^2 \nu_{ek}} E_0^2 \qquad (9)$$

The expressions (8) and (9) are held in the region

$$1 < \frac{E_0^2}{E_{th.}^2} < \frac{\omega_c}{\gamma_c} \qquad (10)$$

Notice must be taken that present results can be important in the low - β plasmas, such as those found in the ionosphere, and some laboratory devices, since $\beta < (T_e/T_i)(k_\perp \rho_i)^2 (m_e/m_i)$ [3]. For such plasmas the turbulent plasma conductivity which is defined by the expression (9) can essentially exceed the classical conductivity due to the electron-ion collisions when the condition $E_0 > E_{th.}$ takes place.

References

1. V.P.Silin (1973) Parametric Effects of High Power Radiation on a Plasma, Nauka Press, Moscow.
2. V.N.Pavlenko, V.G.Paenchenko, S.M.Renenchuk (1986) Sov. Phys. JETP 64, 50.
3. M.Y.Yu, P.K.Shukla (1976) Phys. Letters 58A, 175.
4. V.N.Pavlenko, V.G.Panchenko, P.K.Shukla (1989) Fiz. Plazmy (to be published).

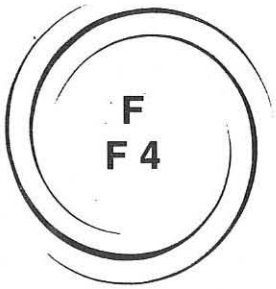

PLASMA HEATING AND CURRENT DRIVE

ALFVÉN WAVE AND OTHER RF HEATING METHODS

F4

COMPARISON OF THE DRIVEN KINETIC ALFVEN WAVES OBSERVED IN THE TCA TOKAMAK WITH NUMERICAL SIMULATIONS.

K. Appert, G.G. Borg, B. Joye, A.J. Knight, J.B. Lister, J. Vaclavik, H. Weisen

Centre de Recherches en Physique des Plasmas
Association Euratom – Confédération Suisse
Ecole Polytechnique Fédérale de Lausanne
21, av. des Bains, CH-1007 Lausanne/Switzerland

INTRODUCTION

The TCA tokamak (R = 0.61m, a = 0.18m, $B_T \leq 1.5$ T, $n_e(0) \leq 1.8 \cdot 10^{20}$ m^{-3}, $I_p \leq 170$ kA) is equipped with four top-bottom antenna pairs to define the toroidal mode number n. An Alfvén resonance is excited whenever the local Alfvén velocity v_A matches the externally imposed wave velocity $\omega/k_{\parallel}$. In the large aspect ratio approximation this condition can be written as

$$\omega^2\rho(r) = (n + m/q(r))^2 (B_T^2/\mu_0 R^2) (1 - \omega^2/\omega^2_{ci}) \qquad (1),$$

where ρ is the mass density and q the safety factor. Fig. 1 shows the resonance position as a function of the central density for two sets of mode numbers considered here, (n,m)=(2,0) and (-1,-1), with B_T = 1.5 T in a deuterium plasma, as relevant to our experimental conditions. The density profile was assumed to be parabolic and the current profile of the form $j(r) = j(0)(1-r^2/a^2)^{2.2}$ such that q(0)=1 and q(a)=3.2.

At high temperatures ($v_e \geq v_A$), kinetic theory predicts mode conversion at the resonance layer from the fast magnetosonic wave to a radially inward propagating wave with a large electrostatic component and an associated density perturbation[1]. The density modulation is detected using the phase contrast diagnostic installed on TCA[2]. It is similar to a laser imaging interferometer and is equipped with a 30 element HgCdTe infrared detector array and coherent amplification for 16 channels. Owing to the essentially cylindrical symmetry of the waves, the pattern of the line integrated density perturbation remains closely related to the original radial wave pattern. To a first approximation the local amplitude is multiplied by an effective integration length $L_{eff} = (2\pi r/k_r)^{0.5}$, where k_r is the radial wavenumber of the wave.

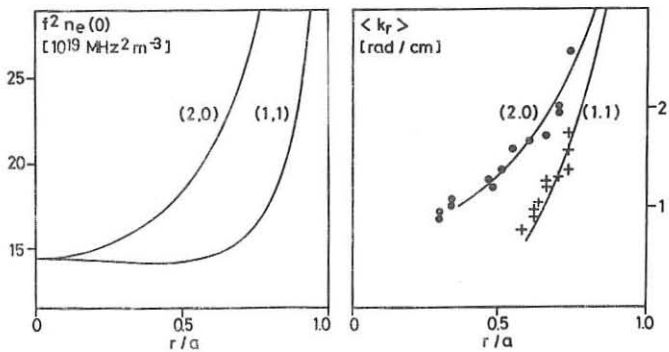

Fig. 1. Resonance curves for TCA conditions. Fig. 2 Mean radial wavenumber as function of position.

EXPERIMENTAL OBSERVATIONS

Fig. 3 shows examples of radial profiles of the amplitude and phase ($\psi(r)$) of the driven density fluctuations at different line densities with (n,m) = (-1,-1) and (2,0), and $P_{rf} \cong 40$ kW. At densities near the threshold below which the resonances are not in the plasma, the oscillations have the character of standing waves (constant phase profiles except for jumps of π). At higher densities they have a prevailingly propagating character (sloping phase profiles), with wavelengths that become shorter as the resonance layers move away from the plasma center. We shall only discuss the case of propagating waves in this paper.

Near resonance it is difficult to compare a local wavenumber ($d\psi/dr$) with theory because it varies rapidly from zero to a finite value. On fig. 2 we have instead plotted the average wavenumber $\langle k_r \rangle$ over the first cycle of inward propagation as a function of peak position. The solid lines were obtained from the approximate dispersion relation for the Kinetic Alfvén Wave expressed as

$$k_r \rho_i (3/4 + T_e/T_i)^{0.5} = ((\omega^2 - k_{||}^2 v_A^2)/ k_{||}^2 v_A^2))^{0.5} \qquad (2),$$

where ρ_i is the ion Larmor radius. The resonance profiles from fig. 1 were used together with a combined temperature profile $T_e + 3/4\ T_i$ assumed to be a parabola squared with a central value of 1 keV, in accordance with temperature measurements on TCA. Again $\langle k_r \rangle$ is an average over the first cycle and is plotted as a function of resonance position. The smaller $\langle k_r \rangle$ for (-1,-1) are a result of the shallowness of the (-1,-1) resonance profile. These waves remain closer to resonance and therefore maintain a longer wavelength. Propagating waves with wavenumbers significantly smaller than indicated on fig. 2 are not observed. Closer to

the thresholds only standing waves occur. In the conditions of the TCA tokamak, the KAW is predicted to be strongly electron Landau damped. The fractional damping rate $\delta_e = 1/2\ \pi^{1/2}\ v_a/v_e$ is in the range 0.2 (near the plasma centre where $T_e \cong 800$ eV) to 0.5 for a (-1,-1) KAW near r/a = 0.7 where $T_e \cong 200$ eV. This is in good agreement with our observation that the amplitude e-folding lengths estimated inward from the amplitude maxima are about one wavelength in the core region, but can be as small as 0.4 wavelength near r/a = 0.7.

COMPARISON WITH NUMERICAL CALCULATIONS

Numerical simulations of KAW excitation were performed in cylindrical geometry using the ISMENE kinetic code which includes Landau damping, transit time magnetic pumping and certain equilibrium gradient terms[3,4], and uses the formulation of Vaclavik[5] for the local power absorption. The profiles of plasma parameters used were similar to the above mentioned and the frequency was 2 MHz. Fig 4. shows profiles of local electron density fluctuation amplitude and phase for cases that can be compared to the corresponding examples on fig.3. Although there is a striking similarity between the wavefields observed and predicted by kinetic theory, exact matching of the two should not be expected because the details of the wavefields depend on the profiles of plasma parameters, and because fig.3 shows line integrated density oscillations. Absolute amplitudes for a given power agree within a factor of two. In the case of (n,m) = (2,0) direct excitation is poor. As a result the KAW amplitude on fig.4. c) and d) is not much larger than the fast (pump) wave amplitude, leading to oscillation profiles that are not representative of those obtained in a tokamak, where the (2,0) waves are excited efficiently via toroidal coupling by a (2,1) antennae structure. The experimental results should therefore be compared to the wave profiles shown as broken lines, where the fast wave component has been subtracted to show the (2,0) KAW only.

CONCLUSIONS

Experimental observations of the KAW in the TCA tokamak and numerical simulations using the ISMENE kinetic code are in excellent agreement. At a more basic level, the observed radial wavenumbers agree with the KAW dispersion relation. The attenuation of the wave amplitude is consistent with electron Landau damping.

This work was partly supported by the Swiss National Science Foundation.

References :

1. A. Hasegawa and L. Chen, Phys. Rev. Lett. **35** (1975), 370.
2. H. Weisen, Rev. Sci. Instrum. **59** (1988), 1544
3. K. Appert et al., Int. Conf. on Plasma Physics, Kiev, **3** (1987), 172. Also LRP 319/87.
4. Th. Martin and J. Vaclavik, Helvetica Physica Acta **60** (1987), 471.
5. Vaclavik J. and Appert K., Plasma Phys. Contr. Fusion **29** (1987), 257.

Fig. 3 (left)

Experimental profiles of driven KAW's in TCA

Fig. 4 (right)

Simulated profiles of driven KAW's

a),b): (n,m) = (-1,-1)

c),d): (n,m) = (2,0)

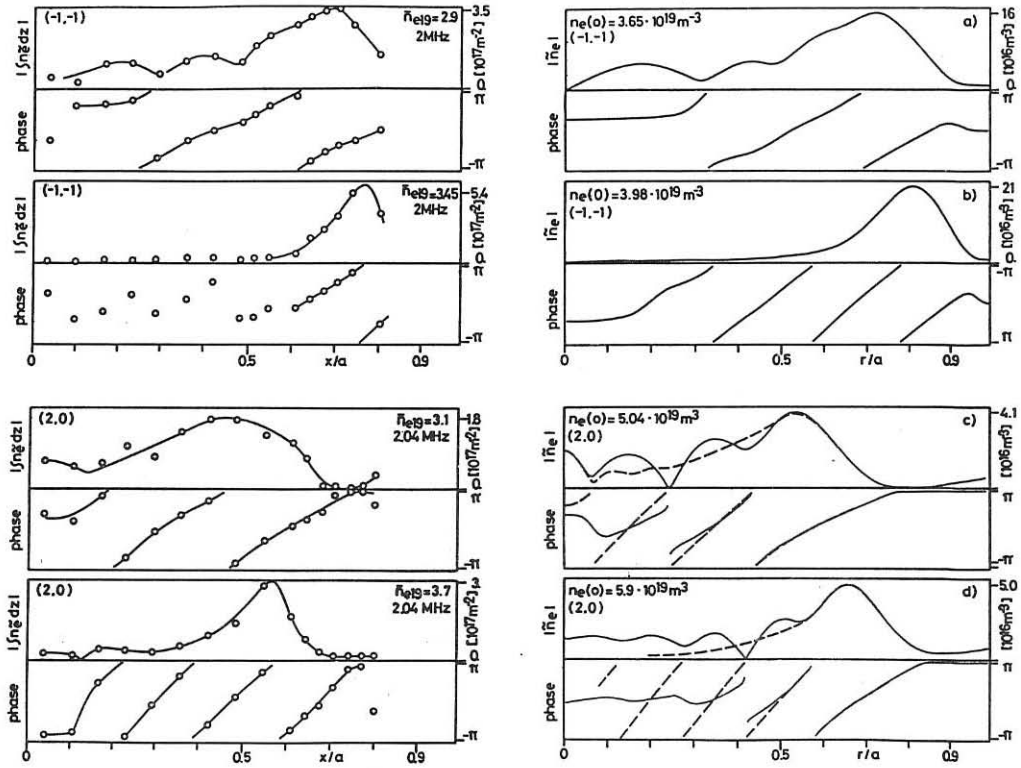

EFFECTS OF THE ALFVEN WAVE HEATING IN THE TCA TOKAMAK DEDUCED FROM THE PLASMA DYNAMICAL RESPONSE

Th. Dudok de Wit, B. Joye, J.B. Lister, J.-M. Moret

Centre de Recherches en Physique des Plasma, Association Euratom-Confédération Suisse
Ecole Polytechnique Fédérale de Lausanne
21, Av. des Bains, CH-1007 Lausanne, Switzerland

Alfvén wave heating as used on TCA has already been shown to have an important effect on most of the plasma parameters amongst which the most noticeable are the electron and ion temperatures, the kinetic energy content inferred from the diamagnetic flux, the Shafranov parameter $\Lambda = \beta_p + li/2 - 1$ deduced from the equilibrium vertical field and above all the plasma density. The spatial distribution of the resonant layers inherent in this kind of rf heating have been found to influence the temporal evolution of most of these parameters. This experimentally appears as a characteristic reduction of their time derivative at the same time as a new resonance layer appears in the plasma center. It is tempting to link these observations with a spatial redistribution of the absorbed power when the resonance surface structure is modified. Nevertheless the impressive density increase present during Alfvén wave heating makes the interpretation of these experiments somewhat difficult if we want to take into account these effects on an equivalent density variation for a purely ohmic shot.

Plasma dynamical response to Alfvén wave heating - Since our experiments are inherently transient, we chose to extensively study the dynamic plasma response [1]. TCA plasmas ($a = 0.18$ m, $R = 0.61$ m, $B_\phi = 1.52$ T) are heated by Alfvén waves at 2.0 to 2.5 MHz launched by 8 phase-coherent antenna array. Dynamical response measurements were performed either by sinusoidally modulating or preprogramming one of the controlable machine parameter such as the rf power or the gas valve. The presented work concentrates on the study the response of the electron temperature in the range of modulation frequencies from 100 Hz to 500 Hz. At these frequencies both the density and the impurity content relative modulations remain much smaller than the soft-X-ray flux modulation. Thus the latter is attributed to a change in the electron temperature.

Profiles of the normalised gain and of the phase of the soft-X-ray response to a modulated rf power (Fig. 1) exhibit two distinct regions separated by a well defined radius. Inside this radius the temperature response profile displays the lowest gains and phases; outside both the gain and the phase increase. We note that that the modulated component of the soft X-ray signal comes mainly from a variation of the base line signal, although it will be shown that the sawtooth activity plays a important role in the electron temperature response. The presence of an electron thermal energy source associated with this perturbation is identified by the lowest value point on the phase profile, i.e. toward the inner side of the separation radius. At the highest studied frequencies, this thermal energy source lags the rf power by 180^o. This shows that the electron temperature perturbation is not produced by directly thermalising the wave energy but by an indirect mechanism. Moreover, it has been possible to establish that this phase profile is independent of the resonance layer position. Two situations are shown in Fig. 1 where the resonant surface structure was modified by

either a density or a frequency change. In the first case - low density or high frequency - all the resonance surfaces are in the plasma periphery while in the second case a new resonance layer has just appeared in the plasma center. Both conditions lead to the same, indistinguishable, phase profile. In fact, this same temperature response was produced by modulating the electron density with gas puffing in purely ohmic conditions. The apparent thermal energy source and the abrupt increase of the delay are associated with the q=1 surface and may be explained by modifications of the sawtooth activity. This unsuspected but natural reaction of the electron temperature to density variations is described in detail in a companion paper [2].

A comparison of the two cases presented in Fig. 1 shows that there is a significant difference in the electron temperature modulation amplitude. The relative gain is from 2 to 4 times bigger when all resonance layers are near the plasma edge compared with the case possessing a dominant central resonance surface. This considerable global decrease of the plasma response amplitude may well be the cause of the observed discontinuity in the time evolution of the plasma parameters when a new continuum is crossed. The unsuspected character of this observation should be emphasised : either gas puffing, producing mainly a modifiction of the edge density, or Alfvén wave heating, and the unavoidable presence of resonance surfaces in the plasma periphery, can induce a change in the energy content in the plasma bulk. With the available experimental results it is, however, not yet possible to determine whether this is the consequence of a modification of the density or the temperature in the plasma periphery.

Superposition of rf power and gas valve modulation - It has been previously established that most of the electron temperature variation during rf heating is an intrinsic reaction of the plasma to a change in the density. Under these circumstances it is obviously much more difficult to observe any experimental evidence of direct rf heating. Gas puffing may be used to control the density modulation due to the rf field. To achieve this the rf power and gas valve were modulated at the same frequency with a phase and amplitude relationship adjusted to minimise the line average density variation. This should leave an electron temperature modulated component which is directly driven by the modulated rf power. Figure 2 shows the amplitude profile of the soft-X-ray flux in three cases: with a modulation of the rf power only, with a modulation of the valve and finally with the described superposition. The experiment was caried out at 100 Hz with a maximum peak to peak rf power modulation limited to 20 kW by the gas valve dynamic range. Also indicated in the figure is the expected signal amplitude in the plasma center if this rf power was spacially uniformly absorbed. The central electron temperature response is compatible within the margin of error with a zero or a uniform heating although the plasma parameters and the heating scheme were set up so as to guarantee the presence of a resonance surface in the central part of the discharge. Only the outermost soft-X-ray channels displaid a larger residual oscillation. The phase of this oscillation with respect to the rf power is estimated to lie between 115^{o} and 140^{o}, a value which exceeds 90^{o} and which is incompatible with direct heating. It should be noted that it is difficult to guarantee that everywhere in the discharge the density variation was cancelled to a sufficiently low level since only the line integrated density modulation was minimised.

Discussion - In conclusion, although the presented experiments were designed to give the best chance to observe any direct electron heating by absorption of Alfvén waves, no clear answer was obtained. The error bar may be reduced by averaging results over many discharges which is hoped to be sufficient to resolve this question.

The theory of the Alfvén wave physics predicts that an inward propagating kinetic

Alfvén wave is created by wave conversion at the resonance layer. This wave is then absorbed by Landau damping over a few wave lengths, quantitatively a few centimeters. The density perturbation associated with this wave has been observed and is in agreement with theory [3]. Quantitativly, if all of the coupled power were thermalised by this channel, a localised modulation of the electron temperature would have been visible. We are forced to consider the possibility of a large fraction of the rf power being dissipated by another mechanism. This could be explained by the very different ratio between the wave phase velocity and the electron thermal velocity in the edge and central part of the plasma column. This hypothesis is supported by the observation of improved heating at low plasma current where the electron temperature is smaller. Experiments will be carried out in a near future to see if this ratio is a key parameter in the processes of Alfvén wave thermalisation.

This work was supported in party by the Fonds National Suisse de la Recherche Scientifique.

References:

[1] B. Joye et al., Plasma Phys. and Contr. Fusion **30** (1988) 743.

[2] Th. Dudok de Wit et al., this conference.

[3] R. Behn et al., Plasma Phys. and Contr. Fusion **29** (1987) 75.

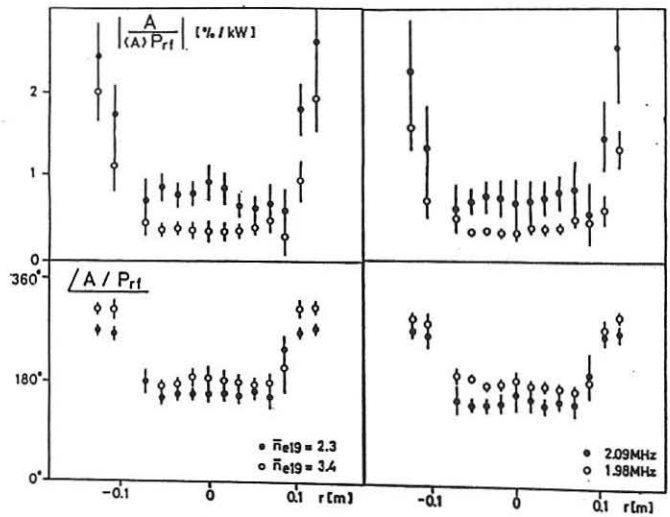

↑ Fig. 1 Relative gain and phase profile of the response of the Soft X-ray with RF modulation before and after crossing the DAW resonant surface a) by increasing the density, b) by increasing the Alfvén frequency.

↓ Fig. 2 Relative gain profile of the response of the Soft X-ray during either RF power modulation (o), gas valve modulation (•) or gas valve and power countermodulation resulting in a minimum density variation (+). The arrow gives the level of the expected amplitude for a uniform energy deposition.

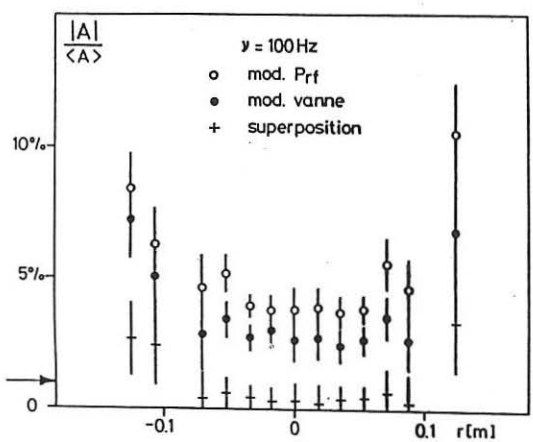

ANTENNA PLASMA INTERACTION AND HARMONIC GENERATION IN ALFVEN WAVE HEATING

G.G. Borg, S. Dalla Piazza, Y. Martin, A. Pochelon, F. Ryter and H. Weisen

Centre de Recherches en Physique des Plasma, Association Euratom-Confédération Suisse
Ecole Polytechnique Fédérale de Lausanne
21, Av. des Bains, CH-1007 Lausanne, Switzerland

*Max-Planck-Institut fur Plasmaphysik, D-8046 Garching, Munich, F.R.G.

Introduction Additonal plasma heating by Alfven waves (AWH) has been studied on TCA for some years. Although considerable agreement between fundamental wave and coupling phenomena has been observed [1,2], the heating results have always been poor and difficult to interpret. Only recently has energy deposition within the plasma been shown to be determined mostly by the density rise [4] and ohmic effects and not by Alfven resonant absorption within the plasma [3].

In TCA, the standard AWH antennae are unshielded and are in direct contact with the plasma scrape off layer (SOL) in the shadow of the limiter. In this paper we test the hypothesis that a Langmuir current (resistive and capacitive [5]), henceforth referred to as the default current, flows from the antennae to the plasma on application of RF potential and we estimate the parasitic power deposited at the plasma SOL interface.

Experiment In TCA there are four pairs of antennae spaced at 90^0 intervals around the machine. In each pair there is one antenna on top and one on the bottom of the plasma. AWH is normally effected by applying approximately 30kW of RF power per antenna at 2.04 MHz. If desired, these antennae can be artificially polarised negatively with respect to machine earth by a biasing circuit coupled to the antenna RF lines. One of the TCA antennas is shown in Fig. 1. We monitor the current entering each terminal of one of its three bar pairs by Rogowski coils. In addition, we monitor the RF potential with respect to the machine earth by one voltage divider on each terminal. The signals obtained are therefore proportional to the time derivatives of the current and the voltage. Under normal conditions and according to the prescription for AWH, a large antenna current, the circulating current, flows in one terminal, through the antenna bars, and out the other terminal. If a default current flows from the antenna into the plasma then the current entering one terminal of the antenna is no longer

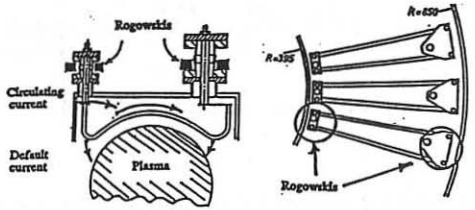

Fig. 1 AWH antenna showing the paths of the circulating current and the default currents for symmetric excitation.

equal to the current leaving the other terminal. Subtraction of the two Rogowski signals therefore permits a measurement of the default current, which must flow from the high power generator, through the terminals of the antenna, and into the SOL.

Under normal conditions the TCA antennae are excited symmetrically at RF with respect to machine earth (the terminals of the antenna are excited in push-pull) and are electrically floating at DC with respect to the plasma. The default currents entering each terminal of the antenna should then be more or less equal. Since these currents consist mainly of a rectified electron current flowing in each terminal on positive half-cycles of the terminal voltage, we predicted a default current signal at the second harmonic of the Alfvén generator frequency (2.04 MHz). The prediction was confirmed by an experiment in which a top and a bottom pair of antennae were excited (Fig 2a). The signal waveform obtained is independent of the chosen antenna poloidal phasing. The magnitude of the default current is typically 0.02 to 0.05 of the circulating antenna current for our conditions. This could explain a substantial part of the measured Alfvén power if the individual default currents flowing in both terminals are in phase with their terminal voltages, as will be shown later, and the other, unmonitored, bar pairs have similar default currents.

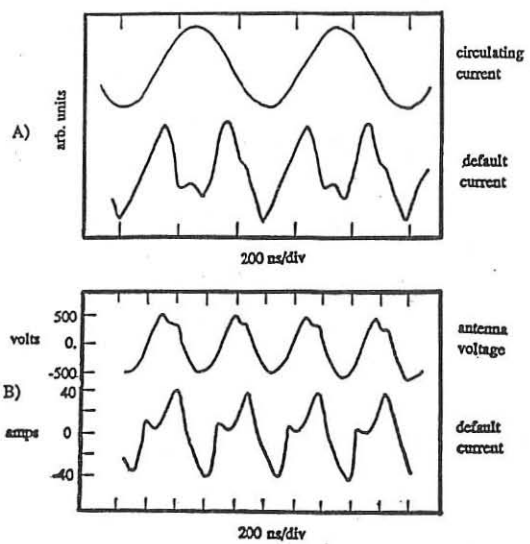

Fig. 2 Typical signal traces showing the time derivatives of the antenna potential, the circulating current and the default current.
a) Symmetric excitation.The default current trace shows the sum of the default currents entering at both antenna terminals.
b) Asymmetric excitation with one side of the antenna at machine earth. The signals are calibrated for the first harmonic at 2.04 MHz.

The default current has some interesting properties. Firstly, the current drawn from the plasma by a passive antenna circuit when RF is applied at another toroidally separated antenna is of the same order as the directly excited default current measured on the excited antenna. This means that different antennae interact. Indeed, observation of the default current of one antenna whilst all eight antennae were excited revealed a very complicated waveform consisting of mainly first and second harmonic signals. Second, in the case of relatively high power excitation, the default current does not depend on the artificial polarisation applied to the antenna when this polarisation is more negative than the natural polarisation. According to simple floating probe theory, an oscillating potential applied to a floating metallic object in a plasma will draw a DC current until the object has charged sufficiently negative to equalise the average ion and electron currents on each half-cycle [6]. This is similar to the technique of grid-leak bias used in circuits involving electron tubes. If a more negative potential is applied to the object, then any increase in RF current must be due to an ion current which causes a DC current to flow to the polarisation source. This increase in RF current is small due to the low ion thermal velocity.

It is not possible to measure the individual default currents in each antenna terminal using the above experimental technique. In order to measure the power deposited in the plasma edge it is therefore necessary to excite the antenna in such a way that the default current enters through a single known terminal. The time averaged product of this current with the measured terminal voltage with respect to machine earth then gives the parasitic power.

This was achieved by grounding one side of the antenna so that all points along the antenna bars oscillate in phase. In this case, for a plasma of static potential, we may hypothesise that only the active side of the antenna sources a default current. A typical unintegrated default current is shown in Fig. 2b with the corresponding unintegrated terminal potential trace. Note that the second harmonic of Fig. 2a for the case of symmetric excitation has largely disappeared; in agreement with the hypothesis.

The default current in this experiment has half the amplitude of the circulating current since the antenna potential was fixed at DC earth. In this case the antenna never attains the negative polarisation necessary to reduce the large electron current on positive half-cycles of the oscillating potential to the value of the ion current on negative half-cycles and hence extinguish the DC current. As a result the power estimated is not directly relatable to that measured in the symmetric, floating antenna case. The power, 10 kW, calculated from the trace for this bar pair corresponds to a total antenna power between 20 and 30 kW assuming that the other outside bar pair behaves identically and depending on how much default current can be drawn along field lines by the centre bar pair. Unfortunately, due to the asymmetrical load, the normal AWH power measurement diagnostic was made nonoperational by this experiment so that a direct comparison is not available. Nonetheless, this magnitude of parasitic power would represent approximately 240 kW of wasted power if all eight antennae were excited asymmetrically in the same way with one terminal at machine earth. The AWH RF power is calculated by a voltage measurement across the symmetric RF power line and by a measurement of the average current in the line. This measurement is therefore expected to include the default current power.

The presence of some second harmonic on the default current with asymmetric excitation (Fig. 2b) is poorly understood, however unlike the first harmonic (2.04 MHz) the second harmonic is strongly fluctuating and varies considerably with plasma conditions. It could have two origins. The first is that the plasma potential oscillation produces a current component into the antenna. The second is that the second harmonic is a natural trait of the high voltage, high frequency Langmuir current effect in the SOL. In this case the characteristic can be checked by disconnecting completely one side of the antenna so that no circulating current flows and the antenna potential is uniform along the length of the antenna

bars. The fact that the default current flows from one terminal to the plasma can be checked by measuring the harmonics of the individual Rogowski currents.

The difference in the amplitude of the observed default current signals in the symmetric and asymmetric excitation experiments may be due to the natural polarisation of the antenna in the symmetric case and the non polarisation in the asymmetric case. It may also be due to the fact that a good portion of the first harmonic of the default currents flowing to the SOL in the symmetric case are cancelled during addition of the Rogowski signals.The natural polarisation of the antenna can be preserved during asymmetric experiments by connecting a low impedance capacitor from the antenna terminal to ground instead of making a direct connection. In this way one should obtain a default current of similar magnitude to that seen in the symmetric, floating antenna experiments.

During AWH with symmetrical excitation, harmonics have been observed on the magnetic wave field and ion saturation current signals in the SOL. The second harmonic (4.08 MHz) has been shown in some cases to be 50% of the fundamental signal. All harmoncs of the ion saturation current measured by a Langmuir probe, positioned far from the excited antenna, peak around the antenna radius. Such harmonics however have only been detected in the SOL. They have not been detected deeper in the plasma by the density fluctuation imaging diagnostic. Their level within the plasma does not exceed the sensitivity threshold of the Kinetic Alfven Wave amplitude at the applied frequency. It has been suggested [7] that these harmonics are due to the Langmuir effect at the antenna-SOL interface. An experiment with asymmetrical excitation has been performed in which the harmonics of the default current were measured as a function of the harmonics of the toroidal component of the magnetic wave field during an RF power scan. Since it is known that the amplitude of these harmonics all decrease with the negative level of artificial polarisation, the antenna was grounded as in the case of the default current power measurement to eliminate the effect of the antenna natural polarisation on the SOL. Asymmetrical excitation also permits excitation of a default current in a single antenna terminal to provide a single source of the plasma wavefields. It was predicted that the level of the harmonics (4.08, 5.12 and 8.16 MHz) of the plasma signal would increase linearly with those of the default current. Experiments however are still preliminary and have not yet provided clean enough signals for a valid comparison.

Conclusion Experimental results have been presented which form the first stage of a study of the plasma-antenna parasitic interaction during AWH in TCA. The results demonstrate that it is physically feasible to obtain a direct measurement of the power dissipated by the default current at the antenna-SOL interface and the measurement indicates that 20 - 30 kWs is delivered to the SOL in the particular case of the asymmetrically excited antenna when grounded directly at the machine earth.

Acknowledgements This work was partly supported by the Fonds National de la Recherche Scientifique.

References

[1] Weisen H. et. al., this conference.
[2] Collins G. A. et. al., (1986) Phys. Fluids 29, p. 2260.
[3] Joye B. et. al., (1988) Plas. Phys. and Contr. Fus. 30, p. 743.
[4] Appert K. et. al., (1987) Int. Conf. on Plas. Phys., Kiev.
[5] De Chambrier A. et. al., (1980) 4th Int. Symp. on Heating in Tor. Plas. Vol. 1., p. 193.
[6] Butler H.S. et al. (1963) Phys. Fluids 6, p. 1346.
[7] Dalla Piazza S. (1988) Rapport de Diplôme, Internal report CRPP-EPFL.

ALFVEN WAVE EXPERIMENTS ON THE TORTUS TOKAMAK

M.J. Ballico, M. Bowden, G.F. Brand, M.H. Brennan, R.C. Cross, P. Fekete and B.W. James

School of Physics, University of Sydney, NSW 2006, Australia

Introduction

Results are presented on the first observations of the Discrete Alfven Wave (DAW) and the first measurements of laser scattering off the kinetic Alfven wave in the TORTUS tokamak. TORTUS is a relatively small device, with major radius R = 0.44m, minor radius 0.1m and has previously been operated routinely with $B_\phi = 0.7$ T, $I_p = 20$ kA and $n_e \sim 1 \times 10^{19}$ m^{-3}. Under these conditions, and over a wide frequency range (1 – 14 MHz), there has been no evidence of the DAW modes observed [1] on TCA. Recently, a minor upgrade of TORTUS has permitted routine operation at $B_\phi = 1.0$ T, $I_p = 30$ kA, $q(a) \sim 5$ and $n_e \sim 1 - 4 \times 10^{19}$ m^{-3}. At the operating frequency, 3.2 MHz, chosen for this study, DAW modes are observed clearly at both low and high densities. The appearance of DAW modes appears to be due to a steeper current profile at the higher plasma currents now generated in TORTUS. The general behaviour of DAW modes is in fact quite sensitive to the density and current profiles, indicating that DAW modes should provide a useful current profile diagnostic.

A total of 6 identical antennas is installed in TORTUS, arranged as 3 pairs at 3 toroidal locations. Each pair consists of a top and bottom electrostatically shielded antenna [2] which can be phased to excite either even or odd poloidal (m) modes. The array can also be phased to select the toroidal (n) mode number and its sign. Each antenna pair is driven separately by a 20 kW amplifier and up to 40 kW of rf power can be delivered to the plasma. By comparison, the ohmic heating power, at $I_p = 30$ kA, is typically 50kW. The results presented in this paper were all obtained with only one of the 3 antenna pairs active, phased to excite odd m modes, in order to excite both $n = 1$ and $n = 2$ modes during a single discharge. Modes with $n > 2$ are not observed at $f = 3.2$ MHz and at densities $n_e < 4 \times 10^{19}$ m^{-3}.

Previously, we have observed Alfven resonance layers in TORTUS using magnetic probes, but only at relatively low values of the plasma current [3]. At high I_p, magnetic probes can be used only in the plasma edge, to monitor DAW and guided modes and to determine the n, m mode spectrum. The Alfven resonance layer is now probed with a submillimetre laser system to detect the density perturbations associated with the kinetic Alfven wave (KAW). The KAW has a radial wavelength ~ 1 cm and generates density fluctuations $\Delta n_e/n_e \sim 0.001$ at a power level ~ 20 kW. DAW modes are not detected by the laser system since the radial wavelength is typically ~ 5 cm and the corresponding density fluctuations are much smaller.

The submillimetre source is a 20 mW optically pumped formic acid vapour laser operating at 433 μm [4]. The laser is used in a far forward scattering system [5] in which radiation

after passing along a vertical chord of the plasma is focussed onto a Schottky diode detector. Density fluctuations associated with the KAW perturb the beam, causing fluctuations in the laser power reaching the diode. The amplitude and phase of the detected signal, at the wave frequency, are measured using quadrature RF mixing techniques. This system has no spatial resolution along the beam. The transverse resolution is determined by the 8mm beam width.

An alternative scattering system, sharing the same optics, has also been developed using a 10 W step tunable gyrotron [6] operating at $\sim$ 175 Ghz (1.7mm) and with a beam width of 4 cm. However, the only scattering results presented below are those obtained with the laser system.

Experimental results

Typical data for DAW mode excitation in a hydrogen plasma is shown in Fig. 1. The antenna resistance, R_{ant}, is the equivalent series resistance of each antenna, with the vacuum resistance subtracted. The occurence of DAW modes is indicated by sharp peaks in the edge wave magnetic fields, and a significant increase in antenna resistance. The dominant wave field component at the plasma edge is the b_θ component. Although a DAW mode is a global mode, the edge wave fields are calculated to be about two orders of magnitude smaller than the wave fields at the centre of the plasma. The mode is therefore not excited directly by the external antennas, but requires the fast wave to transport energy from the external antennas to the center of the plasma. DAW modes can be excited by driving only one antenna pair, as in Fig. 1, or by appropriate phasing of all three antenna pairs. Better coupling to any individual mode is obtained by phasing the three antenna pairs, but a wider spectrum of modes can be studied by driving only one pair of antennas.

In Fig. 1, the most obvious indication of a DAW mode appears on the b_θ trace, which shows two distinct peaks, the first at $t \approx 6$ ms and the second at $t \approx 11.5$ ms. The first peak corresponds to an $n = +1$, $m = -1$ mode which appears at a line average density $\overline{n}_e = 1.5 \times 10^{19}$ m^{-3} and the second peak is due to an $n = +2$, $m = -1$ mode which appears at $\overline{n}_e = 4.3 \times 10^{19}$ m^{-3}. The sign notation used in this paper is such that $k_\parallel = (n + m/q)/R$ in the cylindrical approximation, for perturbations of the form $\exp[i(kz + m\theta - \omega t)]$. The edge safety factor $q(a) \approx -5$ in Fig. 1, I_p and B_ϕ being in opposite directions. Negative m DAW modes are excited preferentially since the wave fields extend over a wider cross-section of the plasma for left-hand polarised shear wave modes than for right-handed ($m > 0$) modes.

The appearance of a DAW mode is not especially evident in the R_{ant} trace when only one antenna pair is driven. A much larger increase in R_{ant} is observed when all 3 antenna pairs are driven. The main features of interest in the R_{ant} trace shown in Fig. 1 are (a) the very low level of background loading prior to the appearance of the $n = 1$ mode and (b) a significant increase in R_{ant} when the $n = 1$ mode appears and again when the $n = 2$ mode appears. These results show clearly that very little energy is deposited in the plasma edge and that essentially all of the power delivered to the plasma is deposited in the $n = 1$ and $n = 2$ Alfven resonance layers.

Scattering of the laser beam is observed at all radii immediately following the disappearance of the $n = +2$ DAW mode. As shown in Fig. 1, there are two distinct peaks in

the scattered signals occuring at slightly different times during the discharge. The radial structure of each peak is shown in Fig. 2. We interpret the scattered signals to represent scattering from Alfven resonance layers in the plasma. The first scattering peak, at $t \sim 11.6$ ms, indicates an Alfven resonance surface at $r/a \sim 0.6$. The second peak, at $t \sim 13.5$ ms shows an Alfven resonance surface at $r/a \sim 0.5$.

Further experimental work will be required to provide a more comprehensive account of the results presented in this paper. We are at present obtaining density profiles and further scattering data at small angles. This data is needed to interpret the radial structure of the scattered signals shown in Fig. 2. At present, the phase information obtained from laser scattering is ambiguous since the phase profiles can be interpreted either in terms of a radial shift in the position of the Alfven resonance layer or as a radial propagating KAW.

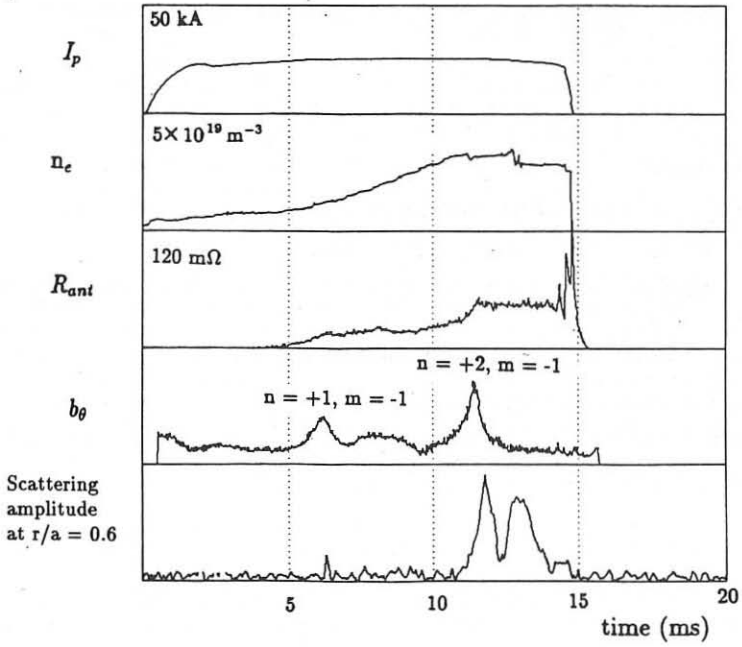

Fig. 1 Typical experimental data at $f = 3.2$ MHz

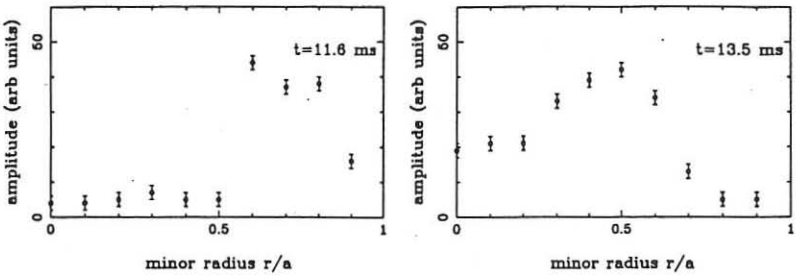

Fig. 2 Scattering signal amplitude vs r/a at (a) $t = 11.6$ ms and (b) $t = 13.5$ ms.

References

[1] G.A. Collins et al., *Phys. Fluids* **29** (1986) 2260.

[2] M.J. Ballico et al., *Plas. Phys. Contr. Fusion* **30** (1988) 1331.

[3] M.J. Ballico et al., *14th Eur. Conf. on Contr. Fus. and Plasma Heating*, Madrid (1987) Vol. 11D, Part III, p. 865.

[4] L.B. Whitbourn et al., *Infrared Physics* **28** (1988) 7.

[5] D.E. Evans et al., *Plasma Physics* **24** (1982) 819.

[6] G.F. Brand in *Infrared and Millimeter Waves* (Ed. K.J. Button, Academic Press) **14** (1985) 371.

ALFVEN AND FAST MAGNETOSONIC WAVE EXCITATION BY HIGH ENERGY ION BEAM IN TOKAMAK PLASMA

Yegorenkov V.D., Stepanov K.N.

Kharkov Institute of Physics and Technology,
the Ukrainian SSR Academy of Sciences, 310108 Kharkov, USSR

Abstract. For the toroidal plasma model as a hollow cylinder with the toroidal magnetic field $\propto 1/R$ it is shown that global Alfven waves in the absence of conversion are excited by resonant ions at the cyclotron resonance under the anomalous Doppler-effect conditions. In the presence of Alfven wave conversion into the kinetic Alfven wave the instability for ITER parameters appears to be impossible because of strong electron Cherenkov absorption.

On injecting fast neutral beams in tokamak plasma with the aim of heating and current drive various instabilities may develop [1]. This problem has become especially actual in connection with the ITER project [2] (R =5÷6m, a =2m, $b/a \leq 2$, $\overline{T}$ =10÷30keV, $\overline{n}$ =0.7÷2.0·10^{20}m^{-3}, I_p =15÷30MA, B_o =5T), which puts forward not only the task of plasma heating to the break-even temperature but also the provision of prolonged discharge sustainment with the help of neutral beam injection (injection power P_{CD}=100MW). To approach the central part of such a discharge the neutral atom energies $\mathcal{E}_o = m_i v_o^2/2$ =0.7÷2.0MeV are required. Under these conditions the beam velocity v_o exceeds the Alfven velocity and as this report shows it becomes possible to excite Alfven (AW) and fast magnetosonic (FMSW) waves with frequencies of the order of ion cyclotron frequency by fast ions appearing in plasma as a result of neutral injection at the cyclotron resonance under the anomalous Doppler effect conditions (Sagdeev-Shafranov instability [3]). AW and FMSW as well as short wavelength ion cyclotron wave excitation by the ion beam with Maxwellian distribution over velocities under the anomalous Doppler-effect conditions was considered previously [4,5] and, recently, in connection with the neutral injection [6].

On tangential injection of neutral beam into the plasma as a result of ionization an ion beam with anisotropic distribution function is formed. If one neglects the scattering of fast ions over angles, their diffusion in velocity space and accounts only for collisional slowing-down by electrons and ions then the steady state distribution function of fast ions has the form[7]

$f(v_\perp, v_\parallel) = 3p\tau_0 [2\pi (v^3 + v_c^3)]^{-1} \delta(\cos\vartheta - \cos\vartheta_0)$, (1)
for $v < v_0$ and $f = 0$ for $v > v_0$, where ϑ_0 is the angle between the injection direction and the magnetic field, $v = \sqrt{v_\perp^2 + v_\parallel^2}$, $\vartheta = \operatorname{arctg}(v_\perp / v_\parallel)$, $v_c = [(3\sqrt{\pi}/4)(m_e/m_i)]^{1/3} v_{Te}$, $\tau_0 = \tau_s / 3$, τ_s is the energy exchange time between the fast ions and plasma, $p = Q/\mathcal{E}_0$, Q is the specific injection power. To obtain (1) for $v \sim v_0$ it is assumed, that $v_{Ti} \ll v \ll v_{Te}$ (for ITER $v_0 \lesssim 1.5 \cdot 10^9$ cm/sec, $v_{Te} \approx 5 \cdot 10^9$ cm/sec, $v_{Ti} \lesssim 10^8$ cm/sec). The conditions for neglecting scattering and diffusion of fast ions imply that $v \gg v_c$. This condition does not hold for ITER parameters chosen ($v_c \approx 10^9$ cm/sec $\sim v_0$). However, the calculations of the fast ion distribution function performed with the account of scattering over angles show that in the region $v \sim v_c \lesssim v_0$ it is numerically close to (1). The deviation is essential only in the velocity region that is considerably less than v_0. Small group of resonant particles with $v \sim v_0$ is responsible for the excitation of waves therefore for estimates we may use $f(v_\perp, v_\parallel)$ in the form (1). Beam density and toroidal electric current density due to ions (which, on neglecting toroidicity for $Z_{eff} = 1$, we consider to be compensated by electrons) accounting for (1) will be $n_b = p\tau_0 \ln(1+\alpha^{-3})$, $j_{\parallel b} = p\tau_0 v_0 \cos\vartheta_0 \chi(\alpha)$, $\chi(\alpha) = 1 - \frac{\alpha}{2}\left[\ln\frac{\sqrt{1-\alpha+\alpha^2}}{1+\alpha} + \sqrt{3}\operatorname{arctg}\frac{\sqrt{3}\alpha}{2-\alpha} + \frac{\pi}{2\sqrt{3}}\right]$, where $\alpha = v_c^3/v_0^3$. For ITER at $\mathcal{E}_0 = 1.5$ MeV, $P_{CD} = 100$ MW and $\cos\vartheta_0 = 0.8$ one obtains $Q = 0{,}1$ W/cm^3, $n_b = 10^{12}$ cm^3, $j_{\parallel b} = 110$ A/cm^2 and total ion current $J_b = j_{\parallel b} \pi a^2 = 25$ MA.

If one neglects the finite Larmor radius effects for plasma ions, then the frequencies and wave vectors of AW's and FMSW's will be connected by the relation

$$\mathcal{M}_0 = \mathcal{N}_\perp^2 (\mathcal{N}_\parallel^2 - \varepsilon_1) + (\mathcal{N}_\parallel^2 - \varepsilon_1)^2 - \varepsilon_2^2 = 0 \qquad (2)$$

and the growth rate is equal to $\gamma_b = \sum_n \gamma_b^{(n)}$, where

$$\gamma_b^{(n)} = \mathcal{M}_b^{(n)} / (\partial \mathcal{M}_0 / \partial\omega)|_{\omega = \omega(\vec{k})},$$

$$\mathcal{M}_b^{(n)} = -\frac{4\pi^2 e^2}{m_b \omega^2} \int d^3v\, v_\perp^2 \left(\frac{n\omega_{cb}}{v_\perp}\frac{\partial f_b}{\partial v_\perp} + k_\parallel \frac{\partial f_b}{\partial v_\parallel}\right) \delta(\omega - k_\parallel v_\parallel - n\omega_{cb}) \Delta, \qquad (3)$$

$$\Delta = \frac{n^2 J_n^2}{s^2} \left[\mathcal{N}^2 (1 + \cos^2\theta) - 2(\varepsilon_1 + \varepsilon_2)\right] - 2\frac{n}{s} J_n J_{n-1} (\mathcal{N}_\parallel^2 - \varepsilon_1 - \varepsilon_2) + J_{n-1}^2 (\mathcal{N}_\parallel^2 - \varepsilon_1),$$

$J_n = J_n(s)$ are Bessel functions, $s = k_\perp v_\perp / \omega_{cb}$, $\mathcal{N}_\parallel = k_\parallel c/\omega$, $\mathcal{N}_\perp = k_\perp c/\omega$,

$\varepsilon_1 = \sum_\beta \omega_{p\beta}^2 / (\omega_{c\beta}^2 - \omega^2)$, $\varepsilon_2 = \sum_\beta (\omega/\omega_{c\beta}) \omega_{p\beta}^2 / (\omega_{c\beta}^2 - \omega^2)$.

For the function (1) formula (3) reads

$$\mathcal{M}_b^{(n)} = -\frac{12\pi^2 e^2 p\tau_0}{m_b \omega^2 / k_\parallel |} \operatorname{tg}\vartheta_0 \left(-n k_\perp \frac{s}{s^3 + s_c^3 \sin^3\vartheta_0} \frac{\partial}{\partial s} s^2 \Delta + \right. \qquad (4)$$

$$\left. + k_\parallel \operatorname{tg}\vartheta_0 \frac{\partial}{\partial s} \frac{s^4}{s^3 + s_c^3 \sin^3\vartheta_0} \Delta\right),$$

$s_c = k_\perp v_c / \omega_{cb}$, $v_\perp = v_\parallel \operatorname{tg}\vartheta_0$, $v_\parallel = (\omega - n\omega_{cb})/k_\parallel$.

These waves are absorbed by electrons and ions of the plasma. The growth rate of the electron Cherenkov damping may be found e.g. in [8]. For ITER $\omega \ll \kappa_{\parallel} v_{Te}$ and $\gamma_e \sim (m_e v_{Te}/m_i v_A)\omega$, and the ion cyclotron damping is essential for AW's at $\Omega = \omega/\omega_{ci} \approx 1$ [8]

$$\gamma_i = (\sqrt{\pi}/2)(1+\cos^2\theta)^{-1/2}(1-\Omega)^{5/2}(v_A/v_{Ti})\exp(-z_i^2),$$

where $z_i = (\omega-\omega_{ci})/\sqrt{2}\kappa_{\parallel}v_{Ti}$, $\cos\theta = \kappa_{\parallel}/\kappa$. To the order of magnitude for AW and FMSW $\omega \sim \kappa_{\parallel} v_A \sim \omega_{ci}$ $(\kappa_{\perp} \sim \kappa_{\parallel})$ and for $v_{\parallel res} = (\omega + n|\omega_{cb}|)/\kappa_{\parallel} \lesssim v_0$

$$\gamma \sim (n_b/n_p)\omega, \quad n = -1, -2, \ldots, \; s \lesssim 1. \qquad (5)$$

For ITER conditions in d-plasma FMSW is not excited because for it the resonant particle velocity $v_{\parallel res} = (\omega + |n|\omega_{cb})/\kappa_{\parallel}$ appears to exceed v_0 whereas for AW $v_{\parallel res}$ is somewhat less than v_0 for $\Omega \approx 0.5 \div 0.7$.

Local consideration is valid if the wavepacket is amplified in its region of localization ΔR, viz.

$$\tau = \operatorname{Im}\kappa \Delta R = \gamma \Delta R / v_{gR} \gg 1, \qquad (6)$$

where $v_{gR} = \partial\omega/\partial\kappa_R$ is the group velocity. In this case the wavepacket on the distance ΔR will attain the nonlinear regime. For ITER $n_b/n_p \sim 10^{-2}$, $\kappa_A = 0.4$ cm^{-1}, $v_{gR} \sim 6\cdot 10^8$ cm/sec, $\Delta R \sim 10^2$ cm, $\tau < 1$ and one obtains that $\tau < 1$ and condition (6) fails. To clear out the question of instability excitation for the case $\tau < 1$ one should consider the problem of global Alfwen waves excitation by the beam in the toroidal tokamak plasma. We discuss this problem in the simplest model of a hollow plasma cylinder $R_0 - a < R < R_0 + a$ in the magnetic field $B_\varphi = B_0 R_0/R$ (a is the small plasma radius, R_0 is the distance between the cylinder axis and the plasma column centre, i.e. the large radius of the torus). For AW $\propto \exp[i(\kappa_z z + l\varphi - \omega t)]$ natural frequencies are determined from the quantization condition

$$\int_{R_1}^{R_2} \kappa_R(R)\,dR = (n + 1/2)\pi, \quad (n \gg 1), \qquad (7)$$

where R_1, R_2 are the reflection points for AW ($\kappa_R = 0$ for $R = R_{1,2}$), $\kappa_R = (\omega^2 N_\perp^2/c^2 - \kappa_\varphi^2 - \kappa_z^2)^{1/2}$, $\kappa_\varphi = l/R$.

The instability in this case is absolute and its growth rate is equal to (see also [9])

$$\gamma^{(n)} = \frac{\omega^2}{2c^2}\int_{R_1}^{R_2}\frac{dR}{\kappa_R}\,\frac{D^{(n)}(R)}{(\varepsilon_\parallel - N_\parallel^2)^2}\left[\int_{R_1}^{R_2} dR\,\partial\kappa_R/\partial\omega\right]^{-1}, \qquad (8)$$

$$D^{(n)}(R) = \frac{4\pi^2 e^2}{m_b\omega^2}\int d^3v\, v_\perp^2\left(\frac{n\omega_{cb}}{v_\perp}\frac{\partial f_b}{\partial v_\perp} + \kappa_\parallel\frac{\partial f_b}{\partial v_\parallel}\right)\left[(\varepsilon_\parallel - N_\parallel^2)J_n' - \varepsilon_2\frac{n}{s}J_n\right]^2\delta(\omega - \kappa_\parallel v_\parallel - n\omega_{cb}).$$

For ITER conditions the growth rate (8) coincides with (5) to the order of magnitude. If one of the reflection points for AW is absent (it occurs when there is a point inside the plasma $R = R_\infty$ where $\varepsilon_\parallel = N_\parallel^2$) then at $R = R_\infty$ the conversion of AW to the short wavelength kinetic AW takes place. The dispersion of these waves is determined in this region by the equation

$$N_{\perp\pm}^2 = \left[\varepsilon_1 - N_\parallel^2 \pm \sqrt{(\varepsilon_1 - N_\parallel^2)^2 + 4A\varepsilon_2^2}\right]/2A, \quad (9)$$

where $A = \varepsilon_1^2 \frac{\omega^2}{\omega_{pe}^2}\frac{v_{Te}^2}{c^2} + \sum_\beta \frac{\omega_{p\beta}^2}{\omega_{c\beta}^2 - \omega^2}\frac{3\omega^2}{4\omega_{c\beta}^2 - \omega^2}\frac{v_{T\beta}^2}{c^2}$.

If one departs from the conversion point in the weak density direction the expression (9) reduces to (2) in which $\varepsilon_1 \approx N_\parallel^2$ and if one moves in the large density direction $N_\perp^2$ grows: $N_\perp^2 = (\varepsilon_1 - N_\parallel^2)/A$. Sufficiently far from the point $R = R_\infty$ the magnitude κ_R becomes large $\kappa_R \sim \omega_{ci}/v_{Ti}$, in this region $\kappa_\perp$ is determined from the equation

$$\mathcal{D}^{(o)} = \varepsilon_{11} + N_\parallel^2\left[N^2(\kappa_\parallel v_{Te}/\omega_{pe})^2 - 1\right]^{-1} = 0, \quad (10)$$

where $\varepsilon_{11} = \frac{\omega_{pi}^2}{\kappa^2 v_{Ti}^2}\left[1 - \sum_n A_n \omega/(\omega - n\omega_{ci})\right]$, $A_n = e^{-\mu} I_n(\mu)$,

Local growth rate is equal to $\gamma = \gamma_6 - \gamma_e$, $\mu = \kappa_\perp^2 v_{Ti}^2/\omega_{ci}^2$. where

$$\gamma_6 = \delta\varepsilon_{11}/(\partial\mathcal{D}^{(o)}/\partial\omega),$$

$$\gamma_e = \sqrt{\pi}\,\frac{\omega/\sqrt{2}\kappa_\parallel v_{Te}}{\partial\mathcal{D}^{(o)}/\partial\omega}\,\frac{N_\parallel^2 N^2(\kappa_\parallel v_{Te}/\omega_{pe})^2}{\left[N^2(\kappa_\parallel v_{Te}/\omega_{pe})^2 - 1\right]^2}, \quad (11)$$

$$\delta\varepsilon_{11} = -\frac{4\pi^2 e^2}{m_6\omega^2}\int d^3v\, v_\perp^2\left(\frac{n\omega_{c6}}{v_\perp}\frac{\partial f_6}{\partial v_\perp} + \kappa_\parallel\frac{\partial f_6}{\partial v_\parallel}\right)\frac{n^2 J_n^2}{s^2}\,\delta(\omega - \kappa_\parallel v_\parallel - n\omega_{c6}).$$

To the order of magnitude at $\kappa_\perp v_{Ti} \sim \omega_{ci}$ we obtain for ITER that

$$\gamma_6/\omega \sim (n_6 v_A/n_p v_\parallel)(v_{Ti}/v_\perp)^3 < 10^{-4},$$

$$\gamma_e/\omega \sim \omega/\kappa_\parallel v_{Te} \sim v_A/v_{Te} \sim 10^{-1},$$

i.e. the small scale ion cyclotron waves in the region $\kappa_\perp v_{Ti} \sim \omega_{ci}$ are strongly damped and their excitation is impossible.

References

1. H.L.Berk et al. Nuclear Fusion, 15, N5, 819 (1975).
2. N.Fujisawa, Summary Report of Neutral Beam ITER CD and Heating Techn.Meeting, July, (1988).
3. R.Z.Sagdeev, V.D.Shafranov, ZhETF, 39, 181 (1960) (In Russian).
4. A.B.Kitsenko, K.N.Stepanov, ZhTF, 31, 167 (1961) (In Russian).
5. D.G.Lominadze, K.N.Stepanov. Nuclear Fusion, 4,281 (1964).
6. S.-I.Itoh et al. Plasma Phys.Contr.Fus.26,N11, 1311 (1984).
7. J.G.Gordey, M.J.Houghton, Nuclear Fusion, 13,N2,215(1973).
8. A.I.Akhiezer et al. Plasma Electrodynamics, Pergamon Press, vol.1 (1975).
9. B.Coppi et al. Phys.Fl. 29 (12), 4060 (1986).

NONLINEAR TRANSFORMATION OF ALFVEN WAVES.

V.P.Sidorov, T.R.Soldatenkov, V.S.Tsypin.
Sukhumi Institute of Physics and Technology, Sukhumi, USSR.

Linear transformation of waves over the Alfven frequency range ($\omega \simeq K_{\parallel} C_A$) is studied thoroughly enough for the present (see Refs. /1/,/2/ and the References cited therein). A theory of linear transformation of a fast Alfven wave (FAW) into a short-wavelength slow mode (SAW) which is afterwards electron-absorbed due to Landau damping serves as a basis for high-frequency (HF) plasma heating concepts. Practically always, the HF field amplitude attains large values close to the points of linear transformation and, therefore, near these points, development of nonlinear processes should be expected. In the present paper, the electrical wave field effect on dispersion properties of plasma is studied.

In the generally accepted approach for deriving the dispersion equation, we take nonlinear terms into consideration. For a cold plasma, within the geometrical optics approximation, we have a system of equations (in x , y , z coordinates, $\vec{B}_0 = \vec{e}_z B_0$; the x -coordinate is chosen along the wave vector $\vec{K}_\perp$):

$$(N^2 \delta_{ik} - N_i N_k - \varepsilon_{ik}^{(s)}) E_k^{(s)} = U_i^{(s)} , \qquad (1)$$

where the harmonics number is $s = \pm 1, \pm 2$; $\vec{N} = \frac{c\vec{K}}{\omega}$.

Such being the case,

$$\vec{U}^{(\pm 1)} = \pm \frac{4\pi i}{\omega} \sum_\alpha e_\alpha n_{0\alpha} \left\{ \vec{v}_{\alpha\pm 1}^{(n)} + \frac{\vec{v}_{\alpha\mp 1}^{(\ell)}}{c} \left[\left(\vec{N} \vec{v}_{\alpha\pm 2} \right) + \frac{1}{c} \left(\vec{N} \vec{v}_{\alpha\pm 1}^{(\ell)} \right)^2 \right] + \right.$$
$$\left. + \frac{\vec{v}_{\alpha\pm 2}}{c} \left(\vec{N} \vec{v}_{\alpha\mp 1}^{(\ell)} \right) \right\} ; \qquad \vec{v}_{\alpha s} = \vec{v}_{\alpha s}^{(\ell)} + \vec{v}_{\alpha s}^{(n)} ;$$

$$\vec{U}^{(\pm 2)} = \pm \frac{2\pi i}{\omega} \sum_\alpha e_\alpha n_{0\alpha} \left\{ \vec{v}_{\alpha\pm 2}^{(n)} + \frac{\vec{v}_{\alpha\pm 1}^{(\ell)}}{c} \left(\vec{N} \vec{v}_{\alpha\pm 1}^{(\ell)} \right) \right\} ; \qquad (2)$$

$$\vec{v}^{(\ell)}_{\alpha s} = \left(1 - \frac{s^2\omega^2}{\omega^2_{B\alpha}}\right)^{-1} \frac{c}{B_0}\left\{\left[\vec{E}, \vec{e}_z\right] - \frac{is\omega}{\omega_{B\alpha}}\vec{E}^{(s)}_{\perp}\right\} + \frac{ie_\alpha}{s\omega M_\alpha}\vec{e}_z E^{(s)}_{\parallel},$$

$$\vec{v}^{(n)}_{\alpha s} = \left(1 - \frac{s^2\omega^2}{\omega^2_{B\alpha}}\right)^{-1} \frac{1}{\omega_{B\alpha}}\left\{\left[\vec{D}^{(n)}_{\alpha s}, \vec{e}_z\right] - \frac{is\omega}{\omega_{B\alpha}}\vec{D}^{(n)}_{\alpha s\perp}\right\} + \frac{i}{s\omega}\vec{e}_z D^{(n)}_{\alpha s\parallel},$$

$$\vec{D}^{(n)}_{\alpha\pm 1} = \pm\frac{i\omega}{c}\left\{\vec{v}^{(\ell)}_{\alpha\mp 1}\left(\vec{N}\vec{v}_{\alpha\pm 2}\right) - 2\vec{v}_{\alpha\pm 2}\left(\vec{N}\vec{v}^{(\ell)}_{\alpha\mp 1}\right)\right\} + \frac{e_\alpha}{M_\alpha c}\left\{\vec{N}\left(\vec{v}_{\alpha\pm 2}\vec{E}^{(\pm 1)}\right) + \right.$$

$$\left. + 2\vec{N}\left(\vec{v}^{(\ell)}_{\alpha\mp 1}\vec{E}^{(\pm 2)}\right) - \vec{E}^{(\pm 1)}\left(\vec{N}\vec{v}_{\alpha\pm 2}\right) - 2\vec{E}^{(\pm 2)}\left(\vec{N}\vec{v}^{(\ell)}_{\alpha\mp 1}\right)\right\},$$

$$\vec{D}^{(n)}_{\alpha\pm 2} = \mp\frac{i\omega}{c}\vec{v}^{(\ell)}_{\alpha\pm 1}\left(\vec{N}\vec{v}^{(\ell)}_{\alpha\pm 1}\right) + \frac{e_\alpha}{M_\alpha c}\left\{\vec{N}\left(v^{(\ell)}_{\alpha\pm 1}\vec{E}^{(\pm 1)}\right) - \vec{E}^{(\pm 1)}\left(\vec{N}\vec{v}^{(\ell)}_{\alpha\pm 1}\right)\right\}.$$

From Eq. (1) it follows that the dispersion harmonics may be reduced to:

$$\Delta_1 = \left(A_1 + A_2/\Delta_2\right)\left|E_{\pm 1x}\right|^2, \tag{3}$$

where

$$\Delta_s = \varepsilon_1^{(s)} N_\perp^4 + \left[\left(\varepsilon_1^{(s)} + \varepsilon_3^{(s)}\right)\left(N_\parallel^2 - \varepsilon_1^{(s)}\right) + \varepsilon_2^{(s)2}\right] N_\perp^2 + \tag{4}$$

$$+ \varepsilon_3^{(s)}\left[\left(N_\parallel^2 - \varepsilon_1^{(s)}\right)^2 - \varepsilon_2^{(s)2}\right],$$

while the right-hand side in Eq. (3) is a nonlinear contribution.

Expressions for second harmonics, $\vec{E}^{(\pm 2)}$, as it is seen from Eq. (1), have the following shape

$$\vec{E}^{(\pm 2)} = f\left(\vec{U}^{(\pm 2)}, \hat{\varepsilon}^{s}, N_\perp, N_\parallel\right)\Big/\Delta_2 . \tag{5}$$

The denominator, Δ_2, in Eq. (5), may turn into zero for certain values of the X-coordinate, i.e., the birth of second harmonics may be of resonance type. These points are found as follows. From the condition for Δ_1 and Δ_2 to be nullified, one derives an equation to define the values of

N^2 at the points of resonance:

$$aN^6+bN^4+cN^2+d=0, \qquad (6)$$

where

$$a=\frac{\varepsilon_3^{(3)}}{\varepsilon_1^{(3)}}-\frac{\varepsilon_3^{(K)}}{\varepsilon_1^{(K)}}, \quad b=\frac{\varepsilon_3^{(3)}\varepsilon_3^{(K)}}{\varepsilon_1^{(3)}\varepsilon_1^{(K)}}\left(\varepsilon_1^{(3)}-\varepsilon_1^{(K)}\right)-2\left(\varepsilon_3^{(3)}-\varepsilon_3^{(K)}\right)+\beta_3\frac{\varepsilon_3^{(K)}}{\varepsilon_1^{(K)}}-\beta_K\frac{\varepsilon_3^{(3)}}{\varepsilon_1^{(3)}},$$

$$c=\frac{\varepsilon_3^{(3)}\varepsilon_3^{(K)}}{\varepsilon_1^{(3)}\varepsilon_1^{(K)}}\left(\varepsilon_1^{(K)}\beta_K-\varepsilon_1^{(3)}\beta_3\right)+\left(\varepsilon_3^{(3)}-2\varepsilon_3^{(K)}\right)\beta_3-\left(\varepsilon_3^{(K)}-2\varepsilon_3^{(3)}\right)\beta_K,$$

$$d=\varepsilon_3^{(3)}\varepsilon_3^{(K)}\left(\beta_3-\beta_K\right)-\left(\varepsilon_3^{(3)}-\varepsilon_3^{(K)}\right)\beta_3\beta_K, \qquad \beta_3=\frac{\varepsilon_1^{(3)2}-\varepsilon_2^{(3)2}}{\varepsilon_1^{3}}.$$

The coefficients a and d are small as well as $\mu=m_e/m_i$ with respect to b and c. Therefore, the roots may be found by means of sequential approximations. The root

$$N^2=-\frac{d}{c}-\frac{bd^2}{c^3} \qquad (7)$$

is of greatest interest (within the accuracy of μ). In what follows, we shall take note of this root. The remaining pair of roots lie either within the region of strong skinning or beyond the Alfven frequency interval.

Plasma density values at the point of resonance are found from the condition:

$$N_{\parallel}^2\simeq\frac{1}{2}\left(\varepsilon_1^{(3)}+\varepsilon_1^{(K)}-\frac{\varepsilon_2^{(3)2}}{\varepsilon_1^{(3)}}-\frac{\varepsilon_2^{(K)2}}{\varepsilon_1^{(K)}}\right), \qquad (8)$$

while $N_\perp^2\simeq -N_{\parallel}^2$.

Calculations of harmonics (Eq. 5) amplitudes (and, as a consequence, those of the coefficient for transforming first harmonics into second ones) result in the following expressions:

$$E_x^{(\pm2)}=\mp\frac{i}{\Delta_2}\frac{\gamma^6\mu N_\perp}{4\gamma(1-4\gamma^2)}\frac{E_x^{(\pm1)2}}{B_0}(1-3\gamma^2)(1+4\gamma^2),$$

$$E_y^{(\pm2)}=\frac{3}{2}\frac{\gamma^6}{\Delta_2(1-4\gamma^2)^2}\frac{E_x^{(\pm1)2}}{B_0}(1-5\gamma^2-4\gamma^4), \qquad (9)$$

$E_z^{(\pm 2)} \sim \mathcal{M}\left(E_x^{(\pm 2)}, E_y^{(\pm 2)}\right)$; $\quad \gamma = \frac{c}{c_A}$, $\quad \nu = \frac{\omega}{\omega_{Bi}}$.

Resonant generation of second harmonics may be considerable due to smallness of the resonance denominator, . The coefficients, A_1 and A_2 in Eq. (3) are of the following types:

$$A_1 = \gamma^{12} N_\perp^2 (1-8\nu^2) \Big/ \nu^2 B_0^2 (1-\nu^2)(1-4\nu^2)^3,$$
$$A_2 = 2\gamma^6 N_\perp^2 \Big/ \mathcal{M} B_0^2 (1-\nu^2)(1-4\nu^2). \qquad (10)$$

Thus, it follows from the dispersion equation (Eq. 3) analysis, with Eq. (10) taken into consideration, that alongside with the gyrotropy, there exists an additional coupling between fast Alfven waves and slow ones due to nonlinear effects and, as a result, nonlinear transformation of Alfven waves may take place. Near the points with $\Delta_2 = 0$, this coupling is of resonant character. Here, second harmonics of HF fields are generated via resonances. It is seen from the analysis of Exps. (9) and (10) that for $\omega = \omega_{Bi}/2$ second harmonic amplitudes and nonlinear coupling between FAW and SAW may become intensified.

REFERENCES.

1. T.Stix, D.Swanson. Foundations of Plasma Physics edited by R.Z.Sagdeev and M.Rosenbluth, Moscow, Energoizdat publishers, vol. 1, pp. 283-333.
2. A.G.Elfimov, A.G.Kirov, V.P.Sidorov. High-Frequency Plasma Heating, 1983. Gorky All-Union Conference Proceedings, p. 211.

EFFECTS OF TOKAMAK PLASMA PRESSURE ON DISCRETE SPECTRUM OF ALFVÉN WAVE

Qiu Xiaoming ang Xue Siwen

(Southwestern Institute of Physics, P.O.Box 15,
Leshan, Sichuan, P.R.China)

Based on ideal MHD equations including a term of plasma pressure, in the cylindrical approximation of tokamak configuration, an eigen-equation for the radial displacement of Alfvén wave perturbation is derived as follows

$$\frac{d}{dr}\left[\left(1+\frac{\Gamma\beta}{2}\cdot\frac{A}{\rho\omega^2}\right)\frac{B^2A}{N_i}\cdot\frac{1}{r}\frac{d}{dr}(r\xi_r)\right]+\left(\mu_0A-r\frac{d}{dr}\left(\frac{B_\theta}{r}\right)^2\right.$$

$$\left.-\left(1-\frac{\Gamma\beta}{2}\cdot\frac{F^2}{\mu_0\rho\omega^2}\right)\cdot\frac{4k^2B^2B_\theta^2}{\mu_0N_i\gamma^2}+\frac{r}{\mu_0}\frac{d}{dr}\left[\left(1+\frac{\Gamma\beta}{2}\cdot\frac{A}{\rho\omega^2}\right)\cdot\frac{2kB_\theta GB^2}{N_ir^2}\right]\right)\xi_r=0 \qquad (1)$$

where $N_i=N-\frac{\Gamma\beta}{2}\frac{A}{\rho\omega^2}\frac{F^2+G^2}{\mu_0}$,

and other symbols are the same as Ref. [1]. Eq.(1) reduces to the basic equation (2) in Ref. [1] when β tends to zero. On performing a WKB analysis of this equation we obtain the dispersion relation of Alfvén wave discrete spectrum

$$\omega^2=\omega_A^2-\frac{1}{\mu_0\rho k_r^2}\left[\left(\frac{G}{B}\right)^2r\frac{d}{dr}\left(\frac{B_\theta}{r}\right)^2+\left(\frac{G}{B}\right)^2r\frac{d}{dr}\left(\frac{2kB_\theta B^2}{r^2G}\right)-4k^2\left(\frac{B_\theta}{r}\right)^2\right.$$

$$\left.\cdot\left(1-\frac{\Gamma\beta}{2}\right)\right] \qquad (2)$$

where k_r is radial wavenumber.

From Eqs.(1) and (2), one sees that the effect of plasma β on Alfvén wave discrete spectrum appears to be less because of $\Gamma\beta/2$ is small.

However, it should be noted that the poroidal field B_θ varies with plasma pressure because the relation between B_θ and p is determined by the equilibrium equation $\nabla p=\vec{J}\times\vec{B}$. Therefore, the effects of plasma pressure(or β) on Alfvén wave discrete spectrum, as we see it, could not be small. In the present paper, we concentrate our attention onto this point. For this purpose, we choose the following profiles of the equilibrium current and density

$$J_\theta=0, \qquad J_z=J_z(0)(1-x^2)^{\kappa_1},$$

$$\rho=\rho(0)\{(1-\Delta)[1-x^2]^{\kappa_2}+\Delta\},$$

where $x=r/a$, a is the minor radius of tokamak plasma and the exponents κ_1 and κ_2 are free parameters. In order to calculate the dependence of Alfvén wave discrete spectrum on plasma β we indroduce a new parameter $\alpha=1/q(0)$ ($q(0)$ is satefy factor at the center of tokamak plasma) instead of β. According to Amper's law

$$\oint\vec{B}\cdot d\vec{l}=\int\vec{J}\cdot d\vec{s},$$

$$B_\theta=\frac{\mu_0 J_z(0)a}{2(\kappa_1+1)}\frac{1}{x}[1-(1-x^2)^{\kappa_1+1}]$$

and $J_z(0)$ is determined from α

$$\alpha=\frac{R}{B_t}\left(\frac{B_\theta}{r}\right)\Big|_{r=a}=\frac{\mu_0 J_z(0)a}{2}\cdot\frac{1}{B_t\epsilon}\qquad\left(\epsilon=\frac{a}{R}\right),$$

where R is the major radius of tokamak plasma. In follows that

$$B_\theta=\frac{\alpha\epsilon B_t}{(\kappa_1+1)}[1-(1-x^2)^{\kappa_1+1}]\frac{I}{x}.$$

In the cylindrical approximation of tokamak configuration, the equilibrium equation $\nabla p=\vec{J}\times\vec{B}$ reduces to

$$-\frac{dp}{dx}=J_z\cdot B_\theta.$$

Solving this equation yields

$$p(x)=p(1)+\frac{\alpha^2\epsilon^2B_t^2}{\mu_0(\kappa_2+1)}\sum_{i=1}^{\kappa_2+1}\frac{(1-x^2)^{\kappa_1+i}}{\kappa_2+i}$$

From the definition

$$\beta=\frac{2\mu_0 p}{B^2},\qquad \beta(0)=\frac{2\alpha^2\epsilon^2}{(\kappa_2+1)}\sum_{i=1}^{\kappa_2+1}\frac{1}{\kappa_2+i},$$

where boundary pressure is ignored. It shows that β increases with α-increasing. In addition, from Suydam criterion we have

$$\alpha < \frac{\kappa_i}{8 \cdot \epsilon} .$$

In the present case, the position n_c' of accumulation point is determined by $n_c' = \alpha \cdot n_c$, where n_c is the position of accumulation point on the coordinate axis for the toroidal mode number n defined in Ref. [1]. This indicates that, with α-varying, the discrete spectra of Alfvén wave move upon the coodinate axis for toroidal mode number n.

We have employed the finite element method[2] to calculate the discrete spectra of Alfvén wave for α=0.8, 1, 1.5, respectively. In the numerical calculation we choose the following values for the parameters

$$\kappa_i = 4 , \qquad \kappa_p = 1 ,$$
$$B_t = 1 , \qquad \Delta = 0.05 ,$$
$$R = 1 , \qquad \epsilon = 0.2787 .$$

The calculated results are shown as Figs. 1—4, where Fig.4 corresponds to Fig. 2 in Ref. [1]. Our numerical results also verify the moving mentioned above. However, the calculated results exhibit that the effect of plasma pressure on the shape of discrete spectra is not obvious.

References

1. K. Appert, et al., Plasma Phys. 24(1982)1147.
2. K. Appert, et al., Computer Physics Communications 10(1975)11.

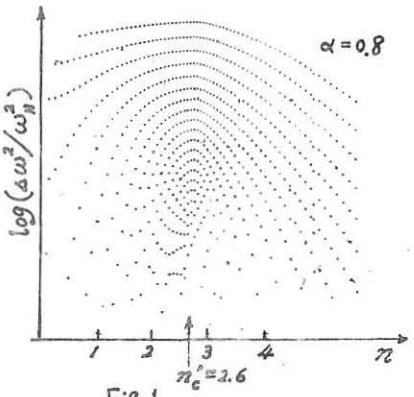

Fig. 1

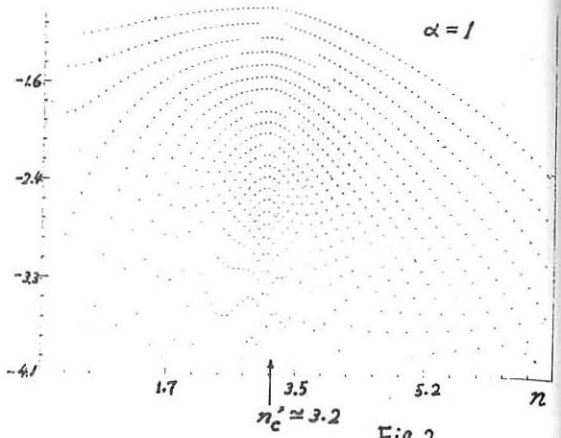

Fig. 2

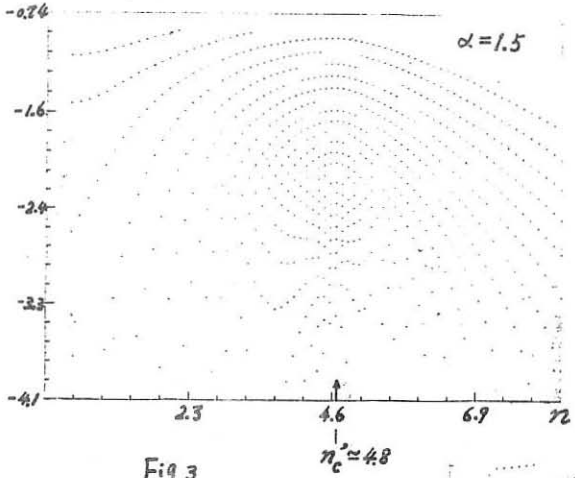

Fig. 3

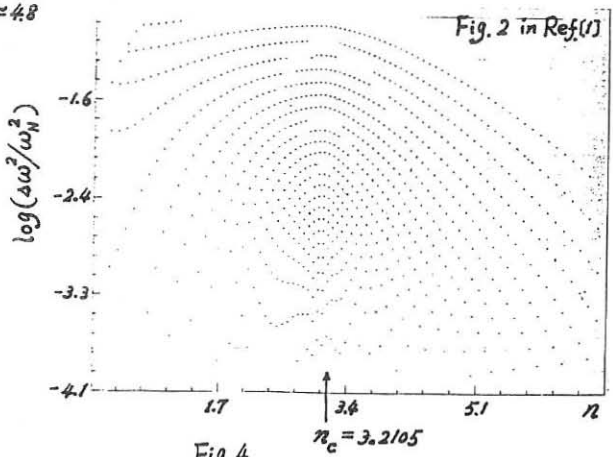

Fig. 4

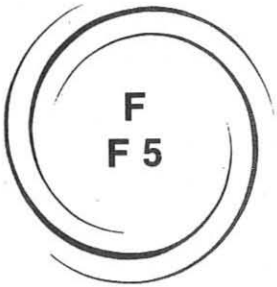

PLASMA HEATING AND CURRENT DRIVE

NEUTRAL BEAM HEATING (NBH)

NEUTRAL BEAM HEATING OF TEXTOR

H. Conrads, H. Euringer, F. Hoenen, G. Fuchs, H. Kever, M. Lochter
U. Samm, J. Schlüter, H. Soltwisch, J. Ongena*, R. Uhlemann, G. Waidmann,
** G. Wang, G. Wolf, TEXTOR-Team, ALT-Team, NBI-Team, ICRH-Team*

Institut für Plasmaphysik, Kernforschungsanlage Jülich GmbH
* Association KFA/EURATOM, P.O.B. 1913, 5170 Jülich, FRG
Koninklijke Militaire School, Laboratorium voor Plasmafysica
** Ave. de la Renaissance 30, 1040 Brüssel, Belgien
Southwestern Institute of Physics, P.O.Box 15, Leshan, Sichuan
People's Republic of China

Introduction

The TEXTOR Tokamak has been designed for technology oriented research /1/ and is extensively used for systematic studies of the plasma adjacent to the limiters and wall and for the application and the development of novel limiters and coatings of surfaces facing the plasma. Carbonization /2/ and boronization /3/ of liner and limiters and the pump limiters ALT I /4/ and ALT II /5/ are some of the improvements of the last years.

It is intended for the TEXTOR programme to have the plasma boundary layer and the loads to the limiters close to the conditions in large devices as JET, DIII - D, JT60, and TFTR. ICR-heating of TEXTOR increased the loads to the liner and the limiters significantly /6/. The addition of neutral beams of similar power will enlarge the range of parameters further. This paper presents first results of plasma heating in TEXTOR by two neutral beams, each of 1.2 MW power at 47 kV, with co, counter, or balanced injection of hydrogen into a deuterium plasma tangentially.

Performance of the Neutral Beams

Each beamline is equipped with one ion source of the type "JET-PINI", which was modified in reducing the number of grids to three and in enlarging the extraction area of the arc, which required a rearrangement of the permanent magnets to a checker-board configuration for full illumination of the extraction grid. The rated data are: 55 kV, 88 A, i.e. 4.8 MW over 10 sec. The final qualification tests of the beam lines delivered the following data of the sources /7/ as used for this paper:

Beam voltage:	47 kV
beam current:	73 A
total beam power:	3.4 MW
neutral beam power:	1.16 MW
pulse length:	3.4 sec
divergence:	0.95 degree
beam diameter:	0.3 m at plasma penetration
species fraction:	61 : 23 : 16 % (H+, H2+, H3+)

The different losses of the ion- and neutralized beam respectively in travelling from the source to the torus i.e. the beam tansmission have been measured by calorimetric methods. An overview of results is given in figure 1.

Plasma Parameters during Co-Injection

Most of the results obtained so far are found from hydrogen co-injection. Fig.2 shows the central electron temperature measured by the electron cyclotron radiation, the central density taken by an HCN-interferometer, the plasma current, and the global neutron yield, all as functions of time during injection starting 0.3 sec after plasma build-up and lasting over 2.7 sec. The injection is overlapping the current build-up, and decay phase, i.e. covers the whole flat top phase (at 460 kA), which could be stretched by 0.5 sec compared to the ohmically heated plasmas. The toroidal field amounted to 2.25 T and the plasma radii were 1.82 m and 0.40 m respectively. The response of the electron and ion temperatures - the latter deduced from the global neutron emission - to the onset of injection are prompt, whereas the density evolution is more closely following the plasma current. Time integrated neutron spectra taken by a novel ionization chamber delivered peak ion temperatures of 1.6 keV.

During the 2.7 sec of injection, the number of injected particles into the plasma is about 4xE20 particles. The total number of particles in the plasma never exceeds 3xE20. The ratio of hydrogen- to deuterium-fluxes close to the wall indicates that fuelling of the plasma by hydrogen from the beam contributes less than 20 %.

During injection the plasma remains free of contaminations as found by space and time resolved bolorimetric measurements, shown in figure 3. The radiation close to 0.3 m of minor radius remains 100 mW per cc, i.e. about 400 kW for the annulus. The emission of the plasma core remains below the sensitivity of the bolometer, i.e. below 10 mW per cc for all time slots taken up to 2.7 sec. The total power input was 1.5 MW. The total plasma energy measured by the compensated magnetic loop remains close to 85 kJ over 2 sec, and the energy confinement time never drops below 55 ms.

Temperature and Density Profiles during Combined Co- and Counter-Injection

Figure 4 shows the profiles for 6 characteristic phases prior to injection (A), during counter - (B), counter/co- at the beginning (C), and close to the end (D), co-injection (E), and the late ohmic phase of the discharge (F). All data are taken at the time of peak amplitude of the sawteeth. Each beam had 1 MW power at 47 kV.The central electron temperature is doubled. The temperature gradient stays constant inboard, whereas outboard it steepens with increasing power. The density profiles within 80 % of the minor radius show a similar but weaker trend. T_e reaches the highest value always at the beginning of the combined heating, whereas the maximum of the density occurs later and seems to be more determined by the inventory of the wall. For the discharge shown in figure 4, density peaks occur at the end of combined injection. The temperature profiles retain regions of concave curvature during all phases. This indentation of the profile close to the q=1 surface is considered to be essential for the existence of $q<1$ values on axis /8/. The density profiles show this indentation only during the early phase of heating. The differences in the temperature and density profiles during co- and counter-injection (phase (E) and (B) respectively) are small and so are the changes in energy confinement.

Confinement and Fluxes to the Wall

The energy confinement time during an ohmically heated discharge in a carbonized TEXTOR with wall temperatures well above 300 C is typically 120 ms. By applying 1 MW of co- or counter-injection into TEXTOR, the average value of energy confinement time is about one half of the above value. Two MW of balanced injection reduces this value to one third. Figure 5 shows the measured density dependence of the energy confinement time for different discharges with currents between 220 kA to 460 kA. For comparison the calculated dependence of energy confinement time on the density is added according to the Kaye-Goldston scaling /9/. At the highest plasma current, the confinement times achieved with co-injection are in agreement with Kaye-Goldston, whereas for lower currents, when part of the current may be generated by the neutral beam, confinement is significantly better than Kaye-Goldston predictions.

The particle fluxes measured at the limiter /10/ increase during combined heating by a factor 5, i.e. by the same amount as the additional power. The assumption that the flux is proportional to the added heating power is consistent with the measured radiation losses as a function of the plasma density shown in figure 6. Contrary to ohmically heated plasmas, the radiation losses remain small with increasing density. The loads to the ALT-II blades /11/ are increased by more than a factor 20 compared to an ohmically heated plasma. The boundary layer in TEXTOR now is getting closer to the conditions of the boundary layer of JET. The measurements in TEXTOR suggest that heat transfer from the plasma to the wall during neutral beam heating occurs primarily at the limiters of TEXTOR.

/1/ H. Conrads, Proc. 10th Symp. on Fusion Technology (1978), Vol 1, pp 25-31, Pergamon Press
/2/ J. Winter, J. Nucl. Mat. 145-147 (1987), p. 131
/3/ F. Waelbroeck et al., Plasma Physics and Controlled (15th EPS-Meeting on Plasma Physics) 30 to be published 1989
/4/ K.H. Dippel et al., J. of Nucl. Materals 145-147 (1987), pp 3-14
/5/ D.M. Goebel et al., to be published in J. of Nucl. Materials 1989
/6/ R. Weynants et al., IAEA-CN-50/E-2-1, Nice 1988, to be published in Nuclear Fusion 1989
/7/ R. Uhlemann et al., Proc. 15th Symp. on Fusion Technology (1988) to be published by North Holland 1989
/8/ H. Soltwisch et al., Proc. 11th Int. Conf. Plasma Physics and Controlled Fusion Research, Kyoto 1986, Vol 1, p. 263
/9/ S.M. Kaye, R.I. Goldston, Nuclear Fusion, Vol 25, No. 1, 1985, p. 65
/10/ U. Samm et al., this conference
/11/ J. Watkins et al., this conference

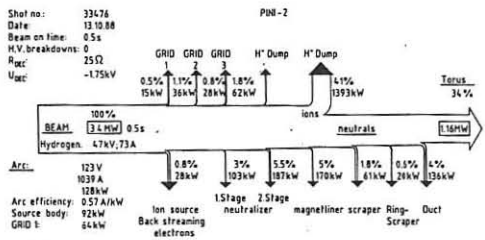

Fig.1

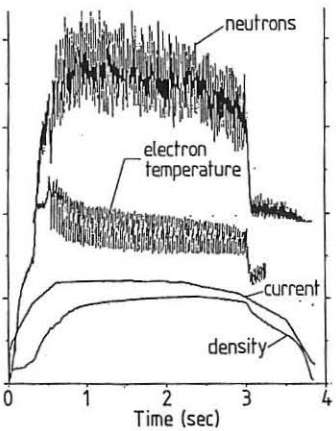

Fig.2

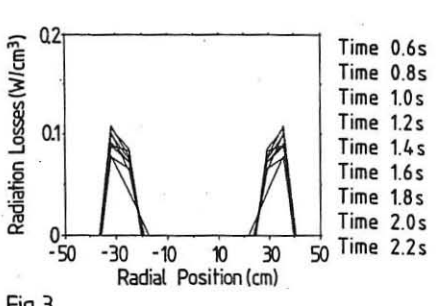

Fig.3

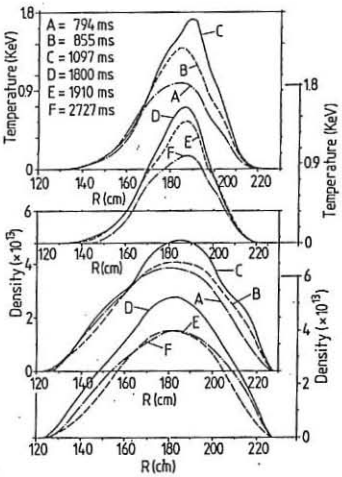

Fig.4

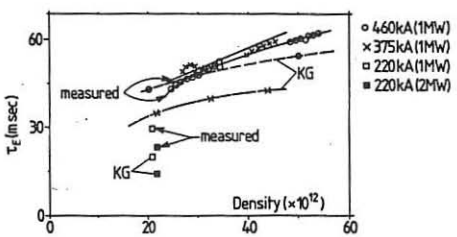

Fig.5

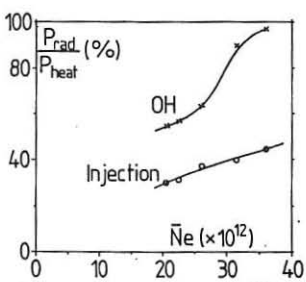

Fig.6

FAST IONS LOSSES DURING NEUTRAL BEAM INJECTION IN TORE-SUPRA

P. Grua and J.P. Roubin

Association EURATOM-CEA sur la Fusion Contrôlée
CEN Cadarache B.P. n°1, 13108 Saint-Paul-lez-Durance, France

INTRODUCTION

Future neutral beam injection experiments in the Tore-Supra tokamak have two charasteristics of major importance concerning fast ions confinement: a high toroidal field ripple and a quasi-perpendicular injection angle. We present a Fokker-Planck calculation of the fast ions losses occuring in such a configuration. Then, we test the sensitivity of these losses to various plasma parameters, and we determine the most favorable heating scenarios.

NBI AND TOROIDAL FIELD RIPPLE IN TORE-SUPRA

The Tore-Supra neutral beam injection system [1] will have a total power capability of 9 MW (D^0, 100 keV) or 4 MW (H^0,80 keV). Two boxes are in co and one in counter-injection. Each box provides two beams in a quasi perpendicular injection geometry: Tangency major radius of the beams R_T=1.24 m (R_{axis} = 2.44 m, α_{axis}=60°). The beam ions born between the outer edge (plasma minor radius a=0.80 m) and r=0.25 m execute banana orbits.

The toroidal field created by the 18 superconducting coils has a high toroidal modulation going from $\delta=2\ 10^{-4}$ up to $\delta=7\ 10^{-2}$ at the outer edge. As a consequence, for standard discharges (I_p=1.7 MA), there is an important zone inside the plasma where local magnetic wells exist along field lines. In this region, the ripple is "effective" ($\delta^*>0$) and the beam ions on banana orbits can entrap the local magnetic wells [2] and leave the plasma before their complete thermalisation. Figure 1 shows the flux surfaces, the contour $\delta^*=0$ where the modulation along a field line vanishes and the position of the banana tips of fast ions first orbits.

FOKKER-PLANCK CALCULATION OF FAST ION LOSSES

We have developed a Fokker-Planck calculation in order to test the sensitivity of the ripple losses to plasma and beam parameters. A complete description of this code, a comparison with Monte-Carlo simulations and with TFR experimental results can be found in [3]. The present version of the code includes improvements concerning the magnetic configuration description (Shafranov shift, horizontal and vertical displacements) and the modelisation of the ripple losses operator. Our calculation is based on the stationnary Fokker-Planck equation for fast ions:

$$\frac{1}{\tau_s v^2}\frac{\partial}{\partial v}(v^3+v_c^3)f + \frac{1}{2\tau_{ii}}\frac{\partial}{\partial \mu}(1-\mu^2)\frac{\partial}{\partial \mu}f + \dot{n}_b\,\delta(v-v_0)\delta(\mu-\mu_0)/\,2\pi v_0^2 + R(f) = 0$$

where τ_s, τ_{ii} are the slowing down and ion-ion collision times, v_c is the critical velocity and $\mu=v_{//}/v$. The first and second terms represent collisionnal effects: drag and angular scattering in the Legendre operator approximation (the energy diffusion is neglected). The third term is the source and the fourth is an operator modelling the ripple losses. In the previous version of the code [3], it is simply written as $R(f)= - f /<\tau_r>$ where $<\tau_r>$ is an averaged ripple loss time. This operator applies the losses to the whole distribution function, whereas only the trapped ions are concerned: this leads to overestimate the losses, especially in the case of tangential injection. To overcome this difficulty, we now write the operator as $R(f)=W(\mu,\mu_{trap})f/<\tau_r>$, where $W(\mu,\mu_{trap})$ is defined by $W=1$ for $\mu<\mu_{trap}$ and $W=0$ for $\mu>\mu_{trap}$, and applies the losses to the trapped ions only. In this case, the solution of the Fokker-Planck equation is obtained after an expansion of R(f) on the Legendre polynomials and a matrix inversion. An iterative procedure is then used in order to insure the coherence of $<\tau_r>$ with the solution f.

The characteristic loss time is defined by $1/<\tau_r>=1/<\tau_1>+1/<\tau_2>$ where the averages are taken over the trapped ions distribution $1/<\tau> = \int f/\tau\, d^3v \;/\; \int f\, d^3v$.

– τ_1 is a characteristic loss time due to trapping in the local wells. This loss term is largely dominant in the effective ripple zone. To compute τ_1, we use the expression given in [2]: $\tau_1=\tau_b/F$ where τ_b is the bounce period and F is the trapping rate per bounce taking into account collisionnal and collisionless trapping mechanisms.

– τ_2 is a loss time that models the effect of banana drift diffusion: This term dominates the transport in the zones where the ripple is not effective. We define it as $\tau_2 = \Delta r^2 / 2D$. D is the ripple-plateau diffusion coefficient and Δr is the averaged distance between the banana tip and the contour where the modulation vanishes.

RESULTS FOR A STANDARD CASE

Figure 2 shows the computed ripple losses for a Tore-Supra standard case: Deuterium plasma, R_0=236cm, a=80cm, I_p=1.7 MA, B=4T, parabolic density profile ($<n_e>=5\ 10^{19}\ m^{-3}$), parabolic squared temperature profile, $T_e(0)$=3 keV, 100 keV (full energy) D^0 neutrals. The local ripple lost fraction $g_r(r)$ (defined as the power lost on a given magnetic surface divided by the power injected on this surface) increases dramatically from the center to the edge. The losses increase rapidly around r= 40 cm: Above this radius the banana tips stay in the effective ripple zone and the ions are lost before thermalisation because $<\tau_r> << \tau_s,\tau_{ii}$. For smaller radii the beam ion transport is due to banana drift diffusion. This mechanism feeds the poor confinement zone with fast ions born in the central part of the plasma and is responsible for substantial losses in the region 35cm<r<50cm. The global losses $G_r(r)$, computed with a classical beam deposition code, are also displayed: They represent the power lost fraction integrated up to a given radius. The total fraction lost is very important for the standard case: $G_r(a)\approx 50\%$.

MINIMISATION OF THE LOSSES

Two main approaches can be examined in order to reduce these dramatic losses.

- for a given plasma geometry (R_{axis},a,B_φ, B_θ), one may try to minimize the beam ions deposition in the poor confinement region: the most sensible parameter in this case is the plasma density (average and profile)
- for given plasma profiles, one may try to expand the good confinement zone: in this case the plasma position inside the vacuum chamber plays the major role.

Effect of plasma density:

Figure 3 shows the total lost fraction (ripple and shine-through) as a function of the volume averaged density for three differents peaking factors $n_e(0)/\langle n_e\rangle$=1.9, 2.6 and 4.0 (the other plasma parameters are the standard ones). For a fixed peaking factor, the losses can be reduced by a decrease in the density down to 2.5 10^{19} that gives a more central fast ions deposition. A further decrease in the density results in a dramatic increase of the losses due to the shine-through fraction. For a fixed average density, the losses can always be decreased by peaking the density profile. However, for these plasmas with standard minor radius a=80cm, the losses remain important: 25% for $\langle n_e\rangle \approx 2.5\ 10^{19}$ and $n_e(0)/\langle n_e\rangle$=4.

Displacements of the plasma column inside the vacuum vessel:

If the plasma minor radius is reduced and the plasma pushed on the inner wall, the good confinement zone becomes more important and this leads to reduced losses. Figure 4 displays the effect of plasma position (the plasma parameters are the standard ones excepted a=70 cm). For a plasma with no vertical displacement (Δz=0 cm) the total ripple loss fraction is $G_r(a)$ = 32% instead of 50% in the standard case. Beam ions are captured and lost in the zone z>0 because they drift towards the top of the vacuum vessel: if the plasma is displaced in the vertical direction towards the bottom of the vacuum vessel, the good confinement zones are no more symmetric with respect to the equatorial plane and the upper one becomes bigger. As shown in figure 4, for Δz=-10 cm we get $G_r(a)$ = 23%. To further reduce the losses, one main combine the favorable effects of plasma position and density profile peaking: for Δz=-10 cm, $n_e(0)/\langle n_e\rangle$=4.0, a=70 cm losses are reduced to $G_r(a)$ = 15%.

CONCLUSION

Fokker-Planck calculations predict important fast ions losses during NBI in Tore-Supra (up to 50% of the injected power for standard operation). These losses are mainly due to beam ions on banana orbits with tips in the effective ripple zone. Plasma position inside the vacuum vessel as well as density (average and profile) are sensible parameters. For smaller, inner wall limited plasmas (a=70cm) and for peaked density profiles, losses can be reduced to smaller values (≈25%). A vertical displacement of the plasma column in the opposite direction of the ion drift velocity can also improve fast ion confinement.

REFERENCES

[1] Bottiglioni, F. et al., 15th SOFT, Utrecht, September 88, paper B42.

[2] Goldston, R.J., Towner, H.H., J. Plasma Phys. **26** (1981) 283.

[3] Tuszewski, M., Roubin, J.P., Nucl. Fusion **28** (1988) 499.

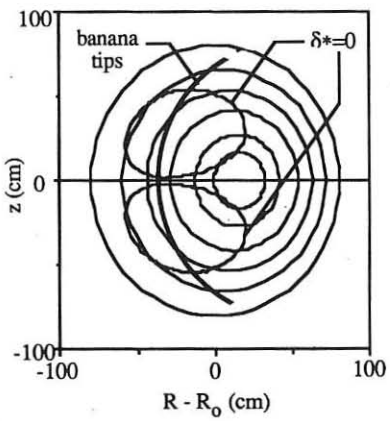

Fig. 1: $\delta^*=0$ contours and position of the first orbits banana tips (D^0 100 keV)

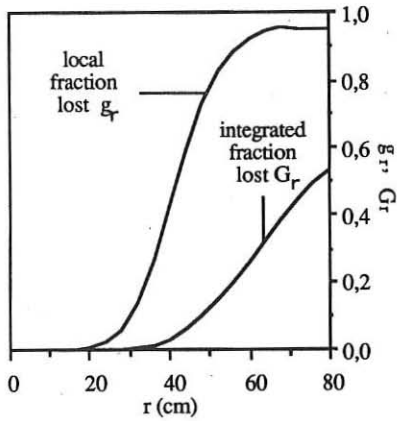

Fig. 2: Ripple losses (local and integrated) for a T-S standard case

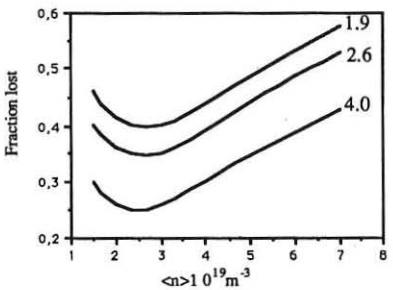

Fig. 3: Effect of plasma density on total losses (ripple + shine-through) for three peaking factors $n_e(0)/<n_e>$=1.9, 2.6 and 4.0

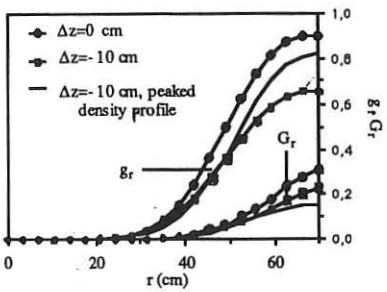

Fig. 4: Effect of plasma position on ripple losses (local and integrated)

NEW APPROACHES TO NEUTRALIZERS FOR NEGATIVE ION BEAMS

H.J. Hopman*, P. Vallinga+ and D.C. Schram+

*The NET Team,c/o Max-Planck-Institut für Plasmaphysik
Boltzmannstr. 2, D-8046 Garching bei München, FRG
+Eindhoven University of Technology, Den Dolech 2
P.O. Box 513, NL-5600 Eindhoven, The Netherlands

INTRODUCTION. To achieve non–inductive current drive and/or heating in the plasma core of future large tokamaks (NET, ITER) by means of neutral beam injection, a particle energy of 1 to 1.5 MeV is required. Such neutral beams are generated by acceleration and subsequent neutralization of D^- ions. Two approaches are being considered to improve the efficiency of the neutralizer cell beyond that of a simple gas cell (calculated efficiency $\eta_g \simeq 55\%$). They are: partial energy recovery in combination with a gas target, which might allow an efficiency $\eta_{er} \simeq 72\%$, and a neutralizer with a plasma target generated by cascaded arcs, for which an efficiency $\eta_p \simeq 85\%$ could be possible.

PARTIAL ENERGY RECOVERY. In a direct energy recovery scheme (ER), the non–neutralized fraction of the beam coming out of the neutralizer is electrostatically decelerated to the ion source potential [1]. This way, these ions do no longer form a load on the full voltage power supply, and the system efficiency is raised. However, if the gas density in the neutralizer is optimized by maximizing the fraction of neutrals in the outgoing beam, nearly equal fractions of D^- and D^+ ions emerge from the neutralizer. Therefore, to make ER work, one needs to increase the charge fraction that can be decelerated to source potential, i.e. that of the negative ions. For this, one has to reduce the gas target density below the optimum, at the cost of also reducing the equivalent neutral beam current produced by the system.

From a source a current i_s of D^- ions is extracted and accelerated through a potential V_b. We assume a constant gas density n_g over the length l of the neutralizer. Beyond the gas cell the particle fractions are separated. The D^+ fraction, η^+, is considered lost; it is collected at full energy on a dump. The D^- fraction, η^-, is

retarded to a potential $V_r << V_b$. Experiments [1] indicate that a large fraction, g, of the current carried by the retarded D^- ions can be recovered, providing $V_r \simeq 0.05\ V_b$. Then, a second term contributing to losses in the drain current, i.e. the current delivered by the high voltage supply, is $(1 - g)\eta^- i_s$. When also including the D^o fraction, η^o, there are three fractions that add up to a drain current $(1 - g\eta^-)i_s$. We can now define the fraction of neutral particles relative to the drain current,

$$D^o_r = \eta^o i_s/(1 - g\eta^-)i_s = \eta^o/(1 - g\eta^-),$$

where D^o_r is the high voltage power supply efficiency; $g = 0$ describes the case without ER.

The relevant processes in the neutralizer cell are one and two electron loss suffered by D^-, with cross sections σ_{-10} and σ_{-11}, and ionization of D^o, σ_{01}. The three reactions are described by a set of first order linear differential equations in the densities of the three species involved, which is easily solved [2]. In a negative ion based system, all particles have the same energy. Therefore, the current fractions are at the same time the particle fractions. As a result, we can relate the power supply efficiency to the neutralizer target density $n_g l$ via the cross sections.

Figure 1 presents the current fractions in the beam leaving the neutralizer, relative to the drain current. We have chosen $V_b = 1$ MeV. The values of the cross sections have been taken from Horiike et al. [3]. For the recovered fraction we used the value $g = 0.9$ quoted by Fumelli et al. [1]. Results have been obtained taking ER into account (full line) and without (dashed line). We observe that the efficiency increases from $\approx$ 55% without ER to nearly 75% with ER at the respective optimum target densities. This improvement is weakly dependent on the beam energy.

To maintain the same equivalent current in the neutral beam produced by the system, the source extraction area must be increased by a factor $S_r = (D^o_g)_m/D^o_g(n_g l)$. where D^o_g is the neutral fraction in case no ER is applied, and the index m denotes its maximum value. The function S_r is depicted in Fig. 1. It is seen that at a 10% increase in source area (vertical dashed line in Fig. 1), the efficiency could be 72%.

PLASMA NEUTRALIZERS. The plasma target in a plasma neutralizer has to fulfil the following demands: degree of ionization $\alpha > 0.3$, target thickness $\simeq 10^{19}$ m^{-2} [4]. It is expected that these demands can be met by the plasma flame expanding from a cascaded arc. In such an arc, gas is admitted into an arc channel with a diameter of 2 to 4 mm and a length of $\approx$ 60 mm. In the arc channel the gas will become partially ionized. At the anode side the plasma expands into vacuum at

supersonic velocities. In the expansion chamber a shock wave occurs at an axial distance of about 50 mm from the anode. The kinetic energy of the highly directed motion is now partially converted into thermal energy. After the shock wave has been crossed, a subsonic but fast flowing (1000 m/s) plasma has been created. The so produced plasma flame has a diameter l of about 10 cm, and is approximately of the required target thickness (10^{19} m^{-2}) in the direction perpendicular to the plasma flow. One flame might possibly form the plasma target for one row of say 20 D^- beamlets emerging from a negative ion source.

With the use of an expanding plasma, the electric and magnetic fields are confined to the plasma production section, i.e. the cascaded arc, so that the flame, which is a recombining plasma, will have negligibly small fields. As a consequence, these plasmas are quiescent and the beam divergence is not modified by micro fields. A numerical model has been developed in order to calculate the relevant plasma parameters in the arc channel, such as the degree of ionization, plasma velocity, discharge pressure, electron temperature and heavy particle temperature. A quasi one–dimensional approach is followed, and the model is essentially based on the mass, momentum and energy conservation laws.

In the flame the transported energy P_b is equal to $n_e w l^2 E_{ion}$, where E_{ion} is the ionization energy of the gas, and w is the plasma velocity. This energy is provided by the arc with overall efficiency η, i.e. $P_b = \eta P_{arc}$. Typical efficiencies in the cascaded arc sources are: $\eta \simeq 10\%$ to 30%. In order to obtain the required target thickness, a minimum beam power P_b of about 2 kW is needed. Consequently, an arc input power of about 10 kW would be required. Figure 2 shows the ionization degree α, as well as the molecular, the atomic, and the electron density, as a function of the axial position in the cascaded arc. For this case the arc current is 75 A, the voltage is 100 V, the diameter is 3.5 mm, the length is 60 mm, and the gas flow is 200 sccs.

REFERENCES

[1] M. Fumelli, F. Jequier, J. Pamela, 15th Eur. Conf. Controlled Fusion and Plasma Heating, Europhysics Abstracts, S. Pesic, J. Jaquinot Eds., Vol. 12B (1988)part III, p.1077.

[2] K.H. Berkner, R.V. Pyle, J.W. Stearns, Nuclear Fusion 15 (1975) 249.

[3] H.Horiike, Y. Ohara, Y. Okumura, T. Shibata, S. Tanaka, Japan Atomic Energy Research Institute Report JAERI–M86–064 (1986).

[4] K.H. Berkner, R.V. Pyle, S.E. Savas, K.R. Stavas, Brookhaven National Lab. Report BNL 51304, Upton NY USA, (1980), p.291.

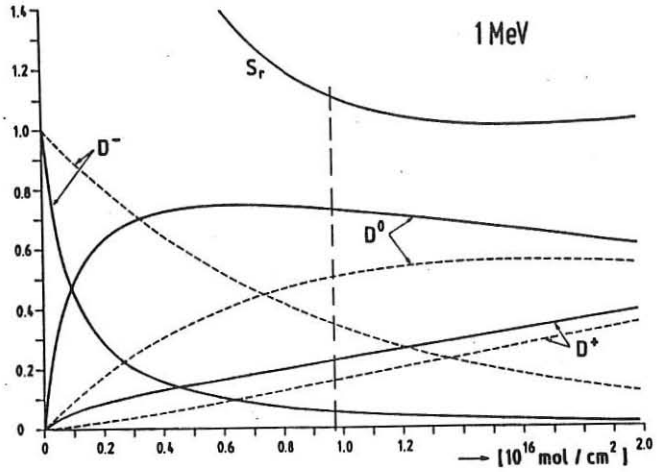

FIGURE 1. Particle fractions in a 1MeV deuterium beam exiting from a neutralizer.

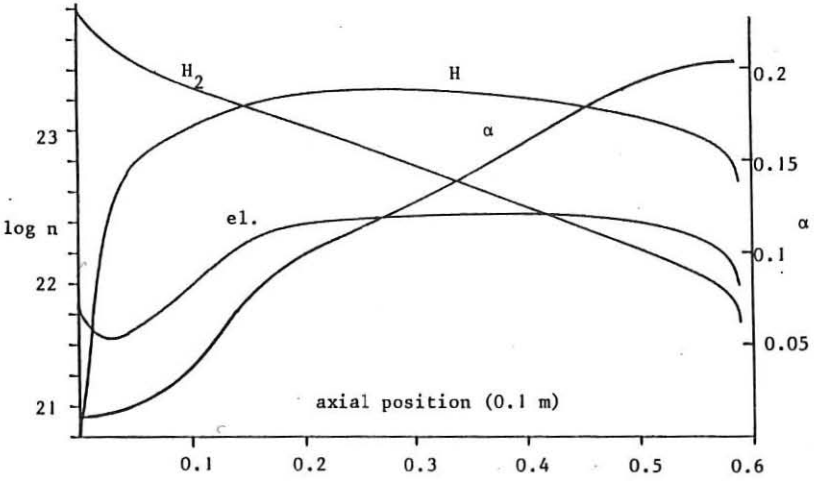

FIGURE 2. The ionization degree α, the molecular, the atomic, and the electron density, as a function of the axial position in the cascaded arc.

RESPONSIBLE AUTHOR

INDEX *

* (First author is listed when responsible author was not indicated)